



UNIVERSIDADE ESTADUAL DE CAMPINAS
FACULDADE DE ENGENHARIA QUÍMICA

GIANI DE VARGAS BRIÃO

**RECOVERY OF RARE EARTH METALS NEODYMIUM AND DYSPROSIUM
FROM SECONDARY SOURCES BY ADSORPTION ON EXPANDED
VERMICULITE CLAY**

***RECUPERAÇÃO DE METAIS TERRAS RARAS NEODÍMIO E DISPRÓSIO DE
FONTES SECUNDÁRIAS POR ADSORÇÃO EM VERMICULITA EXPANDIDA***

Campinas - SP

2022

GIANI DE VARGAS BRIÃO

**RECOVERY OF RARE EARTH METALS NEODYMIUM AND DYSPROSIUM
FROM SECONDARY SOURCES BY ADSORPTION ON EXPANDED
VERMICULITE CLAY**

***RECUPERAÇÃO DE METAIS TERRAS RARAS NEODÍMIO E DISPRÓSIO DE
FONTES SECUNDÁRIAS POR ADSORÇÃO EM VERMICULITA EXPANDIDA***

Doctoral Thesis presented to the Faculty of
Chemical Engineering of the University of
Campinas as part of the requirements for the
degree of Doctor in Chemical Engineering.

*Tese de Doutorado apresentada à Faculdade
de Engenharia Química da Universidade
Estadual de Campinas como parte dos
requisitos para a obtenção do título de Doutora
em Engenharia Química.*

Orientadora: Prof^a. Dr^a. Melissa Gurgel Adeodato Vieira

Coorientadora: Prof^a. Dr^a. Meuris Gurgel Carlos da Silva

ESTE TRABALHO CORRESPONDE À
VERSÃO FINAL DA TESE DEFENDIDA
PELA ALUNA GIANI DE VARGAS BRIÃO
E ORIENTADA PELA PROF^a. DR^a.
MELISSA GURGEL ADEODATO VIEIRA.

Campinas - SP

2022

Ficha catalográfica
Universidade Estadual de Campinas
Biblioteca da Área de Engenharia e Arquitetura
Rose Meire da Silva - CRB 8/5974

B76r Brião, Giani de Vargas, 1991-
Recovery of rare earth metals neodymium and dysprosium from secondary sources by adsorption on expanded vermiculite clay / Giani de Vargas Brião. – Campinas, SP : [s.n.], 2022.

Orientador: Melissa Gurgel Adeodato Vieira.
Coorientador: Meuris Gurgel Carlos da Silva.
Tese (doutorado) – Universidade Estadual de Campinas, Faculdade de Engenharia Química.

1. Metais de terras raras. 2. Compostos de neodímio. 3. Lantanídeos. 4. Vermiculita. 5. Adsorção. I. Vieira, Melissa Gurgel Adeodato, 1979-. II. Silva, Meuris Gurgel Carlos da, 1955-. III. Universidade Estadual de Campinas. Faculdade de Engenharia Química. IV. Título.

Informações Complementares

Título em outro idioma: Recuperação de metais terras raras neodímio e disprósio de fontes secundárias por adsorção em vermiculita expandida

Palavras-chave em inglês:

Rare earth metals

Neodymium compounds

Lanthanides

Vermiculite

Adsorption

Área de concentração: Engenharia Química

Titulação: Doutora em Engenharia Química

Banca examinadora:

Melissa Gurgel Adeodato Vieira [Orientador]

Regina de Fátima Peralta Muniz Moreira

Maria Helena Araujo

Heloise de Oliveira Pastore Jensen

José Roberto Guimarães

Data de defesa: 03-10-2022

Programa de Pós-Graduação: Engenharia Química

Identificação e informações acadêmicas do(a) aluno(a)

- ORCID do autor: <https://orcid.org/0000-0003-1300-9592>

- Currículo Lattes do autor: <http://lattes.cnpq.br/5341892469921144>

FOLHA DE APROVAÇÃO

Tese de Doutorado defendida por Giani de Vargas Brião e aprovada em 03 de outubro de 2022 pela banca examinadora constituída pelos professores doutores:

Profa. Dra. Melissa Gurgel Adeodato Vieira - Presidente e Orientadora

Faculdade de Engenharia Química – FEQ/UNICAMP

Profa. Dra. Regina de Fátima Peralta Muniz Moreira

Universidade Federal de Santa Catarina – UFSC

Profa. Dra. Maria Helena Araujo

Universidade Federal de Minas Gerais – UFMG

Profa. Dra. Heloise de Oliveira Pastore Jensen

Instituto de Química – IQ/UNICAMP

Prof. Dr. José Roberto Guimarães

Faculdade de Engenharia Civil, Arquitetura e Urbanismo– FECFAU/UNICAMP

A Ata da Defesa, assinada pelos membros da Comissão Examinadora, consta no SIGA/Sistema de Fluxo de Dissertação/Tese e na Secretaria do Programa da Unidade.

Acknowledgments

The preparation of this thesis and my entire academic trajectory were only possible due to the excellent support network that I had by my side. So, I thank God for providing the strength I needed to face the challenges and for watching over my family and me all these years.

I thank my family, which I love deeply, for always being by my side on this long journey at the academy, especially my parents, for all the encouragement and help since the first school tasks in childhood. To them, I dedicate my most sincere thanks for the affection and love with which they educated my brothers and me. Mom, thank you for being my best friend and for all the listening and valuable advice. Dad, thank you for always being my partner and example of how to deal healthily with professional and personal life. I am also very grateful to my dear grandma, an example of determination and courage for overcoming all adversity with love.

I want to thank my husband, who closely followed the entire trajectory of my doctorate, all the difficulties, and all the victories. Thank you for being this partner who has supported me and my dreams since our relationship began. Thank you for staying by my side, even though you know that the life of a researcher will require a lot of my time and dedication. Thank you for your love and for the beautiful family we are building.

I thank my friends, whether from academia or not, who have entertained, distracted, listened, helped, and contributed to completing my Ph.D. Thank all my friends in Campinas, a city that welcomed me very well, especially my homemates from “Casa Curie”, Lucília, Renan, Raíssa, Lucas, and Raoni. Thank you so much for making my days happier, even in one of the saddest moments I’ve ever lived, the height of the COVID-19 pandemic. I also thank my longtime friends, Diana and Nando, a couple that I have the pleasure of being a maid of honor; thank you for being present even with the distance.

I am incredibly grateful to all my laboratory colleagues. Friends of LEA/LEPA, thank you for the emotional and technical help these four years, for receiving me so well, and for making our work environment warmer. You have certainly contributed a lot to my personal and professional development.

I would like to thank the Coordination for the Improvement of Higher Education Personnel (CAPES) for providing me an international exchange through the PrInt program at the University of Aveiro (UA)/Portugal. I thank professors Tito, Carlos, and Cláudia for having received me with such affection at the UA, to which I am also very grateful. I thank you for the work we did together, for the partnership we established, and for the friendship. Thank you, Cláudia, for being with me in the day-to-day laboratory, supporting all the activities, and

especially helping me in the moments when the longing for the family almost made me give up.

Thank you, professors Melissa and Meuris, for agreeing to guide me and offering all the technical, financial, and intellectual support necessary to prepare this thesis. Thank you for the autonomy you gave me in conducting the research; this contributed a lot to my growth as a researcher. In particular, I would like to thank Professor Melissa for the times she encouraged me and for her emotional support during my exchange, a very challenging time due to the “saudade” and the pandemic. Also, I thank you for having believed in my potential. Today I feel like a much more prepared researcher after learning with these excellent professionals. Thank you for contributing so much to my professional improvement.

I thank the Unicamp and the “*Faculdade de Engenharia Química*” for the excellent infrastructure and support for developing this thesis. I am also grateful to the teachers and collaborators for contributing to my professional growth with their superb work. Also, I want to thank the professors Regina de Fátima Peralta Muniz Moreira, Maria Helena Araujo, Heloise de Oliveira Pastore Jensen and José Roberto Guimarães who accept to evaluate my thesis in this defense exam. Thank you for your time and dedication.

Thanks to the CAPES for funding my sandwich doctorate through the PrInt program (Proc. N° 88887.571776/2020-00), the National Council for Scientific and Technological Development (Proc. N° 308046/2019-6, and Proc. 147606/2018-7) for funding my doctoral scholarship that generated this thesis. And the Research Support Foundation of the State of São Paulo – Brazil (FAPESP) (Proc. 2019/11353-8 and 2017/18236-1) for financial support.

I extend my thanks to those not mentioned above but who somehow contributed to the development of this thesis and my academic and professional evolution.

To all, my sincere thanks.

Agradecimentos

A preparação desta tese bem como toda a minha trajetória acadêmica somente foram possíveis devido a uma grande rede de apoio que tive ao meu lado. Por isso agradeço a Deus por ter fornecido a força necessária para enfrentar os desafios, e por ter zelado por mim e pela minha família todos estes anos.

Agradeço a minha família, a qual amo profundamente, por terem sempre estado ao meu lado nessa longa caminhada na academia, em especial aos meus pais por todo o incentivo e ajuda desde as primeiras tarefas escolares na infância. À eles dedico meu mais sincero obrigada pelo carinho e amor com que educaram a mim e aos meus irmãos. Mãe, obrigada por ser minha melhor amiga, por todo o puxão de orelha e pelos valiosos conselhos. Pai, obrigada por ser meu parceiro em todos os momentos e por ser meu exemplo de como lidar de forma saudável com a vida profissional e pessoal. Sou muito grata também a minha querida avó que sempre foi exemplo de determinação e coragem por superar toda a adversidade com muito amor.

Agradeço o meu marido, que acompanhou de perto toda a trajetória do meu doutorado, todas as dificuldades, e todas as vitórias. Obrigada por ter sido este companheiro que me apoia e dá suporte para meus sonhos desde o começo do nosso relacionamento. Obrigada por ter ficado ao meu lado mesmo sabendo que a vida de pesquisadora exigirá muito do meu tempo e dedicação. Obrigada pelo seu amor e pela família linda que estamos construindo.

Dedico um agradecimento especial aos meus amigos, sejam da academia ou não, que me divertiram, distraíram, ouviram, ajudaram e contribuíram para que eu chegasse à conclusão do doutorado. Obrigada a todos os amigos que fiz na cidade de Campinas, cidade que me acolheu muitíssimo bem, em especial my homemates da Casa Curie, Lucília, Renan, Raíssa, Lucas, e Raoni. À vocês meu muito obrigada por fazerem meus dias mais felizes, até mesmo num dos momentos mais tristes que já vivi, o auge da pandemia de COVID-19. Também agradeço meus amigos de longa data, Diana e Nando, casal que tenho prazer de ser madrinha de casamento, obrigada por se fazerem presentes mesmo com a distância.

Faço um agradecimento especial a todos os colegas de laboratório. Amigos do LEA/LEPA, obrigada pela ajuda emocional e técnica durante esses 4 anos, obrigada por me receberem tão bem, e por fazerem o nosso ambiente de trabalho mais caloroso. Com certeza vocês contribuíram muito para o meu desenvolvimento pessoal e profissional.

Sou grata à Coordenação de Aperfeiçoamento de Pessoal de Nível Superior (CAPES) por me proporcionar um intercâmbio internacional através do programa PrInt na

Universidade de Aveiro (UA)/Portugal. Agradeço aos professores Tito, Carlos, e Cláudia por terem me recebido com tanto carinho na Universidade de Aveiro, a qual também sou muito grata. Agradeço pelo trabalho que fizemos juntos, pela parceria que firmamos e pela amizade. Obrigada Cláudia por estar comigo no dia-a-dia do laboratório, auxiliando em todas as atividades, e, especialmente, obrigada por me ajudar nos momentos em que a saudade da família quase me fez sucumbir.

Obrigada professoras Melissa e Meuris por terem aceito me orientar, por terem oferecido todo o suporte técnico, financeiro, intelectual necessário para a elaboração desta tese. Obrigada pela autonomia que deram na condução da pesquisa, isso contribuiu muito para o meu crescimento como pesquisadora. Em especial, direciono um agradecimento a professora Melissa por todas as vezes que me incentivou, pelo apoio emocional durante o meu intercâmbio, momento bastante desafiador devido a saudade e a pandemia. Inclusive, agradeço por sempre acreditar no meu potencial. Hoje me sinto uma pesquisadora muito mais preparada depois de conviver e aprender com essas excelentes profissionais. Obrigada por terem contribuído tanto na minha formação.

Agradeço a Unicamp e a Faculdade de Engenharia Química, pela excelente infraestrutura para o desenvolvimento desta tese. Sou grata também pelos professores, e todos os funcionários por terem colaborado para o meu crescimento profissional com os seus trabalhos excelentes. Também quero agradecer aos professores Regina de Fátima Peralta Muniz Moreira, Maria Helena Araujo, Heloise de Oliveira Pastore Jensen e José Roberto Guimarães que aceitaram avaliar minha tese neste exame de defesa. Obrigado pelo seu tempo e dedicação.

Obrigada a CAPES pelo financiamento do meu doutorado sanduíche pelo programa PrInt (Proc. Nº 88887.571776/2020-00), ao Conselho Nacional de Desenvolvimento Científico e Tecnológico (Proc. Nº 308046/2019-6 and Proc. Nº 147606/2018-7) pelo custeio da minha bolsa de doutorado que gerou a presente tese. E, a Fundação de Amparo à Pesquisa do Estado de São Paulo – Brasil (FAPESP) (Proc. 2019/11353-8 e 2017/18236-1) pelo suporte financeiro.

Estendo meus agradecimentos a todos que não foram citados anteriormente, mas que de alguma forma colaboraram para o desenvolvimento da presente tese, e para minha formação acadêmica e profissional.

A todos, meus sinceros agradecimentos.

ABSTRACT

Rare earth metals (REM), such as neodymium (Nd) and dysprosium (Dy), are critical resources due to the growing future supply risk and the high employment in strategic segments such as high-tech equipment production and clean energy technologies. The predicted REM scarcity scenario motivates the scientific community to find alternative ways to recover Nd and Dy from secondary sources, such as permanent magnets. Among the technologies that have been studied, the adsorption into a hydrometallurgical route has gained attention due to its simplicity, efficiency in concentrating REM, and selectivity. The present thesis investigates the Nd and Dy recovery from aqueous solutions by adsorption and desorption in batch and fixed-bed operations mode using expanded vermiculite (low-cost and available clay material) as adsorbent. Important criteria such as operational conditions optimization, kinetics, equilibrium, thermodynamics, desorption, selectivity, and reusability were investigated, as well as the efficiency to remove REM from a simulated permanent magnet leachate solution. Besides, characterization analyses were done to evaluate the adsorbent morphology, crystallinity, composition, textural and structural properties pre and post the adsorption and desorption steps. The best pH ($3.3 \leq \text{pH} \leq 3.5$), adsorbent dosage between 14 and 12.8 g/L, and particle size of 0.855 mm were determined by response surface and machine learning techniques, achieving Nd and Dy adsorption percentages around 99.0%. The PSO model described both kinetics behaviors; however, different equilibrium times were required for each metal for higher concentrations. The exchange with the interlayer magnesium rules the overall Nd and Dy adsorption mechanism. Maximum adsorption capacities for Nd and Dy of 0.48 mmol/g at 283 K and 0.9 mmol/g at 298K were obtained by the equilibrium isotherms modeled by Langmuir and Brunauer-Emmett-Teller equations. The Nd and Dy adsorption thermodynamics had exothermic and endothermic natures, respectively. The highest Nd and Dy desorption efficiencies were achieved using a solid/liquid ratio of 7.31 g/L and 14 g/L, with calcium chloride (0.3 mol/L) and magnesium nitrate (0.2 mol/L) eluent solutions, with a contact time of 3 h, correspondingly. In batch and fixed-bed modes, the cyclic reuses showed replicable adsorption and desorption efficiencies along with the cycles. The vermiculite was selective for Nd and Dy adsorption from mixtures obeying the follow order: Dy > Pb > Ni > Cd > Cu, and Nd > Ni > Zn > Cu > Pb. In column dynamic studies, at the best conditions, the breakthrough and exhaustion capacities were 0.26 and 0.40 mmol/g for Nd and 0.31 and 0.42 mmol/g for Dy. Also, empirical and mass transfer models fit well the breakthrough curves, useful for scale-up purposes. The continuous desorption of the vermiculite bed could concentrate Nd and Dy 25.2 and 41.2 times, respectively. The vermiculite performance from a complex mixture of metals (Fe, Nd, Ni, Zn, Pr, Dy, Co, Mn, and Al) that compound the permanent magnets (Nd-Fe-B) showed that high adsorption capacities were achieved, but the selectivity towards REM reduced significantly. However, chelant agents could desorb Nd selectively. With the adsorption of Nd and Dy, the vermiculite surface area of 10 m²/g was reduced to half of the original, and the desorption could not regenerate it completely. The adsorbent also presented homogeneous composition, mesoporosity, and thermal stability before and after the Nd and Dy adsorption and subsequent reuses. Composition and functional group analyses confirmed the aluminum-iron-magnesium silicate composition of the vermiculite. Thus, expanded vermiculite showed advantageous properties to the adsorption and recovery of Nd and Dy, such as high adsorption capacities, physic-chemical stability in multiple uses, and potential for the selective recovery of REM.

Keywords: Rare earth metals. Neodymium. Dysprosium. Vermiculite. Adsorption

RESUMO

Metais de terras raras (REM), como neodímio (Nd) e disprósio (Dy), são recursos críticos devido ao crescente risco de oferta no futuro e ao alto emprego em segmentos estratégicos como produção de equipamentos de alta tecnologia e de energia limpa. O cenário de escassez de REM motiva a comunidade científica a encontrar formas alternativas de recuperar Nd e Dy de fontes secundárias, como os ímãs permanentes. Dentre as tecnologias que vêm sendo estudadas, a adsorção em uma rota hidrometalúrgica tem ganhado destaque devido à sua simplicidade, eficiência na concentração de REM e seletividade. A presente tese investiga a recuperação de Nd e Dy de soluções aquosas por adsorção e dessorção em modo batelada e em leito fixo usando vermiculita expandida (material argiloso de baixo custo e disponível) como adsorvente. Critérios importantes como otimização das condições operacionais, cinética, equilíbrio, termodinâmica, dessorção, seletividade e reutilização foram investigados, bem como a eficiência para remover REM do lixiviado de ímãs permanentes. Além disso, análises de caracterização foram feitas para avaliar a morfologia, cristalinidade, composição, propriedades estruturais e texturais do adsorvente nas etapas pré e pós adsorção e dessorção. O melhor pH ($3,3 \leq \text{pH} \leq 3,5$), dosagem de adsorvente entre 14 e 12,8 g/L e tamanho de partícula de 0,855 mm foram determinados por análise de superfície de resposta e técnicas de inteligência artificial, atingindo percentuais de adsorção de Nd e Dy em torno de 99,0%. O modelo PSO descreveu ambos comportamentos cinéticos; no entanto, tempos de equilíbrio foram diferentes para cada metal em concentrações mais altas. A troca com o magnésio das intercâmbias da argila rege o mecanismo geral de adsorção de Nd e Dy. Capacidades máximas de adsorção para Nd e Dy de 0,48 mmol/g a 283 K e 0,9 mmol/g a 298 K foram obtidas pelas isotermas de equilíbrio modeladas pelas equações de Langmuir e Brunauer-Emmett-Teller. A termodinâmica de adsorção de Nd e Dy teve natureza exotérmica e endotérmica, respectivamente. As maiores eficiências de dessorção de Nd e Dy foram alcançadas usando uma relação sólido/líquido de 14 g/L e 7,31 g/L, com soluções eluentes de cloreto de cálcio (0,3 mol/L) e nitrato de magnésio (0,2 mol/L), com um contato tempo de 3 h, correspondentemente. Nos modos batelada e leito fixo, os reusos cíclicos mostraram eficiências de adsorção e dessorção replicáveis. A vermiculita foi seletiva para adsorção de Nd e Dy a partir de misturas obedecendo a seguinte ordem: Dy > Pb > Ni > Cd > Cu, e Nd > Ni > Zn > Cu > Pb. Em estudos dinâmicos em coluna, nas melhores condições, as capacidades de ruptura e exaustão foram 0,26 e 0,40 mmol/g para Nd e 0,31 e 0,42 mmol/g para Dy. Além disso, os modelos empíricos e de transferência de massa se ajustaram bem às curvas de ruptura, úteis para fins de aumento de escala. A dessorção contínua do leito de vermiculita conseguiu concentrar Nd e Dy 25,2 e 41,2 vezes, respectivamente. O desempenho da vermiculita a partir de uma mistura complexa de metais (Fe, Nd, Ni, Zn, Pr, Dy, Co, Mn e Al) que compõem os ímãs Nd-Fe-B, indicou que altas capacidades de adsorção foram alcançadas, mas a seletividade para REM foi reduzida significativamente. No entanto, agentes quelantes puderam dessorver Nd seletivamente. Com a adsorção de Nd e Dy, a área superficial da vermiculita de 10 m²/g foi reduzida à metade, e a dessorção não conseguiu regenerá-la completamente. O adsorvente também apresentou composição homogênea, mesoporosidade e estabilidade térmica antes e após a adsorção de Nd e Dy e reusos subsequentes. Análises de composição e grupos funcionais confirmaram a composição de silicato de alumínio-ferro-magnésio da vermiculita. Também evidenciaram que o mecanismo de troca iônica teve papel fundamental na adsorção de Nd e Dy pela vermiculita expandida. Assim, a vermiculita expandida apresentou propriedades vantajosas para a adsorção e recuperação de Nd e Dy, como alta capacidade de adsorção, estabilidade físico-química em múltiplos usos, e potencial para a recuperação seletiva de REM.

Palavras-chave: Metais terras raras. Neodímio. Disprósio. Vermiculita. Adsorção

CONTENTS

CHAPTER 1. INTRODUCTION AND OBJECTIVES.....	18
1.1 MOTIVATION AND RELEVANCE	18
1.2 OBJECTIVES.....	19
1.2.1 General Objectives	19
1.2.2 Specific Objectives.....	19
1.3 THESIS STRUCTURE	20
CHAPTER 2. LITERATURE REVIEW	24
2.1 INTRODUCTION	25
2.2 NEODYMIUM AND DYSPROSIUM: CRITICALITY AND CIRCULAR ECONOMY	26
2.3 PERMANENT MAGNET SCRAP AS A SECONDARY SOURCE OF RARE EARTH METALS	28
2.4 REUSE, RECYCLING, AND RECOVERY OF NdFeB MAGNETS	29
2.5 ROLE, EFFICIENCY, AND POTENTIALITY OF THE ADSORPTION IN THE NEODYMIUM AND DYSPROSIUM RECOVERY FROM NdFeB MAGNETS IN HYDROMETALLURGICAL ROUTES	30
2.6 SINGLE ADSORPTION AND DESORPTION OF NEODYMIUM AND DYSPROSIUM IN BATCH MODE.....	31
2.6.1 Adsorbent Materials.....	37
2.6.2 Operational Conditions.....	39
2.6.3 Kinetics	41
2.6.4 Equilibrium	42
2.6.5 Thermodynamics	43
2.6.6 Reuse.....	44
2.6.7 Selectivity.....	46
2.7 NEODYMIUM AND DYSPROSIUM ADSORPTION FROM MIXTURES ON BATCH MODE AND CONTINUOUS FIXED BED	47
2.8 CONTRIBUTION OF ND AND DY RECOVERY BY ADSORPTIVE PROCESSES TO THE DEVELOPMENT OF THE CIRCULAR ECONOMY: CHALLENGES AND PROSPECTS	52
2.9 CONCLUSIONS	57
ACKNOWLEDGMENT	58
REFERENCES	58

CHAPTER 3. NEODYMIUM ADSORPTION ON EXPANDED VERMICULITE: KINETICS, SELECTIVITY, AND DESORPTION	72
3.1 INTRODUCTION	73
3.2 MATERIALS AND METHODS	74
3.2.1 Adsorbate (neodymium) and adsorbent (expanded vermiculite)	74
3.2.2 Adsorbent characterization	75
3.2.3 Adsorption experiments	75
3.2.3.1 <i>Optimization of the experimental conditions</i>	76
3.2.3.2 <i>Adsorption kinetic</i>	77
3.2.3.2.1 <i>Mathematical modeling</i>	77
3.2.3.3 <i>Ion exchange</i>	78
3.2.4 Desorption experiments	79
3.2.5 Selectivity.....	80
3.3 RESULTS AND DISCUSSION.....	80
3.3.1 Characterization	80
3.3.2 Adsorption of neodymium	83
3.3.2.1 <i>Optimization of experimental conditions of adsorption</i>	83
3.3.2.2 <i>Adsorption kinetics</i>	87
3.3.2.3 <i>Ion Exchange</i>	90
3.3.3 Neodymium adsorption mechanism	92
3.3.4 Neodymium desorption	93
3.3.5 Selectivity.....	95
3.4 CONCLUSION	96
FUNDING	97
ACKNOWLEDGMENTS	97
REFERENCES	97
CHAPTER 4. NEODYMIUM ADSORPTION ON EXPANDED VERMICULITE IN BATCH MODE: EQUILIBRIUM, THERMODYNAMICS, AND REUSE.....	105
4.1 INTRODUCTION	106
4.2 MATERIALS AND METHODS	107
4.2.1 Materials.....	107
4.2.2 Characterization	107
4.2.3 Adsorption Experiments	107
4.2.3.1 <i>General</i>	108

4.2.3.2 Adsorption kinetics	108
4.2.3.3 Adsorption equilibrium.....	109
4.2.3.4 Thermodynamic	110
4.2.4. Criteria for the quality of the model fit	112
4.2.5. Desorption Experiments.....	112
4.2.6 Cost analysis at lab scale	113
4.3 RESULTS AND DISCUSSION.....	113
4.3.1 Characterization analyses.....	113
4.3.2 Kinetics of adsorption	118
4.3.3 Equilibrium of adsorption	119
4.3.4 Thermodynamic.....	122
4.3.5 Neodymium Desorption	124
4.3.5.1 Optimization of desorption conditions	124
4.3.5.2 Cycles of adsorption/desorption	126
4.3.6 Cost analysis at lab scale	127
4.4 CONCLUSION	128
FUNDING	128
ACKNOWLEDGMENTS	128
REFERENCES	128
CHAPTER 5. NEODYMIUM RECOVERY ON EXPANDED VERMICULITE: CONTINUOUS FIXED-BED ADSORPTION AND DESORPTION	136
5.1 INTRODUCTION.....	137
5.2 MATERIAL AND METHODS.....	138
5.2.1 Neodymium solutions	138
5.2.2 Adsorbent	139
5.2.3 Dynamic Column System.....	139
5.2.4 Fixed-bed adsorption experiments.....	139
5.2.4.1 Flow rate and inlet concentration effect.....	140
5.2.4.2 Adsorption-desorption cycles.....	140
5.2.5 Fixed-bed adsorption modeling.....	141
5.2.6 Adsorbent characterization after adsorption/desorption cycles	143
5.3 RESULTS AND DISCUSSION.....	144
5.3.1 Effect of the flow rate	144
5.3.2 Effect of the inlet concentration	145

5.3.3 Mathematical modeling.....	146
5.3.4 Adsorption-desorption cycles	149
5.3.5 Adsorbent characterization after adsorption/desorption cycles	152
5.4 CONCLUSION	157
FUNDING	158
ACKNOWLEDGMENTS	158
REFERENCES	158
CHAPTER 6. OPTIMIZATION OF THE DYSPROSIUM ADSORPTION ON EXPANDED VERMICULITE.....	165
6.1 INTRODUCTION	166
6.2 MATERIALS AND METHODS	167
6.2.1 Adsorption Experiments	167
6.2.2 Response Surface Methodology	169
6.2.3 Machine learning techniques	170
6.2.3.1 <i>Artificial Neural Network</i>	170
6.2.3.2 <i>The adaptive neuro-fuzzy inference system</i>	171
6.2.4 Assessment of data correlation quality	172
6.2.5 Adsorbent characterization	172
6.3 RESULTS AND DISCUSSION.....	173
6.3.1 Response surface methodology	173
6.3.3 Machine learning	179
6.3.3.1 <i>Dataset</i>	179
6.3.3.2 <i>Artificial neural network</i>	180
6.3.3.3 <i>Adaptive neuro-fuzzy inference system</i>	182
6.3.4 Overall discussion	184
6.3.5 Adsorbent characterization	185
6.4 CONCLUSIONS	189
ACKNOWLEDGMENTS	189
REFERENCES	190
CHAPTER 7. DYSPROSIUM ADSORPTION ON EXPANDED VERMICULITE IN BATCH MODE: KINETICS, SELECTIVITY AND DESORPTION	198
7.1 INTRODUCTION	199
7.2 MATERIALS AND METHODS	200
7.2.1 Adsorption experiments: general aspects.....	200

7.2.2 Adsorption kinetics experiment	200
7.2.3 Adsorption kinetics modelling	201
7.2.4 Selectivity	203
7.2.5 Desorption	203
7.2.6 Adsorbent characterization	204
7.3 RESULTS AND DISCUSSION	204
7.3.1 Adsorption and ion exchange kinetics	204
7.3.2 Selectivity	209
7.3.3 Desorption	211
7.3.4 Adsorbent characterization	213
7.4 CONCLUSIONS	216
ACKNOWLEDGMENTS	217
REFERENCES	217
CHAPTER 8. DYSPROSIUM ADSORPTION ON EXPANDED VERMICULITE IN BATCH MODE: EQUILIBRIUM, THERMODYNAMICS, REUSE	224
8.1 INTRODUCTION	225
8.2 MATERIAL AND METHODS	226
8.2.1 Vermiculite performance in the rare earth adsorption	226
8.2.2 Equilibrium and thermodynamics	226
8.2.3 Desorption	228
8.2.4 Dysprosium concentration measuring	228
8.2.5 Adsorbent characterization	228
8.3 RESULTS AND DISCUSSION	229
8.3.1 Vermiculite performance in the rare earth adsorption	229
8.3.2 Equilibrium and thermodynamics	230
8.3.3 Desorption	233
8.3.4 Adsorbent characterization	237
8.4 CONCLUSION	239
FUNDING	239
ACKNOWLEDGMENTS	239
REFERENCES	239
CHAPTER 9. DYSPROSIUM RECOVERY ON EXPANDED VERMICULITE: CONTINUOUS FIXED-BED ADSORPTION AND DESORPTION	248
9.1 INTRODUCTION	249

9.2 MATERIALS AND METHODS	250
9.2.1 Adsorbate and adsorbent	250
9.2.2 Adsorption and desorption on continuous fixed bed	250
9.2.2.1 <i>Column system</i>	250
9.2.2.2 <i>Fixed bed efficiency parameters</i>	251
9.2.2.3 <i>Fluid dynamic and inlet concentration effect</i>	251
9.2.2.4 <i>Cycles of reuse</i>	252
9.2.2.5 <i>Dy selectivity from a multimetal solution</i>	253
9.2.3 Adsorbent characterization	253
9.3 RESULTS AND DISCUSSION	254
9.3.1 Fluid dynamics and inlet concentration effect	254
9.3.2 Batch and fixed-bed equilibrium	258
9.3.3 Cycles of reuse	259
9.3.3.1 <i>Adsorbent characterization after adsorption/desorption cycles</i>	261
9.3.4 Selectivity	265
9.4 CONCLUSION	268
ACKNOWLEDGMENTS	268
REFERENCES	269
CHAPTER 10. RECOVERY OF REM FROM Nd-Fe-B MAGNET LEACHATE	274
10.1 INTRODUCTION	275
10.2 MATERIALS AND METHODS	276
10.2.1 Adsorbent Material	276
10.2.2 Adsorption experiments	276
10.2.2.1 <i>Binary system</i>	276
10.2.2.2 <i>Simulated permanent magnet leachate</i>	278
10.3 RESULTS AND DISCUSSION	279
10.3.1 Binary System	279
10.3.2 Simulated permanent magnet leachate	281
10.4 CONCLUSION	284
ACKNOWLEDGMENTS	284
REFERENCES	285
CHAPTER 11. GENERAL DISCUSSION	288
CHAPTER 12. GENERAL CONCLUSIONS AND PERSPECTIVES	296
CHAPTER 13. SCIENTIFIC PRODUCTION OF THE PERIOD (2018/2-2022/2)	299

GENERAL REFERENCES	304
APPENDIX A. SUPPLEMENTARY MATERIALS	308
APPENDIX B. LICENCES OF THE PUBLISHED ARTICLES.....	323

CHAPTER 1. INTRODUCTION AND OBJECTIVES

1.1 MOTIVATION AND RELEVANCE

The group of rare earth metals (REM) is a group composed of the 15 metals of the lanthanide series in addition to scandium and yttrium. They are majority applied in conventional markets such as oil catalytic cracking, but also in novel high-tech and green energy applications, which corresponds 41% of the REM consumption (CHARALAMPIDES *et al.*, 2015). In the new market segments, dysprosium, neodymium, and praseodymium are responsible for about 85% of the REM application, due to its application for the manufacture of permanent magnets (NdFeB).

Dy and Nd are considered critical and scarce, therefore needing, in the medium and long term, to increase production to attend the growing demand (JOWITT *et al.*, 2018). Nevertheless, increasing production would increase the environmental impacts caused by REM mining, such as: presence of radioactive thorium and uranium together with ores of rare earth elements; use of large amounts of water, and application of strong acids (BALARAM, 2019). Thus, to meet this increasing demand, the recovery of these metals from industrial effluents as well as the solid waste is necessary to minimize the impacts caused by mining and to move the REM market to a circular economy (JOWITT *et al.*, 2018; ZHANG; XU, 2016). Besides, Junne *et al.* (2020) predicted diverse green energy scenarios up to 2050, where the highest annual demand for neodymium and dysprosium could exceed 3 to 9 times (Nd) and 7 to 35 times (Dy) the mining quantities. Those future scenarios indicate the vast relevance of Nd and Dy on the feasibility of further sustainable development based on renewable energy. Also, those predictions show the inherent need for high rare earth recycling rates to supply the future demand.

Currently, regardless of the final use, REMs are not recovered in large quantities as recycling is not mandatory and the prices of rare earth elements still do not make recycling competitive (CHARALAMPIDES *et al.*, 2015). In waste electrical and electronic equipments recycling plants, many electronic components are ground and their magnetic components, mainly Fe and Nd, tend to follow the ferrous scrap current, which is very diluted and difficult to recover from the REM. Thus, an adaptation of current metallurgy technologies is necessary to recover REM from scrap containing magnets in low concentrations (YANG *et al.*, 2017).

A method that has several advantages in dilute systems is adsorption due to its high efficiency, ability to concentrate and desorb (recover) the adsorbate (DA COSTA; DA SILVA;

VIEIRA, 2022). In the literature, there are works on the adsorption of Nd and Dy proposing adsorbent materials such as: macroporous chitosan membrane (LIU *et al.*, 2017), phosphorus-functionalized nanoporous carbon (SAHA *et al.*, 2017), mesoporous silica functionalized with carboxyl group (KANEKO *et al.*, 2018) and films with two layers of ion-printed polymers (ZHENG *et al.*, 2018). However, the above cited papers have some lacks regarding the economic viability of the adsorbent materials, accurate modeling, development of the desorption towards the REM recovery and reusability, studies of continuous fixed-bed mode, and complete studies of the adsorption in actual or simulated samples.

Vermiculite, an abundant clay mineral, is a promisor adsorbent for REM based on the high cation exchange capacity, negative charge, improved surface area, especially the expanded form, and physic-chemical stability of the material composed of hydrated magnesium-iron-aluminum phyllosilicate (ARRUDA, 2005). Also, vermiculite has presented great adsorption results removing noble and toxic metals (CHEN *et al.*, 2018; DŁUGOSZ; BANACH, 2018; FREITAS; ALMEIDA; VIEIRA, 2017; MORAES *et al.*, 2019). Another relevant criterion is that in Brazil, specifically, this material is quite available, as it holds 14.7% of world reserves (PAULA; CARVALHÃES, 2018), which motivates even more the deep investigation of this national resource for REM adsorption.

Thus, the recovery of Nd and Dy from end-of-life NdFeB magnets by means of adsorption on vermiculite presents itself as an innovative alternative, mainly due to the absence of studies on the adsorption of REM using it as an adsorbent, due to the low-cost and availability of the material. Besides that, the study focused on desorption (recovery of REM), on fixed-bed adsorption, and application on real waste treatment will also contribute with the advance of REM recovery knowledge area.

1.2 OBJECTIVES

1.2.1 General Objectives

Evaluate Nd and Dy recovery from aqueous solutions through adsorption and desorption on expanded vermiculite as a viable adsorbent in batch and continuous fixed-bed operation.

1.2.2 Specific Objectives

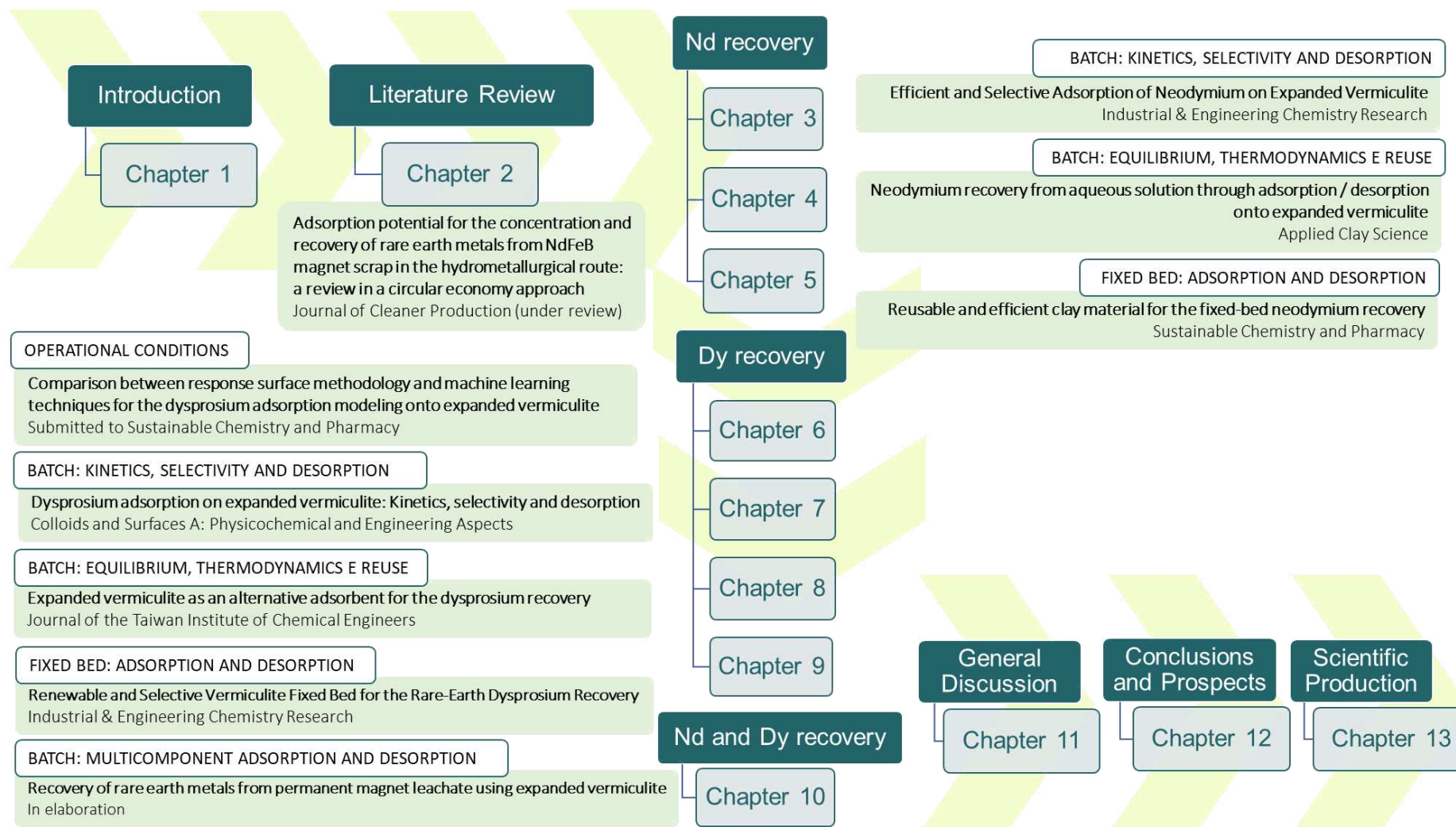
- Characterize the vermiculite regarding morphology, functional groups, textural properties, structure, and composition before and after the Nd and Dy adsorption and after multiple reuses.

- Define the operating conditions, in batch and dynamic (fixed bed), of the single adsorption Nd and Dy on expanded vermiculite.
- Analyze the kinetics of adsorption of the REM.
- Evaluate and model the Nd and Dy adsorption equilibrium on expanded vermiculite.
- Examine the thermodynamics of the proposed adsorption operation.
- Investigate suitable eluents for the REM recovery.
- Determine the best desorption experimental conditions.
- Evaluate the reusability and recovery efficiency of the adsorbent over cyclic reuses (batch and fixed-bed).
- Fit phenomenological and empirical mathematical models to the experimental data in the dynamic system.
- Investigate the selectivity towards Nd and Dy from mixtures with other metals.
- Evaluate the REM adsorption and desorption performance from a simulated Nd-Fe-B magnet leachate.

1.3 THESIS STRUCTURE

The present document is divided into 13 chapters containing an introduction, literature review, experimental findings of the study developed in the LEA/LEPA lab of the University of Campinas that were distributed in seven articles, one chapter addressing the results obtained in the exchange period at the CICECO - Aveiro Institute of Materials group of the University of Aveiro, general discussion, conclusions, and prospects, and scientific production of the period. Figure 1.1 illustrates this thesis's content.

Figure 1.1 Thesis Structure



Chapter 1 addresses an introduction that comprises the motivation and relevance of the Nd and Dy recovery by adsorption on expanded vermiculite, objectives, and thesis structure outline.

Chapter 2 is a current literature review about the adsorption potential to recover Nd and Dy from spent NdFeB magnets. This paper intends to collaborate with the scientific community as a recent and reliable information source that brings a systematic view of the adsorption's role, challenges, and perspectives on the recovery of Nd and Dy from this secondary source and then contributes to boosting the circular economy of REM. In the thesis scope, this chapter also aims to orient the reader where the proposed study is included in the actual REM recovery research scenario.

Chapters 3, 4, and 5 are the sections destined for the neodymium adsorption and recovery on expanded vermiculite. Chapter 3 presents the optimization of operational conditions, Nd adsorption kinetic, ion exchange, selectivity, and eluent determination (batch mode), including virgin and Nd-loaded vermiculite characterization. Chapter 4, in turn, focuses on equilibrium, desorption optimization, cyclic reuse, and Nd recovery in a batch operation. This chapter analyzes virgin vermiculite regarding morphology, textural properties, X-ray diffraction, and thermal behavior. Chapter 5 is the report of the neodymium adsorption and desorption study in a fixed bed operation, where the best flow rate and inlet concentration were determined, modeling, cyclic process, and the characterization of the adsorbent material after five cycles of uses were performed.

Chapters 6, 7, 8, and 9 are the papers addressed to the dysprosium adsorption investigation, also on expanded vermiculite. Chapter 6 compares three methodologies, response surface response, artificial neural network, and adaptive neuro-fuzzy inference system, to optimize and predict the effects of pH, adsorbent dosage, and size on the Dy adsorption efficiency. Chapter 7 shows the study of dysprosium adsorption and desorption regarding kinetics, magnesium exchange, selectivity, and elution (obtainment of the best conditions), and the vermiculite characterization after the Dy adsorption. Chapter 8 studies the Dy adsorption equilibrium and reusability using expanded vermiculite in batch mode. Furthermore, the morphology, crystalline structure, thermal stability, and composition of the spent adsorbent are discussed in this section. Chapter 9, analogously to Chapter 5, presents the Dy adsorption and desorption in a continuous operation (fixed bed); nevertheless, in this section, the Dy selectivity and concentration potential of the process was investigated.

Chapter 10 presents some of results from the exchange period at the University of Aveiro (Portugal) from September 2021 to March 2022. This collaboration was financed by the

“Programa Institucional de Internacionalização da Coordenação de Aperfeiçoamento de Pessoal de Nível Superior” (CAPES-PrInt). The host group was the CICECO – Aveiro Institute of Materials, in which the professors Dr. Carlos Manuel Silva and Dr. Tito Trindade were the research supervisors. During the exchange, we tested expanded vermiculite and vermiculite-based adsorbents to recover Nd and Dy from binary and simulated wastewater systems. However, only the findings of the expanded vermiculite are discussed in the chapter due to the direct pertinence to the thesis theme.

Chapter 11 is the overall discussion of the chapter's main findings. In this section, the results of both metal adsorption and desorption, as well as the adsorbent characterization, are linked, compared, and discussed, giving the reader a general explanation of the phenomenon involved in each metal adsorption on expanded vermiculite.

Chapter 12 comprises the general conclusions and perspectives of the work. In this section are presented: the findings of the studies attempting to attend all the objectives; the doctorate activities chronogram, including the steps to be done for the final thesis presentation; and pertinent suggestions for further studies.

Chapter 13 is the complete scientific production of the doctorate period, comprising published and submitted papers, book chapters, and complete articles and abstracts in congress proceedings.

The final sections of the present work are general references and appendices A and B, where the supplementary material and copyright of the papers are shown, respectively.

CHAPTER 2. LITERATURE REVIEW

Adsorption potential for the concentration and recovery of rare earth metals from NdFeB magnet scrap in the hydrometallurgical route: a review in a circular economy approach¹

Giani de Vargas Brião, Meuris Gurgel da Silva, Melissa Gurgel Adeodato Vieira

*School of Chemical Engineering, University of Campinas (UNICAMP), ZIP code 13083-852,
Campinas, São Paulo, Brazil*

Abstract

Rare earth metals (REM) are critical resources, and future supply concerns governments, economy experts, and scientists worldwide. Neodymium and dysprosium metals are paramount for the rise of clean energy technologies due to their use in NdFeB magnets in electric vehicles and wind turbines. Scarcity, supply risk, and importance to the renewable energy field motivate the recovery of Nd and Dy from secondary sources, moving the typical production chain towards a circular economy. Diverse approaches have been investigated to recuperate Nd and Dy; among them, adsorption has grown in interest due to the simplicity, low cost, ability to concentrate the metals, and high efficiency. This Review aims to present the potential, challenges, and prospects of adsorption in hydrometallurgical routes of REM recovery from spent NdFeB magnets. The current literature has been extensively reviewed, and the adsorbent properties, kinetics, equilibrium, thermodynamics, selectivity, reusability, multicomponent adsorption, and fixed-bed applications have been critically discussed concerning the potential to concentrate and recover REM from magnet scraps. Thus, this work reports state-of-the-art recovery of Nd and Dy from a residue rich in REM through the incorporation of the adsorption and desorption in hydrometallurgical routes contributing to the REM circular economy.

Keywords: *Rare earth metals, circular economy, neodymium, dysprosium, recovery, adsorption.*

¹ Manuscript published in *Journal of Cleaner Production* (2022).

DOI: 10.1016/j.jclepro.2022.135112. Reprinted with the journal's permission (Appendix B.1).

2.1 INTRODUCTION

High-technology and environmental applications of rare earth metals (REMs), lanthanoids, scandium, and yttrium have grown considerably in variety and importance. REMs are more abundant than many common industrial metals; nevertheless, the "rare" aspect is due to the low number and non-homogenous distribution of exploitable ore deposits around the globe (United States Geological Survey (USGS), 2020). Among all REMs, neodymium (Nd) and dysprosium (Dy) are especially critical resources due to their significant relevance to the progress of clean energy technologies (Jyothi et al., 2020). These metals are mainly applied in the factory of NdFeB magnets employed in wind turbines and electric motors, which the demand is predicted to increase by 26 % by 2030 (Schulze and Buchert, 2016). The Nd and Dy growing demand could exceed 9 and 35 times the extraction volumes up to 2050, respectively (Junne et al., 2020), which exhibit the need for a movement toward a rare earth circular economy to supply the future green energy demand (Dang et al., 2021; Korhonen et al., 2018).

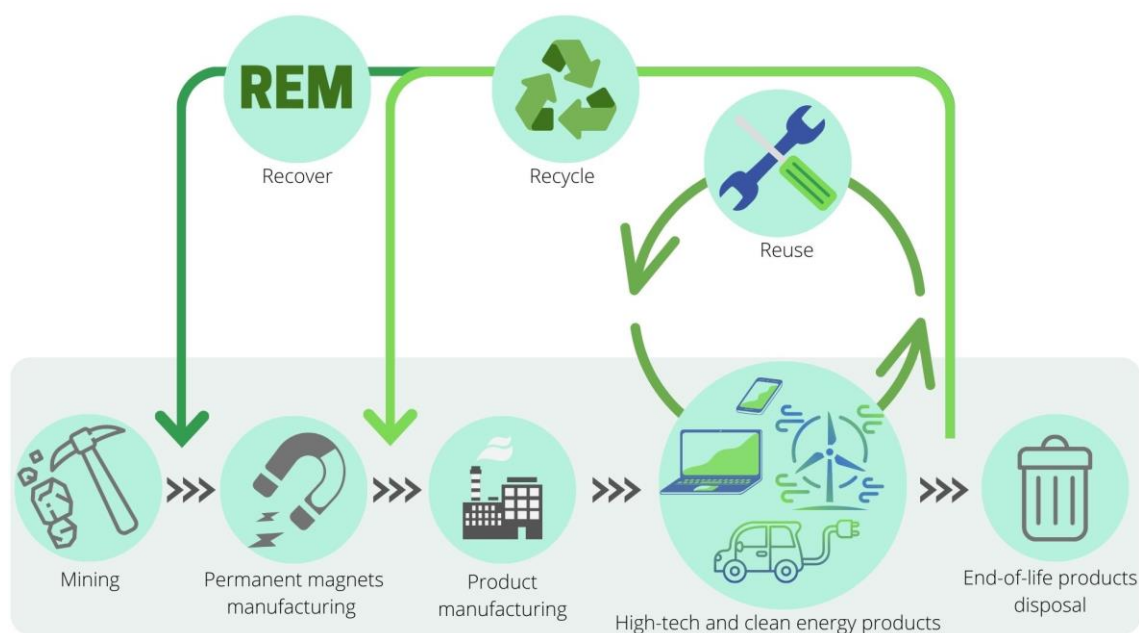
E-waste may become one of the most promising candidates for REM extraction (Dang et al., 2021). Among them, NdFeB magnet scraps from hard disks have gained special attention lately due to the rare earth content (32%) (München and Veit, 2017). However, extracting rare earths from end-of-life electronics is still challenging and not industrially applicable (Trench and Sykes, 2020), which motivates the development of reuse, recycling, and recovery technology to achieve the desired circular economy (Figure 2.1). Direct reuse and direct recycling are the most recommendable strategies, however, disassembling and impurities in the shredded magnets have made these approaches unfeasible until now (Walzberg et al., 2022). Thus, alternative sources and processes for the recovery of Nd and Dy have gained the scientific community's attention, such as the hydrometallurgical processes applied to NdFeB magnet scraps (Yuksekdag et al., 2022). Usually, the methods employed during hydrometallurgical treatment of rare earth resources mainly include leaching, solvent extraction, ion exchange, and precipitation, which varies depending on the recovered metals (Kumari et al., 2018). Hydro-processing approaches are very efficient for REM recovery from several wastes. However, adsorption is more advantageous at low concentrations than typical hydrometallurgy practices since it is more straightforward, efficient, and economical (Jyothi et al., 2020).

Opare et al. (2021) pointed out that adsorption and membrane separation has an intermediate maturity compared to other technologies. Reviews have been published prospecting the potential of prominent adsorbent matrixes to recover REM from aqueous media such as nanomaterials (Kegl et al., 2020), carbon-based nanomaterials (Cardoso et al., 2019),

and biosorbents (Costa et al., 2020). The works cited above comprise REM sorption (general) in different solid materials focusing on the peculiarities and perspectives of each adsorbent. More recently, using a different approach, de Farias et al. (2021) evaluated the adsorption of the rare earth metal cerium considering a circular economy context essential for a sustainable REM market. Despite the high quality of the literature research done by the papers cited above, there is still a lack of a highly specialized review about the sorption processes in hydrometallurgical routes to recover Nd and Dy from secondary sources. That would allow a holistic view of the adsorption's actual contribution to the circular economy of Nd and Dy.

This paper's primary goal is to critically compile and discuss the most recent findings in the adsorption of neodymium and dysprosium to present the potential of sorption processes to concentrate REM in hydrometallurgical treatments of NdFeB magnets from electronic scrap.

Figure 2.1 – Circular economy of Nd and Dy



2.2 NEODYMIUM AND DYSPROSIUM: CRITICALITY AND CIRCULAR ECONOMY

The International Union of Pure and Applied Chemistry recommends the rare earth metals (REM) nomenclature to the group formed by lanthanides, scandium, and yttrium. Also, they are classified as light and heavy rare earth metals depending on the presence of paired electrons on the valence orbital (Connelly et al., 2005; IUPAC, 1970). Thus, the light rare earth metals are from lanthanum to gadolinium and scandium; the other REMs are heavy rare earth metals

(Haque et al., 2014). REM presents similar properties due to their oxidative state that is majority trivalent, having just a few differences regarding the solubility and complex formation due to the lanthanide contraction effect (Charalampides and Vatalis, 2015; Rosental, 2005).

REMs are usually found together in the form of phosphates, carbonates, nitrates, and silicates as part of the chemistry of a host mineral. The most viable ores for REM extraction are bastnaesite ((La, Ce, Nd)CO₃F), xenotime ((Y, Dy, Yb)PO₄), and monazite ((La, Ce, Th)PO₄) (Sousa Filho and Serra, 2014). According to Charalampides et al. (2015), in 2010, about 54,000 tons of rare earths were produced from bastnaesite in iron ore, 12,000 tons from bastnaesite, and 11,000 tons from monazite and xenomite. China has the largest reserves of REMs in the world (80%) and is the primary producer (Charalampides et al., 2015).

The rare earth metals have been applied in the factory of magnets, batteries, metallic alloys, catalysis, petroleum refining, polishing, additives for glasses, luminophores, ceramics, and others (Jowitt et al., 2018). Due to their fundamental role in developing strategic areas, such as energy, defense, and health, and the scarcity of exploitable ores, many REMs are considered critical materials. Cardoso et al. (2019) pointed out that Dy, Nd, Tb, Y, and Eu are critically at-risk marketable elements in balancing the importance of clean energy development and supply risk. The relevance of Dy and Nd to the renewable energy field development is because these metals compose permanent magnets used in electric automobiles and eolic turbines. Also, those magnets are widely applied in computer hard disks implying that Nd and Dy are crucial to the clean energy sector and the high-tech products industry (Tesfaye et al., 2021).

The high supply risk, Chinese monopoly, growing demand, and strategic interest in the clean energy sector move the Nd and Dy market towards a circular economy, i.e., towards the substitution of the linear extraction, production, use, and disposal by a 'closing-the-loop' production (Dang et al., 2021; Korhonen et al., 2018). Also, the REMs circular economy would reduce the environmental impacts of mining (Favot and Massarutto, 2019; Jowitt et al., 2018; Zhang and Xu, 2016) and can make more rentable REM recovery. Therefore, to achieve the circular economy goal, Nd and Dy's recovery from secondary sources must still be implemented industrially.

Electronic and electrical equipment wastes (WEEE) are the primary alternative supplies of REM (Swain and Mishra, 2019). However, neodymium and dysprosium have also been found in acid mine drainage (Zhao et al., 2007), red mud (Khairul et al., 2019), acid leachate of landfills (Gutiérrez-Gutiérrez et al., 2015), wastewater treatment sludge (Gao et al., 2012; Kawasaki et al., 1998; Yessoufou et al., 2017), magnetic waste sludge from a NdFeB magnet factory (Rabatho et al., 2013), which potentially can contaminate water resources. Hence,

recovering REM from residues and wastewaters is necessary to meet the rising demand and mitigate environmental impacts (Zhang and Xu, 2016).

2.3 PERMANENT MAGNET SCRAP AS A SECONDARY SOURCE OF RARE EARTH METALS

REM-based permanent magnets have been present in several segments of modern life and are fundamental for developing the renewable energy field (Opare et al., 2021). They are more expensive than the classical ferrite magnets. However, rare earth magnets have superior magnetic properties (~10 times), allowing applications in various high-performance sectors (Minowa, 2008). Rare earth magnets are divided into SmCo type and NdFeB type magnets, with 98% of rare earth magnets being NdFeB type (Stegen, 2015).

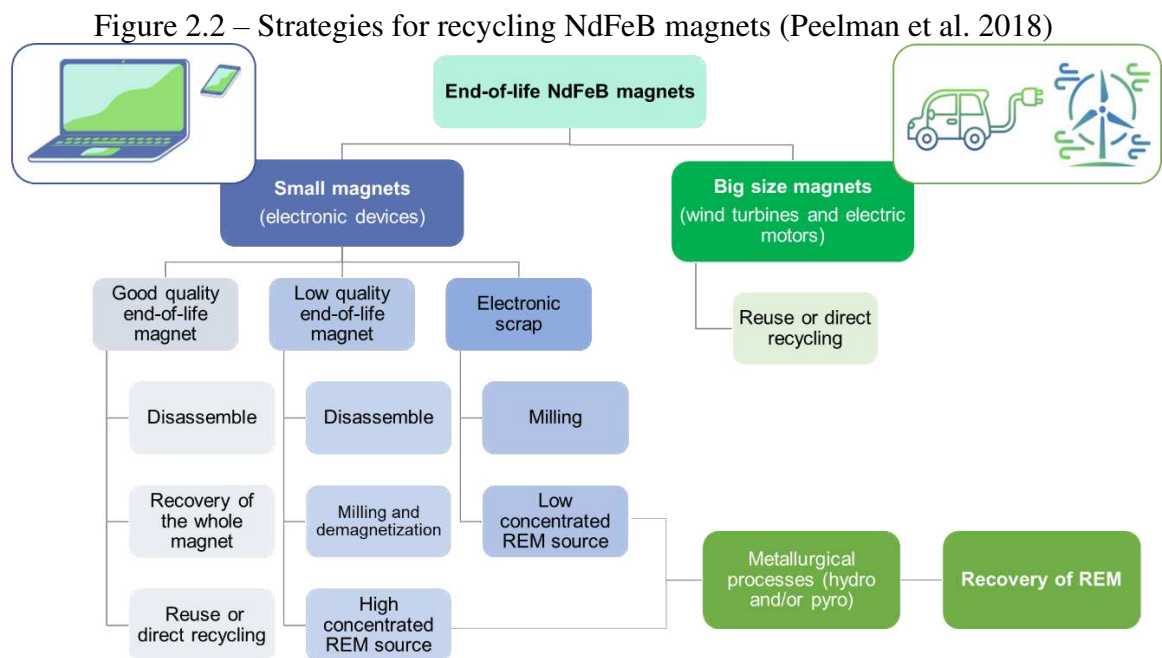
The NdFeB magnet's composition varies according to each application's requirements. Approximately 32% of the NdFeB magnet for hard disks is composed of rare earths, the main ones being Nd (~25 %) and Pr (~4%), followed by Dy (3%)(München and Veit, 2017). The Dy content contributes to the stability at high temperatures, where a maximum of 5% is usually applied in magnets for automotive and wind energy fields (Tesfaye et al., 2021).

According to Schulze and Buchert (2016), the NdFeB magnet demand for electric vehicles and wind turbines is predicted to increase by 20 and 26 % from 2020 to 2030. Besides, Junne et al. (2020) predicted diverse green energy scenarios up to 2050, where the highest annual demand for neodymium and dysprosium could exceed 3 to 9 times (Nd) and 7 to 35 times (Dy) the mining quantities. Those future scenarios indicate the vast relevance of Nd and Dy on the feasibility of further sustainable development based on renewable energy. Also, those predictions show the inherent need for high rare earth recycling rates to supply the future demand.

Depending on the application, NdFeB magnets can have different life cycles: from 2-3 years for electronic products to 20-30 years for wind turbines. Magnets' weights range from 1 g in electronic equipment, 1 kg in electric and hybrid vehicle engines, and 1000-2000 kg in modern wind turbine generators (Peelman et al., 2018). HDDs offer the benefit of being available in larger quantities than newer NdFeB applications and could serve as a secondary REE source shortly (Schulze and Buchert, 2016).

2.4 REUSE, RECYCLING, AND RECOVERY OF NdFeB MAGNETS

Due to the difficulty of obtaining the rare earth metals Nd and Dy (critical and scarce elements), several methods of recycling NdFeB magnets have been proposed, such as direct reuse, reprocessing, and hydrometallurgical and pyrometallurgical methods for REM recovery (Figure 2.2).



Direct reuse is the most economical and environmentally viable due to the low energy cost, the absence of chemical reagents' consumption, and the non-generation of waste. However, it is only appropriate for easily accessible and large magnets such as those from wind turbines and large electric generators. For small pieces, manual separation is still a challenge. According to Peelman et al. (2018), purchasing rare earth metals from primary production sources is easier and cheaper than reprocessing complex scrap material, especially for small-scale products. In actual WEEE plants, many electrical and electronic components are ground without manual disassembling of the magnets, and their magnetic members tend to follow the ferrous scrap current, which is very diluted and challenging to recover REM.

Reprocessing the magnet alloys (direct recycling) after hydrogen decrepitation is particularly feasible for hard drives since the energy consumption is lower than required in metallurgical methods, and there is no waste generation. However, this method is not applicable

for recycling mixed electronic scrap and oxidized magnets, and a high hydrogen supply is a prerequisite for this technology.

Hydrometallurgical methods such as leaching, separation, and precipitation are appropriate for all sorts of magnets. Nonetheless, for the pyrometallurgical liquid phase processes, only non-oxidized magnets can be melted directly, and for the gas phase, the application extends to the oxidized alloys, too (Peelman et al., 2018; Xu et al., 2018a). Comparing hydro and pyrometallurgical methods, the pyrometallurgical route does not generate effluents, and fewer processing steps are required. However, the pyrometallurgical process consumes large amounts of energy, produces significant solid waste quantity, demands chlorine gas consumption, and can generate corrosive aluminum chloride, which improves the cost of emissions treatment (Zhang et al., 2020).

2.5 ROLE, EFFICIENCY, AND POTENTIALITY OF THE ADSORPTION IN THE NEODYMIUM AND DYSPROSIUM RECOVERY FROM NdFeB MAGNETS IN HYDROMETALLURGICAL ROUTES

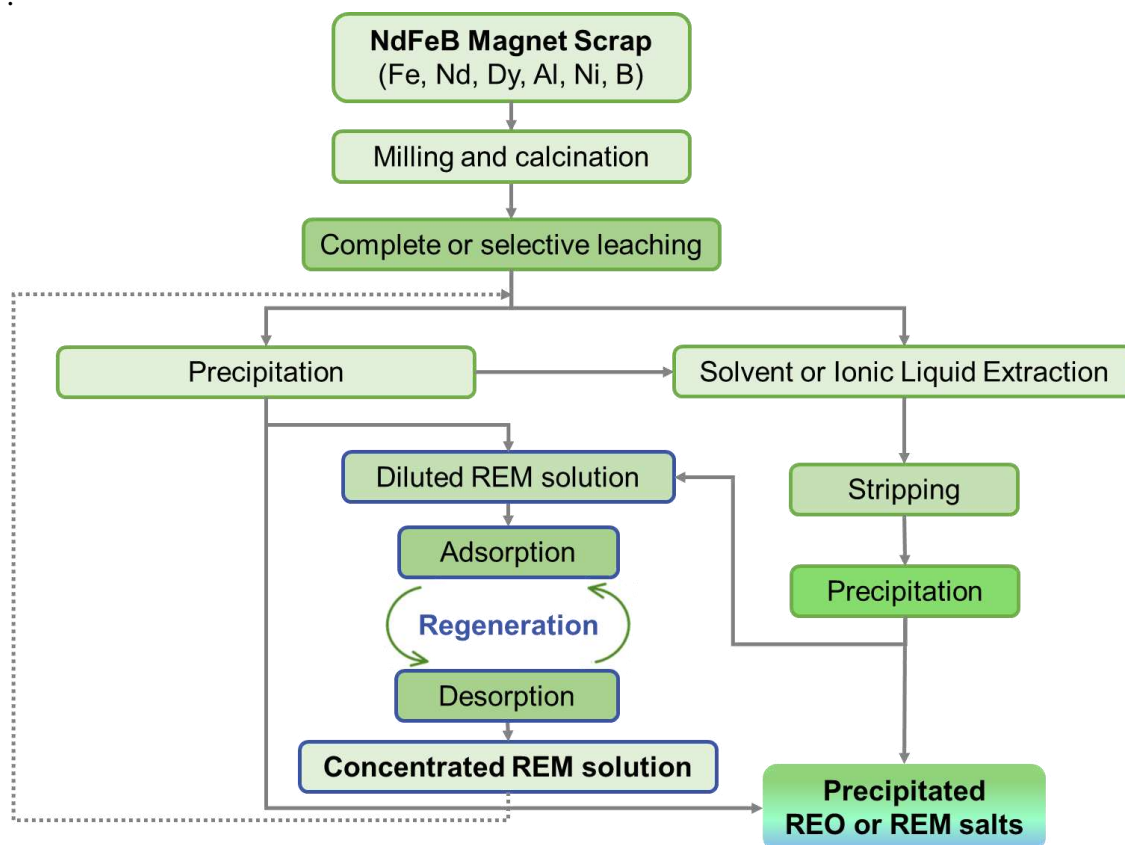
The hydrometallurgical recovery process consists of leaching (digestion, dissolution) of the powder of crushed material to reach a REM-rich aqueous phase liquor for further reprocessing; and solvent extraction or ion exchange of the REM from the REM-rich aqueous liquors, followed by stripping of the extracted species, and precipitation or electro deposition or further reprocessing of the strip solution (Gergorić, 2018).

Despite the classic hydrometallurgical methods presenting satisfactory results for concentrated systems, an adaptation of current metallurgy technologies is still necessary to recover REM from scrap in low concentrations (Yang et al., 2017). Furthermore, without a preconcentration system and innovative technologies, the low content of scrap will hardly be industrially recovered (Dudarko et al., 2022; Yamada et al., 2018). Adsorption has excellent potential to overcome this issue because it became advantageous mainly in diluted systems, where the adsorbent saturation is delayed (Costa et al., 2020). Figure 2.3 shows an overall methodology for recovering REM-rich magnet scrap by hydrometallurgical methods, including adsorption as a selective (preferable) preconcentration system.

Typically, adsorption is a tertiary process (purification) in a standard water treatment plant, where flocculation, coagulation, precipitation, and biological treatments are the primary and secondary processes. However, according to Figure 3, in the REM recovery by a hydrometallurgical approach, adsorption followed by desorption can reconcentrate the REMs

selectively. Once an REM-rich solution is produced, the typical hydrometallurgical processes can be applied efficiently to produce high purity REM.

Figure 2.3 Schematic representation of a hydrometallurgical route with adsorption and desorption reconcentration system



2.6 SINGLE ADSORPTION AND DESORPTION OF NEODYMIUM AND DYSPROSIUM IN BATCH MODE

Due to the simplicity, low cost, and high efficiency, several studies have evaluated the adsorption of neodymium and dysprosium as an alternative to concentrate and recover those critical metals. Thus, Table 2.1 summarizes the main findings of relevant works published in the last five years regarding the Nd and Dy single adsorption in batch mode.

Table 2.1 – Main Nd and Dy adsorption and desorption results of the recent literature.

(continues)

REM	Adsorbent	Adsorption conditions	Kinetics		Equilibrium		Thermodynamic	Cyclic reuses			Selectivity	Ref.
			Model	Rate constant	Model	Parameters		Eluent	Adsorption	Desorption		
Nd	Ion imprinted xanthan gum-layered double hydroxide nanocomposite	$C_{ads} = 3$ g/L pH 4.0	PFO	0.08 min^{-1}	Freundlich	$n = 1.63$ $K_F = 1.94$	Endothermic Spontaneous $\Delta S > 0$	HNO ₃ 0.1 mol/L	~ 85 % (1 st) 45 % (5 th)	-	-	(Iftekhhar et al., 2018b)
Nd	Polyamide magnetic calcium alginate composite	$C_{ads} = 0.8$ g/L 180 rpm pH 5.0	PSO	0.013 g/mg.min	Langmuir	$q_m = 71.4$ mg/g $K_L = 0.88$ L/mg	Endothermic Spontaneous $\Delta S > 0$	HNO ₃ 0.2 mol/L	96.1 % (1 st) 91.7 % (4 th)	89% (1 st)	-	(Javadian et al., 2020a)
Nd	Carboxyl-functionalized porous carbon derived from ZIF-8	$C_{ads} = 1$ g/L $C_i \geq 500$ mg/L pH 6.0	PSO	0.000262 g/mg.min	Langmuir	$q_m = 175$ mg/g $K_L = 0.00411$ L/mg	Endothermic Spontaneous $\Delta S > 0$	HCl 0.1 mol/L	~ 120 mg/g (1 st) 105 mg/g (5 th)	-	Nd >> Fe > Al > Mg > Ca > Na	(Ahmed et al., 2021)
Nd	Poly(Itaconic Acid)/Magnetite Sepiolite Composite	$C_{ads} = 0.8$ g/L $C_i \geq 250$ mg/L pH 7.0	PSO	0.01 g/mg.min	Langmuir	$q_m = 151.5$ mg/g $K_L = 0.16$ L/mg	Endothermic Spontaneous $\Delta S > 0$	HCl 0.01 mol/L	~ 38 mg/g (1 st) 36 mg/g (6 th)	~95% (1 st) 93 % (6 th)	Er > Nd > Ce > Fe > Al > Mg > Ca > K > Na	(Bai et al., 2020)
Nd	Chitosan-Mn-Ferrite Magnetic Beads	$C_{ads} = 1$ g/L $C_i \geq 200$ mg/L pH 4.0 150 rpm	PSO	0.0023 g/mg.min	Sips	$q_{mS} = 44.3$ mg/g $K_S = 0.01$ L/mg $m_S = 0.63$	-	Methanol 98%	~80% (1 st) 50% (4 th)	~95% (1 st) 55 % (4 th)	-	(Durán et al., 2020)
Nd	Fumarate polystyrene microspheres	$C_{ads} = 0.8$ g/L pH 5.0 150 rpm	PSO	0.0556 g/mg.min	Langmuir	$q_m = 43.1$ mg/g $K_L = 0.04$ L/mg	No effect of temperature	HNO ₃ 0.50 mol/L	-	-	U > Nd	(Elsalamouny et al., 2017)

Table 2.1 – Main Nd and Dy adsorption and desorption results of the recent literature.

(continues)

REM	Adsorbent	Adsorption conditions	Kinetics		Equilibrium		Thermodynamic	Cyclic reuses			Selectivity	Ref.
			Model	Rate constant	Model	Parameters		Eluent	Adsorption	Desorption		
Nd	Thiourea modified Amberlite XAD7	$C_{ads} = 4$ g/L $C_i \geq 400$ mg/L pH 6.0 200 rpm	PSO	483.2 g/mg.min	Sips	$q_{mS} = 74.9$ mg/g $K_S = 6.42$ L/mg $m_S = 2.16$	Endothermic Spontaneous $\Delta S > 0$	HCl 15% v/v	98.7 % (1 st) 20.7 % (11 th)	85.6 % (1 st) 19.2 % (11 th)	-	(Negrea et al., 2020)
Nd	Diglycolic acid-functionalized electrospun polystyrene nanofibers	$C_{ads} = 0.75$ g/L $C_i \geq 180$ mg/L pH 6.0 200 rpm	-	-	Langmuir	$q_m = 146.2$ mg/g $K_L = 0.0036$ L/mg	-	HNO ₃ 1 mol/L	-	~100 % (1 st) 92 % (4 th)	-	(Pereao et al., 2020)
Nd	Diglycolic acid-functionalized polyethylene terephthalate nanofibers	$C_{ads} = 0.75$ g/L $C_i \geq 180$ mg/L pH 6.0 200 rpm	-	-	Langmuir	$q_m = 123.9$ mg/g $K_L = 0.00027$ L/mg	-	HNO ₃ 1 mol/L	-	-	-	(Pereao et al., 2021)
Nd	Benzene triamide-tetraphosphonic acid immobilized on mesoporous silica	$C_{ads} = 1$ g/L pH 6.0 200 rpm	PSO	0.086 g/mg.min	Langmuir	$q_m = 129.8$ mg/g $K_L = 0.88$ L/mg	-	HCl 0.5 mol/L	100 % (1 st) 88 % (5 th)	-	Y > Nd > Ce > La	(Ravi et al., 2018)
Nd	Expanded Vermiculite	$C_{ads} = 14$ g/L pH 3.3 $C_i \geq 1731$ mg/L	PSO	0.0007 g/mg.min	Langmuir	$q_m = 56.3$ mg/g $K_L = 0.25$ L/mg	Exothermic Spontaneous $\Delta S > 0$	CaCl ₂ 0.3 mol/L	~ 99% in five cycles	~70% (1 st) 96 % (5 th)	Nd > N i > Zn > Cu > Pb	(Brião et al., 2020; G. de V. Brião et al., 2021b)

Table 2.1 – Main Nd and Dy adsorption and desorption results of the recent literature.

(continues)

REM	Adsorbent	Adsorption conditions	Kinetics		Equilibrium		Thermodynamic	Cyclic reuses			Selectivity	Ref.
			Model	Rate constant	Model	Parameters		Eluent	Adsorption	Desorption		
Nd	Porous Covalent Polymers Comprising a Phosphite Skeleton	$C_{ads} = 1$ g/L $C_i \geq 500$ mg/L pH 5.0	PSO	0.000691 g/mg.min	Langmuir	$q_m = 321.0$ mg/g $K_L = 1.19$ L/mg	Endothermic Spontaneous $\Delta S > 0$	HNO ₃ 2 mol/L	~98% (1 st) 94 % (10 th)	-	Eu > Nd > Ce > La Nd >> Fe > Al > Cu > Mg	(Ravi et al., 2019)
Nd	Jordanian diatomaceous earth	$C_{ads} = 4$ g/L $C_i \geq 50$ mg/L pH 5.0 150 rpm	PSO	0.099 g/mg.min	Langmuir	$q_m = 169.5$ mg/g $K_L = 0.181$ L/mg	Exothermic Spontaneous $\Delta S > 0$	H ₃ PO ₄ 0.05 mol/L EDTA 0.05 mol/L		85% (1 st)		(Hamadneh et al., 2019)
Nd	Functionalized magnetic ferrite	$C_{ads} = 0.5$ g/L pH 8.16 NaCl 1N	PSO	0.38 g/mg.min	Langmuir	$q_m = 25.6$ mg/g; $K_L = 3.01$ L/mg	-	HNO ₃ 0.05 N	-	100% (1 st) 95% (5 th)	Nd >> Ca = Mg = Na = K ~ 0	(Tu et al., 2019)
Nd	Imprinted mesoporous cellulose nanocrystals films	$C_{ads} = 1$ g/L $C_i \geq 150$ mg/L; pH 4.0	PSO	0.00018 g/mg.min	Langmuir	$q_m = 23.0$ mg/g $K_L = 0.13$ L/mg	-	Acetic acid 1:9 v/v	~ 18 mg/g (1 st) 15 mg/g (5 th)	-	Nd >> La = Gd = Dy = Tb	(Zheng et al., 2019)
Dy	Polyamide magnetic calcium alginate composite	$C_{ads} = 0.8$ g/L 180 rpm pH 5.0	PSO	0.012 g/mg.min	Langmuir	$q_m = 99.9$ mg/g $K_L = 0.36$ L/mg	Endothermic Spontaneous $\Delta S > 0$	HNO ₃ 0.2 mol/L	96.8 % (1 st) 93.6 % (4 th)	95% (1 st)	-	(Javadian et al., 2020b)
Dy	Oxidized carbon nanotubes, graphene oxide, ion-imprinted polymer composite	$C_{ads} = 1$ g/L $C_i \geq 200$ mg/L pH 4.0	PSO	0.00093 g/mg.min	Langmuir	$q_m = 48.14$ mg/g $K_L = 0.64$ L/mg	Endothermic Spontaneous $\Delta S > 0$	Acetic acid 10% v/v	34 mg/g (1 st) 30 mg/g (5 th)	-	-	(Zheng et al., 2020)

Table 2.1 – Main Nd and Dy adsorption and desorption results of the recent literature.

(continues)

REM	Adsorbent	Adsorption conditions	Kinetics		Equilibrium		Thermodynamic	Cyclic reuses			Selectivity	Ref.
			Model	Rate constant	Model	Parameters		Eluent	Adsorption	Desorption		
Dy	Hybrid Lewis base ligand functionalized alumina-silica based composite	$C_{ads} = 1$ g/L pH 4.0	-	-	Langmuir	$q_m = 125.5$ mg/g $K_L = 1.62$ L/mg	-	HNO ₃ 0.30 mol/L	100 % (1 st) 90 % (6 th)	-	Dy = Lu > Ca ~ Mg ~ Zn ~ Na ~ K	(Awual et al., 2017)
Dy	Phosphate functionalized Silica/polyvinyl imidazole core-shell nanoparticles	$C_{ads} = 0.3$ g/L $C_i \geq 300$ mg/L pH 4.0 150 rpm	PSO	0.00083 g/mg.min	Frendlich	$n = 1.71$ $K_F = 128$	Endothermic Spontaneous $\Delta S > 0$	HCl 0.1 mol/L	~ 100 mg/g (1 st) 85 mg/g (5 th)	-	-	(Ettehad Gargari et al., 2017)
Dy	Carboxyl-functionalized mesoporous silica	$C_i \geq 10$ mg/L pH 1.75	-	-	Langmuir	$q_m = 44.8$ mg/g	-	HNO ₃ 1 mol/L	-	~ 100% in five cycles	Dy >>> Cu = Zn = Fe = Nd ~ 0	(Kaneko et al., 2018)
Dy	Ion imprinted macroporous chitosan membrane	$C_{ads} = 1$ g/L $C_i \geq 200$ mg/L pH 7.0	PSO	0.00263 g/mg.min	Langmuir	$q_m = 28.0$ mg/g $K_L = 0.0363$ L/mg	-	HCl 1 mol/L	~ 24 mg/g (1 st) 20mg/g (5 th)	-	Dy > Tb > Pr > Nd > Fe	(Liu et al., 2017)
Dy	Modified Metal-Organic Frameworks	$C_{ads} = 0.5$ g/L pH 5.3 200 rpm 30° C	PSO	0.000172 g/mg.min	-	-	Endothermic Spontaneous $\Delta S > 0$	HNO ₃ 0.01 mol/L	~ 75 mg/g (1 st) 70 mg/g (4 th)	-	Dy >> Mn > Ca > Mg = Co > Ni	(Pei et al., 2021)
Dy	Expanded Vermiculite	$C_{ads} = 12.8$ g/L pH 3.5 $C_i \geq 1950$ mg/L	PSO	0.0013 g/mg.min	BET	$q_m = 55.25$ mg/g $K_{BET} = 0.14$ L/mg $K_u = 0.0006$ L/mg	Endothermic Spontaneous $\Delta S > 0$	Mg(NO ₃) ₂ 0.25 mol/L	~99% in five cycles	87% (1 st) 100 % (5 th)	Dy > Pb > Ni > Cd > Cu	(G. de V. Brião et al., 2021a; G. V. Brião et al., 2021)

Table 2.1 – Main Nd and Dy adsorption and desorption results of the recent literature.

(conclusion)

REM	Adsorbent	Adsorption conditions	Kinetics		Equilibrium		Thermodynamic	Cyclic reuses			Selectivity	Ref.
			Model	Rate constant	Model	Parameters		Eluent	Adsorption	Desorption		
Dy	Polyurethane sponge-supported graphene oxide–titanium phosphate	$C_{ads} = 0.06$ g/L $C_i \geq 100$ mg/L 200 rpm	PSO	0.001 g/mg.min	Langmuir	$q_m = 576.2$ mg/g $K_L = 0.16$ L/mg	-	HCl 1 mol/L	~ 380 mg/g (1 st) 170 mg/g (4 th)	-	-	(Peng et al., 2021)
Dy	Hierarchical porous ZIF-8 nanoparticles	$C_{ads} = 0.25$ g/L $C_i = 12$ mg/L pH 7.0 300 rpm	PSO	0.026 g/mg.min	Langmuir	$q_m = 430$ mg/g $K_L = 0.25$ L/mg	Endothermic Spontaneous $\Delta S > 0$	Acetonitrile at 55°C	-	> 90 % in three cycles	Dy > Sm >> La > Ni > Ca > Mg	(Abdel-Magied et al., 2019)
Dy	Sericin and alginate blend beads	$C_{ads} = 10$ g/L $C_i = 237.3$ mg/L 200 rpm	PFO	0.009 min ⁻¹	-	-	-	Ca(NO ₃) ₂ / HNO ₃ 0.1 mol/L	94% (1 st) 98% (4 th)	> 98% in four cycles	-	(da Costa et al., 2021)
Dy	Benzylphosphate-based covalent porous organic polymers	$C_{ads} = 1$ g/L $C_i \geq 500$ mg/L pH 6.5 200 rpm	PSO	-	Langmuir	$q_m = 301.9$ mg/g $K_L = 0.18$ L/mg	-	HCl 0.25 mol/L	~98% (1 st) 90 % (10 th)	~96% (1 st) 88% (10 th)	Dy > Zr> Zn > Cu > Mg > K	(Ravi et al., 2022)
Dy	Bacterial cellulose nanofibrous ion-imprinted aerogel	$C_{ads} = 1$ g/L $C_i \geq 200$ mg/L pH 4.0	PSO	0.005 g/mg.min	Langmuir	$q_m = 49.9$ mg/g $K_L = 0.13$ L/mg	Endothermic Spontaneous $\Delta S > 0$	Acetic acid 10% v/v	~ 40 mg/g (1 st) 33 mg/g (5 th)	-	Dy > Pr = Nd	(Zheng et al., 2022b)
Dy	GO and polyethyleneimine ionic imprinted cellulose nanocrystal aerogel	$C_{ads} = 1$ g/L $C_i \geq 200$ mg/L pH 5.0	PSO	0.157 g/mg.min	Langmuir	$q_m = 36.5$ mg/g $K_L = 0.397$ L/mg	Endothermic Spontaneous $\Delta S > 0$	Acetic acid 10% v/v	~ 36 mg/g (1 st) 28 mg/g (5 th)	-	Dy >> Pr = Nd	(Zheng et al., 2022a)

2.6.1 Adsorbent Materials

The adsorbent matrix is the “core” of an adsorptive process. A technically viable adsorbent preferably should have a high internal volume accessible to the components to be removed from the fluid (McCABE et al., 2000). Adsorbents can be carbonaceous or inorganic, synthetic, or natural. Table 2.1 shows that diverse adsorbent materials have been applied to the adsorption and recovery of Nd and Dy, such as polymer-based materials (da Costa et al., 2021), metal-organic frameworks (Abdel-Magied et al., 2019 ; Pei et al., 2021), functionalized silica (Ravi et al., 2018), carbon-based materials (Zheng et al., 2022a), magnetic particles (Tu et al., 2019), and others (Hamadneh et al., 2019; Brião et al., 2020).

Polymer-based adsorbents such as composites, usually formed using fillers such as metal, metal oxides, and natural fibers, have been presenting great adsorptive responses for environmental remediation due to their exclusive properties, such as improved durability, processing capability, high functionality, and a large surface area, and low cost (Yaashikaa et al., 2022). For rare earth selective adsorption, ion-imprinted polymer-based (IIP) adsorbents have been gaining attention. The preparation usually involves complexing a ligand and a metal ion to create specific binding sites after metal leaching (Branger et al., 2013).

Metal-organic frameworks (MOF) are innovative adsorbents with unique structural diversity from the coordination bonds between the inorganic metal atoms, isolated polyhedral and small clusters that act as nodes, and organic ligands (di-, tri-, or tetra-dentate) that link the node (Ibrahim et al., 2021). MOFs present unique properties such as high specific surface area, tunable pore sizes, and excellent thermal and chemical stability (Parmar et al., 2021). However, these materials have weak metallic cation interactions, needing modifications or functionalization to improve rare earth recovery.

Silica-based adsorbents with micro or mesoporosity, significant surface areas, good mechanical, chemical, and thermal stabilities, availability, and low cost, have excellent properties for adsorption. Nevertheless, silica-based materials have strong and sometimes irreversible non-selective adsorption because their surface consists of acidic silanol (Zeb et al., 2020). Microporous silica is silica beads, alunite, perlite, and zeolites, and mesoporous silica includes the Mobile Composition of Matter (MCM) family and the Santa Barbara Amorphous (SBA) family (Diagboya and Dikio, 2018). To improve the affinity for rare earth metals, silica-based adsorbents are usually

functionalized with aliphatic and aromatic oxygen, nitrogen, and sulfur-containing groups (Cashin et al., 2018).

Carbon-based adsorbents are materials composed of carbon nanotubes (CNTs), graphene oxide, nanoporous carbon, nanodiamond, fullerenes, and graphitic carbon nitride, and their derivatives such as polymer, ceramics, and magnetic composites (Prediger et al., 2022). CNTs own cylindrical carbon structures with extraordinary properties such as lightweight, small size with a high aspect ratio, good tensile strength, and good conducting characteristics, making them useful as fillers in different materials such as polymers, metallic surfaces, and ceramics (Ibrahim, 2013). Graphene derivatives can be formed by the incorporation of large oxygen-containing functional groups to get graphene oxide (GO) and reduced graphene oxide (rGO) (Khurana et al., 2017). According to Smith et al. (2019), GO is similar to graphene but contains functional groups such as hydroxyl, alkoxy, carbonyl, and carboxylic acid. These oxygenated groups are responsible for conferring to GO significant adsorptive rare earth metals (cations) potential and easy functionalization to form composites. Polymeric carbon composites have been applied as adsorbents due to their high porosity structure, different functional groups, large specific surface area, and the possibility of π interactions with the adsorbate. Magnetic carbon-based adsorbents are advantageous due to their easy separation from aqueous solution by the exposition to an external magnetic field.

Magnetic nanoparticles were usually made of iron oxides such as magnetite (Fe_3O_4), maghemite ($\gamma\text{-Fe}_2\text{O}_3$), and hematite ($\alpha\text{-Fe}_2\text{O}_3$); however, they can also be originated from oxides of metals Co, Ni, Cu, and Mn (Mehta et al., 2015). These materials can be used directly as adsorbents or modified to achieve higher adsorption capacities and selectivity or also used in the adsorbent composition to improve the solid/liquid separation. The surface of magnetic nanoparticles can be doped with functional groups, enhancing the colloidal stability and avoiding the typical nanomaterial problem of agglomerations (da Silva et al., 2021; de Andrade et al., 2021; Phouthavong et al., 2022).

Other alternative adsorbents or components of the adsorbents shown in Table 2.1 were diatomaceous earth (sedimentary rock), sepiolite, and expanded vermiculite (clay materials), both natural soil materials whose main composition is silica, alumina, and iron oxides. Clay materials present excellent adsorptive properties for cations as the REMs, such as high negatively charged surface, high cation exchange capacity, low cost, and availability (de Gisi et al., 2016; Valaskova

and Martynková, 2012). Moreover, naturally, REMs have a high attraction to clay materials, one of the REM deposits varieties (ion-adsorption clay) (Alshameri et al., 2019; Borst et al., 2020) that also motivates the study of clay-based adsorbents for REM recovery.

2.6.2 Operational Conditions

Adsorption is an operation that efficiency depends on certain conditions such as the adsorbent mass, particle's dimension, shape, porous structure, solution pH, temperature, and adequate mixing to guarantee the proper adsorbate/adsorbent contact time, and adsorbate initial concentration, among others. Non-optimized operational conditions can lead to low adsorption capacity or removal percentage, which is highly undesirable to further applications.

Adsorbent dosage is a factor intrinsically related to the economy of an adsorptive separation process. The higher the affinity between the adsorbate/adsorbent, the lower the adsorbent dosage needed to reach high adsorption efficiencies. The increase in adsorbent concentration translates into increased active adsorption sites (Iftekhhar et al., 2018a). From Table 2.1, the adsorbent dosage varied from the magnitude order of 10^{-2} to 14 g/L. The extensive range occurs because of the different adsorbent efficiencies and initial REM concentrations evaluated in the studies; the more concentrated the solution, the higher the adsorbent dosage needed.

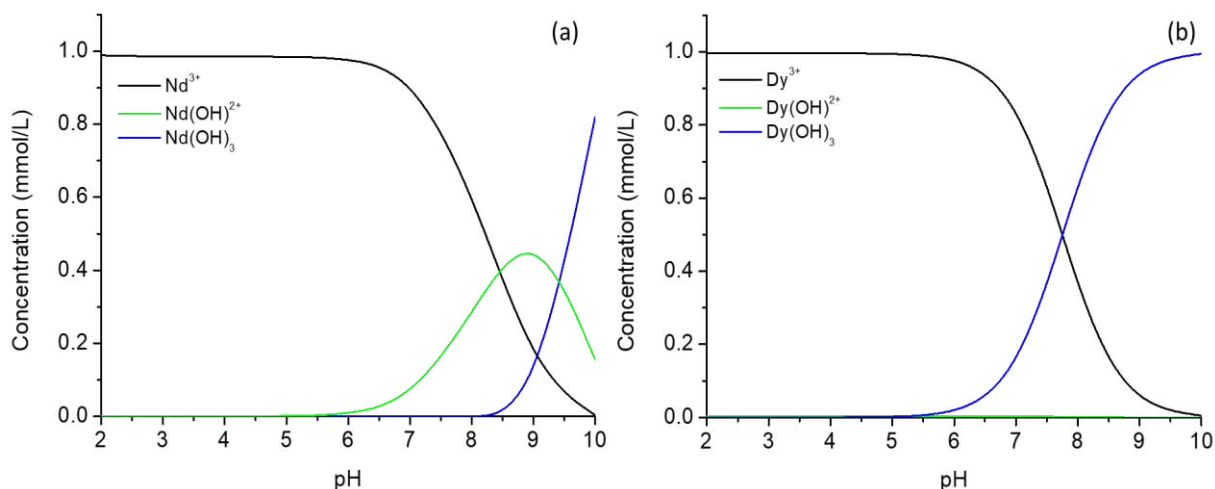
The initial Nd and Dy concentrations ranged from 5 to 500 mg/L. Usually, in adsorption studies, the initial concentration range is defined by the concentration of the interest adsorbate in the real wastewaters and effluents and according to the measurement technique's sensibility. However, in the Nd and Dy adsorption studies, just a few mentioned the concentration of secondary sources to simulate in their studies. That occurs because the composition of NdFeB magnets can vary significantly according to the application, and so do the leachates and possible solutions that would be submitted to the adsorption studies. Table 2.1 presents the main components' concentration of magnet scraps leachates, where the Nd and Dy concentrations were in the range of 100 to 3300 mg/L for Nd and 6 to 1800 mg/L for Dy, respectively. The leachates achieved lower iron contents due to the pH adjustment to 3.6 and 3.8 (Brewer et al., 2019a; Önal et al., 2017) and precipitation and separation of the significant iron content. Considering the process proposed in Figure 2.3, just diluted residual solutions would be sent to the adsorption step. Thus, the concentration range presented in the studies in Table 2.1 (5 - 500 mg/L) addresses the actual conditions.

Table 2.2 – Permanent magnets scrap leaching composition.

Concentration (mg/L)				Leaching	Ref.
Pr	Nd	Dy	Fe		
29.73	106.74	6.09	329.22	H ₂ SO ₄	(Brewer et al., 2019a)
1493	28570	1771	63700	HCl	(Klemettinen et al., 2021)
24200	24000	159	86100	H ₂ SO ₄	(Klemettinen et al., 2021)
73.00	2722.0	301.0	28.0	H ₂ SO ₄	(Önal et al., 2017)
1140	3290	540	13350	HCl	(Ni'am et al., 2020)

pH significantly impacts the adsorbent's overall efficiency in the REM adsorption because it affects the surface charge of the adsorbents, the degree of ionization, and the species of the adsorbate in solution (Olu-Owolabi et al., 2021). Nd (a) and Dy (b) species distribution according to the solution pH is shown in Figure 2.4, in which for pH < 5.5, only the trivalent forms of Nd and Dy are present, respectively. For pH > 5.5, the hydroxide species are formed.

Figure 2.4. Nd (a) and Dy (b) speciation as a function of the solution pH



The pH range applied in the sorption studies presented in Table 2.1 is from 1.75 to 8.16; however, 52% of the papers used $5.0 \leq \text{pH} \leq 6.0$, despite the different adsorbent natures. According to the works of Riaño and Binnemans (2015), Gergoric et al. (2019), and Xu et al. (2018a), who

propose hydrometallurgical treatments for the recovery of rare earths from discarded magnets, the pH of the leachate was approximately 2.

2.6.3 Kinetics

The adsorption kinetics determines the feasibility and the mass transfer mechanism involved in the process because it points out the time needed to reach the equilibrium and, by modeling, informs the adsorption rates.

In the last years, many mathematical models have been proposed to describe adsorption kinetics; they can be classified as kinetic reaction-based, empirical, and mass transfer-based models (Wang and Guo, 2020). The most used adsorption kinetic models are the pseudo-first-order (PFO)(Lagergren, 1898) and pseudo-second-order (PSO)(Ho and McKay, 1998), represented by Equations 1 and 2.

$$q_t = q_e(1 - e^{-k_1 t}) \quad (2.1)$$

$$q_t = \frac{k_2 q_e^2 t}{1 + k_2 q_e t} \quad (2.2)$$

Where k_1 (1/min) and k_2 (g/(mmol. min)) are the PFO and PSO apparent rate constants, q_t and q_e are the adsorption capacities at a specific time, and the equilibrium (mmol/g), and t is the time (min).

In the kinetic modeling of the studies exposed in Table 2.1, PSO was the model that better represented the experimental data. Since the model assumes that the rate-limiting step is chemical sorption (Ho and Mckay, 1999), the adsorption of Nd and Dy occurs by valence forces through sharing or exchanging electrons with the adsorbates. Despite the widespread application, the PSO model has some drawbacks due to the influence of the adsorbent and adsorbate concentration on the sorption rate, which means that the k_2 and q_e parameters are valid just for the experimental conditions applied in the kinetic study. Thus, the comparison between the adsorption kinetics of different systems should be made carefully, and it is just valid for similar adsorbate/adsorbent concentrations (Bullen et al., 2021). Due to those limitations, despite the easy use of the PSO model, more meaningful models should be applied for scale-up purposes, such as mass transfer-

based models that can predict the mass transfer resistances of sorption operation (Wang and Guo, 2020).

2.6.4 Equilibrium

Information on the adsorption equilibrium is essential for analyzing the adsorption process, as they indicate an adsorbent's maximum adsorption capacity and saturation rate. There are several isotherm models available to fit experimental data and to describe the adsorption equilibrium in a liquid phase, including Freundlich (Freundlich, 1906), Langmuir (Langmuir, 1918), BET for liquid phase (Wang et al., 1998), Sips (Sips, 1948), and Dubinin-Radushkevich (Dubinin and Radushkevich, 1947), among others.

According to Table 2.1, the adsorption equilibrium of Nd and Dy is commonly described by Langmuir (Equation 2.3), Freundlich (Equation 2.4), and Sips (Equation 2.5) models.

$$q_e = \frac{q_m K_L C_e}{1 + (K_L C_e)} \quad (2.3)$$

$$q_e = K_F C_e^{n_F} \quad (2.4)$$

$$q_e = \frac{q_{mS} K_S C_e^{m_S}}{1 + (K_S C_e)^{m_S}} \quad (2.5)$$

Where K_L is the Langmuir constant (L/mg), q_m is the maximum adsorption capacity (mg/g), K_F (L/g) is the Freundlich constant, n_F is the heterogeneity constant ($0 < n_F < 1$), q_{mS} is the Sips maximum adsorption capacity (mg/g), K_S is the Sips constant (L/mg), and m_S is the Sips heterogeneity factor.

Langmuir isotherm, which represents most of the equilibrium systems from Table 2.1, assumes that maximum adsorption occurs when a saturated monolayer of adsorbate is held on the adsorbent surface, that all sites have the energy (homogenous), and that there is no lateral interaction between adsorbate on the monolayer. Table 2.1 also presents the parameters q_m and K_L , which can be compared, indicating which adsorbent material has higher Nd and Dy adsorption potential.

The highest q_m was achieved using porous covalent organic polymers comprising a phosphite skeleton and polyurethane sponge-supported graphene oxide–titanium phosphate for Nd and Dy, respectively. The authors justified that the high adsorption capacity (321.0 mg/g) of the first adsorbent (Ravi et al., 2019) occurs by the presence of many binding phosphate groups in the network. The authors of the second one (Peng et al., 2021) explained that the excellent adsorption capacity (576.2 mg/g) is due to the well-dispersed structure of the titanium phosphate on the sponge as active adsorption sites. In both studies, the phosphorus-based functional groups were responsible for the adsorption by electrostatic interactions and surface coordination complexation mechanisms.

The lowest q_m was 23.0 and 28.0 mg/g for the adsorption of Nd on ion-imprinted mesoporous cellulose nanocrystal films (Zheng et al., 2019) and Dy on ion-imprinted macroporous chitosan membranes (Liu et al., 2017). Both materials applied the ion-imprinted technique on porous biopolymers. As discussed above, ion-imprinted polymers have been gaining attention due to their ability to improve the polymeric adsorbent's selectivity. However, the process still needs further development since the polymers can present low surface areas, poor mass transfer, and binding kinetics (Kusumkar et al., 2021). The synthesis of high porous composites with ion-imprinted polymers could be an alternative to solve some issues also regarding the IIP's lower reusability and large-scale production.

2.6.5 Thermodynamics

The effect of temperature on the adsorption performance is essential to determine the thermodynamic nature of the process. To estimate the adsorption energy of Gibbs (ΔG_{ads}°), the classic Van't Hoff (Van't Hoff, 1884) equation (Equation 2.6) is applied.

$$\Delta G_{ads}^\circ = -RT \ln K_e \quad (2.6)$$

T is the temperature (K), R is the ideal gas constant (8.314 J/mol K), and K_e is the equilibrium constant.

There are many approaches to calculating the K_e from the isotherm equilibrium constants; nonetheless, Ghosal and Gupta (2017), Lima et al. (2019), and Liu (2009) pointed out that the metal activity coefficient at equilibrium (γ_e) should be considered, especially for charged adsorbates as the metals. In the case of the adsorption equilibrium following the Langmuir relation,

as usually occurs (Table 2.1), the K_e can be calculated by Equation 7 using a reference concentration (1 mmol/L). However, the γ_e is often considered equal to 1, and the K_L is applied as K_e .

$$K_e = \frac{K_L}{\gamma_e} \cdot (1 \text{ mol} \cdot \text{L}^{-1}) \quad (2.7)$$

Thus, ΔG_{ads}^o can be associated with the adsorption enthalpy (ΔH_{ads}^o) and entropy (ΔS_{ads}^o) by Equation 2.8.

$$\Delta G_{ads}^o = \Delta H_{ads}^o - T\Delta S_{ads}^o \quad (2.8)$$

Finally, ΔH_{ads}^o and ΔS_{ads}^o are estimated using the slope of the curve $\ln K_e$ versus $1/T$ (Equation 2.9).

$$\ln K_e = \frac{-\Delta H_{ads}^o}{RT} + \frac{\Delta S_{ads}^o}{R} \quad (2.9)$$

If $\Delta H_{ads}^o > 0$, the adsorption is endothermic; if $\Delta H_{ads}^o < 0$, is exothermic. The ΔS_{ads}^o indicates the randomness degree of the system, and the ΔG_{ads}^o the spontaneity of the process. Also, the magnitude of the ΔH_{ads}^o can inform if the process occurs by chemisorption or physisorption. From Table 2.1, most thermodynamic studies indicate that the sorption of Nd and Dy is positively affected by the temperature increase (endothermic character).

The decrease of ΔG_{ads}^o with temperature means that metal binding is enhanced at higher temperatures. Meanwhile, the absolute values of ΔH_{ads}^o are systematically below the absolute values of $T\Delta S_{ads}^o$, which confirms that the adsorption of Nd and Dy is controlled by entropic changes due to the improved disorder of the solid/liquid interface than by enthalpy variation (Thomas, 1961).

2.6.6 Reuse

Desorption and regeneration are essential aspects that rule the economy and sustainability of effluent treatment technologies (Lata et al., 2015). Therefore, regeneration should be performed efficiently and without damage to mechanical and adsorption properties (Gkika et al., 2022;

Thomas and Crittenden, 1998). The rare earth metals case is even more critical because it involves the concentration and recovery of the metals with high added value due to the scarcity and criticality. In addition, the concentration and recovery of REM are crucial to return these metals to the production chain, contributing to the circular economy. As mentioned above, the selection of the papers cited in Table 2.1 has been made based on their desorption/reuse studies due to the relevance of this topic for the REM recovery purpose.

Table 2.1 shows that the eluents most used are strong acids (HNO_3 , HCl), followed by acetic acid, organic solvents (acetonitrile and methanol), and mixtures of inorganic salts ($\text{Ca}(\text{NO}_3)_2$, CaCl_2 , $\text{Mg}(\text{NO}_3)_2$), complexing agents (EDTA), and acids (H_3PO_4 and HNO_3). The determination of the better eluent depends on the adsorption mechanism, nature/stability of the adsorbent, and preferably based on cost-effectiveness and "eco-friendliness". Strong acids efficiently lixiviate the adsorbed REM; regardless, they may damage the adsorbent along with the cycles. Organic solvents as eluents should be avoided because of their toxicities. One of the advantages of the adsorption process over solvent extraction, for example, is the non-generation of significant amounts of harmful effluents to treat. Thus, designing sustainable eluting strategies is still challenging for further REM recovery adsorptive processes.

The adsorptive efficiency, along with the cycles, is an essential criterion of reusability of the adsorbent. The studies evaluated from 4 to 11 cycles of adsorption/desorption, of which five cycles is the mode of the set. Some authors preferred to report the results in removal percentage (%) and others by adsorption capacity (mg/g); nonetheless, both efficiency parameters are equally important. A suitable adsorbent must have a high adsorption capacity. Also, especially for the REM separation, operation conditions must be optimized to achieve high removal efficiencies since, more critical than the great use of the adsorbent, the principal objective is to reincorporate these metals into the productive chain. The most resistant adsorbent that supported six successive uses, losing just 5% of the original capacity, was the poly(itaconic acid)/magnetite sepiolite composite (Bai et al., 2020). The eluent used was hydrochloric acid (0.01 mol/L). The inorganic-based adsorbent made by engineered clay may have contributed to the material's stability. Regarding the desorption efficiencies exclusively, the most reproductive process was the recovery of Dy from carboxyl-functionalized mesoporous silica using nitric acid (1 mol/L) as eluent. The recovery efficiency of 100% was practically constant along with the five cycles (Kaneko et al., 2018).

Most of the studies presented in Table 2.1 evaluated their reuse tests based on the adsorptive response along with the cycles, and few of them only reported desorption efficiencies (Abdel-Magied et al., 2019; Hamadneh et al., 2019; Kaneko et al., 2018; Pereao et al., 2020; Tu et al., 2019). However, some of them balanced both criteria (Bai et al., 2020; da Costa et al., 2021; Negrea et al., 2020; Ravi et al., 2022), presenting adsorption and desorption results along with the reuses. So, comparing both performances, the benzylphosphate-based covalent porous organic polymer (Ravi et al., 2022) could efficiently adsorb Dy ($q_m = 301.9$ mg/g), and, during ten cycles of reuse, the adsorbent just decreased 8% of the adsorption (98 to 90%) and desorption (96 to 88%) efficiencies. The eluent used was hydrochloric acid (0.25 mol/L). This outstanding performance was attributed to the high stability of the material to a wide range of pH (1 - 13) proved by FT-IR analysis and to the high functionalization with phosphate that acts as a hard Lewis base binding efficiently the Dy³⁺ions.

2.6.7 Selectivity

Selectivity is critical in rare earth recovery since the REM on secondary sources is mainly mixed with several other metals and interferents (Wang et al., 2017). Also, the selectivity between the rare earth metals is compulsory since they are known for their similar properties that difficult their separation and purification. According to Charalampides et al. (2015), no other group of the periodic system presents such similarity as REM. They usually have a 3+ oxidation state and very close ionic radii, which the replacement of one REM by another is free from impediments in several adsorbent sites. However, REM presents slight differences among themselves regarding the solubility of their compounds or the formation of complexes. Thus, the selectivity tests of Table 2.1 evaluated the Nd and Dy selectivity from a solution containing different groups of metals (Ahmed et al., 2021; Brião et al., 2020; G. de V. Brião et al., 2021a, 2021b; G. V. Brião et al., 2021; Pei et al., 2021; Ravi et al., 2022; Tu et al., 2019) and investigated the affinity between the rare earths (Abdel-Magied et al., 2019; Awual et al., 2017; Bai et al., 2020; Elsalamouny et al., 2017; Kaneko et al., 2018; Ravi et al., 2019, 2018).

From a mixture of bi- and monovalent metals, REM can be selectively adsorbed due to the higher positive charge that is attracted strongly to the negatively charged sites in the adsorbent surface (Abdel-Magied et al., 2019). The selectivity order of the adsorbent material from Table 2.1 was justified repeatedly by the hard and soft acid/base theory, in which hard Lewis bases

($-\text{PO}_3^{2-}$, COOH , carbonyls, amino groups) binds preferably to hard Lewis's acids as rare earth metals (REM^{3+}) with the smallest ionic radii by coordination complexes (Abdel-Magied et al., 2019; Liu et al., 2017; Ravi et al., 2022, 2019). In the case of the ion-imprinted polymer-based adsorbents, the steric effect of the imprinted cavities also plays a relevant role in the selection mechanism (Liu et al., 2017).

2.7 NEODYMIUM AND DYSPROSIUM ADSORPTION FROM MIXTURES ON BATCH MODE AND CONTINUOUS FIXED BED

Literature reporting complete study of multicomponent (Nd and Dy) adsorption on batch mode (Table 2.3) and continuous fixed-bed studies (Table 2.4) are discussed separately from the single adsorption on batch mode (Table 2.1) because their approaches and findings are distinct.

Complete studies of Nd and Dy adsorption (Table 2.3) from multicomponent solutions (binary, ternary, or other possible mixtures, including actual samples containing Nd and Dy), differently from the monocomponent studies, scrutinizes the competitive and/or synergic effects of the metal's adsorption on the kinetics, equilibrium, and desorption behavior.

The Nd and Dy adsorption studies from binary and ternary mixtures showed that, in general, the PSO models govern the kinetics, which agrees with the monocomponent studies.

According to Table 2.3, the multicomponent equilibrium was not modeled mathematically, except for the binary Nd and Dy adsorption on ion-imprinted mesoporous bilayer film, which Langmuir model described the equilibrium behavior (Zheng et al., 2018). Besides the well-known isothermal models, there are also multiadsorbate isotherm equations such as the ideal adsorbed solution theory, the most applied multicomponent model, that permit the prediction of mixture adsorption equilibria without being linked to a particular single-solute isotherm model (Radke and Prausnitz, 1972; Worch and Eckhard, 2012). Such accurate competitive adsorption modeling is still lacking in REM adsorption studies.

Table 2.3 – Adsorption of Nd and Dy (multicomponent studies) on batch mode.

Adsorbent	Adsorbate Mixture	Adsorption conditions	Kinetics	Equilibrium	Selectivity	Desorption	Reuse (adsorptive performance)	Ref.
Organophosphorous loaded octadecyl methacrylate film	Binary Dy and Nd (100 mg/L each)	150 rpm pH 2.0 $A_{\text{film}} = 4 \text{ cm}^2$ $V = 50 \text{ mL}$	-	Nd = 1.0 mg/g Dy = 26.0 mg/g	Dy >> Nd	HCl (1 M)	Dy = 25.3 mg/g (2 nd) Nd = 0.8 mg/g (2 nd)	(Hoshina et al., 2020)
Ionic imprinted mesoporous bilayer films	Binary Nd and Dy (50 mg/L each)	$C_{\text{ads}} = 1 \text{ g/L}$ pH 4.0	PSO	Langmuir Nd ($q_m = 13.2 \text{ mg/g}$ and $K_L = 0.09 \text{ L/mg}$) Dy ($q_m = 18.6 \text{ mg/g}$ and $K_L = 0.11 \text{ L/mg}$)	Dy > Nd > (Pr, Tb, and Fe)	Temperature Stripping (313 K)	Nd = 15% (1 st) - 12 % (5 th) Dy = 10% (1 st) - 8 % (5 th)	(Zheng et al., 2018)
Amorphous zirconium phosphate	Ternary Nd, Dy, Co (0.01 to 10 mM each)	$C_{\text{ads}} = 5 \text{ g/L}$ pH 3.0 60 rpm	PSO	Nd = 86.5 mg/g Dy = 113.7 mg/g Co = 5.59 mg/g	Dy ~ Nd > Co	H ₂ SO ₄ (1M) Nd = 85% Dy = 83%	-	(Xu et al., 2018b)

Regarding the selectivity experiments, the higher selectivity between Dy and Nd was achieved by the organophosphorus-loaded octadecyl methacrylate film, followed by ionic imprinted mesoporous bilayer films, which performance in the Nd and Dy selective adsorption was attributed to the combination of the organosilane chelation and dual-template docking oriented ionic imprinting process. These findings are comparable to those achieved by the selectivity tests in Table 2.1, in which the phosphorous functionalization and ion-imprinted processes are the most efficient in improving the REM selectivity.

The desorption step occurred majority using strong acids (HCl and H₂SO₄) as the single desorption (Table 2.1). However, thermal stripping at 313 K (Zheng et al., 2018), a moderate temperature, was also used as a more cost-effective and less dangerous alternative to acid elution. Yet, the reusability tests evaluated just a few cycles and used the adsorptive performance as efficiency criteria, neglecting the desorption/recovery. Thus, future studies should also deeply investigate the reusability of the adsorbents in cyclic adsorption and desorption of mixtures in batch mode.

As shown in Table 2.1, many studies addressed the adsorption of Nd and Dy in batch mode, and some novel adsorbent materials achieved remarkable potential. However, batch adsorptive processes are generally limited to treating small volumes of effluents in industrial applications, and continuous fixed-bed adsorption systems are indicated to treat large amounts of wastewater. Ergo, the study and development of continuous fixed-bed studies are needed to advance the REM adsorption towards actual applications. A literature review limited to the published papers of the last five years was done regarding the Nd and Dy fixed-bed adsorption with a focus on recovery, and just a few articles were found, which the main findings are demonstrated in Table 2.4.

The liquid is fed continuously to the top or bottom of a stationary adsorbent bed in dynamic fixed bed REM adsorption systems. When maximum adsorption capacity is reached, the bed is regenerated and reused. The studies presented in Table 2.4 were conducted on a lab scale, in which the columns applied have small dimensions, the bed volumes do not surpass 7.85 mL, and the flow rates are smaller than 2 mL/min.

Table 2.4 – Adsorption of Nd and Dy (multicomponent studies) on continuous fixed-bed mode.

Adsorbent	Adsorbate Mixture	Adsorption conditions	Fixed-bed efficiency	Selectivity	Reusability	Ref.
Agarose beads functionalized with lanmodulin protein	Nd (28.9 mg/L)	$H = 5$ cm $D_i = 0.5$ cm $BV = 0.94$ mL $Q = 0.5$ mL/min pH 3.0	Nd (0.832 mg/g)	Nd = Y = La = Dy = Lu (no interference of competing ions)	Eluent: HCl (pH 1.5) CF = 14 No reduction of efficiency along 10 cycles	(Dong et al., 2021)
<i>Escherichia coli</i> encapsulated in permeable polyethylene glycol diacrylate	Nd (0.5 mg/L)	$H = 20$ cm $D_i = 0.5$ cm $BV = 7.85$ mL $Q = 1.93$ mL/min pH 6.0	Nd (2.6 mg/g)	Dy > Nd > Pr > (Zn, Co, Ni, Fe, Mn)	Eluent: citrate 10 mmol/L Desorption: 94% CF = 6 0.21 mg/g (1 st) to 0.18 mg/g (9 th)	(Brewer et al., 2019b)
Organophosphorous loaded octadecyl methacrylate	Binary Dy and Nd (100 mg/L each)	$D_i = 0.7$ cm $BV = 0.2$ mL $Q = 0.33$ mL/min pH 2.0	Dy (43.6 mg/g) Nd (4.2 mg/g)	Dy >> Nd	Eluent: HCl 1 mol/L Desorption: Dy 99% and Nd 98% CF _{Dy} = 3.73 and CF _{Nd} = 0.38 Almost same behavior at the second use	(Hoshina et al., 2020)
Amorphous zirconium phosphate	Ternary Nd, Dy, Co (0.01 mmol/L each)	$H = 5.5$ cm $D_i = 1$ cm $BV = 4.32$ mL $Q = 0.144$ mL/min pH 1.8	Dy (86.1 mg/g) Nd (39.9 mg/g) Co (0.5 mg/g)	Dy > Nd >> Co	Eluent: HNO ₃ (from 0.1 to 0.5 mol/L) Desorption: Dy 97.5%, Nd 78.3%, Co 0% CF _{Dy} = 17 and CF _{Nd} = 13	(Xu et al., 2018b)
Expanded Vermiculite	Nd (72.1 mg/L)	$H = 7$ cm $D_i = 0.7$ cm $BV = 2.69$ mL $Q = 0.25$ mL/min pH = 3.3	Nd (57.7 mg/g)	-	Eluent: CaCl ₂ 0.3 mol/L Desorption: 69.7%*; CF= 25.0* 57.7 mg/g (1 st) to 54.8 mg/g (5 th)	(Brião et al., 2022b)
	Dy (81.2 mg/L)	$H = 7$ cm $D_i = 0.7$ cm $BV = 2.69$ mL $Q = 0.25$ mL/min pH = 3.5	Dy (68.3 mg/g)	Dy >> Pb > Ni > Cd > Cu	Eluent: Mg(NO ₃) ₂ 0.25 mol/L Desorption: 94.7%*; CF= 41.2* 68.25 mg/g (1 st) to 65.0 mg/g (5 th)	(Brião et al., 2022a)

* Average value along with the cycles

Comparing the bed efficiencies (Equation 2.10), the amorphous zirconium phosphate achieved the highest adsorption capacity for Dy (86.1 mg/g) and expanded vermiculite for Nd (57.7 mg/g).

$$q_e = \frac{C_0 Q}{1000m} \int_0^{t_e} \left(1 - \frac{C}{C_0}\right) dt \quad (2.10)$$

Where C_0 is the metal inlet concentration (mmol/L or mg/L); Q is the flow rate (ml/min); m is the adsorbent mass (g); t_e is the exhaustion time (min), and C is the metal outlet concentration (mmol/L or mg/L).

The equilibrium adsorption capacities achieved in fixed-bed mode are different from those achieved in batch mode by the same adsorbent (Table 2.3) due to the different concentrations used in each study and because of the limitations of mass transfer and axial dispersion of the fixed-bed operation, which leads to lower adsorption capacity than batch mode (Chatterjee et al., 2018; Costa et al., 2020). However, comparing the range of the adsorption capacities of Table 2.1 and Table 2.4, the studies monocomponent in batch mode reached much higher adsorption capacities because many of the more efficient adsorbents of Table 2.1 have the size in nanoscale that leads to improved surface areas, such as the porous covalent organic polymers comprising a phosphite skeleton (Ravi et al., 2019) and polyurethane sponge-supported graphene oxide–titanium phosphate (Peng et al., 2021). The nano adsorbents, despite their high surface area, fast kinetics, and high adsorption capacities, are unfeasible for fixed-bed applications due to the bed packing limitations and obstruction of the inlet flow. Thus, highly efficient adsorbents for the Nd and Dy uptake still need to be developed regarding their morphology and stability for fixed-bed operations.

The selectivity was also evaluated in the fixed-bed studies, in which the agarose beads functionalized with protein and encapsulated bacteria in permeable polyethylene glycol diacrylate are highly selective towards REM compared to light and base metals. Organophosphorous-loaded octadecyl methacrylate has a more considerable affinity towards Dy than Nd, and amorphous zirconium phosphate can efficiently separate Dy and Nd from a mixture with cobalt.

The reusability in a fixed-bed operation is also an essential factor to be evaluated, as it determines the economic viability of the process. In the studies in Table 2.4, the most used eluents were strong acids that showed high desorption efficiency. Also, the step-by-step

desorption experiments by (Xu et al. (2018b)), in which nitric acid in different concentrations was applied at specific elution times, showed that distinguishable peaks of release could be achieved to improve the separation. The studies exhibited concentration factors (CF) from 0.38 (Hoshina et al., 2020) to 41.2 (Brião et al., 2022a), showing that the elution of the expanded vermiculite bed was able to concentrate 41.2 times the original inlet solution. The study developed for Hoshina et al. (2020) achieved distinct CF for the REMs; Dy was about ten times more concentrated in the eluate than Nd, indicating the high separation efficacy of the process due to the highly selective adsorption. In general, the agarose beads and expanded vermiculite presented excellent reproducibility, corroborating the stability of the adsorbent materials.

2.8 CONTRIBUTION OF ND AND DY RECOVERY BY ADSORPTIVE PROCESSES TO THE DEVELOPMENT OF THE CIRCULAR ECONOMY: CHALLENGES AND PROSPECTS

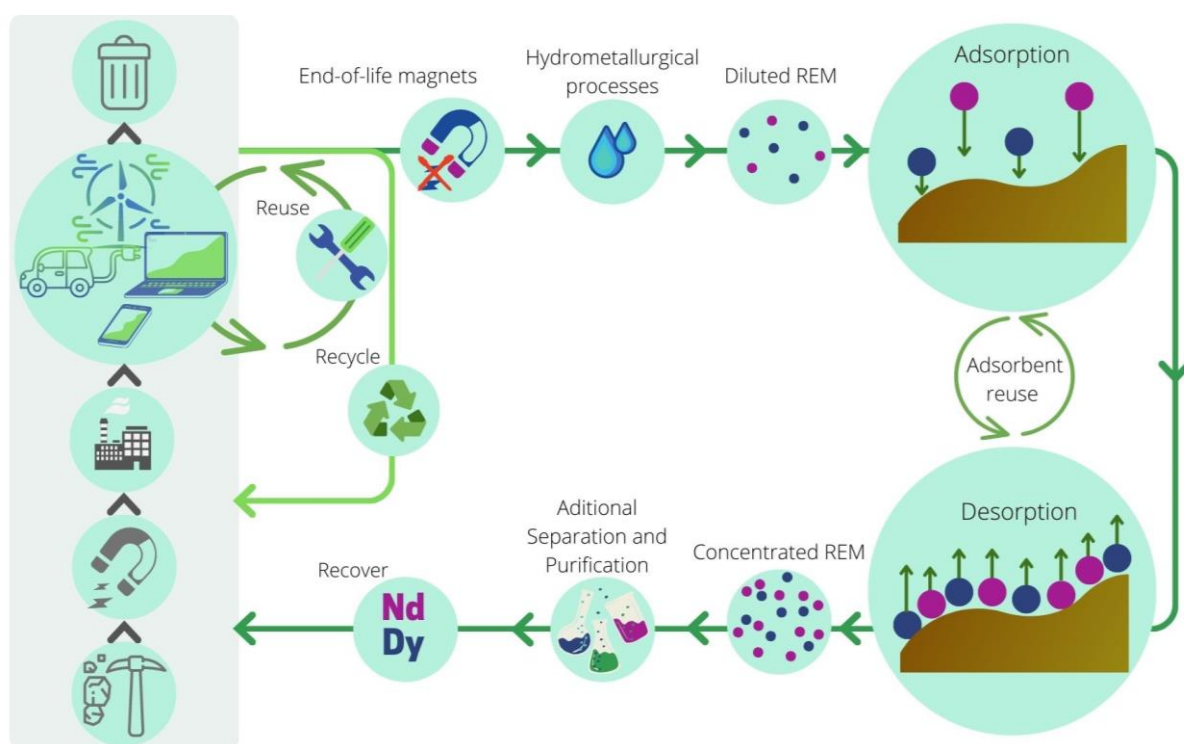
As mentioned above, e-waste could become one of the most promising candidates for NdFeB magnet recycling and REM extraction (Dang et al., 2021). NdFeB recycling, despite the challenging disassembly, presented expressive gains in environmental and economic aspects compared to primary production (Wang et al., 2022), so much so that some factories have already started marketing recycled magnets, such as the Okon Metals INC. (USA) and the HyproMag Ltd. (UK).

Despite the greater maturity of recycling technologies, REM recovery of NdFeB magnets is still under development. However, Amato et al. (2019) pointed out that secondary Nd productions from permanent magnets can reduce CO₂ emissions by 6 times and 7.1 times the production cost compared to the primary, which confirms the possible advantage derived from the extraction of REMs from permanent magnets from both environmental and the economic point of view. Considering the recovery of Nd from spent hard disk magnets by hydrometallurgical processes, the recent life cycle assessment (LCA) and economic analysis performed by Karal et al. (2021) indicated that the scaled-up Nd metal recovery system would reduce environmental impacts, such as climate change from 30.5 to 22.8 kg CO₂ eq, terrestrial ecotoxicity from 0.47 to 0.16 kg 1,4 dichlorobenzene eq (1,4 DCB eq), freshwater and marine aquatic ecotoxicity from 16.0 to 13.8 kg 1,4 DCB eq, and 6.74 to 4.75 x 10⁵ kg 1,4 DCB eq, respectively, ozone layer depletion from 3.96 to 2.70 x 10⁻⁶ kg CFC-11 eq, human toxicity from 72.8 to 52.5 kg 1,4 DCB eq, and depletion of abiotic resources – fossil fuels from 440 to 297

MJ. And Nd recovery would lower the production cost of Nd-Fe-B magnets from 8.55 to 3.98 USD/kg, reducing 53.3%.

In this context, where the hydrometallurgical processes are an advantageous alternative, the present Review evidenced that many studies have been carried out on the recovery of Nd and Dy, critical REMs present in NdFeB magnets, from aqueous solutions by sorption processes, which have the potential to reconcentrate and reintroduce these metals to the market, contributing for production and closed cycle of consumption (Figure 2.5). This work shows that diverse adsorbent materials have been applied in the adsorption and recovery of Nd and Dy, such as ion-imprinted polymers, carbon-based materials, metal-organic frameworks, magnetic particles, clays, and functionalized silica. The advantages and disadvantages of these materials are compiled in Table 2.5.

Figure 2.5 – Contribution of Nd and Dy recovery by adsorptive processes to the circular economy



Danaci et al. (2021) pointed out promising adsorbents should be highly efficient, reusable, and selective. Also, it should exhibit tolerance to impurities, rapid mass transfer, sufficiently high density, low cost, and low environmental and safety impacts to be viable for large-scale applications. The adsorbent materials used for REM adsorption reviewed in this study (Table

2.5) fulfilled many of the above criteria, especially in relation to optimal textural properties, stability, cost, and versatility. Yet, most materials have a similar drawback, the need for functionalization or modification to achieve high levels of selectivity.

Considering essential factors such as efficiency, selectivity, and stability, the most promising adsorbents were the phosphorus-functionalized polymer-based adsorbents that achieved high adsorption capacities of 321.0 mg/g (Ravi et al., 2019), and 576.2 mg/g (Peng et al., 2021) for Nd and Dy, respectively; and attained remarkable selectivity among rare earth metals (Hoshina et al., 2020), where phosphate improved surface coordination complexation mechanisms. However, the raw material to synthesize the adsorbents can also have lower yields, increasing the final cost of the adsorbents, making REM recovery less competitive with primary extraction. Thus, alternative raw materials such as agro-industrial wastes biomasses, abundant minerals (zeolites and clays), and biopolymers should be applied for the sustainable production of adsorbents to promote REM circularity.

Table 2.5 – Main advantages and drawbacks of each adsorbent matrix.

Adsorbent	Advantages	Disadvantages
Polymer-based	<ul style="list-style-type: none"> • Easy functionalization • Ecofriendly (biopolymers) • Low cost • High adsorption capacity and selectivity • Possible to apply the ion-impression technique 	<ul style="list-style-type: none"> • Price of the ion-impression • Scalability of the use of biopolymers • Need of functionalization or modification to enhance selectivity
Carbon-based	<ul style="list-style-type: none"> • Presence of hydroxyl, carbonyl, and carboxyl groups • High surface area • Ecofriendly (activate carbon from biomass) 	<ul style="list-style-type: none"> • Functionalization is recommended for the selective adsorption of REM • Complex surface structures highly dependent on the raw materials, pre-treatment, and production methods • Cost of the GO and derivatives
MOF	<ul style="list-style-type: none"> • High specific surface area • Tunable pore sizes • Thermal and chemical stability 	<ul style="list-style-type: none"> • Weak interactions • Need of modifications or functionalization to improve REM recovery
Magnetic nanoparticles	<ul style="list-style-type: none"> • High surface area 	<ul style="list-style-type: none"> • Colloidal instability • Agglomeration • Environmental issues

	<ul style="list-style-type: none"> • It can be used in the adsorbent composition to improve the S/L separation • Easy doping with functional groups 	
Clays	<ul style="list-style-type: none"> • Negatively charged surface • High cation exchange capacity • Low cost • Availability 	<ul style="list-style-type: none"> • Need for functionalization and modifications to achieve a high level of selectivity • Low resistance at extreme pHs
Silica-based	<ul style="list-style-type: none"> • Significant surface area • Mechanical, chemical, and thermal stabilities • Simple chemical synthesis • Availability and scalability • Possibility to immobilize various functional groups 	<ul style="list-style-type: none"> • Non-selective adsorption • Need of functionalization with aliphatic and aromatic oxygen, nitrogen, and sulfur-containing groups • Low resistance at high pH

Moreover, the kinetic, equilibrium, and thermodynamic findings showed that, in general, the adsorption of neodymium and dysprosium was described by chemical and endothermic sorption, in which the adsorbent saturation forms homogenous monolayers of adsorbate. Reuse tests indicated that strong acids had the best recovery response. The best adsorption/desorption efficiency was achieved using a covalent porous organic polymer based on benzylphosphate as adsorbent and hydrochloric acid (0.25 mol/L) as eluent, which only reduced 8% of the original adsorption (98 %) and desorption (96 %) efficiencies along with ten cycles of reuse. The selectivity of the adsorbents was governed by the Lewis's theory, in which hard bases ($-\text{PO}_3^{2-}$, COOH , carbonyls, amino groups) bind preferentially to REM hard Lewis acids with the smallest ionic radii. The few studies of Nd and Dy adsorption from binary and ternary mixtures corroborate the findings of adsorption of a single metal in batch mode. The main results in continuous fixed bed were related to the selectivity and reuse experiments that achieved an effective separation and concentration of REM using strong acids (usual), thermal stripping, and step-by-step procedures, which are significant indicators for the efficient recovery of Nd and Dy in real and large-scale applications.

The findings of recent studies discussed in this work indicate the potential of adsorptive processes to recover Nd and Dy in hydrometallurgical routes. However, some gaps should be explored in future research for the processes to reach a higher level of maturity, such as accurate modeling, development of novel desorption processes towards REM recovery, reuse and

sustainability, further studies in continuous fixed-bed system in laboratory and pilot scales, and complete investigations of the adsorption in real or simulated samples.

The studies on REM adsorption are deficient in adsorption modeling. Mass transfer models are rarely applied, the competitive adsorption is usually not mathematically described, and the breakthrough curves usually are not used to obtain kinetic rates and mass transfer coefficients that are indispensable for scale-up purposes. Besides the classical mathematical modeling approaches, machine learning methodologies have been gaining attention in environmental remediation (Dotto and McKay, 2020). They can be an alternative to predict the multivariate REM adsorption and desorption.

Regardless of the significant number of studies of Nd and Dy adsorption in batch mode (Table 2.1), just a few works investigate the REM adsorption and desorption in fixed-bed operations (Table 2.4). Convoluting this scenario, the adsorbent reusability and the REM recovery are scarcely pondered at once. Due to the high added value of REMs, in the REM recovery, adsorption and desorption efficiencies must be increased over the cycles to consider this sorbent technically viable, differently for environmental remediation where the adsorbent regeneration is the main desorption goal. Another exciting trend in the desorption process is the reuse of the eluent along with the cycles that would produce more REM-rich eluate (much more concentrated), meaning higher recovery efficiency; would reduce the eluent consumption and cost; would lead to a lower generation of hazardous effluents and consequently lower cost with the effluent treatment, improving the overall process sustainability.

The lack of fixed-bed studies can be related to the adsorbent-specific morphology required for this operation mode. Nanosorbents, for example, despite their many advantages, are materials unable to be used in fixed-bed due to the limitations of packing and solid/liquid separation. Thus, besides sustainability and cost-effectiveness of the adsorbents, the morphology and size should be included as decisive criteria for Nd, and Dy adsorption from secondary sources, since that, for industrial scale, the fixed-bed operation is the most recommended.

Another point to be further developed is the evaluation of the adsorptive performance of the materials using actual samples; in the case proposed in this study, recovering REM from spent NdFeB magnets by hydrometallurgical routes applying sorbents to reconcentrate and recover the interesting REM. Besides that, acid mine drainage, red mud, acid leachate of landfills, wastewater treatment sludge, and pre-consumer NdFeB magnets residue should be considered potential secondary sources of REM.

In addition to the demand for more experimental studies, review work should also be performed addressing desorption and recovery, including mechanism, safety, environmental impacts, and cost of the eluents. In the same way as this present review, the potential of the adsorption to recover REM from other secondary sources should be reviewed to compile the main composition of these sources, as adsorption could contribute to the concentration of REM, contributing to this construction, thus, of a complete view of the real scenario of the REM recovery. Following the structure of other interesting review works (Cardoso et al., 2019; Costa et al., 2020; Kegl et al., 2020), the polymer-based adsorbents that had the most outstanding selectivity results could be explored in detail in a review of their unique physicochemical properties, functionalization methods, and their effect on REM selective and reproductive adsorption.

Thereby, the state-of-the-art of Nd and Dy recovery from secondary sources by adsorption moves towards the development of novel, selective, stable, and eco-friendly adsorbents with low cost and high availability that are the same inherent characteristics as the desirable sorbent for environmental remediation and water purification for both batch and fixed-bed operation modes. However, for the REM recovery purpose, the desorption process plays an important role. It still needs to be developed to guarantee the sorbent's complete regeneration, concentrate/recover the interesting REM, and allow multiple uses of the sorbent and the eluent solution. Those criteria are fundamental to integrating the adsorption operation in the hydrometallurgical routes for the REM recovery, regressing to the productive chain, and improving the circular economy of rare earth metals.

2.9 CONCLUSIONS

The recovery by hydro processing of rare earth metals from NdFeB magnets has been widely studied, as well as the recovery by adsorptive processes that have gained notorious attention lately due to their excellent performance in diluted systems. This article reviewed recent studies that managed the adsorption and desorption (recovery) of Nd and Dy, in which adsorbent matrices, kinetics, equilibrium, thermodynamics, selectivity towards Nd and Dy, and reuse in batch mode and fixed bed were discussed in detail. Novel adsorbents such as ion-imprinted polymers, high porous carbon-based materials, and metal-organic frameworks were the most applied materials in the literature. The kinetic, equilibrium, and thermodynamic findings indicated the predominance of chemical sorption, formation of monolayers, and a positive effect of temperature (endothermic). The best reuse performance was achieved using a

porous phosporous-based polymer as adsorbent and hydrochloric acid as eluent, maintaining high adsorption and desorption efficiencies with ten cycles of use. Lewis theory governed the selectivity of adsorbents, where functionalization with acid groups and ion-imprinting techniques had the most significant responses. Only a few relevant works focused on the complete study of competitive adsorption, evaluating synthetic and real samples, and application in continuous fixed bed. In these cases, the adsorption capacities were much lower than those found in single adsorption studies, which means that the synthesis of adsorbents still needs to be enhanced in future studies to achieve real applications. Further research on the modeling of competitive REM adsorption and development of novel desorption processes for REM recovery and reuse should also be performed. Thus, despite the promising results, the adsorption processes must be improved to reach the highest levels of maturity necessary for large-scale operation to advance towards the REM circular economy.

ACKNOWLEDGMENT

This work was funded by São Paulo Research Foundation/FAPESP (Grant #2017/18236-1), Brazilian National Council for Scientific and Technological Development/CNPq (Grant # 308046/2019-6 and Grant # 147606/2018-7), and Coordination for the Improvement of Higher Education Personnel/CAPES (Financial code 001).

REFERENCES

- Abdel-Magied, A.F., Abdelhamid, H.N., Ashour, R.M., Zou, X., Forsberg, K., 2019. Hierarchical porous zeolitic imidazolate frameworks nanoparticles for efficient adsorption of rare-earth elements. *Microporous and Mesoporous Materials* 278, 175–184. <https://doi.org/10.1016/j.micromeso.2018.11.022>
- Ahmed, I., Bhattacharjee, S., Lee, C.S., Kang, K.K., Ahn, J.W., Ahn, W.S., 2021. Aqueous Nd³⁺ capture using a carboxyl-functionalized porous carbon derived from ZIF-8. *J Colloid Interface Sci* 594, 702–712. <https://doi.org/10.1016/j.jcis.2021.03.036>
- Alshameri, A., Wei, X., Wang, H., Fuguo, Y., Chen, X., He, H., Yan, C., Xu, F., 2019. A Review of the Role of Natural Clay Minerals as Effective Adsorbents and an Alternative Source of Minerals, in: *Minerals*. IntechOpen. <https://doi.org/10.5772/intechopen.87260>
- Amato, A., Becci, A., Birloaga, I., de Michelis, I., Ferella, F., Innocenzi, V., Ippolito, N.M., Pillar Jimenez Gomez, C., Vegliò, F., Beolchini, F., 2019. Sustainability analysis of

- innovative technologies for the rare earth elements recovery. *Renewable and Sustainable Energy Reviews* 106, 41–53. <https://doi.org/10.1016/j.rser.2019.02.029>
- Awual, M.R., Alharthi, N.H., Okamoto, Y., Karim, M.R., Halim, M.E., Hasan, M.M., Rahman, M.M., Islam, M.M., Khaleque, M.A., Sheikh, M.C., 2017. Ligand field effect for Dysprosium(III) and Lutetium(III) adsorption and EXAFS coordination with novel composite nanomaterials. *Chemical Engineering Journal* 320, 427–435. <https://doi.org/10.1016/j.cej.2017.03.075>
- Bai, B., Zhang, Z., Zhao, X., 2020. Enhanced Adsorption of Rare Earth Elements by a Poly(Itaconic Acid)/Magnetite Sepiolite Composite. *Anal Lett* 54, 1881–1899. <https://doi.org/10.1080/00032719.2020.1828907>
- Borst, A.M., Smith, M.P., Finch, A.A., Estrade, G., Villanova-de-Benavent, C., Nason, P., Marquis, E., Horsburgh, N.J., Goodenough, K.M., Xu, C., Kynický, J., Geraki, K., 2020. Adsorption of rare earth elements in regolith-hosted clay deposits. *Nat Commun* 11, 4386. <https://doi.org/10.1038/s41467-020-17801-5>
- Branger, C., Meouche, W., Margailan, A., 2013. Recent advances on ion-imprinted polymers. *React Funct Polym* 73, 859–875. <https://doi.org/10.1016/j.reactfunctpolym.2013.03.021>
- Brewer, A., Dohnalkova, A., Shutthanandan, V., Kovarik, L., Chang, E., Sawvel, A.M., Mason, H.E., Reed, D., Ye, C., Hynes, W.F., Lammers, L.N., Park, D.M., Jiao, Y., 2019a. Microbe Encapsulation for Selective Rare-Earth Recovery from Electronic Waste Leachates. *Environ Sci Technol* 53, 13888–13897. <https://doi.org/10.1021/acs.est.9b04608>
- Brewer, A., Dohnalkova, A., Shutthanandan, V., Kovarik, L., Chang, E., Sawvel, A.M., Mason, H.E., Reed, D., Ye, C., Hynes, W.F., Lammers, L.N., Park, D.M., Jiao, Y., 2019b. Microbe Encapsulation for Selective Rare-Earth Recovery from Electronic Waste Leachates. *Environ Sci Technol* 53, 13888–13897. <https://doi.org/10.1021/acs.est.9b04608>
- Brião, G. de V., Agostinho, F.A., da Silva, M.G.C., Vieira, M.G.A., 2022a. Renewable and Selective Vermiculite Fixed Bed for the Rare-Earth Dysprosium Recovery. *Ind Eng Chem Res.* <https://doi.org/10.1021/acs.iecr.2c01265>
- Brião, G. de V., da Silva, M.G., Vieira, M.G.A., 2021a. Expanded vermiculite as an alternative adsorbent for the dysprosium recovery. *J Taiwan Inst Chem Eng* 127, 228–235. <https://doi.org/10.1016/j.jtice.2021.08.022>

- Brião, G. de V., da Silva, M.G.C., Vieira, M.G.A., 2022b. Reusable and efficient clay material for the fixed-bed neodymium recovery. *Sustain Chem Pharm* 25, 100623. <https://doi.org/10.1016/j.scp.2022.100623>
- Brião, G. de V., da Silva, M.G.C., Vieira, M.G.A., 2021b. Efficient and Selective Adsorption of Neodymium on Expanded Vermiculite. *Ind Eng Chem Res* 60, 4962–4974. <https://doi.org/10.1021/acs.iecr.0c05979>
- Brião, G. de V., Silva, M.G.C. da, Vieira, M.G.A., 2020. Neodymium recovery from aqueous solution through adsorption/desorption onto expanded vermiculite. *Appl Clay Sci* 198, 105825. <https://doi.org/10.1016/j.clay.2020.105825>
- Brião, G.V., da Silva, M.G.C., Vieira, M.G.A., 2021. Dysprosium adsorption on expanded vermiculite: Kinetics, selectivity and desorption. *Colloids Surf A Physicochem Eng Asp* 630, 127616. <https://doi.org/10.1016/j.colsurfa.2021.127616>
- Bullen, J.C., Saleesongsom, S., Gallagher, K., Weiss, D.J., 2021. A Revised Pseudo-Second-Order Kinetic Model for Adsorption, Sensitive to Changes in Adsorbate and Adsorbent Concentrations. *Langmuir* 37, 3189–3201. <https://doi.org/10.1021/acs.langmuir.1c00142>
- Cardoso, C.E.D., Almeida, J.C., Lopes, C.B., Trindade, T., Vale, C., Pereira, E., 2019. Recovery of rare earth elements by carbon-based nanomaterials—a review. *Nanomaterials*. <https://doi.org/10.3390/nano9060814>
- Cashin, V.B., Eldridge, D.S., Yu, A., Zhao, D., 2018. Surface functionalization and manipulation of mesoporous silica adsorbents for improved removal of pollutants: A review. *Environ Sci (Camb)*. <https://doi.org/10.1039/c7ew00322f>
- Charalampides, G., Vatalis, K.I., 2015. Global Production Estimation of Rare Earth Elements and Their Environmental Impacts on Soils. *Journal of Geoscience and Environment Protection* 03, 66–73. <https://doi.org/10.4236/gep.2015.38007>
- Charalampides, G., Vatalis, K.I., Apostoplos, B., Ploutarch-Nikolas, B., 2015. Rare Earth Elements: Industrial Applications and Economic Dependency of Europe. *Procedia Economics and Finance* 24, 126–135. [https://doi.org/10.1016/S2212-5671\(15\)00630-9](https://doi.org/10.1016/S2212-5671(15)00630-9)
- Chatterjee, S., Mondal, S., De, S., 2018. Design and scaling up of fixed bed adsorption columns for lead removal by treated laterite. *J Clean Prod* 177, 760–774. <https://doi.org/10.1016/j.jclepro.2017.12.249>
- Connelly, N.G., Damhus, T., Hartshorn, R.M., Hutton, A.T., 2005. Nomenclature of Inorganic Chemistry: IUPAC Recommendations 2005. The Royal Society of Chemistry.

- Costa, T.B. da, Silva, M.G.C. da, Vieira, M.G.A., 2020. Recovery of rare-earth metals from aqueous solutions by bio/adsorption using non-conventional materials: a review with recent studies and promising approaches in column applications. *Journal of Rare Earths* 38, 339–355. <https://doi.org/10.1016/j.jre.2019.06.001>
- da Costa, T.B., da Silva, M.G.C., Vieira, M.G.A., 2021. Recovery of dysprosium by biosorption onto a biocomposite from sericin and alginate. *Journal of Water Process Engineering* 44. <https://doi.org/10.1016/j.jwpe.2021.102388>
- da Silva, T.L., da Costa, T.B., Neves, H.S. de C., da Silva, M.G.C., Vieira, M.G.A., 2021. Methods of Synthesis of Magnetic Adsorbents. pp. 25–58. https://doi.org/10.1007/978-3-030-64092-7_2
- Danaci, D., Webley, P.A., Petit, C., 2021. Guidelines for Techno-Economic Analysis of Adsorption Processes. *Frontiers in Chemical Engineering* 2. <https://doi.org/10.3389/fceng.2020.602430>
- Dang, D.H., Thompson, K.A., Ma, L., Nguyen, H.Q., Luu, S.T., Duong, M.T.N., Kernaghan, A., 2021. Toward the Circular Economy of Rare Earth Elements: A Review of Abundance, Extraction, Applications, and Environmental Impacts. *Arch Environ Contam Toxicol*. <https://doi.org/10.1007/s00244-021-00867-7>
- de Andrade, J.R., Brião, G. de V., da Silva, M.G.C., Vieira, M.G.A., 2021. Removal of Emerging Pollutants Using Magnetic Adsorbents. pp. 187–222. https://doi.org/10.1007/978-3-030-64092-7_7
- de Farias, A.B.V., da Costa, T.B., da Silva, M.G.C., Vieira, M.G.A., 2021. Cerium recovery from aqueous solutions by bio/adsorption: A review in a circular economy context. *J Clean Prod*. <https://doi.org/10.1016/j.jclepro.2021.129395>
- de Gisi, S., Lofrano, G., Grassi, M., Notarnicola, M., 2016. Characteristics and adsorption capacities of low-cost sorbents for wastewater treatment: A review. *Sustainable Materials and Technologies* 9, 10–40. <https://doi.org/10.1016/j.susmat.2016.06.002>
- Diagboya, P.N.E., Dikio, E.D., 2018. Silica-based mesoporous materials; emerging designer adsorbents for aqueous pollutants removal and water treatment. *Microporous and Mesoporous Materials*. <https://doi.org/10.1016/j.micromeso.2018.03.008>
- Dong, Z., Mattocks, J.A., Deblonde, G.J.P., Hu, D., Jiao, Y., Cotruvo, J.A., Park, D.M., 2021. Bridging Hydrometallurgy and Biochemistry: A Protein-Based Process for Recovery and Separation of Rare Earth Elements. *ACS Cent Sci* 7, 1798–1808. <https://doi.org/10.1021/acscentsci.1c00724>

- Dotto, G.L., McKay, G., 2020. Current scenario and challenges in adsorption for water treatment. *J Environ Chem Eng* 8. <https://doi.org/10.1016/j.jece.2020.103988>
- Dubinín, M.M., Radushkevich, L.V., 1947. The equation of the characteristic curve of activated charcoal. *Proceedings of the Academy of Sciences of USSR* 55, 331.
- Dudarko, O., Kobylinska, N., Kessler, V., Seisenbaeva, G., 2022. Recovery of rare earth elements from NdFeB magnet by mono- and bifunctional mesoporous silica: Waste recycling strategies and perspectives. *Hydrometallurgy* 210. <https://doi.org/10.1016/j.hydromet.2022.105855>
- Durán, S.V., Lapo, B., Meneses, M., Sastre, A.M., 2020. Recovery of neodymium (III) from aqueous phase by chitosan-manganese-ferrite magnetic beads. *Nanomaterials* 10, 1–12. <https://doi.org/10.3390/nano10061204>
- Elsalamouny, A.R., Desouky, O.A., Mohamed, S.A., Galhoum, A.A., Guibal, E., 2017. Evaluation of adsorption behavior for U(VI) and Nd(III) ions onto fumarated polystyrene microspheres. *J Radioanal Nucl Chem* 314, 429–437. <https://doi.org/10.1007/s10967-017-5389-5>
- Ettehadí Gargari, J., Sid Kalal, H., Shakeri, A., Khanchi, A., 2017. Synthesis and characterization of Silica/polyvinyl imidazole/H₂PO₄-core-shell nanoparticles as recyclable adsorbent for efficient scavenging of Sm(III) and Dy(III) from water. *J Colloid Interface Sci* 505, 745–755. <https://doi.org/10.1016/j.jcis.2017.06.059>
- Favot, M., Massarutto, A., 2019. Rare-earth elements in the circular economy: The case of yttrium. *J Environ Manage* 240, 504–510. <https://doi.org/10.1016/j.jenvman.2019.04.002>
- Freundlich, H.M.F., 1906. Over the Adsorption in Solution. *J. Phy. Chem* 57, 385–470.
- Gao, L., Kano, N., Sato, Y., Li, C., Zhang, S., Imaizumi, H., 2012. Behavior and distribution of heavy metals including rare earth elements, thorium, and uranium in sludge from industry water treatment plant and recovery method of metals by biosurfactants application. *Bioinorg Chem Appl* 2012. <https://doi.org/10.1155/2012/173819>
- Gergorić, M., 2018. *Hydrometallurgical Treatment of Neodymium Magnet Waste* (Gothenburg, Sweden 2018). Chalmers University of Technology.
- Gergoric, M., Barrier, A., Retegan, T., 2019. Recovery of Rare-Earth Elements from Neodymium Magnet Waste Using Glycolic, Maleic, and Ascorbic Acids Followed by Solvent Extraction. *Journal of Sustainable Metallurgy* 5, 85–96. <https://doi.org/10.1007/s40831-018-0200-6>

- Ghosal, P.S., Gupta, A.K., 2017. Determination of thermodynamic parameters from Langmuir isotherm constant-revisited. *J Mol Liq* 225, 137–146. <https://doi.org/10.1016/j.molliq.2016.11.058>
- Gkika, D.A., Mitropoulos, A.C., Kyzas, G.Z., 2022. Why reuse spent adsorbents? The latest challenges and limitations. *Science of the Total Environment*. <https://doi.org/10.1016/j.scitotenv.2022.153612>
- Gutiérrez-Gutiérrez, S.C., Coulon, F., Jiang, Y., Wagland, S., 2015. Rare earth elements and critical metal content of extracted landfilled material and potential recovery opportunities. *Waste Management* 42, 128–136. <https://doi.org/10.1016/j.wasman.2015.04.024>
- Hamadneh, I., Alatawi, A., Zalloum, R., Albuqain, R., Alsotari, S., Khalili, F.I., Al-Dujaili, A.H., 2019. Comparison of Jordanian and standard diatomaceous earth as an adsorbent for removal of Sm(III) and Nd(III) from aqueous solution. *Environmental Science and Pollution Research* 26, 20969–20980. <https://doi.org/10.1007/s11356-019-05294-9>
- Haque, N., Hughes, A., Lim, S., Vernon, C., 2014. Rare Earth Elements: Overview of Mining, Mineralogy, Uses, Sustainability and Environmental Impact. *Resources* 3, 614–635. <https://doi.org/10.3390/resources3040614>
- Ho, Y.S., McKay, G., 1999. Pseudo-second order model for sorption processes, *Process Biochemistry*. [https://doi.org/10.1016/S0032-9592\(98\)00112-5](https://doi.org/10.1016/S0032-9592(98)00112-5)
- Ho, Y.S., McKay, G., 1998. A Comparison of Chemisorption Kinetic Models Applied to Pollutant Removal on Various Sorbents. *Process Safety and Environmental Protection* 76, 332–340. <https://doi.org/10.1205/095758298529696>
- Hoshina, H., Chen, J., Amada, H., Seko, N., 2020. Chain entanglement of 2-ethylhexyl hydrogen-2-ethylhexylphosphonate into methacrylate-grafted nonwoven fabrics for applications in separation and recovery of Dy (III) and Nd (III) from aqueous solution. *Polymers (Basel)* 12, 1–12. <https://doi.org/10.3390/polym12112656>
- HyproMag Ltd., n.d. Rare Earth Magnetic Recycling [WWW Document]. URL <https://hypromag.com/> (accessed 10.16.22).
- Ibrahim, A.O., Adegoke, K.A., Adegoke, R.O., AbdulWahab, Y.A., Oyelami, V.B., Adesina, M.O., 2021. Adsorptive removal of different pollutants using metal-organic framework adsorbents. *J Mol Liq*. <https://doi.org/10.1016/j.molliq.2021.115593>
- Ibrahim, K.S., 2013. Carbon nanotubes-properties and applications: a review. *Carbon letters* 14, 131–144. <https://doi.org/10.5714/cl.2013.14.3.131>

- Iftekhar, S., Ramasamy, D.L., Srivastava, V., Asif, M.B., Sillanpää, M., 2018a. Understanding the factors affecting the adsorption of Lanthanum using different adsorbents: A critical review. *Chemosphere*. <https://doi.org/10.1016/j.chemosphere.2018.04.053>
- Iftekhar, S., Srivastava, V., Hammouda, S. ben, Sillanpää, M., 2018b. Fabrication of novel metal ion imprinted xanthan gum-layered double hydroxide nanocomposite for adsorption of rare earth elements. *Carbohydr Polym* 194, 274–284. <https://doi.org/10.1016/j.carbpol.2018.04.054>
- IUPAC, 1970. Pure and Applied Chemistry Nomenclature of Inorganic Chemistry 116.
- Javadian, H., Ruiz, M., Taghvai, M., Sastre, A.M., 2020a. Novel magnetic nanocomposite of calcium alginate carrying poly(pyrimidine-thiophene-amide) as a novel green synthesized polyamide for adsorption study of neodymium, terbium, and dysprosium rare-earth ions. *Colloids Surf A Physicochem Eng Asp* 603, 125252. <https://doi.org/10.1016/j.colsurfa.2020.125252>
- Javadian, H., Ruiz, M., Taghvai, M., Sastre, A.M., 2020b. Novel magnetic nanocomposite of calcium alginate carrying poly(pyrimidine-thiophene-amide) as a novel green synthesized polyamide for adsorption study of neodymium, terbium, and dysprosium rare-earth ions. *Colloids Surf A Physicochem Eng Asp* 603. <https://doi.org/10.1016/j.colsurfa.2020.125252>
- Jowitt, S.M., Werner, T.T., Weng, Z., Mudd, G.M., 2018. Recycling of the rare earth elements. *Curr Opin Green Sustain Chem* 13, 1–7. <https://doi.org/10.1016/j.cogsc.2018.02.008>
- Junne, T., Wulff, N., Breyer, C., Naegler, T., 2020. Critical materials in global low-carbon energy scenarios: The case for neodymium, dysprosium, lithium, and cobalt. *Energy* 211, 118532. <https://doi.org/10.1016/j.energy.2020.118532>
- Jyothi, R.K., Thenepalli, T., Ahn, J.W., Parhi, P.K., Chung, K.W., Lee, J.Y., 2020. Review of rare earth elements recovery from secondary resources for clean energy technologies: Grand opportunities to create wealth from waste. *J Clean Prod*. <https://doi.org/10.1016/j.jclepro.2020.122048>
- Kaneko, T., Nagata, F., Kugimiya, S., Kato, K., 2018. Optimization of carboxyl-functionalized mesoporous silica for the selective adsorption of dysprosium. *J Environ Chem Eng* 6, 5090–5098. <https://doi.org/10.1016/j.jece.2018.09.018>
- Karal, E., Kucuker, M.A., Demirel, B., Coptu, N.K., Kuchta, K., 2021. Hydrometallurgical recovery of neodymium from spent hard disk magnets: A life cycle perspective. *J Clean Prod* 288. <https://doi.org/10.1016/j.jclepro.2020.125087>

- Kawasaki, A., Kimura, R., Arai, S., 1998. Rare earth elements and other trace elements in wastewater treatment sludges. *Soil Sci Plant Nutr* 44, 433–441. <https://doi.org/10.1080/00380768.1998.10414465>
- Kegl, T., Košak, A., Lobnik, A., Novak, Z., Kralj, A.K., Ban, I., 2020. Adsorption of rare earth metals from wastewater by nanomaterials: A review. *J Hazard Mater.* <https://doi.org/10.1016/j.jhazmat.2019.121632>
- Khairul, M.A., Zanganeh, J., Moghtaderi, B., 2019. The composition, recycling and utilisation of Bayer red mud. *Resour Conserv Recycl* 141, 483–498. <https://doi.org/10.1016/j.resconrec.2018.11.006>
- Khurana, I., Saxena, A., Bharti, Khurana, J.M., Rai, P.K., 2017. Removal of Dyes Using Graphene-Based Composites: a Review. *Water Air Soil Pollut* 228. <https://doi.org/10.1007/s11270-017-3361-1>
- Klemettinen, A., Žak, A., Chojnacka, I., Matuska, S., Leśniewicz, A., Wełna, M., Adamski, Z., Klemettinen, L., Rycerz, L., 2021. Leaching of rare earth elements from ndfeb magnets without mechanical pretreatment by sulfuric (H_2SO_4) and hydrochloric (hcl) acids. *Minerals* 11. <https://doi.org/10.3390/min11121374>
- Korhonen, J., Honkasalo, A., Seppälä, J., 2018. Circular Economy: The Concept and its Limitations. *Ecological Economics* 143, 37–46. <https://doi.org/10.1016/j.ecolecon.2017.06.041>
- Kumari, A., Jha, M.K., Pathak, D.D., 2018. Review on the Processes for the Recovery of Rare Earth Metals (REMs) from Secondary Resources. pp. 53–65. https://doi.org/10.1007/978-3-319-72350-1_5
- Kusumkar, V.V., Galamboš, M., Viglašová, E., Daňo, M., Šmelková, J., 2021. Ion-imprinted polymers: Synthesis, characterization, and adsorption of radionuclides. *Materials* 14, 1–29. <https://doi.org/10.3390/ma14051083>
- Lagergren, S., 1898. About the theory of so-called adsorption of soluble substances. *Kungliga Suensk Vetenskapsak ademiens Handlingar* 24, 1–39.
- Langmuir, I., 1918. The Adsorption of Gases on Plane Surfaces of Glass Mic and Platinum. *Journal of American Chemiscal Society* 40, 1361–1403.
- Lata, S., Singh, P.K., Samadder, S.R., 2015. Regeneration of adsorbents and recovery of heavy metals: a review. *International Journal of Environmental Science and Technology* 12, 1461–1478. <https://doi.org/10.1007/s13762-014-0714-9>

- Lima, E.C., Hosseini-Bandegharai, A., Moreno-Piraján, J.C., Anastopoulos, I., 2019. A critical review of the estimation of the thermodynamic parameters on adsorption equilibria. Wrong use of equilibrium constant in the Van't Hoof equation for calculation of thermodynamic parameters of adsorption. *J Mol Liq* 273, 425–434. <https://doi.org/10.1016/j.molliq.2018.10.048>
- Liu, Enli, Xu, X., Zheng, X., Zhang, F., Liu, Enxiu, Li, C., 2017. An ion imprinted macroporous chitosan membrane for efficiently selective adsorption of dysprosium. *Sep Purif Technol* 189, 288–295. <https://doi.org/10.1016/j.seppur.2017.06.079>
- Liu, Y., 2009. Is the Free Energy Change of Adsorption Correctly Calculated? *J Chem Eng Data* 54, 1981–1985. <https://doi.org/10.1021/je800661q>
- McCABE, W.L., SMITH, J.C., HARRIOTT, P., 2000. *Unit Operations of Chemical Engineering*, 6th ed. Mc Graw Hill, USA.
- Mehta, D., Mazumdar, S., Singh, S.K., 2015. Magnetic adsorbents for the treatment of water/wastewater-A review. *Journal of Water Process Engineering*. <https://doi.org/10.1016/j.jwpe.2015.07.001>
- Minowa, T., 2008. Rare earth magnets: Conservation of energy and the environment, in: *Resource Geology*. Blackwell Publishing Ltd, pp. 414–422. <https://doi.org/10.1111/j.1751-3928.2008.00073.x>
- München, D.D., Veit, H.M., 2017. Neodymium as the main feature of permanent magnets from hard disk drives (HDDs). *Waste Management*. <https://doi.org/10.1016/j.wasman.2017.01.032>
- Negrea, P., Gabor, A., Davidescu, C.M., Ciopec, M., Negrea, A., Duteanu, N., 2020. Kinetics and thermodynamics modeling of Nd(III) removal from aqueous solution using modified Amberlite XAD7. *Journal of Rare Earths* 38, 306–314. <https://doi.org/10.1016/j.jre.2019.04.023>
- Ni'am, A.C., Wang, Y.F., Chen, S.W., Chang, G.M., You, S.J., 2020. Simultaneous recovery of rare earth elements from waste permanent magnets (WPMs) leach liquor by solvent extraction and hollow fiber supported liquid membrane. *Chemical Engineering and Processing - Process Intensification* 148. <https://doi.org/10.1016/j.cep.2020.107831>
- Okon Metals INC., n.d. Rare Earth/Neodymium Magnet Recycling [WWW Document]. URL <https://www.okonmetals.com/rare-earthneodymium-magnet-recycling> (accessed 10.16.22).

- Olu-Owolabi, B.I., Diagboya, P.N., Mtunzi, F.M., Düring, R.-A., 2021. Utilizing eco-friendly kaolinite-biochar composite adsorbent for removal of ivermectin in aqueous media. *J Environ Manage* 279, 111619. <https://doi.org/10.1016/j.jenvman.2020.111619>
- Önal, M.A.R., Borra, C.R., Guo, M., Blanpain, B., van Gerven, T., 2017. Hydrometallurgical recycling of NdFeB magnets: Complete leaching, iron removal and electrolysis. *Journal of Rare Earths* 35, 574–584. [https://doi.org/10.1016/S1002-0721\(17\)60950-5](https://doi.org/10.1016/S1002-0721(17)60950-5)
- Opare, E.O., Struhs, E., Mirkouei, A., 2021. A comparative state-of-technology review and future directions for rare earth element separation. *Renewable and Sustainable Energy Reviews* 143, 110917. <https://doi.org/10.1016/j.rser.2021.110917>
- Parmar, B., Bisht, K.K., Rajput, G., Suresh, E., 2021. Recent advances in metal-organic frameworks as adsorbent materials for hazardous dye molecules. *Dalton Transactions*. <https://doi.org/10.1039/d0dt03824e>
- Peelman, S., Venkatesan, P., Abrahami, S., Yang, Y., 2018. Recovery of REEs from End-of-Life Permanent Magnet Scrap Generated in WEEE Recycling Plants. pp. 2619–2631. https://doi.org/10.1007/978-3-319-95022-8_221
- Pei, L., Zhao, X., Liu, B., Li, Z., Wei, Y., 2021. Rationally Tailoring Pore and Surface Properties of Metal-Organic Frameworks for Boosting Adsorption of Dy³⁺. *ACS Appl Mater Interfaces* 13, 46763–46771. <https://doi.org/10.1021/acsami.1c14302>
- Peng, X., Mo, S., Li, R., Li, J., Tian, C., Liu, W., Wang, Y., 2021. Effective removal of the rare earth element dysprosium from wastewater with polyurethane sponge-supported graphene oxide–titanium phosphate. *Environ Chem Lett* 19, 719–728. <https://doi.org/10.1007/s10311-020-01073-y>
- Pereao, O., Laatikainen, K., Bode-Aluko, C., Fatoba, O., Omoniyi, E., Kochnev, Y., Nechaev, A.N., Apel, P., Petrik, L., 2021. Synthesis and characterisation of diglycolic acid functionalised polyethylene terephthalate nanofibers for rare earth elements recovery. *J Environ Chem Eng* 9. <https://doi.org/10.1016/j.jece.2021.105902>
- Pereao, O., Laatikainen, K., Bode-Aluko, C., Kochnev, I., Fatoba, O., Nechaev, A.N., Petrik, L., 2020. Adsorption of Ce³⁺ and Nd³⁺ by diglycolic acid functionalised electrospun polystyrene nanofiber from aqueous solution. *Sep Purif Technol* 233. <https://doi.org/10.1016/j.seppur.2019.116059>
- Phouthavong, V., Yan, R., Nijpanich, S., Hagio, T., Ichino, R., Kong, L., Li, L., 2022. Magnetic Adsorbents for Wastewater Treatment: Advancements in Their Synthesis Methods. *Materials*. <https://doi.org/10.3390/ma15031053>

- Prediger, P., Vieira, M.G.A., Camparotto, N.G., de Figueiredo Neves, T., da Silva, P.M.M., de Vargas Brião, G., 2022. Adsorption and Desorption Aspects of Carbon-Based Nanomaterials: Recent Applications for Water Treatments and Toxic Effects, in: Liquid and Crystal Nanomaterials for Water Pollutants Remediation. CRC Press, Boca Raton, pp. 59–87. <https://doi.org/10.1201/9781003091486-4>
- Rabatho, J.P., Tongamp, W., Takasaki, Y., Haga, K., Shibayama, A., 2013. Recovery of Nd and Dy from rare earth magnetic waste sludge by hydrometallurgical process. *J Mater Cycles Waste Manag* 15, 171–178. <https://doi.org/10.1007/s10163-012-0105-6>
- Radke, C.J., Prausnitz, J.M., 1972. Thermodynamics of multi-solute adsorption from dilute liquid solutions. *AIChE Journal* 18, 761–768. <https://doi.org/10.1002/aic.690180417>
- Ravi, S., Kim, S.Y., Bae, Y.S., 2022. Novel benzylphosphate-based covalent porous organic polymers for the effective capture of rare earth elements from aqueous solutions. *J Hazard Mater* 424. <https://doi.org/10.1016/j.jhazmat.2021.127356>
- Ravi, S., Lee, Y.R., Yu, K., Ahn, J.W., Ahn, W.S., 2018. Benzene triamido-tetraphosphonic acid immobilized on mesoporous silica for adsorption of Nd³⁺ ions in aqueous solution. *Microporous and Mesoporous Materials* 258, 62–71. <https://doi.org/10.1016/j.micromeso.2017.09.006>
- Ravi, S., Puthiaraj, P., Yu, K., Ahn, W.S., 2019. Porous Covalent Organic Polymers Comprising a Phosphite Skeleton for Aqueous Nd(III) Capture. *ACS Appl Mater Interfaces* 11, 11488–11497. <https://doi.org/10.1021/acsami.9b00546>
- Riaño, S., Binnemans, K., 2015. Extraction and separation of neodymium and dysprosium from used NdFeB magnets: An application of ionic liquids in solvent extraction towards the recycling of magnets. *Green Chemistry* 17, 2931–2942. <https://doi.org/10.1039/c5gc00230c>
- Rosental, S., 2005. 30. Terras Raras 629–653.
- Schulze, R., Buchert, M., 2016. Estimates of global REE recycling potentials from NdFeB magnet material. *Resour Conserv Recycl* 113, 12–27. <https://doi.org/10.1016/j.resconrec.2016.05.004>
- Sips, R., 1948. On the structure of a catalyst surface. *J Chem Phys* 16, 490–495. <https://doi.org/10.1063/1.1746922>
- Smith, A.T., LaChance, A.M., Zeng, S., Liu, B., Sun, L., 2019. Synthesis, properties, and applications of graphene oxide/reduced graphene oxide and their nanocomposites. *Nano Materials Science* 1, 31–47. <https://doi.org/10.1016/j.nanoms.2019.02.004>

- Sousa Filho, P.C. de, Serra, O.A., 2014. Rare Earths in Brazil: Historical aspects, production, and perspectives. *Quim Nova* 37, 753–760. <https://doi.org/10.5935/0100-4042.20140121>
- Stegen, K.S., 2015. Heavy rare earths, permanent magnets, and renewable energies: An imminent crisis. *Energy Policy* 79, 1–8. <https://doi.org/10.1016/j.enpol.2014.12.015>
- Swain, N., Mishra, S., 2019. A review on the recovery and separation of rare earths and transition metals from secondary resources. *J Clean Prod* 220, 884–898. <https://doi.org/10.1016/j.jclepro.2019.02.094>
- Tesfaye, F., Peng, H., Zhang, M., 2021. Advances in the Circular Economy of Lanthanides. *Jom* 73, 16–18. <https://doi.org/10.1007/s11837-020-04493-x>
- Thomas, J.M., 1961. The existence of endothermic adsorption. *J Chem Educ* 38, 138. <https://doi.org/10.1021/ed038p138>
- Thomas, W.J., Crittenden, B., 1998. Fundamentals of adsorption equilibria. *Adsorption Technology & Design* 31–65. <https://doi.org/10.1016/B978-075061959-2/50004-5>
- Trench, A., Sykes, J.P., 2020. Rare Earth Permanent Magnets and Their Place in the Future Economy. *Engineering* 6, 115–118. <https://doi.org/10.1016/j.eng.2019.12.007>
- Tu, Y.-J., You, C.-F., Lo, S.-C., Chan, T.-S., Chung, C.-H., 2019. Recycling of neodymium enhanced by functionalized magnetic ferrite. *Environ Technol* 40, 1592–1604. <https://doi.org/10.1080/09593330.2018.1426643>
- United States Geological Survey (USGS), 2020. Mineral Commodity Summaries, U.S Department OF The Interior, U.S Geological Survey. <https://doi.org/https://doi.org/10.3133/mcs2020>
- Valaskova, M., Martynková, G.S., 2012. Vermiculite: Structural Properties and Examples of the Use, in: *Clay Minerals in Nature - Their Characterization, Modification and Application*. InTech, p. 64. <https://doi.org/10.5772/51237>
- Van't Hoff, J.H., 1884. *Etudes de dynamique chimique*. Frederik Muller, Amsterdam.
- Walzberg, J., Burton, R., Zhao, F., Frost, K., Muller, S., Carpenter, A., Heath, G., 2022. An investigation of hard-disk drive circularity accounting for socio-technical dynamics and data uncertainty. *Resour Conserv Recycl* 178, 106102. <https://doi.org/10.1016/j.resconrec.2021.106102>
- Wang, J., Guo, X., 2020. Adsorption kinetic models: Physical meanings, applications, and solving methods. *J Hazard Mater* 390, 122156. <https://doi.org/10.1016/j.jhazmat.2020.122156>

- Wang, J., Huang, C.P., Allen, H.E., Cha, D.K., Kim, D.-W., 1998. Adsorption Characteristics of Dye onto Sludge Particulates.
- Wang, M., Tan, Q., Chiang, J.F., Li, J., 2017. Recovery of rare and precious metals from urban mines—A review. *Front Environ Sci Eng* 11, 1–17. <https://doi.org/10.1007/s11783-017-0963-1>
- Wang, Y., Sun, B., Gao, F., Chen, W., Nie, Z., 2022. Life cycle assessment of regeneration technology routes for sintered NdFeB magnets. *International Journal of Life Cycle Assessment* 27, 1044–1057. <https://doi.org/10.1007/s11367-022-02081-6>
- Worch, Eckhard, 2012. *Adsorption Technology in Water Treatment*. De Gruyter, Berlin/Bosto.
- Xu, J., Koivula, R., Zhang, W., Wiikinkoski, E., Hietala, S., Harjula, R., 2018a. Separation of cobalt, neodymium and dysprosium using amorphous zirconium phosphate. *Hydrometallurgy* 175, 170–178. <https://doi.org/10.1016/j.hydromet.2017.11.010>
- Xu, J., Koivula, R., Zhang, W., Wiikinkoski, E., Hietala, S., Harjula, R., 2018b. Separation of cobalt, neodymium and dysprosium using amorphous zirconium phosphate. *Hydrometallurgy* 175, 170–178. <https://doi.org/10.1016/j.hydromet.2017.11.010>
- Yaashikaa, P.R., Senthil Kumar, P., Karishma, S., 2022. Review on biopolymers and composites – Evolving material as adsorbents in removal of environmental pollutants. *Environ Res* 212, 113114. <https://doi.org/10.1016/j.envres.2022.113114>
- Yamada, E., Murakami, H., Nishihama, S., Yoshizuka, K., 2018. Separation process of dysprosium and neodymium from waste neodymium magnet. *Sep Purif Technol* 192, 62–68. <https://doi.org/10.1016/j.seppur.2017.09.062>
- Yang, Y., Walton, A., Sheridan, R., Güth, K., Gauß, R., Gutfleisch, O., Buchert, M., Steenari, B.-M., van Gerven, T., Jones, P.T., Binnemans, K., 2017. REE Recovery from End-of-Life NdFeB Permanent Magnet Scrap: A Critical Review. *Journal of Sustainable Metallurgy* 3, 122–149. <https://doi.org/10.1007/s40831-016-0090-4>
- Yessoufou, A., Ifon, B.E., Suanon, F., Dimon, B., Sun, Q., Dedjiho, C.A., Mama, D., Yu, C.P., 2017. Rare earth and precious elements in the urban sewage sludge and lake surface sediments under anthropogenic influence in the Republic of Benin. *Environ Monit Assess* 189. <https://doi.org/10.1007/s10661-017-6331-6>
- Yuksekdag, A., Kose-Mutlu, B., Siddiqui, A.F., Wiesner, M.R., Koyuncu, I., 2022. A holistic approach for the recovery of rare earth elements and scandium from secondary sources under a circular economy framework – A review. *Chemosphere*. <https://doi.org/10.1016/j.chemosphere.2022.133620>

- Zeb, S., Ali, N., Ali, Z., Bilal, M., Adalat, B., Hussain, S., Gul, S., Ali, F., Ahmad, R., Khan, S., Iqbal, H.M.N., 2020. Silica-based nanomaterials as designer adsorbents to mitigate emerging organic contaminants from water matrices. *Journal of Water Process Engineering* 38. <https://doi.org/10.1016/j.jwpe.2020.101675>
- Zhang, L., Xu, Z., 2016. A review of current progress of recycling technologies for metals from waste electrical and electronic equipment. *J Clean Prod* 127, 19–36. <https://doi.org/10.1016/j.jclepro.2016.04.004>
- Zhang, Y., Gu, F., Su, Z., Liu, S., Anderson, C., Jiang, T., 2020. Hydrometallurgical Recovery of Rare Earth Elements from NdFeB Permanent Magnet Scrap: A Review. *Metals (Basel)* 10, 841. <https://doi.org/10.3390/met10060841>
- Zhao, F., Cong, Z., Sun, H., Ren, D., 2007. The geochemistry of rare earth elements (REE) in acid mine drainage from the Sitai coal mine, Shanxi Province, North China. *Int J Coal Geol* 70, 184–192. <https://doi.org/10.1016/j.coal.2006.01.009>
- Zheng, X., Sun, W., Li, A., Wang, B., Jiang, R., Song, Z., Zhang, Y., Li, Z., 2022a. Graphene oxide and polyethyleneimine cooperative construct ionic imprinted cellulose nanocrystal aerogel for selective adsorption of Dy(III). *Cellulose* 29, 469–481. <https://doi.org/10.1007/s10570-021-04299-3>
- Zheng, X., Sun, W., Li, A., Zhang, Y., Li, Z., 2022b. Bacterial cellulose nanofibrous ion imprinted aerogel for highly efficient recognition and adsorption of Dy(III). *Process Safety and Environmental Protection* 160, 70–79. <https://doi.org/10.1016/j.psep.2022.01.077>
- Zheng, X., Zhang, Y., Bian, T., Wang, D., Li, Z., 2019. One-step fabrication of imprinted mesoporous cellulose nanocrystals films for selective separation and recovery of Nd(III). *Cellulose* 26, 5571–5582. <https://doi.org/10.1007/s10570-019-02482-1>
- Zheng, X., Zhang, Y., Zhang, F., Li, Z., Yan, Y., 2018. Dual-template docking oriented ionic imprinted bilayer mesoporous films with efficient recovery of neodymium and dysprosium. *J Hazard Mater* 353, 496–504. <https://doi.org/10.1016/j.jhazmat.2018.04.022>
- Zheng, X., Zhang, Y., Bian, T., Zhang, Y., Li, Z., Pan, J., 2020. Oxidized carbon materials cooperative construct ionic imprinted cellulose nanocrystals films for efficient adsorption of Dy(III). *Chemical Engineering Journal* 381, 122669. <https://doi.org/10.1016/j.cej.2019.122669>

CHAPTER 3. NEODYMIUM ADSORPTION ON EXPANDED VERMICULITE: KINETICS, SELECTIVITY, AND DESORPTION

Efficient and selective adsorption of neodymium on expanded vermiculite²

Giani de Vargas Brião, Meuris Gurgel Carlos da Silva, Melissa Gurgel Adeodato Vieira

University of Campinas, School of Chemical Engineering, Albert Einstein Avenue, 500, 13083-852 Campinas, Brazil

ABSTRACT

In this study, expanded vermiculite was applied to the adsorption of neodymium from aqueous solution with a focus on the description of the kinetic, mechanism of adsorption, determination of the best eluent, and selectivity. The expanded vermiculite was characterized before and after the adsorption process by morphology, composition, textural properties (specific surface area, density, and porosity), and functional groups. The adsorption experiments showed that, under the optimal conditions, using 0.7 g of adsorbent and at pH 3.3, the efficiency achieved an enhanced adsorption percentage of 98.7%, which represents an adsorption capacity of 0.205 mmol/g. The external mass and the diffusional resistance controlled the mass transfer, and the ion exchange occurred mainly with magnesium cation. The proposed mechanism of adsorption was cation exchange in the interlayer region of the vermiculite and the formation of outer-sphere complexes. Calcium chloride was the most suitable eluent, regarding efficiency and low toxicity. The adsorbent preferably adsorbed neodymium from a multimetal solution, achieving enhanced values of selectivity. Regarding the characterization, expanded vermiculite presented a well-organized structure, a lamellar morphology, and typical functional groups as Al-O and Si-O. Thus, expanded vermiculite adsorbed neodymium quickly and efficiently, and the ion exchange mechanism of adsorption allows selective adsorption of neodymium and safe desorption by the exchange with Ca^{2+} .

Keywords: adsorption, neodymium, vermiculite, kinetic, desorption, selectivity.

² Manuscript published in *Industrial & Engineering Chemistry Research* (2021).
DOI: 10.1021/acs.iecr.0c05979. Reprinted with the journal's permission (Appendix B.2).

3.1 INTRODUCTION

Neodymium (Nd) is a rare earth element with atomic number 60, electronic configuration [Xe] 4f⁴6s², and abundance 33-41 ppm ¹. Neodymium, like other rare earth metals (REM), is on the list of critical materials because of its scarcity and its growing demand related to technological application ², which motivates the recovery of these metals from secondary sources. Besides the economic and productive aspects, environmental issues related to the detrimental effect of rare earth metals on the development of plants ^{3,4} and animals ⁵ have been caused concern. Electronic and electrical equipment wastes are the main secondary sources of REM ⁶. However, rare earth metals, including neodymium, have been found in different residuals and wastewaters, such as acid mine drainage ⁷, red mug ⁸, acid leachate of landfills ⁹, wastewater treatment sludge ¹⁰⁻¹², which potentially can contaminate water resources. Thus, the recovery of REM from effluents and solid wastes is essential to attend to the growing demand, minimize environmental impacts ^{2,13}, and guarantee the water and groundwater quality for future generations.

There are several methods to separate and purify these ions, including classical hydrometallurgical processes (leaching, chemical precipitation, and solvent extraction), ion exchange, and adsorption ¹⁴. Leaching followed by extraction of neodymium has been proposed by several authors by using alternative solvents ¹⁵⁻¹⁷. However, despite the high recovery of REM, solvent extraction is a high cost and complex process that generate large volumes of waste ¹⁸. Adsorption, in turn, has stood out for its simplicity, high efficiency, capacity to concentrate, and desorb (recovery) the adsorbate from diluted solutions ^{19,20}. One of the determining factors for the overall adsorption efficiency is the type of adsorbent matrix applied.

Clay minerals are outstanding adsorbent of cationic pollutants and have significant potential as an alternative source of REM ²¹. However, further development of clay mineral applications still needs to be studied for getting the best adsorption and the best extraction of the loaded REM (desorption) ²². Operational parameters such as mass transfer mechanism and desorption, from the perspective of safety and sustainability, have been neglected in works that applied clay minerals to adsorb neodymium ²³⁻²⁶. As well, the selective adsorption of rare earth metals from multicomponent systems, which is the current focus of many studies ²⁷⁻³¹, is still explored insufficiently regarding the applying of clay-based adsorbents.

Vermiculite is a clay mineral that is non-toxic to the environment, available, and low-cost ^{21,32}. It is also a potential adsorbent for the neodymium recovery because has exchangeable

cations in the interlayer spaces that compensate part of the negative charge that provides a great cation exchange capacity ³³. Another property that favors its use as an adsorbent is the high surface area and porosity provide by thermal or chemical expansion process ³⁴. Vermiculite has been successfully applied to remove heavy metals ^{35–37}, and recently presented favorable results in the neodymium adsorption, regarding equilibrium, thermodynamic, and reusability aspects ²⁶.

This work goals to scrutinize the kinetics, mechanism of neodymium adsorption, desorption (determination of the best eluent), selectivity on expanded vermiculite in batch mode. For that, optimal parameters for the adsorption as pH, amount of adsorbent, and particle size were determined by a central composite design of experiments. Then, kinetic experiments were performed to comprehend the mechanism of adsorption. Desorption experiments gave information about the adsorbent regeneration and the capacity to recover neodymium using different eluents. Also, a study about the selectivity of the vermiculite to adsorb neodymium from a multicomponent solution containing Pb^{2+} , Ni^{2+} , Cu^{2+} , and Zn^{2+} was performed. Furthermore, the interactions between neodymium and expanded vermiculite were discussed by the characterization analysis of functional groups, morphology, chemical composition, and textural properties.

3.2 MATERIALS AND METHODS

3.2.1 Adsorbate (neodymium) and adsorbent (expanded vermiculite)

The different neodymium solutions applied in the experiments were prepared by dilutions of a “stock” solution. This “stock” solution was made with the dissolution of 5 g of neodymium (III) nitrate hexahydrate ($\text{Nd}(\text{NO}_3)_3 \cdot 6\text{H}_2\text{O}$, Aldrich, 99.9%) in 200 mL of deionized water.

The neodymium concentration on the aqueous solutions was determined by spectrophotometry UV- visible (UVmini-1240, Shimadzu) through the addition of the xylenol orange (0.0045 mol/L) as a complexing agent. The wavelength of maximum absorbance of the xylenol orange was 575 nm ³⁸. The complex was formed in a volumetric flask (10 mL) by the addition of 2 mL of the metal solution, 3 mL of xylenol orange, and filled the volume with a buffer solution of acetic acid/sodium acetate (pH 5.6).

Brasil Minérios S.A. donated the adsorbent matrix, expanded vermiculite. The material was used as received, without pre-treatment.

3.2.2 Adsorbent characterization

Expanded vermiculite (EV) was characterized before and after the adsorption process by morphology, composition, textural properties (specific surface area, density, and porosity), and functional groups. The saturated expanded vermiculite sample will be denoted as EV-Nd. Regarding the morphology, images, semi-quantitative evaluation of composition, and elements map on the adsorbent surface were observed by scanning electron microscopy and energy dispersive X-ray spectrometry (SEM-EDS) (LEO 440i, LEO). The specific surface area was obtained by the Brunauer-Emmet-Teller (BET) method³⁹ from the isotherm of adsorption and desorption of nitrogen. The surface area analyzer ANOVA-e (Quantachrome) was utilized with the pressure range from 10 to 800 mmHg, the time of vermiculite treatment (degas) was 3 hours at 200°C. The bulk density was analyzed by mercury porosimetry (Auto Pore IV, Micromeritics). Helium picnometry measured the real density (Accupyc II 1340, Micromeritics). The porosimetry (ε_p) was calculated according to Equation 3.1. Chemical ligands and functional groups were verified by Fourier-transform infrared spectroscopy (FT-IR), ranging from 4000 to 400 cm^{-1} and with a resolution of 4 cm^{-1} in the spectrometer Nicolet 6700 (Thermo Scientific). Complementary characterization analyses such as thermal analysis, X-ray diffraction, and nitrogen physisorption isotherm were discussed in a previous work²⁶.

$$\varepsilon_p = 1 - (\rho_b / \rho_r) \quad (3.1)$$

Where ε_p is the porosity, ρ_b is the bulk density (kg/m^3) and ρ_r is the real density (kg/m^3).

3.2.3 Adsorption experiments

All the experiments were performed in a batch mode with an agitation speed of 200 rpm at room temperature (25°C). Optimal pH, adsorbent mass, and particle size were determined conforming to section 2.3.1. pH was controlled by the addition of a few drops of nitric acid (0.1 mol/L). Equations 3.2 to 3.5 calculated the adsorption capacity ($q/\text{mmol/g}$), removal percentage ($\%R$), desorption capacity ($q_d/\text{mmol/g}$), desorption percentage ($\%D$), respectively.

$$q = \frac{C_0 - C_f}{m} V \quad (3.2)$$

$$\%R = \frac{C_0 - C_f}{C_0} 100 \quad (3.3)$$

$$q_{el} = \frac{C_f}{m} V \quad (3.4)$$

$$\%D = \frac{q_{el}}{q} 100 \quad (3.5)$$

Where C_0 is the initial concentration (mmol/L), C_f is the final concentration at a given time (mmol/L), V is the solution volume (L) and m is the adsorbent mass (g).

3.2.3.1 Optimization of the experimental conditions

Particle size (A), adsorbent amount (B), and pH (C) were varied by a rotational central composite design (RCCD) to optimize the removal percentage ($\%R$) (response variable). Therefore, the experiment plan was composed of 8 runs (2^3 design), 6 runs (axial points), and 3 runs (central point triplicate), in which the contact time was 24h. The RCCD levels, from $-\alpha$ to $+\alpha$, for A , B , and C , varied from 0.48 to 1.3 mm, 0.163 to 0.836 g, and 1.3 to 4.7, respectively. The complete experimental domain is presented in Table S1 (Appendix A.1).

The pH range (1.3 to 4.7) was based on the low pH of the potential effluents that contain Nd ($\cong 2.0$)^{40–42} and on the maximum pH in which the majority of species in solution is Nd³⁺ ($\cong 6.0$)⁴³. Besides, the metallic speciation in the function of the pH was simulated using the free software Visual Minteq 3.0 to confirm the prevalence of Nd³⁺. The separation of the expanded vermiculite according to its particle size was performed by a set of sieves (40 to 12 mesh) on a vibratory base (Produtest). The mass of the adsorbent range was chosen to guarantee the availability of the process (low adsorbent amounts).

The variance analysis test (ANOVA) with a confidence interval of 95% and the generation of the surface responses were performed on Statistics 8.0 software. An empiric-squared model was determined to obtain the $\%R$ (Equation 3.6). This model was submitted to a backward elimination to improve the adjustment.

$$\%R = b_0 + b_1A + b_2B + b_3C + b_{11}A^2 + b_{22}B^2 + b_{33}C^2 + b_{12}AB + b_{13}AC + b_{23}BC \quad (3.6)$$

Where $\%R$ is the predicted value of the removal percentage (response variable), b_0 is the mean, A , B , and C are the factors, b_1 , b_2 , b_3 are linear coefficients, b_{12} , b_{13} , and b_{23} are cross-product coefficients, and b_{11} , b_{22} , and b_{33} are quadratic coefficients. The best model obtained was validated by an adsorption experiment (triplicate) with the optimized parameters from the RSM analysis.

3.2.3.2 Adsorption kinetic

Three different Nd solutions (1.0, 3.0, and 5.0 mmol/L) were put on contact with expanded vermiculite under mechanical agitation. Few milliliters were taken at certain intervals of time and filtered using a syringe filter (Chromafil Xtra PES-20/25). The supernatant concentrations were measured by complexation (section 3.2.1).

3.2.3.2.1 Mathematical modeling

The pseudo-first-order (PFO) (Equation 3.7)⁴⁴, pseudo-second-order (PSO) (Equation 3.8)⁴⁵, Weber-Morris intra-particle diffusion (Equation 3.9)⁴⁶, external mass transfer (Equation 10), Boyd (equations 3.11-3.14)⁴⁷ were adjusted to the kinetic data.

$$q_t = q_e(1 - e^{-k_1 t}) \quad (3.7)$$

$$q_t = \frac{k_2 q_e^2 t}{1 + k_2 q_e t} \quad (3.8)$$

$$q_t = k_p \sqrt{t} + I \quad (3.9)$$

Where k_1 is the pseudo-first-order rate constant (1/min); k_2 is the pseudo-second-order rate constant (g/mmol.min), k_p is the rate constant of intraparticle diffusion (mmol/g. $\sqrt{\text{min}}$) and I is the term that refers to the boundary layer. The higher I value, the higher the boundary layer effect on the mass transfer. Also, q_t and q_e are the adsorption capacity at time t and the equilibrium (mmol/g) respectively.

When there is an equilibrium condition on the interface between particle surface and film, Equation 3.10 can describe the external mass transfer⁴⁸.

$$\frac{dC}{dt} = k_f S(C - C_s); t = 0, C = C_0 \quad (3.10)$$

Where k_f is the external mass transfer coefficient (m/min), S is the surface area per volume unit (m^{-1}), and C_s is the adsorbate concentration on the interface solid-liquid (mmol/L).

The Boyd diffusion model can predict which step limits the mass transfer process of adsorption. According to this method, the solute fraction adsorbed until an instant t ($F(t)$) can be calculated by Equation 3.11 and 3.12.

$$F(t) = \frac{q_t}{q_e} \quad (3.11)$$

$$F(t) = 1 - \frac{6}{\pi^2} \sum_{n=1}^{\infty} \frac{1}{n^2} e(-n^2 B_t) \quad (3.12)$$

B_t can be calculated by equations 3.13 and 3.14 through a simplification of Equation 3.12 by Fourier transform and numeric integration.

$$0 \leq F \leq 0.85: B_t = 2\pi - \frac{\pi^2 F}{3} - 2\pi \left(1 - \frac{\pi F}{3}\right)^{1/2} \quad (3.13)$$

$$0.85 < F \leq 1: B_t = -0.4977 - \ln(1 - F) \quad (3.14)$$

The plot of B_t versus t specifies the rate-limiting step. If the slope can be represented by a linear equation with a linear coefficient equal a 0, intraparticle diffusion governs the process, otherwise, film diffusion is the rate-limiting step. The angular coefficient (B) of the linear fit of the B_t versus t , is related to the effective diffusivity according to Equation 3.15⁴⁹.

$$B = \frac{D_{ef}\pi^2}{r^2} \quad (3.15)$$

Where D_{ef} is the effective coefficient of diffusion of the metal on the adsorbent (m^2/min) and r is the average size of particles adsorbent (m).

The quality of the mathematical model adjust to experimental data was evaluated by determination coefficient (R^2), adjusted determination coefficient (R_a^2).

3.2.3.3 Ion exchange

The ion exchange process was evaluated along time. Expanded vermiculite (14 g/L) was mixed to a neodymium solution (1 mmol/L), at 200 rpm, 25°C, and pH 3.3 until the equilibrium.

Aliquots were removed along the time, centrifuged and the metal concentration in the fluid phase was measured using an atomic absorption spectrophotometer (AA 7000, Shimadzu). Also, a blank test using deionized water under the same conditions was performed to discount the metal dissolution.

The exchange capacity of the expanded vermiculite was evaluated according to the SW/846 Method 9081 from Environmental Protection Agency ⁵⁰, in which 100 ml of ammonium acetate (3 mol/L) was put in contact with 2.5 g of expanded vermiculite, and agitated for 24 hours. The concentration from the stoichiometric relation (Equation 3.16) of the cation exchange was compared to the experimental data.

$$z_A B_{ads}^{z_B+} + z_B A_{sol}^{z_A+} \leftrightarrow z_A B_{sol}^{z_B+} + z_B A_{ads}^{z_A+} \quad (3.16)$$

Where cations A and B have z_A and z_B charges (valence); the index ads refers to the adsorbent and sol denotes the solution.

3.2.4 Desorption experiments

In a previous work ²⁶, cycles of adsorption and desorption were performed using CaCl_2 as eluent. However, other potential eluents were not evaluated. Thus, in the present work, the elution step includes the evaluation of the desorption capacity of different eluents aiming for the recovery of neodymium and the regeneration of the vermiculite. To conduct the desorption experiments, firstly, there was the adsorbent “saturation” with a neodymium solution (1 mmol/L) at the proportion of 0.7 g of adsorbent each 50 mL of metal solution. The eluents tested are nitric acid (HNO_3 , Anidrol 65%), sulfuric acid (H_2SO_4 , Dinâmica 99%), hydrochloric acid (HCl , Dinâmica 36.5%), acetic acid (CH_3COOH , Dinâmica 99.7%), potassium chloride (KCl , Dinâmica 99%), sodium chloride (NaCl , Vetec 99%), sodium nitrate (NaNO_3 , Dinâmica 99%), and calcium chloride (CaCl_2 , Dinâmica 99%). These eluents were determined because acids and salts have known elution capacity for metals ⁵¹, also, they are selected because they allow the complexation reaction between the metal and methyl orange, for the determination of the metal by UV- visible spectrophotometry. The concentration of the eluent solutions was 0.1 mol/L. The time of contact for the desorption essay was 1 hour and it was performed in triplicate.

3.2.5 Selectivity

Rare earth metals are found in aqueous solution, mixed with base metals (iron, aluminum, nickel, zinc, selenium, indium, gallium), noble (copper, palladium or gold, silver), and toxic substances (mercury, beryllium, lead, arsenic, cadmium, antimony, and plastics) ⁵². Thus, the selectivity of the vermiculite toward Nd(III) was tested in an adsorption experiment in presence of other metals, nickel, lead, zinc, and copper. A solution containing 1 mmol/L of each metal, i.e, totalizing 5 mmol/L was put in contact with the vermiculite in the optimal adsorbent dosage (14 g/L) for 18 hours, at pH ~ 3.0, agitated at 200 rpm. The order of magnitude for the metal concentration of the metals was based on the work of Gao et al.¹⁰.

The experiment was made in triplicate. The multicomponent solution was prepared by the dissolution of nickel nitrate ($\text{Ni}(\text{NO}_3)_2 \cdot 6\text{H}_2\text{O}$, Dinâmica 98%), lead nitrate ($\text{Pb}(\text{NO}_3)_2$, Sigma Aldrich 99.9%), zinc nitrate ($\text{Zn}(\text{NO}_3)_2 \cdot 6\text{H}_2\text{O}$, Synth 99.0%), copper nitrate ($\text{Cu}(\text{NO}_3)_2 \cdot 3\text{H}_2\text{O}$, Dinâmica 98%), and neodymium nitrate ($\text{Nd}(\text{NO}_3)_3 \cdot 6\text{H}_2\text{O}$, Aldrich, 99.9%). The concentration of the metals was measured by atomic absorption spectroscopy (AA7000, Shimadzu).

The selectivity coefficient ($S_{Nd/M}$) was defined as a ratio of the distribution coefficient between Nd(III) and other metal Equation (3.17) ⁵³.

$$S_{Nd/M} = \frac{K_d(Nd)}{K_d(M)} \quad \text{with} \quad K_d = \frac{q_e}{C_e} \quad (3.17)$$

Where K_d (L/g) is the distribution coefficient of the selected metal ion between the adsorbent and solution; C_e (mmol/L) and q_e (mmol/g) are the concentration and adsorption capacities of the metal ion at the equilibrium.

3.3 RESULTS AND DISCUSSION

3.3.1 Characterization

Figure 3.1(a) shows the FT-IR spectra for expanded vermiculite before and after the neodymium adsorption. Both had a large and intense absorption band at the region of 3200-3570 cm^{-1} , referring to the axial vibrations of free OH of the groups as SiO-H, in addition to the absorbed water molecules in the interlayer of the vermiculite ⁵⁴. Another band of medium

intensity is observed at $\sim 1640\text{ cm}^{-1}$, which relates the symmetric angular deformation of the O-H bond (water molecules) to the exchangeable cations of the clay. The attenuation of this band after the adsorption of neodymium suggests that happened the substitution of the exchangeable ions by Nd^{3+} ⁵⁵⁻⁵⁷. At $\sim 1001\text{ cm}^{-1}$, there is the characteristic band of the asymmetric stretch of Si-O-Si and Si-O-Al of the tetrahedral and octahedral lamellar faces. Two peaks in the expanded vermiculite spectra at 739 cm^{-1} and 667 cm^{-1} indicate the deforming vibrations of Al-OH and R-O-Si (R = Fe, Al, Mg, etc.), respectively. The band of medium intensity at 447 cm^{-1} is related to the deforming vibration of Si-O-Mg ^{56,58}. In the EV-Nd spectra, there is a reduction in the signal intensity in the bands at 657 cm^{-1} and 456 cm^{-1} , which suggests that cations (Fe, Al, Mg) may have been extracted from the octahedral layer. The intense peak at 1384.33 cm^{-1} can be associated with the NO_3^- ion from the dissociation of the nitrate salt used in the neodymium solutions ⁵⁷, in which a small fraction of the partially dissociate ion (NdNO_3^{2+}) is also presented in the solution at pH 3.3, i.e., both Nd^{3+} and NdNO_3^{2+} species were adsorbed on the expanded vermiculite.

Figure 3.1(b) has the SEM images in the amplification of 150 times for the expanded vermiculite before and after the neodymium adsorption, the EV-Nd at 1000 times of amplification, and the neodymium map over the expanded vermiculite. Figure 3.1(b) images confirmed that the sheet arrangement characteristic of a phyllosilicate material as the vermiculite. Comparing the images of EV and EV-Nd, it is evident that the vermiculite lost part of the expansion with the adsorption process. The original expansion of the multilayers was achieved by a quick thermal treatment, in which the interlamellar water vaporized ⁵⁹. Thus, the reduction of the lamellar space was due to the rehydration of the material during the adsorption process. The neodymium mapping using EDS on SEM evidenced the neodymium was effectively loaded on the planar region and the lamellar space.

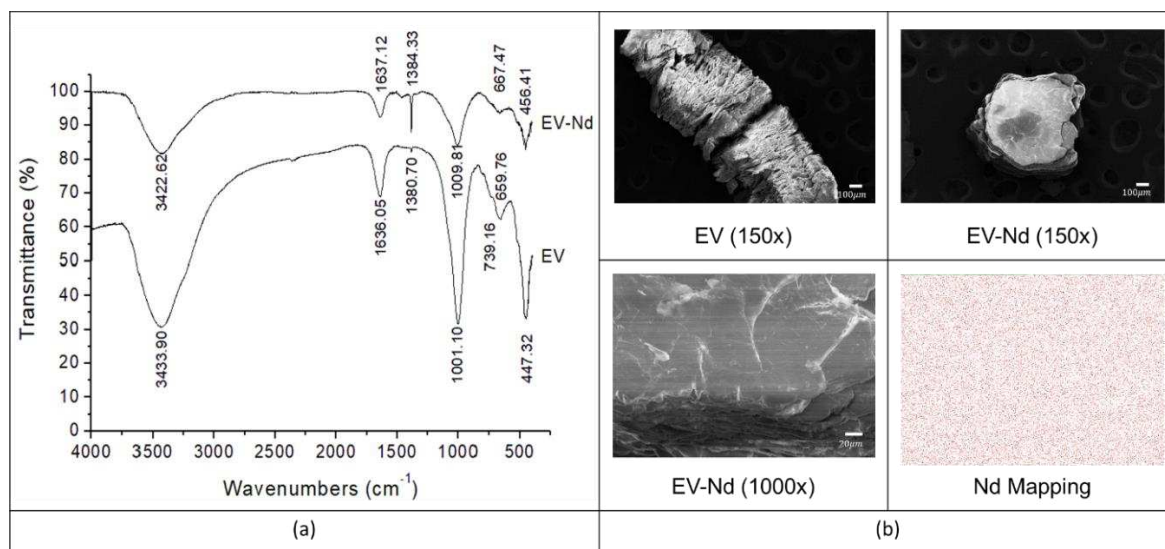


Figure 3.1. FT-IR spectrum (a) and SEM images (b) for vermiculite before (EV) and after the neodymium adsorption (EV-Nd)

The energy dispersive X-ray spectrometry analysis (SEM-EDS) of the lamellar region of expanded vermiculite shows the weight percentage of each element in Table 3.1, which reveals that EV-Nd, comparing to EV, had a reduction of the titanium and iron content, the absence of chromium and potassium, and an increase in the aluminum percentage. The absence of potassium and chromium, and the expressive reduction of iron reveals that these metals were resealed into the solution during the adsorption of neodymium at saturation condition. EV-Nd exhibited a neodymium content of 3.62%, confirming the effective adsorption of the metal. The elements that constitute the samples EV are typical of the vermiculite structure^{37,57,60–62}.

Table 3.1. Weight composition by chemical element in EV and EV-Nd.

Element	Weight composition (%)	
	EV	EV-Nd
Mg	15.7 ± 0.69	15.9 ± 0.76
Al	7.63 ± 0.31	8.35 ± 0.61
Si	21.8 ± 0.51	22.7 ± 0.74
Ti	0.83 ± 0.11	0.54 ± 0.29
Cr	0.50 ± 0.12	-
Fe	7.49 ± 0.35	2.83 ± 0.74
K	0.21 ± 0.01	-
O	45.9 ± 0.03	45.9 ± 0.72
Nd	-	3.62 ± 1.18

Table 3.2. Specific surface area and bulk density of the expanded vermiculite.

Sample	S_{BET} (m ² /g)*	Bulk density (kg/m ³)	Real density (kg/m ³)	Porosity (ϵ_p)
EV	9.877	264.5	2,167.5	0.88
EV-Nd	5.440	553.0	2,582.6	0.78

*From Brião et al. ²⁶

In Table 3.2 the BET surface areas, bulk, and real densities, and porosities of EV and EV-Nd are reported, according to the analysis of the isotherm of adsorption and desorption of N₂, to the mercury intrusion porosimetry, and the helium picnometry, respectively. The BET surface areas of the samples EV and EV-Nd were 9.877 and 5.440 m²/g, correspondently. The decrease of the BET surface area of the vermiculite may due to the occupation of available sites for N₂ adsorption by the loaded neodymium. The results of mercury porosimetry demonstrate that the bulk density of EV-Nd (553.0 kg/m³) is higher than the EV (264.15 kg/m³). Hillier, Marwa, and Rice ⁶² found a very similar bulk density value for EV expanded at 900°C being 241 kg/m³. The real density of EV samples (2,167.5 kg/m³) was also lower than for EV-Nd (2,582.6 kg/m³). These results indicated that the neodymium adsorption process promoted a loss of the expansion between the layers of vermiculite, and consequently, a decrease of volume and an increase of the densities of the material, which corroborates with Figure 3.1(b). The adsorption of neodymium also decreased the porosity of the material, however, VE-Nd presents a high porosity (78%), typical for the expanded vermiculites ⁶³.

3.3.2 Adsorption of neodymium

3.3.2.1 Optimization of experimental conditions of adsorption

Table 3.3 compiles the experimental configuration of the RCCD and the results of the neodymium adsorption on expanded vermiculite. The values of q and % R varied from 0.106 to 0.770 mmol/g, and from 37.5 to 98.4%, respectively, which indicates that the range of the experimental design variables affected the results effectively. Figure 3.2 presents the Pareto diagram (Figure 3.2(a)) and the surface response (Figure 3.2(b)).

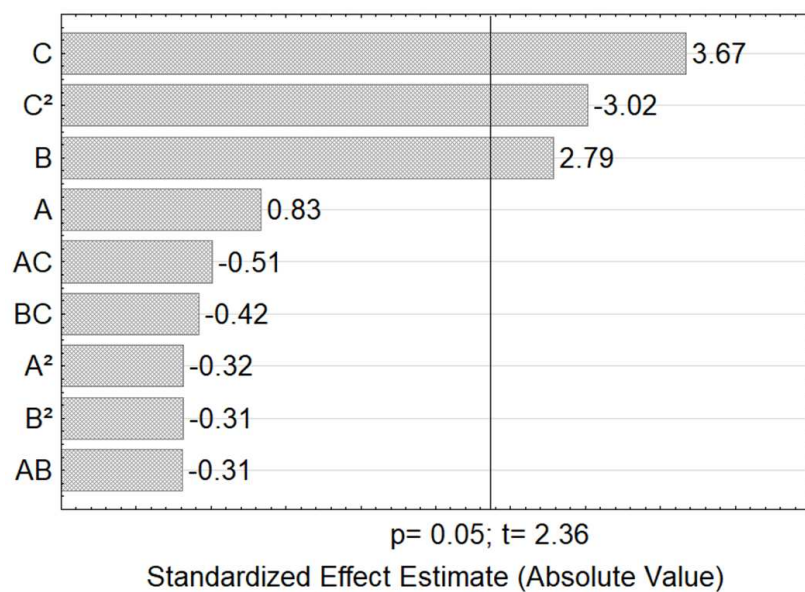
Table 3.3 The capacity of adsorption (q) and removal percentage ($\%R$) of Nd adsorption on expanded vermiculite.

Run	A	B	C	q mmol/g	$\%R$
1	0.65	0.3	2	0.255	54.1
2	1.01	0.3	2	0.311	66.0
3	0.65	0.7	2	0.170	84.2
4	1.01	0.7	2	0.186	92.1
5	0.65	0.3	4	0.339	71.8
6	1.01	0.3	4	0.374	79.4
7	0.65	0.7	4	0.197	97.4
8	1.01	0.7	4	0.196	96.8
9	0.46	0.5	3	0.257	90.7
10	1.3	0.5	3	0.271	95.7
11	0.85	0.164	3	0.770	88.9
12	0.85	0.836	3	0.167	98.2
13	0.85	0.5	1.32	0.106	37.5
14	0.85	0.5	4.68	0.279	98.4
15	0.85	0.5	3	0.271	93.5
16	0.85	0.5	3	0.271	93.8
17	0.85	0.5	3	0.274	94.5

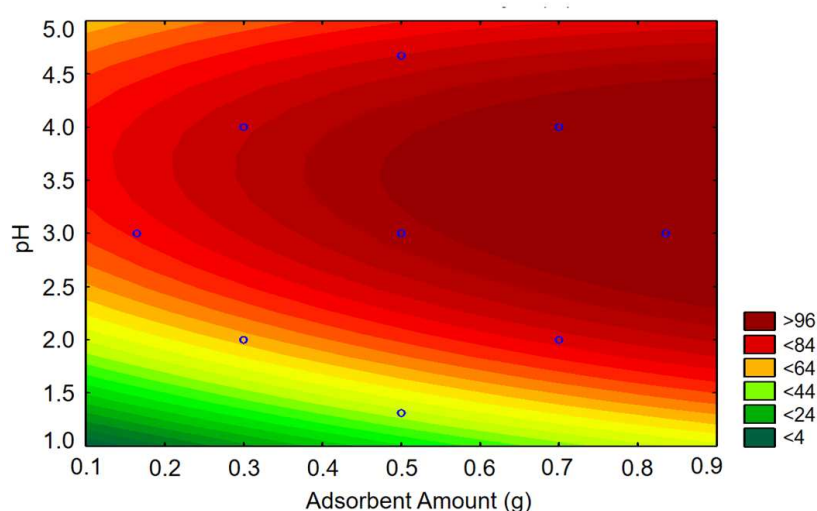
Pareto diagram, according to the student test (t), indicated that linear pH (C), quadratic pH (C^2), and linear adsorbent amount (B) were significant at a 95% confidence interval. The linear and quadratic effects of the particle size were not statistically significant.

According to Ikenyiri and Ukpaka ⁶⁴, the effect of particle size (A) on adsorption is associated with changes in physical-chemical interface properties due to the influence on the characteristic of grains and crystals. However, the linear and quadratic (A and A^2) statistical evaluation expressed the non-significance of the particle size on the Nd removal percentage ($\%R$).

Figure 3.2(a) also demonstrates that the linear effect of the adsorbent amount (B) was significant and positive, which was expected because, as the mass of adsorbent in the system is greater, the number of active sites available for adsorption increases, thus also increasing the removal percentage.



(a)



(b)

Figure 3.2. Pareto chart of standardized effects (a) and response surface of Nd removal percentage as function of pH and adsorbent amount (b)

pH affects the surface charge of the adsorbents, the degree of ionization, and the species of the adsorbate, which influences the adsorbent's efficiency⁶⁵. Figure 3.2(a) emphasizes that the pH effect, both linear and quadratic (C and C²), was significant in the adsorption of Nd in expanded vermiculite. A study on the distribution of zeta potential as a function of pH defined the zero charge point of expanded vermiculite as being at pH 2.9⁶⁶. That is, the EV surface

potential is positive below 2.9 and negative for higher pH. Thus, according to Table 3.3, for pH lower than the zero charge point, the Nd adsorption was quite reduced, since the surface had a positive charge that possibly repelled the neodymium cations. At low pHs, there is also competition between Nd^{3+} and H^+ .

The highest value of %R was obtained with the range of pH 3.0 - 5.0 (Figure 3.2(b)) because in this intermediary pH, the effect of the competition of hydrogen ions was reduced and the precipitation was avoided ^{67,68}, which is confirmed by the simulation of the metallic speciation (Figure 3). According to Figure 3.3, the trivalent form of the neodymium (Nd^{3+}) was predominant on the range of pH applied, and then, at pHs above 7.0, the insoluble form of neodymium turns present in the solution. However, the effluents from the hydrometallurgical process to recover rare earth metals usually have a low pH (<2.0) ⁴⁰⁻⁴². Thus, the condition to achieve optimal %R was considered an adsorbent mass of 0.7 g and pH~3.0.

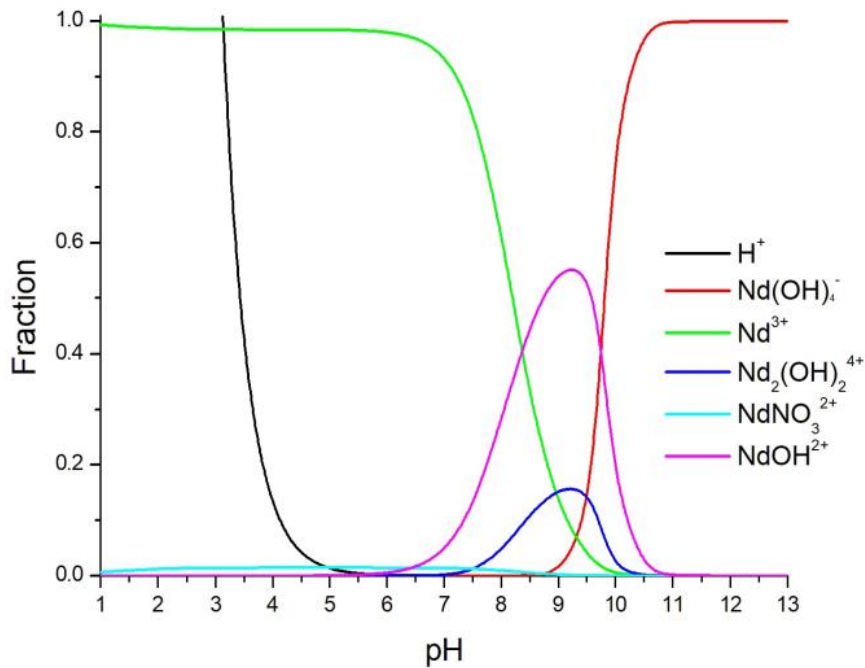


Figure 3.3. Metallic speciation of neodymium (1 mmol/L)

The quadratic model with coded variables that considered just the significant factors and interactions denoted the data with a determination coefficient of R^2 0.8234. This model is presented in Equation 3.18.

$$\%R = 94.12_{(\pm 6.42)} + 8.37_{(\pm 3.00)}B + 11.01_{(\pm 3.00)}C - 10.13_{(\pm 3.35)}C^2 \quad (3.18)$$

According to the test F, the value calculated (F_{calc}) was 4.75 times higher than the tabled value (F_{tab}), i.e., the variance analysis (ANOVA) results (Table 3.4) confirmed that the model (Equation 18) is statically significant, with a confidence interval of 95%.

Table 3.4. ANOVA of the quadratic model of neodymium removal (%R) (confidence interval of 95%)

Source of variation	SS	df	MS	F_{calc}	F_{tab}
Regression	3843.2	3	1281.1	16.2	3.41
Residues	1024.8	13	78.8		
Total	4868.0	16			

To confirm the application of the model to predict the neodymium removal percentage in expanded vermiculite, the validation test was performed in triplicate under the best conditions found by the optimization of parameters, pH= 3.3, adsorbent mount= 0.7 g, and particle size= 0.855 mm. The result of the removal percentage obtained experimentally was $98.7 \pm 0.008 \%$ ($q = 0.205 \pm 0.003$ mmol/g) and the one calculated using the model was $103.4 \pm 6.35 \%$. The experimental result was higher than any result of Table 3.3, showing that there was an effective optimization of the conditions, maximizing the response variable (% R). Under the optimal conditions applied, the model predicted a removal percentage of 103.4%. The difference between the experimental and the model was only 4.7%, indicating certain accuracy of the model. However, the model, due to its empirical nature, is not based on a mass balance that restricts 100% as the maximum value.

3.3.2.2 Adsorption kinetics

The adsorption kinetics is fundamental to determine the viability and the mass transfer mechanism involved in the process ⁶⁵. Figure 3.4 shows the kinetic behavior of the adsorption of neodymium for three distinct initial concentrations 1.0, 3.0, and 5.0 mmol/L, and the plot of the kinetic models. The kinetic parameters obtained through the fit of PFO, PSO, Weber-Morris intraparticle diffusion model, Boyd diffusion, and external mass transfer (film diffusion) are compiled in Table 3.5.

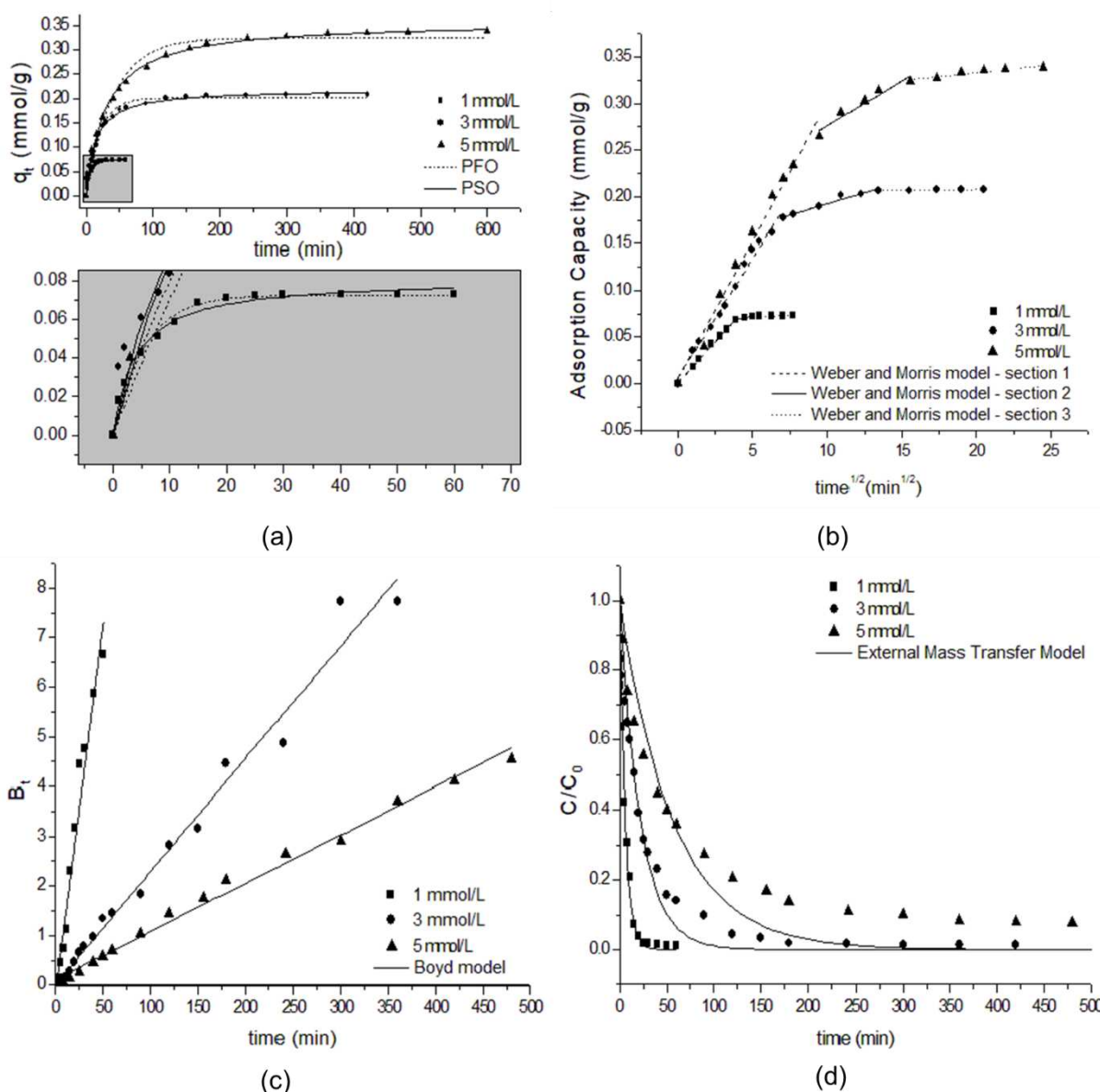


Figure 3.4. Neodymium adsorption capacity over time and plot of the kinetic models: PFO and PSO (a), intraparticle diffusion (b), Boyd diffusion (c) and external mass transfer (d)

According to Figure 3.4(a), with the increase of the concentration of adsorbate, the time to reach the equilibrium increased as well. For the lowest concentration (1.0 mmol/L) the equilibrium time was about 25 min, for 3.0 mmol/L the equilibrium was achieved at 180 min, and for the highest concentration (5.0 mmol/L) the equilibrium time was 360 min. At short times, the neodymium adsorption rate was high, because the adsorbate has all adsorption sites available. With the advancing of time, the sites were continuously occupied until reaching the equilibrium (plateau), when the rate of adsorption is equal to the rate of desorption⁶⁵. The amounts adsorbed at the equilibrium for the initial concentrations 1.0, 3.0, and 5.0 mmol/L were

0.073, 0.21, and 0.34 mmol/g, respectively. The amounts adsorbed increased proportionally with the initial concentration because higher initial concentrations of the adsorbate augmented the driving force (concentration gradient) to overcome the mass transfer resistance between the aqueous and the solid phase ^{69,70}. However, a maximum adsorption capacity was not achieved, which means that the active sites of the expanded vermiculite were not saturated in these conditions. Brião et al. ²⁶ indicated that the maximum adsorption capacity of the expanded vermiculite from the Langmuir isotherm was 0.39 mmol of Nd³⁺/g.

Comparing the PFO and PSO (Table 3.5), models based on reaction kinetic models, the adjust criteria (R_a^2) indicated that PSO had the best fit to the data for all concentrations. The model, however, did not predict satisfactorily the experimental q at the equilibrium time for 1.0 mmol/L. The rate constants (k_2) were 3.1, 0.33, and 0.096 g.mmol/min at 1.0, 3.0, and 5.0 mmol/L, respectively, showing that the rate of adsorption was strongly influenced by the initial concentration ⁷¹, and decreased with increasing C_0 ⁷².

The fit of the mass transfer models of Weber-Morris, Boyd, and the external mass transfer are presented in Figure 3.4(b), Figure 3.4(c), and Figure 3.4(d), respectively. The multilinearity evidenced in Figure 3.4(b) pointed out that the kinetic process of neodymium adsorption has a multistep mechanism being: (1) film diffusion (2) intraparticle diffusion and (3) fast adsorption onto the adsorbent ⁷³. Analyzing the plot of B_t versus t (Figure 3.4(c)), from the Boyd model, the data could be effectively fitted by linear equations. According to Figure 3.4(d), the external mass transfer model fitted worse the data as the C_0 increased.

The intraparticle diffusion coefficient (k_p) from the Weber-Morris model was estimated from the fit of the second linear section ⁷⁴ (Figure 3.4(b)). According to Table 3.5, the k_p and I were higher as the initial concentration increased. The intercept I is related to the boundary layer thickness ⁷⁵, which means that the effect of the boundary layer also became more expressive with the increment of C_0 .

The high R_a^2 values from the Boyd model fit to the kinetic data indicated that the B_t in the function of t could be considered a linear relationship (Table 3.5). However, these equations have linear coefficients (C) -0.071, 0.02, and 0.1, i.e. the plot does not pass through the origin, which means that the intraparticle diffusion does not control the overall process rate ⁴⁹. The effective diffusivities (D_{ef}) for the neodymium concentration 1.0, 3.0, and 5.0 mmol/L, were 27.4, 4.46, and 1.81×10^{-10} m²/min, respectively. D_{ef} values in the same order of magnitude were determined for Na⁺ diffusion on vermiculite ^{76,77}.

Table 3.5. Parameters from the fit of the kinetic models.

Model	Parameters	Neodymium initial concentration (mmol/L)		
		1.0	3.0	5.0
PFO	q_1 (mmol/g)	0.073	0.20	0.32
	k_1 (1/min)	0.18	0.050	0.025
	R^2	0.987	0.975	0.977
	R_a^2	0.985	0.973	0.975
PSO	q_2 (mmol/g)	0.081	0.22	0.36
	k_2 (g.mmol/min)	3.1	0.33	0.096
	R^2	0.990	0.988	0.997
	R_a^2	0.989	0.987	0.996
Weber-Morris	k_p ($\times 10^3$ mmol/g.min ^{1/2})	3.5	4.8	9.6
	I (mmol/g)	0.055	0.14	0.18
	R^2	0.990	0.983	0.971
	R_a^2	0.960	0.958	0.923
Boyd	B	0.15	0.024	9.7×10^{-3}
	C	-0.071	0.02	0.1
	D_{ef} ($\times 10^{10}$ m ² /min)	27.4	4.46	1.81
	R^2	0.986	0.992	0.996
	R_a^2	0.970	0.984	0.992
External Mass Transfer	k_f ($\times 10^6$ m//min)	1.23	0.33	0.13
	R^2	0.985	0.968	0.922
	R_a^2	0.985	0.968	0.922

Table 3.5 shows that the external mass transfer coefficients (k_f) obtained for 1.0, 3.0 and 5.0 mmol/L, respectively, were 1.23, 0.33 and 0.13×10^{-6} m/min. The negative effect of the neodymium concentration in the film transfer rate (k_f) can be explained by the competition for the active sites at higher neodymium concentration or limitation of the binding capacity of vermiculite ⁷⁸.

Comparing R_a^2 of the three models of mass transfer, the external mass transfer had the best fit for 1 mmol/L, and the Boyd model had the best adjustment for the 3 and 5 mmol/L. Thus, the ion diffusion from the exterior of the adsorbent into the cleavages is more relevant as the Nd³⁺ initial concentration increases.

3.3.2.3 Ion Exchange

Considering the SEM-EDS result, the cations selected to analyze the exchange with neodymium along with time were Mg²⁺ and K⁺ (Figure 3.5(a)). Chromium was not considered because Cr³⁺ concentration was lower than the sensitivity of the atomic absorption equipment.

Thus, the release of Mg^{2+} and K^+ , by the saturation with NH_4^+ , were evaluated to quantify the cation exchange in the total process of sorption. The Mg^{2+} and K^+ exchange capacity was 141.24 and 1.84 cmol/kg, respectively, totalizing 143.08 cmol/kg. Wang and Wang ⁷⁹ affirmed that vermiculites have a cation exchange capacity between 100 and 150 cmol/kg, which agrees with the experimental value obtained by the present study.

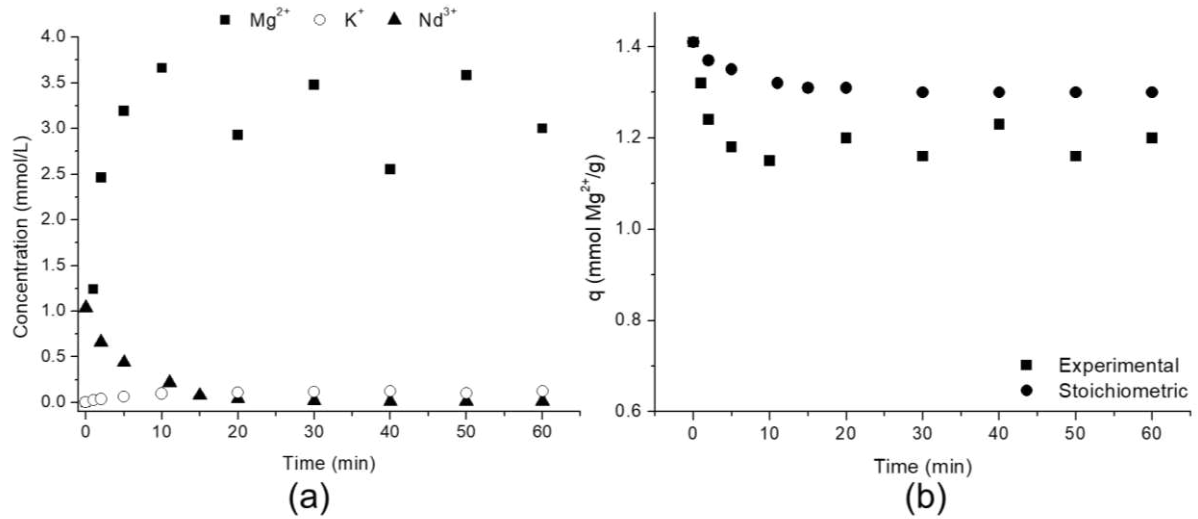


Figure 3.5. Kinetic of the magnesium and potassium release, and adsorption of neodymium (a), and theoretical and experimental kinetic of magnesium release in terms of sorption capacity (b)

Figure 3.5(a) indicates that the magnesium was much more released compared to the potassium, confirming that vermiculite preferably exchanges divalent cation (Ca, Mg), over monovalent (Na, K), and trivalent (Cr) ⁸⁰. The unstable behavior of the magnesium release after 10 min may be due to the different affinity of the vermiculite for each metal. As the higher the concentration of the light metals in the solution, the higher is the competition for the finite bindings sites, the material have also a preference for exchange magnesium, which may cause the adsorption of the already desorbed Mg^{2+} , causing this oscillating concentration ^{81,82}.

Due to the high release of magnesium, the stoichiometric reaction of cation exchange in the sorption of neodymium can be simplified to consider just the shift of Mg^{2+} (Equation 3.19). Thus, theoretically, a neodymium cation is adsorbed, for each 3/2 displaced magnesium cation.



The magnesium theoretical concentration calculated from the neodymium concentration at equilibrium was 1.1 times lower than the experimental, indicating that the release of Mg^{2+} does not follow the stoichiometric relation of 3:2. Regarding the exchange capacity (Figure 3.5 (b)), at the beginning of the sorption of neodymium, the expanded vermiculite has the maximum exchangeable magnesium amount of 1.41 mmol/g. At the end of the process, the capacity was reduced theoretically to 1.3 mmol/g and experimentally to 1.2 mmol/g. In the vermiculite structure, magnesium is a dominant cation in the octahedral layer and an exchangeable cation in the interlayer space^{33,83}. The higher experimental release comparing to the theoretical one suggests that also magnesium of the octahedral layer may have been released⁸⁴. These statements corroborate with the FT-IR interpretation about the extraction of some cations, including magnesium, from the octahedral layer.

3.3.3 Neodymium adsorption mechanism

The sorption of the metal can occur by diverse mechanisms as ion exchange, surface complexation, and direct bonding of metal cations to the surface of clays⁸⁵. According to Malandrino et al.⁸⁶ and Wang and Wang⁷⁹ the main mechanisms of adsorption of metals on vermiculite are cation exchange and the inner-sphere and outer-sphere complexes through Si-O and Al-O groups at the vermiculite particle.

Considering the FT-IR findings for the neodymium adsorption and the results of magnesium and potassium release, the cation exchange mechanism is confirmed. The attenuation of the band $\sim 1640\text{ cm}^{-1}$ and the reduction of the intensity at 657 cm^{-1} and 456 cm^{-1} suggest that neodymium substituted exchangeable cations (interlayer) and that the magnesium was also extracted from the octahedral sheet, respectively. The desorption using CaCl_2 as eluent affirms that the adsorption process develops weak interactions between the vermiculite and neodymium. Based on that, it is possible to deduce that the electrostatic interaction between the neodymium ions and negative permanent charge (outer-sphere complexes) occurs preferably to the formation of inner-sphere complexes by the direct interaction to Si-O and Al-O (more energetic bonds). According to the mechanisms proposed by Han et al.⁸⁷, Padilla-Ortega et al.⁶⁶, and Węgrzyn et al.⁸⁸ and to the experimental findings of the present work, the estimated mechanism of the neodymium adsorption is majority ion exchange and outer-sphere complexation.

The mass transfer results indicated that there is a resistance to the transfer in the external film and then neodymium diffuses between the layers of vermiculite. Once in the interlayer space, the neodymium ion exchange with magnesium, also, on the planar regions, neodymium bond physically to the vermiculite surface outer-sphere complexes. To ratify the adsorption mechanism proposed, further analysis such as X-ray photoelectron spectroscopy and extended X-ray absorption fine structure spectroscopy should be performed.

3.3.4 Neodymium desorption

To determine the best eluent to regenerate the adsorbent and to recover the neodymium, the desorption performance of eight eluents is compared in Figure 3.6. With an eluent concentration of 0.1 mol/L, the best desorption percentage was achieved using nitric acid, followed by calcium chloride, hydrochloric acid, potassium chloride, sulfuric acid, sodium nitrate, acetic acid, and sodium chloride. Due to the highest desorption efficiencies of the nitric acid and calcium chloride at 0.1 mol/L, their performances at 0.5 mol/L were compared to verify how the concentration can affect the desorption efficiency of these eluents. It was evidenced that, using more concentrated eluent solutions, the desorption percentage was increased, and on these conditions, calcium chloride turns slightly more efficient (43.2%) than nitric acid (41.0%).

Strong acids had a great elution capacity for metals, however, due to the mineral composition of the vermiculite, they also lixiviate metals of the vermiculite structure (dissolution of Fe and Al oxide/silicate adsorption surfaces)⁵¹. Another disadvantage is the safety of the use of strong acids, according to the globally harmonized system (GHS) health hazard classification system, the sulfuric, nitric, and hydrochloric acids are classified as skin corrosion/irritation and serious eye damage/irritation substances. Calcium chloride, nonetheless, can regenerate the vermiculite surface without causing structural damage, due to the exchange with the loaded Nd^{3+} . Thus, considering efficiency and safety, the more recommendable eluent between those tested in this study is calcium chloride.

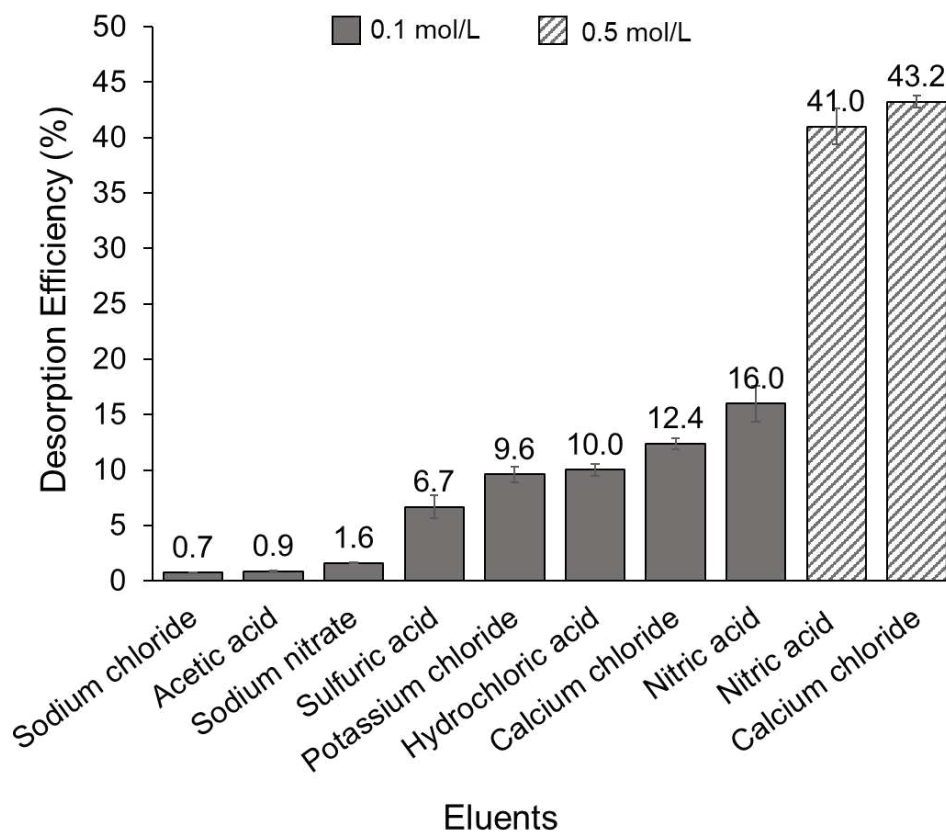


Figure 3.6. Desorption percentage of Nd^{3+} by different eluting agents

To associate our desorption results with other studies in the literature, Table S2 (Appendix A.1) presents some elution processes to recovery neodymium to compare them regarding efficiency and safety, in which methanol (MeOH) and strong acids (HCl and HNO_3) had higher elution efficiencies (%*D*) compared to the calcium chloride. According to Birungi et al.⁸⁹, the efficiency of the eluent can be also expressed by the solid/liquid ratio (*S/L*), where the *S* represents the metal-laden adsorbent and the *L* is the eluent volume. Thus, CaCl_2 is also very efficient with an *S/L* value at least 14 times higher than the other eluents. Regarding operational parameters, acidic desorption leads to big amounts of acid effluents to treated before discarding, which translates into an increase in costs and related environmental issues⁹⁰.

The toxicity of the eluents was compared in Table S2 by the lethal dose LD_{50} for oral ingestion in rats according to the safety data sheet of the substances. From the GHS, MeOH and CaCl_2 are considered in category 4 (harmful if swallowed) and HCl and HNO_3 are from category 3 (toxic if swallowed). Comparing directly both eluents from category 3, methanol can cause poisoning due to metabolic acidosis and may lead to blindness, encephalopathy, and/or

multisystem organ failure ⁹¹, and calcium chloride is not a hazardous material, and it even finds many uses in foods and medicines ⁹².

Thus, the ion exchange mechanism involved in the neodymium adsorption on expanded vermiculite makes possible recovery neodymium using CaCl_2 that is less dangerous and easier to handle than those have found in the literature (strong acids and toxic alcohols).

3.3.5 Selectivity

The removal percentage of Pb, Ni, Zn, Cu, and Nd and the selectivity towards neodymium are presented in Figure 3.7. Vermiculite adsorbed more expressively the neodymium (90.8%), followed by nickel (66.1%), zinc (54.2%), copper (37.8%), and lead (23.4%). Among the five metals, Nd^{3+} was preferably adsorbed due to the higher positive charge that increases the electrostatic attraction to the negatively charged surface of the vermiculite. The ionic radii of metals also influences on their affinity to minerals⁹³, for the bivalent ions, lower cations were adsorbed more efficiently and %R decreases following this order: Ni^{2+} (0.72 Å) > Zn^{2+} (0.74 Å) > Cu^{2+} (0.94 Å) > Pb^{2+} (1.20 Å) ^{94,95}. This occurs due to the difficulty of large ions to diffuse inside the lamellar space ⁸⁶. The distribution coefficients and adsorption capacities can be consulted in Table S3 (Supporting Information, Appendix A.1). In a similar selectivity essay, the biosorbent phosphorylated dry baker's yeast removed just 10 % of Cu^{2+} , Cd^{2+} , Zn^{2+} , and Pb^{2+} , and 70 % of the neodymium content ²⁹, indicating that the biomaterial is more selective for neodymium than the expanded vermiculite. Ogata et al ²⁸, in turn, applying a modified silica gel, at pH 1, adsorbed 76% of Dy^{3+} and 23% of Nd^{3+} , and 0% of Cu^{2+} , Fe^{3+} , and Zn^{2+} , which means that the adsorbent presented also a selective adsorption mechanism between the rare earth metals dysprosium and neodymium. Thus, the natural selectivity of the vermiculite due to the electrostatic forces is favorable for the neodymium adsorption from a mixture of bivalent ions. However, further studies of multicomponent adsorption must be performed, mainly from mixtures of rare earth metals, and physical-chemical modifications, such as ligand insertion ^{28,96}, should be proposed to separate REM from each other using this clay as adsorbent.

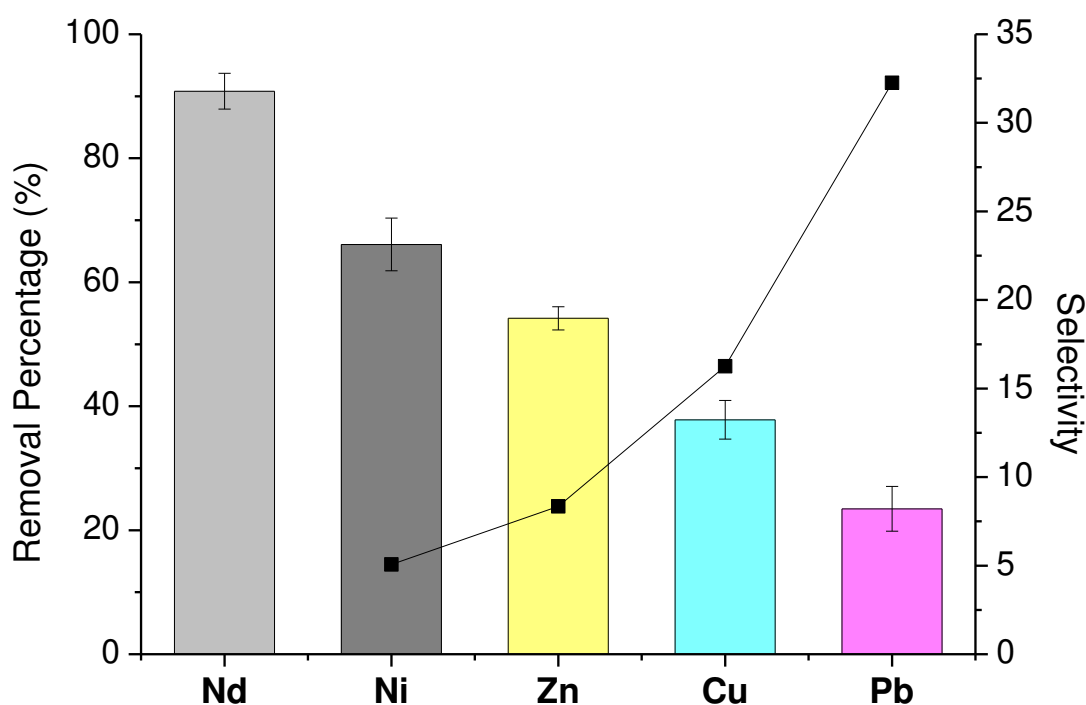


Figure 3.7. Multicomponent adsorption performance of vermiculite

3.4 CONCLUSION

In this work, we investigated the batch adsorption and desorption of neodymium on expanded vermiculite as an alternative adsorbent. The solid material was characterized before and after the adsorption process. The adsorbent before the adsorption presented the typical physic-chemical properties of this expanded phyllosilicate. The adsorption of neodymium, however, caused the material to decrease the specific surface area, to increase the bulk and real density, to release light metals of the interlayer space, to reduce the expansion of the material. The kinetics of adsorption is fast and followed the PSO model, in which the initial concentration affected significantly the rate of adsorption. The mass transfer is controlled by external film and intraparticle diffusion. Magnesium is the main exchangeable cation involved in the sorption of neodymium, and the ion exchange does not follow the stoichiometric relation. The proposed adsorption mechanism is based on ion exchange and formation of outer-sphere complexes, which allows that calcium chloride, a source of Ca^{2+} , to be the most efficient eluent to desorb neodymium. Also, the electrostatic nature of the Nd-clay interactions contributed to the great selectivity over the different classes of metals, heavy (Pb^{2+}), base (Zn^{2+} and Ni^{2+}), and noble (Cu^{2+}) metals, which is evidence that the material may be also selective in the neodymium

adsorption from wastewaters. Therefore, the neodymium recovery from aqueous solution using expanded vermiculite, a minimally treated clay mineral, presented enthusiastic results on a lab-scale. Further studies, however, should be developed to improve the recovery and selectively even from industrial effluents, such as the evaluation of adsorption of neodymium in other operation modes and scales, and from rare earth mixtures.

FUNDING

This work was supported by the Fundação de Amparo à Pesquisa do Estado de São Paulo/FAPESP (Grant # 2017/18236-1 and Grant # 2019/11353-8), Conselho Nacional de Desenvolvimento Científico e Tecnológico/CNPq (Grant # 308046/2019-6 and Grant # 147606/2018-7), Coordenação de Aperfeiçoamento de Pessoal de Nível Superior/CAPES.

ACKNOWLEDGMENTS

The authors are grateful to Brasil Minérios S.A. for donating the expanded vermiculite.

REFERENCES

- (1) Bünzli, J.-C. G. Lanthanides, Physical and Chemical Characteristics. In *Encyclopedia of Metalloproteins*; Kretsinger, R. H., Uversky, V. N., Permyakov, E. A., Eds.; Springer New York: New York, NY, 2013; pp 1135–1142. https://doi.org/10.1007/978-1-4614-1533-6_148.
- (2) Jowitt, S. M.; Werner, T. T.; Weng, Z.; Mudd, G. M. Recycling of the Rare Earth Elements. *Curr. Opin. Green Sustain. Chem.* **2018**, *13*, 1–7. <https://doi.org/10.1016/j.cogsc.2018.02.008>.
- (3) Wang, C.; He, M.; Shi, W.; Wong, J.; Cheng, T.; Wang, X.; Hu, L.; Chen, F. Toxicological Effects Involved in Risk Assessment of Rare Earth Lanthanum on Roots of *Vicia Faba* L. Seedlings. *J. Environ. Sci.* **2011**, *23* (10), 1721–1728. [https://doi.org/10.1016/S1001-0742\(10\)60598-0](https://doi.org/10.1016/S1001-0742(10)60598-0).
- (4) Wang, C.; Zhang, K.; He, M.; Jiang, C.; Tian, L.; Tian, Y.; Wang, X. Mineral Nutrient Imbalance, DNA Lesion and DNA-Protein Crosslink Involved in Growth Retardation of *Vicia Faba* L. Seedlings Exposed to Lanthanum Ions. *J. Environ. Sci.* **2012**, *24* (2), 214–220. [https://doi.org/10.1016/S1001-0742\(11\)60760-2](https://doi.org/10.1016/S1001-0742(11)60760-2).
- (5) Cui, J.; Zhang, Z.; Bai, W.; Zhang, L.; He, X.; Ma, Y.; Liu, Y.; Chai, Z. Effects of Rare Earth Elements La and Yb on the Morphological and Functional Development of Zebrafish Embryos. *J. Environ. Sci.* **2012**, *24* (2), 209–213. [https://doi.org/10.1016/S1001-0742\(11\)60755-9](https://doi.org/10.1016/S1001-0742(11)60755-9).
- (6) Swain, N.; Mishra, S. A Review on the Recovery and Separation of Rare Earths and Transition Metals from Secondary Resources. *J. Clean. Prod.* **2019**, *220*, 884–898. <https://doi.org/10.1016/j.jclepro.2019.02.094>.

- (7) Zhao, F.; Cong, Z.; Sun, H.; Ren, D. The Geochemistry of Rare Earth Elements (REE) in Acid Mine Drainage from the Sitai Coal Mine, Shanxi Province, North China. *Int. J. Coal Geol.* **2007**, *70* (1-3 SPEC. ISS.), 184–192. <https://doi.org/10.1016/j.coal.2006.01.009>.
- (8) Khairul, M. A.; Zanganeh, J.; Moghtaderi, B. The Composition, Recycling and Utilisation of Bayer Red Mud. *Resour. Conserv. Recycl.* **2019**, *141* (November 2018), 483–498. <https://doi.org/10.1016/j.resconrec.2018.11.006>.
- (9) Gutiérrez-Gutiérrez, S. C.; Coulon, F.; Jiang, Y.; Wagland, S. Rare Earth Elements and Critical Metal Content of Extracted Landfilled Material and Potential Recovery Opportunities. *Waste Manag.* **2015**, *42*, 128–136. <https://doi.org/10.1016/j.wasman.2015.04.024>.
- (10) Gao, L.; Kano, N.; Sato, Y.; Li, C.; Zhang, S.; Imaizumi, H. Behavior and Distribution of Heavy Metals Including Rare Earth Elements, Thorium, and Uranium in Sludge from Industry Water Treatment Plant and Recovery Method of Metals by Biosurfactants Application. *Bioinorg. Chem. Appl.* **2012**, *2012*. <https://doi.org/10.1155/2012/173819>.
- (11) Kawasaki, A.; Kimura, R.; Arai, S. Rare Earth Elements and Other Trace Elements in Wastewater Treatment Sludges. *Soil Sci. Plant Nutr.* **1998**, *44* (3), 433–441. <https://doi.org/10.1080/00380768.1998.10414465>.
- (12) Yessoufou, A.; Ifon, B. E.; Suanon, F.; Dimon, B.; Sun, Q.; Dedjiho, C. A.; Mama, D.; Yu, C. P. Rare Earth and Precious Elements in the Urban Sewage Sludge and Lake Surface Sediments under Anthropogenic Influence in the Republic of Benin. *Environ. Monit. Assess.* **2017**, *189* (12). <https://doi.org/10.1007/s10661-017-6331-6>.
- (13) Zhang, L.; Xu, Z. A Review of Current Progress of Recycling Technologies for Metals from Waste Electrical and Electronic Equipment. *J. Clean. Prod.* **2016**, *127*, 19–36. <https://doi.org/10.1016/j.jclepro.2016.04.004>.
- (14) Barros, Ó.; Costa, L.; Costa, F.; Lago, A.; Rocha, V.; Vipotnik, Z.; Silva, B.; Tavares, T. Recovery of Rare Earth Elements from Wastewater Towards a Circular Economy. *Molecules* **2019**, *24* (6), 1005. <https://doi.org/10.3390/molecules24061005>.
- (15) Gergoric, M.; Barrier, A.; Retegan, T. Recovery of Rare-Earth Elements from Neodymium Magnet Waste Using Glycolic, Maleic, and Ascorbic Acids Followed by Solvent Extraction. *J. Sustain. Metall.* **2019**, *5* (1), 85–96. <https://doi.org/10.1007/s40831-018-0200-6>.
- (16) Onoda, H.; Nakamura, R. Recovery of Neodymium from an Iron–Neodymium Solution Using Phosphoric Acid. *J. Environ. Chem. Eng.* **2014**, *2* (2), 1186–1190. <https://doi.org/10.1016/j.jece.2014.04.019>.
- (17) Arellano Ruiz, V. C.; Kuchi, R.; Parhi, P. K.; Lee, J.-Y.; Jyothi, R. K. Environmentally Friendly Comprehensive Hydrometallurgical Method Development for Neodymium Recovery from Mixed Rare Earth Aqueous Solutions Using Organo-Phosphorus Derivatives. *Sci. Rep.* **2020**, *10* (1), 16911. <https://doi.org/10.1038/s41598-020-74041-9>.
- (18) Zhang, Y.; Gu, F.; Su, Z.; Liu, S.; Anderson, C.; Jiang, T. Hydrometallurgical Recovery of Rare Earth Elements from NdFeB Permanent Magnet Scrap: A Review. *Metals (Basel)*. **2020**, *10* (6), 841. <https://doi.org/10.3390/met10060841>.

- (19) Anastopoulos, I.; Bhatnagar, A.; Lima, E. C. Adsorption of Rare Earth Metals: A Review of Recent Literature. *J. Mol. Liq.* **2016**, *221*, 954–962. <https://doi.org/10.1016/j.molliq.2016.06.076>.
- (20) Jyothi, R. K.; Thenepalli, T.; Ahn, J. W.; Parhi, P. K.; Chung, K. W.; Lee, J.-Y. Review of Rare Earth Elements Recovery from Secondary Resources for Clean Energy Technologies: Grand Opportunities to Create Wealth from Waste. *J. Clean. Prod.* **2020**, *267*, 122048. <https://doi.org/10.1016/j.jclepro.2020.122048>.
- (21) Alshameri, A.; Wei, X.; Wang, H.; Fuguo, Y.; Chen, X.; He, H.; Yan, C.; Xu, F. A Review of the Role of Natural Clay Minerals as Effective Adsorbents and an Alternative Source of Minerals. In *Minerals*; IntechOpen, 2019. <https://doi.org/10.5772/intechopen.87260>.
- (22) Diagboya, P. N.; Olu-Owolabi, B. I.; Mtunzi, F. M.; Adebawale, K. O. Clay-Carbonaceous Material Composites: Towards a New Class of Functional Adsorbents for Water Treatment. *Surfaces and Interfaces* **2020**, *19*, 100506. <https://doi.org/10.1016/j.surfin.2020.100506>.
- (23) Wang, J. Adsorption of Aqueous Neodymium, Europium, Gadolinium, Terbium, and Yttrium Ions onto NZVI-Montmorillonite: Kinetics, Thermodynamic Mechanism, and the Influence of Coexisting Ions. *Environ. Sci. Pollut. Res.* **2018**, *25* (33), 33521–33537. <https://doi.org/10.1007/s11356-018-3296-0>.
- (24) Xiao, Y.; Huang, L.; Long, Z.; Feng, Z.; Wang, L. Adsorption Ability of Rare Earth Elements on Clay Minerals and Its Practical Performance. *J. Rare Earths* **2016**, *34* (5), 543–548. [https://doi.org/10.1016/S1002-0721\(16\)60060-1](https://doi.org/10.1016/S1002-0721(16)60060-1).
- (25) Iannicelli-Zubiani, E. M.; Cristiani, C.; Dotelli, G.; Gallo Stampino, P.; Pelosato, R.; Mesto, E.; Schingaro, E.; Lacalamita, M. Use of Natural Clays as Sorbent Materials for Rare Earth Ions: Materials Characterization and Set up of the Operative Parameters. *Waste Manag.* **2015**, *46*, 546–556. <https://doi.org/10.1016/j.wasman.2015.09.017>.
- (26) Brião, G. de V.; Silva, M. G. C. da; Vieira, M. G. A. Neodymium Recovery from Aqueous Solution through Adsorption/Desorption onto Expanded Vermiculite. *Appl. Clay Sci.* **2020**, *198*, 105825. <https://doi.org/10.1016/j.clay.2020.105825>.
- (27) Zhao, L.; Duan, X.; Azhar, M. R.; Sun, H.; Fang, X.; Wang, S. Selective Adsorption of Rare Earth Ions from Aqueous Solution on Metal-Organic Framework HKUST-1. *Chem. Eng. J. Adv.* **2020**, *1* (June), 100009. <https://doi.org/10.1016/j.cej.2020.100009>.
- (28) Ogata, T.; Narita, H.; Tanaka, M. Immobilization of Diglycol Amic Acid on Silica Gel for Selective Recovery of Rare Earth Elements. *Chem. Lett.* **2014**, *43* (9), 1414–1416. <https://doi.org/10.1246/cl.140446>.
- (29) Ojima, Y.; Kosako, S.; Kihara, M.; Miyoshi, N.; Igarashi, K.; Azuma, M. Recovering Metals from Aqueous Solutions by Biosorption onto Phosphorylated Dry Baker's Yeast. *Sci. Rep.* **2019**, *9* (1), 1–9. <https://doi.org/10.1038/s41598-018-36306-2>.
- (30) Bunina, Z. Y.; Bryleva, K.; Yurchenko, O.; Belikov, K. Sorption Materials Based on Ethylene Glycol Dimethacrylate and Methacrylic Acid Copolymers for Rare Earth Elements Extraction from Aqueous Solutions. *Adsorpt. Sci. Technol.* **2017**, *35* (5–6), 545–559. <https://doi.org/10.1177/0263617417701455>.
- (31) Kinemuchi, H.; Ochiai, B. Synthesis of Hydrophilic Sulfur-Containing Adsorbents for

- Noble Metals Having Thiocarbonyl Group Based on a Methacrylate Bearing Dithiocarbonate Moieties. *Adv. Mater. Sci. Eng.* **2018**, 2018, 1–8. <https://doi.org/10.1155/2018/3729580>.
- (32) Srinivasan, R. Advances in Application of Natural Clay and Its Composites in Removal of Biological, Organic, and Inorganic Contaminants from Drinking Water. *Adv. Mater. Sci. Eng.* **2011**, 2011. <https://doi.org/10.1155/2011/872531>.
 - (33) Valaskova, M.; Martynková, G. S. Vermiculite: Structural Properties and Examples of the Use. In *Clay Minerals in Nature - Their Characterization, Modification and Application*; InTech, 2012; Vol. 2, p 64. <https://doi.org/10.5772/51237>.
 - (34) Arruda, G. M. Vermiculite Utilization on the Treatment of Water Contaminated with Organic Compounds; 2 nd Mercosur Congress on Chemical Engineering 4 Mercosur Congress on Process Systems Engineering, 2005; pp 1–10.
 - (35) Freitas, E. D. de; Almeida, H. J. de; Vieira, M. G. A. Binary Adsorption of Zinc and Copper on Expanded Vermiculite Using a Fixed Bed Column. *Appl. Clay Sci.* **2017**, 146 (July), 503–509. <https://doi.org/10.1016/j.clay.2017.07.004>.
 - (36) Długosz, O.; Banach, M. Kinetic, Isotherm and Thermodynamic Investigations of the Adsorption of Ag⁺ and Cu²⁺ on Vermiculite. *J. Mol. Liq.* **2018**, 258, 295–309. <https://doi.org/10.1016/j.molliq.2018.03.041>.
 - (37) Moraes, D. S.; Rodrigues, E. M. S.; Lamarão, C. N.; Marques, G. T.; Rente, A. F. S. New Sodium Activated Vermiculite Process. Testing on Cu²⁺ Removal from Tailing Dam Waters. *J. Hazard. Mater.* **2019**, 366 (September 2018), 34–38. <https://doi.org/10.1016/j.jhazmat.2018.11.086>.
 - (38) Granados-Correa, F.; Vilchis-Granados, J.; Jiménez-Reyes, M.; Quiroz-Granados, L. A. Adsorption Behaviour of La(III) and Eu(III) Ions from Aqueous Solutions by Hydroxyapatite: Kinetic, Isotherm, and Thermodynamic Studies. *J. Chem.* **2013**, 2013. <https://doi.org/10.1155/2013/751696>.
 - (39) Brunauer, S.; Emmett, P. H.; Teller, E. Adsorption of Gases in Multimolecular Layers. *J. Am. Chem. Soc.* **1938**, 60 (2), 309–319. <https://doi.org/10.1021/ja01269a023>.
 - (40) Riaño, S.; Binnemans, K. Extraction and Separation of Neodymium and Dysprosium from Used NdFeB Magnets: An Application of Ionic Liquids in Solvent Extraction towards the Recycling of Magnets. *Green Chem.* **2015**, 17 (5), 2931–2942. <https://doi.org/10.1039/c5gc00230c>.
 - (41) Xu, J. Recovery of Rare-Earth Elements from NdFeB Magnets by Zirconium Phosphate Ion Exchangers, Faculty of Science of the University of Helsinki, 2018.
 - (42) Gergorić, M. Hydrometallurgical Treatment of Neodymium Magnet Waste, Chalmers University of Technology, 2018.
 - (43) Park, H.-J.; Tavlarides, L. L. Adsorption of Neodymium(III) from Aqueous Solutions Using a Phosphorus Functionalized Adsorbent. *Ind. Eng. Chem. Res.* **2010**, 49 (24), 12567–12575. <https://doi.org/10.1021/ie100403b>.
 - (44) Lagergren, S. About the Theory of So-Called Adsorption of Soluble Substances. *K. Svensk Vetenskapsak ademiens Handl.* **1898**, 24, 1–39.
 - (45) Ho, Y. S.; McKay, G. A Comparison of Chemisorption Kinetic Models Applied to

- Pollutant Removal on Various Sorbents. *Process Saf. Environ. Prot.* **1998**, 76 (4), 332–340. <https://doi.org/10.1205/095758298529696>.
- (46) Weber, W. J.; Morris, J. C. Kinetics of Adsorption Carbon from Solutions. *J. Sanit. Engineering Div. Proc.* **1963**, 89, 31–60.
- (47) Boyd, G. E.; Adamson, A. W.; Myers, L. S. The Exchange Adsorption of Ions from Aqueous Solutions by Organic Zeolites. II. Kinetics. *J. Am. Chem. Soc.* **1947**, 69 (11), 2836–2848. <https://doi.org/10.1021/ja01203a066>.
- (48) Furusawa, T.; Smith, J. M. Fluid-Particle and Intraparticle Mass Transport Rates in Slurries. *Ind. Eng. Chem. Fundam.* **1973**, 12 (2), 197–203. <https://doi.org/10.1021/i160046a009>.
- (49) Viegas, R. M. C.; Campinas, M.; Costa, H.; Rosa, M. J. How Do the HSDM and Boyd's Model Compare for Estimating Intraparticle Diffusion Coefficients in Adsorption Processes. *Adsorption* **2014**, 20 (5–6), 737–746. <https://doi.org/10.1007/s10450-014-9617-9>.
- (50) Schweitzer, J.; Muller, G. Test Method 9081: Cation-Exchange Capacity of Soils (Sodium Acetate) <https://www.epa.gov/hw-sw846/sw-846-test-method-9081-cation-exchange-capacity-soils-sodium-acetate>.
- (51) Lata, S.; Singh, P. K.; Samadder, S. R. Regeneration of Adsorbents and Recovery of Heavy Metals: A Review. *Int. J. Environ. Sci. Technol.* **2015**, 12 (4), 1461–1478. <https://doi.org/10.1007/s13762-014-0714-9>.
- (52) Fornalczyk, A.; Willner, J.; Francuz, K.; Cebulski, J. E-Waste as a Source of Valuable Metals. *Arch. Mater. Sci. Eng.* **2013**, 63 (2), 87–92.
- (53) Bui, T. H.; Lee, W.; Jeon, S.-B.; Kim, K.-W.; Lee, Y. Enhanced Gold(III) Adsorption Using Glutaraldehyde-Crosslinked Chitosan Beads: Effect of Crosslinking Degree on Adsorption Selectivity, Capacity, and Mechanism. *Sep. Purif. Technol.* **2020**, 248, 116989. <https://doi.org/10.1016/j.seppur.2020.116989>.
- (54) Coates, J. Encyclopedia of Analytical Chemistry -II Interpretation of Infrared Spectra, A Practical Approach. *Encycl. Anal. Chem.* **2004**, 1–23.
- (55) Alves, A. P. M.; Fonseca, M. G.; Wanderley, A. F. Inorganic-Organic Hybrids Originating from Organosilane anchored onto Leached Vermiculite. *Mater. Res.* **2013**, 16 (4), 891–897. <https://doi.org/10.1590/S1516-14392013005000076>.
- (56) Long, H.; Wu, P.; Yang, L.; Huang, Z.; Zhu, N.; Hu, Z. Efficient Removal of Cesium from Aqueous Solution with Vermiculite of Enhanced Adsorption Property through Surface Modification by Ethylamine. *J. Colloid Interface Sci.* **2014**, 428, 295–301. <https://doi.org/10.1016/j.jcis.2014.05.001>.
- (57) Długosz, O.; Banach, M. Sorption of Ag⁺ and Cu²⁺ by Vermiculite in a Fixed-Bed Column: Design, Process Optimization and Dynamics Investigations. *Appl. Sci.* **2018**, 8 (11). <https://doi.org/10.3390/app8112221>.
- (58) Xu, B.; Ma, H.; Lu, Z.; Li, Z. Paraffin/Expanded Vermiculite Composite Phase Change Material as Aggregate for Developing Lightweight Thermal Energy Storage Cement-Based Composites. *Appl. Energy* **2015**, 160, 358–367. <https://doi.org/10.1016/j.apenergy.2015.09.069>.

- (59) Feng, J.; Liu, M.; Fu, L.; Zhang, K.; Xie, Z.; Shi, D.; Ma, X. Enhancement and Mechanism of Vermiculite Thermal Expansion Modified by Sodium Ions. *RSC Adv.* **2020**, *10* (13), 7635–7642. <https://doi.org/10.1039/D0RA00223B>.
- (60) Maia, F. A. D. Caracterização e Aplicação de Vermiculita Natural e Quimicamente Modificada Na Adsorção de Azul de Metileno, Universidade Federal do Rio Grande do Norte, 2014.
- (61) Cuong, N. D.; Hue, V. T.; Kim, Y. S. Thermally Expanded Vermiculite as a Risk-Free and General-Purpose Sorbent for Hazardous Chemical Spillages. *Clay Miner.* **2019**, *54* (3), 235–243. <https://doi.org/10.1180/clm.2019.34>.
- (62) Hillier, S.; Marwa, E. M. M.; Rice, C. M. On the Mechanism of Exfoliation of ‘Vermiculite.’ *Clay Miner.* **2013**, *48* (4), 563–582. <https://doi.org/10.1180/claymin.2013.048.4.01>.
- (63) Balima, F.; Le Floch, S.; San-Miguel, A.; Reinert, L.; Duclaux, L.; Nguyen, A. N.; Daniel, I.; Brûlet, A.; Gremillard, L.; Pischedda, V. Porosity Evolution of Expanded Vermiculite under Pressure: The Effect of Pre-Compaction. *SN Appl. Sci.* **2019**, *1* (6), 1–9. <https://doi.org/10.1007/s42452-019-0627-9>.
- (64) Ikenyiri, P. N.; Ukpaka, C. P. Overview on the Effect of Particle Size on the Performance of Wood Based Adsorbent. *J. Chem. Eng. Process Technol.* **2016**, *07* (05). <https://doi.org/10.4172/2157-7048.1000315>.
- (65) Olu-Owolabi, B. I.; Diagbaya, P. N.; Mtunzi, F. M.; Düring, R.-A. Utilizing Eco-Friendly Kaolinite-Biochar Composite Adsorbent for Removal of Ivermectin in Aqueous Media. *J. Environ. Manage.* **2021**, *279*, 111619. <https://doi.org/10.1016/j.jenvman.2020.111619>.
- (66) Padilla-Ortega, E.; Leyva-Ramos, R.; Mendoza-Barron, J. Role of Electrostatic Interactions in the Adsorption of Cadmium(II) from Aqueous Solution onto Vermiculite. *Appl. Clay Sci.* **2014**, *88–89*, 10–17. <https://doi.org/10.1016/j.clay.2013.12.012>.
- (67) Burham, N.; Sayed, M. Adsorption Behavior of Cd²⁺ and Zn²⁺ onto Natural Egyptian Bentonitic Clay. *Minerals* **2016**, *129* (6), 1–15. <https://doi.org/https://doi.org/10.3390/min6040129>.
- (68) Khalfa, L.; Cervera, M. L.; Bagane, M.; Souissi-Najar, S. Modeling of Equilibrium Isotherms and Kinetic Studies of Cr (VI) Adsorption into Natural and Acid-Activated Clays. *Arab. J. Geosci.* **2016**, *9* (1), 75. <https://doi.org/10.1007/s12517-015-2104-0>.
- (69) Chowdhury, S.; Saha, P. Sea Shell Powder as a New Adsorbent to Remove Basic Green 4 (Malachite Green) from Aqueous Solutions: Equilibrium, Kinetic and Thermodynamic Studies. *Chem. Eng. J.* **2010**, *164* (1), 168–177. <https://doi.org/10.1016/j.cej.2010.08.050>.
- (70) Xikhongelo, R. V.; Mtunzi, F. M.; Diagbaya, P. N.; Olu-Owolabi, B. I.; Düring, R.-A. Polyamidoamine-Functionalized Graphene Oxide–SBA-15 Mesoporous Composite: Adsorbent for Aqueous Arsenite, Cadmium, Ciprofloxacin, Ivermectin, and Tetracycline. *Ind. Eng. Chem. Res.* **2021**, *acs.iecr.0c04902*. <https://doi.org/10.1021/acs.iecr.0c04902>.
- (71) Ho, Y. S. Review of Second-Order Models for Adsorption Systems. *J. Hazard. Mater.* **2006**, *136* (3), 681–689. <https://doi.org/10.1016/j.jhazmat.2005.12.043>.

- (72) Tan, K. L.; Hameed, B. H. Insight into the Adsorption Kinetics Models for the Removal of Contaminants from Aqueous Solutions. *J. Taiwan Inst. Chem. Eng.* **2017**, *74*, 25–48. <https://doi.org/10.1016/j.jtice.2017.01.024>.
- (73) Kajjumba, G. W.; Emik, S.; Öngen, A.; Kurtulus Özcan, H.; Aydın, S. Modelling of Adsorption Kinetic Processes—Errors, Theory and Application. In *Advanced Sorption Process Applications*; IntechOpen, 2019. <https://doi.org/10.5772/intechopen.80495>.
- (74) Wu, F.-C.; Tseng, R.-L.; Juang, R.-S. Initial Behavior of Intraparticle Diffusion Model Used in the Description of Adsorption Kinetics. *Chem. Eng. J.* **2009**, *153* (1–3), 1–8. <https://doi.org/10.1016/j.cej.2009.04.042>.
- (75) McKay, G. The Removal of Colour from Effluent Using Various Adsorbents—III. Silica: Rate Processes. *Water Res.* **1980**, *14* (1), 15–20. [https://doi.org/10.1016/0043-1354\(80\)90037-8](https://doi.org/10.1016/0043-1354(80)90037-8).
- (76) Yang, W.; Zheng, Y.; Zaoui, A. Swelling and Diffusion Behaviour of Na-Vermiculite at Different Hydrated States. *Solid State Ionics* **2015**, *282*, 13–17. <https://doi.org/10.1016/j.ssi.2015.09.007>.
- (77) Lai, T. M.; Mortland, M. M. Cationic Diffusion in Clay Minerals:II. Orientation Effects. *Clays Clay Miner.* **1968**, *16* (2), 129–136. <https://doi.org/10.1346/CCMN.1968.0160203>.
- (78) Guiza, S.; Hajji, H.; Bagane, M. External Mass Transport Process during the Adsorption of Fluoride from Aqueous Solution by Activated Clay. *Comptes Rendus Chim.* **2019**, *22* (2–3), 161–168. <https://doi.org/10.1016/J.CRCL.2019.02.001>.
- (79) Wang, A.; Wang, W. *Vermiculite Nanomaterials: Structure, Properties, and Potential Applications*; Elsevier Inc., 2019. <https://doi.org/10.1016/B978-0-12-814533-3.00009-0>.
- (80) Seaborn, D. J.; Jameson, G. J. Some Ion Exchange Properties of Exfoliated Vermiculite. *Hydrometallurgy* **1976**, *2*, 141–155.
- (81) Cechinel, M. A. P.; Mayer, D. A.; Pozdniakova, T. A.; Mazur, L. P.; Boaventura, R. A. R.; de Souza, A. A. U.; de Souza, S. M. A. G. U.; Vilar, V. J. P. Removal of Metal Ions from a Petrochemical Wastewater Using Brown Macro-Algae as Natural Cation-Exchangers. *Chem. Eng. J.* **2016**, *286*, 1–15. <https://doi.org/10.1016/j.cej.2015.10.042>.
- (82) Cardoso, S. L.; Costa, C. S. D.; da Silva, M. G. C.; Vieira, M. G. A. Insight into Zinc(II) Biosorption on Alginate Extraction Residue: Kinetics, Isotherm and Thermodynamics. *J. Environ. Chem. Eng.* **2020**, *8* (3), 103629. <https://doi.org/10.1016/j.jece.2019.103629>.
- (83) Ugarte, J. F. de Ol.; Sampaio, J. A.; França., S. C. A. Vermiculita. In *Rochas e Minerais Industriais -CETEM/2008*; 2008; pp 861–887.
- (84) Kalinowski, B. E.; Schweda, P. Rates and Nonstoichiometry of Vermiculite Dissolution at 22°C. *Geoderma* **2007**, *142* (1–2), 197–209. <https://doi.org/10.1016/j.geoderma.2007.08.011>.
- (85) Gu, S.; Kang, X.; Wang, L.; Lichtfouse, E.; Wang, C. Clay Mineral Adsorbents for Heavy Metal Removal from Wastewater: A Review. *Environ. Chem. Lett.* **2019**, *17* (2), 629–654. <https://doi.org/10.1007/s10311-018-0813-9>.
- (86) Malandrino, M.; Abollino, O.; Giacomino, A.; Aceto, M.; Mentasti, E. Adsorption of

- Heavy Metals on Vermiculite: Influence of PH and Organic Ligands. *J. Colloid Interface Sci.* **2006**, 299 (2), 537–546. <https://doi.org/10.1016/j.jcis.2006.03.011>.
- (87) Han, B.; He, B.; Geng, R.; Zhao, X.; Li, P.; Liang, J.; Fan, Q. Ni(II) Sorption Mechanism at the Vermiculite-Water Interface: Effects of Interlayer. *J. Mol. Liq.* **2019**, 274, 362–369. <https://doi.org/10.1016/j.molliq.2018.10.153>.
- (88) Węgrzyn, A.; Chmielarz, L.; Zjezdzałka, P.; Kowalczyk, A.; Jabłońska, M.; Baldrich Tolosa, X.; Michalik, M. Adsorbents for Iron Removal Obtained from Vermiculite. *Acta Geodyn. Geomater.* **2013**, 10 (3), 353–361. <https://doi.org/10.13168/AGG.2013.0034>.
- (89) Birungi, Z. S.; Nkhalambayausi Chirwa, E. M.; Shen, N.; Roestorff, M. Recovery of Rare Earths, Precious Metals and Bioreduction of Toxic Metals from Wastewater Using Algae. In *Emerging Eco-friendly Green Technologies for Wastewater Treatment*; 2020; pp 267–297. https://doi.org/10.1007/978-981-15-1390-9_12.
- (90) Polido Legaria, E.; Rocha, J.; Tai, C.-W.; Kessler, V. G.; Seisenbaeva, G. A. Unusual Seeding Mechanism for Enhanced Performance in Solid-Phase Magnetic Extraction of Rare Earth Elements. *Sci. Rep.* **2017**, 7 (1), 43740. <https://doi.org/10.1038/srep43740>.
- (91) Jacobsen, D.; McMartin, K. E. Alcohols and Glycols. In *Human Toxicology*; Elsevier, 1996; pp 623–648. <https://doi.org/10.1016/B978-044481557-6/50026-5>.
- (92) Garrett, D. E. Calcium Chloride. In *Handbook of Lithium and Natural Calcium Chloride*; Elsevier, 2004; pp 237–457. <https://doi.org/10.1016/B978-012276152-2/50038-4>.
- (93) He, H.; Guo, J.; Xie, X.; Peng, J. Experimental Study of the Selective Adsorption of Heavy Metals onto Clay Minerals. *Chinese J. Geochemistry* **2000**, 19 (2), 105–109. <https://doi.org/10.1007/BF03166865>.
- (94) Persson, I. Hydrated Metal Ions in Aqueous Solution: How Regular Are Their Structures? *Pure Appl. Chem.* **2010**, 82 (10), 1901–1917. <https://doi.org/10.1351/PAC-CON-09-10-22>.
- (95) Marcus, Y. Thermodynamics of Solvation of Ions. Part 5. - Gibbs Free Energy of Hydration at 298.15 K. *J. Chem. Soc. Faraday Trans.* **1991**, 87 (18), 2995–2999. <https://doi.org/10.1039/FT9918702995>.
- (96) Ogata, T.; Narita, H.; Tanaka, M. Rapid and Selective Recovery of Heavy Rare Earths by Using an Adsorbent with Diglycol Amic Acid Group. *Hydrometallurgy* **2015**, 155, 105–109. <https://doi.org/10.1016/j.hydromet.2015.04.015>.

CHAPTER 4. NEODYMIUM ADSORPTION ON EXPANDED VERMICULITE IN BATCH MODE: EQUILIBRIUM, THERMODYNAMICS, AND REUSE

Neodymium recovery from aqueous solution through adsorption/desorption onto expanded vermiculite³

Giani de Vargas Brião, Meuris Gurgel Carlos da Silva, Melissa Gurgel Adeodato Vieira

University of Campinas, School of Chemical Engineering, Albert Einstein Avenue, 500, 13083-852 Campinas, Brazil

ABSTRACT

The noble application of the neodymium on the technological field provides its high aggregate value. However, the future supply depends on the recycle, which still needs the improvement of the classical separation methods. In this study, expanded vermiculite was employed as an adsorbent to neodymium recovery from aqueous solution in batch mode. The specific properties of this phyllosilicate such as the lamellar structure were confirmed by different analytical techniques. The equilibrium of adsorption was well explained by Langmuir achieving the maximum adsorption capacity of 0.48 mmol/g at 283 K. The process was exothermic, spontaneous, and classified as physical adsorption. Desorption experimental conditions were optimized using the response surface methodology. The calcium chloride (0.3 mol/L) as eluent guaranteed a high recovery of neodymium and great reusability to the adsorbent material, achieving an uptake efficiency of 94% and a neodymium recovery of 95% in the fifth cycle. Thus, this commercial clay mineral demonstrated a great potential to recover neodymium from aqueous solution, due to the high adsorption and desorption efficiency after successive cycles of reuse.

Keywords: (Bio)sorption; Rare-earth elements; Toxic metals; Dysprosium biosorption; Sericin and alginate; Chemical crosslinking.

³ Manuscript published in *Applied Clay Science* (2020).

DOI: 10.1016/j.clay.2020.105825. Reprinted with the journal's permission (Appendix B.3).

4.1 INTRODUCTION

Rare earth metals such as the neodymium are classified as critical element for their specific role in the manufacture of some fundamental products to strategic fields, as energy, defense, and medical, also, the supply source is at the moment a Chinese monopoly (Charalampides et al., 2015). Neodymium (Nd), a member of the group of rare earth metals (REM), has its major application in the manufacture of permanent magnets of the NdFeB type used in electric vehicle engines, wind power generation turbines, and electronic devices. The circular economy for critical metals has gain attention in recent years, where the main idea is to substitute the linear material and energy flow that comprises extraction, production, use, and disposal with the adoption of a ‘closing-the-loop’ production (Korhonen et al., 2018). The circular economy of rare earths will minimize the environmental impacts by the mining activities (Zhang and Xu, 2016; Jowitt et al., 2018; Favot and Massarutto, 2019), and can turn the recycle a rentable activity.

The main application of neodymium is on the confection of Nd-Fe-B permanent magnets, and the recovery of Nd from this products implies many technological challenges due to the difficulties in the assemblage of the magnets from small electronic parts (Peelman et al., 2018) and the high dilution of these metals on the scrap flow (Yang et al., 2017). Studies have been proposed some hydrometallurgical methods to recover rare earth from magnet scrap, such as separation using ionic liquid (Riaño and Binnemans, 2015), lixiviation, and selective extraction (Gergoric et al., 2019), and ion exchange (Xu et al., 2018). However, at low concentrations, adsorption is considered an alternative to conventional hydrometallurgy techniques because it is simple, efficient, selective, and cost-effective (Barcelos da Costa et al., 2020; Costa et al., 2020; Jyothi et al., 2020). The adsorption of neodymium has been studied on different adsorbent matrices as acrylic resin (Xiong et al., 2015), biochar (Komnitsas et al., 2017), microalgae (Kucuker et al., 2017), and modified montmorillonite clay (Wang, 2018).

The physic-chemical properties of an adsorbent are fundamental to provide a high affinity to a determinate adsorbate. De Gisi et al. (2016), emphasized the interesting characteristics of clay and clay minerals as adsorbents, such as the negative charge able to be neutralized by the adsorption of cations. Expanded vermiculite is a hydrated magnesium aluminum phyllosilicate, which is exposed to thermal or chemical expansion (Arruda, 2005). Vermiculite has a known high exchange capacity between 120 to 200 cmol/kg (Valaskova and Martynková, 2012) that motivated many studies about the adsorption of precious and toxic metals (Freitas et al., 2017;

Chen et al., 2018; Długosz and Banach, 2018; Moraes et al., 2019). Despite of that, there are no studies on the adsorption of rare earth elements onto vermiculite.

Thus, this work aims to investigate the adsorption and desorption of neodymium using expanded vermiculite as an adsorbent in batch mode. The equilibrium of adsorption, the thermodynamic, and the desorption of neodymium were evaluated. Moreover, the properties of the expanded vermiculite before and after the adsorption were conferred by characterization analysis, such as scanning electron microscopy (SEM), X-ray diffraction (XRD), isotherm of adsorption and desorption of nitrogen, porosimetry by mercury intrusion, and thermogravimetric analysis (TGA) and differential thermal analysis (DTA).

4.2 MATERIALS AND METHODS

4.2.1 Materials

The adsorbent applied in this work was the expanded vermiculite, donated by Brasil Minérios S.A from Goiania/Brazil, with a particle size of 0.855 mm. $\text{Nd}(\text{NO}_3)_3 \cdot 6\text{H}_2\text{O}$ (Aldrich, 99.9%) was applied to make a standard solution that was diluted in deionized water at different concentrations.

4.2.2 Characterization

Expanded vermiculite was characterized before (EV) and after (EV-Nd) the adsorption process. Adsorbent images were made by scanning electron microscopy spectrometry (SEM) (LEO 440i, LEO). The surface area analyzer ANOVA-e (Quantachrome) was utilized to obtain the isotherm of adsorption and desorption of N_2 , with a pressure range from 10 to 800 mmHg. The pore distribution was determined by mercury porosimetry (Auto Pore IV, Micromeritics). The X-ray diffraction analysis occurred in the equipment Philips Analytical X-Ray (X'Pert-MPD), the copper $\text{K}\alpha$ with $\lambda=1.54056 \text{ \AA}$, no monochromator was used, step scan size of 0.05 degree, counting time of 2 s/step. The thermogravimetric and differential thermal analyzes were performed using DTG-60 (Shimadzu), with a gas flow of 50 ml/min, a heating rate of 20 °C/min, and under nitrogen atmosphere.

4.2.3 Adsorption Experiments

4.2.3.1 General

The adsorption of neodymium on expanded vermiculite was evaluated in batch mode, in which Erlenmeyers of 100 mL were agitated at 200 rpm for 24 h, except for the desorption study where the time was varied. The pH of the solutions was maintained around 3.0 by the addition of a few milliliters of HNO₃. Equations 4.1 to 4.4 were applied to calculate the adsorption capacity (q), removal percentage ($\%R$), desorption capacity (q_{el}), desorption percentage ($\%D$), respectively.

$$q = \frac{C_0 - C_f}{m} V \quad (4.1)$$

$$\%R = \frac{C_0 - C_f}{C_0} 100 \quad (4.2)$$

$$q_{el} = \frac{C_f}{m} V \quad (4.3)$$

$$\%D = \frac{q_{el}}{q} 100 \quad (4.4)$$

Where C_0 is the initial concentration (mmol/L), C_f is the final concentration at the equilibrium (mmol/L), V is the solution volume (L) and m is the adsorbent mass (g).

The determination of the neodymium concentration was done by spectrophotometry UV-visible (UVmini-1240, Shimadzu) through the formation of a complex with xylenol orange in a wavelength of 575 nm (maximum absorbance). The complex was formed in a volumetric flask (10 mL) by the addition of 2 mL of the metal solution, 3 mL of xylenol orange (4.5×10^{-4} mol/L), and 5 mL of a buffer solution of acetic acid/sodium acetate (pH 5.6) (Havel et al., 1994; Granados-Correa et al., 2013).

4.2.3.2 Adsorption kinetics

In the kinetic study of the neodymium adsorption on expanded vermiculite was performed, a solution with a neodymium concentration of 0.5 mmol/L was put on contact with the EV under mechanical agitation. Aliquots were collected along to the time and the solid was separated using a syringe filter (Chromafil Xtra PES-20/25). The neodymium concentrations were determined according to section 2.2.1.

The pseudo-first-order (PFO) (Equation 4.5)(Lagergren, 1898)(Lagergren, 1898), pseudo-second-order (PSO) (Equation 4.6) (Ho and McKay, 1998) were adjusted to the kinetic data, in order to obtain the adsorption rate.

$$q_t = q_e(1 - e^{-k_1 t}) \quad (4.5)$$

$$q_t = \frac{k_2 q_e^2 t}{1 + k_2 q_e t} \quad (4.6)$$

Where q_t and q_e are the adsorption capacity at time t and at the equilibrium (mmol/g) respectively; k_1 is the PFO rate constant of adsorption (1/min); k_2 is the PSO rate constant of adsorption (g/mmol.min).

4.2.3.3 Adsorption equilibrium

50 mL of metal solution was mixed with 0.7 g of the adsorbent at 283, 298, 313, and 328 K. The initial concentration of neodymium varied from 1 to 12 mmol/L. The models of adsorption isotherms that associate the C_e (adsorbate concentration (mmol/L) on the solution at equilibrium) with q_e (adsorption capacity (mmol/g) at the equilibrium) applied in this study were Langmuir (Langmuir, 1918) (Equation 4.7), Freundlich (Freundlich, 1906) (Equation 4.8), Sips (Sips, 1948) (Equation 4.9), and Dubinin-Radushkevich (Dubinin and Radushkevich, 1947) (Equations 10-12).

$$q_e = \frac{q_m K_L C_e}{1 + (K_L C_e)} \quad (4.7)$$

$$q_e = K_F C_e^{n_F} \quad (4.8)$$

$$q_e = \frac{q_{mS} K_S C_e^{m_S}}{1 + (K_S C_e)^{m_S}} \quad (4.9)$$

$$q_e = q_m e^{-\beta \varepsilon^2} \quad (4.10)$$

Where K_L is the Langmuir constant (L/mmol) and q_m is the maxima adsorption capacity (mmol/g), K_F (L/g) is the Freundlich constant and n_F is considered the heterogeneity constant ($0 < n_F < 1$), q_{mS} is the Sips maximum adsorption capacity (mmol/g), K_S is the Sips constant

(L/mmol), and m_s is the dimensionless heterogeneity factor, β is the constant associated with the free energy of adsorption (mol^2/J^2) and ε is the Polanyi potential (J/mol).

Equation 4.11 describes the Polanyi potential and Equation 4.12 calculates the free energy of adsorption.

$$\varepsilon = RT \ln \left(1 + \frac{1}{C_e/1000} \right) \quad (4.11)$$

$$E = \frac{1}{\sqrt{2\beta}} \quad (4.12)$$

Where R is the ideal gas constant (8.314 J/mol.K), T is the temperature (K), E is the free energy of adsorption (J/mol).

4.2.3.4 Thermodynamic

To estimate the adsorption energy of Gibbs (ΔG_{ads}°) it was applied to the classic Van't Hoff (1884) equation (Equation 4.13).

$$\Delta G_{ads}^\circ = -RT \ln K_e \quad (4.13)$$

Where T is the temperature (K), R is the ideal gas constant (8.314 J/mol K) e K_e is the equilibrium constant.

K_e was determined according to Ghosal and Gupta (2017), Lima et al. (2019), Liu (2009), considering the relationship between the coefficient of activity of neodymium at equilibrium (γ_e) and the Langmuir constant (Equation 14). Langmuir constant as the equilibrium constant ($K_e = K_L$) was also applied to compare the influence of the acidity on the quality of adjusting (R^2) to obtain the thermodynamic parameters.

$$K_e = \frac{K_L}{\gamma_e} \cdot (1 \text{ mol.L}^{-1}) \quad (4.14)$$

For a more accurate estimation of the equilibrium constant considering the effect of the activity coefficient, the Langmuir isotherm should be plotted as q_{ae} versus a_e (Ghosal and Gupta, 2017), where q_{ae} is calculated by Equation (4.15).

$$q_{ae} = \frac{\gamma_0 C_0 - \gamma_e C_e}{m} V = \frac{a_0 - a_e}{m} V \quad (4.15)$$

In which, a_0 , γ_0 , and a_e are the activity and activity coefficient at the initial stage and the activity at the equilibrium. γ is a function of ionic strength (I) of solute and the charge of solute (z), temperature (T), and dielectric constant of water (ϵ). The activity coefficient at the beginning and at equilibrium can be obtained using Equation 16 (Hückel and Debye, 1923).

$$\log \gamma = -\frac{1.824 \times 10^6}{(\epsilon T)^{3/2}} z^2 \sqrt{I} \quad (4.16)$$

As the adsorption occurs in aqueous media, $\epsilon = 78.54$, and the ionic strength of neodymium (Nd^{3+}) is calculated following Equation 4.17. Based on the speciation of neodymium in an aqueous solution, at low pHs, the main species in solution is Nd^{3+} (Park and Tavlarides, 2010; Brião et al., 2019). Thus, the ionic strength was calculated considering just the concentration (C) and charge of neodymium (z).

$$I = \frac{1}{2} C z^2 \quad (4.17)$$

ΔG_{ads}^o can be related to the adsorption enthalpy (ΔH_{ads}^o) and entropy (ΔS_{ads}^o) conforming Equation 4.18.

$$\Delta G_{ads}^o = \Delta H_{ads}^o - T \Delta S_{ads}^o \quad (4.18)$$

Finally, ΔH_{ads}^o and ΔS_{ads}^o can be estimated, respectively, through the angular and linear coefficients of the slope $\ln K_e$ versus $1/T$ (Equation 4.19).

$$\ln K_e = \frac{-\Delta H_{ads}^o}{RT} + \frac{\Delta S_{ads}^o}{R} \quad (4.19)$$

Isosteric heat is an important thermodynamic parameter that has been discussed in relevant studies of adsorption (Santos et al., 2020). Saha and Chowdhury (2011) affirmed that the isosteric heat of adsorption (ΔH_x , kJ/mol) is defined as the heat determinate at a constant amount of adsorbate adsorbed. Equation 4.20 relates ΔH_x to the C_e .

$$\ln C_e = - \left(\frac{\Delta H_x}{R} \right) \frac{1}{T} + b \quad (4.20)$$

Where b is a constant. The isosteric heat of adsorption is calculated from the slope of the plot of $\ln C_e$ versus $1/T$ by different adsorbed amounts (q_e).

4.2.4. Criteria for the quality of the model fit

The quality of the model adjusts to experimental data was evaluated by determination coefficient (R^2), adjusted determination coefficient (R^2_a), Akaike Information Criterion for small samples (AIC_c), and sum square of errors (SSE).

4.2.5. Desorption Experiments

To conduct the desorption experiments, firstly, the neodymium (1 mmol/L) was loaded on the adsorbent. Calcium chloride (CaCl_2 , Dinâmica 99%) was applied as eluent due to the high desorption capacity presented in a previous study (Nishikawa et al., 2012). The desorption experiments were divided into (i) optimization of the experimental desorption conditions and (ii) cycles of adsorption and desorption under the optimal conditions.

Desorption can be affected by many variables as like eluent concentration, solid/liquid ratio (dosage), time, temperature, pH, agitation speed and others, thus, to optimize the desorption efficiency (%D), we performed a rotational composite central design (RCCD) with central point triplicate, and the response surface methodology (RSM). The design of experiments allows testing hypotheses in the most efficient way while avoiding wrong experimental practices (Santos et al., 2019) and have been applied successfully to the desorption optimization (Amorim et al., 2003; Assoumani et al., 2014; Momina et al., 2019).

The independent variables were eluent concentration (A), time (B), and adsorbent dosage (C). A variance analysis test (ANOVA) with a significance level of 5% and the generation of the surface response was performed on Statistics 8.0 software. Equation 4.21 presents the empiric-squared model proposed to predict the desorption efficiency. The model, after backward elimination, was validated by an adsorption and desorption test (triplicate) under the optimal conditions obtained by RSM analysis.

$$\%D = b_0 + b_1A + b_2B + b_3C + b_{11}A^2 + b_{22}B^2 + b_{33}C^2 + b_{12}AB + b_{13}AC + b_{23}BC \quad (4.21)$$

Where $\%D$ is the desorption percentage (response variable), b_0 is constant (mean), b_1 , b_2 , b_3 are linear coefficients, b_{12} , b_{13} , and b_{23} are cross-product coefficients and b_{11} , b_{22} , and b_{33} are quadratic coefficients (Box et al., 1978). Table 4.1 exhibits the RCCD levels of the experimental domain of neodymium desorption.

Table 4.1. The experimental domain of RCCD for the neodymium desorption from EV

Factor	Code	Levels				
		$-\alpha$	-1	0	+1	$+\alpha$
Eluent concentration (mol/L)	<i>A</i>	0.049	0.15	0.30	0.45	0.55
Time (h)	<i>B</i>	0.49	1.5	3.0	4.5	5.51
Adsorbent dosage (g/L)	<i>C</i>	7.3	10.0	14.0	18.0	20.7

The range of eluent concentration was based on the limitations of the Nd complexation reaction on the eluent matrix. On this range was possible to obtain a linear relation between absorbance and Nd concentration. The maximum time value was determined based on previous work (Nishikawa et al., 2012). The dosage of the adsorbent contains, as the central point, the solid-liquid ratio applied to the adsorption experiments.

4.2.6 Cost analysis at lab scale

In this study, we estimated the cost of the process to recovery 1 g of neodymium from a solution with initial concentration fixed in 1 mmol/L. The price of the main reactants was considered based on the Brazilian market.

4.3 RESULTS AND DISCUSSION

4.3.1 Characterization analyses

Figure 4.1 depicts the SEM images in the amplification of 400 times (a, b) 1800 times (c, d) for the expanded vermiculite before and after the neodymium adsorption. Figure 4.1(a) and Figure 4.1(b) show the expanded vermiculite before the Nd^{3+} adsorption, where evident the lamellar structure with different slit openings. Figure 4.1(c) and Figure 4.1(d), in contrast,

pointed out that there was a loss of expansion and homogenization of layered structure after the Nd^{3+} adsorption.

The isotherms of adsorption and desorption of N_2 (Figure 4.2) of the expanded vermiculite before and after the adsorption do not exhibit plateaus at high relative pressures, therefore they can be classified as H3 (Sing et al., 1985). Such isotherm shape indicates that the material contains both mesopores, which are responsible for the H3 type hysteresis, and macropores, which results in an absence of the plateau (Kuila, 2013). This kind of isotherm is generally observed when there is an aggregate of particles in the form of plates that originate porous as slits, which is a predominant characteristic of the phyllosilicates as the vermiculite. Furthermore, EV has more micropores than EV-Nd, as indicated by a larger adsorbed volume at $P/P_0 < 0.01$. The volumes of micro, meso, and macropores are presented in Table 4.2.

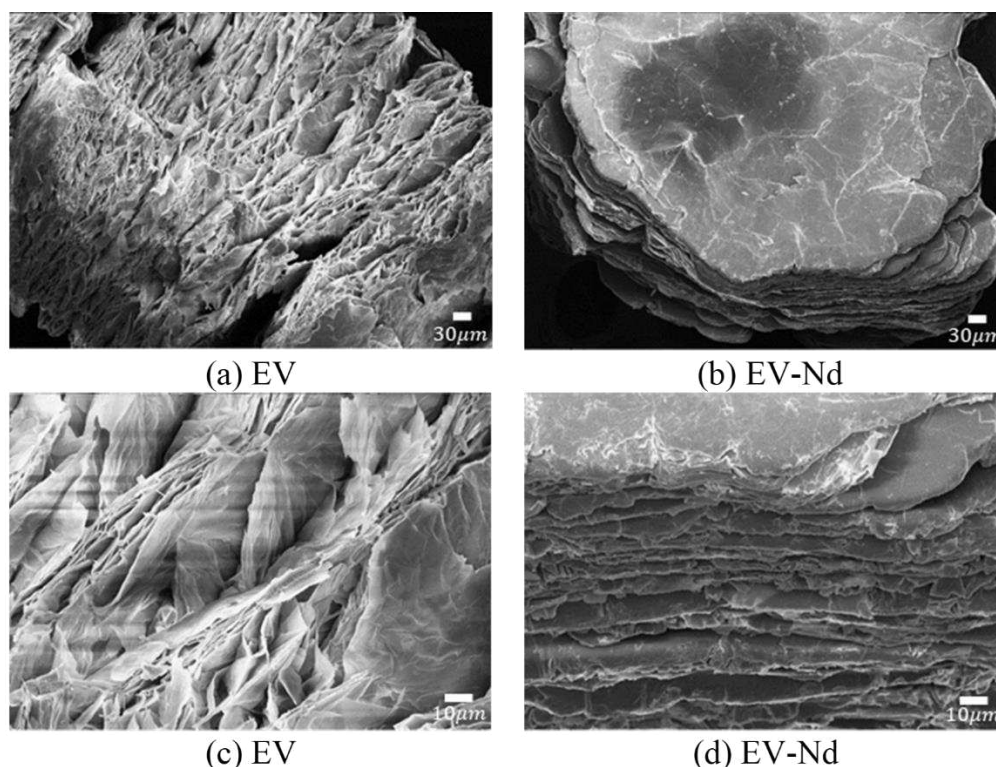


Figure 4.1 – SEM images for vermiculite before (a-c) e after the neodymium adsorption (b-d).

The intrusion of mercury confers information about the porous distribution, considering the porous geometry as a sphere. However, for vermiculite (phyllosilicate), where the openings in the material are in the form of slits (interlayers), the volume of intruded mercury is presented as a function of the opening of the slits, according to the Figure 4.3(a) (Anovitz and Cole, 2015). Figure 4.3(a) shows that EV has slits with the opening of diverse sizes; it is a non-homogenous

distribution along with all range of slits, however, EV presented the maximum volume of the intruded mercury at the slit size of 60 μm . The EV-Nd curve presented a pronounced peak for large slit openings, that can be related to the loss of expansion of the vermiculite that makes the mercury fills the void spaces between particles generating artificial “slits” in the range of 100 μm (Giesche, 2006; Cuong et al., 2019). In the range of slit size lower than 12 μm , both materials presented two evident slits sizes, being 2.68 and 9.74 μm for EV, and 1.79 and 10.95 μm for EV-Nd.

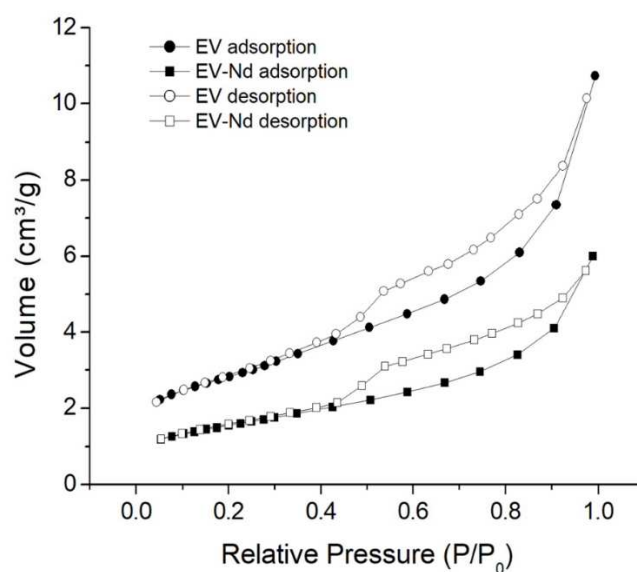


Figure 4.2 – Isotherm of adsorption and desorption of N_2 for EV and EV-Nd.

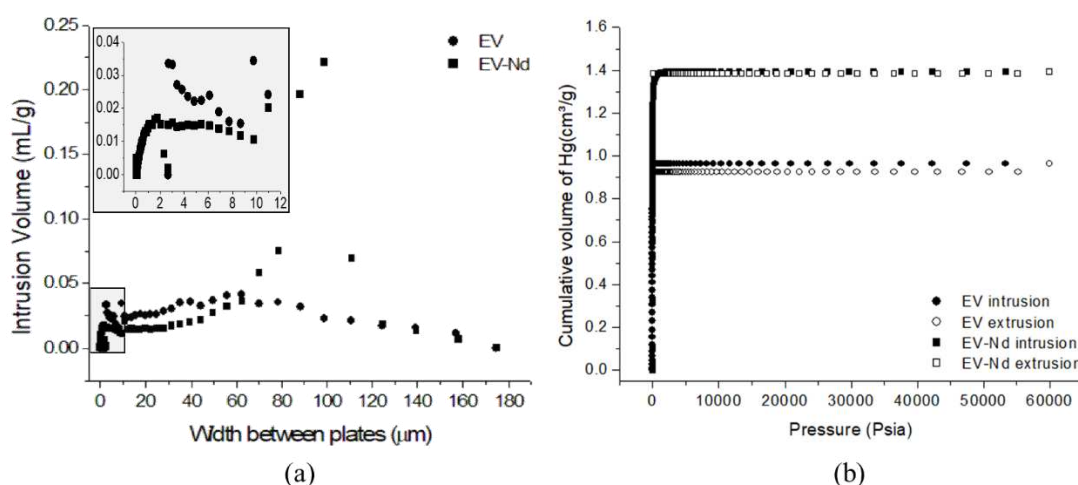


Figure 4.3 – Mercury intrusion volume in function of the width of slits (a) and cumulative volume versus the pressure (b)

Figure 4.3(b) shows the mercury intrusion and extrusion behavior into the vermiculite. The cumulative intruded volume was 0.96 and 1.39 cm³/g, for EV and EV-Nd, indicating that the neodymium adsorption conferred more macropores to the material. The cumulative extruded volume is constant in all ranges of pressure, indicating that the mercury remains confined in samples after the pressure recovering to the initial one. It can be explained by the fact of the mercury extrusion damage the structure of highly compressible clay samples as expanded vermiculite, which can trap mercury into the vermiculite structure (Giesche, 2006).

According to Table 4.2, expanded vermiculite has, majority, a mesoporous structure, with a volume of mesopores equal to 8.26 and 4.66 cm³/g, before and after the adsorption of neodymium. The estimated total pore volume was 10.73 and 5.99 cm³/g, for EV and EV-Nd respectively. This decrease can be attributed to the neodymium uptake on the active sites and loss of expansion. However, the increase of the macropores in the EV-Nd samples may be associated with the collapse of the layers due to the presence of hydroxy-aluminum species in acidic conditions (Malla, 1978).

Table 4.2. Textural properties of the expanded vermiculite before and after the neodymium adsorption

Sample	V_{micro} (cm ³ /g)	V_{meso} (cm ³ /g)	V_{macro} (cm ³ /g)	V_{total} (cm ³ /g)	S_{BET} (m ² /g)
EV	2.47	8.26	0.96	10.73	9.88
EV-Nd	1.33	4.66	1.39	5.99	5.44

Figure 4.4 presents the X-ray diffractogram of EV and EV-Nd and the lattice spaces, which were calculated conforming to the known Bragg's law (Bragg, 1934). Both diffractograms had intense peaks at similar diffraction angles. The samples had reflection (002) at angle 2θ around 6.0°, which is the reflection more characteristic of the vermiculite and confirms that the material has a double water layer between the silicate plates (Marcos et al., 2009; Udoudo et al., 2015). EV-Nd also exhibited a slightly crystal lattice perpendicular to the plane of the silicate layers (14.8 Å) relating to EV (14.1 Å), due to the replacement of interlayer exchangeable cations for neodymium (Walker, 1959). The peaks in 14.1-14.8 Å, 5.0-4.8 Å e 3.6-3.8 Å indicate that vermiculite contains octahedral Mg between the octahedral aluminum and silicate layers (Valaskova and Martynková, 2012; Udoudo et al., 2015). The decrease of the intensity in the diffraction peaks of EV-Nd sample comparing to the EV denotes that the Nd adsorption process has also disorganized the structure of the material. Wang and Wang

(2019) signed that the ion exchange can collapse of the vermiculite interlayer due to the different ionic radii and hydrated energies of the ions.

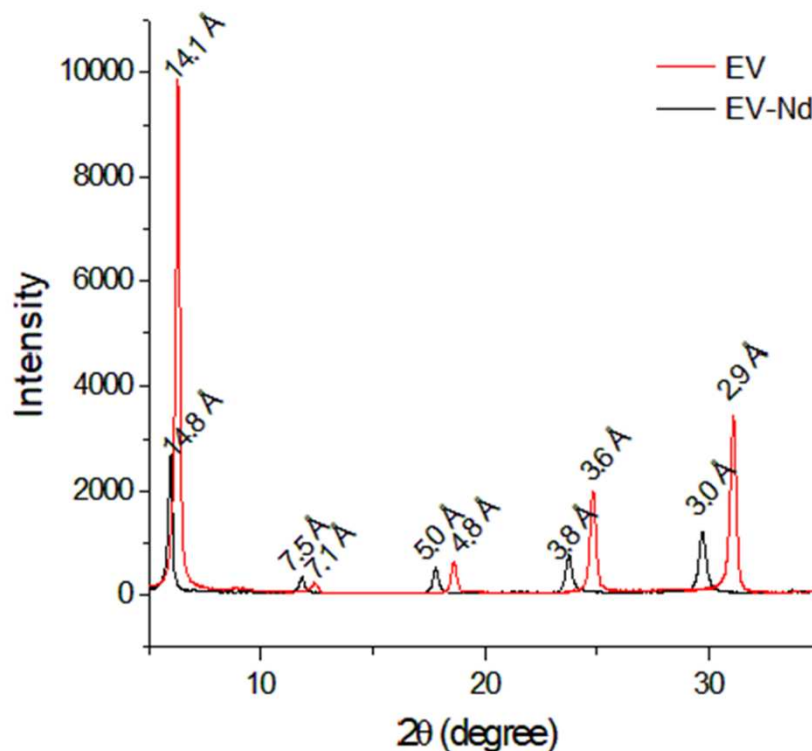


Figure 4.4 – X-ray diffractogram of EV and EV-Nd

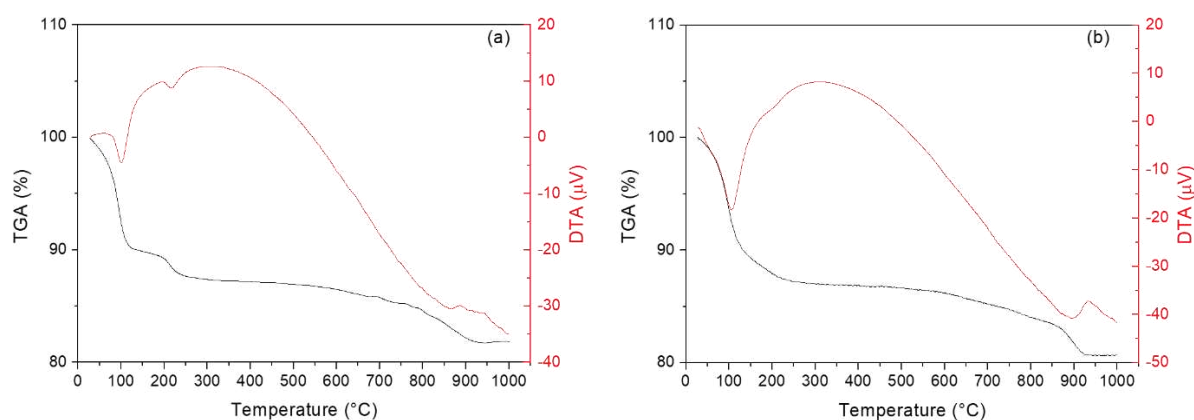


Figure 4.5 – TGA (a) and DTA (b) for EV and EV-Nd samples

According to the TGA curves in Figure 4.5(a), from 25 °C to 1000 °C, four stages for EV sample occurred. In the first stage, from 25°C to 102°C, the removal of the adsorbed water molecules on the vermiculite surface happened and represented a mass loss of 10% (Foldvari, 2011). The subsequent dehydration process between 102°C and 214°C is related to the loss of

the interlayered water molecules and corresponded to a mass loss of 1.4%. The third stage, from 300°C to 860°C, with a mass loss of 5.4%, may be associated with the dehydroxylation. As the EV sample was submitted to temperatures close to 1000°C (fourth stage), a mass loss of 1.7% occurred due to the formation of forsterite ($2\text{MgO} \cdot \text{SiO}_2$), mullite ($\text{Al}_6\text{Si}_4\text{O}_{13}$), and alumina (Al_2O_3) by the thermal decomposition reaction (Feng et al., 2020). After the neodymium adsorption, the TGA curve of the EV-Nd sample showed an analogous tendency to that of the EV sample. On the other hand, it does not present well-demarcated stages of transition between the dehydration of the adsorbed water (106°C) and the interlayered water (~200°C), taking place a continuous mass loss (13%) in the temperature range from 50 to 300 °C. This indicated that EV-Nd dehydration occurred basically to the loss of the surface water. The distinct thermal behavior of EV and EV-Nd, regarding the dehydration may be related to the difference between the degree of coordination (hydration spheres) of the neodymium and the exchangeable cations of the EV (Brigatti et al., 2005; Huo et al., 2012). Regarding specifically the differential thermal analysis (Figure 4.5(b)), endothermic valleys at around 100 °C and 200°C (weak valleys) for both samples are related to the liberating of free water, and the interlayer bounded water releasing temperature, respectively (Huo et al., 2012). Also, none distinct peak between 300 and 850°C was observed due to the slow rate of the dehydroxylation reaction (Foldvari, 2011).

4.3.2 Kinetics of adsorption

The kinetic behavior of the neodymium adsorption on expanded vermiculite is plotted in Figure 4.6 that also presents the PFO and PSO fitting to the data. Regarding the experimental results, the time of equilibrium, with an initial concentration of 0.5 mmol/L, was 12 min, and the capacity of adsorption on the equilibrium was 0.035 mmol/g. Fast adsorption of the neodymium ions was already expected since vermiculite and other clays have shown this behavior in the adsorption of heavy metals such as cadmium and lead (Liu et al., 2016; Chen et al., 2018; Ahmed et al., 2020). This behavior can be attributed to the direct electrostatic attraction and the inner or outer-sphere complexes formation on the surface of the adsorbent (Liu et al., 2016). Table S.1 (Supplementary material, Appendix A.2) summarizes the parameters to determine the quality of fit for both empirical models. PFO presented the best fit to the experimental data, because it presented the highest R^2 , and R^2_{adj} , and the lowest SSE , ARE and AIC_c . Moreover, the q_e predicted by PFO was closer to the experimental value, being 0.035 ± 0.0003 mmol/g, and the rate of adsorption (k_t) was 0.341 ± 0.011 min⁻¹.

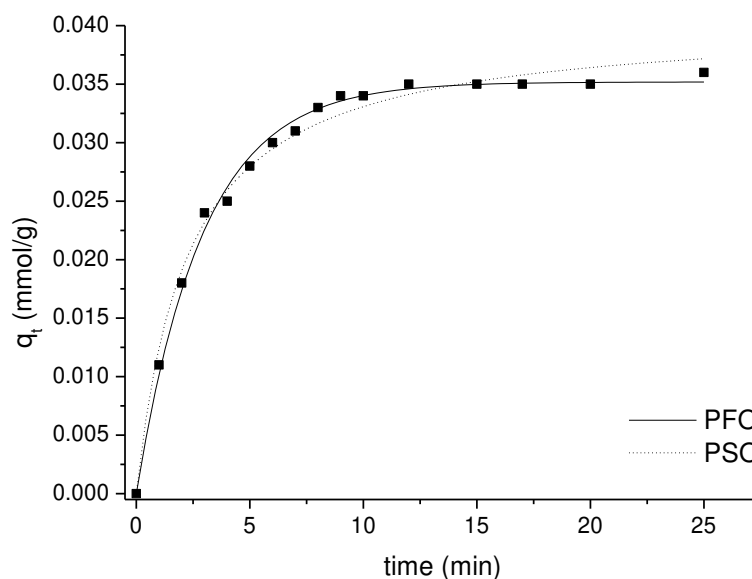


Figure 4.6 – Kinetic of neodymium adsorption

4.3.3 Equilibrium of adsorption

Figure 4.7 exhibits the isotherms of neodymium adsorption in expanded vermiculite at different temperatures. The experimental q_e on the plateau was 0.48, 0.41, 0.38 and 0.37 mmol/g, for 283, 298, 313 and 328 K, respectively. This behavior demonstrates that the temperature affects negatively the adsorption capacity. Figure 4.7 shows that the initial part of the isotherm is vertical, which indicates a high affinity between the solute and the adsorbent. This shape of isotherm is classified as H type (Giles et al., 1960). In addition, this shape of isotherm can indicate that occurred in an exchange of single ions with others of much lower affinity.

In addition, Figure 4.7 plots of Langmuir, Freundlich, Sips, and Dubinin-Radushkevich isotherm models, whose parameters are presented in Table 4.3.

Langmuir model adjusted well the equilibrium data ($R^2 > 0.9$), which implied that the adsorbed solute forms a monolayer and that the adsorption occurred at energetically identical sites. The model also predicted well the maximum adsorption capacity of the expanded vermiculite, being 0.48, 0.39, 0.38, and 0.37, for 283, 298, 313, and 328 K, respectively, which agreed with the experimental data. Sips model also fitted greatly the data, presenting the lowest *SSE* for all temperatures; however, it did not predict well the maximum adsorption capacity obtained experimentally.

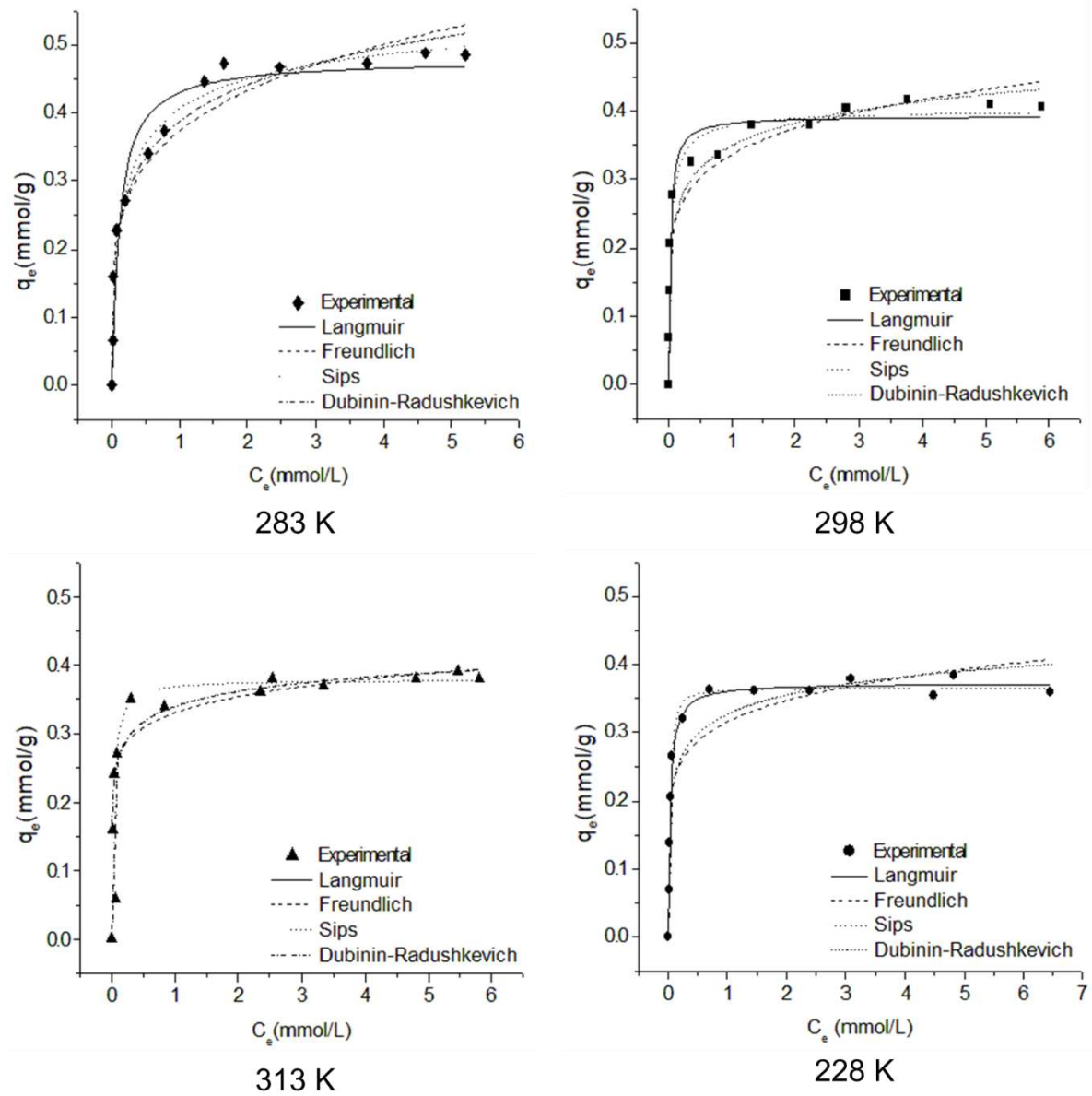


Figure 4.7 – Neodymium adsorption isotherms

Freundlich model, which assumes that the adsorption can occur in heterogeneous sites, and Dubinin-Radushkevich model did not predict satisfactory all the equilibrium data, for temperatures of 313 and 328 K, R^2 was lower than 0.9. However, the values of heterogeneity factor ($n_F < 1$) from the Freundlich model designated that the neodymium adsorption process was favorable (Al-Ghouti and Da'ana, 2020).

Table 4.3. Parameters of adsorption isotherm models

Model	Parameters	Temperature (K)			
		283	298	313	328
Langmuir	q_m (mmol/g)	0.48	0.39	0.38	0.37
	K_L (L/mmol)	8.73	35.67	36.86	29.94
	R^2	0.941	0.974	0.961	0.985
	R^2_a	0.935	0.972	0.957	0.984
	SSE	0.02	0.01	0.002	0.003
	AIC_c	-78.7	-94.1	-88.6	-103.7
	K_F (mmol/g)(mmol/L) ^{-n_F}	0.37	0.34	0.33	0.32
Freundlich	n_F	0.21	0.16	0.10	0.14
	R^2	0.939	0.925	0.836	0.865
	R^2_a	0.934	0.918	0.818	0.852
	SSE	0.021	0.018	0.0089	0.027
	AIC_c	-78.4	-80.3	-72.9	-74.9
	q_{mS} (mmol/g)	0.31	0.19	0.34	1.24
	m_S	0.56	0.79	0.97	1.35
Sips	K_S (L/mmol)	4.28	30.7	37.3	32.0
	R^2	0.969	0.976	0.961	0.990
	R^2_a	0.963	0.971	0.951	0.988
	SSE	0.01	0.01	0.00	0.002
	AIC_c	-83.7	-91.4	-84.7	-105.8
	q_m (mmol/g)	0.77	0.56	0.47	0.50
	β (mol ² /J ²)	2.61x10 ⁻⁹	1.63x10 ⁻⁹	1.02x10 ⁻⁹	1.23x10 ⁻⁹
Dubinin-Radushkevich	E (kJ/mol)	13.8	17.5	22.15	20.19
	R^2	0.938	0.918	0.877	0.832
	R^2_a	0.932	0.910	0.863	0.815
	SSE	0.014	0.01	0.01	0.02
	AIC_c	-83.4	-84.9	-75.4	-71.5

According to Table 4.4, nZVI-M had the highest adsorption capacity followed by the expanded vermiculite, Ca-montmorillonite, clinoptilolite, and kaolin. The adsorbent nZVI-M is a clay mineral (montmorillonite) doped with magnetic nanoparticles, which can have contributed to this great performance to adsorb rare earths. However, the expanded vermiculite is a commercial material that, likewise, achieved a great adsorption capacity even without previous modifications. Symeopoulos et al. (1996), Xiao et al. (2016) and Wang (2018), also

affirmed that the sorption of neodymium uptake had the contribution of the cation exchange mechanism and surface complexation.

Table 4.4. Neodymium adsorption performance of clay mineral adsorbents

Adsorbents	Experimental Conditions	q_m (mmol/g)	Reference
Montmorillonite-supported zero-valent iron nanoparticles (nZVI-M)	C_0 : 1–20 mg/L (0.007 – 0.14 mmol/L); 293 K; pH: 4.7–5.0; contact time: 4 h; adsorbent dosage: 0.5 g/L	1.81	Wang (2018)
Kaolin	C_0 : 10–150 mg/L (0.07 – 1.04 mmol/L); 298 K; pH: 4.8; adsorbent dosage: 25 g/L	0.01	Xiao et al. (2016)
Ca-montmorillonite	C_0 : 19 mmol/L; pH: 5; contact time: 1.5 h; adsorbent dosage: 40 g/L	0.21*	Iannicelli-Zubiani et al. (2015)
Ca-montmorillonite	300.5 K; adsorbent dosage: 10 g/L; contact time: 24 h.	0.18	Symeopoulos et al. (1996)
Clinoptilolite-bearing tuff	300.5 K; adsorbent dosage: 10 g/L; contact time: 24 h.	0.04	Symeopoulos et al. (1996)
Expanded Vermiculite	C_0 : 1 – 12 mmol/L; 200 rpm; 298 K; pH: 3.0 – 3.5; contact time: 24 h; adsorbent dosage: 14 g/L	0.39	This Work

* Calculated using the experimental value of adsorption efficiency (~45%).

4.3.4 Thermodynamic

Figure S.1 (a) (Supplementary material, Appendix A.2) demonstrates that the effect of the temperature over the maximum adsorption capacity does not have linear behavior, mainly because the highest q_m at 283 K. It can be explained because in an adsorption process, depending on the range of temperature studied, physical and chemical adsorption can occur simultaneously on the same surface (Hill, 1997), which turns more difficult to predict the effect of the temperature. Due to the temperature effect to the adsorption capacity did not have a linear behavior in the total range of temperature studied, the thermodynamic parameters were calculated from the equilibrium parameters at temperatures from 298 to 313 K. Figure S.1 (b) evidenced the effect of K_e (calculated though different methods) on the linear relationship between the $\ln K_e$ and $1/T$. The K_e was calculated by $K_e = K_L/\gamma_e$, i.e. considering the activity of neodymium, and $K_e = K_L$ (coefficient of Langmuir as the equilibrium constant).

The estimation of the equilibrium constant considering the activity coefficient improved the linear fit ($R^2 = 0.783$), obtained thermodynamic parameters more reliable. Lima et al. (2019)

assigned that the equilibrium constant expressed regarding activity, instead of concentration (ideal solution), is closer to a real adsorption process. Table 4.5 indicates that the adsorption of neodymium on expanded vermiculite is spontaneous and favorable ($\Delta G_{ads}^o < 0$), exothermic ($\Delta H_{ads}^o < 0$), and increased in the degree of disorder of the adsorbed species ($\Delta S_{ads}^o > 0$). The value of ΔH_{ads}^o -20.5 kJ/mol, classified the process as physisorption, i.e., occurs by Van der Waals and electrostatic forces, and the neodymium adsorbed, on desorption, could return to the bulk solution in its original form (Rouquerol et al., 2012).

Table 4.5. Thermodynamic parameters calculated through different ways to obtain K_e

	T (K)	ΔG_{ads}^o (kJ/mol)	ΔH_{ads}^o (kJ/mol)	ΔS_{ads}^o (kJ/molK)	R^2
$K_e = K_L / \gamma_e$	298	-29.6			
	313	-29.2	-20.5	0.029	0.783
	328	-30.6			
$K_e = K_L$	298	-26.0			
	313	-27.4	-4.60	0.072	0.586
	328	-28.1			

Using the isotherms to obtain C_e for each q_e at different temperatures, the value of the isosteric heat (ΔH_x) was determined from the slope of the plot of $\ln C_e$ versus $1/T$ (Figure 4.8 (a)). As the loading amount increases, R^2 is closer to 1.00, indicating that the value of ΔH_x is more accurate as the saturation is closer. Figure 4.8 (b) reveals that the isosteric heat increases with the increase of the adsorption capacity. The increase of the ΔH_x as high the adsorbate loading can occur due to the formation of a monolayer and is related to a maximum value isosteric heat (Giraldo et al. 2019). This behavior is typical of surfaces without any energetic heterogeneity and occurs due to adsorbate-adsorbate interactions (Siperstein and Gubbins, 2002). According to Saha and Chowdhury (2011), the magnitude of the isosteric heat value gives information about the adsorption mechanism as chemical ion-exchange ($80 < \Delta H_x < 200$ kJ/mol) or physical sorption ($\Delta H_x < 80$ kJ/mol). Thus, the uptake of Nd^{3+} on EV can be classified as physical adsorption, because the maximum value of isosteric heat was 22.4 kJ/mol, which indicated that the interactions between the neodymium and the vermiculite surface may occur by outer-sphere complexes (weak interactions) (Malandrino et al., 2006; Wang and Wang, 2019) through Si-O and Al-O groups.

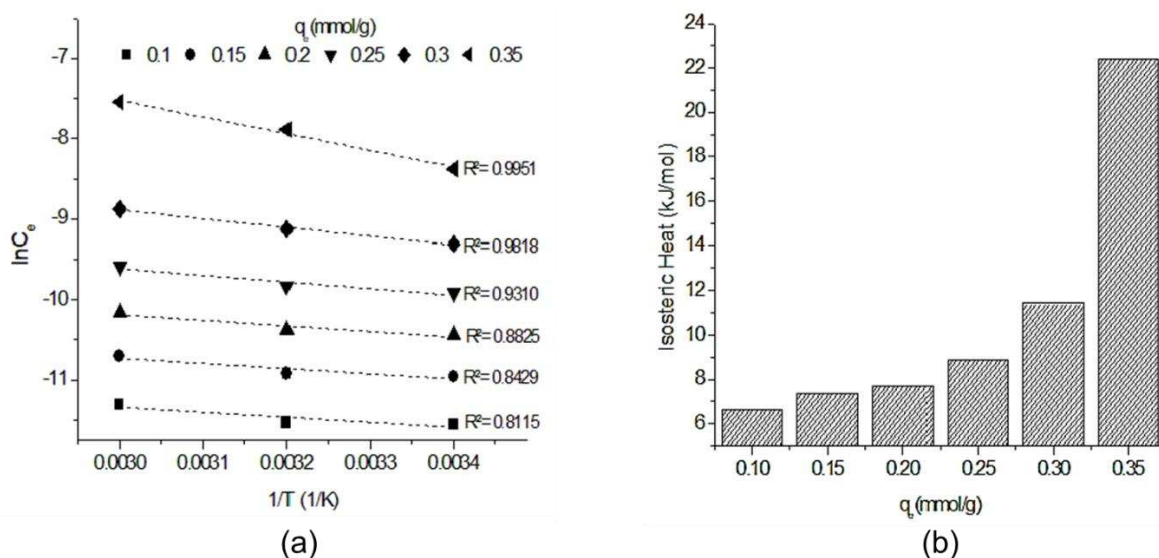


Figure 4.8 – Isosteric Heat: Linear fit of $\ln C_e$ versus $1/T$ (a) and value of isosteric heat for different or different amounts of Nd^{3+} adsorbed on expanded vermiculite

4.3.5 Neodymium Desorption

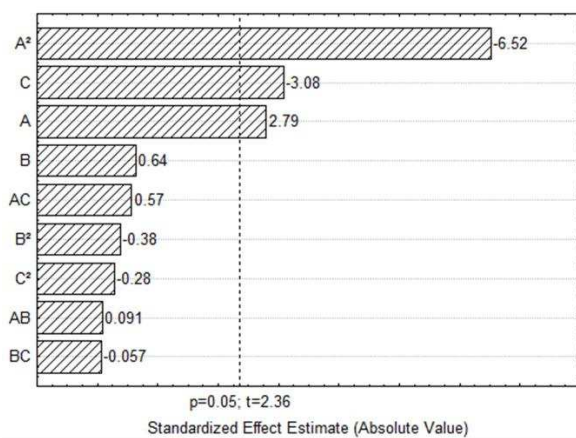
4.3.5.1 Optimization of desorption conditions

To increase the recovery of neodymium, the experimental design proposed was made with 17 runs. It is evident from Table 4.6 that the different experimental conditions of the runs affected $\%D$ and q_{el} . The $\%D$ range achieved was from 8.0 up to 81.0%, and for q_{el} was from 0.006 up to 0.070 mmol/g.

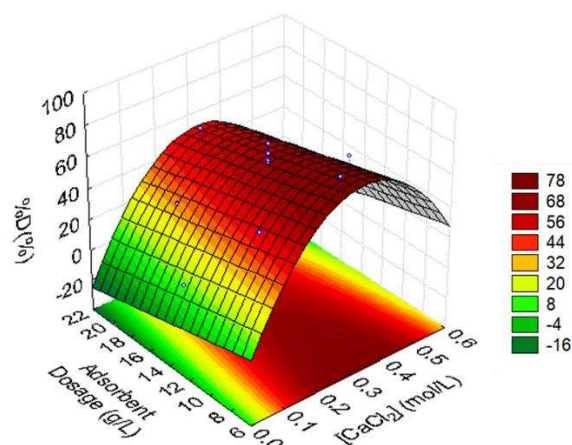
CaCl_2 concentration (A), linear and squared, and dosage of adsorbent (B) had a significant effect on the desorption percentage according to the Pareto chart (Figure 4.9(a)). The CaCl_2 concentration is significant to the overall desorption process because as higher the salt concentration, higher is the action of the electrolyte to recovery the metal, neutralize the active sites, and regenerate the EV surface. The adsorbent dosage had a negative effect on the efficiency of desorption because as higher is the loaded neodymium as lower is the ability to remove it completely due to the limitations of the eluent (saturation).

Table 4.6. %D and q_{el} of Nd adsorption on expanded vermiculite

Run	A	B	C	q_{el} (mmol/g)	%D
1	0.15	1.5	10	0.036	50.2
2	0.45	1.5	10	0.038	52.3
3	0.15	4.5	10	0.036	49.2
4	0.45	4.5	10	0.039	53.6
5	0.15	1.5	18	0.024	33.3
6	0.45	1.5	18	0.031	43.2
7	0.15	4.5	18	0.024	32.8
8	0.45	4.5	18	0.031	42.6
9	0.05	3	14	0.006	8.0
10	0.55	3	14	0.031	43.2
11	0.30	0.49	14	0.045	62.2
12	0.30	5.51	14	0.054	74.2
13	0.30	3	7.31	0.070	81.0
14	0.30	3	20.64	0.041	56.9
15	0.30	3	14	0.046	63.6
16	0.30	3	14	0.046	63.8
17	0.30	3	14	0.049	68.1



(a)



(b)

Figure 4.9 – Pareto diagram (a) and response surface of %D (b)

The quadratic model with coded variables of the significant factors had a $R^2 = 0.8901$ to fit the data and it is presented in Equation 4.22.

$$\%D = 63.91_{(\pm 2.07)} + 6.26_{(\pm 1.70)}A - 15.56_{(\pm 1.75)}A^2 - 6.50_{(\pm 1.70)}C \quad (4.22)$$

The variance analysis (ANOVA) indicated that the model of Equation 4.22 is significant with an interval of confidence of 95% (Table 4.7). In which, the value calculated (F_{calc}) was 10.44 times higher than the tabled value (F_{tab}).

Table 4.7. ANOVA of the quadratic model for the desorption percentage (confidence interval of 95%)

Source of variation	SS	df	MS	F_{calc}	F_{tab}
Regression	4206.46	3	1402.153	35.61	3.41
Residual	511.81	13	39.37		
Total SS	4718.27	16			

Figure 4.9(b) shows the response surface (%D) behavior according to adsorbent dosage and CaCl_2 concentration. The optimal region of the surface is achieved at low adsorbent dosages and intermediary eluent concentrations. Thus, the adsorbent dosage of 7.31 g/L (inferior level of the factor ($-\alpha$)) and CaCl_2 concentration of 0.3 mol/L (central point) were the best conditions for the desorption experiments. To confirm that, the model validation was performed with a contact time of 3 hours. The time was not significant to the model, this way, the time of 3 hours was determined to guarantee the equilibrium and to be the central point (Table 4.1), giving more information about the experimental error. The experimental value of desorption efficiency was $80.71 \pm 4.99 \%$, and the %D from the model was $70.41 \pm 5.33\%$. Thus, the model did not predict efficiently the real desorption efficiency, however, the experimental %D shows that the desorption procedure is reproducible because of the similarity to the value obtained in Table 4.6 (13th run), at same experimental conditions.

4.3.5.2 Cycles of adsorption/desorption

The neodymium recovery and the adsorbent regeneration capacity was evaluated in 5 cycles of adsorption/desorption (Figure 4.10). The adsorption efficiency was higher than 94% in all cycles. However, the desorption efficiency did not have a monotonous behavior along with the cycles. The %D decreases from the first to the second cycle and increases until the fifth, achieving the maximum efficiency of 95%. This behavior can be attributed to the remained ions on the adsorbent at the first cycles, which will be desorbed in the posterior desorption processes. The improvement of the desorption efficiency along the cycle's hints that

the CaCl_2 is proper to recover the neodymium from the adsorbent. The loss of the adsorbent due to the separation process (filtration) along the cycles is also shown in Figure 4.10. Considering the decay as a line, the rate of adsorbent loss along the cycles (slope) was -5.77% ($R^2 = 0.8817$). The high adsorption efficiency even in the fifth run evidenced that the expanded vermiculite has great stability and potential of regeneration. These characteristics are desirable to become the adsorption process viable on a large scale, however, an improvement of the solid-liquid separation efficiency is recommended.

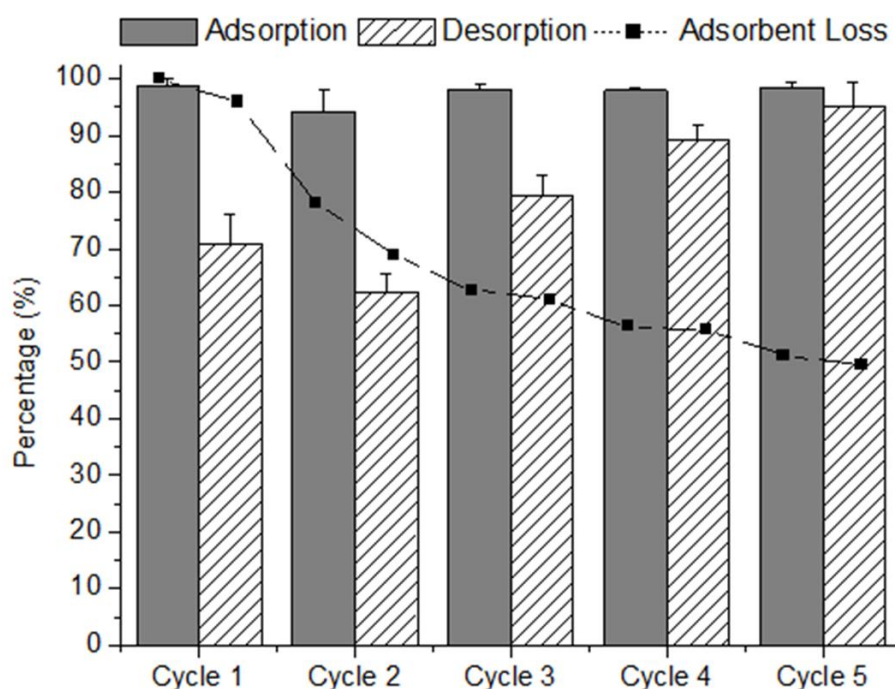


Figure 4.10 – Cycles of adsorption and desorption of neodymium using expanded vermiculite

4.3.6 Cost analysis at lab scale

Table S.2 (Supplementary material, Appendix A.2) presents the estimation for the process cost at lab scale. In the analysis, the price paid for the acquisition of the main reactants in Brazil was considered, with the exception of the adsorbent that was donated, thus the cost was estimated based on the Padilla (2017) report. According to the results, the major cost was related to the eluent CaCl_2 , being it the critical point to be evaluated in further economic studies, in the pilot and large scale, to turn the process rentable. The cost of the adsorbent is low because the vermiculite is a cheap material ($\$0.85/\text{kg}$) (Padilla, 2017). Regarding the neodymium recovery, it was considered an efficiency of 80%, an average of the desorption efficiencies along with the cycles, so, if the process occurred in one cycle, to recovery 1 g of neodymium it

would be necessary to treat 8.68 L with a concentration of 1 mmol/L (0.144 g/L). The neodymium could be commercialized for \$45.00/kg, value of neodymium oxide in the market in 2019 (United States Geological Survey (USGS), 2020), or more, depending on the purity of the neodymium obtained.

4.4 CONCLUSION

In this work, we evaluated the efficiency of adsorption of expanded vermiculite to recovery neodymium. The adsorption and desorption were evaluated in batch mode. The inceptive and saturated adsorbent were characterized. The adsorption of neodymium made the expanded vermiculite lose part of the expansion, disorganized the crystalline structure, and uniformed the slits size distribution. Langmuir isotherm model described the equilibrium data with q_m of 0.48 mmol/g, for 283 K. The adsorption of neodymium can be considered thermodynamically spontaneous and feasible, exothermic, and a reversible phenomenon. The neodymium recovery using CaCl_2 as eluent was efficient, achieving high desorption performances along with five cycles of adsorption/desorption. Moreover, the application of expanded vermiculite, a commercial clay mineral, to recovery neodymium from aqueous solution exhibited great primary results, which indicates the potential of this material to an industrial application after further economic and upscale studies.

FUNDING

This work was supported by the Fundação de Amparo à Pesquisa do Estado de São Paulo/FAPESP (Proc. 2017/18236-1), Conselho Nacional de Desenvolvimento Científico e Tecnológico/CNPq (Proc. 308046/2019-6 and Proc. 147606/2018-7), Coordenação de Aperfeiçoamento de Pessoal de Nível Superior/CAPES.

ACKNOWLEDGMENTS

The authors are grateful to Brasil Minérios S.A. for donating the expanded vermiculite.

REFERENCES

Ahmed, Z., Wu, P., Jiang, L., Liu, J., Ye, Q., Yang, Q., Zhu, N., 2020. Enhanced simultaneous adsorption of Cd(II) and Pb(II) on octylamine functionalized vermiculite. *Colloids Surfaces A Physicochem. Eng. Asp.* 604, 125285.

- <https://doi.org/10.1016/j.colsurfa.2020.125285>
- Al-Ghouti, M.A., Da'ana, D.A., 2020. Guidelines for the use and interpretation of adsorption isotherm models: A review. *J. Hazard. Mater.* 393, 122383. <https://doi.org/10.1016/j.jhazmat.2020.122383>
- Amorim, W.B., Hayashi, A.M., Pimentel, P.F., Silva, M.G.C. d., 2003. A study of the process of desorption of hexavalent chromium. *Brazilian J. Chem. Eng.* 20, 283–289. <https://doi.org/10.1590/S0104-66322003000300008>
- Anovitz, L.M., Cole, D.R., 2015. Characterization and analysis of porosity and pore structures. *Rev. Mineral. Geochemistry* 80, 61–164. <https://doi.org/10.2138/rmg.2015.80.04>
- Arruda, G.M., 2005. Vermiculite utilization on the treatment of water contaminated with organic compounds. 2nd Mercosur Congress on Chemical Engineering 4 Mercosur Congress on Process Systems Engineering, pp. 1–10.
- Assoumani, A., Margoum, C., Guillemain, C., Coquery, M., 2014. Use of experimental designs for the optimization of stir bar sorptive extraction coupled to GC–MS/MS and comprehensive validation for the quantification of pesticides in freshwaters. *Anal. Bioanal. Chem.* 406, 2559–2570. <https://doi.org/10.1007/s00216-014-7638-6>
- Barcelos da Costa, T., Carlos da Silva, M.G., Adeodato Vieira, M.G., 2020. Development of a natural polymeric bioadsorbent based on sericin, alginate and POLY(VINYL alcohol) for the recovery of ytterbium from aqueous solutions. *J. Clean. Prod.* 123555. <https://doi.org/10.1016/j.jclepro.2020.123555>
- Box, E.G.P., Hunter, W.G.E., Hunter, J.S., 1978. *Statistics for experimenters: an introduction to design, data analysis, and model building*.
- Bragg, W.L., 1934. *The Crystalline State: Volume I*. The Macmillan Company, New York.
- Brião, G. V., Silva, M.G.C., Vieira, M.G.A., 2019. Ensaios de afinidade de íons terras raras em concentrado de vermiculita e vermiculita expandida, in: *Simpósio Comemorativo Dos 40 Anos Da Área de Sistemas Particulados (AP1) Do DEQ/UFSCar*. pp. 497–505.
- Brigatti, M.F., Colonna, S., Malferrari, D., Medici, L., Poppi, L., 2005. Mercury adsorption by montmorillonite and vermiculite: A combined XRD, TG-MS, and EXAFS study. *Appl. Clay Sci.* 28, 1–8. <https://doi.org/10.1016/j.clay.2004.03.006>
- Charalampides, G., Vatalis, K.I., Apostoplos, B., Ploutarch-Nikolas, B., 2015. Rare Earth Elements: Industrial Applications and Economic Dependency of Europe. *Procedia Econ. Financ.* 24, 126–135. [https://doi.org/10.1016/S2212-5671\(15\)00630-9](https://doi.org/10.1016/S2212-5671(15)00630-9)
- Chen, L., Wu, P., Chen, M., Lai, X., Ahmed, Z., Zhu, N., Dang, Z., Bi, Y., Liu, T., 2018.

- Preparation and characterization of the eco-friendly chitosan/vermiculite biocomposite with excellent removal capacity for cadmium and lead. *Appl. Clay Sci.* 159, 74–82. <https://doi.org/10.1016/j.clay.2017.12.050>
- Costa, T.B. da, Silva, M.G.C. da, Vieira, M.G.A., 2020. Recovery of rare-earth metals from aqueous solutions by bio/adsorption using non-conventional materials: a review with recent studies and promising approaches in column applications. *J. Rare Earths* 38, 339–355. <https://doi.org/10.1016/j.jre.2019.06.001>
- Cuong, N.D., Hue, V.T., Kim, Y.S., 2019. Thermally expanded vermiculite as a risk-free and general-purpose sorbent for hazardous chemical spillages. *Clay Miner.* 54, 235–243. <https://doi.org/10.1180/clm.2019.34>
- De Gisi, S., Lofrano, G., Grassi, M., Notarnicola, M., 2016. Characteristics and adsorption capacities of low-cost sorbents for wastewater treatment: A review. *Sustain. Mater. Technol.* 9, 10–40. <https://doi.org/10.1016/j.susmat.2016.06.002>
- Długosz, O., Banach, M., 2018. Sorption of Ag⁺ and Cu²⁺ by vermiculite in a fixed-bed column: Design, process optimization and dynamics investigations. *Appl. Sci.* 8. <https://doi.org/10.3390/app8112221>
- Dubinin, M.M., Radushkevich, L.V., 1947. The equation of the characteristic curve of activated charcoal. *Proc. Acad. Sci. USSR* 55, 331.
- Favot, M., Massarutto, A., 2019. Rare-earth elements in the circular economy: The case of yttrium. *J. Environ. Manage.* 240, 504–510. <https://doi.org/10.1016/j.jenvman.2019.04.002>
- Feng, J., Liu, M., Fu, L., Zhang, K., Xie, Z., Shi, D., Ma, X., 2020. Enhancement and mechanism of vermiculite thermal expansion modified by sodium ions. *RSC Adv.* 10, 7635–7642. <https://doi.org/10.1039/d0ra00223b>
- Foldvari, M., 2011. Handbook of thermo-gravimetric system of minerals and its use in geological practice, Occasional papers of the geological institute of Hungary.
- Freitas, E.D. de, Almeida, H.J. de, Vieira, M.G.A., 2017. Binary adsorption of zinc and copper on expanded vermiculite using a fixed bed column. *Appl. Clay Sci.* 146, 503–509. <https://doi.org/10.1016/j.clay.2017.07.004>
- Freundlich, H.M.F., 1906. Over the Adsorption in Solution. *urnal Phys. Chem.* 57, 385–470.
- Gergoric, M., Barrier, A., Retegan, T., 2019. Recovery of Rare-Earth Elements from Neodymium Magnet Waste Using Glycolic, Maleic, and Ascorbic Acids Followed by Solvent Extraction. *J. Sustain. Metall.* 5, 85–96. <https://doi.org/10.1007/s40831-018->

0200-6

- Ghosal, P.S., Gupta, A.K., 2017. Determination of thermodynamic parameters from Langmuir isotherm constant-revisited. *J. Mol. Liq.* 225, 137–146. <https://doi.org/10.1016/j.molliq.2016.11.058>
- Giesche, H., 2006. Mercury porosimetry: A general (practical) overview. Part. Part. Syst. Charact. 23, 9–19. <https://doi.org/10.1002/ppsc.200601009>
- Giles, C.H., Macewan, T.H., Nakhwa, S.N., Smith, D., 1960. Studies in Adsorption. Part XI.* A System of Classification of Solution Adsorption Isotherms, and its Use in Diagnosis of Adsorption Mechanisms and in Measurement of Specific Surface Areas of Solids. *J. Chem. Soc.* 3973–3993.
- Giraldo, L., Rodriguez-Estupiñán, P., Moreno-Piraján, J.C., 2019. Isosteric heat: Comparative study between Clausius-Clapeyron, CSK and adsorption calorimetry methods. *Processes* 7. <https://doi.org/10.3390/pr7040203>
- Granados-Correa, F., Vilchis-Granados, J., Jiménez-Reyes, M., Quiroz-Granados, L.A., 2013. Adsorption behaviour of La(III) and Eu(III) ions from aqueous solutions by hydroxyapatite: Kinetic, isotherm, and thermodynamic studies. *J. Chem.* 2013. <https://doi.org/10.1155/2013/751696>
- Havel, J., Moreno, C., Hrdlička, A., Valiente, M., 1994. Spectrophotometric determination of rare earth elements by flow injection analysis based on their reaction with xylenol orange and cetylpyridinium bromide. *Talanta* 41, 1251–1254. [https://doi.org/10.1016/0039-9140\(93\)E0044-E](https://doi.org/10.1016/0039-9140(93)E0044-E)
- Hill, C.G.J., 1997. An introduction to chemical engineering kinetics & reactor design, Chemical Engineering Science. John Wiley & Sons. <https://doi.org/10.1016/j.ces.2007.03.016>
- Ho, Y.S., McKay, G., 1998. A Comparison of chemisorption kinetic models applied to pollutant removal on various sorbents. *Process Saf. Environ. Prot.* 76, 332–340. <https://doi.org/10.1205/095758298529696>
- Hückel, P., Debye, E., 1923. The theory of electrolytes. I. Freezing point depression and related phenomena (Translation). *Phys. Zeitschrift* 24, 185–206.
- Huo, X., Wu, L., Liao, L., Xia, Z., Wang, L., 2012. The effect of interlayer cations on the expansion of vermiculite. *Powder Technol.* 224, 241–246. <https://doi.org/10.1016/j.powtec.2012.02.059>
- Jowitt, S.M., Werner, T.T., Weng, Z., Mudd, G.M., 2018. Recycling of the rare earth elements. *Curr. Opin. Green Sustain. Chem.* 13, 1–7. <https://doi.org/10.1016/j.cogsc.2018.02.008>

- Jyothi, R.K., Thenepalli, T., Ahn, J.W., Parhi, P.K., Chung, K.W., Lee, J.-Y., 2020. Review of rare earth elements recovery from secondary resources for clean energy technologies: Grand opportunities to create wealth from waste. *J. Clean. Prod.* 267, 122048. <https://doi.org/10.1016/j.jclepro.2020.122048>
- Komnitsas, K., Zaharaki, D., Bartzas, G., Alevizos, G., 2017. Adsorption of Scandium and Neodymium on Biochar Derived after Low-Temperature Pyrolysis of Sawdust. *Minerals* 7, 200. <https://doi.org/10.3390/min7100200>
- Korhonen, J., Honkasalo, A., Seppälä, J., 2018. Circular Economy: The Concept and its Limitations. *Ecol. Econ.* 143, 37–46. <https://doi.org/10.1016/j.ecolecon.2017.06.041>
- Kucuker, M.A., Wieczorek, N., Kuchta, K., Coptý, N.K., 2017. Biosorption of neodymium on *Chlorella vulgaris* in aqueous solution obtained from hard disk drive magnets. *PLoS One* 12, e0175255. <https://doi.org/10.1371/journal.pone.0175255>
- Kuila, U., 2013. Measurement and interpretation of porosity and pore size distribution in mudrocks: The hole story of shales. Colorado School of Mines.
- Lagergren, S., 1898. About the theory of so-called adsorption of soluble substances. *K. Suensk Vetenskapsak ademiens Handl.* 24, 1–39.
- Langmuir, I., 1918. The Adsorption of Gases on Plane Surfaces of Glass Mic and Platinum. *J. Am. Chemiscal Soc.* 40, 1361–1403.
- Lima, E.C., Hosseini-Bandegharai, A., Moreno-Piraján, J.C., Anastopoulos, I., 2019. A critical review of the estimation of the thermodynamic parameters on adsorption equilibria. Wrong use of equilibrium constant in the Van't Hoof equation for calculation of thermodynamic parameters of adsorption. *J. Mol. Liq.* 273, 425–434. <https://doi.org/10.1016/j.molliq.2018.10.048>
- Liu, C., Wu, P., Zhu, Y., Tran, L., 2016. Simultaneous adsorption of Cd²⁺ and BPA on amphoteric surfactant activated montmorillonite. *Chemosphere* 144, 1026–1032. <https://doi.org/10.1016/j.chemosphere.2015.09.063>
- Liu, Y., 2009. Is the Free Energy Change of Adsorption Correctly Calculated? *J. Chem. Eng. Data* 54, 1981–1985. <https://doi.org/10.1021/je800661q>
- Malandrino, M., Abollino, O., Giacomino, A., Aceto, M., Mentasti, E., 2006. Adsorption of heavy metals on vermiculite: Influence of pH and organic ligands. *J. Colloid Interface Sci.* 299, 537–546. <https://doi.org/10.1016/j.jcis.2006.03.011>
- Malla, P.B., 1978. Vermiculite, in: *Sedimentology, Encyclopedia of Earth Science*. Springer Berlin Heidelberg, pp. 1265–1269. https://doi.org/10.1007/3-540-31079-7_248

- Marcos, C., Arango, Y.C., Rodriguez, I., 2009. X-ray diffraction studies of the thermal behaviour of commercial vermiculites. *Appl. Clay Sci.* 42, 368–378. <https://doi.org/10.1016/j.clay.2008.03.004>
- Momina, Rafatullah, M., Ismail, S., Ahmad, A., 2019. Optimization Study for the Desorption of Methylene Blue Dye from Clay Based Adsorbent Coating. *Water* 11, 1304. <https://doi.org/10.3390/w11061304>
- Moraes, D.S., Rodrigues, E.M.S., Lamarão, C.N., Marques, G.T., Rente, A.F.S., 2019. New sodium activated vermiculite process. Testing on Cu²⁺ removal from tailing dam waters. *J. Hazard. Mater.* 366, 34–38. <https://doi.org/10.1016/j.jhazmat.2018.11.086>
- Nishikawa, E., Neto, A.F.A., Vieira, M.G.A., 2012. Equilibrium and thermodynamic studies of zinc adsorption on expanded vermiculite. *Adsorpt. Sci. Technol.* 30, 759–772. <https://doi.org/10.1260/0263-6174.30.8-9.759>
- Padilla, A.J., 2017. 2017 Minerals Yearbook. US Geol. Surv.
- Park, H.-J., Tavlarides, L.L., 2010. Adsorption of Neodymium(III) from Aqueous Solutions Using a Phosphorus Functionalized Adsorbent. *Ind. Eng. Chem. Res.* 49, 12567–12575. <https://doi.org/10.1021/ie100403b>
- Peelman, S., Venkatesan, P., Abrahami, S., Yang, Y., 2018. Recovery of REEs from End-of-Life Permanent Magnet Scrap Generated in WEEE Recycling Plants. pp. 2619–2631. https://doi.org/10.1007/978-3-319-95022-8_221
- Riaño, S., Binnemans, K., 2015. Extraction and separation of neodymium and dysprosium from used NdFeB magnets: An application of ionic liquids in solvent extraction towards the recycling of magnets. *Green Chem.* 17, 2931–2942. <https://doi.org/10.1039/c5gc00230c>
- Rouquerol, F., Rouquerol, J., Sing, K.S.W., Llewellyn, P., Maurin, G., 2012. Adsorption by Powders and Porous Solids, 2nd ed. Elsevier, San Diego. <https://doi.org/10.1016/C2010-0-66232-8>
- Saha, P., Chowdhury, S., 2011. Insight Into Adsorption Thermodynamics, Thermodynamics. <https://doi.org/10.5772/13474>
- Santos, C.P., Rato, T.J., Reis, M.S., 2019. Design of Experiments: A comparison study from the non-expert user's perspective. *J. Chemom.* 33, 1–18. <https://doi.org/10.1002/cem.3087>
- Santos, N.T. das G., Moraes, L.F., da Silva, M.G.C., Vieira, M.G.A., 2020. Recovery of gold through adsorption onto sericin and alginate particles chemically crosslinked by proanthocyanidins. *J. Clean. Prod.* 253, 119925. <https://doi.org/10.1016/j.jclepro.2019.119925>

- Sing, K.S.W., Everett, D.H., Haul, R.A.W., Moscou, L., Pierotti, R.A., Rouquerol, J., Siemieniewska, T., 1985. Reporting physisorption data for gas/solid systems. *Pure Appl. Chem.* 57, 603–619.
- Siperstein, F.R., Gubbins, K.E., 2002. Influence of synthesis conditions on surface heterogeneity of M41 type materials studied with lattice Monte Carlo, *Studies in Surface Science and Catalysis*. Elsevier Masson SAS. [https://doi.org/10.1016/s0167-2991\(02\)80192-6](https://doi.org/10.1016/s0167-2991(02)80192-6)
- Sips, R., 1948. On the structure of a catalyst surface. *J. Chem. Phys.* 16, 490–495. <https://doi.org/10.1063/1.1746922>
- Symeopoulos, B., Soupioni, M., Misaelides, P., Godelitsas, A., Barbayiannis, N., 1996. Neodymium sorption by clay minerals and zeoliferous rocks. *J. Radioanal. Nucl. Chem. Lett.* 212, 421–429. <https://doi.org/10.1007/BF02163287>
- Udoudo, O., Folorunso, O., Dodds, C., Kingman, S., Ure, A., 2015. Understanding the performance of a pilot vermiculite exfoliation system through process mineralogy. *Miner. Eng.* 82, 84–91. <https://doi.org/10.1016/j.mineng.2015.03.023>
- United States Geological Survey (USGS), 2020. Mineral Commodity Summaries, U.S Department OF The Interior, U.S Geological Survey. <https://doi.org/https://doi.org/10.3133/mcs2020>
- Valaskova, M., Martynková, G.S., 2012. Vermiculite: Structural Properties and Examples of the Use, in: *Clay Minerals in Nature - Their Characterization, Modification and Application*. InTech, p. 64. <https://doi.org/10.5772/51237>
- Van't Hoff, J.H., 1884. *Etudes de dynamique chimique*. Frederik Muller, Amsterdam.
- Walker, G.F., 1959. Diffusion of Exchangeable Cations in Vermiculite. *Nature* 184, 1392–1393. <https://doi.org/10.1038/1841392a0>
- Wang, A., Wang, W., 2019. Vermiculite nanomaterials: Structure, properties, and potential applications, *Nanomaterials from Clay Minerals: A New Approach to Green Functional Materials*. Elsevier Inc. <https://doi.org/10.1016/B978-0-12-814533-3.00009-0>
- Wang, J., 2018. Adsorption of aqueous neodymium, europium, gadolinium, terbium, and yttrium ions onto nZVI-montmorillonite: kinetics, thermodynamic mechanism, and the influence of coexisting ions. *Environ. Sci. Pollut. Res.* 25, 33521–33537. <https://doi.org/10.1007/s11356-018-3296-0>
- Xiao, Y., Huang, L., Long, Z., Feng, Z., Wang, L., 2016. Adsorption ability of rare earth elements on clay minerals and its practical performance. *J. Rare Earths* 34, 543–548.

[https://doi.org/10.1016/S1002-0721\(16\)60060-1](https://doi.org/10.1016/S1002-0721(16)60060-1)

- Xiong, C., He, R., Pi, L., Li, J., Yao, C., Jiang, J., Zheng, X., 2015. Adsorption of Neodymium(III) on Acrylic Resin (110 Resin) from Aqueous Solutions. *Sep. Sci. Technol.* 50, 564–572. <https://doi.org/10.1080/01496395.2014.955204>
- Xu, J., Koivula, R., Zhang, W., Wiikinkoski, E., Hietala, S., Harjula, R., 2018. Separation of cobalt, neodymium and dysprosium using amorphous zirconium phosphate. *Hydrometallurgy* 175, 170–178. <https://doi.org/10.1016/j.hydromet.2017.11.010>
- Yang, Y., Walton, A., Sheridan, R., Güth, K., Gauß, R., Gutfleisch, O., Buchert, M., Steenari, B.-M., Van Gerven, T., Jones, P.T., Binnemans, K., 2017. REE Recovery from End-of-Life NdFeB Permanent Magnet Scrap: A Critical Review. *J. Sustain. Metall.* 3, 122–149. <https://doi.org/10.1007/s40831-016-0090-4>
- Zhang, L., Xu, Z., 2016. A review of current progress of recycling technologies for metals from waste electrical and electronic equipment. *J. Clean. Prod.* 127, 19–36. <https://doi.org/10.1016/j.jclepro.2016.04.004>

CHAPTER 5. NEODYMIUM RECOVERY ON EXPANDED VERMICULITE: CONTINUOUS FIXED-BED ADSORPTION AND DESORPTION

Reusable and efficient clay material for the fixed-bed neodymium recovery⁴

Giani de Vargas Brião, Meuris Gurgel Carlos da Silva, Melissa Gurgel Adeodato Vieira

University of Campinas, School of Chemical Engineering, Albert Einstein Avenue, 500, 13083-852 Campinas, Brazil

ABSTRACT

Neodymium is an essential resource for the future development of clean energy. Its future supply is a global concern motivating the application of different adsorbent materials to recover neodymium from secondary sources. However, there is a lack of studies of adsorption with scale-up potential. This work aims to recuperate neodymium from aqueous solution through dynamic adsorption in a fixed-bed of expanded vermiculite, an abundant clay mineral with excellent adsorbent properties. For that, the flow rate and concentration optimization, mathematical modeling; cycles of adsorption and desorption; and the extensive characterization of the regenerated adsorbent matrix were carried out. The main findings of the study are the column high adsorption capacity 0.40 mmol/g; the effective modeling of the column by modified dose-response and DualSD model, being useful for scale-up purposes; the constant bed efficiency along with the cycles and the well succeed neodymium recovery (96% in the third cycle) and concentration (28.4 times). Besides that, the structural composition was maintained, attesting to the physical and chemical stability of the material. Thus, the neodymium continuous recovery from aqueous solution through successive cycles of adsorption and desorption on an expanded vermiculite fixed-bed has high potential for scale-up and rare earth rich wastewater treatment studies.

Keywords: neodymium; recovery; vermiculite; fixed-bed.

⁴ Manuscript published in *Sustainable Chemistry and Pharmacy* (2022).

DOI: 10.1016/j.scp.2022.100623. Reprinted with the journal's permission (Appendix B.4).

5.1 INTRODUCTION

Rare earth metals (REM), composed of lanthanides, yttrium, and scandium, have been widely applied in the technological field and low-carbon economy (Dang et al., 2021). Neodymium, light rare earth with atomic number 60, atomic mass 144.242 u., and electronic distribution of [Xe] 4f⁴6s² is mainly used in permanent magnets (NdFeB type) applied to the manufacture of wind turbines and electric vehicles, i.e., the neodymium offer is intrinsically related to the clean energy development (Yang et al., 2017). Nowadays, the insufficiency of economic and operational primary sources is compelling for nations to invest in recycling rare earth metals from pre-consumer scrap, industrial effluents, and end-of-life products (Jha et al., 2016). It is possible to recover REM by directly recycling manufacturing scrap/residues, urban mining end-of-life products, and industrial waste (solid/liquid) (Kumari et al., 2018).

There are methods to separate, purify, and preconcentrate the REMs from wastewaters, such as adsorption, liquid–liquid extraction, chemical precipitation, and ion exchange (Anastopoulos et al., 2016). Solvent extraction is the most commercialized technology for REM separation. However, despite the large processing capacity, it consumes many organic reactants with challenging regeneration, and it is not recommended to treat low-concentration rare earth solutions (Chen et al., 2022). Adsorption, in turn, is a unit operation widely applied for wastewater treatment (Arasi et al., 2021; Hachoumi et al., 2019; Mandal et al., 2020; Paziresh et al., 2021) that has gained attention for REM recovery because it is simple, cost-effective, and highly efficient at dilute systems (Costa et al., 2020; Hidayah and Abidin, 2017). Also, the adsorption can be selective and achieve high concentration factors (Asadollahzadeh et al., 2020; Chen et al., 2022).

Many studies of adsorption in batch mode evaluated the removal of neodymium using several adsorbent matrices (Table 5.1). Among them, vermiculite stood out because of its great reusability potential (Brião et al., 2020). Vermiculite is a clay mineral that presents a permanent negative charge and a high cationic exchange capacity (Campos et al., 2009), which improves the potential for rare earth cations adsorption. Besides that, when it is abruptly heated at high temperatures, the vermiculite produces an expanded structure with excellent textural properties for the adsorption purpose, such as a large pore volume and surface area, good chemical stability, and a low bulk density (Duman and Tunç, 2008; Huo et al., 2012).

Despite the high number of studies of rare earth adsorption on batch mode, there is a scarcity of studies discussing the adsorption/desorption cycles in fixed-bed operation for

recovery of REMs regeneration of the adsorbent (Costa et al., 2020). Agreeing to this scenario just a few works addressed the analysis of the reusability of the adsorbent and the Nd recovery simultaneously (Brewer et al., 2019; Park and Tavlarides, 2010). Moreover, there is a lack of studies about the application of viable adsorbents, with physical-chemical stability, low-cost and availability, in fixed-bed operation that is essential to move the REM recovery research towards an industrial scale (Callura et al., 2021; Patel, 2019).

Table 5.1. Adsorbent materials applied to the neodymium adsorption on batch mode.

Adsorbent	* q_{max} (mmol/g)	**Reusability	Reference
nZVI-montmorillonite	1.81	-	(Wang, 2018)
Expanded Vermiculite	0.39	98.8 % - 98.5% (5 cycles)	(Brião et al., 2021, 2020)
Kaolin	0.011	-	(Xiao et al., 2016)
Acrylic resins	2.13	-	(Xiong et al., 2015)
Functionalized magnetic nanoparticles	0.59	-	(Ashour et al., 2017)
Functionalized chitosan magnetic nanoparticles	0.35	100% - 95.1% (5 cycles)	(Galhoum et al., 2015)
Functionalized silica	2.08	-	(Polido Legaria et al., 2017)
Mesoporous Amine-Functionalized Polymer/SiO ₂ Composite	1.06	69.2 % - 66.4% (5 cycles)	(Salih et al., 2021)

* Maximum adsorption capacity estimated by Langmuir model

Therefore, this work goals to study the cyclic uptake and recovery of neodymium in a fixed-bed column of expanded vermiculite, based on promisor results of reusability presented by the adsorbent in batch mode and on the lack of studies addressing the recovery of neodymium through cycles of adsorption and desorption in the dynamic fixed-bed mode. To achieve this objective, the present study was divided into the optimization of operation variables as inlet flow and concentration; mathematical modeling; cycles of adsorption and desorption; and extensive characterization of the regenerated adsorbent.

5.2 MATERIAL AND METHODS

5.2.1 Neodymium solutions

Neodymium solutions were made by dissolving 5g of neodymium nitrate $\text{Nd}(\text{NO}_3)_3 \cdot 6\text{H}_2\text{O}$ (Aldrich, 99.9%) in 200 mL of deionized water. Successive dilutions in deionized water with

pH 3.5 were done at the desired concentration for the experiments. The pH was adjusted using drops of HNO₃ solution (0.5 mol/L).

Complexes of neodymium and xylenol orange were used to quantify the neodymium concentration by ultraviolet-visible spectroscopy (UVmini-1240, Shimadzu) in a wavelength of 575 nm (Granados-Correa et al., 2013; Havel et al., 1994).

5.2.2 Adsorbent

Commercial expanded vermiculite (EV) particles, provided by Brasil Minérios S.A., were the adsorbent material of this study.

5.2.3 Dynamic Column System

For all the adsorption experiments, a glass column with an inner diameter of 0.7 cm and a height of 10 cm was used. 0.4 g of expanded vermiculite filled the column, corresponding to a bed depth of proximally 7 cm. The column was sealed with glass fiber to avoid carrying adsorbent particles and then attached to a peristaltic pump Masterflex L/S (Cole-Parmer, USA) and a programmable aliquot collector FC203 (Gilson, Brazil). The system was continually fed in an upward flow with the neodymium solution at pH 3.5, while aliquots from the outlet of the column were taken at predetermined times. All experiments were carried out at room temperature (~25 °C).

5.2.4 Fixed-bed adsorption experiments

The effect of flow and inlet concentration were evaluated. The reusability of the bed in adsorption and desorption cycles was also assessed. The column efficiency was determined by the adsorption capacity q_i (mmol/g) and neodymium removal percentage R_i (%), in which $i = b$ corresponds to the breakthrough point ($C/C_0 = 0.05$), and $i = e$ refers to the exhaustion point ($C/C_0 = 0.95$); and by the mass transfer zone height (H_{MTZ}) (Equations 5.1 to 5.5).

$$q_b = \frac{C_0 Q}{1000m} \int_0^{t_b} \left(1 - \frac{C}{C_0}\right) dt \quad (5.1)$$

$$q_e = \frac{C_0 Q}{1000m} \int_0^{t_e} \left(1 - \frac{C}{C_0}\right) dt \quad (5.2)$$

$$R_b = \frac{q_b m}{C_0 Q t_b} 100 \quad (5.3)$$

$$R_e = \frac{q_e m}{C_0 Q t_e} 100 \quad (5.4)$$

$$H_{MTZ} = \left(1 - \frac{q_b}{q_e}\right)L \quad (5.5)$$

Where C_0 is the neodymium inlet concentration (mmol/L); Q is the neodymium solution flow rate (ml/min); m is the amount of vermiculite (g); t_b and t_e are the breakthrough and saturation time (min); C is the neodymium concentration at the outlet (mmol/L), and L is the bed depth (cm).

5.2.4.1 Flow rate and inlet concentration effect

The neodymium concentration was initially fixed at 1.0 mmol/L, and the runs with flow rates of 0.25, 0.50, 1.0, and 1.50 mL/min were performed to analyze the flow rate effect on the breakthrough curves. In the inlet concentration-effect study, the adequate flow rate was kept constant, and neodymium concentrations of 0.25, 0.5, and 1.0 mmol/L were evaluated. The more adequate experimental conditions of Q and C_0 were employed to study the recovery of neodymium and the adsorbent regeneration by the cyclic adsorption/desorption process.

5.2.4.2 Adsorption-desorption cycles

The reusability test was performed using the eluent CaCl_2 (0.3 mol/L), defined in the previous work (Brião et al., 2020). The column was submitted to five adsorption-desorption runs to simultaneously evaluate the neodymium recovery and the EV regeneration. Between each adsorption and desorption step, the column was washed with deionized water for 30 minutes. The elution capacity (q_{el} /mmol/g) and percentage ($E/\%$) were determinate by Equations 5.6 and 5.7.

$$q_{el} = \frac{Q}{m} \int_0^t C_{el} dt \quad (5.6)$$

$$E = \frac{q_{el}}{q_e} 100 \quad (5.7)$$

Where C_{el} is the neodymium concentration in the eluate (mmol/L) and t is the time (min). Also, a concentration factor (CF) was calculated as the maximum concentration ratio from the elution curve (C_{max}) and the inlet concentration C_0 . This factor indicates how much the metal was concentrated in the eluate compared to the inlet solution of the adsorption step (Lodeiro et al., 2006).

5.2.5 Fixed-bed adsorption modeling

Classical fixed-bed adsorption models such as Thomas, modified dose-response model (MDR), and Yoon-Nelson were fitted to the experimental data by nonlinear fitting carried out in OriginPro 8 software. Also, models based on mass conservation law were fitted to the data. Maple 17 was employed to perform the simulations and numerical resolutions. The determination coefficient (R^2), and corrected Akaike information criterion (AIC_c) were the parameters of fit quality (Hurvich and Tsai, 1989).

The Thomas model (Thomas, 1944), MDR model (Yan et al., 2001), Yoon-Nelson model (Yoon and Nelson, 1984) are presented in Equation 5.8, 5.9 and 5.10.

$$\frac{C}{C_0} = \frac{1}{1 + \exp\left[\frac{k_{Th}}{Q}(q_{Th}m - C_0Qt)\right]} \quad (5.8)$$

$$\frac{C}{C_0} = 1 - \frac{1}{1 + \left(\frac{C_0Qt}{q_Ym}\right)^{a_Y}} \quad (5.9)$$

$$\frac{C}{C_0} = \frac{1}{1 + \exp(k_{YN}\tau - k_{YN}t)} \quad (5.10)$$

Where k_{Th} (L/mmol.min) and q_{Th} (mmol/g) are the Thomas kinetic constant and bed adsorption capacity; a_Y (dimensionless) and q_Y (mmol/g) are the Yan constant and adsorption capacity at exhaustion; k_{YN} and τ (min) are the Yoon-Nelson kinetic constant (1/min) and the time for the saturation of half of the adsorbent amount.

The models based on the mass transfer mechanism fitted to the data were the instantaneous local equilibrium (ILE) (Georgin et al., 2020) and the dual-site diffusion (DualSD)(de Andrade et al., 2020). Both models consider the thermodynamic equilibrium

between the liquid phase and the solid (adsorbent) and that the properties of the liquid and solid phases are not altered during the process. Hence, the material balance is represented by Equation 5.11.

$$\frac{\partial C}{\partial t} = D_a \frac{\partial^2 C}{\partial z^2} - u_0 \frac{\partial C}{\partial z} - \frac{\rho_B}{\varepsilon} \frac{\partial q}{\partial t} \quad (5.11)$$

Where: D_a (cm²/min) is the axial dispersion coefficient; u_0 (cm/min) is the interstitial velocity; ρ_B (g/L) is the fixed-bed density, and ε is the void fraction.

The focal statement of the ILE model is the quick mass transfer between the phases and the local solid-liquid equilibrium in each segment of the fixed-bed (Georgin et al., 2020). Thus, the adsorption rate ($\partial q / \partial t$) of the Equation 5.11 can be rewritten in terms of the Langmuir equilibrium model (Langmuir, 1918), as shown in Equation 5.12.

$$\frac{\partial q}{\partial t} = \frac{\partial}{\partial t} \left(\frac{q_{max} K_L C}{1 + K_L C} \right) \quad (5.12)$$

Where: q_{max} (mmol/g) and K_L (L/mmol) are the Langmuir's constants, determined in previous work (Brião et al., 2020).

Differently to ILE model, the DualSD model assumes that there are two different adsorption sites at the adsorbent surface, which results in two mass transfer resistance coefficients, so the first term in Equation 5.11 ($\partial q / \partial t$) can be substituted as follows:

$$\frac{\partial q}{\partial t} = \frac{\partial q_1}{\partial t} + \frac{\partial q_2}{\partial t} \quad (5.13)$$

$$\frac{\partial q_1}{\partial t} = k_{s1} \left(\alpha \left(\frac{q_{max} K_L C}{1 + K_L C} \right) - q_1 \right) \quad (5.14)$$

$$\frac{\partial q_2}{\partial t} = k_{s2} \left((1 - \alpha) \left(\frac{q_{max} K_L C}{1 + K_L C} \right) - q_2 \right) \quad (5.15)$$

In which, q_i (mmol/g) is the amount adsorbed and k_{si} (1/min) is the mass transfer coefficient of each type of adsorption site; where $i=1$ or $i=2$ refer to the type-1 and type-2 sites, correspondingly, and α (dimensionless) is the contribution fraction of type-1 sites on the total adsorbed.

In the ILE model, the axial dispersion coefficient is predicted by the fitting, and, in DualSD, D_a is calculated to be an inlet parameter for the simulation according to Equation 5.16.

$$D_a = u_0 d_p \left(\frac{20 \frac{kT}{6\pi\tilde{\eta}_l r_i} \cdot 6 \times 10^5}{\varepsilon u_0 d_p} + \frac{1}{2} \right) \quad (5.16)$$

Where: d_p is adsorbent particle size (cm); k is the Boltzmann constant (1.3807×10^{-23} J/K), T is the temperature (K), r_i is the ionic radius (1.163 Å) and $\tilde{\eta}_l$ is the ion micro-viscosity (31.67×10^{-4} kg/m.s) (Mauerhofer et al., 2004).

5.2.6 Adsorbent characterization after adsorption/desorption cycles

The expanded vermiculite used in the present work was characterized, previously, before and after the neodymium adsorption (Brião et al., 2021, 2020). In this work, the regenerated expanded vermiculite (EVreg) was characterized after the cycles of adsorption and desorption, regarding the textural properties, morphology (images, semi-quantitative evaluation of composition), functional groups, structure, thermal stability, and zeta potential (Table 5.2).

Table 5.2. Characterization analysis of the adsorbent after the cycles of adsorption and desorption

Analyzes	Equipment	Conditions
Scanning electron microscopy and energy dispersive X-ray spectrometry (SEM-EDS)	LEO 440i, LEO	Metallization with gold (2 min), 10/20 kV, 50/600 pA.
Physical adsorption and desorption of nitrogen.	ANOVA-e (Quantachrome)	Pressure range from 10 to 800 mmHg, degas treatment for 3 hours at 200°C
Mercury porosimetry	Auto Pore IV (Micromeritics)	Pressure from 0.10 to 60000.00 psia
Helium picnometry	Accupyc II 1340 (Micromeritics)	10 cycles, cycle fill pressure of 16.000 psig, equilibration rate of 0.0500 psig/min.
Fourier-transform infrared spectroscopy (FT-IR)	Spectrometer Nicolet 6700 (Thermo Scientific)	KBr pastilles, wavelength from 4000 to 400 cm^{-1} and resolution of 4 cm^{-1}
X-ray diffraction	Philips Analytical X-Ray (X'Pert-MPD)	Cu K α with $\lambda=1.54056$ Å, step size 0.05 degree with 2 s/step
Thermogravimetric and differential thermal analyses	DTG-60 (Shimadzu)	N ₂ flow of 50 ml/min, a heating rate of 20 °C/min
Zeta potential	SurPASS (Anton Paar)	Acid titration (HNO ₃ 0.5 mol/L), ammonium acetate electrolyte (1 mmol/L)

5.3 RESULTS AND DISCUSSION

5.3.1 Effect of the flow rate

The flow rate is one of the most relevant parameters that determine the overall adsorption efficiency of a fixed-bed column. Figure 5.1 shows the breakthrough curves for the adsorption of neodymium on the expanded vermiculite bed with different flow rates. According to Figure 5.1, it was evidenced that the flow rate decreased as the breakthrough time increased. The flow rate is intrinsically related to the contact time between the adsorbate and adsorbent, which affects the mass transfer rate. For higher flow rates, the adsorbent is saturated faster than for lower ones. The flow rate of 0.25 mL/min affected more significantly the breakthrough time. Table 5.3 presents the effect of flow rate in the efficiency parameters for the neodymium adsorption on expanded vermiculite.

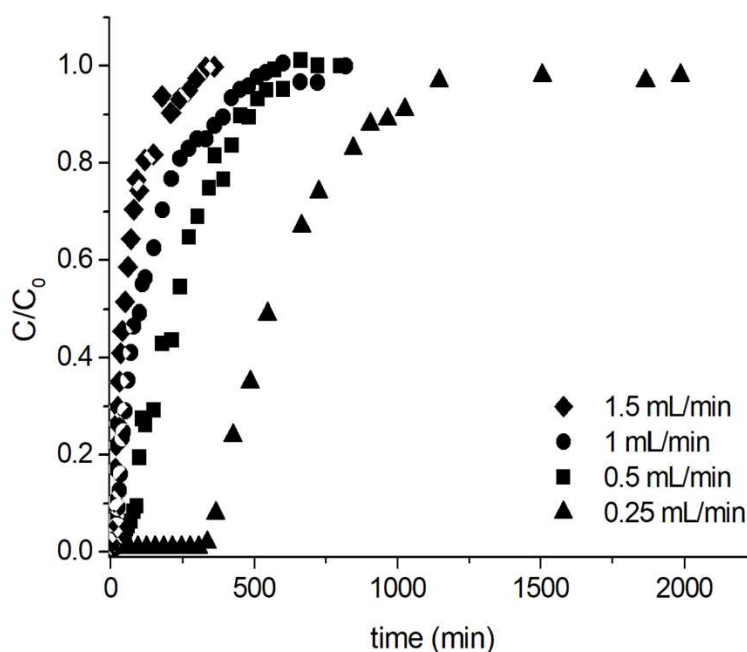


Figure 5.1. Effect of the flow rate on the breakthrough curves $C_0 = 1$ mmol/L

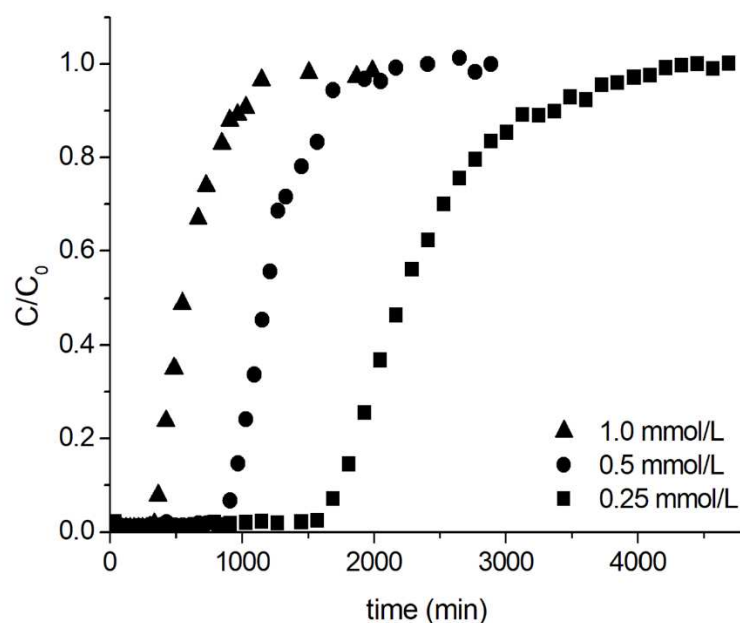
Table 5.3 indicated that for flow rates higher than 0.5 mL/min, q_b was very low compared to the flow rate of 0.25 mL/min. Besides that, other efficiency parameters also indicated that the best operation flow was 0.25 mL/min, such as the highest values of q_b , q_e , and R_e . Also, the breakthrough curve was closer to the ideal due to the lowest mass transfer zone height of 3.37 cm. Thus, the concentration-effect study was performed with a fixed flow rate of 0.25 mL/min.

Table 5.3. Parameters of adsorption efficiency for $C_0 = 1$ mmol/L at different flow rates.

Q (mL/min)	q_b (mmol/g)	q_e (mmol/g)	H_{MTZ} (cm)	R_b (%)	R_e (%)
0.25	0.24	0.45	3.37	99.2	42.7
0.5	0.09	0.39	5.43	98.0	37.7
1.0	0.05	0.37	6.02	100.0	27.7
1.5	0.03	0.29	6.28	98.0	21.1

5.3.2 Effect of the inlet concentration

Feed concentration is another important variable that affects the performance of a fixed-bed adsorber. Figure 5.2 presents breakthrough curves with different feed concentrations at the same flow rate (0.25 mL/min) to study how the neodymium concentration affects column efficiency.

Figure 5.2. Effect of the inlet concentration on the breakthrough curves $Q = 0.25$ mL/min

According to Figure 5.2, it is perceptible that the more diluted the inlet concentration, the higher the breakthrough time. Also, for the inlet concentration of 0.25 mmol/L, the breakthrough curve is less steep than the curves for higher inlet concentrations, which corroborates more mass-transfer resistance at this condition. Table 5.4 presents the adsorption parameters of the breakthrough curve for each inlet concentration.

Table 5.4. Parameters of adsorption efficiency for $Q = 0.25$ mL/min at different inlet concentrations.

C_0 (mmol/L)	q_b (mmol/g)	q_e (mmol/g)	H_{MTZ} (cm)	R_b (%)	R_e (%)
0.25	0.24	0.37	2.39	98.3	54.2
0.5	0.26	0.40	2.37	98.9	52.7
1.0	0.24	0.45	3.37	99.2	42.7

Analyzing each parameter of the adsorption efficiency in Table 5.4, we can notice that the q_b for all the inlet concentrations was almost the same (~ 0.25 mmol/g). However, the q_e increased as more concentrated was the inlet concentration. This occurs because increasing initial neodymium concentration promotes a driving force capable of surpassing the mass-transfer resistance (Patel, 2019). R_b and R_e were inversely affected by the inlet concentration increase. The highest R_b (99.2 %) was achieved with 1.0 mmol/L (highest C_0), while the highest R_e (54.2%) occurred at 0.25 mmol/L (lowest C_0). However, the mass-transfer zone does not have a monotonous behavior with the increase of the inlet concentration. With 1.0 mmol/L, the H_{MTZ} was 3.37 cm, representing around 50% of bed depth, and for the 0.5 and 0.25 mmol/L, the H_{MTZ} was 2.37 and 2.39 cm, around 34% of the bed depth. The closer the column is operated to the ideal condition, the more efficient is the mass-transfer zone (D. Barros et al., 2013). Therefore, the ideal situation means $H_{MTZ} = 0$. Based on the above, the best inlet concentration to operate the fixed-bed was 0.5 mmol/L because it presented a slightly higher q_b and the minimal H_{MTZ} . Thus, the study with the reusability of the fixed-bed along with cycles of adsorption and desorption was performed with $Q = 0.25$ mL/L and $C_0 = 0.5$ mmol/L.

5.3.3 Mathematical modeling

The accurate mathematical modeling to predict the fixed-bed adsorption parameters is essential for scale-up purposes (Ronda et al., 2018; Xu et al., 2013). In this paper, the classical empirical models of Thomas, MDR, Yoon-Nelson, and the mass-transfer models of DualSD and ILE were fitted to the breakthrough data, which the fitting results are presented in Table 5.5 and in Figure S.1 (Appendix A.3)

Table 5.5. Parameters from Thomas, modified dose-response (MDR), Yoon-Nelson, Dual site diffusion (DualSD), and Instantaneous local equilibrium (ILE) model calculated for neodymium adsorption on expanded vermiculite bed.

	C_0 (mmol/L)	1.0	1.0	1.0	1.0	0.5	0.25
Model	Q (mL/min)	1.5	1.0	0.5	0.25	0.25	0.25
	q_e (mmol/g)	0.29	0.37	0.39	0.45	0.40	0.37
Thomas	k_{Th} (L/mmol/min)	0.038	0.018	0.013	0.007	0.012	0.012
	q_{Th} (mmol/g)	0.22	0.29	0.28	0.42	0.38	0.36
	R^2	0.9547	0.9531	0.9838	0.9887	0.9876	0.9935
	AIC_c	-141.0	-178.3	-229.4	-171.2	-187.0	-273.2
MDR	a_Y	1.59	1.61	2.42	4.53	6.76	6.79
	q_Y (mmol/g)	0.18	0.24	0.32	0.40	0.38	0.35
	R^2	0.9962	0.9950	0.9923	0.9967	0.9929	0.9973
	AIC_c	-210.2	-258.9	-258.2	-206.1	-204.7	-309.7
Yoon-Nelson	k_{YN} (min ⁻¹)	0.037	0.017	0.012	0.0084	0.0059	0.0030
	τ (min)	56.3	120.5	240.4	592.1	1,231.8	2,286.1
	R^2	0.9547	0.9531	0.9838	0.9887	0.9876	0.9935
	AIC_c	-141.0	-178.3	-229.4	-171.2	-187.0	-273.2
DualSD	k_{S1} (min ⁻¹)	0.020	0.043	0.0053	0.0061	0.0045	0.0023
	k_{S2} (min ⁻¹)	0.0023	0.0059	5.44×10^{-12}	0.0075	0.010	0.0029
	D_a (cm ² /min)	0.187	0.127	0.067	0.037	0.037	0.037
	A	0.55	0.081	0.981	1.000	1.000	1.000
	q_e predicted (mmol/g)	0.33	0.39	0.33	0.33	0.73	1.17
	R^2	0.9952	0.9984	0.9932	0.9620	0.9678	0.8503
	AIC_c	-197.3	-295.2	-257.9	-125.7	-152.2	-139.7
ILE	D_a (cm ² /min)	2.28×10^8	8.87×10^7	9.20×10^8	3.40×10^7	3.15×10^1	2.32×10^7
	R^2	0.3498	0.6454	0.8427	0.9375	0.9692	0.9066
	AIC_c	-65.3	-104.7	-140.1	-122.3	-158.5	-163.8

According to the quality of fit criteria, the modified dose-response had the best adjustment, achieving the highest R^2 and the lowest AIC_c for most of the operational conditions evaluated. Also, the adsorption capacity at exhaustion forecasted by the model was closer to the experimental as the flow rate and inlet concentration reduced. The a_Y constant was maximum and practically the same (~ 6.8) for the best conditions evaluated ($Q = 0.25$ mL/min, and $C_0 = 0.5$ and 0.25 mmol/L), which suggests that there is a stabilization tendency of the a_Y

for low concentrations when the fixed bed works more efficiently. Thus, the value of $a_Y = 6.8$ may be helpful in further simulations studies for a lower C_0 range. Therefore, the MDR parameters q_Y (mmol/g) and a_Y were obtained from accurate nonlinear regression ($R^2 > 0.9923$), the model could predict the best performances of the bed, which indicates that MDR parameters can be useful for scale-up simulations to lead pilot or industrial scales.

The Thomas model that originates the MDR improvement (Yan et al., 2001) did not have the best fit. However, it could predict better the maximum adsorption capacity of the bed for the smallest concentrations. This model assumes the second-order reversible reaction kinetics and the Langmuir isotherm, which agreed with the kinetic and equilibrium characteristics of the system studied in previous work (Brião et al., 2020). The Yoon-Nelson model presented the same R^2 and AIC_c as the Thomas model because it can be written with an equivalent mathematical expression (Calero et al., 2009; Oliveira et al., 2018), with different variables and physical meanings. Despite the inferior fit to the experimental data, these models also give meaningful and precise information about the kinetic rate constants, equilibrium capacity of the bed, and time of 50% saturation. Thomas model indicated a kinetic constant magnitude order of 0.01 L/mmol/min for the lowest concentrations and flow rates. Also, the time of 50 % saturation predicted by Yoon-Nelson was very close to the experimental ones.

Thus, from the empirical models evaluated in this study, the modified dose-response model was the most recommended for predicting the breakthrough curves of the neodymium adsorption on expanded vermiculite. However, Thomas and Yoon-Nelson parameters can also assist in further simulations.

The DualSD model derives from linear driving force models and assumes that kinetic behaviors are due to two kinds of adsorption sites on the adsorbent. DualSD model fitted well the data ($R^2 > 0.96$) for almost all the conditions studied, except for the lowest concentration ($C_0 = 0.25$ mmol/L). The mass transfer coefficient k_{S1} decreased with the decreasing inlet concentration, agreeing to the experimental results that show a slower adsorption process with the reduction of the C_0 . At the same time, k_{S2} presented fluctuating values according to the variation of the flow rate and the inlet concentration. With the variation of the inlet concentration at 0.25 mL/min, the type1-site was the only adsorption site that contributed to the total amount adsorbed ($\alpha = 1.000$). Thus, the adsorption at the lowest flow rate ($Q = 0.25$ mL/min), independently of the inlet concentration, occurred more significantly in just one type of adsorption site. The axial dispersion calculated by Equation 16, an inlet parameter for the

DualSD model, is proportional to the interstitial velocity, i.e., D_a decreased as the flow rate decreased.

The ILE model did not predict the data satisfactorily at high flow rates ($R^2 < 0.85$), and the axial dispersion obtained by the ILE simulation was much higher than the D_a calculated (Equation 5.16). The ILE model fitted better the data ($R^2 = 0.9692$) when $Q = 0.25$ mL/min and $C_0 = 0.5$ mmol/L. This experimental condition was considered the most efficient, having the lowest H_{MTZ} (Table 5.4), which agrees with the great fit of the ILE model. ILE model represents a fixed-bed system without mass transfer resistance, i.e., much more the ILE model fitted the data, lower is the mass transfer resistance, closer to the ideal is the adsorption system, lower the H_{MTZ} .

Comparing both models based on the mass conservation law, the DualSD and ILE, overall DualSD adjusted the breakthrough data better than ILE. This indicates that the mass transfer resistance cannot be neglected, corroborating that the axial dispersion (D_a), as a hydrodynamic phenomenon, is independent of the intraparticle mass transport and did not significantly affect the mass transfer mechanism (Ko et al., 2003). From the analysis of Figure S.1, it is noted that the models that fitted better the data had different adjustments for shorter and longer times in the study of the concentration effect ($Q = 0.25$ mL/min). DualSD adjusted the breakthrough point better, and Thomas fitted the exhaustion better, except for the more diluted condition ($C_0 = 0.25$ mmol/L).

5.3.4 Adsorption-desorption cycles

The capacity to concentrate and recover the adsorbate is a great advantage of the adsorption compared to another separation process. However, the feasibility of the process is related to the reusability potential of the adsorbent material. A successful desorption operation must be capable of discharging the adsorbed rare-earth ions and guarantee the effective regeneration of the bed (Costa et al., 2020). Figure 5.3 demonstrates the curves of five cycles of the neodymium adsorption (a) and desorption (b) on expanded vermiculite. Figure 5.3(a) shows that the breakthrough time of all cycles was closer, indicating that the adsorbent does not lose efficiency significantly along with the cycles. Figure 5.3(b) presented the typical desorption curves with a pronounced peak in the desorbate concentration (Worch, 2012). The neodymium desorption occurred very quickly, which enriched the outlet solution, achieving a maximum of 14 mmol/l in the third cycle. Respectively, Table 5.6 summarizes the adsorption and desorption results for each cycle.

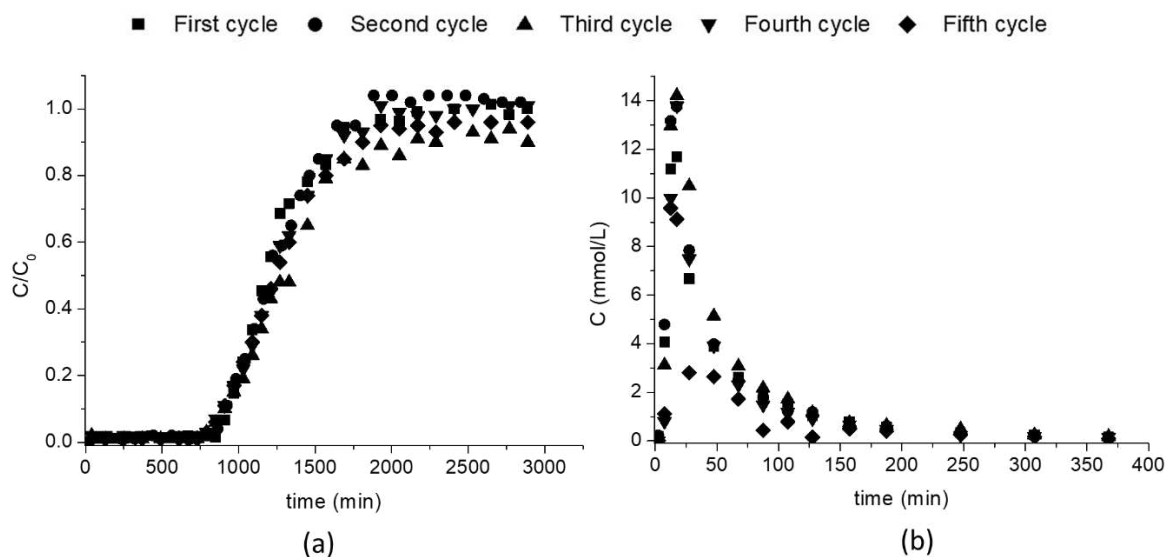


Figure 5.3. Cycles of neodymium adsorption (a) and desorption (b). $C_0 = 0.5$ mmol/L; $Q = 0.25$ mL/min; $C_{CaCl_2} = 0.3$ mol/L

The results in Table 5.6 show that the column increased its efficiency on the second cycle and lost part of it on the third one; after that, the bed maintained the performance until the last adsorption. However, along with the cycles, q_b and q_e deviated just ± 0.01 and ± 0.02 mmol/g, indicating that the column could reproduce the original performance without significant loss of efficiency. On the second adsorption, the breakthrough time and adsorption capacity increased. Moreover, the column saturated faster ($t_e = 1883$ min), achieving a removal efficiency of 65.0% with the lowest mass-transfer zone height. This behavior may be related to the exchange with the interlayer magnesium in the neodymium adsorption on the expanded vermiculite (Han et al., 2019; Padilla-Ortega et al., 2014; Węgrzyn et al., 2013). The negatively charged silicate sheet have distinct attractiveness for the interlayer Mg and the Ca from the eluent (Wild and Keay, 1964), which may contribute to the improvement of the adsorption efficiency at the second cycle.

The neodymium elution results present in Table 5.6 showed a non-monotonous behavior. An interesting observation is that the elution did not achieve 100% in any cycle, but it did not significantly compromise the adsorption efficiency of the column (Table 5.5). The elution using a source of Ca^{2+} as an exchangeable ion showed to be very efficient to recover neodymium, achieving high CF from 19.2 (5th cycle) to 28.4 (3rd cycle), with an average CF of 25.2 ± 3.9 . The third elution step could regenerate 96% of the bed, achieving an elution of 0.39

mmol/g and a concentration factor of 28.4, i.e., the solution from the elution (maximum peak) was 28.4 times more concentrated than the inlet solution of the adsorption step.

Table 5.6. Parameters of neodymium adsorption and desorption efficiency along with five cycles of reuse.

Cycle	Adsorption							Desorption			
	t_b (min)	q_b (mmol/g)	R_b (%)	t_e (min)	q_e (mmol/g)	R_e (%)	H_{MTZ} (cm)	q_{el} (mmol/g)	E (%)	C_{max} (mmol/L)	CF
1°	847.5	0.26	98.9	2407.5	0.40	52.7	2.37	0.24	62.1	11.7	23.4
2°	863.0	0.26	98.6	1883.0	0.37	65.0	2.13	0.24	66.2	13.8	27.6
3°	790.0	0.23	98.9	2170.0	0.41	62.6	2.97	0.39	96.0	14.2	28.4
4°	790.0	0.23	98.2	1930.0	0.37	64.7	2.65	0.28	75.5	13.8	27.6
5°	790.0	0.23	98.9	1930.0	0.38	66.3	2.72	0.19	48.9	9.58	19.2

Table 5.7 compiles the main results of reusability and neodymium recovery of some adsorbents to compare with the expanded vermiculite performance. Thus, just works with more than one cycle of adsorption/desorption were selected. The adsorbents presented in Table 5.7 have different origins; the phosphorus-based sol-gel is composed of clusters of phosphoric acid on the silica structure, the microbe beads are formed by the encapsulation of *Escherichia coli* cells by a polymeric matrix, and the expanded vermiculite is the thermal exfoliated form of the clay mineral vermiculite. The nature and composition of the adsorbents are directly related to the adsorption efficiency and stability along with the cycles. The biosorbent based on cell biomass has adsorption capacities much lower than the other adsorbents. Also, the neodymium desorption did not achieve a high concentration factor. In turn, the phosphorus-based sol-gel adsorbent that was synthesized to overcome the low applicability of the chelating resins attained great results of adsorbent reusability. The adsorbent lost just 19% of its original efficiency after twenty reuses. The expanded vermiculite had the highest adsorption capacities with a loss of just 5% along with the cycles, also achieved the highest concentration factor. These great results indicated that the continuous adsorption in an expanded vermiculite bed and desorption with calcium chloride is a promisor operation to recover neodymium due to the stability of this inorganic adsorbent.

Table 5.7. Comparison of reusability and neodymium recovery of different adsorbent matrices.

Adsorbent	Experimental Conditions				Eluent	Reusability	CF (1 st cycle)	Reference
	C_0 mmol/L	Q mL/min	pH	Column		q_e (mmol/g)		
Phosphorus-based sol-gel	1.0	0.83	3.2	$m = 0.3$ g $d_i = 0.7$ cm	1 M HNO_3	0.3 (1 st) 0.24 (20 th)	19*	(Park and Tavlariades, 2010)
Microbe beads	0.5	1.0	6.0	$d_i = 0.5$ cm $L = 15$ cm	0.01 M sodium citrate	0.018 (1 st) 0.012 (9 th)	6	(Brewer et al., 2019)
Expanded Vermiculite	0.5	0.25	3.5	$m = 0.4$ g $d_i = 0.7$ cm $L = 7.0$ cm	0.3 M $CaCl_2$	0.40 (1 st) 0.38 (5 th)	23.4	This work

* From a multicomponent experiment

5.3.5 Adsorbent characterization after adsorption/desorption cycles

Table 5.8 summarizes the surface and porous characteristics of the adsorbent before (EV) and after the neodymium adsorption (EV-Nd) and after the reuse (EVreg). The specific mass (ρ), the volume of the micro (V_{micro}) and mesopores (V_{meso}) were obtained by Helium picnometry, the bulk density (ρ_b) and the volume of macropores (V_{macro}) by mercury porosimetry, the particle porosity (ε_p) was calculated according to Equation 5.17. The isotherm of nitrogen adsorption and desorption provided the specific surface area by the Brunauer-Emmet-Teller (BET) method (Brunauer et al., 1938).

$$\varepsilon_p = 1 - (\rho_b / \rho) \quad (5.17)$$

The bulk density of the EVreg sample increased compared to the EV and EV-Nd, due to the structure compaction. The rehydration of interlayer sheets of the expanded silicates causes the loss of expansion, which means less void volume and greater bulk density. The specific mass of the EVreg is comparable to the EV one because Nd^{3+} was exchanged by Ca^{2+} , which agrees with the composition analysis (Table 5.9). The porosity and the surface area of the EVreg reduced compared to the original adsorbent (EV), indicating that the material lost part of the available adsorption sites along with the cycles of adsorption and desorption due to the reduction of the interlayer space and to the loaded calcium that filled the slits (pores). The volume of micro, meso, and macropores for EVreg were 1.46, 7.81, and 0.96 cm³/g, respectively, indicating a slight reduction in the volume of all classes of pores, compared to the

EV, except for macropores that maintained the same volume. The slight decrease in the total volume of pores indicated that even after five reusing cycles, the material was adequately regenerated with the proposed desorption method.

Table 5.8. Textural properties of the adsorbent.

Properties	EV*	EV-Nd*	EVreg
Specific mass (kg/m ³)	2167.5	2582.6	2,544.0
Bulk density (kg/m ³)	264.5	553	1,205
Porosity	0.88	0.79	0.53
Surface area (m ² /g)	9.88	5.44	8.78
V_{micro} (cm ³ /g)	2.47	1.33	1.46
V_{meso} (cm ³ /g)	8.26	4.66	7.81
V_{macro} (cm ³ /g)	0.96	1.39	0.96
Total pore volume (cm ³ /g)	10.73	5.99	10.23

* Results presented in previous work (Brião et al., 2020).

Table 5.9. Composition of the adsorbent before (EV), after the neodymium adsorption (EV-Nd), and after five cycles of adsorption/desorption (EVreg)

Element	Weight composition (%)		
	EV*	EV-Nd*	EVreg
Mg	15.7 ± 0.69	15.9 ± 0.76	14.15 ± 0.34
Al	7.63 ± 0.31	8.35 ± 0.61	7.36 ± 0.29
Si	21.8 ± 0.51	22.7 ± 0.74	21.84 ± 0.24
Cl	-	-	0.33 ± 0.19
Ca	-	-	3.35 ± 0.66
Ti	0.83 ± 0.11	0.54 ± 0.29	0.56 ± 0.08
Cr	0.50 ± 0.12	-	0.15
Fe	7.49 ± 0.35	2.83 ± 0.74	6.31 ± 1.03
Ni	-	-	0.09
K	0.21 ± 0.01	-	-
Nd	-	3.62 ± 1.18	0.51 ± 0.28
O	45.9 ± 0.03	45.9 ± 0.72	45.34 ± 0.13

* Results presented in previous work (Brião et al., 2021).

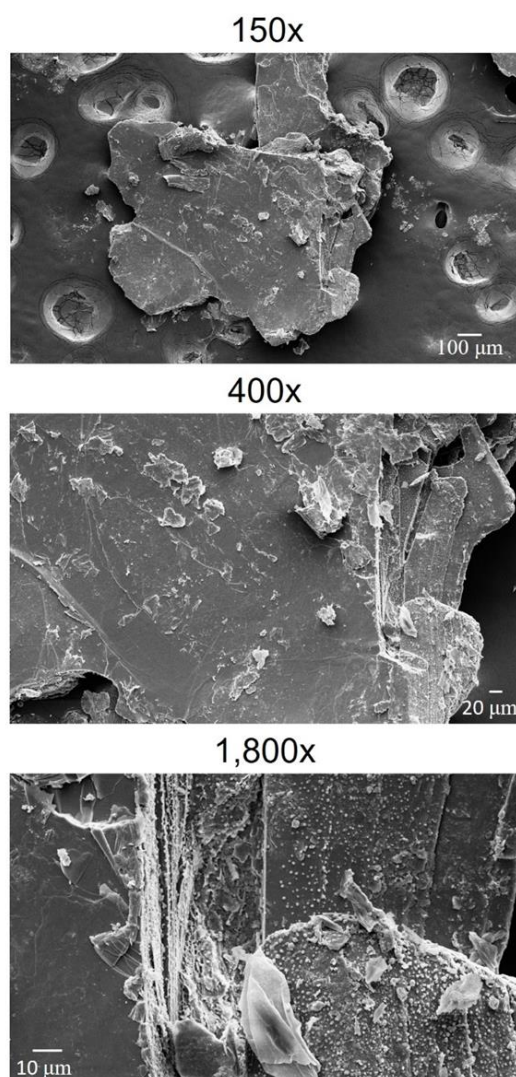


Figure 5.4. SEM images of EVreg

The SEM images (Figure 5.4) of the EVreg under different amplifications shows that the consecutive runs of adsorption and desorption made the thermally expanded mineral return the compacted form because the vermiculite plates are significantly closer to another. Also, on the reused material's surface are presented fragments that indicate that some damage to the EV structure occurred along with the cycles. The composition by EDS (Table 5.9) was determined in three different SEM images to obtain an error of the composition. Cr and Ni were found in just one image of EVreg; consequently, the percentage does not present a standard deviation. Both samples' material composition showed trace elements as Cr, K, Ni, Ti. For the regenerated adsorbent, Cl and Nd were included as trace elements. The primary mechanism of desorption

in which the loaded neodymium (Nd^{3+}) was exchanged with the Ca^{2+} of the eluent solution was confirmed because the percentage of the adsorbed neodymium (3.62%) after the adsorption is significantly closer to the loaded calcium in the EV after the regeneration (3.35%). Also, the percentage of the residual neodymium in the adsorbent is meager, indicating that the recovery was well executed. Regarding the structural elements of the adsorbent, Mg, Si, and Al, (Suvorov and Skurikhin, 2003) they were maintained even after the five series of adsorption/desorption, which represents that the composition integrity of the adsorbent was preserved.

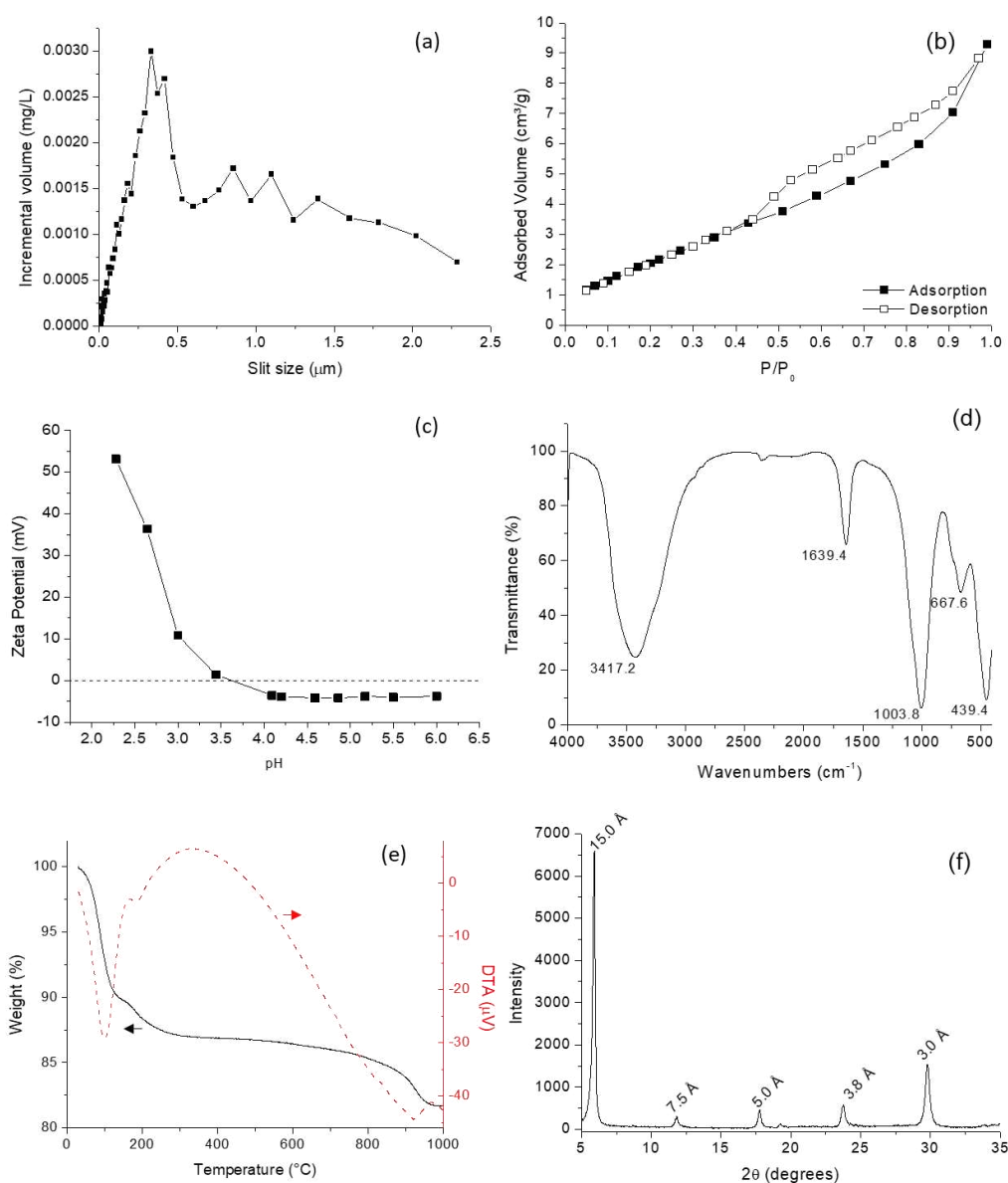


Figure 5.5. Characterization of regenerated expanded vermiculite (EVreg): Pore-size distribution (a); Isotherm of adsorption and desorption of N_2 (b); Zeta potential (c); FT-IR spectra (d); Thermo-gravimetric analysis (e) XRD spectrum (f)

Figure 5.5 (a) shows the pore-size distribution of the EVreg by the intrusion of Hg. The curve has one pronounced peak with a slit size of 0.3 μm , being the primary type of slit of the regenerated vermiculite. This value is much lower than the slit openings of the material before and after the adsorption. EV and EV-Nd presented bimodal distributions for slits $<12 \mu\text{m}$, with peaks at 2.68 and 9.74 μm for EV and 1.79 and 10.95 μm for EV-Nd (Brião et al., 2020). This significant reduction of the slits sizes indicated that the material effectively lost its expansion during the adsorption cycles.

In the same way as the raw adsorbent, EVreg presented an isotherm of physisorption of nitrogen (Figure 5.5 (b)) that does not have a plateau at high relative pressures being categorized as H3 (Brião et al., 2020; Sing et al., 1985). This behavior was expected because it is typical of phyllosilicates. Compounds with a structure in which silicate tetrahedrons (central silicon atom surrounded by four oxygen atoms) are arranged in sheets such as vermiculite (Brindley, 1981). Thus, it is possible to assume that the material maintained the structural form along with the five cycles.

The potential of the adsorbent surface influences the efficiency, as well as the overall mechanism of adsorption. The isoelectric point is a pH value at which the sum of the positive and negative charges on the material surface is zero. The zeta potential of the EVreg is presented in Figure 5.5 (c). The zeta potential values were negative for pH higher than 3.6 (isoelectric point), being constant (-5 mV) for pH higher than 4.0. The typical isoelectric point of the vermiculite is 2.9 (Duman and Tunç, 2008), which is lower than that for EVreg (3.6). Hence, after the consecutive reuses, the adsorbent neutralized part of the negative surface charge and the electrostatic attraction between the adsorbent and adsorbate was reduced along with the cycles.

The FTIR spectra (Figure 5.5 (d)) of the regenerated vermiculite present the O-H stretching vibration associated with the interlayer water at 3717.2 cm^{-1} . The absorption band at 1639.4 cm^{-1} also indicates the bend deformation of the O-H of water (Coates, 2004). The acute peak at 1003.8 cm^{-1} and 667.6 cm^{-1} , respectively, assigned the Si-O stretching and Al-O bending vibration. The peak at 439.4 points to the Si-O-Mg bending vibration (Duman and Tunç, 2008). The peaks relatives of Si-OH (3570 cm^{-1}) and Al-OH ($\sim 800 \text{ cm}^{-1}$) were not present, which may be associated with the substitution of the proton (H^+) for other cations in the process of adsorption (Nd^{3+}) and desorption (Ca^{2+}).

Clay minerals have known thermal stability, their small weight loss in a heating process is due mainly by water vaporization (Velde and Druc, 1998). Figure 5.5 (e) corroborated the

thermal stability of the vermiculite even after the successive cycles of adsorption/desorption of neodymium. With the temperature increment from 30 to 1000°C, the material just lost 18.3% of the mass. The significant loss of weight is due to the dehydration that the peak (~100°C) is referent to the adsorbed water. The step between 180-200°C is the escape the water bound to the exchangeable cations (Foldvari, 2011). The slow dehydroxylation process, which occurs in the 300–900 °C range, was responsible for just 2.3% of the lost weight. At high temperatures (900-950°C) occurs the thermal decomposition reaction of the structural elements of the vermiculite (Mg, Al, and Si) forming crystalline phases such as mullite, alumina, forsterite, enstatite (Feng et al., 2020; Foldvari, 2011).

According to Figure 5.5 (f), in which the X-ray diffractogram of the regenerated adsorbent is presented, the reflection (002) at angle 2θ around 6.0° indicated that the vermiculite maintained the dual water layer between the silicate sheets ($[\text{Si}_2\text{O}_2^{-5}]_n$) (Udoudo et al., 2015). The layer-to-layer distance increased from 14.1 Å in the original material (Brião et al., 2020) to 15.0 Å in the EVreg, indicating an increase in the number of interlayer H_2O molecules (Lanson et al., 2015). This is reasonable because the EVreg results from 5 cycles of adsorption and desorption where the samples were in contact with aqueous solutions interruptedly, which hydrated the interlayer space effectively. The basal diffraction intensities follow the typical sequence of the vermiculite pattern, in which the hkl 004 (7.5 Å), 006 (5.0 Å), 008 (3.8 Å), and 010 (3.0 Å) presented growing intensities (Wiewióra, 2003). The lattice spaces were obtained according to Bragg's law (Bragg, 1934).

5.4 CONCLUSION

The dynamic adsorption of neodymium on expanded vermiculite was optimized for varying flow rate and concentration, mathematical models were fitted to the data, cycles of adsorption and desorption were performed, and the material after the cycles was characterized by several analyses. According to the optimization phase, the adsorption efficiency increased as the flow rate reduced, and the flow rate of 0.25 mL/min was determined as the best flow condition. However, when the concentration-effect was studied, the intermediate concentration (0.5 mmol/L) presented the best adsorption performance, achieving a utile capacity of 0.26 mmol/g, an equilibrium capacity of 0.40 mmol/g, and a mass transfer zone height of 2.37 cm. The MDR fitted the data better than the other classical models. Comparing the fit of the mass transfer-based models to the data, the DualSD had a better adjustment than ILE, indicating that

the mass transfer resistance cannot be neglected, and that the axial dispersion does not affect the system significantly. The dynamic adsorption of neodymium in five cycles of adsorption and desorption had significantly closer breakthrough times, which indicates that the adsorbent did not lose significant efficiency along with the cycles. Moreover, the desorption process was able to recover and concentrate the neodymium achieving 96% of efficiency in the third cycle. After all the saturation and regeneration steps, the adsorbent lost part of the original negative charge and part of the expansion; however, it maintained the same structural composition, indicating that the material is resistant to several reuses. Thus, due to the great and reproducible adsorption and desorption performance in successively reuses, the expanded vermiculite is a promisor adsorbent to be applied to treat effluents containing neodymium; however, more studies on a laboratory and pilot scale still need to be carried out.

FUNDING

This work was supported by São Paulo Research Foundation/FAPESP (Grant # 2017/18236-1 and Grant # 2019/11353-8), Brazilian National Council for Scientific and Technological Development/CNPq (Grant # 308046/2019-6 and Grant # 147606/2018-7), and Coordination for the Improvement of Higher Education Personnel/CAPES.

ACKNOWLEDGMENTS

The authors thank Brasil Minérios S.A. for providing the adsorbent material.

REFERENCES

- Anastopoulos, I., Bhatnagar, A., Lima, E.C., 2016. Adsorption of rare earth metals: A review of recent literature. *Journal of Molecular Liquids* 221, 954–962. <https://doi.org/10.1016/j.molliq.2016.06.076>
- Arasi, M.A., Salem, A., Salem, S., 2021. Production of mesoporous and thermally stable silica powder from low grade kaolin based on eco-friendly template free route via acidification of appropriate zeolite compound for removal of cationic dye from wastewater. *Sustainable Chemistry and Pharmacy* 19, 100366. <https://doi.org/10.1016/j.scp.2020.100366>

- Asadollahzadeh, M., Torkaman, R., Torab-Mostaedi, M., 2020. Extraction and Separation of Rare Earth Elements by Adsorption Approaches: Current Status and Future Trends. *Separation and Purification Reviews*. <https://doi.org/10.1080/15422119.2020.1792930>
- Ashour, R.M., El-sayed, R., Abdel-Magied, A.F., Abdel-khalek, A.A., Ali, M.M., Forsberg, K., Uheida, A., Muhammed, M., Dutta, J., 2017. Selective separation of rare earth ions from aqueous solution using functionalized magnetite nanoparticles: kinetic and thermodynamic studies. *Chemical Engineering Journal* 327, 286–296. <https://doi.org/10.1016/j.cej.2017.06.101>
- Bragg, W.L., 1934. *The Crystalline State: Volume I*. The Macmillan Company, New York.
- Brewer, A., Dohnalkova, A., Shutthanandan, V., Kovarik, L., Chang, E., Sawvel, A.M., Mason, H.E., Reed, D., Ye, C., Hynes, W.F., Lammers, L.N., Park, D.M., Jiao, Y., 2019. Microbe Encapsulation for Selective Rare-Earth Recovery from Electronic Waste Leachates. *Environmental Science & Technology* 53, 13888–13897. <https://doi.org/10.1021/acs.est.9b04608>
- Brião, G. de V., da Silva, M.G.C., Vieira, M.G.A., 2021. Efficient and Selective Adsorption of Neodymium on Expanded Vermiculite. *Industrial & Engineering Chemistry Research* [acs.iecr.0c05979](https://doi.org/10.1021/acs.iecr.0c05979). <https://doi.org/10.1021/acs.iecr.0c05979>
- Brião, G. de V., Silva, M.G.C. da, Vieira, M.G.A., 2020. Neodymium recovery from aqueous solution through adsorption/desorption onto expanded vermiculite. *Applied Clay Science* 198, 105825. <https://doi.org/10.1016/j.clay.2020.105825>
- Brindley, G.W., 1981. Phyllosilicates, in: *Mineralogy*. Springer, Boston, MA., pp. 369–376. https://doi.org/10.1007/0-387-30720-6_100
- Brunauer, S., Emmett, P.H., Teller, E., 1938. Adsorption of Gases in Multimolecular Layers. *Journal of the American Chemical Society* 60, 309–319. <https://doi.org/10.1021/ja01269a023>
- Calero, M., Hernáinz, F., Blázquez, G., Tenorio, G., Martín-Lara, M.A., 2009. Study of Cr (III) biosorption in a fixed-bed column. *Journal of Hazardous Materials* 171, 886–893. <https://doi.org/10.1016/j.jhazmat.2009.06.082>
- Callura, J.C., Shi, Q., Dzombak, D.A., Karamalidis, A.K., 2021. Selective recovery of rare earth elements with ligand-functionalized polymers in fixed-bed adsorption columns. *Separation and Purification Technology* 265, 118472. <https://doi.org/10.1016/j.seppur.2021.118472>
- Campos, A., Moreno, S., Molina, R., 2009. Characterization of vermiculite by XRD and spectroscopic techniques. *Earth Sciences Research Journal* 13, 108–118.

- Chen, Z., Li, Z., Chen, J., Kallem, P., Banat, F., Qiu, H., 2022. Recent advances in selective separation technologies of rare earth elements: a review. *Journal of Environmental Chemical Engineering* 10, 107104. <https://doi.org/10.1016/j.jece.2021.107104>
- Coates, J., 2004. Encyclopedia of Analytical Chemistry -Interpretation of Infrared Spectra, A Practical Approach. *Encyclopedia of Analytical Chemistry* 1–23.
- Costa, T.B. da, Silva, M.G.C. da, Vieira, M.G.A., 2020. Recovery of rare-earth metals from aqueous solutions by bio/adsorption using non-conventional materials: a review with recent studies and promising approaches in column applications. *Journal of Rare Earths*. <https://doi.org/10.1016/j.jre.2019.06.001>
- D. Barros, M.A.S., A., P., A., E., 2013. General Aspects of Aqueous Sorption Process in Fixed Beds, in: *Mass Transfer - Advances in Sustainable Energy and Environment Oriented Numerical Modeling*. InTech. <https://doi.org/10.5772/51954>
- Dang, D.H., Thompson, K.A., Ma, L., Nguyen, H.Q., Luu, S.T., Duong, M.T.N., Kernaghan, A., 2021. Toward the Circular Economy of Rare Earth Elements: A Review of Abundance, Extraction, Applications, and Environmental Impacts. *Archives of Environmental Contamination and Toxicology* 81. <https://doi.org/10.1007/s00244-021-00867-7>
- de Andrade, J.R., Oliveira, M.F., Canevesi, R.L.S., Landers, R., da Silva, M.G.C., Vieira, M.G.A., 2020. Comparative adsorption of diclofenac sodium and losartan potassium in organophilic clay-packed fixed-bed: X-ray photoelectron spectroscopy characterization, experimental tests and theoretical study on DFT-based chemical descriptors. *Journal of Molecular Liquids* 312, 113427. <https://doi.org/10.1016/j.molliq.2020.113427>
- Duman, O., Tunç, S., 2008. Electrokinetic properties of vermiculite and expanded vermiculite: Effects of pH, clay concentration and mono- and multivalent electrolytes. *Separation Science and Technology* 43, 3755–3776. <https://doi.org/10.1080/01496390802219109>
- Feng, J., Liu, M., Fu, L., Zhang, K., Xie, Z., Shi, D., Ma, X., 2020. Enhancement and mechanism of vermiculite thermal expansion modified by sodium ions. *RSC Advances* 10, 7635–7642. <https://doi.org/10.1039/d0ra00223b>
- Foldvari, M., 2011. Handbook of thermo-gravimetric system of minerals and its use in geological practice, Occasional papers of the geological institute of Hungary.
- Galhoun, A.A., Mahfouz, M.G., Abdel-Rehem, S.T., Gomaa, N.A., Atia, A.A., Vincent, T., Guibal, E., 2015. Diethylenetriamine-functionalized chitosan magnetic nano-based particles for the sorption of rare earth metal ions [Nd(III), Dy(III) and Yb(III)]. *Cellulose* 22, 2589–2605. <https://doi.org/10.1007/s10570-015-0677-0>

- Georgin, J., Franco, D., Drumm, F.C., Grassi, P., Netto, M.S., Allasia, D., Dotto, G.L., 2020. Powdered biosorbent from the mandacaru cactus (*cereus jamacaru*) for discontinuous and continuous removal of Basic Fuchsin from aqueous solutions. *Powder Technology* 364, 584–592. <https://doi.org/10.1016/j.powtec.2020.01.064>
- Granados-Correa, F., Vilchis-Granados, J., Jiménez-Reyes, M., Quiroz-Granados, L.A., 2013. Adsorption behaviour of La(III) and Eu(III) ions from aqueous solutions by hydroxyapatite: Kinetic, isotherm, and thermodynamic studies. *Journal of Chemistry* 2013. <https://doi.org/10.1155/2013/751696>
- Hachoumi, I., Tatár, E., Mihucz, V.G., Orgován, G., Záray, G., el Antri, S., Lazar, S., 2019. Pod razor (*Ensis siliqua*) shell powder as cost-effective biomineral for removal of nickel(II), copper(II) and zinc(II) from artificially contaminated industrial wastewater. *Sustainable Chemistry and Pharmacy* 12, 100137. <https://doi.org/10.1016/j.scp.2019.100137>
- Han, B., He, B., Geng, R., Zhao, X., Li, P., Liang, J., Fan, Q., 2019. Ni(II) sorption mechanism at the vermiculite-water interface: Effects of interlayer. *Journal of Molecular Liquids* 274, 362–369. <https://doi.org/10.1016/j.molliq.2018.10.153>
- Havel, J., Moreno, C., Hrdlička, A., Valiente, M., 1994. Spectrophotometric determination of rare earth elements by flow injection analysis based on their reaction with xylenol orange and cetylpyridinium bromide. *Talanta* 41, 1251–1254. [https://doi.org/10.1016/0039-9140\(93\)E0044-E](https://doi.org/10.1016/0039-9140(93)E0044-E)
- Hidayah, N.N., Abidin, S.Z., 2017. The evolution of mineral processing in extraction of rare earth elements using solid-liquid extraction over liquid-liquid extraction: A review. *Minerals Engineering* 112, 103–113. <https://doi.org/10.1016/j.mineng.2017.07.014>
- Huo, X., Wu, L., Liao, L., Xia, Z., Wang, L., 2012. The effect of interlayer cations on the expansion of vermiculite. *Powder Technology* 224, 241–246. <https://doi.org/10.1016/j.powtec.2012.02.059>
- Hurvich, C.M., Tsai, C.L., 1989. Regression and time series model selection in small samples. *Biometrika* 76, 297–307. <https://doi.org/10.1093/biomet/76.2.297>
- Jha, M.K., Kumari, A., Panda, R., Rajesh Kumar, J., Yoo, K., Lee, J.Y., 2016. Review on hydrometallurgical recovery of rare earth metals. *Hydrometallurgy* 165, 2–26. <https://doi.org/10.1016/j.hydromet.2016.01.035>
- Ko, D.C.K., Porter, J.F., McKay, G., 2003. Mass transport model for the fixed bed sorption of metal ions on bone char. *Industrial and Engineering Chemistry Research* 42, 3458–3469. <https://doi.org/10.1021/ie020505t>

- Kumari, A., Jha, M.K., Pathak, D.D., 2018. Review on the Processes for the Recovery of Rare Earth Metals (REMs) from Secondary Resources. pp. 53–65. https://doi.org/10.1007/978-3-319-72350-1_5
- Langmuir, I., 1918. The Adsorption of Gases on Plane Surfaces of Glass Mic and Platinum. *Journal of American Chemiscal Society* 40, 1361–1403.
- Lanson, B., Ferrage, E., Hubert, F., Prêt, D., Mareschal, L., Turpault, M.-P., Ranger, J., 2015. Experimental aluminization of vermiculite interlayers: An X-ray diffraction perspective on crystal chemistry and structural mechanisms. *Geoderma* 249–250, 28–39. <https://doi.org/10.1016/j.geoderma.2015.03.005>
- Lodeiro, P., Herrero, R., Sastre de Vicente, M.E., 2006. Batch desorption studies and multiple sorption–regeneration cycles in a fixed-bed column for Cd(II) elimination by protonated *Sargassum muticum*. *Journal of Hazardous Materials* 137, 1649–1655. <https://doi.org/10.1016/j.jhazmat.2006.05.003>
- Mandal, A., Bar, N., Das, S.K., 2020. Phenol removal from wastewater using low-cost natural bioadsorbent neem (*Azadirachta indica*) leaves: Adsorption study and MLR modeling. *Sustainable Chemistry and Pharmacy* 17, 100308. <https://doi.org/10.1016/j.scp.2020.100308>
- Mauerhofer, E., Zhernosekov, K., Rösch, F., 2004. Limiting transport properties and hydration numbers of actinyl ions in pure water. *Radiochimica Acta* 92, 5–10. <https://doi.org/10.1524/ract.92.1.5.25405>
- Oliveira, M.F., de Souza, V.M., da Silva, M.G.C., Vieira, M.G.A., 2018. Fixed-Bed Adsorption of Caffeine onto Thermally Modified Verde-lodo Bentonite. *Industrial & Engineering Chemistry Research* 57, 17480–17487. <https://doi.org/10.1021/acs.iecr.8b03734>
- Padilla-Ortega, E., Leyva-Ramos, R., Mendoza-Barron, J., 2014. Role of electrostatic interactions in the adsorption of cadmium(II) from aqueous solution onto vermiculite. *Applied Clay Science* 88–89, 10–17. <https://doi.org/10.1016/j.clay.2013.12.012>
- Park, H.-J., Tavlarides, L.L., 2010. Adsorption of Neodymium(III) from Aqueous Solutions Using a Phosphorus Functionalized Adsorbent. *Industrial & Engineering Chemistry Research* 49, 12567–12575. <https://doi.org/10.1021/ie100403b>
- Patel, H., 2019. Fixed-bed column adsorption study: a comprehensive review. *Applied Water Science* 9, 1–17. <https://doi.org/10.1007/s13201-019-0927-7>
- Paziresh, F., Salem, A., Salem, S., 2021. Super effective recovery of industrial wastewater contaminated by multi-disperse dyes through hydroxyapatite produced from eggshell. *Sustainable Chemistry and Pharmacy* 23, 100501. <https://doi.org/10.1016/j.scp.2021.100501>

- Polido Legaria, E., Samouhos, M., Kessler, V.G., Seisenbaeva, G.A., 2017. Toward Molecular Recognition of REEs: Comparative Analysis of Hybrid Nanoadsorbents with the Different Complexonate Ligands EDTA, DTPA, and TTHA. *Inorganic Chemistry* 56, 13938–13948. <https://doi.org/10.1021/acs.inorgchem.7b02056>
- Ronda, A., Martín-Lara, M.A., Osegueda, O., Castillo, V., Blázquez, G., 2018. Scale-up of a packed bed column for wastewater treatment. *Water Science and Technology* 77, 1386–1396. <https://doi.org/10.2166/wst.2018.020>
- Salih, K.A.M., Hamza, M.F., Mira, H., Wei, Y., Gao, F., Atta, A.M., Fujita, T., Guibal, E., 2021. Nd(III) and Gd(III) Sorption on Mesoporous Amine-Functionalized Polymer/SiO₂ Composite. *Molecules* 26, 1049. <https://doi.org/10.3390/molecules26041049>
- Sing, K.S.W., Everett, D.H., Haul, R.A.W., Moscou, L., Pierotti, R.A., Rouquerol, J., Siemieniewska, T., 1985. Reporting physisorption data for gas/solid systems. *Pure and Applied Chemistry* 57, 603–619.
- Suvorov, S.A., Skurikhin, V. V., 2003. Vermiculite - A promising material for high-temperature heat insulators. *Refractories and Industrial Ceramics* 44, 186–193. <https://doi.org/10.1023/A:1026312619843>
- Thomas, H.C., 1944. Heterogeneous Ion Exchange in a Flowing System. *Journal of the American Chemical Society* 66, 1664–1666. <https://doi.org/10.1021/ja01238a017>
- Udoudo, O., Folorunso, O., Dodds, C., Kingman, S., Ure, A., 2015. Understanding the performance of a pilot vermiculite exfoliation system through process mineralogy. *Minerals Engineering* 82, 84–91. <https://doi.org/10.1016/j.mineng.2015.03.023>
- Velde, B., Druc, I.C., 1998. Archaeological ceramic materials: origin and utilization, *Natural science in archaeology*.
- Wang, J., 2018. Adsorption of aqueous neodymium, europium, gadolinium, terbium, and yttrium ions onto nZVI-montmorillonite: kinetics, thermodynamic mechanism, and the influence of coexisting ions. *Environmental Science and Pollution Research* 25, 33521–33537. <https://doi.org/10.1007/s11356-018-3296-0>
- Węgrzyn, A., Chmielarz, L., Zjezdzałka, P., Kowalczyk, A., Jabłońska, M., Baldrich Tolosa, X., Michalik, M., 2013. Adsorbents for iron removal obtained from vermiculite. *Acta Geodynamica et Geomaterialia* 10, 353–361. <https://doi.org/10.13168/AGG.2013.0034>
- Wiewióra, A., 2003. Particle size distribution in sonicated high- and low-charge vermiculites. *Applied Clay Science* 24, 51–58. [https://doi.org/10.1016/S0169-1317\(03\)00133-9](https://doi.org/10.1016/S0169-1317(03)00133-9)

- Wild, A., Keay, J., 1964. Cation-Exchange Equilibria With Vermiculite. *Journal of Soil Science* 15, 135–144. <https://doi.org/10.1111/j.1365-2389.1964.tb02214.x>
- Worch, E., 2012. Desorption and reactivation. *Adsorption Technology in Water Treatment*. <https://doi.org/10.1515/9783110240238.253>
- Xiao, Y., Huang, L., Long, Z., Feng, Z., Wang, L., 2016. Adsorption ability of rare earth elements on clay minerals and its practical performance. *Journal of Rare Earths* 34, 543–548. [https://doi.org/10.1016/S1002-0721\(16\)60060-1](https://doi.org/10.1016/S1002-0721(16)60060-1)
- Xiong, C., He, R., Pi, L., Li, J., Yao, C., Jiang, J., Zheng, X., 2015. Adsorption of Neodymium(III) on Acrylic Resin (110 Resin) from Aqueous Solutions. *Separation Science and Technology* 50, 564–572. <https://doi.org/10.1080/01496395.2014.955204>
- Xu, Z., Cai, J., Pan, B., 2013. Mathematically modeling fixed-bed adsorption in aqueous systems. *Journal of Zhejiang University SCIENCE A* 14. <https://doi.org/10.1631/jzus.A1300029>
- Yan, G., Viraraghavan, T., Chen, M., 2001. A new model for heavy metal removal in a biosorption column. *Adsorption Science and Technology* 19, 25–43. <https://doi.org/10.1260/0263617011493953>
- Yang, Y., Walton, A., Sheridan, R., Güth, K., Gauß, R., Gutfleisch, O., Buchert, M., Steenari, B.-M., van Gerven, T., Jones, P.T., Binnemans, K., 2017. REE Recovery from End-of-Life NdFeB Permanent Magnet Scrap: A Critical Review. *Journal of Sustainable Metallurgy* 3, 122–149. <https://doi.org/10.1007/s40831-016-0090-4>
- Yoon, Y.H., Nelson, J.H., 1984. Application of Gas Adsorption Kinetics I. A Theoretical Model for Respirator Cartridge Service Life. *American Industrial Hygiene Association Journal* 45, 509–516. <https://doi.org/10.1080/15298668491400197>

CHAPTER 6. OPTIMIZATION OF THE DYSPROSIUM ADSORPTION ON EXPANDED VERMICULITE

Critical rare earth metal adsorption onto expanded vermiculite: accurate modeling through response surface methodology and machine learning techniques⁵

Giani de Vargas Brião^a, Dison Stracke Pflingsten Franco^b, Flávio Vasconcelos da Silva^a,
Meuris Gurgel Carlos da Silva^a, Melissa Gurgel Adeodato Vieira^{a,*}

^a *University of Campinas – School of Chemical Engineering, Campinas, Brazil.*

^b *Universidad de la Costa – Department of Civil and Environmental, Barranquilla, Colombia.*

ABSTRACT

The circular economy of rare earth metals (REM), such as dysprosium, is essential for a sustainable future in clean energy and high-tech fields. Adsorption has gained attention to recover and reintegrate REM into the productive chain; however, accurate modeling of adsorptive processes still needs to be addressed, which delays further scale-up studies. Thus, this paper studied the adsorption of Dy on expanded vermiculite and applied novel empirical methods, such as artificial neural networks (ANN) and adaptive neuro-fuzzy inference system (ANFIS), and the classical response surface methodology (RSM) for modeling of dysprosium recovery as a function of adsorbent size, mass, and pH of the solution, variables often ignored in the mathematical modeling of adsorption. In our work, the effect of each operational parameter on Dy removal efficiency was examined by the RSM approach, in which only the adsorbent dosage and pH were the significant factors. So, ANFIS with two input membership functions (Gaussian type) was the most accurate procedure to predict and model the dysprosium removal efficiency ($R^2 = 0.99681$). Also, vermiculite removed dysprosium with high efficiency (99.2%) under the best experimental conditions, at pH around 3.5 and adsorbent mass of 0.64 g, indicating an effective process optimization. The loaded vermiculite, after the adsorption, was characterized by textural and thermal properties that confirmed the stability of the material. Thus, according to basic operational parameters, accurate modeling of the Dy adsorption on expanded vermiculite (a low-cost, available, and non-toxic material) can improve adsorption technology's maturity to reconcentrate and recover rare earth metals.

Keywords: dysprosium, adsorption, vermiculite, RSM, machine learning

⁵ Manuscript published in *Sustainable Chemistry and Pharmacy* (2023).

DOI: 10.1016/j.scp.2022.100938. Reprinted with the journal's permission (Appendix B.5).

6.1 INTRODUCTION

Dysprosium (Dy) is heavy rare earth metal (REM) that is primarily used in the manufacturing of permanent magnets (Nd-Fe-B) (Constantinides, 2012) used in wind turbines and electric vehicles, meaning dysprosium and rare earth metals play an essential role in developing renewable energy (Elshkaki and Graedel, 2014). However, increasing demand and risk supply make REM recovery from secondary sources essential to provide a circular economy and a sustainable energy sector in the future (Ambaye et al., 2020). REM recovery by hydrometallurgical routes generally has poor separation performance for dilute systems and environmental issues (Yoon et al., 2016), which can be tackled through adsorption, a reliable, low-cost, and simple process (Costa et al., 2020).

The adsorption efficiency and cost-effectiveness are directly related to the nature of the adsorbent. Currently, many adsorbents have been used to recover REM, such as clay materials (Sáez et al., 2021), modified zeolites (Yue et al., 2021), phosphogypsum (Hagag et al., 2019), microbial biomass (Shen et al., 2021), polymer-based sorbents (Ali et al., 2021; da Costa et al., 2022, 2021a, 2021b; Peng et al., 2021; Zhang et al., 2020). Expanded vermiculite has beneficial properties as a suitable adsorbent (Valkov and Simha, 2012), as this clayey mineral with a hydrated magnesium-aluminum-iron phyllosilicate structure has a high cation exchange capacity and a large surface area (Li et al., 2021; Udoudo et al., 2015). Besides, unlike the engineered adsorbents with a complex synthesis route and high cost, vermiculite is a natural and economical material for large-scale use in the recovery of rare earth (Li et al., 2021).

The adsorption efficiency depends not only on the unique characteristics of the adsorbent but also on different operating conditions, such as adsorbent mass, particle size, pH, temperature, contact time, adsorbate concentration, presence of interferents, among others (Iftekhhar et al., 2018), and proper modeling of the effect operational parameters on adsorption performance is essential to achieve industrial scales (Dotto and McKay, 2020). There are very accurate phenomenological and empirical models in the literature describing adsorption kinetics, equilibrium concentration (isotherms), and thermodynamics. Nevertheless, the influence of adsorbent mass, particle size, and pH on the adsorption potential is usually determined by investigating each effect individually without proper modeling.

Thus, to fill this gap, empirical and artificial intelligence approaches, such as response surface methodology (RSM), artificial neural networks (ANN), and adaptive neuro-fuzzy inference system (ANFIS), have been successfully applied to adsorption modeling (Dolatabadi

et al., 2020, 2018; Fan et al., 2017; Franco et al., 2020; Gokhale et al., 2020; Igwegbe et al., 2019; Sivamani et al., 2022; Talib et al., 2019). The RSM is an efficient tool mainly because it scrutinizes the influence of each factor on the response of interest (Box and Wilson, 1951). Still, it is not versatile enough to describe behaviors beyond linear and quadratic relationships. Machine learning techniques such as ANN and ANFIS, in turn, have outstanding learning algorithm performance and an elevated ability to differentiate between the input and output relationships for diverse nonlinear systems (Franco et al., 2020; Igwegbe et al., 2019; Talib et al., 2019), which leads to a higher prediction capability. ANFIS, a neural network combined with a fuzzy inference system, generally has advantages in terms of superior speed, fault tolerance, and adaptability (Jang, 1993).

Thus, this work aims to investigate and model the removal of dysprosium by varying the pH, particle size, and mass of vermiculite by profiting from the advantages of both RSM and machine learning approaches, i.e., scrutinize the effect of each variable by response surface methodology and provide accurate modeling of the operational parameters, usually neglected, on the Dy adsorption efficiency by machine learning. Furthermore, the study intends to evaluate the adsorbate-adsorbent interaction by textural and thermal characterization analyses to assess the feasibility of applying vermiculite in dysprosium adsorption, which would contribute to the future scale-up of the REM recovery sector.

6.2 MATERIALS AND METHODS

6.2.1 Adsorption Experiments

A series of experiments were done following a rotational central composite design (RCCD) varying particle size, adsorbent mass, and pH to scrutinize the effect of each variable over the Dy adsorption efficiency and to determine the best operational conditions by response surface methodology.

New experiments were performed varying just the significant parameters pointed by the RSM, and this data was the input for ANN and ANFIS, approaches rarely applied in the recovery of rare earth metals research field, used to refine the modeling of the significant effects over the removal percentage.

The adsorbent used in this study, the expanded vermiculite, was produced by Brasil Minérios S/A. The material was sieved to separate different granulometric fractions through a set of sieves (40 to 12 mesh) on a vibrating base (Produtest).

A dysprosium solution (3.0 mmol/L) was prepared from a stock solution in which 5.0 g of dysprosium (III) pentahydrate nitrate (Aldrich, 99.9%) was dissolved in 100 mL of acidified water ($\text{pH} \cong 5.0$) by addition of nitric acid (0.1 mol/L).

The agitation was done in an incubator shaker (SI-600R Jeio Tech), in which the fixed parameters were rotation (200 rpm), time (24 h), temperature (25 °C), volume (50 mL), and concentration of the Dy^{3+} solution (3 mmol/L). A few drops of nitric acid (0.1 mol/L) and ammonium hydroxide (0.1 mol/L) were added to control the pH of the experiment. The adsorbent mass range was chosen to ensure process availability (low amounts of adsorbent). Furthermore, the pH range was based on the typical pH of effluents that may contain Dy ($\cong 2.0$) (Gergoric et al., 2019; Riaño and Binnemans, 2015; Zhang and Xu, 2016) and on the pH of the $\text{Dy}(\text{OH})_3$, precipitable specie, formation in an aqueous medium ($\cong 6.0$).

The solid phase (adsorbent) was separated by centrifugation at 4000 rpm for 10 min (CENCE L600 centrifuge), and the supernatant was filtrated with a syringe filter (Macherey-Nagel, porous of 0.45 μm). Dysprosium concentration was measured using atomic absorption spectroscopy (Shimadzu, AA7000).

The adsorption capacity (q) and the removal percentage ($\%R$) were determined by Equations 6.1 and 6.2, respectively.

$$q = \frac{(C_0 - C)V_{sol}}{m_{ads}} \quad (6.1)$$

$$\%R = \frac{(C_0 - C)}{C_0} 100 \quad (6.2)$$

Where C_0 is the initial concentration (mmol/L), C is the concentration after a specific contact time (mmol/L), V_{sol} is the volume of the metallic solution (L), and m_{ads} is the adsorbent mass (g).

6.2.2 Response Surface Methodology

Multiple factors potentially affect the adsorption process. Therefore, in this study, particle size (A), adsorbent mass (B), and pH (C) were varied by a rotational central composite design (RCCD) to optimize the %R (response variable). Seventeen runs were carried out following the RCCD, consisting of eight factorial points, six axial points, and three central points. RSM was applied to this dataset.

The RSM is widely applied to optimize products and processes, as it allows the discovery of significant factors, accurate modeling, and optimization (Costa et al., 2011). In the present study, the analysis of variance (ANOVA) test, with a significance level of 0.05, and the surface responses were performed using the Statistica software version 7.0 (StatSoft, Inc.). An empiric-squared model (Equation 6.3) was initially fitted to the data, and backward elimination was conducted to enhance the adjustment.

$$Y = \beta_0 + \sum_{i=1}^k \beta_i x_i + \sum_{i=1}^k \beta_{ii} x_i^2 + \sum_{i=1}^k \sum_{j=1}^k \beta_{ij} x_i x_j + \varepsilon \quad (6.3)$$

Where Y is the predicted response (removal percentage), x_i and x_j are the independent variables (CCD factors), ε is the random error, and β_0 , β_i , β_{ii} , and β_{ij} are the polynomial coefficients (model constant, linear coefficient, quadratic coefficient, and cross-product coefficient, respectively).

Complementary analyses were done to comprehend the role of pH in the mechanism of dysprosium adsorption: analysis of the expanded vermiculite zeta potential and the metallic speciation of dysprosium. The zeta potential of the adsorbent was measured by acid titration (HNO_3 0.5 mol/L) in ammonium acetate electrolyte (1 mmol/L) using a SurPASS (Anton Paar). The dysprosium species distribution as a pH function was simulated using Visual Minteq software.

Once the optimal conditions of pH, mass of adsorbent, and particle size were defined, an experimental validation was carried out in triplicate, maintaining the same rotation speed (200 rpm), initial concentration (3.0 mmol/L), and solution volume (50 mL) of the RCCD, to verify the accuracy of the RSM to model and optimize the adsorption of dysprosium on expanded vermiculite.

6.2.3 Machine learning techniques

The ANN and ANFIS were designed considering the significant input variables on the output (Dy removal percentage). The development and training of the networks were performed in MATLAB scripts using a total data of 24 points. The data were normalized and denormalized as needed. Different architectures of both neural networks were tested several times regarding their predictability to avoid local minimum.

6.2.3.1 Artificial Neural Network

Artificial neural networks (ANNs) are computational models with interconnected nodes inspired by neurons in the human brain or neural biology (Izadkhah, 2022) that can trace nonlinear relationships between input and output parameters. ANN architectures are constructed by different layers, such as input, output, and hidden layers. In the layers, there are activation functions that manage the training in the algorithm. Each neuron has specific weight and bias values that rule the optimization procedure (Ghaedi and Vafaei, 2017). Therefore, ANN can mathematically be represented by Equation 6.4 (Pauletto et al., 2020).

$$Y = f_1 \left(\sum_{j=1}^n w_{kj} \left[f_2 \left(\sum_{i=1}^m w_{ji} X_i + b_j \right) \right] + b_k \right) \quad (6.4)$$

Where Y is the output vector, X is the input vector, w and b are the weights and biases between the layers, n is the number of neurons at hidden layers, m is the number of inputs variables, and i, j, k corresponds to the input, hidden and output layers, respectively. Besides, f_1 and f_2 are the activation functions at the output and hidden layers, respectively.

This work analyzed ANN architectures with different neurons in the hidden layer, in a typical shallow neural network, by the minimum mean square error (MSE). The Levenberg–Marquardt algorithm (Levenberg, 1944; Marquardt, 1963), often the fastest backpropagation algorithm, was the training function of the network architectures developed in MATLAB 2018a software, and the activation function “*tansig*” (Equation 6.5) and “*purelin*” (Equation 6.6) were used at the hidden and output layers, respectively, as a standard two-layer feedforward network. In this case, 70% of the data were used randomly for training, 15% for validation, and 15% for test.

$$f(x) = \frac{2}{(1 + e^{-2x})} - 1 \quad (6.5)$$

$$f(x) = x \quad (6.6)$$

6.2.3.2 The adaptive neuro-fuzzy inference system

One of the most common neuro-fuzzy systems is the ANFIS system introduced by (Jang, 1993), which combines fuzzy logic and neural network. If the desired input-output data sets are available for a fuzzy system, the membership function (MF) and rule table for a fuzzy model can be designed using the neural network training method (Bose, 2021). ANFIS combines the advantages of the ANN and FIS and avoids their shortcomings. Therefore, it provides better generalization performance, archives highly nonlinear mapping, and provides stable solutions (Shafiullah et al., 2022). ANFIS network comprises five layers: fuzzy layer, product layer, normalized layer, de-fuzzy layer, and total output layer (Kurtgoz and Deniz, 2018).

In this paper, the fuzzy interference system applied to ANFIS was implemented through the “*genfis1*” function of MATLAB 2018a that returns a Takagi-Sugeno type FIS (Takagi and Sugeno, 1985) using a grid partition of the input and output data provided. The Gaussian membership function (“*gaussmf*”) was applied to both inputs (Equation 6.7) since this MF is widely used due to its smoothness and concise notation (Hameed, 2011; Sadollah, 2018).

$$f(x, \sigma, c) = e^{-((x-c)^2 / 2\sigma^2)} \quad (6.7)$$

Where x is the input and σ and c are the function parameters.

The number of membership functions referring to the minimal *MSE* was evaluated to determine the best ANFIS architecture. 70% of the data was used for training and 30% for checking randomly (“*randperm*” function). The network was simulated using the hybrid method, the combination of least-squares estimation, and the backpropagation algorithm. The defuzzification was done by the weighted average method; and the output membership functions were linear.

6.2.4 Assessment of data correlation quality

The statistical criteria to estimate the goodness of fit were the coefficient of determination (R^2) (Equation 6.8), which indicates the relationship between observed and predicted values, and the MSE (Equation 6.9), which informs whether the data are concentrated around the best fit curve, prediction error (Saber et al., 2021). The MSE criteria were selected because it is differentiable, can be optimized better, penalizes even minor errors by squaring them, and is very sensitive to outliers (Aditya Mishra, 2020). The post-metric R^2 was chosen to verify how much of the total variance in the target is explained by variance in the regression line (Hiregoudar, 2020).

$$R^2 = 1 - \frac{\sum_{i=1}^N (y_i - \hat{y}_i)^2}{\sum_{i=1}^N (y_i - \bar{y})^2} \quad (6.8)$$

$$MSE = \frac{1}{N} \sum_{i=1}^N (\hat{y}_i - y_i)^2 \quad (6.9)$$

Where N is the number of experimental points, y_i and \hat{y}_i are the observed and the predicted values, respectively, and \bar{y} is the mean of the observed values.

6.2.5 Adsorbent characterization

Accurate modeling of adsorption phenomena considering the effect of operational parameters is usually ignored. The same occurs with the characterization of the adsorbent after sorption to verify the stability of the material. In this work, expanded vermiculite loaded with dysprosium (V-Dy), the solid sample collected after adsorption, was characterized in terms of textural and thermal properties. The textural properties evaluated are the Brunauer–Emmett–Teller surface area ($S_{BET}/m^2/g$) (Brunauer et al., 1938) (Equations S1-S2, Supplementary Information), real ($\rho/g/cm^3$) and bulk ($\rho_{bulk}/g/cm^3$) densities, particle porosity (ϵ_p , Equation A3). The instruments used were an ANOVA-e surface area analyzer (Quantachrome), Auto Pore IV mercury porosimeter (Micromeritics), and Accupyc II 1340 Helium pycnometer (Micromeritics). A thermogravimetric and differential thermal analysis by DTG-60 (Shimadzu) was conducted to investigate the material's thermal stability after adsorption. More details on the characterization procedure can be found in **Table S1** (Supplementary Information, Appendix A.4).

6.3 RESULTS AND DISCUSSION

6.3.1 Response surface methodology

The results of adsorption capacity and percentage of Dy removal of the rotational central composite design are exhibited in **Table 6.1**, in which the %*R* wide-ranging from 27.6% (run 13) to 99.1% (run 8), and the *q* passed from 0.08 mmol/g (run 13) to 0.37 mmol/g (run 6), indicating that the factors affected the response variable (%*R*) and the adsorption capacity.

Table 6.1 RCCD for the Dy adsorption capacity (*q*) and removal percentage (%*R*) on vermiculite as a function of particle size (*A*), adsorbent amount (*B*), and pH (*C*).

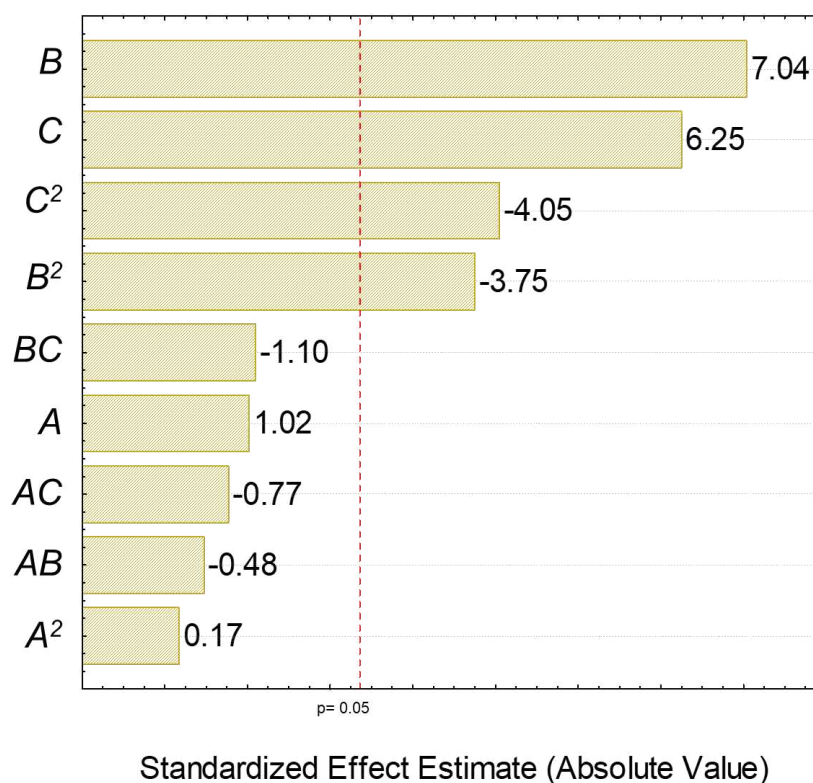
Run	Independent Variables			Coded Variables			<i>q</i> (mmol/g)	% <i>R</i>
	<i>A</i> (mm)	<i>B</i> (g)	pH	<i>A</i> (mm)	<i>B</i> (g)	<i>C</i>		
1	0.65	0.300	2.0	-1	-1	-1	0.20	42.2
2	1.09	0.300	2.0	+1	-1	-1	0.26	55.8
3	0.65	0.700	2.0	-1	+1	-1	0.16	80.6
4	1.09	0.700	2.0	+1	+1	-1	0.18	89.3
5	0.65	0.300	4.0	-1	-1	+1	0.35	73.9
6	1.09	0.300	4.0	+1	-1	+1	0.37	79.6
7	0.65	0.700	4.0	-1	+1	+1	0.20	98.9
8	1.09	0.700	4.0	+1	+1	+1	0.20	99.1
9	0.48	0.500	3.0	- α	0	0	0.27	94.1
10	1.30	0.500	3.0	+ α	0	0	0.27	97.3
11	0.85	0.163	3.0	0	- α	0	0.28	32.1
12	0.85	0.836	3.0	0	+ α	0	0.17	98.8
13	0.85	0.500	1.3	0	0	- α	0.08	27.6
14	0.85	0.500	4.7	0	0	+ α	0.28	98.9
15	0.85	0.500	3.0	0	0	0	0.27	95.8
16	0.85	0.500	3.0	0	0	0	0.27	95.6
17	0.85	0.500	3.0	0	0	0	0.27	95.8

The standardized effects of the independent inputs and their relations to the response variable (%*R*) are presented in **Fig 6.1** (Pareto Chart) to understand how much each factor

affected the response. Effects were considered significant when the t -value was greater than ± 2.365 (t -student test for seven degrees of freedom (fd) and had $p < 0.05$). Factors that significantly affected the %R with 95% confidence were: the amount of adsorbent (g) and pH, both in linear form (B , C) and squared form (B^2 , C^2). Particle size (A , A^2), and all interactions between factors (AC , BC , AB) were insignificant. The complete table of the estimated effects can be consulted in the supplementary material (**Table S2**, Appendix A.4).

A simulation of Dy speciation (**Fig 6.2 (a)**) and the zeta potential of the material (**Fig 6.2 (b)**) were evaluated to elucidate the effect of pH on the adsorbate and adsorbent. The highest effect on %R was the adsorbent mass (g) followed by pH, both positive. The squared effects (B^2 , C^2) were smaller than the linear and negative ones. The positive effect of the adsorbent mass on the %R can be explained because the adsorbent dosage increases the available sites to adsorb metallic ions. While the positive effect of pH is due to the increase in the negative charge of vermiculite with the intensification of pH, which improves the electrostatic attraction of the cations.

Fig 6.1 Pareto chart (standardized effects on percentage of Dy removal)



The species in solution in the pH range studied (1.3 until 4.7) are essentially Dy^{3+} and H^+ (**Fig 6.2(a)**). For $\text{pH} < 2.9$, hydrogen is the dominant species in the medium, while for $\text{pH} > 2.9$, the Dy^{3+} has the highest concentration in the medium. As the pH increases, the H^+ concentration drops to zero ($\text{pH} \sim 5.0$). This behavior explains the positive effect of pH for the adsorption of Dy, since the augment in pH diminishes the competition between Dy^{3+} and H^+ for the known negatively charged sorption sites of vermiculite. In the analysis of vermiculite zeta potential (**Fig 6.2 (b)**), the isoelectric point was determined at $\text{pH} = 2.5$, i.e., at this pH value, the sum of the positive and negative charges on the vermiculite surface was zero (Duman and Tunç, 2008). When the $\text{pH} >$ zero charge potential, the surface of the vermiculite is negatively charged, promoting an attraction of Dy^{3+} cations, which also justifies the positive effect of pH on the adsorption of dysprosium. The effect of pH can be evidenced by comparing the results of **Table 6.1** (runs 13 and 14), where only pH was varied; at pH 1.3, the %R was 27.6%, and at pH 4.8, the %R was 98.9%.

Fig 6.2 Dysprosium speciation diagram (a) and vermiculite zeta potential of the (b)

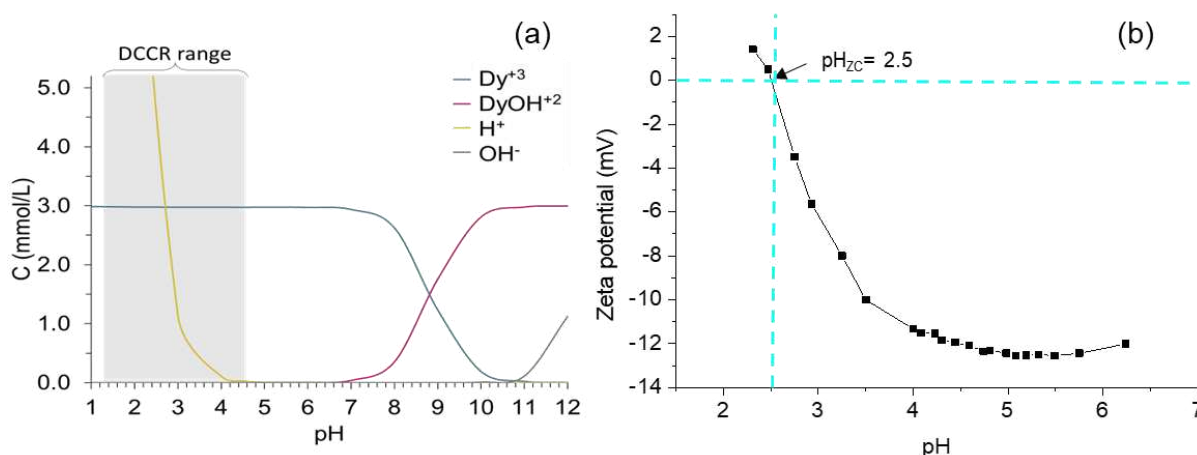


Table S3 (Appendix A.4) presents the variance analysis (ANOVA) for the completed model with main and interaction effects. The complete model (Equation 3) was significant with 95% confidence, although the model considers the non-significant effects. It could be concluded by $F_{\text{cal}}/F_{\text{tab}} = 3.7$. The model adjusted the data with an R^2 of 0.9455 and an adjusted determination coefficient (R^2_{adj}) of 0.8755. However, the ANOVA of the reduced model (**Table 6.2**) after the backward elimination (Equation 10), i.e., elimination of the non-significant effects, showed an $F_{\text{cal}}/F_{\text{tab}} = 10.8$, an $R^2 = 0.9217$ and an $R^2_{\text{adj}} = 0.8949$. The estimated effects of the reduced model are available in **Table S4** (Appendix A.4).

Table 6.2 ANOVA for the reduced squared model ($\alpha = 0.05$) for %R prediction.

Source	<i>SS</i>	<i>fd</i>	<i>MS</i>	<i>F_{calc}</i>	<i>F_{calc}</i> / <i>*F_{tab}</i>
Regression	9078.4	4	2269.6	35.1	10.8
Error	776.9	12	64.7		
Total	9855.4	16			

* $F_{tab} = 3.26$

The increase of the F-test value from 3.7 to 10.8, and the R^2_{adj} from 0.8755 to 0.8949 indicated that the reduced model is more significant than the completed model. The reduced model was chosen to represent the %R because it presented $F_{cal}/F_{tab} > 10$; a ratio recommended in the literature to consider a helpful regression for forecasting purposes (de Barros Neto et al., 2010). The observed versus predicted values (**Fig 6.3**) and the response surface (**Fig 6.4**) were based on the %R model of Equation 10 for normalized values of B (adsorbent mass) and C (pH).

$$\%R = 96.58 + 16.74B + 14.91C - 10.09B^2 - 10.90C^2 \quad (10)$$

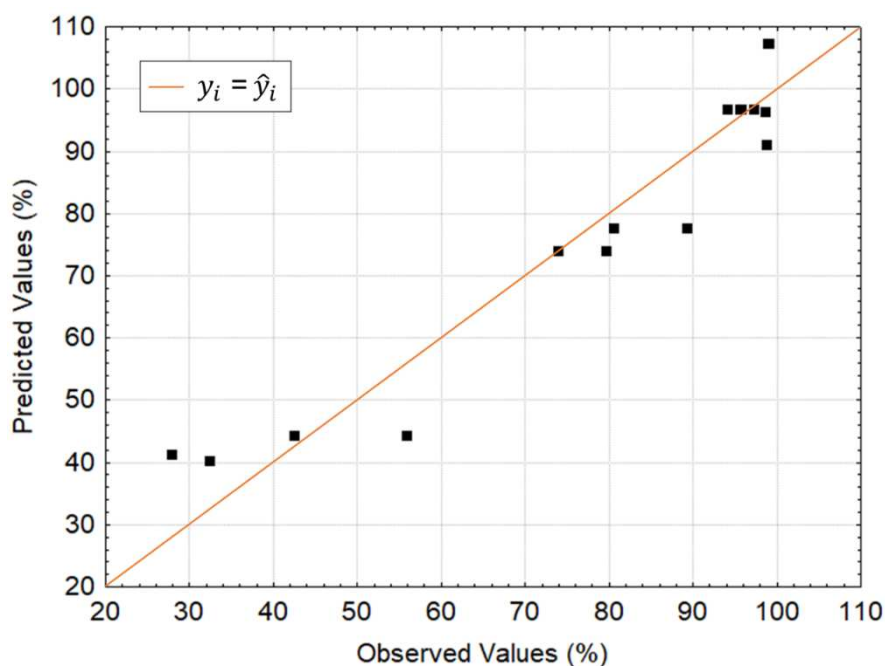
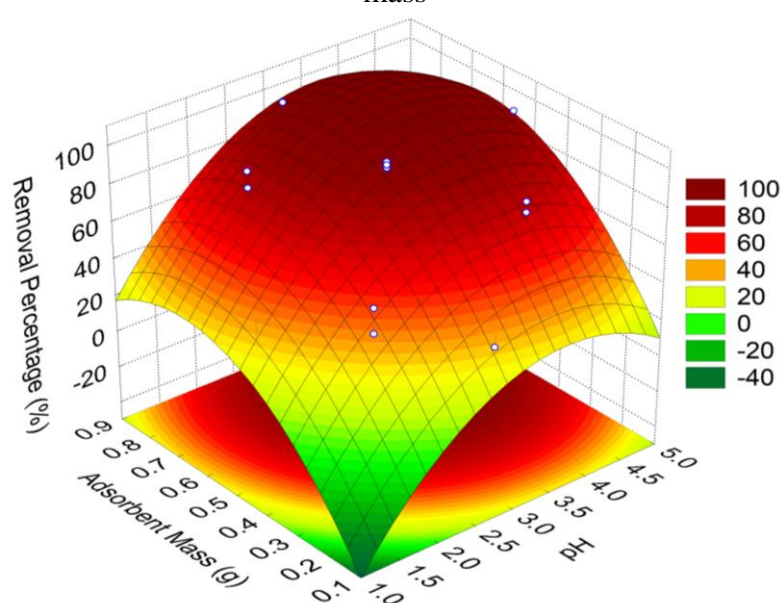
Fig 6.3 Predicted versus observed values (RSM)

Fig 6.3 indicated that the model predicted the data better for high %*R* values than for lower values (< 60%), meaning that the model is more reliable in interpreting the zone of maximum dysprosium removal. **Fig 6.4** presents the %*R* response surface as a function of pH and amount of adsorbent (g) (significant factors), where a region of maximum removal percentage can be observed. The highest values of %*R* were found at pH around 3.5 and with an amount of adsorbent between 0.5 to 0.8 g. The critical values obtained by the Statistica software were pH equal to 3.5 and adsorbent mass equal to 0.64 g.

Fig 6.4 Response surface of the percentage of Dy removal as a function of pH and adsorbent mass



The results of the validation test under optimal conditions were $q = 0.23$ mmol/g and %*R* = 99.2 ± 0.10 %. The %*R* experimentally obtained by validation test was higher than the %*R* shown in **Table 6.1**, which means that optimization (maximization of %*R*) was achieved. The model predicted a removal percentage of 106.5%, with an *MSE* of 53.8. Thus, the model is not precise enough to predict the Dy removal percentage indicating the limitation of RSM modeling.

In **Table 6.3**, there is a comparison between the present study and other works on dysprosium adsorption. The data in **Table 6.3** were obtained from studies on the effect of adsorbent mass and pH. The mass of the adsorbent was recalculated to a volume of 50.0 mL (solution volume of this study).

Table 6.3 shows that the Dy³⁺ removal percentage on the expanded vermiculite was 99.2 %, similar to other results, and the adsorption capacity achieved was higher than most.

However, the initial Dy concentration from this study is much higher than other C_i . Consequently, due to the presence of more Dy ions in the solution, the highest mass of adsorbent was used in this study. Comparing expanded vermiculite (present study) with the functionalized silica that used the lowest initial concentration, the expanded vermiculite attained the same removal percentage for a solution 4,838.7 times more concentrated using just 2.56 times more adsorbent mass.

Table 6.3 Comparison between different optimal conditions for Dy³⁺ adsorption

Adsorbent	C_i (mmol/L)	pH	Adsorbent mass (g)	%R	q (mmol/g)	Reference
Ion-imprinted mesoporous silica	0.3	2.0	0.05	*34	0.10	(Zheng et al., 2016)
Chemically activated carbon	0.03	4.0	0.075	94	*0.19	(Alcaraz et al., 2019)
Phycally activated carbon	0.03	4.0	0.075	100	*0.21	(Kegl et al., 2019)
γ -Fe ₂ O ₃ -NH ₄ OH@SiO ₂ nanoparticles	0.002	7.0	0.15	90	*6.0x10 ⁻⁴	(Berijani et al., 2012)
Functionalized silica	6.2x10 ⁻⁴	5.0	0.25	100	*2.0x10 ⁻⁵	(Abdel-Magied et al., 2019a)
Hierarchical zeolitic imidazolate frameworks nanoparticles	0.074	7.0	0.012	*95.8	0.28	(Abdel-Magied et al., 2019a)
Expanded Vermiculite	3.0	3.5	0.64	99.2	0.27	Present Work

* Calculated from reported data (values not shown in the original article).

Comparing optimal pH conditions, studies were conducted over a wide range of pHs, from 2.0 to 7.0. . It is very close to the pH of the permanent magnet leachate, pH= 3.6 (Brewer et al., 2019), which means an advantage for the practical use of vermiculite for concentration and REM recovery from REM-rich secondary source. The best pH defined by the present study is intermediate. It is very close to the pH of the permanent magnet leachate, pH= 3.6 (Brewer et al., 2019), which means an advantage for the practical use of vermiculite for concentration and REM recovery from REM-rich secondary sources. At pH 7.0 (Abdel-Magied et al., 2019b; Kegl et al., 2019) the insoluble form of dysprosium is formed (Dy(OH)₃) even in small amounts (Fig 6.2 (a)). Therefore, precipitation of Dy may have been included as a result of adsorption. Dy adsorption at pH 2.0 is unusual due to high competition with H⁺ (Zheng et al., 2016). Regardless, the authors considered this condition optimal because, in acid media, the adsorbent adsorption capacity (IMS) towards Dy³⁺ is not only based on the chelating capacity, but also on the spatial structure for the coordination of Dy³⁺-conferred by the imprint process.

6.3.3 Machine learning

6.3.3.1 Dataset

The dataset used to train the networks and for the prediction (**Table 6.4**) is composed of 24 experimental points, in which only the significant parameters pointed out by the ANOVA/RSM (vermiculite mass and pH) were varied, and their response to the Dy removal percentage was evaluated experimentally. Very distinct removal percentages were achieved (from 10.4 to 99.4 %), corroborating the significant effect of vermiculite mass and solution pH on Dy uptake performance. **Table 6.4** also presents the values of the normalized data. This data shows characteristics of a good quality dataset, such as reliability, since they come from a rigorous experimental procedure and correct feature representation (normalization)(Shanker et al., 1996). The statistical indices of the dataset are presented in **Table S5** (SI, Appendix A.4).

Table 6.4 ANN and ANFIS dataset

Raw data			Normalized data [-1,1]		
Adsorbent Mass (g)	pH	%R (%)	Adsorbent Mass (g)	pH	%R (%)
0.164	3.0	32.10	-0.73	-0.28	-0.51
0.836	3.0	98.80	0.85	-0.28	0.99
0.500	1.32	27.60	0.06	-1.00	-0.61
0.500	4.68	98.90	0.06	0.44	0.99
0.500	3.0	95.80	0.06	-0.28	0.92
0.500	3.0	95.60	0.06	-0.28	0.91
0.500	3.0	95.80	0.06	-0.28	0.92
0.500	2.0	80.49	0.06	-0.71	0.57
0.500	2.5	89.64	0.06	-0.50	0.78
0.500	3.0	97.75	0.06	-0.28	0.96
0.500	3.5	98.02	0.06	-0.07	0.97
0.500	4.0	98.62	0.06	0.15	0.98
0.500	4.5	98.52	0.06	0.36	0.98
0.500	5.5	98.69	0.06	0.79	0.98
0.500	6.0	98.59	0.06	1.00	0.98
0.050	5.0	10.45	-1.00	0.57	-1.00
0.200	5.0	59.25	-0.65	0.57	0.10
0.350	5.0	90.62	-0.29	0.57	0.80
0.500	5.0	98.21	0.06	0.57	0.97
0.650	5.0	99.03	0.41	0.57	0.99
0.750	5.0	99.26	0.65	0.57	1.00
0.900	5.0	99.40	1.00	0.57	1.00

0.640	3.5	99.20	0.39	-0.07	1.00
0.500	5.0	97.10	0.06	0.57	0.95

6.3.3.2 Artificial neural network

Two neurons in the input layer, three in the hidden layer, and one in the output layer composed the best architecture of the artificial neural network (**Fig. 6.5**) to predict the removal of Dy by varying the mass of vermiculite and the pH of the solution. This configuration achieved the lowest *MSE* in the test procedure (**Fig S1**, Appendix A.4). The leaning curve (**Fig S.2**, Appendix A.4) showed that the training and validation error decreased to the point of stability, in which the *MSE* for training, validation, and test were, respectively, 2.81×10^{-4} , 8.70×10^{-2} , 6.92×10^{-5} . The optimal weights were 0.008, -0.710, and 1.302, and the biases were 1.947, -2.623, and 1.868. These low errors mean that the ANN was well-trained and validated, which led to a good fit in the test step.

Fig 6. 5 Artificial neural network architecture

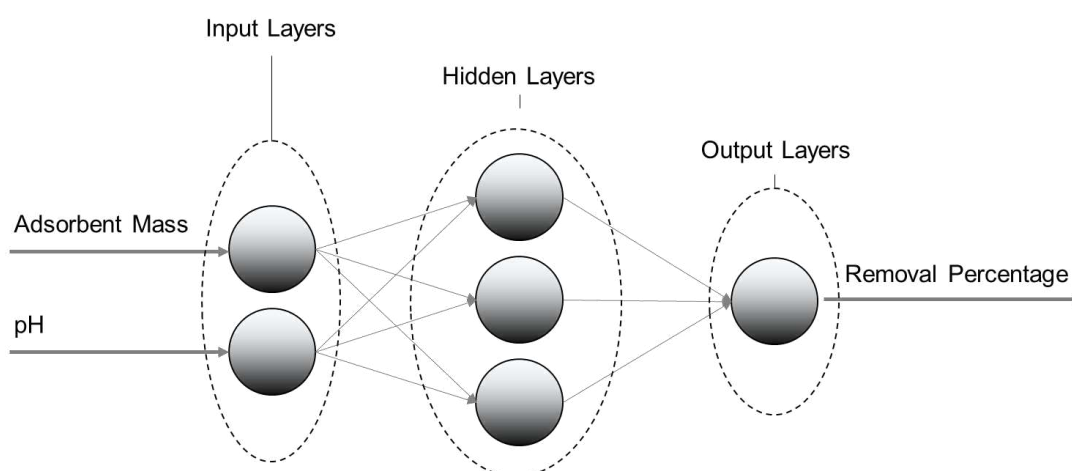


Fig 6.6 shows the fitting results of the training, validation, and check, which high *R* of the training and validation, 0.99970 and 0.99992, respectively, corroborates that the network was trained adequately. However, a lower *R*= 0.94175 was achieved in the test, which means that the regression model could not explain all the variation of the actual values from the mean value, despite the low *MSE* mentioned above (6.92×10^{-5}). Thus, the ANN was trained satisfactorily by the data and could predict well the Dy removal. However, the generalization by the regression was not very close to the ideal (*R* = 1).

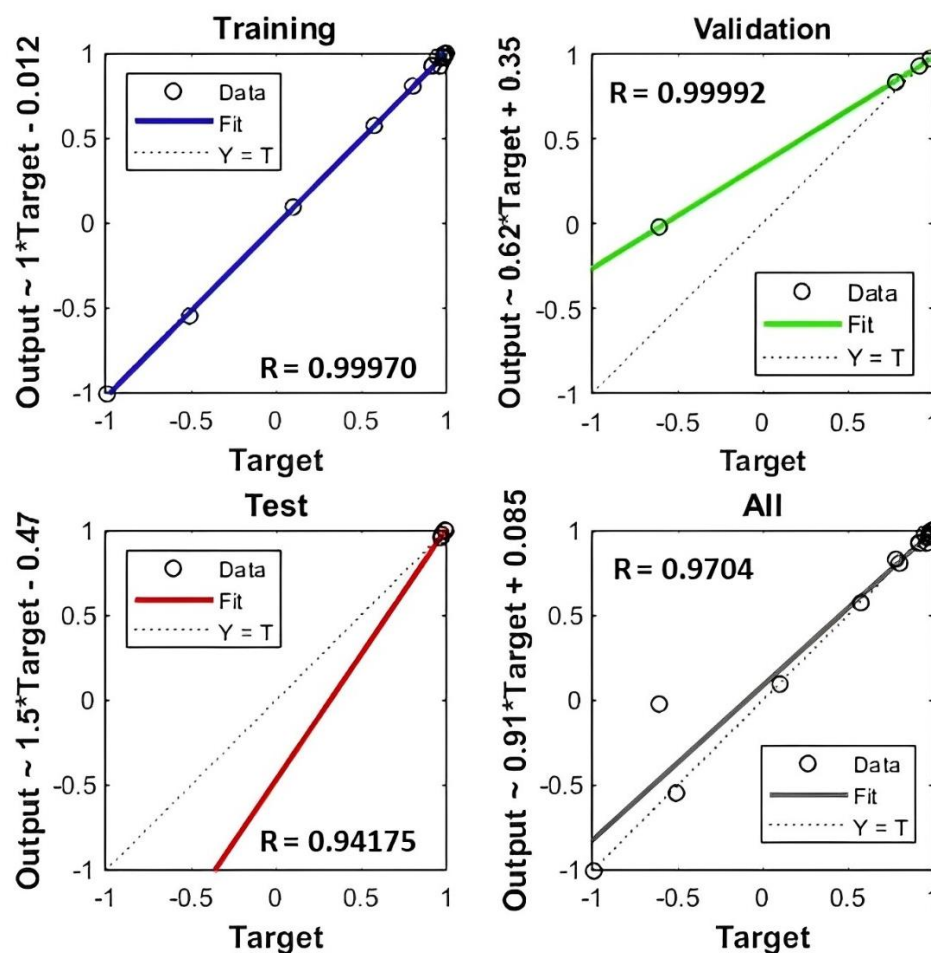
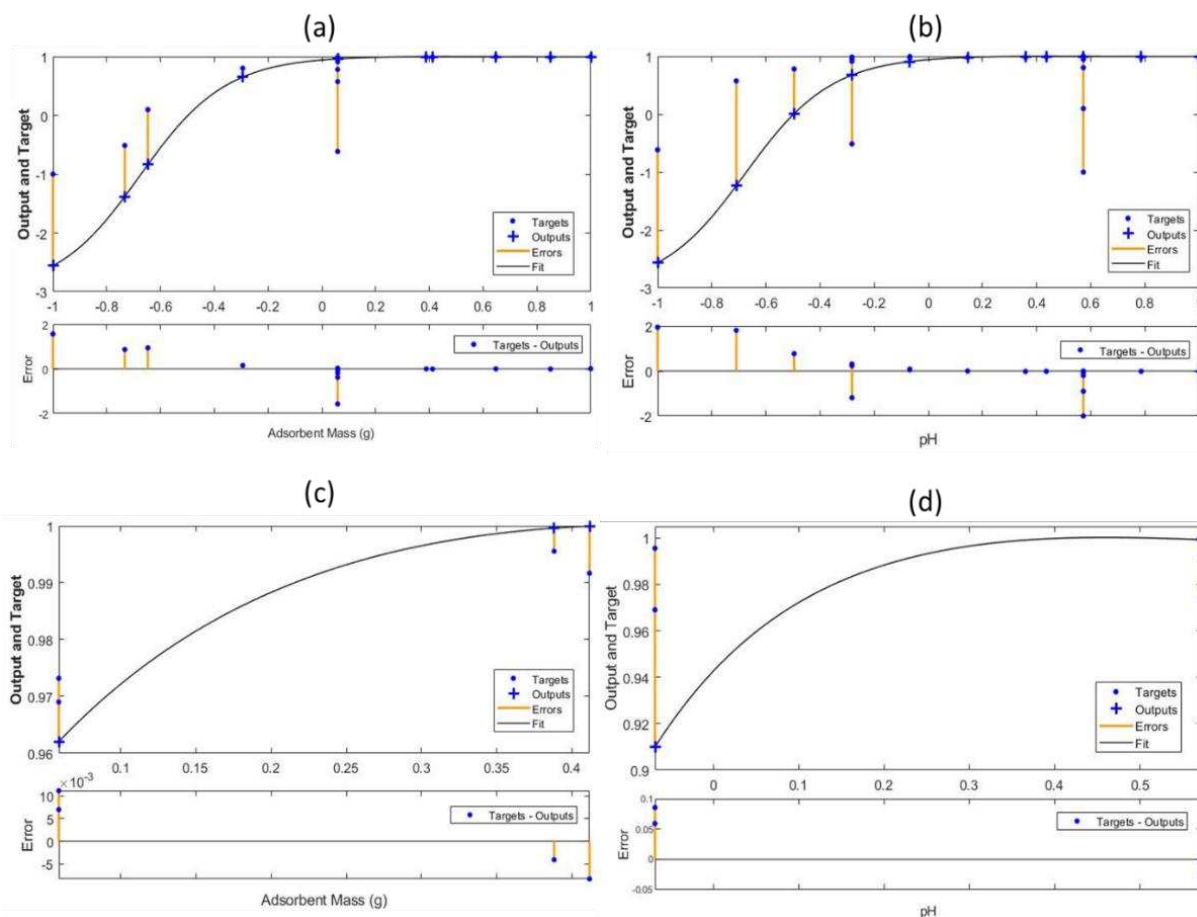
Fig 6.6 Predicted versus observed values (ANN)

Fig 6.7 represents the function fit for both normalized inputs, adsorbent mass (**Fig 6.7(a,c)**), and pH (**Fig 6.7(b,d)**) for training and testing. For the training (**Fig 6.7(a)** and **Fig 6.7(b)**), the best fit occurred, in general, in the region of the maximum removal percentage, at a higher adsorbent dosage (> 0.64 g) and pH between 3.0 and 5.0. In the test, the predicted (output) and the target values presented low errors between them (**Fig 6.7(c)** and **Fig 6.7(d)**), mainly for the highest removal percentages, which agrees with the training performance that was most effective under the best conditions. Also, the network was able to predict better the effect of vermiculite mass on Dy removal (smaller errors) than pH, corroborating the significance order indicated by the RSM.

Fig 6.7 Percentage of dysprosium removal predicted by ANN in training and test as a function of adsorbent mass (a,c) and pH (b,d)



Therefore, the ANN was precise in predicting Dy removal percentage from the data; nevertheless, modeling the dysprosium adsorption efficiency on expanded vermiculite varying the dosage of the adsorbent and the pH should still be improved.

6.3.3.3 Adaptive neuro-fuzzy inference system

Different numbers of input membership functions (Gaussian type) were investigated, and the simplest configuration, 2 MF for input 1 (adsorbent mass) and 2MF for input 2 (pH), was the most predictive, i.e., achieved the lowest *MSE* in the check step (**Fig S3**, Appendix A.4). The learning curve of this ANFIS design (**Fig S4**, Appendix A.4) shows that the training and check errors were reduced until the stabilization. **Fig 6.8** represents the best ANFIS architecture

for the percentage of dysprosium removal on expanded vermiculite in terms of adsorbent amount and medium pH, with 2 Gaussian MF for each input, creating four rules, with eight nonlinear and 12 linear parameters. The statistical parameters for the ANFIS fit are R^2 of 0.99936 and 0.99681, and MSE of 2.71×10^{-4} and 2.61×10^{-4} for training and checking, respectively, which indicates the excellent fit to the experimental data.

Fig 6.8 Illustration of the final ANFIS architecture simplification

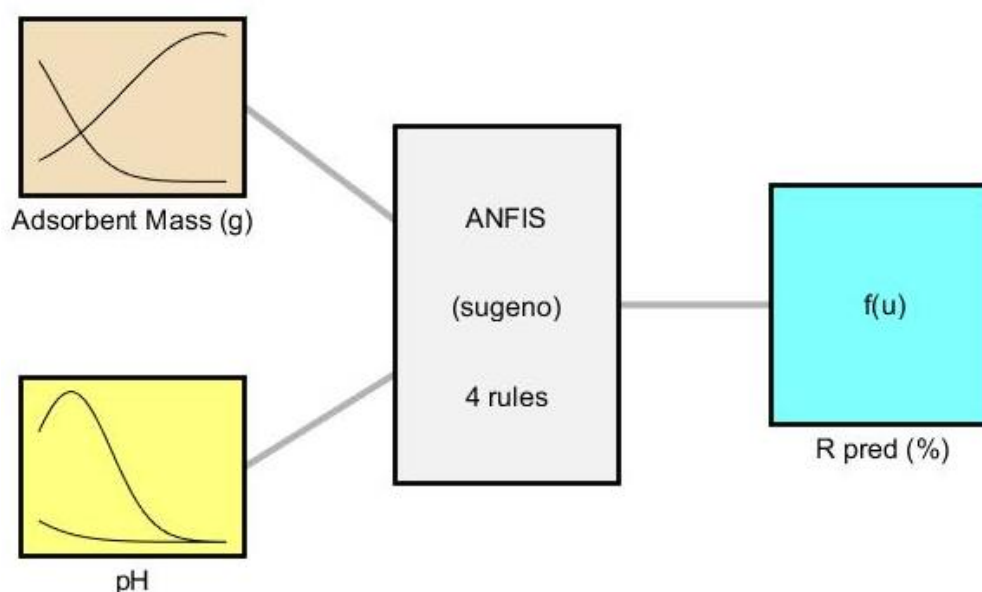
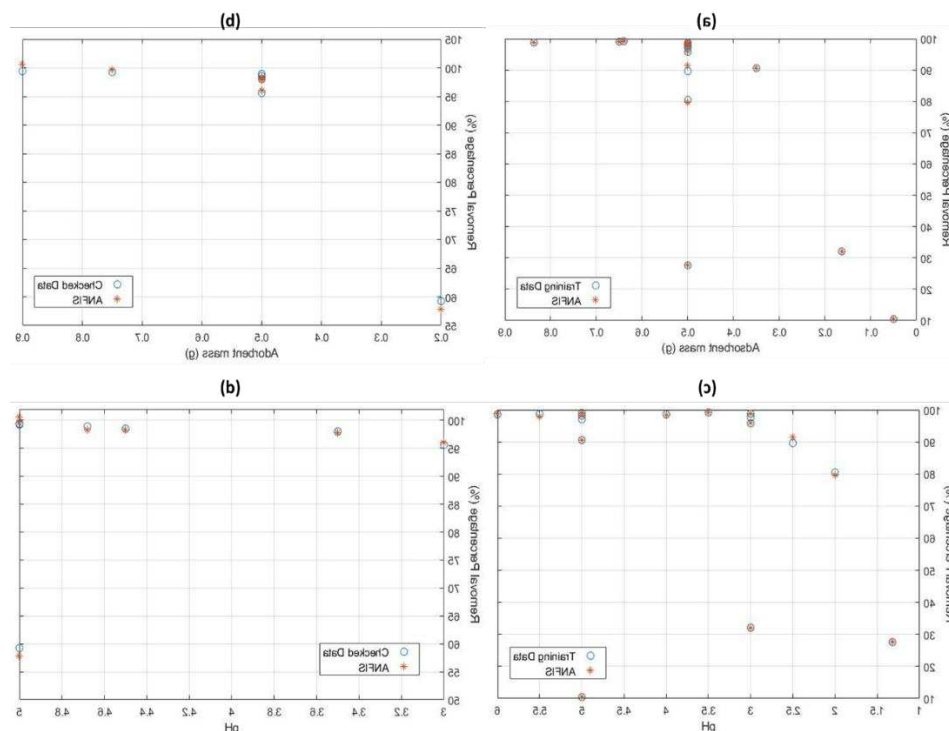


Fig 6.9 Percentage of dysprosium removal predicted by ANFIS in training and check as a function of adsorbent mass (a,c) and pH (b,d)



The predicted versus observed values (**Fig 6.9**) for the training (**Fig 6.9 (a, c)**) and check (**Fig 6.9 (b, d)**) steps for both inputs showed that the network was very well trained, i.e., the ANFIS could learn with the input data leading to minor errors. Also, in the check, the network predicted precisely the Dy removal percentage in practically all the range of adsorbent mass and pH studied, which is very advantageous for practical applications where pH can change abruptly in a plant for the Dy recovery from secondary sources such as acid mine drainage water, leachate of NdFeB magnets, red mug, among others.

6.3.4 Overall discussion

The RSM is a powerful tool to identify the relevant independent variables for specific responses, where critical information can be obtained due to its statistical formalism, such as the effect of the input variables on the response variable. In this paper, the RSM showed that the vermiculite particle size was insignificant for the removal of Dy from aqueous solutions and pointed out the great relevance of the adsorbent mass and pH. Also, the best Dy removal occurred at pH 3.5 and an adsorbent mass of 0.64 g. However, modeling the adsorption efficiency of Dy as a function of these parameters was not very accurate, as ANN and ANFIS, which is in agreement with other adsorption studies (Onu et al., 2021; Saber et al., 2021; Shojaeimehr et al., 2014). This result may be related to the limitation of the RSM modeling,

which assumes beforehand a quadratic model (second-order), unlike the machine learning approaches (ANN and ANFIS), which are based on the biological information processing system that allows a better fit to the data due to the nonlinearity and noise insensitivity (Basheer and Hajmeer, 2000; Franco et al., 2020).

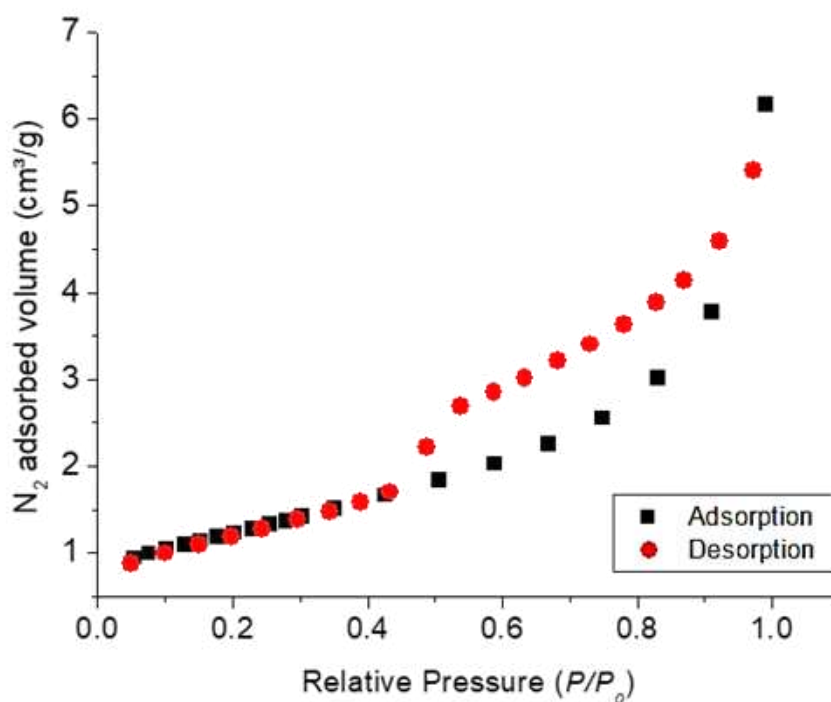
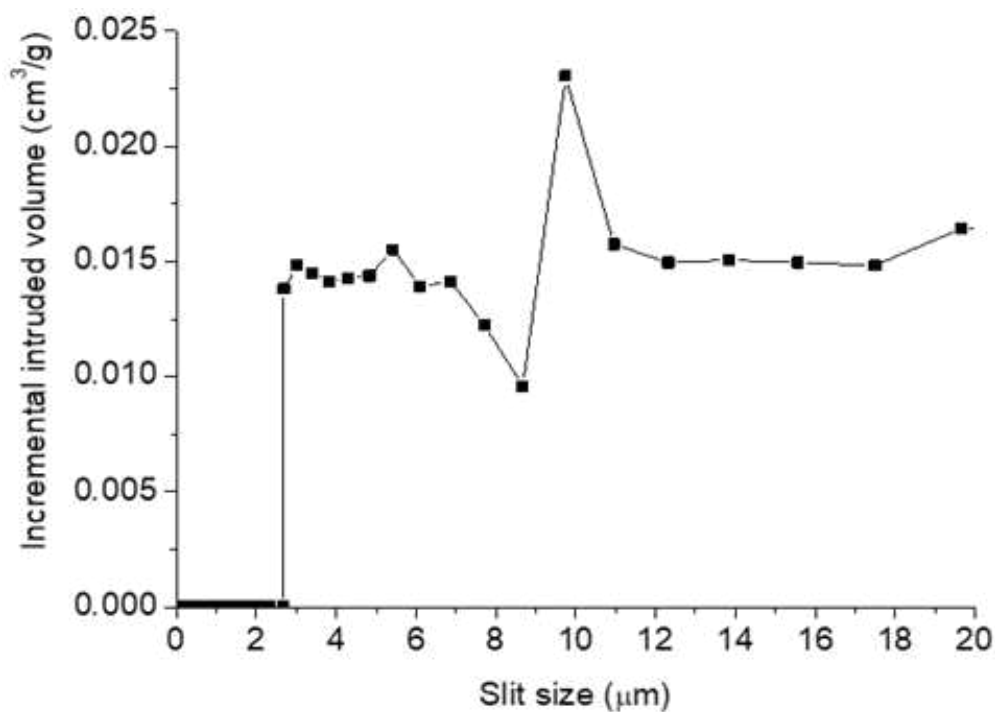
When comparing the predictability of ANN and ANFIS, repeatedly in the literature, ANFIS has a better response than ANN for optimizing and predicting adsorptive processes (Onu et al., 2021; Souza et al., 2018; Wong et al., 2020). As ANFIS combines a neural network learning proficiency and fuzzy logic reasoning abilities, it groups advantages from both methodologies (Dolatabadi et al., 2020); thus, ANFIS could better predict and model the percentage of dysprosium removal in this study.

Therefore, this study showed that ANFIS with 2 Gaussian MFs for each input could model the efficiency of dysprosium adsorption as a function of adsorbent properties (size and mass) and pH. Also, since the ANFIS can be retrained at any time with new data, this modeling strategy is relevant for scale-up processes.

6.3.5 Adsorbent characterization

Adsorption is an interfacial phenomenon; consequently, the adsorbent textural properties have an essential role in the adsorption potential. It determines the area, type, form, and size of pores available for the adsorbate. **Fig 6.10**, the isotherm of physical sorption of nitrogen on dysprosium-loaded vermiculite (V-Dy), has the characteristic hysteresis shape of phyllosilicates. According to (Thommes et al. 2015), in a report of the International Union of Pure and Applied Chemistry (IUPAC), the sorption isotherm shape is a particular case of type IV, in which the adsorption branch is type II and the desorption has a hysteresis loop H3. The N₂ adsorption with no plateau at high P/P_0 indicates the presence of macropores [46]. The H3 loop is caused by non-rigid aggregates of plate-like particles as certain clay materials, including vermiculite [47,48].

The porous distribution according to the mercury intruded volume (**Fig 6.12**) was obtained considering the pores as opened slits, typical of clay minerals as vermiculite [49]. **Fig 6.12** demonstrates V-Dy has a median intruded volume of 0.015 cm³/g along with the range of 2.5 to 20 µm, with a more pronounced peak at 10 µm. Thus, after the adsorption of dysprosium, the material presented a diversified macropores distribution. The volume of macropores of V-Dy is 0.74 cm³/g, lower than the material before the adsorption (0.96 cm³/g) [50].

Fig 6.10 Isotherm of N₂ adsorption and desorption of V-Dy**Fig 6.11** Macropores size distribution of V-Dy

Textural properties of the loaded adsorbent and the virgin expanded vermiculite are summarized in **Table 6.4**. The properties evaluated are the BET surface area (S_{BET}), real (ρ) and bulk (ρ_{bulk}) densities, and particle porosity (ε_p).

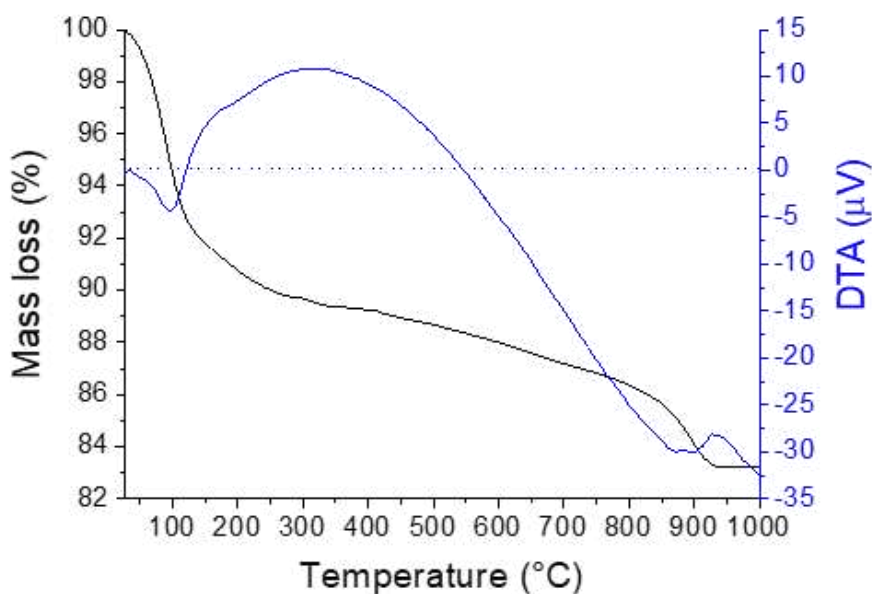
Table 6.4 Comparison of the textural properties of V-Dy and the original adsorbent

Samples	S_{BET} (m ² /g)	ρ (g/cm ³)	ρ_{bulk} (g/cm ³)	ε_p	Reference
Expanded Vermiculite	9.877	2.167	0.264	0.88	(Brião et al. 2020, 2021a)
V-Dy	4.382	2.612	0.741	0.72	This work

The S_{BET} of the V-Dy was reduced to 4.382 m²/g compared to the adsorbent before the dysprosium adsorption, which means a loss of 44.36% of surface area. V-Dy's real and bulk densities were 2.612 and 0.741 g/cm³, both higher than the original. The increase of the material density diminishes the void spaces and leads to a lower particle porosity of 0.72. This reduction of surface area, porosity, and density increment is related to the rehydration effect on the expanded vermiculite structure [51] and the effective dysprosium adsorption on the vermiculite surface. The expanded vermiculite was formed by thermal treatment at 900°C that vaporized the interlayer water and enlarged the lamellar spaces of the material, increasing the surface area. Therefore, when the material was put in an aqueous solution, the rehydration compacts the "accordion" shape slightly. In addition, the reduction of the surface area is associated with the effective adsorption of dysprosium that occupies the active sites of V-Dy samples, reducing the available surface of the material and consequently blocking the N₂ physisorption.

Fig 6.12 is the thermal analysis of the vermiculite after the dysprosium adsorption, in which the dehydration process is the most significant mass loss mechanism of the material. From the TGA until proximately 250 °C, the free water, and the water coordinate to the interlayer cations were vaporized [52], reducing the sample to 90% of the original weight. In the intermediary temperature from 450 to 850 °C occurred the structural dehydroxylation process, a slow release of OH groups bound in the vermiculite [53]. For 850 < T < 1000°C, new phases of Mg-Al silicates are formed [54]. The DTA indicates an endothermic effect at 98°C related to the loss of the adsorbed water; around 200 °C, there is a slight inflection in the curve regarding the dehydration of the bounded water. The exothermic peak around 950 °C indicates the crystallization of new phases [53].

Fig 6.12 Thermogravimetric analysis (TGA) and differential thermal analysis (DTA) of V-Dy



The V-Dy dehydration was continuous while, for the original adsorbent [50], the dehydration occurred in two well distinct steps. That is related to the hydration phenomena of the interlayer's cations. The expanded vermiculite originally had magnesium as the exchangeable cation, with a coordination number (CN) of 6 [55]. During the sorption process, Dy (III), which has a coordination number of 8 or 9 [56], replaces Mg (II) in an ion-exchange reaction. Dysprosium in the first and second hydration shells affects around 17 water molecules/Dy³⁺, and Magnesium 10.3 water molecules/Mg²⁺[57]. Thus, the two layers of water surrounding the interlayer cations are stronger attracted by Dy than by Mg, which contributed to the imperceptible transition between the first stage of dehydration ("free" water) and the second stage (coordinate water). Also, the V-Dy had even a lower total mass loss (16.8 %) than expanded vermiculite (18.2 %), indicating that the dysprosium adsorption improved the material's thermal stability.

Therefore, the textural characterization analyses of the V-Dy indicated that the adsorbent reduced the surface area and the macropores volume and increased the bulk and real densities due to the recompactation (rehydration), and to the effective adsorption of dysprosium on vermiculite surface. The thermal analyses indicated that the interlayer ion-exchange mechanism plays a significant role in the dysprosium uptake on the expanded vermiculite, which influenced even the material's thermal stability.

6.4 CONCLUSIONS

Operational parameters are very often neglected in typical adsorption process modeling. This work applied statistical (ANOVA/RSM) and artificial intelligence (ANN and ANFIS) approaches to predict the percentage of dysprosium removal from aqueous solution using expanded vermiculite in the function of particle size, adsorbent mass, and pH. Moreover, the sorption process was evaluated through the characterization of Dy-loaded-solid.

The RSM pointed out that the adsorbent mass and pH are statistically significant to the Dy adsorption efficiency. The optimal values of %*R* are obtained in pH 3.5 and with 0.64 g of adsorbent. The final RSM model, excluding particle size effect (insignificant), fitted the data with an R^2 of 0.9217, and a high validation error (~ 7%) shows that the model is not precise enough in the Dy removal prediction in the function of pH and adsorbent amount. ANN with three hidden neurons trained using the Levenberg-Marquardt backpropagation algorithm fitted the data with an *R* of 0.94175, predicting the efficiency of dysprosium adsorption more accurately than RSM. Nonetheless, ANFIS, composed of 2 Gaussian MFs for each input, showed a higher correlation coefficient in training (0.99936) and checking (0.99681), demonstrating a superior capacity for learning and generalization than ANN.

Regarding the Dy-loaded vermiculite characterization, the loaded adsorbent material has the typical layered structure of phyllosilicates, with non-uniform pore distribution. Also, the adsorbent reduced the BET surface area (4.382 m²/g) and porosity (0.72) and increased the bulk (0.741 g/cm³) and real (2.612 g/cm³) densities compared to the pristine. Thus, textural properties of the material, such as surface area, changed throughout the process; however, the thermogravimetric analysis pointed to the high thermal stability of vermiculite even after dysprosium adsorption.

Therefore, vermiculite is a stable phyllosilicate material that can uptake dysprosium efficiently from aqueous solutions. The adsorbent mass and pH effects are modeled accurately by ANFIS, which can help improve process control and cost-effectiveness in further applications.

ACKNOWLEDGMENTS

This work was supported by the Fundação de Amparo à Pesquisa do Estado de São Paulo (FAPESP) (Proc. 2017/18236-1), Coordenação de Aperfeiçoamento de Pessoal de Nível Superior (CAPES), Conselho Nacional de Desenvolvimento Científico e Tecnológico (CNPq) (Proc. 308046/2019-6). The adsorbent material was donated by Brasil Minérios S/A.

REFERENCES

- Abdel-Magied, A.F., Abdelhamid, H.N., Ashour, R.M., Zou, X., Forsberg, K., 2019a. Hierarchical porous zeolitic imidazolate frameworks nanoparticles for efficient adsorption of rare-earth elements. *Microporous and Mesoporous Materials* 278, 175–184. <https://doi.org/10.1016/j.micromeso.2018.11.022>
- Abdel-Magied, A.F., Abdelhamid, H.N., Ashour, R.M., Zou, X., Forsberg, K., 2019b. Hierarchical porous zeolitic imidazolate frameworks nanoparticles for efficient adsorption of rare-earth elements. *Microporous and Mesoporous Materials* 278. <https://doi.org/10.1016/j.micromeso.2018.11.022>
- Aditya Mishra, 2020. Metrics to Evaluate your Machine Learning Algorithm [WWW Document]. Towards Data Science. URL <https://towardsdatascience.com/metrics-to-evaluate-your-machine-learning-algorithm-f10ba6e38234> (accessed 11.6.22).
- Alcaraz, L., Escudero, M.E., Alguacil, F.J., Llorente, I., Urbieto, A., Fernández, P., López, F.A., 2019. Dysprosium Removal from Water Using Active Carbons Obtained from Spent Coffee Ground. *Nanomaterials* 9, 1372. <https://doi.org/10.3390/nano9101372>
- Ali, A.H., Dakroury, G.A., Hagag, M.S., Abdo, Sh.M., Allan, K.F., 2021. Sorption of Some Rare Earth Elements from Acidic Solution onto Poly(acrylic acid-co-acrylamide/16, 16-dimethylheptadecan-1-amine) Composite. *J Polym Environ.* <https://doi.org/10.1007/s10924-021-02271-7>
- Ambaye, T.G., Vaccari, M., Castro, F.D., Prasad, S., Rtimi, S., 2020. Emerging technologies for the recovery of rare earth elements (REEs) from the end-of-life electronic wastes: a review on progress, challenges, and perspectives. *Environmental Science and Pollution Research* 27. <https://doi.org/10.1007/s11356-020-09630-2>
- Anovitz, L.M., Cole, D.R., 2015. Characterization and analysis of porosity and pore structures. *Rev Mineral Geochem* 80, 61–164. <https://doi.org/10.2138/rmg.2015.80.04>
- Basheer, I.A., Hajmeer, M., 2000. Artificial neural networks: fundamentals, computing, design, and application. *J Microbiol Methods* 43, 3–31. [https://doi.org/10.1016/S0167-7012\(00\)00201-3](https://doi.org/10.1016/S0167-7012(00)00201-3)
- Berijani, S., Ganjali, M.R., Sereshti, H., Norouzi, P., 2012. A selective modified nanoporous silica as sorbent for separation and preconcentration of dysprosium in water samples prior to ICP-OES determination. *Int J Environ Anal Chem* 92, 355–365. <https://doi.org/10.1080/03067319.2010.551120>

- Bobrowski, A., Kaczmarska, K., Sitarz, M., Drożyński, D., Leśniak, M., Grabowska, B., Nowak, D., 2021. Dehydroxylation of perlite and vermiculite: Impact on improving the knock-out properties of moulding and core sand with an inorganic binder. *Materials* 14. <https://doi.org/10.3390/ma14112946>
- Bock, C.W., Kaufman, A., Glusker, J.P., 1994. Coordination of water to magnesium cations. *Inorg Chem* 33, 419–427. <https://doi.org/10.1021/ic00081a007>
- Boruah, A., Rasheed, A., Mendhe, V.A., Ganapathi, S., 2019. Specific surface area and pore size distribution in gas shales of Raniganj Basin, India. *J Pet Explor Prod Technol* 9, 1041–1050. <https://doi.org/10.1007/s13202-018-0583-8>
- Bose, B.K., 2021. Neural network and applications, in: *Power Electronics and Motor Drives*. Elsevier, pp. 875–1014. <https://doi.org/10.1016/b978-0-12-821360-5.00012-9>
- Box, G.E.P., Wilson, K.B., 1951. On the Experimental Attainment of Optimum Conditions. *Journal of the Royal Statistical Society: Series B (Methodological)* 13, 1–38. <https://doi.org/10.1111/j.2517-6161.1951.tb00067.x>
- Brewer, A., Dohnalkova, A., Shutthanandan, V., Kovarik, L., Chang, E., Sawvel, A.M., Mason, H.E., Reed, D., Ye, C., Hynes, W.F., Lammers, L.N., Park, D.M., Jiao, Y., 2019. Microbe Encapsulation for Selective Rare-Earth Recovery from Electronic Waste Leachates. *Environ Sci Technol* 53, 13888–13897. <https://doi.org/10.1021/acs.est.9b04608>
- Brião, G. de V., Silva, M.G.C. da, Vieira, M.G.A., 2020. Neodymium recovery from aqueous solution through adsorption/desorption onto expanded vermiculite. *Appl Clay Sci* 198, 105825. <https://doi.org/10.1016/j.clay.2020.105825>
- Brunauer, S., Emmett, P.H., Teller, E., 1938. Adsorption of Gases in Multimolecular Layers. *J Am Chem Soc* 60, 309–319. <https://doi.org/10.1021/ja01269a023>
- Constantinides, S., 2012. The Important Role of Dysprosium in Modern Permanent Magnets [WWW Document]. Arnold Magnetic Technologies Corporation. URL <https://www.arnoldmagnetics.com/wp-content/uploads/2017/10/Important-Role-of-Dysprosium-in-Modern-Permanent-Magnets-150906.pdf>
- Costa, T.B. da, Silva, M.G.C. da, Vieira, M.G.A., 2020. Recovery of rare-earth metals from aqueous solutions by bio/adsorption using non-conventional materials: a review with recent studies and promising approaches in column applications. *Journal of Rare Earths*. <https://doi.org/10.1016/j.jre.2019.06.001>

- Costa, N.R., Lourenço, J., Pereira, Z.L., 2011. Desirability function approach: A review and performance evaluation in adverse conditions. *Chemometrics and Intelligent Laboratory Systems* 107, 234–244. <https://doi.org/10.1016/j.chemolab.2011.04.004>
- da Costa, T.B., da Silva, M.G.C., Vieira, M.G.A., 2022. Effective recovery of ytterbium through biosorption using crosslinked sericin-alginate beads: A complete continuous packed-bed column study. *J Hazard Mater* 421, 126742. <https://doi.org/10.1016/j.jhazmat.2021.126742>
- da Costa, T.B., da Silva, M.G.C., Vieira, M.G.A., 2021a. Recovery of dysprosium by biosorption onto a biocomposite from sericin and alginate. *Journal of Water Process Engineering* 44. <https://doi.org/10.1016/j.jwpe.2021.102388>
- da Costa, T.B., da Silva, M.G.C., Vieira, M.G.A., 2021b. Biosorption of lanthanum using sericin/alginate/polyvinyl alcohol beads as a natural cation exchanger in a continuous fixed-bed column system. *Colloids Surf A Physicochem Eng Asp* 627, 127233. <https://doi.org/10.1016/j.colsurfa.2021.127233>
- de Barros Neto, B., Scarminio, I.S., Bruns, R.E., 2010. *Como fazer experimentos*, 4th ed. Bookman, Porto Alegre.
- Dolatabadi, M., Mehrabpour, M., Esfandyari, M., Ahmadzadeh, S., 2020. Adsorption of tetracycline antibiotic onto modified zeolite: Experimental investigation and modeling. *MethodsX* 7. <https://doi.org/10.1016/j.mex.2020.100885>
- Dolatabadi, M., Mehrabpour, M., Esfandyari, M., Alidadi, H., Davoudi, M., 2018. Modeling of simultaneous adsorption of dye and metal ion by sawdust from aqueous solution using of ANN and ANFIS. *Chemometrics and Intelligent Laboratory Systems* 181, 72–78. <https://doi.org/10.1016/j.chemolab.2018.07.012>
- Dotto, G.L., McKay, G., 2020. Current scenario and challenges in adsorption for water treatment. *J Environ Chem Eng* 8. <https://doi.org/10.1016/j.jece.2020.103988>
- Duman, O., Tunç, S., 2008. Electrokinetic properties of vermiculite and expanded vermiculite: Effects of pH, clay concentration and mono- and multivalent electrolytes. *Sep Sci Technol* 43, 3755–3776. <https://doi.org/10.1080/01496390802219109>
- Elshkaki, A., Graedel, T.E., 2014. Dysprosium, the balance problem, and wind power technology. *Appl Energy* 136, 548–559. <https://doi.org/10.1016/j.apenergy.2014.09.064>
- Fan, M., Hu, J., Cao, R., Xiong, K., Wei, X., 2017. Modeling and prediction of copper removal from aqueous solutions by nZVI/rGO magnetic nanocomposites using ANN-GA and ANN-PSO. *Sci Rep* 7, 1–14. <https://doi.org/10.1038/s41598-017-18223-y>

- Feng, J., Liu, M., Fu, L., Zhang, K., Xie, Z., Shi, D., Ma, X., 2020. Enhancement and mechanism of vermiculite thermal expansion modified by sodium ions. *RSC Adv* 10, 7635–7642. <https://doi.org/10.1039/d0ra00223b>
- Franco, D.S.P., Duarte, F.A., Salau, N.P.G., Dotto, G.L., 2020. Analysis of indium (III) adsorption from leachates of LCD screens using artificial neural networks (ANN) and adaptive neuro-fuzzy inference systems (ANIFS). *J Hazard Mater* 384, 121137. <https://doi.org/10.1016/j.jhazmat.2019.121137>
- Gergoric, M., Barrier, A., Retegan, T., 2019. Recovery of Rare-Earth Elements from Neodymium Magnet Waste Using Glycolic, Maleic, and Ascorbic Acids Followed by Solvent Extraction. *Journal of Sustainable Metallurgy* 5, 85–96. <https://doi.org/10.1007/s40831-018-0200-6>
- Ghaedi, A.M., Vafaei, A., 2017. Applications of artificial neural networks for adsorption removal of dyes from aqueous solution: A review. *Adv Colloid Interface Sci.* <https://doi.org/10.1016/j.cis.2017.04.015>
- Gokhale, N.A., Trivedi, N.S., Mandavgane, S.A., Kulkarni, B.D., 2020. Biomass ashes as potent adsorbent for pesticide: prediction of adsorption capacity by artificial neural network. *International Journal of Environmental Science and Technology* 17, 3209–3216. <https://doi.org/10.1007/s13762-020-02645-9>
- Hagag, M.S., Morsy, A.M.A., Ali, A.H., El-Shiekh, A.S., 2019. Adsorption of Rare Earth Elements onto the Phosphogypsum a Waste Byproduct. *Water Air Soil Pollut* 230. <https://doi.org/10.1007/s11270-019-4362-z>
- Hameed, I.A., 2011. Using Gaussian membership functions for improving the reliability and robustness of students' evaluation systems. *Expert Syst Appl* 38, 7135–7142. <https://doi.org/10.1016/j.eswa.2010.12.048>
- Hiregoudar, S., 2020. Ways to evaluate regression models [WWW Document]. Towards Data Science. URL <https://towardsdatascience.com/ways-to-evaluate-regression-models-77a3ff45ba70> (accessed 11.6.22).
- Iftekhar, S., Ramasamy, D.L., Srivastava, V., Asif, M.B., Sillanpää, M., 2018. Understanding the factors affecting the adsorption of Lanthanum using different adsorbents: A critical review. *Chemosphere*. <https://doi.org/10.1016/j.chemosphere.2018.04.053>
- Igwegbe, C.A., Mohmmadi, L., Ahmadi, S., Rahdar, A., Khadkhodaiy, D., Dehghani, R., Rahdar, S., 2019. Modeling of adsorption of Methylene Blue dye on Ho-CaWO₄ nanoparticles using Response Surface Methodology (RSM) and Artificial Neural Network (ANN) techniques. *MethodsX* 6, 1779–1797. <https://doi.org/10.1016/j.mex.2019.07.016>

- Izadkhah, H., 2022. Basic structure of neural networks, in: *Deep Learning in Bioinformatics*. Elsevier, pp. 67–93. <https://doi.org/10.1016/b978-0-12-823822-6.00011-1>
- Jang, J.-S.R., 1993. ANFIS: adaptive-network-based fuzzy inference system. *IEEE Trans Syst Man Cybern* 23. <https://doi.org/10.1109/21.256541>
- Kawano, M., Tomita, K., 1991. Dehydration and rehydration of saponite and vermiculite. *Clays Clay Miner* 39, 174–183. <https://doi.org/10.1346/CCMN.1991.0390209>
- Kegl, T., Ban, I., Lobnik, A., Košak, A., 2019. Synthesis and characterization of novel γ -Fe₂O₃-NH₄OH@SiO₂(APTMS) nanoparticles for dysprosium adsorption. *J Hazard Mater* 378, 120764. <https://doi.org/10.1016/j.jhazmat.2019.120764>
- Kofod, N., Arppe-Tabbara, R., Sørensen, T.J., 2019. Electronic Energy Levels of Dysprosium(III) ions in Solution. Assigning the Emitting State and the Intraconfigurational 4f–4f Transitions in the Vis–NIR Region and Photophysical Characterization of Dy(III) in Water, Methanol, and Dimethyl Sulfoxide. *J Phys Chem A* 123, 2734–2744. <https://doi.org/10.1021/acs.jpca.8b12034>
- Kurtgoz, Y., Deniz, E., 2018. Comparison of ANN, Regression Analysis, and ANFIS Models in Estimation of Global Solar Radiation for Different Climatological Locations, in: *Exergetic, Energetic and Environmental Dimensions*. Elsevier Inc., pp. 133–148. <https://doi.org/10.1016/B978-0-12-813734-5.00008-1>
- Levenberg, K., 1944. A Method for the Solution of Certain Nonlinear Problems in Least Squares. *Q Appl Math* 2, 164–168.
- Li, T.-T., Liu, P., Wang, H., Dai, W., Wang, J., Wang, Z., Shiu, B.-C., Lou, C.-W., Lin, J.-H., 2021. Preparation and characteristics of flexible polyurethane foam filled with expanded vermiculite powder and concave-convex structural panel. *Journal of Materials Research and Technology* 12, 1288–1302. <https://doi.org/10.1016/j.jmrt.2021.03.045>
- Lowell, S., Shields, J.E., Thomas, M.A., Thommes, M., 2004. *Characterization of Porous Solids and Powders: Surface Area, Pore Size and Density*, Particle Technology Series. Springer Netherlands, Dordrecht. <https://doi.org/10.1007/978-1-4020-2303-3>
- Marquardt, D.W., 1963. An Algorithm for Least-Squares Estimation of Nonlinear Parameters. *Journal of the Society for Industrial and Applied Mathematics* 11, 431–441. <https://doi.org/10.1137/0111030>
- Moraes, D.S., Rodrigues, E.M.S., Lamarão, C.N., Marques, G.T., Rente, A.F.S., 2019. New sodium activated vermiculite process. Testing on Cu²⁺ removal from tailing dam waters. *J Hazard Mater* 366, 34–38. <https://doi.org/10.1016/j.jhazmat.2018.11.086>

- Onu, C.E., Nwabanne, J.T., Ohale, P.E., Asadu, C.O., 2021. Comparative analysis of RSM, ANN and ANFIS and the mechanistic modeling in eriochrome black-T dye adsorption using modified clay. *S Afr J Chem Eng* 36, 24–42. <https://doi.org/10.1016/j.sajce.2020.12.003>
- Patra, A., Roy, S., Saha, S., Palit, D.K., Mondal, J.A., 2020. Observation of Extremely Weakly Interacting OH ($\sim 3600\text{ cm}^{-1}$) in the Vicinity of High Charge Density Metal Ions (M^{z+} ; $z = 1, 2, 3$): A Structural Heterogeneity in the Extended Hydration Shell. *The Journal of Physical Chemistry C* 124, 3028–3036. <https://doi.org/10.1021/acs.jpcc.9b09692>
- Pauletto, P.S., Dotto, G.L., Salau, N.P.G., 2020. Optimal artificial neural network design for simultaneous modeling of multicomponent adsorption. *J Mol Liq* 320. <https://doi.org/10.1016/j.molliq.2020.114418>
- Peng, X., Mo, S., Li, R., Li, J., Tian, C., Liu, W., Wang, Y., 2021. Effective removal of the rare earth element dysprosium from wastewater with polyurethane sponge-supported graphene oxide–titanium phosphate. *Environ Chem Lett* 19. <https://doi.org/10.1007/s10311-020-01073-y>
- Riaño, S., Binnemans, K., 2015. Extraction and separation of neodymium and dysprosium from used NdFeB magnets: An application of ionic liquids in solvent extraction towards the recycling of magnets. *Green Chemistry* 17, 2931–2942. <https://doi.org/10.1039/c5gc00230c>
- Saber, WEIA, El-Naggar, N.E.A., El-Hersh, M.S., El-khateeb, A.Y., Elsayed, A., Eldadamony, N.M., Ghoniem, A.A., 2021. Rotatable central composite design versus artificial neural network for modeling biosorption of Cr^{6+} by the immobilized *Pseudomonas alcaliphila* NEWG-2. *Sci Rep* 11, 1–15. <https://doi.org/10.1038/s41598-021-81348-8>
- Sadollah, A., 2018. Introductory Chapter: Which Membership Function is Appropriate in Fuzzy System?, in: *Fuzzy Logic Based in Optimization Methods and Control Systems and Its Applications*. InTech. <https://doi.org/10.5772/intechopen.79552>
- Sáez, P., Rodríguez, A., Gómez, J.M., Paramio, C., Fraile, C., Díez, E., 2021. H-Clinoptilolite as an Efficient and Low-Cost Adsorbent for Batch and Continuous Gallium Removal from Aqueous Solutions. *Journal of Sustainable Metallurgy*. <https://doi.org/10.1007/s40831-021-00437-0>
- Shafiullah, M., Abido, M.A., Al-Mohammed, A.H., 2022. Artificial intelligence techniques, in: *Power System Fault Diagnosis*. Elsevier, pp. 69–100. <https://doi.org/10.1016/b978-0-323-88429-7.00007-2>
- Shanker, M., Hu, M.Y., Hung, M.S., 1996. Effect of data standardization on neural network training. *Omega (Westport)* 24, 385–397. [https://doi.org/10.1016/0305-0483\(96\)00010-2](https://doi.org/10.1016/0305-0483(96)00010-2)

- Shen, J., Liang, C., Zhong, J., Xiao, M., Zhou, J., Liu, Jun, Liu, Juan, Ren, S., 2021. Adsorption behavior and mechanism of *Serratia marcescens* for Eu(III) in rare earth wastewater. *Environmental Science and Pollution Research*. <https://doi.org/10.1007/s11356-021-14668-x>
- Shojaeimehr, T., Rahimpour, F., Khadivi, M.A., Sadeghi, M., 2014. A modeling study by response surface methodology (RSM) and artificial neural network (ANN) on Cu²⁺ adsorption optimization using light expanded clay aggregate (LECA). *Journal of Industrial and Engineering Chemistry* 20, 870–880. <https://doi.org/10.1016/j.jiec.2013.06.017>
- Sing, K.S.W., Williams, R.T., 2004. Physisorption hysteresis loops and the characterization of nanoporous materials. *Adsorption Science and Technology* 22, 773–782. <https://doi.org/10.1260/0263617053499032>
- Sivamani, S., Prasad, B.S.N., Nithya, K., Sivarajasekar, N., Hosseini-Bandegharai, A., 2022. Back-propagation neural network: Box–Behnken design modelling for optimization of copper adsorption on orange zest biochar. *International Journal of Environmental Science and Technology* 19, 4321–4336. <https://doi.org/10.1007/s13762-021-03411-1>
- Souza, P.R., Dotto, G.L., Salau, N.P.G., 2018. Artificial neural network (ANN) and adaptive neuro-fuzzy interference system (ANFIS) modelling for nickel adsorption onto agro-wastes and commercial activated carbon. *J Environ Chem Eng* 6, 7152–7160. <https://doi.org/10.1016/j.jece.2018.11.013>
- Takagi, T., Sugeno, M., 1985. Fuzzy identification of systems and its applications to modeling and control. *IEEE Trans Syst Man Cybern SMC-15*, 116–132. <https://doi.org/10.1109/TSMC.1985.6313399>
- Talib, N.S.R., Halmi, M.I.E., Ghani, S.S.A., Zaidan, U.H., Shukor, M.Y.A., 2019. Artificial Neural Networks (ANNs) and Response Surface Methodology (RSM) Approach for Modelling the Optimization of Chromium (VI) Reduction by Newly Isolated *Acinetobacter radioresistens* Strain NS-MIE from Agricultural Soil. *Biomed Res Int* 2019. <https://doi.org/10.1155/2019/5785387>
- Thommes, M., Kaneko, K., Neimark, A. V., Olivier, J.P., Rodriguez-Reinoso, F., Rouquerol, J., Sing, K.S.W., 2015. Physisorption of gases, with special reference to the evaluation of surface area and pore size distribution (IUPAC Technical Report). *Pure and Applied Chemistry* 87, 1051–1069. <https://doi.org/10.1515/pac-2014-1117>
- Udoudo, O., Folorunso, O., Dodds, C., Kingman, S., Ure, A., 2015. Understanding the performance of a pilot vermiculite exfoliation system through process mineralogy. *Miner Eng* 82, 84–91. <https://doi.org/10.1016/j.mineng.2015.03.023>

- Valkov, M., Simha, G., 2012. Vermiculite: Structural Properties and Examples of the Use, in: Clay Minerals in Nature - Their Characterization, Modification and Application. InTech. <https://doi.org/10.5772/51237>
- Wong, Y.J., Arumugasamy, S.K., Chung, C.H., Selvarajoo, A., Sethu, V., 2020. Comparative study of artificial neural network (ANN), adaptive neuro-fuzzy inference system (ANFIS) and multiple linear regression (MLR) for modeling of Cu (II) adsorption from aqueous solution using biochar derived from rambutan (*Nephelium lappaceum*) pee. *Environ Monit Assess* 192. <https://doi.org/10.1007/s10661-020-08268-4>
- Yoon, H.-S., Kim, C.-J., Chung, K.-W., Kim, S.-D., Lee, J.-Y., Kumar, J.R., 2016. Solvent extraction, separation and recovery of dysprosium (Dy) and neodymium (Nd) from aqueous solutions: Waste recycling strategies for permanent magnet processing. *Hydrometallurgy* 165, 27–43. <https://doi.org/10.1016/j.hydromet.2016.01.028>
- Yue, L., Xie, Q., Yang, Y., Li, J., Li, X., 2021. Preparation of SBA-15 surface lanthanum ion-imprinted polymer and its adsorption properties. *Polymer Bulletin* 78. <https://doi.org/10.1007/s00289-020-03395-x>
- Zhang, L., Xu, Z., 2016. A review of current progress of recycling technologies for metals from waste electrical and electronic equipment. *J Clean Prod* 127, 19–36. <https://doi.org/10.1016/j.jclepro.2016.04.004>
- Zhang, Yi, Zheng, X., Bian, T., Zhang, Yuzhe, Mei, J., Li, Z., 2020. Phosphorylated-CNC/MWCNT thin films-toward efficient adsorption of rare earth La(III). *Cellulose* 27. <https://doi.org/10.1007/s10570-020-03012-0>
- Zheng, X., Liu, E., Zhang, F., Yan, Y., Pan, J., 2016. Efficient adsorption and separation of dysprosium from NdFeB magnets in an acidic system by ion-imprinted mesoporous silica sealed in a dialysis bag. *Green Chemistry* 18. <https://doi.org/10.1039/C6GC01426G>

CHAPTER 7. DYSPROSIUM ADSORPTION ON EXPANDED VERMICULITE IN BATCH MODE: KINETICS, SELECTIVITY AND DESORPTION

Dysprosium adsorption on expanded vermiculite: kinetics, selectivity, and desorption⁶

Giani de Vargas Brião, Meuris Gurgel Carlos da Silva, Melissa Gurgel Adeodato Vieira

University of Campinas, School of Chemical Engineering, Albert Einstein Avenue, 500, 13083-852 Campinas, Brazil

ABSTRACT

Dysprosium obtainment from secondary sources is a current theme in the scientific scenario due to the high demand and environmental issues related to primary production. Hydrometallurgy applied to urban mines can be a potential alternative to separate and recover critical metals as dysprosium. Thus, the present work evaluates the dysprosium adsorption, a secondary separation process in the hydrometallurgical routes, onto expanded vermiculite through kinetic, selectivity, and desorption aspects. The adsorption process had a kinetic governed by the external mass transfer model, in which the primary mechanism of adsorption is the ion exchange. The adsorption efficiency of vermiculite towards dysprosium from a multicomponent solution indicated that the vermiculite adsorbed preferably Dy (97.6%) followed by Pb (80.1%) > Ni (70.1%) > Cd (52.0%) > Cu (51.7%). A desorption efficiency of 89% was reached using magnesium nitrate hexahydrate as eluent (0.2 mol/L), contact time (3 h), and solid/liquid ratio (14 g/L) determined by surface response methodology from a rotational central composite design of experiments. The characterization of the loaded adsorbent indicated that vermiculite, after the adsorption of dysprosium, lost expansion, enlarged the interlayer space due to the exchange of magnesium, and maintained its alumino-phyllsilicate characteristic composition. Therefore, the adsorption of dysprosium is efficient, fast, selective, and did not promote relevant structural changes in the adsorbent structure. Moreover, the very successful dysprosium desorption favors expanding vermiculite as adsorbent in further applications.

Keywords: rare earth metal, dysprosium, adsorption, vermiculite, recovery.

⁶ Manuscript published in *Colloids and Surfaces A: Physicochemical and Engineering Aspects* (2021). DOI: 10.1016/j.colsurfa.2021.127616. Reprinted with the journal's permission (Appendix B.6).

7.1 INTRODUCTION

Dysprosium (Dy) is a heavy rare earth metal (REM) whose main application is the manufacturing of permanent magnets (Nd-Fe-B type), in which Dy improves the resistance to demagnetization and its high-temperature performance [1]. These permanent magnets compose wind turbines, electric vehicles, computer hard disks, which means that dysprosium plays an essential role in developing clean energies and in the high-tech electronic industry [2]. However, robust mitigation strategies are necessary to reduce the environmental consequences from the global production of REM for magnets in the future [3], and REM efficient recovery technologies from secondary sources are fundamental to move toward the ideal circular economy [2,4].

Hydrometallurgy applied to urban mines, which contain a high concentration of rare earth metals, can be a potential alternative to recover these metals [5]. Among the different methods to separate, purify and preconcentrate the REMs, adsorption is one of the most promising due to its simplicity, high efficiency, and practical applicability in dilute systems [6]. Regarding the dysprosium adsorption, active carbons [7], functionalized and modified silica [8], zeolitic imidazolate frameworks [9], and ion-imprinted polymer-based adsorbents [10,11] have been recently employed. However, despite the multiple advantages, the adsorption method for rare earth recovery still needs to be improved to achieve higher selectivity, resistance to many cycles of use, more facilitated desorption and faster kinetics to be effectively mature for industrial-scale operation [4].

Vermiculite is hydrated magnesium–aluminum–iron phyllosilicate widely available [12,13]. When heated at high temperatures, this mineral steams the interlayer water, causing an expansion of the interlayer space [12,14]. After the expansion process, the vermiculite presents a higher surface area, enhancing its applicability as an adsorbent [14]. Vermiculite and vermiculite-based adsorbents have been applied to remove toxic and trace natural metals [15–18]. Recently, the expanded vermiculite was studied to recover the light rare earth metal neodymium, achieving high adsorption capacities [19,20], which indicates that the material could be efficient for dysprosium. However, although the known adsorptive properties of clay minerals as the high cation exchange capacity [21], dysprosium adsorption on expanded vermiculite or other clay minerals is still unexplored.

Thus, this work's central goal is to investigate an available and low-costly adsorbent as the expanded vermiculite for dysprosium adsorption as a viable alternative for dysprosium

recovery. Likewise, this work specifically aims to study the adsorption kinetics, investigate the ion exchange mechanism involved in the dysprosium sorption, and evaluate the material's selectivity toward dysprosium from a multicomponent solution capacity to recover the loaded metal through a desorption step. The adsorbent material also was characterized according to functional groups, morphological properties, and composition.

7.2 MATERIALS AND METHODS

7.2.1 Adsorption experiments: general aspects

For all experiments, the expanded vermiculite (Brazil Minérios S/A) was applied as adsorbent in batch mode. Dysprosium solutions were prepared from a stock solution formed by the addition of 5.0 g of dysprosium (III) pentahydrate nitrate (Aldrich, 99.9%) in 100 mL of acidified aqueous solution ($\text{pH} \cong 5.0$) with the insertion of small volumes of nitric acid (0.1 mol/L).

The samples were centrifuged at 4000 rpm for 10 min (CENCE L600 centrifuge), and the supernatant was filtrated with a syringe filter (Chromafil Xtra, porous of 0.20 μm). Atomic absorption spectroscopy (Shimadzu, AA7000) determined the metal concentration in all experiments.

Equations 7.1 and 7.2 determine the adsorption efficiency parameters considered along with this work, such as adsorption capacity ($q/\text{mmol/g}$) and removal percentage ($R/\%$).

$$q = \frac{(C_0 - C)V_{sol}}{m_{ads}} \quad (7.1)$$

$$R = \frac{(C_0 - C)}{C_0} 100 \quad (7.2)$$

Where C_0 and C are the concentrations at the beginning and at a specific time (mmol/L), respectively; V_{sol} refers to the metallic solution volume (L); m_{ads} is the vermiculite weight (g).

7.2.2 Adsorption kinetics experiment

The expanded vermiculite adsorption capacity and the time were evaluated, putting in contact the adsorbent to a volume of dysprosium solution ($C_0 = 1.0, 3.0$, and 5.0 mmol/L). The

adsorbent dosage was 12.8 g/L, and the pH was maintained around 3.5. These operating conditions were determined previously [22]. The system was mixed by a constant mechanical agitation (200 rpm) promoting the efficient dispersion of the solid and mixture of the system. Samples were collected at predetermined times and filtered.

The ion exchange in clays has an essential role in their sorption mechanism. In this case, the Brazilian vermiculite has magnesium (Mg^{2+}) as the principal exchangeable cation [23]. Thus, in the kinetic essay using 1.0 mmol/L of dysprosium, the magnesium concentration was measured to investigate the ion exchange mechanism.

7.2.3 Adsorption kinetics modelling

Kinetic constants were obtained by the nonlinear fitting of models to the data, such as the pseudo-first-order (PFO) [24] and pseudo-second-order (PSO) [25], Equations 7.3 and 7.4, respectively.

$$q_t = q_e(1 - e^{-k_1 t}) \quad (7.3)$$

$$q_t = \frac{k_2 q_e^2 t}{1 + k_2 q_e t} \quad (7.4)$$

Where k_1 (1/min) and k_2 (g/(mmol.min)) are the PFO and PSO apparent rate constants, q_t and q_e are the adsorption capacities at a specific time and at the equilibrium (mmol/g), and t is the time (min).

The mass transfer mechanism was evaluated by the fitting of the Weber-Morris model [26](Equation 7.5), Boyd model [27,28] (Equations 7.6 – 7.9), and the external mass transfer (EMT) models (Equation 7.10).

$$q_t = k_p \sqrt{t} + I \quad (7.5)$$

Where, in the Weber-Morris model (Equation 5), k_p is the intraparticle diffusion rate constant (mmol/(g.min^{1/2})), and I refers to the boundary layer thickness.

$$F = \frac{q_t}{q_e} = 1 - \frac{6}{\pi^2} \sum_{n=1}^{\infty} \frac{1}{n^2} e(-n^2 B_t) \quad (7.6)$$

$$0 \leq F \leq 0.85: B_t = 2\pi - \frac{\pi^2 F}{3} - 2\pi \left(1 - \frac{\pi F}{3}\right)^{1/2} \quad (7.7)$$

$$0.85 < F \leq 1: B_t = -0.4977 - \ln(1 - F) \quad (7.8)$$

$$B = \frac{D_{ef}\pi^2}{r^2} \quad (7.9)$$

The intraparticle diffusion model (Equation 6) proposed by Boyd et al. [28] was solved by Reichenberg [27] using Fourier Transform and numeric integration, which originates the relations 7.7 and 7.8, where F is the adsorbed fraction until an instant t . If a linear equation can represent the slope of B_t versus t , passing through the origin, intraparticle diffusion is the slowest transfer process; else, film diffusion is the limiting step. The effective diffusivity ($D_{ef}/\text{m}^2/\text{min}$) determines the curve declination (B), following Equation 9 [29], in which r is the characteristic dimension of particles (m).

The EMT model (Equation 7.10) considers the external diffusion as the slowest step, and the equilibrium occurs on the solid surface, i.e., intraparticle distribution is instantaneous. The external mass transfer coefficient ($k_{ext}/\text{m}/\text{min}$) was determined by numerical solution from Maple 17. The other parameters of the EMT model are the surface area per gram ($S/\text{m}^2/\text{g}$) and the dysprosium concentration on the solid-liquid interface ($C_s/\text{mmol}/\text{L}$).

$$\frac{dC}{dt} = \frac{mS}{V} \cdot k_{ext}(C - C_s); \quad t = 0, C = C_0 \quad (7.10)$$

The statistical parameters to estimate the quality of fit of the kinetic models to the data were coefficient of determination (R^2) (Equation 7.11), corrected Akaike information criterion (AIC_c) (Equation 7.12), and average relative error (ARE) (Equation 7.13) [30–32].

$$R^2 = 1 - \frac{\sum_{i=1}^N (y_i - \hat{y}_i)^2}{\sum_{i=1}^N (y_i - \bar{y})^2} \quad (7.11)$$

$$AIC_c = N \cdot \ln \left(\sum_{i=1}^N \frac{(Y_i - \hat{Y}_i)^2}{N} \right) + 2p + \frac{2p(p+1)}{N-p-1} \quad (7.12)$$

$$ARE = \frac{1}{N} \sum_{i=1}^N \left| \frac{\hat{y}_i - y_i}{y_i} \right| \cdot 100 \quad (7.13)$$

Where N is the number of points, y_i and \hat{y}_i are the experimental and predicted values, \bar{y} is the mean of the experimental values, p is the number of the estimable parameters +1 (variance) [33].

7.2.4 Selectivity

The affinity and selectivity between dysprosium and vermiculite from a multimetal solution was evaluated to simulate an effluent or wastewater condition. The equimolar multi-component solution (5 mmol/L) consisted of the dissolution of $\text{Ni}(\text{NO}_3)_2 \cdot 6\text{H}_2\text{O}$ (Dinâmica 98%), $\text{Pb}(\text{NO}_3)_2$ (Sigma Aldrich 99.9%), $\text{Cd}(\text{NO}_3)_2 \cdot 4\text{H}_2\text{O}$ (Sigma Aldrich 99.9%), $\text{Cu}(\text{NO}_3)_2 \cdot 3\text{H}_2\text{O}$ (Dinâmica 98%), $\text{Dy}(\text{NO}_3)_3 \cdot 5\text{H}_2\text{O}$ (Aldrich, 99.9%). This solution was brought into contact with the vermiculite in the same experimental conditions of the kinetic essays over 18 hours. The experiment was made in triplicate. The removal percentage (Equation 7.2) and the selectivity coefficient ($S_{Dy/M}$) (Equation (7.14)) were the parameters evaluated.

$$S_{Dy/M} = \frac{K_{d(Dy)}}{K_{d(M)}} \quad \text{with} \quad K_d = \frac{q_e}{C_e} \quad (7.14)$$

Where K_d (L/g) is the partition coefficient between the solid and bulk phases; C_e (mmo/L) is the concentration at the equilibrium [34].

7.2.5 Desorption

Desorption is essential for an efficient concentration and recovery of rare earth metals through adsorptive processes [35]. Brião et al. [19], in the study of neodymium adsorption on expanded vermiculite, pointed out that the elution process using calcium chloride should be improved to guarantee viability. Thus, in this work, we tested nitrate of magnesium as eluent ($\text{Mg}(\text{NO}_3)_2 \cdot 6\text{H}_2\text{O}$) to be a source of Mg^{2+} cations in an aqueous solution to regenerate the exchangeable cations from the vermiculite interlayer. To define the best eluent concentration, time, and solid/liquid ratio and to maximize the desorption percentage (%D), a rotational central composite design (RCCD) followed by a response surface analysis was conducted. Temperature (25°C), agitation (200 rpm), and volume of solution (50 mL) were then fixed parameters. The loaded vermiculite used in the desorption essays was obtained by a dysprosium adsorption process using 50 mL of a Dy solution of 1 mmol/L, which was put in contact with 0.64 g of expanded vermiculite for one hour at 200 rpm.

Eluent concentration (*A*), time (*B*), and solid/liquid ratio (*C*) were varied in an experimental design of 17 runs (factorial points (2^3), axial points (6), and central points (3)). The variance analysis (ANOVA) and the surface responses were generated using Statistics 6.0 software. The non-significant terms were removed from the empiric-squared model to represent the response variable better. A desorption experiment was repeated three times under the best conditions to validate the model's prediction ability.

7.2.6 Adsorbent characterization

The raw adsorbent was prior characterized in previous works [19,20]. In this work, the solid sample collected after the adsorption process (Verm-Dy) was characterized to describe details of the adsorbent-adsorbate interaction. The performed analyzes were scanning electron microscopy (SEM) and energy-dispersive X-ray spectroscopy (EDS) (LEO 440i, LEO); Fourier-transform infrared spectroscopy (FT-IR) (Nicolet 6700, Thermo Scientific); and X-ray diffraction (Philips Analytical X-Ray, X'Pert-MPD), with the copper $K\alpha$ with $\lambda=1.54056 \text{ \AA}$, step scan size of 0.05 degree, 2.0 s/step.

7.3 RESULTS AND DISCUSSION

7.3.1 Adsorption and ion exchange kinetics

Adsorption kinetics is one of the main factors contributing to the applicability of any adsorbent [31]. Fig. 7.1(a) presents the kinetic of dysprosium adsorption on expanded vermiculite from three initial concentrations (1, 3, and 5 mmol/L). The adsorption capacity augmented quickly at the first period of contact, and then gradually, the adsorption rates reduced in the intermediary times until reaching the equilibrium. The equilibrium times and adsorption capacities increased as the initial concentration increased. The equilibrium times were 40, 150, and 180 min, and the adsorption capacities (equilibrium) were 0.085, 0.200, and 0.322 mmol/g, for the initial concentration of 1.0, 3.0, and 5.0 mmol/L, respectively. The behavior in that the adsorption capacity increased with the initial concentration occurred because the initial dysprosium concentrations offer a significant driving force to surpass the mass transfer resistance of the metal among liquid and solid phases [36]. Thus, in the concentration range studied, augmenting initial concentrations favors the adsorption efficiency. The kinetic parameters from each model adjustment are summarized in Table 7.1 and the respective curves of the models fitting to the kinetic data in Fig. 7.1.

Table 7.1. Adjustment of the reaction and mass transfer kinetic models

Model	Parameters	Dysprosium Concentration (mmol/L)		
		1.0	3.0	5.0
PFO	k_1 (1/min)	0.105	0.032	0.047
	q_e (mmol/g)	0.086	0.200	0.312
	R^2	0.9977	0.9938	0.9597
	AIC_c	-158.7	-138.0	-161.8
	$ARE(\%)$	5.52	5.45	7.18
PSO	k_2 (g/(mmol.min))	1.450	0.190	0.214
	q_e (mmol/g)	0.097	0.223	0.333
	R^2	0.9832	0.9921	0.9923
	AIC_c	-147.0	-134.0	-278.2
	$ARE(\%)$	5.60	4.27	2.42
Weber and Morris	k_p (mmol/(g.min ^{1/2}))	0.010	0.007	0.009
	I (mmol/g)	0.028	0.113	0.192
	R^2	0.9622	0.9400	0.8427
	AIC_c	-36.6	-30.2	-47.1
	$ARE(\%)$	0.99	1.61	2.95
Boyd	B	0.110	0.023	0.014
	C	-0.303	-0.149	0.148
	D_{ef} (m ² /min)	8.17 x 10 ⁻⁹	1.72 x 10 ⁻⁹	1.05 x 10 ⁻⁹
	R^2	0.9823	0.9960	0.9634
	AIC_c	-8.59	-17.9	-18.8
External Mass Transfer	$ARE(\%)$	24.7	17.9	4.83
	k_{ext} (m/min)	8.18 x 10 ⁻⁷	2.29 x 10 ⁻⁷	2.86 x 10 ⁻⁷
	R^2	0.9967	0.9975	0.9807
	AIC_c	-162.2	-141.4	-129.5
	$ARE(\%)$	5.45	5.47	7.18

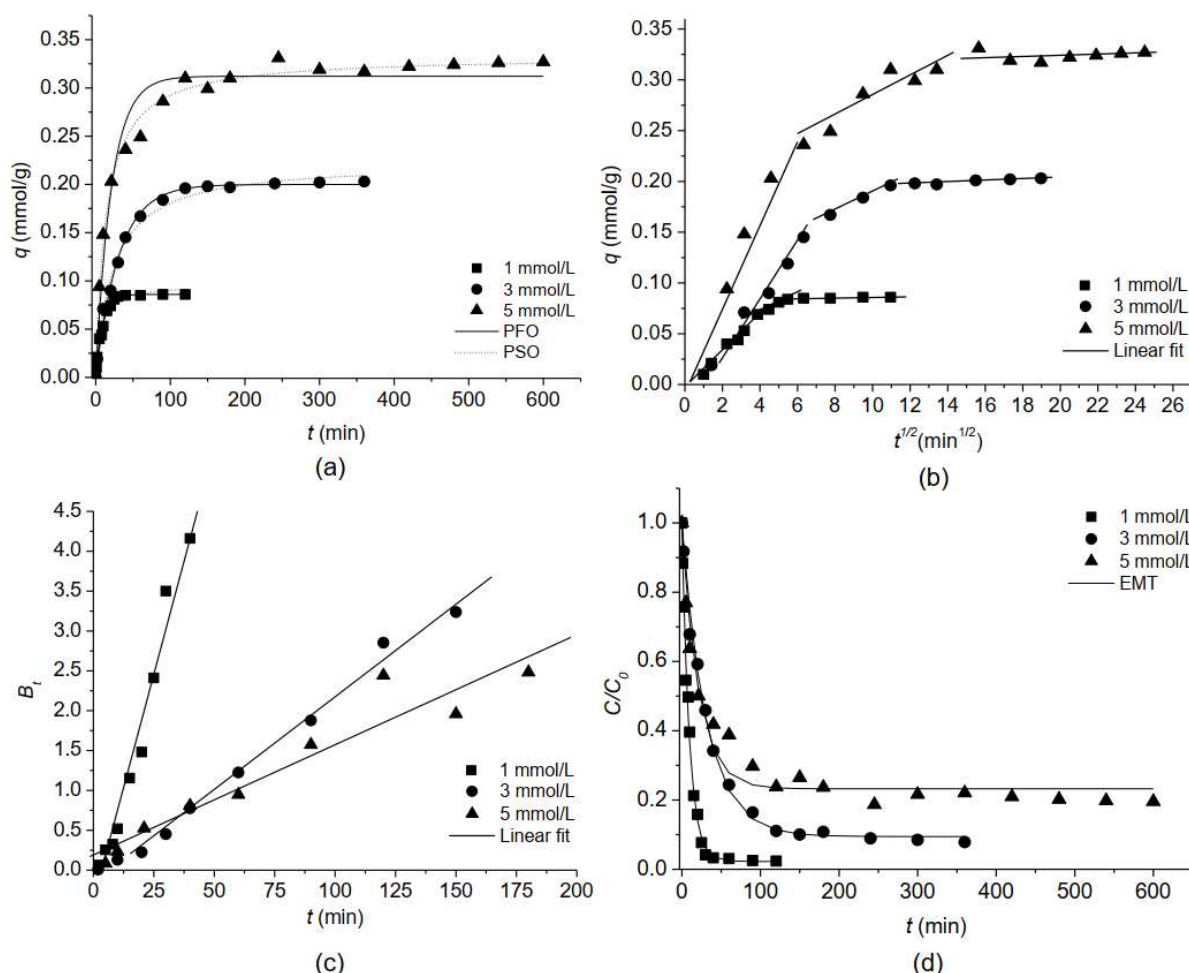


Fig. 7.1. Curves of the fitted kinetic models: PFO and PSO (a), Weber and Morris (b), Boyd (c), and ETM (d)

Comparing the PFO and PSO kinetic models, the adjustment criteria ($R^2 \sim 1.0$) indicated that both models fitted well with the data. The PFO and PSO fitting was performed using the data from the beginning of the process, far from the equilibrium ($F \leq 0.85$) [30,31,37]. According to the *ARE*, PSO had the best fit to the data for 3.0 and 5.0 mmol/L. The model, however, overestimated the q_e at the equilibrium if compared to the experimental values (Fig. 7.1 (a)). The apparent rate constants (k_2) were 1.450, 0.190, 0.214 g/(mmol.min) at 1.0, 3.0, and 5.0 mmol/L, respectively, showing that, for the highest concentrations, the apparent rate of adsorption was not affected significantly with the increase of the C_0 , approximating to a typical rate constant behavior, which the value is independent of operating parameters [31].

The Weber and Morris model (Fig. 7.1 (b)) had a multilinear behavior, which indicates that the adsorption is controlled by multiple processes [31], external transfer from the bulk phase to the adsorbent surface, intraparticle diffusion from the external surface into the

vermiculite slits, and adsorption of the dysprosium in the active sites [32]. The linear regression results from the second zone (intraparticle diffusion) are presented in Table 7.1, in which k_p is 0.010, 0.007 and 0.009 mmol/(g.min^{1/2}), for 1.0, 3.0 and 5.0 mmol/L, respectively. The intraparticle diffusion coefficient did not decrease proportionally to the decrease of the C_0 . However, as the C_0 increased, the boundary layer effect increased too, conforming to the intercept values $I = 0.028, 0.113, 0.192$ mmol/g, which indicates that C_0 increases retarded the intraparticle diffusion [38].

Straight lines could describe Bt versus t , $R^2 > 0.96$ (Fig. 7.1 (c)); however, they did not pass through the origin. Thus, the intraparticle diffusion does not control the adsorption process, which corroborates the multilinear plot from the Weber and Morris model. The effective diffusivities were (D_{ef}) 8.17, 1.72, 1.05×10^{-9} m²/min, from the 1.0, 3.0 and 5.0 mmol/L.

EMT described the dysprosium adsorption kinetic (Fig. 7.1 (d)) adequately achieving the best-fit parameters, highest R^2 , and low $AICc$ and ARE , which indicates that the transfer in the external film is the limiting stage. The k_{ext} decreased from 8.18, 2.29, 2.86×10^{-7} m/min with the increase of C_0 . The high cation exchange capacity of the vermiculite and the pores in the form of slits, confirmed by the ion exchange experiment and the characterization analyses, respectively, can explain higher external transfer resistance. Inglezakis and Pouloupoulos [39] pointed out that high ion exchange capacities lead to great driving forces in the adsorbents and the pores in the form of slits facilitate the pore diffusion.

In literature, the dysprosium adsorption kinetic was studied in batch mode using different adsorbent matrices. Parameters such as equilibrium time (t_e), PSO rate constants (k_2), and adsorption capacities (q_e) of similar studies conducted at the same temperature and with an approximate ratio of adsorbate/adsorbent concentration were evaluated to compare the kinetic performances of different adsorbents to the vermiculite one (Table A.1, Appendix A.5). Hierarchical porous zeolitic imidazolate frameworks nanoparticles (ZIF-8 NPs) presented k_2 equal to 4.22 g/(mmol.min) and q_e of 0.29 mmol/g at 420 min [9]. Ion imprinted macroporous chitosan membrane (IIMCM) adsorbed dysprosium with a rate of 0.43 g/(mmol.min), achieving an adsorption capacity of 0.15 mmol/g in 240 min [10]. The adsorbent composed of oxidized carbon nanotubes (O-CNC/MWCNC), graphene oxide (GO), ion-imprinted cellulose (IIC) achieved a q_e of 0.22 mmol/g at 240 min with an apparent adsorption rate of 0.13 (g/(mmol.min)) [11]. Expanded vermiculite presented k_2 equal to 1.45, 0.19 and 0.21 g/(mmol.min), achieving adsorption capacities of 0.085 mmol/g (40 min), 0.2 mmol/g (150 min) and 0.32 mmol/g (180 min), for the C_0 equal to 1.0, 3.0 and 5.0 mmol/L, respectively.

Comparing the findings from Table A.1(Appendix A.5), for adsorbate/adsorbent concentration ratio around 0.05 ± 0.01 , the rate of Dy adsorption of on expanded vermiculite, for 3.0 and 5.0 mmol/L, was higher than k_2 of the O-CNC/MWCNC/GO/IIC composites, and lower than ZIF-8 NPs and IIMCM. Despite the higher adsorption rate, ZIF-8 NPs achieved an adsorption capacity lower than the expanded vermiculite for $C_0 = 5.0$ mmol/L. Therefore, the kinetic of the dysprosium adsorption on expanded vermiculite is comparable to the kinetic performance of more complex and engineered adsorbents, indicating the potential of the material for future studies of pre-treatments, functionalization, and production of composites for the application in the recovery of rare-earth metals.

Magnesium is the principal exchangeable cation in vermiculite, and it also constitutes the octahedral sheet and the interlayer space [40,41]. Thus, the magnesium concentration in the solution during the dysprosium adsorption (Fig. 2 (a)) was evaluated. The magnesium release was shown in terms of q (mmol/g), the total exchange capacity, 1.41 mmol/g, which was determined by uptake and release of ammonium ions from one molar ammonium acetate solution at pH 7.0 [42].

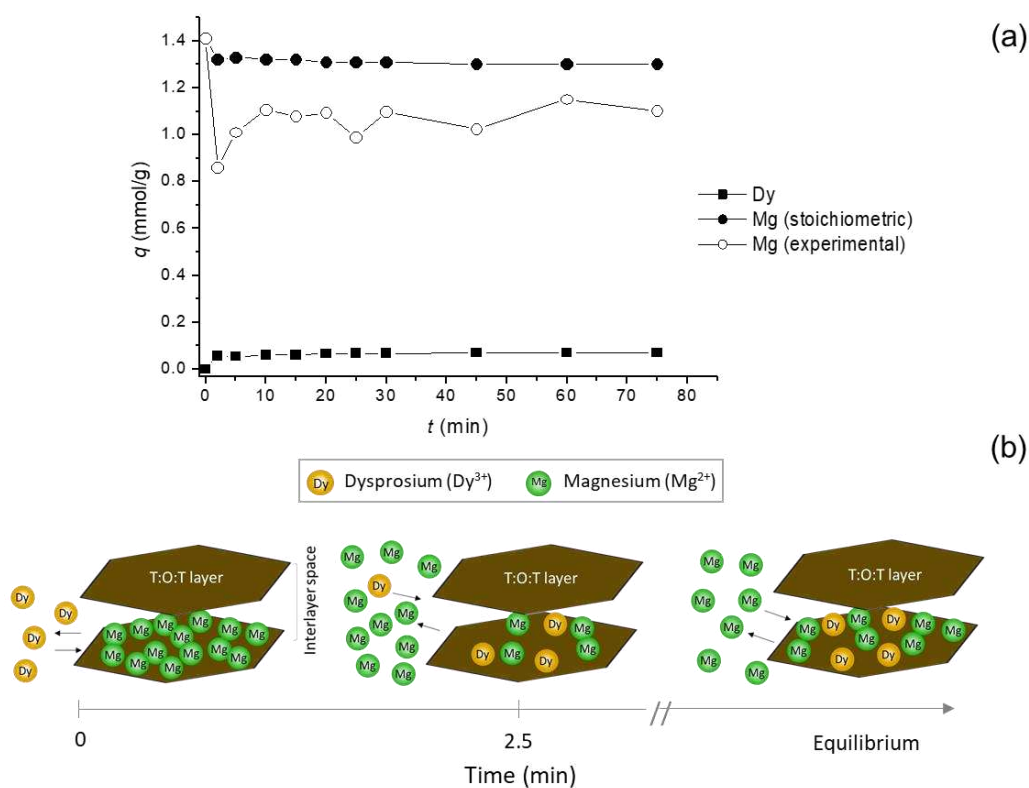
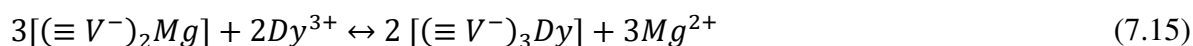


Fig. 7.2. Theoretical and experimental kinetic profiles of magnesium release during the Dy adsorption (a) and representation of the ion exchange mechanism in the dysprosium adsorption (b)

Based on the charge of the dysprosium (Dy^{3+}) and magnesium (Mg^{2+}), the stoichiometric relation would determine that for each 3 displaced magnesium, 2 dysprosium cations are adsorbed, theoretically (Equation 7.15). However, the magnesium concentration released during the experiment was higher than the theoretical one. Thus, at equilibrium, the theoretical magnesium retained on the adsorbent (mmol/g) was 1.3 mmol/g, being 1.2 times higher than the experimental (1.1 mmol/g).



Which $\equiv V^-$ is the negatively charged surface of vermiculite.

Another particular characteristic of the magnesium kinetic release is that a significant quantity of magnesium is unloaded at the beginning of the process. After this peak (overshoot), the light metal (Mg^{2+}) is progressively readsorbed until the equilibrium, presenting oscillations in the q values. The dysprosium is quickly adsorbed, promoting the overshoot of magnesium, due to the higher attraction of the trivalent cation to the negatively charged tetrahedral–octahedral–tetrahedral (T:O:T) aluminosilicate layers in a competitive adsorption process [43,44]. The dysprosium adsorption capacity did not oscillate as the magnesium release; thus, the proposed mechanism (Fig. 2(b)) shows that, in the exchanging sites, Mg^{2+} (solution) substitutes the Mg^{2+} originally retained, while Dy^{3+} continued adsorbed. Thus, the exchange occurs not only by the balancing ion but also by a competition effect [45] that determines selectivity and elution mechanisms.

7.3.2 Selectivity

Rare earth metals usually are mixed with base, noble, and toxic metals in wastewaters, which require further separation and purification [5]. Therefore, the speciation diagram of all metals in solution in function of pH, the removal percentage for each metal, and the selectivity towards dysprosium are presented in Fig. 3. At pH=3.5, pH of the experiment, the monoatomic ions are the predominant species, with the presence of the partially ionized nitrate forms in a much lower concentration (Fig. 7.3 (a)). Thus, for the discussion of the selectivity of the vermiculite, just the bivalent and trivalent (Dy) cations will be mentioned.

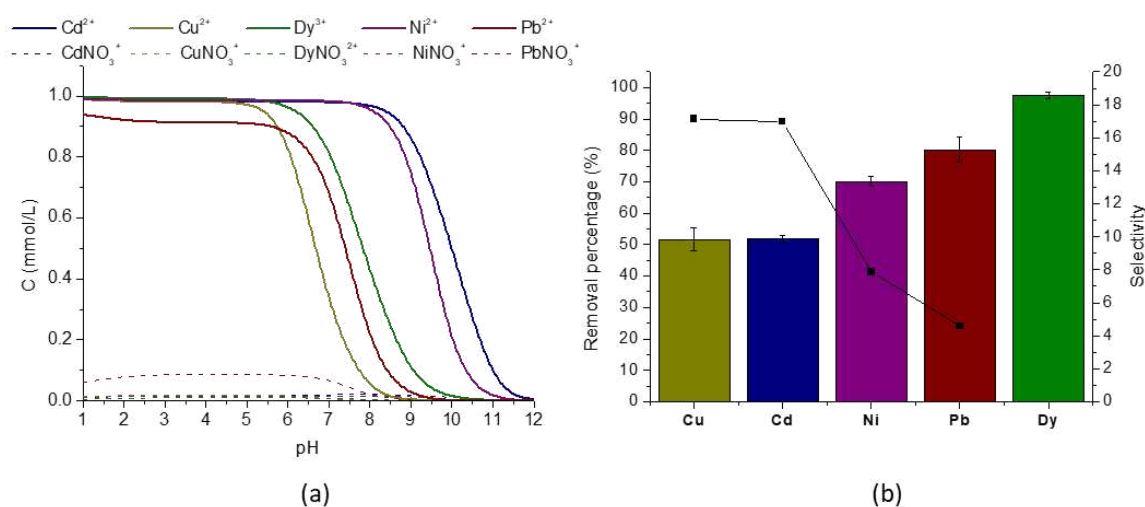


Fig. 7.3. Multimetal speciation (a), removal percentage, and selectivity (b) toward Dy

According to Fig. 7.3 (b), vermiculite adsorbed the metals in that descending order: Dy (97.6%) > Pb (80.1%) > Ni (70.1%) > Cd (52.0%) > Cu (51.7%). Many factors influence the affinity between ions and adsorbent, such as charge, hydrated radius, mass, and hydration energy [46]. Vermiculite is negatively charged because of the replacement of Si^{4+} and Al^{3+} by other cations [47], which implies a high electrostatic attraction by highly charged cations as dysprosium (trivalent) among the other metals (bivalent). Among the other cations, the affinity order was influenced, the majority, by the hydration energy. Ions of lower hydration energy would easily be fixed to the interlayer due to their facilitated partial dehydration (loss of coordinated water) [48]. The ascendant order of hydration energy is Pb (1425 kJ/mol), Cd (1755 kJ/mol), Ni (1980 kJ/mol), Cu (2010 kJ/mol) [49], which agrees with the experimental results, with the exception for nickel (0.72 Å) that had enhanced affinity due to the similar hydrated ionic ratio of magnesium (0.76 Å), the major exchangeable ion from the interlayer space [48,50]. Ergo, the different affinities between trivalent and bivalent cations and vermiculite are determined by distinct factors, such as charge, hydration energy, and ionic radii. However, the selectivity of the vermiculite must be improved to achieve optimal dysprosium or rare earth separation efficiency. Thus, other strategies of structural and chemical modifications, such as ligand insertion [51,52], should be developed to enhance the natural selectivity of this material and separate REM from other metals; moreover, separated them from each other.

7.3.3 Desorption

The results of elution capacity and D_y from the RCCD are displayed in Table 7.2. The %D varied from 8.2% to 89.4%, and the q_{el} changed from 0.0071 mmol/g to 0.0769 mmol/g, which indicates that the factors effectively affected the desorption efficiency. The standardized effects of the independent variables and their interactions on the desorption percentage are presented in Fig. 7.4 (a) (Pareto Chart) to comprehend how significantly each factor influenced the response. The effects in which t value was higher than ± 2.365 (t -student test for seven freedom degrees (fd)) and had the $p < 0.05$ were considered significant.

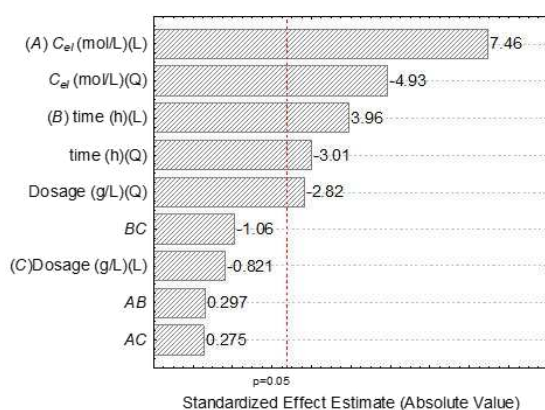
Table 7.2. Dy desorption performance according to %D and q_{el} .

Run	Factors			Coded Factors			q_{el} (mmol/g)	%D
	A C_{el} (mol/L)	B time (h)	C Dosage (g/L)	A	B	C		
1	0.1	1.5	10.0	-1	-1	-1	0.0212	24.6
2	0.3	1.5	10.0	+1	-1	-1	0.0630	73.3
3	0.1	4.5	10.0	-1	+1	-1	0.0501	58.2
4	0.3	4.5	10.0	+1	+1	-1	0.0732	85.2
5	0.1	1.5	18.0	-1	-1	+1	0.0320	37.2
6	0.3	1.5	18.0	+1	-1	+1	0.0549	63.9
7	0.1	4.5	18.0	-1	+1	+1	0.0260	30.3
8	0.3	4.5	18.0	+1	+1	+1	0.0747	86.9
9	0.032	3.0	14.0	$-\alpha$	0	0	0.0071	8.20
10	0.368	3.0	14.0	$+\alpha$	0	0	0.0646	75.2
11	0.2	0.49	14.0	0	$-\alpha$	0	0.0284	33.0
12	0.2	5.51	14.0	0	$+\alpha$	0	0.0706	82.1
13	0.2	3.0	7.31	0	0	$-\alpha$	0.0524	61.0
14	0.2	3.0	20.64	0	0	$+\alpha$	0.0492	57.2
15	0.2	3.0	14.0	0	0	0	0.0717	83.3
16	0.2	3.0	14.0	0	0	0	0.0756	88.0
17	0.2	3.0	14.0	0	0	0	0.0769	89.4

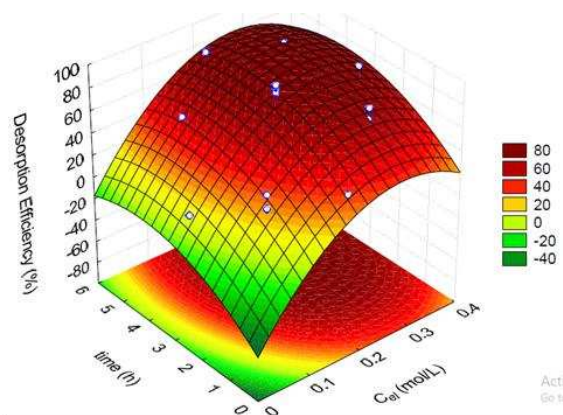
The eluent concentration was the factor that affected more significantly the dysprosium desorption, followed by time and the quadratic effect of the dosage. After the eluent's nature, the eluent concentration is the most critical factor influencing the desorption efficiency [53,54], which justifies the high C_{el} effect on the dysprosium recovery. The interactions between the factors were not significant, as well the linear solid/liquid ratio effect. Table 7.3 presents the variance analysis (ANOVA) for the reduced model that considers just the significant parameters, with a significance level (α) of 0.05.

Table 7.3. ANOVA for the reduced squared model ($\alpha = 0.05$)

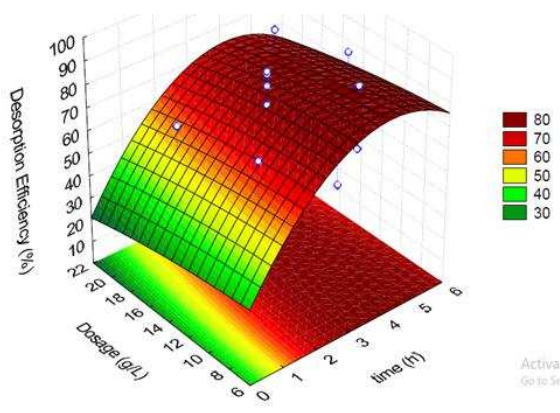
Source of variation	Reduced squared model ($F_{\text{tab}} = 3.20$)				
	SS	fd	MS	F_{calc}	$F_{\text{calc}}/F_{\text{tab}}$
Regression	9,644.6	5	1,928.9	24.4	7.64
Error	867.7	11	78.8	-	-
Total	10,512.3	16	-	-	-



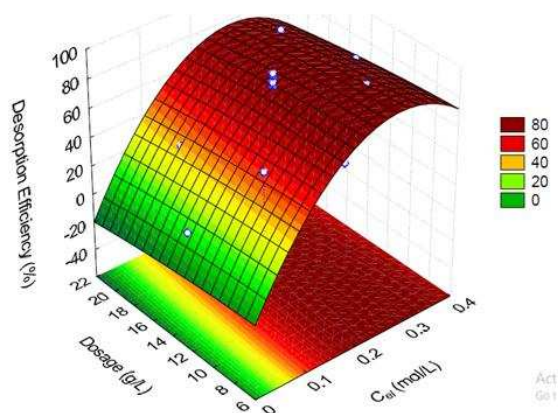
(a)



(b)



(c)



(d)

Fig. 7.4. Pareto chart (standardized effects on Dy removal percentage) (a), response surfaces of the dysprosium desorption efficiency as a function of time and eluent concentration (b), dosage and time (c) and dosage, and eluent concentration (d)

After the backward elimination, the ANOVA of the reduced model showed $F_{\text{calc}}/F_{\text{tab}} = 7.64$, $R^2 = 0.9174$, and $R_{\text{adj}}^2 = 0.8799$, indicating that the model is predictive. The response surfaces (Fig. 7.4 (b), Fig. 7.4 (c), and Fig. 7.4 (d)) were elaborated from the %D model of Equation 7.16 that excluded non-significant effects.

$$\%D = 86.3_{\pm 5.1} + 19.8_{\pm 2.4}A - 14.4_{\pm 2.6}A^2 + 10.6_{\pm 2.4}B - 8.9_{\pm 2.7}B^2 - 8.4_{\pm 2.7}C^2 \quad (7.16)$$

The response surface of Fig. 7.4 (b) that corresponds to the desorption percentage as a function of the most significant factors (eluent concentration and contact time) shows that the efficiency had a maximum in the region between 0.2 and 0.3 mol/L of eluent and 3 and 5 hours. Fig. 7.4 (c) and Fig. 7.4 (d) evidenced the slight influence of the dosage in the desorption efficiency, i.e., in the surface shape. Thus, the optimum operating conditions defined by the RSM analysis were C_{el} of 0.25 mol/L, time of 4 hours and dosage of 14 g/L, in which the predicted desorption efficiency is 95.8 %.

In a design of experiments, an experimental confirmation is required to verify that the system operates or behaves consistently with some theory or practical limitations to effectively validate the conclusions from the experiment [55]. The validation test at the best conditions from RSM achieved an experimental value of the desorption efficiency of 84.0 ± 2.6 %, which means a relative difference of 12.3 % between the predicted (95.8%) and the observed, indicating that the model was not able to predict satisfactorily the desorption efficiency at this condition. Based on the experimental results of the RCCD (Table 7.2), the highest %D was achieved at the central point; thus, another triplicate (validation) was performed at this condition. The new validation test reached a $\%D = 89.1 \pm 4.3$ %, which agrees with the model prediction of 86.3 %, representing a relative error of 3.1 % and indicating the higher reproducibility of the experiment at this condition. Thus, the best validated conditions for the desorption are C_{el} of 0.2 mol/L, time of 3 hours and dosage of 14 g/L.

Compared to analogous studies from the literature, dysprosium was desorbed from oxidized multiwalled carbon nanotubes [56] and from amorphous zirconium phosphate [57] with an efficiency of 70% and 83%, using nitric and sulfuric acid, respectively. Thus, the desorption efficiency of 89.1% achieved in this work is higher than those found in the literature. Furthermore, using a source of magnesium cations for the dysprosium desorption and adsorbent regeneration represents a safer process than the typical elution by strong acids.

7.3.4 Adsorbent characterization

In Fig. 7.5 (a) and Fig. 7.5 (b), SEM images of the lamellar region of two distinct particles at 1800 times of amplification, the ordered layers of the dysprosium-loaded vermiculite were evidenced. The space between the lamellas was much lower than 10 μm (scale reference), which

means that the material is not as expanded as the original due to rehydration. The original expanded material has slit openings of 60 μm , proximately [19]. Fig. 7.5 (c) and Fig. 7.5 (d) show the EDS mapping for dysprosium (green dots) on the vermiculite surface and Fig. 7.5 (e) the EDS spectra for Verm-Dy sample. Due to the uniform distribution of the dysprosium on the vermiculite, we infer that the adsorbate was homogeneously adsorbed on the surface. The EDS spectra evidences the relevant content of dysprosium on Verm-Dy, which is confirmed by Table 7.4 (Verm-Dy composition estimation from the EDS analysis).

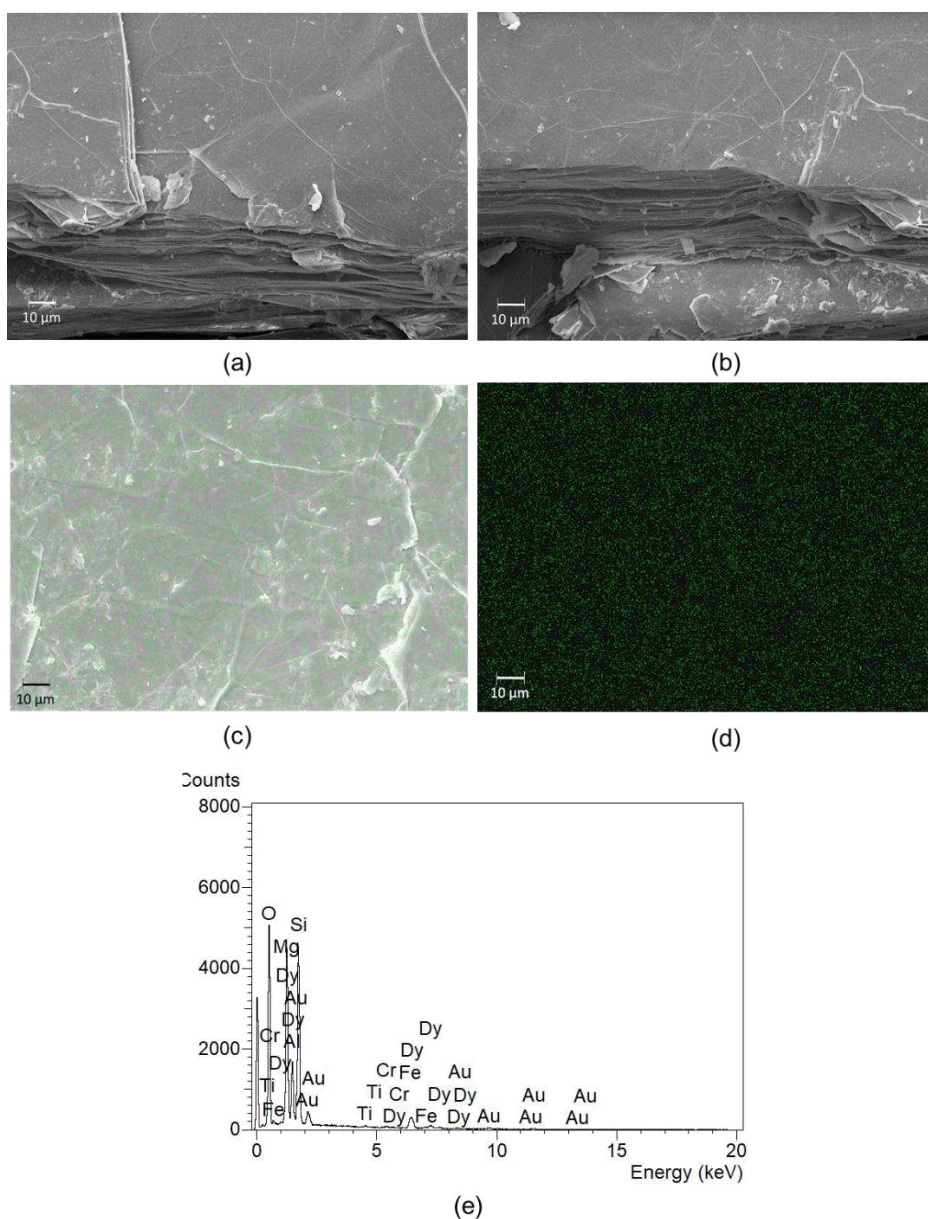


Fig. 7.5. SEM images (a,b), EDS mapping for dysprosium (green dots) (c,d) and the EDS spectra (e) of dysprosium-loaded vermiculite (Verm-Dy)

From Table 7.4, silicon, magnesium, aluminum, and iron are the main components of Verm-Dy, which agrees to the well-known structure of the vermiculite that is a hydrated, magnesium–iron–aluminum trioctahedral sheet silicate [58]. Titanium and chromium are trace elements. Thus, the composition of Verm-Dy indicates that the dysprosium adsorption did not significantly alter the chemical structure of the adsorbent. Also, the percentage of dysprosium from mass and molar basis, 6.97 % and 0.94 %, respectively, confirmed the effective adsorption of dysprosium.

Table 7.4. Composition of Verm-Dy from EDS analysis

Component	Verm-Dy	
	Element (%)	Atomic (%)
Mg	15.5 ± 1.8	14.0 ± 1.5
Al	6.98 ± 0.2	5.70 ± 0.2
Si	21.2 ± 0.2	16.6 ± 0.2
Ti	0.54 ± 0.3	0.25 ± 0.2
Cr	0.41 ± 0.2	0.18 ± 0.1
Fe	4.30 ± 1.2	1.70 ± 0.5
Dy	6.97 ± 0.7	0.94 ± 0.1
O	44.0 ± 0.4	60.6 ± 0.4

The IR spectra (Fig. 7.6 (a)) exhibited a strong band at 3417 cm^{-1} relative to the O–H stretching vibration of the hydration water and bound Si–OH groups [59,60]. Another band related to the hydration water molecules was noted at around 1644 cm^{-1} (O–H bending vibrations) [61]. The peak at 1384 cm^{-1} is relative to the adsorbed nitrate [62,63], confirming the simulation of the dysprosium speciation at pH 3.5 (Fig. A.1, Appendix A.5), in which DyNO_3^{2+} , even in a minimal concentration, was also present in the aqueous solutions. The band at 1007 cm^{-1} identified stretching vibrations of Si–O groups. Although, Al–O and Si–O out-of-plane vibrations were observed by the band at 670 cm^{-1} , and the band at 449 cm^{-1} indicated the Si–O–Si bending vibrations [64].

Fig. 7.6 (b) is the X-ray diffractogram of Verm-Dy, in which the 2nd, 4th, 6th, 8th, and 10th order reflections were located at 14.9, 7.4, 5.0, 3.7, and 3.0 Å, respectively. According to Walker [65], the XRD reflection of the distance between layers for clay minerals is characterized as 002 reflections (2nd order). For the 2:1 type clay minerals, as the vermiculite, bihydrated layers of water molecules in interlayer space produce a 002 reflection at around 15 Å [41,66,67], which agrees to the experimental value. The original adsorbent had a basal spacing of 14.1 Å [19]. Therefore, the dysprosium adsorption enlarged the interlayer space of

the material. This phenomenon occurs due to the rehydration of the material and the replacement of interlayer magnesium by dysprosium with a larger ionic radius and a higher coordination number [65]. The 6th, 8th, and 10th reflections showed the growing intensities typical for vermiculites [68].

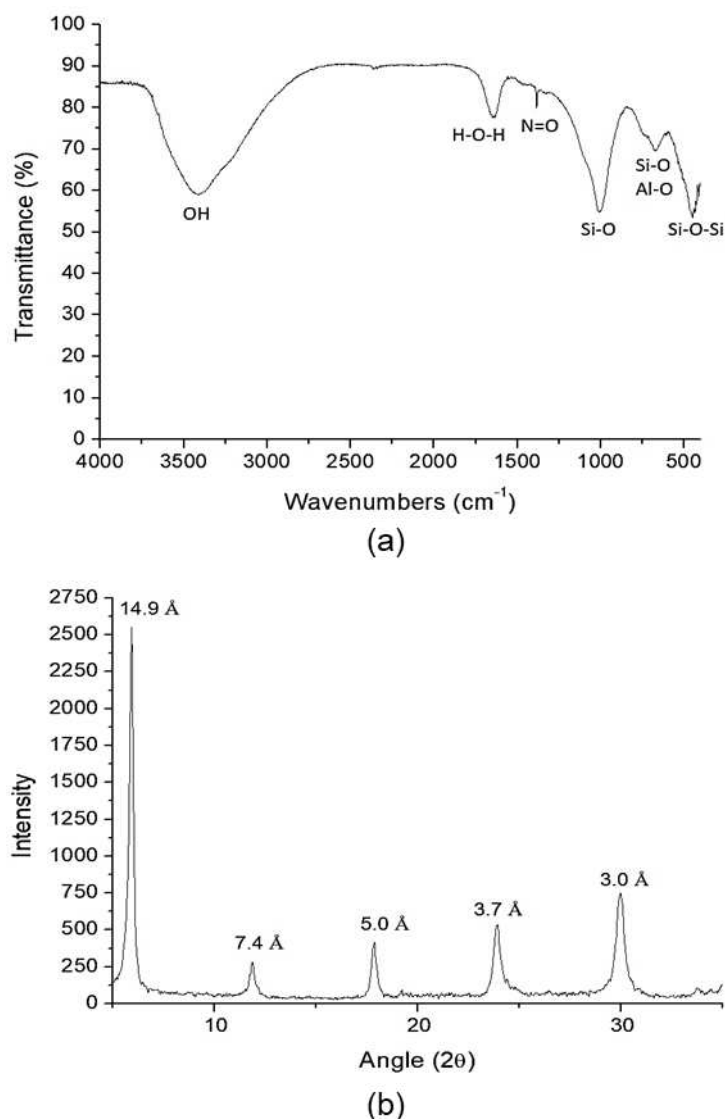


Fig. 7.6. FT-IR spectra (a) and XRD pattern (b) of Verm-Dy

7.4 CONCLUSIONS

Relevant parameters for efficient recovery of dysprosium through adsorption on expanded vermiculite, such as adsorption kinetics, selectivity, and desorption, were investigated in this paper. Dysprosium adsorption kinetic is fast, controlled by external mass transfer, and the exchange with interlayer magnesium is an essential mechanism involved in

the sorption process. The expanded vermiculite shows an ordered affinity sequence to adsorb cations from different groups: Dy > Pb > Ni > Cd > Cu influenced by charge, hydration energies, and ionic radii. The desorption process is significantly influenced by eluent concentration, contact time, and dosage of loaded adsorbent. The best-operating conditions were considered 0.2 mol/L, contact time of 3 h, and dosage of 14 g/L, achieving an experimental desorption efficiency of 89.1 ± 4.3 %. According to the analyses of the solid material after the dysprosium adsorption, the typical crystalline structure is maintained; however, the process enlarges the interlayer space due to rehydration and exchange of magnesium for dysprosium, a larger cation. Regarding the composition, Dy achieves a significant percentage of 6.97% on the total mass of the loaded adsorbent. From the FTIR, the known bonds Si-O and Al-O from clay materials are also preserved. Thus, the adsorption of dysprosium is efficient, fast, selective, and does not compromise the adsorbent structure, indicating resistance for multiple reuses that should be evaluated in further studies.

ACKNOWLEDGMENTS

This work was financed by the Fundação de Amparo à Pesquisa do Estado de São Paulo (FAPESP) (Grants # 2017/18236-1 and 2019/11353-8), Coordenação de Aperfeiçoamento de Pessoal de Nível Superior (CAPES) (Financial code – 001), Conselho Nacional de Desenvolvimento Científico e Tecnológico (CNPq) (Grants # 406193/2018-5 and 308046/2019-6). The adsorbent material was provided by Brasil Minérios S/A.

REFERENCES

- [1] S. Constantinides, The Important Role of Dysprosium in Modern Permanent Magnets, Arnold Magn. Technol. Corp. (2012) 10. <https://www.arnoldmagnetics.com/wp-content/uploads/2017/10/Important-Role-of-Dysprosium-in-Modern-Permanent-Magnets-150906.pdf>.
- [2] F. Tesfaye, H. Peng, M. Zhang, Advances in the Circular Economy of Lanthanides, Jom. 73 (2021) 16–18. <https://doi.org/10.1007/s11837-020-04493-x>.
- [3] S. Langkau, M. Erdmann, Environmental impacts of the future supply of rare earths for magnet applications, J. Ind. Ecol. (2020) 1–17. <https://doi.org/10.1111/jiec.13090>.
- [4] R.K. Jyothi, T. Thenepalli, J.W. Ahn, P.K. Parhi, K.W. Chung, J.Y. Lee, Review of rare earth elements recovery from secondary resources for clean energy technologies: Grand

- opportunities to create wealth from waste, *J. Clean. Prod.* 267 (2020) 122048. <https://doi.org/10.1016/j.jclepro.2020.122048>.
- [5] M. Wang, Q. Tan, J.F. Chiang, J. Li, Recovery of rare and precious metals from urban mines—A review, *Front. Environ. Sci. Eng.* 11 (2017). <https://doi.org/10.1007/s11783-017-0963-1>.
- [6] I. Anastopoulos, A. Bhatnagar, E.C. Lima, Adsorption of rare earth metals: A review of recent literature, *J. Mol. Liq.* 221 (2016) 954–962. <https://doi.org/10.1016/j.molliq.2016.06.076>.
- [7] L. Alcaraz, M.E. Escudero, F.J. Alguacil, I. Llorente, A. Urbieto, P. Fernández, F.A. López, Dysprosium Removal from Water Using Active Carbons Obtained from Spent Coffee Ground, *Nanomaterials*. 9 (2019) 1372. <https://doi.org/10.3390/nano9101372>.
- [8] T. Kegl, I. Ban, A. Lobnik, A. Košak, Synthesis and characterization of novel $\gamma\text{-Fe}_2\text{O}_3\text{-NH}_4\text{OH@SiO}_2(\text{APTMS})$ nanoparticles for dysprosium adsorption, *J. Hazard. Mater.* 378 (2019) 120764. <https://doi.org/10.1016/j.jhazmat.2019.120764>.
- [9] A.F. Abdel-Magied, H.N. Abdelhamid, R.M. Ashour, X. Zou, K. Forsberg, Hierarchical porous zeolitic imidazolate frameworks nanoparticles for efficient adsorption of rare-earth elements, *Microporous Mesoporous Mater.* 278 (2019) 175–184. <https://doi.org/10.1016/j.micromeso.2018.11.022>.
- [10] E. Liu, X. Xu, X. Zheng, F. Zhang, E. Liu, C. Li, An ion imprinted macroporous chitosan membrane for efficiently selective adsorption of dysprosium, *Sep. Purif. Technol.* 189 (2017) 288–295. <https://doi.org/10.1016/j.seppur.2017.06.079>.
- [11] X. Zheng, Y. Zhang, T. Bian, Y. Zhang, Z. Li, J. Pan, Oxidized carbon materials cooperative construct ionic imprinted cellulose nanocrystals films for efficient adsorption of Dy(III), *Chem. Eng. J.* 381 (2020) 122669. <https://doi.org/10.1016/j.cej.2019.122669>.
- [12] O. Udoudo, O. Folorunso, C. Dodds, S. Kingman, A. Ure, Understanding the performance of a pilot vermiculite exfoliation system through process mineralogy, *Miner. Eng.* 82 (2015) 84–91. <https://doi.org/10.1016/j.mineng.2015.03.023>.
- [13] R. de F. Paula, C. Carvalhães, Vermiculita, in: *Sumário Miner. 2016*, Departamento Nacional de Produção Mineral, Brasília, 2018: pp. 110–111.
- [14] M. Valaskova, G.S. Martynková, Vermiculite: Structural Properties and Examples of the Use, in: *Clay Miner. Nat. - Their Charact. Modif. Appl.*, InTech, 2012: p. 64. <https://doi.org/10.5772/51237>.

- [15] V.E. dos Anjos, J.R. Rohwedder, S. Cadore, G. Abate, M.T. Grassi, Montmorillonite and vermiculite as solid phases for the preconcentration of trace elements in natural waters: Adsorption and desorption studies of As, Ba, Cu, Cd, Co, Cr, Mn, Ni, Pb, Sr, V, and Zn, *Appl. Clay Sci.* 99 (2014) 289–296. <https://doi.org/10.1016/j.clay.2014.07.013>.
- [16] D.R. Ferreira, J.A. Thornhill, E.I.N. Roderick, Y. Li, The Impact of pH and Ion Exchange on 133 Cs Adsorption on Vermiculite, *J. Environ. Qual.* 47 (2018) 1365–1370. <https://doi.org/10.2134/jeq2018.01.0043>.
- [17] E.D. de Freitas, H.J. de Almeida, M.G.A. Vieira, Binary adsorption of zinc and copper on expanded vermiculite using a fixed bed column, *Appl. Clay Sci.* 146 (2017) 503–509. <https://doi.org/10.1016/j.clay.2017.07.004>.
- [18] E. Nishikawa, A.F.A. Neto, M.G.A. Vieira, Equilibrium and thermodynamic studies of zinc adsorption on expanded vermiculite, *Adsorpt. Sci. Technol.* 30 (2012) 759–772. <https://doi.org/10.1260/0263-6174.30.8-9.759>.
- [19] G. de V. Brião, M.G.C. da Silva, M.G.A. Vieira, Neodymium recovery from aqueous solution through adsorption/desorption onto expanded vermiculite, *Appl. Clay Sci.* 198 (2020) 105825. <https://doi.org/10.1016/j.clay.2020.105825>.
- [20] G. de V. Brião, M.G.C. da Silva, M.G.A. Vieira, Efficient and Selective Adsorption of Neodymium on Expanded Vermiculite, *Ind. Eng. Chem. Res.* (2021) acs.iecr.0c05979. <https://doi.org/10.1021/acs.iecr.0c05979>.
- [21] A. Alshameri, X. Wei, H. Wang, Y. Fuguo, X. Chen, H. He, C. Yan, F. Xu, A Review of the Role of Natural Clay Minerals as Effective Adsorbents and an Alternative Source of Minerals, in: *Minerals*, IntechOpen, 2019. <https://doi.org/10.5772/intechopen.87260>.
- [22] G. de V. Brião, T.L. da Silva, M.G.C. da Silva, M.G.A. Vieira, Response surface methodology approach for optimization of dysprosium adsorption onto expanded vermiculite, in: D.C.S. de Azevedo, M. Bastos-Neto (Eds.), *13th Brazillian Meet. Adsorpt.*, Imprensa Universitaria, 2021: pp. 492–497. <https://doi.org/10.51996/9786588492529>.
- [23] D.G. Schulze, Clay Minerals, in: *Encycl. Soils Environ.*, Elsevier, 2005: pp. 246–254. <https://doi.org/10.1016/B0-12-348530-4/00189-2>.
- [24] S. Lagergren, About the theory of so-called adsorption of soluble substances., *K. Suensk Vetenskapsak Ademiens Handl.* 24 (1898) 1–39.
- [25] Y.S. Ho, G. McKay, A Comparison of chemisorption kinetic models applied to pollutant removal on various sorbents, *Process Saf. Environ. Prot.* 76 (1998) 332–340.

- <https://doi.org/10.1205/095758298529696>.
- [26] W.J. Weber, J.C. Morris, Kinetics of adsorption carbon from solutions, *J. Sanit. Engineering Div. Proc.* 89 (1963) 31–60.
 - [27] D. Reichenberg, Properties of Ion-Exchange Resins in Relation to their Structure. III. Kinetics of Exchange, *J. Am. Chem. Soc.* 75 (1953) 589–597. <https://doi.org/10.1021/ja01099a022>.
 - [28] G.E. Boyd, A.W. Adamson, L.S. Myers, The Exchange Adsorption of Ions from Aqueous Solutions by Organic Zeolites. II. Kinetics, *J. Am. Chem. Soc.* 69 (1947) 2836–2848. <https://doi.org/10.1021/ja01203a066>.
 - [29] R.M.C. Viegas, M. Campinas, H. Costa, M.J. Rosa, How do the HSDM and Boyd's model compare for estimating intraparticle diffusion coefficients in adsorption processes, *Adsorption*. 20 (2014) 737–746. <https://doi.org/10.1007/s10450-014-9617-9>.
 - [30] J.-P. Simonin, On the comparison of pseudo-first order and pseudo-second order rate laws in the modeling of adsorption kinetics, *Chem. Eng. J.* 300 (2016) 254–263. <https://doi.org/10.1016/j.cej.2016.04.079>.
 - [31] J. Wang, X. Guo, Adsorption kinetic models: Physical meanings, applications, and solving methods, *J. Hazard. Mater.* 390 (2020) 122156. <https://doi.org/10.1016/j.jhazmat.2020.122156>.
 - [32] K.L. Tan, B.H. Hameed, Insight into the adsorption kinetics models for the removal of contaminants from aqueous solutions, *J. Taiwan Inst. Chem. Eng.* 74 (2017) 25–48. <https://doi.org/10.1016/j.jtice.2017.01.024>.
 - [33] C.M. Hurvich, C.L. Tsai, Regression and time series model selection in small samples, *Biometrika*. 76 (1989) 297–307. <https://doi.org/10.1093/biomet/76.2.297>.
 - [34] T.H. Bui, W. Lee, S.-B. Jeon, K.-W. Kim, Y. Lee, Enhanced Gold(III) adsorption using glutaraldehyde-crosslinked chitosan beads: Effect of crosslinking degree on adsorption selectivity, capacity, and mechanism, *Sep. Purif. Technol.* 248 (2020) 116989. <https://doi.org/10.1016/j.seppur.2020.116989>.
 - [35] T.B. da Costa, M.G.C. da Silva, M.G.A. Vieira, Recovery of rare-earth metals from aqueous solutions by bio/adsorption using non-conventional materials: a review with recent studies and promising approaches in column applications, *J. Rare Earths*. 38 (2020) 339–355. <https://doi.org/10.1016/j.jre.2019.06.001>.
 - [36] X.-Q. Qiao, F.-C. Hu, F.-Y. Tian, D.-F. Hou, D.-S. Li, Equilibrium and kinetic studies on MB adsorption by ultrathin 2D MoS₂ nanosheets, *RSC Adv.* 6 (2016) 11631–11636.

- <https://doi.org/10.1039/C5RA24328A>.
- [37] S. Azizian, Kinetic models of sorption: A theoretical analysis, *J. Colloid Interface Sci.* 276 (2004) 47–52. <https://doi.org/10.1016/j.jcis.2004.03.048>.
 - [38] F.-C. Wu, R.-L. Tseng, R.-S. Juang, Initial behavior of intraparticle diffusion model used in the description of adsorption kinetics, *Chem. Eng. J.* 153 (2009) 1–8. <https://doi.org/10.1016/j.cej.2009.04.042>.
 - [39] V.J. Inglezakis, S.G. Pouloupoulos, Adsorption and Ion Exchange, in: *Adsorpt. Ion Exch. Catal.*, Elsevier, 2006: pp. 243–353. <https://doi.org/10.1016/B978-044452783-7/50004-5>.
 - [40] Y. Liu, D. Xiao, H. Li, Kinetics and Thermodynamics of Lead (II) Adsorption on Vermiculite, *Sep. Sci. Technol.* 42 (2007) 185–202. <https://doi.org/10.1080/01496390600998045>.
 - [41] S. Hillier, E.M.M. Marwa, C.M. Rice, On the mechanism of exfoliation of ‘Vermiculite,’ *Clay Miner.* 48 (2013) 563–582. <https://doi.org/10.1180/claymin.2013.048.4.01>.
 - [42] J. Schweitzer, G. Muller, Test Method 9081: Cation-Exchange Capacity of Soils (Sodium Acetate), *Hazard. Waste Test Methods / SW-846*. 13 (1986) 1529–1532. <https://www.epa.gov/hw-sw846/sw-846-test-method-9081-cation-exchange-capacity-soils-sodium-acetate>.
 - [43] W. li Xiong, J. Zhang, J. xia Yu, R. an Chi, Competitive adsorption behavior and mechanism for Pb²⁺ selective removal from aqueous solution on phosphoric acid modified sugarcane bagasse fixed-bed column, *Process Saf. Environ. Prot.* 124 (2019) 75–83. <https://doi.org/10.1016/j.psep.2019.02.001>.
 - [44] S.C. Ryu, G. Naidu, H. Moon, S. Vigneswaran, Continuous and selective copper recovery by multi-modified and granulated SBA-15, *Chemosphere*. 271 (2021) 129820. <https://doi.org/10.1016/j.chemosphere.2021.129820>.
 - [45] M.A.S.D. Barros, M.L. Gimenes, M.G.A. Vieira, M.G.C. da Silva, Ion Exchange Fundamentals and New Challenges, in: M. Solecki (Ed.), *Mass Transf. - Adv. Process Model.*, IntechOpen, 2015. <https://doi.org/10.5772/60864>.
 - [46] B. Asgari Lajayer, N. Najafi, E. Moghiseh, M. Mosaferi, J. Hadian, Removal of heavy metals (Cu²⁺ and Cd²⁺) from effluent using gamma irradiation, titanium dioxide nanoparticles and methanol, *J. Nanostructure Chem.* 8 (2018) 483–496. <https://doi.org/10.1007/s40097-018-0292-3>.
 - [47] S. Gu, X. Kang, L. Wang, E. Lichtfouse, C. Wang, Clay mineral adsorbents for heavy

- metal removal from wastewater: a review, *Environ. Chem. Lett.* 17 (2019) 629–654. <https://doi.org/10.1007/s10311-018-0813-9>.
- [48] H. He, J. Guo, X. Xie, J. Peng, Experimental study of the selective adsorption of heavy metals onto clay minerals, *Chinese J. Geochemistry.* 19 (2000) 105–109. <https://doi.org/10.1007/BF03166865>.
- [49] Y. Marcus, Thermodynamics of solvation of ions. Part 5. - Gibbs free energy of hydration at 298.15 K, *J. Chem. Soc. Faraday Trans.* 87 (1991) 2995–2999. <https://doi.org/10.1039/FT9918702995>.
- [50] I. Persson, Hydrated metal ions in aqueous solution: How regular are their structures?, *Pure Appl. Chem.* 82 (2010) 1901–1917. <https://doi.org/10.1351/PAC-CON-09-10-22>.
- [51] T. Ogata, H. Narita, M. Tanaka, Rapid and selective recovery of heavy rare earths by using an adsorbent with diglycol amic acid group, *Hydrometallurgy.* 155 (2015) 105–109. <https://doi.org/10.1016/j.hydromet.2015.04.015>.
- [52] T. Ogata, H. Narita, M. Tanaka, Immobilization of diglycol amic acid on silica gel for selective recovery of rare earth elements, *Chem. Lett.* 43 (2014) 1414–1416. <https://doi.org/10.1246/cl.140446>.
- [53] P.R. Haddad, P.E. Jackson, Chapter 4 Eluents for Ion-Exchange Separations, in: *Ion Chromatogr. Princ. Appl.*, 1990: pp. 79–132. [https://doi.org/10.1016/S0301-4770\(08\)61136-7](https://doi.org/10.1016/S0301-4770(08)61136-7).
- [54] O. Bahadir, Ion-Exchange Chromatography and Its Applications, in: *Column Chromatogr.*, InTech, 2013. <https://doi.org/10.5772/55744>.
- [55] D.C. Montgomery, *Design and Analysis of Experiments*, 8th ed., John Wiley & Sons, Inc., 2013.
- [56] S.M.A. Koochaki-Mohammadpour, M. Torab-Mostaedi, A. Talebizadeh-Rafsanjani, F. Naderi-Behdani, Adsorption Isotherm, Kinetic, Thermodynamic, and Desorption Studies of Lanthanum and Dysprosium on Oxidized Multiwalled Carbon Nanotubes, *J. Dispers. Sci. Technol.* 35 (2014) 244–254. <https://doi.org/10.1080/01932691.2013.785361>.
- [57] J. Xu, R. Koivula, W. Zhang, E. Wiikinkoski, S. Hietala, R. Harjula, Separation of cobalt, neodymium and dysprosium using amorphous zirconium phosphate, *Hydrometallurgy.* 175 (2018) 170–178. <https://doi.org/10.1016/j.hydromet.2017.11.010>.
- [58] A.L. Bush, Construction Materials: Lightweight Aggregates, in: K.H.J. Buschow, R.W. Cahn, M.C. Flemings, B. Ilshner, E.J. Kramer, S. Mahajan, P. Veyssi re (Eds.), *Encycl.*

- Mater. Sci. Technol., Elsevier, 2001: pp. 1550–1558. <https://doi.org/10.1016/B0-08-043152-6/00277-1>.
- [59] J. Hougardy, J.M. Serratosa, W. Stone, H. van Olphen, Interlayer water in vermiculite: thermodynamic properties, packing density, nuclear pulse resonance, and infra-red absorption, *Spec. Discuss. Faraday Soc.* 1 (1970) 187–193. <https://doi.org/10.1039/sd9700100187>.
- [60] V.C. Farmer, *Vibrational Spectroscopy in Mineral Chemistry*, in: *Infrared Spectra Miner.*, Mineralogical Society of Great Britain and Ireland, London, 1974: pp. 1–10. <https://doi.org/10.1180/mono-4.1>.
- [61] M. Ritz, J. Zdrálová, M. Valášková, Vibrational spectroscopy of acid treated vermiculites, *Vib. Spectrosc.* 70 (2014) 63–69. <https://doi.org/10.1016/j.vibspec.2013.11.007>.
- [62] O. Długosz, M. Banach, Sorption of Ag⁺ and Cu²⁺ by Vermiculite in a Fixed-Bed Column: Design, Process Optimization and Dynamics Investigations, *Appl. Sci.* 8 (2018) 2221. <https://doi.org/10.3390/app8112221>.
- [63] J. Coates, *Encyclopedia of Analytical Chemistry - Interpretation of Infrared Spectra, A Practical Approach*, *Encycl. Anal. Chem.* (2004) 1–23. <http://www3.uma.pt/jrodrigues/disciplinas/QINO-II/Teorica/IR.pdf>.
- [64] E. Eren, Removal of copper ions by modified Unye clay, Turkey, *J. Hazard. Mater.* 159 (2008) 235–244. <https://doi.org/10.1016/j.jhazmat.2008.02.035>.
- [65] G.F. Walker, Vermiculites, in: *Soil Components*, Springer Berlin Heidelberg, Berlin, Heidelberg, 1975: pp. 155–189. https://doi.org/10.1007/978-3-642-65917-1_6.
- [66] E. Ferrage, Investigation of the Interlayer Organization of Water and Ions In Smectite from the Combined Use of Diffraction Experiments And Molecular Simulations. a Review of Methodology, Applications, And Perspectives, *Clays Clay Miner.* 64 (2016) 348–373. <https://doi.org/10.1346/CCMN.2016.0640401>.
- [67] L. Ma, X. Su, Y. Xi, J. Wei, X. Liang, J. Zhu, H. He, The structural change of vermiculite during dehydration processes: A real-time in-situ XRD method, *Appl. Clay Sci.* 183 (2019) 105332. <https://doi.org/10.1016/j.clay.2019.105332>.
- [68] A. Wiewióra, Particle size distribution in sonicated high- and low-charge vermiculites, *Appl. Clay Sci.* 24 (2003) 51–58. [https://doi.org/10.1016/S0169-1317\(03\)00133-9](https://doi.org/10.1016/S0169-1317(03)00133-9).

CHAPTER 8. DYSPROSIUM ADSORPTION ON EXPANDED VERMICULITE IN BATCH MODE: EQUILIBRIUM, THERMODYNAMICS, REUSE

Expanded vermiculite as an alternative adsorbent for the dysprosium recovery⁷

Giani de Vargas Brião, Meuris Gurgel Carlos da Silva, Melissa Gurgel Adeodato Vieira

University of Campinas, School of Chemical Engineering, Albert Einstein Avenue, 500, 13083-852 Campinas, Brazil

ABSTRACT

1) Background: Dysprosium (Dy) is a critical resource for developing high-tech green energies, and its growing demand implying the need to recover it from secondary sources. Due to the known stability, availability, and high cation exchange capacity, adsorption on vermiculite can be promisor for this purpose. 2) Methods: This work evaluated the dysprosium adsorption and desorption on expanded vermiculite through experiments of equilibrium, thermodynamic, and reuse cycles. Also, the regenerated material was characterized regarding morphological, compositional, thermal, superficial aspects. 3) Significant Findings: The equilibrium data achieved high adsorption capacities (0.9 mmol/g), and the sigmoidal isotherms indicated a first layer saturation and progressive surface precipitation, which may favor a Dy selective sorption. The process is feasible and spontaneous, endothermic, and classified as physisorption, advantageous for facilitating dysprosium desorption. From the reusability experiments, high efficiencies of adsorption (99%) and desorption (94%) were reached during five cycles, indicating the effective regeneration of the adsorbent and recovery of the adsorbate using a source of magnesium as eluent (magnesium nitrate hexahydrate solution). The characterization analyses corroborated the stability and the renewability of the adsorbent. Thus, the material shows a high adsorption capacity and an easy regeneration compared to other complex adsorbents, giving the vermiculite an expressive potential for future applications in rare earth metals recovery.

Keywords: adsorption, rare earth, recovery, dysprosium, vermiculite

⁷ Manuscript published in *Journal of the Taiwan Institute of Chemical Engineers* (2021). DOI: 10.1016/j.jtice.2021.08.022. Reprinted with the journal's permission (Appendix B.7).

8.1 INTRODUCTION

Dysprosium (Dy) is a heavy rare earth metal (REM), with atomic number 66 and relative atomic mass 162.5 that is extensively applied to the manufacturing of Nd-Fe-B permanent magnets to increase the resistance to demagnetization for uses in hybrid electric vehicles and wind turbines, being thus an essential resource to the development of the renewable energies field [1,2]. Because of their cost and criticality status, there is a great interest in the neodymium and dysprosium recovery from permanent magnets, mainly in regions without the possibility of mining activity [3]. The dysprosium recovery would also avoid environmental impacts generated by the primary production, such as exposition to radioactive metals, consumption of large water amounts, and strong acids in the mines [4,5]. Moreover, it will mitigate water resource contamination, which may further cause harmful effects on human health and aquatic organisms [6,7].

Adsorption and desorption processes have been proposed for the rare earth recovery as an alternative technology to concentrate and separate the metal using various adsorbent matrixes such as graphene oxide based adsorbents [8], brown macroalga [9], functionalized mesoporous silica [10], composite nanomaterials [11,12], polymer-based adsorbents [13]. However, some of these adsorbents have complex routes of synthesis, implying high costs of production, being necessary found abundant and available as a low-cost alternative material.

Rare earth metals have a high affinity to clay minerals due to their high cation exchange capacity, such that one of the primary types of REM deposits is the ion-adsorption clay [14–16]. Because of this affinity and the high availability of clay materials, the study of rare-earth adsorption on clay-based adsorbents has been gain attention [17–23]. Another advantage of using clay minerals is that they are generally inexpensive, easy to mine, and non-toxic, making them eco-friendly materials [24].

Vermiculite, a mica-type trioctahedral silicate clay mineral with a 2:1 layered structure (2 tetrahedral silica sheets: 1 octahedral alumina sheet) [25], presents physical-chemical properties that are very advantageous for the adsorption of metals. This mineral has high ion exchange capacity, which is a consequence of the permanent negative charge [26], the expanded form achieves high surface areas [27], and it is chemical inert, neutral to both alkali and acids, and is biologically resistant [28].

This work goals study the equilibrium isotherm and the thermodynamic of the dysprosium adsorption on vermiculite. Also, it aims to evaluate the reusability and recovery of

Dy through successive cycles of adsorption and desorption and the characterization of the adsorbent after the reuse by morphology, composition, crystalline structure, thermal behavior, and surface properties.

8.2 MATERIAL AND METHODS

8.2.1 Vermiculite performance in the rare earth adsorption

Vermiculite is an aluminum-iron-magnesium silicate, in which the expanded form is obtained industrially by a quick thermal treatment up to 900°C that vaporizes the water content in the interlayer and enlarges lamellar space [29]. Thus, to evaluate the effect of the expansion on the adsorption capacity of vermiculite for different lanthanides, a preliminary study of the adsorptive performance of raw vermiculite and expanded vermiculite (Brazil Minérios, S.A.) to uptake La, Ce, Nd, Yb, and Dy was accomplished. Detailed information can be found in Supplementary Material (Appendix A.6).

Equations 8.1 and 8.2 calculated the efficiency parameters such as adsorption capacity at equilibrium (q_e /mmol/g) and removal percentage (% R /%).

$$q_e = \frac{(C_0 - C_e)}{m} V \quad (8.1)$$

$$\%R = \frac{(C_0 - C)}{C_0} 100 \quad (8.2)$$

Where C_0 is the initial concentration, C_e is the concentration at equilibrium (mmol/L), V is the solution volume (L), and m is the adsorbent mass (g).

8.2.2 Equilibrium and thermodynamics

Isotherms of adsorption, q_e (adsorption capacity (mmol/g) at the equilibrium) versus C_e (adsorbate concentration (mmol/L)), were obtained at different temperatures (25, 35, and 45 °C). Erlenmeyer vessels (100 mL) containing dysprosium solutions (50 mL), with initial concentrations from 1.0 to 12.0 mmol/L, and the expanded vermiculite (0.64 g) were mixed for 24 hours in an incubated shaker (Jeio Tech), at 200 rpm, with pH= 3.5 controlled by the addition of HNO₃ (0.1 mol/L) drops. After the adsorption process, the solid was separated by filtration using syringe filters (Chromafil Xtra PES-20/25), and the filtered was submitted to the AAS

analysis to determine the dysprosium concentration. These conditions were defined in previous work [30].

The Isotherm models of Langmuir [31] and Brunauer, Emmet, and Teller (BET) for solid-liquid systems [32–34] were fitted to the data using the non-linear fitting procedure using the Origin 8.0 software, in which the respective mathematical relations are expressed by Equation 8.3 and 8.4, respectively.

$$q_e = \frac{q_m K_L C_e}{1 + (K_L C_e)} \quad (8.3)$$

K_L (L/mmol) is the Langmuir constant, q_m is the maximum adsorption capacity of the monolayer (mmol/g) predicted by Langmuir.

The BET model is considered a particular form of the Langmuir model. It has the same assumptions of the Langmuir model regarding the homogeneity and saturation of a first layer by adding other simplified assumptions about multilayer formation. The first layer has different energy from the other layers that each other have the same adsorption energy [35].

$$q_e = \frac{q_{BET} K_{BET} C_e}{(1 - K_u C_e)(1 - K_u C_e + K_{BET} C_e)} \quad (8.4)$$

Where q_{BET} is the adsorption capacity of the first layer (mmol/g), K_{BET} is the equilibrium constant of adsorption for the first layer (L/mmol), and K_u is the equilibrium constant of adsorption for upper layers (L/mmol).

Gibbs adsorption energy (ΔG_{ads}^o) was calculated by Van't Hoff (1884) relation (Equation 8.5).

$$\Delta G_{ads}^o = -RT \ln K_e = \Delta H_{ads}^o - T \Delta S_{ads}^o \quad (8.5)$$

Where T is the temperature (K), R is the ideal gas constant (8.314 J/mol K), K_e is the equilibrium constant, ΔH_{ads}^o and ΔS_{ads}^o are the adsorption enthalpy and entropy.

K_e was determined considering the coefficient of activity of dysprosium at equilibrium (γ_e) and the Langmuir constant [19,37–39]. ΔH_{ads}^o and ΔS_{ads}^o can be estimated, respectively, through the angular and linear coefficients of the slope $\ln K_e$ versus $1/T$ (Equation 8.6).

$$\ln K_e = \frac{-\Delta H_{ads}^o}{RT} + \frac{\Delta S_{ads}^o}{R} \quad (8.6)$$

8.2.3 Desorption

Five cycles of adsorption and desorption were carried out to evaluate the recovery of dysprosium and the reusability of the vermiculite. In the adsorption experiments, a dysprosium solution of 1 mmol/L was mixed with the adsorbent (12.8 g/L) for 1 hour at 200 rpm. The desorption, instead, occurred at the best conditions of eluent concentration (0.2 mol/L), solid/ratio (14 g/L), and contact time (3 hours). The experiment occurred at room temperature (25°C). The eluent solution was prepared by dissolution of magnesium nitrate hexahydrate (Dinâmica, 99%) in deionized water, a source of Mg^{2+} , the principal exchangeable cation in the ion exchange mechanism of vermiculite [40]. The parameters of the desorption performance were de capacity of elution q_{el} (mmol/g) (Equation 8.7) and %D (%) (Equation 8.8).

$$q_{el} = \frac{C_f}{m} V \quad (8.7)$$

$$\%D = \frac{q_{el}}{q} 100 \quad (8.8)$$

8.2.4 Dysprosium concentration measuring

The solutions of dysprosium were prepared from the dilution of a stock solution, in which 5.00 g of dysprosium(III) pentahydrate nitrate (Sigma Aldrich, 99.9% trace metals basis) was dissolved in 100 mL of acidified water ($pH \cong 5.0$) with the addition of few drops of nitric acid (0.1 mol/L). The measuring of the dysprosium concentration was performed through atomic absorption spectroscopy (ASS) (Shimadzu, AA7000), in which the detection range is 2 to 20 ppm.

8.2.5 Adsorbent characterization

The virgin adsorbent was already characterized in other studies [18,19]. In our work, the regenerated adsorbent (Verm-Reg), i.e., the solid sample collected after the cycles of reuses, was characterized. Images and the semi-quantitative composition of the samples were observed by scanning electron microscopy and energy dispersive X-ray spectrometry (SEM-EDS) (LEO

440i, LEO). X-ray diffraction analysis was performed in the equipment Philips Analytical X-Ray (X'Pert-MPD). Thermogravimetric and differential thermal analyses used the DTG-60 (Shimadzu), using a 50 mL/min gas flow rate with a rate of 20 °C/min and an inert atmosphere. The isotherm of adsorption and desorption of nitrogen was constructed using the surface area analyzer ANOVA-e (Quantachrome).

8.3 RESULTS AND DISCUSSION

8.3.1 Vermiculite performance in the rare earth adsorption

The knowledge of the lanthanides (Ln (III)) intra-series separation tendency is an essential factor in the investigation of an alternative adsorbent for the rare earth metals recovery [11,12]. Based on that, Figure 8.1 indicates La, Ce, Nd, Yb, and Dy adsorption using raw vermiculite (RV) and expanded vermiculite (EV) as adsorbents. Expanded vermiculite presented an average performance of 26.1% higher than RV, showing that the expansion process effectively improved the adsorption capacity of the material due to the improvement of surface area and porosity and consequently augmented the availability of active sites for adsorption [25].

Both materials removed REM following the order $Yb > Dy > Nd > Ce > La$. Thus, these clay minerals retain more heavy rare earth metals (Yb and Dy) than light ones (La, Ce, and Nd). Despite the higher adsorption of Yb (0.32 mmol/g or 54.9 mg/g), dysprosium (0.31 mmol/g or 50.2 mg/g) was chosen to the study equilibrium, thermodynamic, and reusability on expanded vermiculite because Dy has been cited as a critical and strategic material for many countries [41–43] due to the involvement to the development of clean energies. Also, the relevant findings of reusability of vermiculite in the Nd adsorption [19] also motivate the study of Dy behavior since they can be found together from end-of-life permanent magnets as a source for urban mining activity.

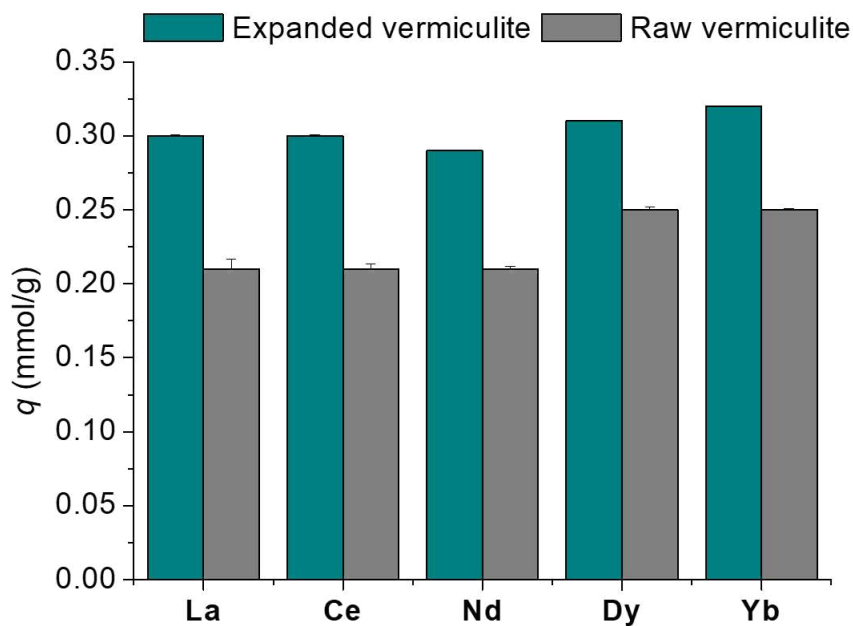


Figure 8.1. Vermiculite performance in the rare earth adsorption.

8.3.2 Equilibrium and thermodynamics

Figure 8.2 groups the adsorption isotherms of dysprosium on expanded vermiculite for the three temperatures. According to Figure 8.2(a), the shape of the curves in the first region of the graphs, until $C_e \sim 3$ mmol/L, indicates that, as more adsorption sites are occupied by dysprosium as hard for the adsorptive find available sites. The presence of a semi-flat region, located in the middle of the graphs, means that a saturation condition is beginning to occur associated with forming an adsorption monolayer. However, since the end of the curve rises again, it demonstrates a renewed availability of adsorption sites [44].

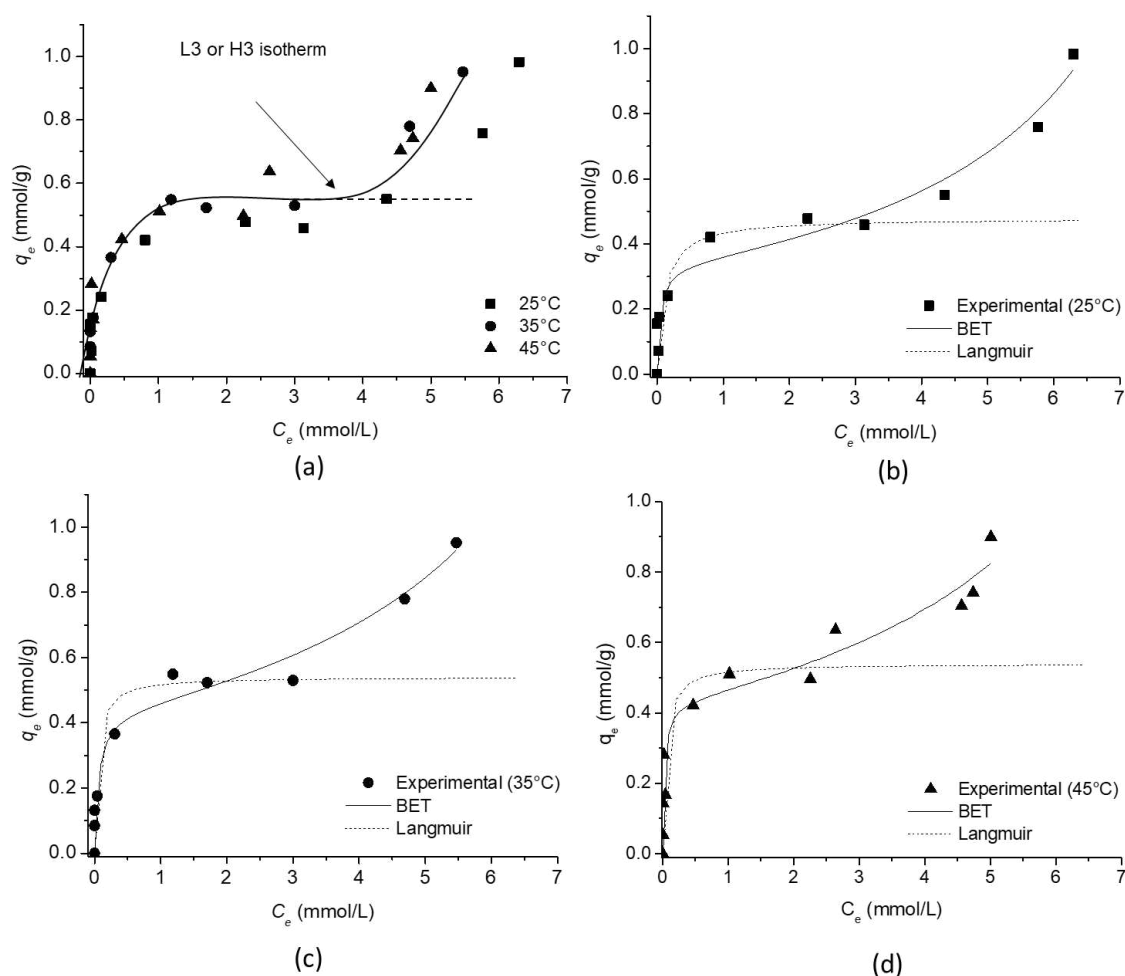


Figure 8.2. Isotherms at 25, 35, and 45°C and theoretical L3/H3 isotherm shape (a). The plot of BET and Langmuir fit the equilibrium isotherms for each temperature 25°C (b), 35°C (c), and 45°C (d).

The shape of the isotherms of Figure 8.2(a) can be considered as Langmuir (L3) or high affinity (H3) types from Giles classification [45]. Langmuir isotherm indicates that the adsorption occurs due to relatively weak forces, such as van der Waals forces, and the H type indicates adsorption by electrostatic forces or chemisorption. In turn, subclass 3 is related to the formation of multilayers [45]. The maximum experimental values of q_e were 0.98, 0.95, and 0.90 mmol/g for the highest initial concentration (12 mmol/L) for the temperatures of 25, 35, and 45°C.

The isotherms L3 and H3 are satisfactorily represented by the BET model, an extension of the Langmuir model for monolayer adsorption to multilayer adsorption [34]. Figure 8.2(b), Figure 8.2(c), and Figure 8.2(d) show the experimental points of the isotherms, and the BET

and Langmuir fitting for the temperatures of 25, 35, and 45°C, in which the parameters from the isotherms adjustment is presented in Table 8.1.

Table 8.1. Parameters of the isotherm models.

Models	Parameters	Temperature (°C)		
		25	35	45
BET	q_{BET} (mmol/g)	0.34	0.44	0.43
	K_{BET} (L/mmol)	22.45	17.35	41.51
	K_u (L/mmol)	0.102	0.097	0.096
	R^2	0.9535	0.9573	0.9328
Langmuir *	q_m (mmol/g)	0.48	0.56	0.54
	K_L (L/mmol)	9.35	8.81	21.42
	R^2	0.8730	0.9173	0.8390
Experimental q_e (mmol/g) **		0.45	0.53	0.50

* For $C_e < 3$ mmol/L

** Semi-flat region

The model BET fitted adequately to the equilibrium data ($R^2 > 0.93$), as expected due to the shape of the curves, in which the amount adsorbed in the first saturated layer (q_{BET}) was 0.34, 0.44, and 0.43 mmol/L, for the temperatures of 25, 35 and 45°C, respectively. The K_{BET} for each temperature was 22.45, 17.35, and 41.51 L/mmol, and K_u was ~ 0.1 L/mmol for all temperatures. The Langmuir parameters obtained by the model's fit to the points until the $C_e \sim 3$ mmol/L, q_m , and K_L were 0.48, 0.56, 0.54 mmol/g, and 9.35, 8.81, 21.42 L/mmol, for T= 25, 35 and 45°C. The q_m from Langmuir is closer to the experimental values obtained by the flat region of the curves than the q_{BET} . For both models, the equilibrium constants for 25 and 35 °C had similar values. They increased significantly for the temperature of 45 °C, which corroborates the initial curve shapes of the isotherms for 25 and 35 °C that are L3 type and for 45 as a high-affinity type (H3).

Considering the coincident assumptions of BET and Langmuir models, the adsorption of dysprosium on expanded vermiculite can be deemed localized over a homogeneous surface,

in which the lateral interaction is neglected. In addition, according to the multilayer approach of the BET isotherm, more than one dysprosium ion can be adsorbed in the same site with different affinities, one on top of the other [33]. The mechanism of adsorption of metals on vermiculite is the ion exchange with light metals from the interlayer space, inner and outer-sphere complexation, and surface precipitation [46]. The sorption of neodymium, a heavy rare-earth metal, on vermiculite occurs mainly by an ion-exchange mechanism, and the saturation forms a monolayer on the surface [18,19]. However, in the adsorption of dysprosium on expanded vermiculite, surface precipitation at high concentrations explains the multilayer formation, where a precipitated layer covers the adsorbed layer [47,48]. These results show that, in competitive adsorption from a multimetal solution, selective sorption can occur depending on the metal of interest affinity to the clay surface or the precipitate surface, blocking or increasing the adsorption of other metals [49].

Through a thermodynamic analysis (Table 8.2), the process is feasible and spontaneous ($\Delta G_{ads}^o < 0$), endothermic ($\Delta H_{ads}^o > 0$), and increases the disorder degree ($\Delta S_{ads}^o > 0$) [50]. Similar endothermic behavior and sigmoidal isotherms were found in the exchange of calcium and potassium in vermiculite [51]. $\Delta H_{ads}^o = 47.1$ kJ/mol is slightly higher than the range of the ion exchange heat (40 kJ/mol), and in the field of the physisorption process ($\Delta H_{ads}^o < 80$ kJ/mol) [52].

Table 8.2. Thermodynamic parameters for the dysprosium adsorption on expanded vermiculite.

Temperature (K)	ΔG_{ads}^o (kJ/mol)	ΔH_{ads}^o (kJ/mol)	ΔS_{ads}^o (kJ/molK)	R^2
298	-28.3			
308	-30.8	47.1	0.242	0.9964
318	-33.1			

8.3.3 Desorption

According to Figure 8.3, vermiculite did not lose the original adsorption efficiency (% $R \sim 99\%$) along to the cycles, indicating that the desorption process using magnesium did not cause damages to the material, allowing the regeneration and reusability. The desorption efficiency floated around an average desorption percentage of 94.6 % during the cycles. Moreover, the desorption process was able to concentrate the dysprosium content in solution around 1.16 times.

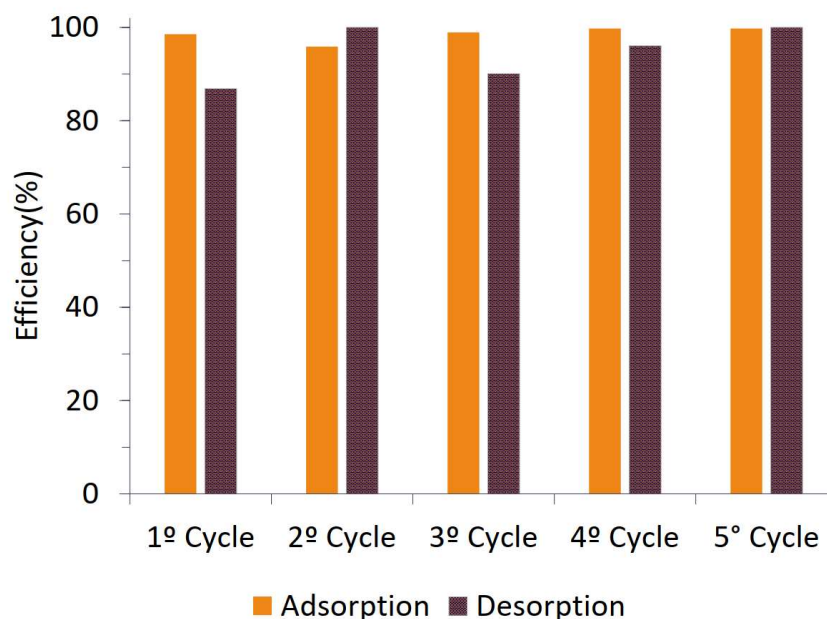


Figure 8.3. Cycles of adsorption and desorption of dysprosium on expanded vermiculite

Regeneration and reusability of the adsorbent are criteria that directly influence the cost-effectiveness of the sorption process [53–56]. Compared to other works from the literature (Table 8.3), this work achieved excellent results in both adsorption and desorption processes, differently from others that focused on the regeneration approach or the desorption efficiency, not on both criteria.

Confronting the adsorption capacity of each adsorbent, the polyurethane sponge supported graphene oxide–titanium phosphate [13] reached the highest q (0.61 mmol/g) after four cycles of reuse; however, compared to the original material, there was a reduction of 76% in the adsorption capacity, while the Dy adsorption on expanded vermiculite maintained constant along of the five cycles. The stability of the material over the cycles brings advantages in economic terms [57], even more for a non-expensive material as the expanded vermiculite, which the average price is \$0.85/kg [58].

Evaluating the desorption performances, engineered adsorbents such as functionalized alumina-silica composite [12], magnetic calcium alginate nanocomposite [59], carboxyl-functionalized mesoporous silica [60] maintained high desorption rates along with five cycles ($\%R > 91\%$); however, vermiculite also performed with high efficiency, from 87% at first cycle to 100% at the fifth. Thus, despite being a simply adsorbent matrix, expanded vermiculite shows expressive potential for successive cycles without loss of efficiency. However, regarding selectivity, engineered and functionalized adsorbents presented advantages due to the insertion

of specific ligands able to separate rare-earth metals from each other since this group of metals is known for similar physical-chemical proprieties, which difficult their purification.

Thus, vermiculite has advantages such as stability, high adsorption capacity at the saturation, high desorption rates even after successive cycles. However, further studies should be performed to verify the selectivity of the vermiculite towards Dy, especially from a mix of rare-earth metals. Also, the insertion of organic ligands should be investigated to improve the selectivity of vermiculite [10,11,61] to develop the full potential of the vermiculite for a scale-up study.

Table 8.3. Comparison of performance of different adsorbents.

Adsorbent	Adsorption Experimental condition	q (mmol/g)	Eluent	Desorption Experimental condition	%D (%)	Reference
Amorphous Zirconium Phosphate	$m_{ads} = 5$ g/L; ternary system (10 mM Co, Dy, Nd)	-	H ₂ SO ₄ (1 mol/L)	S/L = 5 g/L; t = 3 days	83	[62]
Octadecyl methacrylate grafted onto nonwoven fabrics	$m_{ads} = 0.17$ g/L; binary system (Dy 0.62 mM, Nd 0.69 mM); pH = 2.0	0.160 (1 st) 0.155 (2 nd)	HCl (1 mol/L)	V = 50 mL; t = 60 min; T = 298K; 150 rpm	-	[63]
Polyurethane sponge-supported graphene oxide–titanium phosphate	$m_{ads} = 0.1$ g/L; $C_{Dy} = 0.31$ mM	2.50 (1 st) 0.610 (4 th)	HCl (1 mol/L)	V = 10 mL; t = 1 h	-	[13]
Functionalized alumina-silica composite	$m_{ads} = 5$ g/L; $C_{Dy} = 5$ mM; pH = 5.0	-	HNO ₃ (0.3 mol/L)	V = 5 mL; t = 20 min	~100 (1 st) 91% (5 th)	[12]
Magnetic calcium alginate nanocomposite	Ternary system (30 mg/L Dy, Tb, Nd)	-	HNO ₃ (0.2 mol/L)	V = 50 mL; t = 2 h; 180 rpm	96.9 (1 st) 93.6 (5 th)	[59]
Carboxyl-functionalized mesoporous silica	$m_{ads} = 0.2$ g/L; $C_{Dy} = 0.06$ mM; t = 2 h; pH = 1.75	-	HNO ₃ (1 mol/L)	V = 12.5 mL; t = 2 h	~100 (1 st - 5 th)	[60]
Ion imprinted macroporous chitosan membrane	-	~0.140 (1 st) 0.128 (5 th)	HCl (1 mol/L)	48 h	-	[64]
Silica gel modified with diglycol amic acid	$m_{ads} = 10$ g/L; t = 24 h	-	HNO ₃ (1 mol/L)	-	100%	[65]
Ionic imprinted mesoporous bilayer films	Binary system (Nd and Dy); pH = 4.0	*14% (1 st) 15% (5 th)	HCl (1:9 v/v)	One step at 313K, and another at 298K	-	[66]
Expanded Vermiculite	$m_{ads} = 12.8$ g/L; $C_{Dy} = 1.0$ mM; pH = 3.5	0.086 (1 st) 0.087 (5 th)	Mg(NO ₃) ₂ ·6H ₂ O (0.2 mol/L)	S/L = 14 g/L; t = 3 h; 200 rpm; T = 298K	87 (1 st) 100 (5 th)	This work

*Removal percentage

~ Proximate values

8.3.4 Adsorbent characterization

Figure 8.4 (a) and Figure 8.4 (b) are the images of the regenerated adsorbent amplified 400 and 1,800 times, respectively. The original adsorbent, the expanded vermiculite, has large slit openings due to the thermal process that vaporizes the water in the interlayer, which confers a higher surface area and lower density than the raw material mineral [67]. According to Figure 8.4(a), the particle of the regenerated adsorbent has a flat shape, not more the “accordion” form, because the rehydration process compacted the vermiculite structure during the cycles of reuse. Indeed, Figure 8.4(b) shows the layers of the material that are significantly closer to each other.

Figure 8.4(c) presents the element composition of Verm-Reg, in which the silicon, aluminum, and iron contents in the vermiculite were kept along of the cyclic adsorption/desorption processes, compared to the original adsorbent composed by 21.80% of Si, 7.63% of Al, and 7.49% of Fe [18]. The magnesium content was augmented from 15.66% to 17.23% due to the excess of magnesium in the elution process. Thus, the composition of the material after the cycles indicated an effective regeneration and recovery of dysprosium that had an imperceptible content in the regenerated vermiculite composition.

The XRD pattern of the regenerated adsorbent (Figure 8.4(d)) has the 002 reflection at 6.2 degrees of 14.3 \AA , according to Bragg's Law [68], indicating that the interlayer space still presents bihydrated layers of water molecular [69]. The material slightly increased the basal space compared to the virgin adsorbent that showed a 002 reflection of 14.1 \AA [19]. The typical growing intensities of the 004, 006, 008, and 0010 reflections of the vermiculite were also observed in the diffractogram [70]. Thus, the vermiculite maintained its crystalline structure after the cycles of reuse.

The weight loss of the vermiculite due to the temperature increase was around 16.6 % in the range of 28 to 1100 °C (Figure 8.4(e)). Until 110 °C occurs, the dehydration of the surface water, after that the water molecules surrounding the magnesium interlayer cations were extracted until ~ 450 °C [70], the water loss corresponds to 69.2% of the total weight loss. The dehydroxylation reaction caused permanent decomposition of vermiculite structure and started at 450 °C and was completed at ~950 °C [71]. Regarding the DTA analysis, endothermic peaks at 100 and 200°C are evident, related to the two steps of water loss mentioned above. The endothermic peak at 850 °C is associated with the formation of new crystalline phases, and the exothermic peak at 950 °C is related to the enstatite $((\text{Mg}, \text{Fe})_2\text{Si}_2\text{O}_6)$ formation [72]. This thermal behavior was also observed for the

expanded vermiculite samples [19], which indicates that the material maintained structural stability even after several adsorption and desorption processes.

According to Figure 8.4(f), the nitrogen isotherm of adsorption and desorption of Verm-Reg, the shape of the isotherm presents the typical hysteresis of clay materials that are non-rigid aggregates of plate particles, having pores in the form of slits [73,74]. Expanded vermiculite, the original adsorbent, presented the same isotherm shape [19]. The hysteresis loop means slits in the mesopores range, and the absence of a plateau at high P/P_0 also indicates macropores in the structure [73].

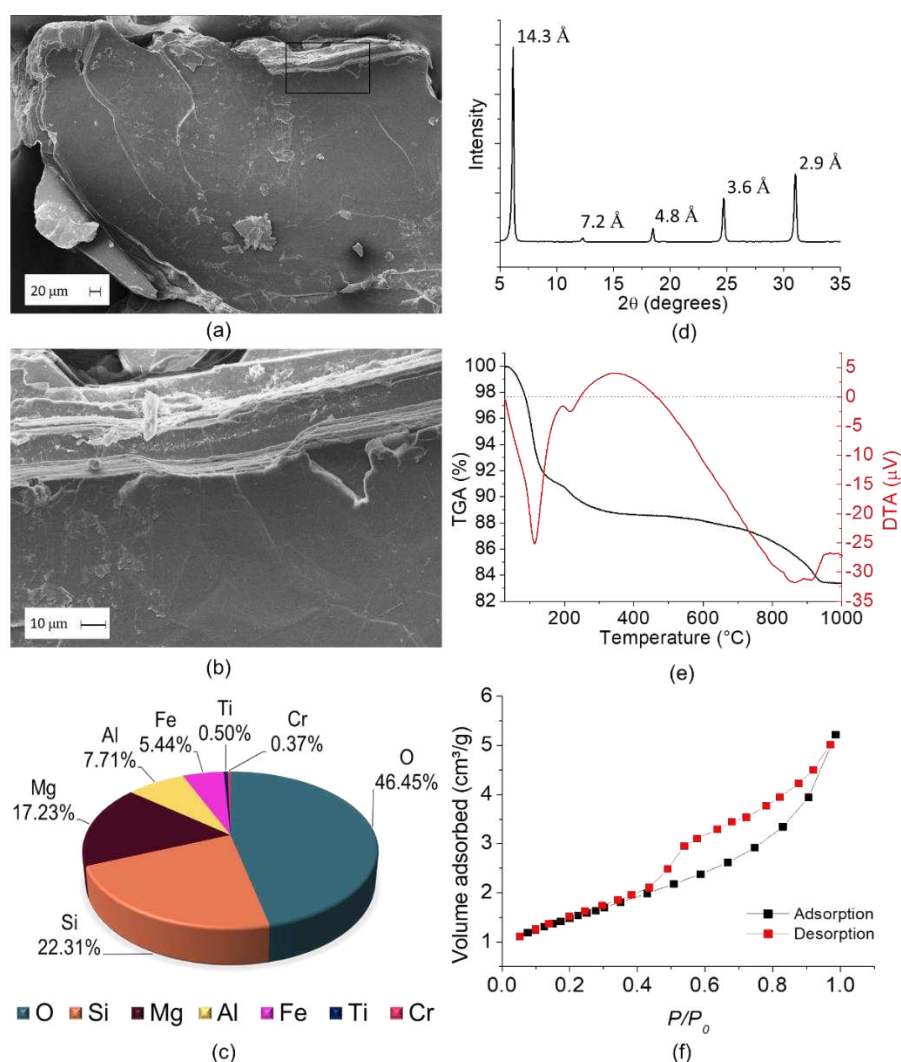


Figure 8.4. Characterization of the regenerated adsorbent: SEM images of the regenerated adsorbent (a, b); semi-quantitative composition from EDS (c); X-ray diffractogram (d); and thermogravimetric analysis (TGA/DTA) (e); Nitrogen isotherm of adsorption and desorption (f).

8.4 CONCLUSION

Expanded vermiculite, an available and cost-effective mineral, was successfully used to recover dysprosium from an aqueous solution. The adsorbent achieved high adsorption capacities, in which the maximum q_e was 0.98 mmol/g at 25°C. The isotherms presented a sigmoidal shape well represented by the multilayer BET model, indicating the formation of a homogeneous first layer and posterior precipitation of the metal over that. The thermodynamic analysis revealed that the adsorption process is endothermic with physical nature. The weak bindings energy between adsorbent-adsorbate allowed to reach desorption efficiencies around 94.6 % during five reuse cycles, which is comparable to the efficiency of other more complex matrices such as functionalized adsorbents. The characterization analyses of SEM-EDS, XRD, DTG/DTA, and N₂ adsorption and desorption indicated that the material lost part of the original expansion and was completed regenerated (no Dy content), maintained the crystalline structure, thermal stability, and meso/macroporosity. Thus, the expanded vermiculite presents advantages as simplicity, high efficiency, and stability; and future selectivity investigations should be investigated to evaluate this promisor alternative adsorbent in the rare earth elements wastewater treatment.

FUNDING

This work was supported by São Paulo Research Foundation/FAPESP (Grant # 2017/18236-1 and Grant # 2019/11353-8). Brazilian National Council for Scientific and Technological Development/CNPq (Grant # 308046/2019-6 and Grant # 147606/2018-7), and Coordination for the Improvement of Higher Education Personnel/CAPES (Financial code 001).

ACKNOWLEDGMENTS

The authors thank Brasil Minérios S.A. for providing the adsorbent material.

REFERENCES

- [1] Dent PC. Rare earth elements and permanent magnets (invited). J Appl Phys 2012;111:1–7. <https://doi.org/10.1063/1.3676616>.

- [2] Ni'am AC, Wang Y-F, Chen S-W, You S-J. Recovery of rare earth elements from waste permanent magnet (WPMs) via selective leaching using the Taguchi method. *J Taiwan Inst Chem Eng* 2019;97:137–45. <https://doi.org/10.1016/j.jtice.2019.01.006>.
- [3] Smith Stegen K. Heavy rare earths, permanent magnets, and renewable energies: An imminent crisis. *Energy Policy* 2015;79:1–8. <https://doi.org/10.1016/j.enpol.2014.12.015>.
- [4] Jha MK, Kumari A, Panda R, Rajesh Kumar J, Yoo K, Lee JY. Review on hydrometallurgical recovery of rare earth metals. *Hydrometallurgy* 2016;165:2–26. <https://doi.org/10.1016/j.hydromet.2016.01.035>.
- [5] Balaram V. Rare earth elements: A review of applications, occurrence, exploration, analysis, recycling, and environmental impact. *Geosci Front* 2019;10:1285–303. <https://doi.org/10.1016/j.gsf.2018.12.005>.
- [6] Malhotra N, Hsu H, Liang S, Roldan MJM, Lee J, Ger T, et al. An Updated Review of Toxicity Effect of the Rare Earth Elements (REEs) on Aquatic Organisms. *Animals* 2020;10:1663. <https://doi.org/10.3390/ani10091663>.
- [7] Rim KT, Koo KH, Park JS. Toxicological evaluations of rare earths and their health impacts to workers: A literature review. *Saf Health Work* 2013;4:12–26. <https://doi.org/10.5491/SHAW.2013.4.1.12>.
- [8] Xu X, Jiang X-Y, Jiao F-P, Chen X-Q, Yu J-G. Tunable assembly of porous three-dimensional graphene oxide-corn zein composites with strong mechanical properties for adsorption of rare earth elements. *J Taiwan Inst Chem Eng* 2018;85:106–14. <https://doi.org/10.1016/j.jtice.2017.12.024>.
- [9] Vijayaraghavan K, Rangabhashiyam S, Ashokkumar T, Arockiaraj J. Assessment of samarium biosorption from aqueous solution by brown macroalga *Turbinaria conoides*. *J Taiwan Inst Chem Eng* 2017;74:113–20. <https://doi.org/10.1016/j.jtice.2017.02.003>.
- [10] Kubra KT, Salman MS, Hasan MN, Islam A, Teo SH, Hasan MM, et al. Sustainable detection and capturing of cerium(III) using ligand embedded solid-state conjugate adsorbent. *J Mol Liq* 2021;338:116667. <https://doi.org/10.1016/j.molliq.2021.116667>.
- [11] Rahman MM, Awual MR, Asiri AM. Preparation and evaluation of composite hybrid nanomaterials for rare-earth elements separation and recovery. *Sep Purif Technol* 2020;253:117515. <https://doi.org/10.1016/j.seppur.2020.117515>.
- [12] Awual MR, Alharthi NH, Okamoto Y, Karim MR, Halim ME, Hasan MM, et al. Ligand field

- effect for Dysprosium(III) and Lutetium(III) adsorption and EXAFS coordination with novel composite nanomaterials. *Chem Eng J* 2017;320:427–35. <https://doi.org/10.1016/j.cej.2017.03.075>.
- [13] Peng X, Mo S, Li R, Li J, Tian C, Liu W, et al. Effective removal of the rare earth element dysprosium from wastewater with polyurethane sponge-supported graphene oxide–titanium phosphate. *Environ Chem Lett* 2021;19:719–28. <https://doi.org/10.1007/s10311-020-01073-y>.
- [14] Borst AM, Smith MP, Finch AA, Estrade G, Villanova-de-Benavent C, Nason P, et al. Adsorption of rare earth elements in regolith-hosted clay deposits. *Nat Commun* 2020;11:4386. <https://doi.org/10.1038/s41467-020-17801-5>.
- [15] Chen Z, Zhang Z, Liu D, Chi X, Chen W, Chi R. Swelling of clay minerals during the leaching process of weathered crust elution-deposited rare earth ores by magnesium salts. *Powder Technol* 2020;367:889–900. <https://doi.org/10.1016/j.powtec.2020.04.008>.
- [16] Alshameri A, Wei X, Wang H, Fuguo Y, Chen X, He H, et al. A Review of the Role of Natural Clay Minerals as Effective Adsorbents and an Alternative Source of Minerals. *Minerals*, IntechOpen; 2019. <https://doi.org/10.5772/intechopen.87260>.
- [17] Feng X, Onel O, Council-Troche M, Noble A, Yoon RH, Morris JR. A study of rare earth ion-adsorption clays: The speciation of rare earth elements on kaolinite at basic pH. *Appl Clay Sci* 2021;201:105920. <https://doi.org/10.1016/j.clay.2020.105920>.
- [18] Brião G de V, da Silva MGC, Vieira MGA. Efficient and Selective Adsorption of Neodymium on Expanded Vermiculite. *Ind Eng Chem Res* 2021;acs.iecr.0c05979. <https://doi.org/10.1021/acs.iecr.0c05979>.
- [19] Brião G de V, Silva MGC da, Vieira MGA. Neodymium recovery from aqueous solution through adsorption/desorption onto expanded vermiculite. *Appl Clay Sci* 2020;198:105825. <https://doi.org/10.1016/j.clay.2020.105825>.
- [20] Iannicelli-Zubiani EM, Cristiani C, Dotelli G, Gallo Stampino P, Pelosato R, Mesto E, et al. Use of natural clays as sorbent materials for rare earth ions: Materials characterization and set up of the operative parameters. *Waste Manag* 2015;46:546–56. <https://doi.org/10.1016/j.wasman.2015.09.017>.
- [21] Xiao Y, Huang L, Long Z, Feng Z, Wang L. Adsorption ability of rare earth elements on clay minerals and its practical performance. *J Rare Earths* 2016;34:543–8.

- [https://doi.org/10.1016/S1002-0721\(16\)60060-1](https://doi.org/10.1016/S1002-0721(16)60060-1).
- [22] Cristiani C, Bellotto M, Dotelli G, Latorrata S, Ramis G, Gallo Stampino P, et al. Rare Earths (La, Y, and Nd) Adsorption Behaviour towards Mineral Clays and Organoclays: Monoionic and Trionic Solutions. *Minerals* 2020;11:30. <https://doi.org/10.3390/min11010030>.
 - [23] Qiu T, Qiu S, Wu H, Yan H, Li X, Zhou X. Adsorption of hydrated $[Y(OH)_2]^+$ on kaolinite (001) surface: Insight from DFT simulation. *Powder Technol* 2021;387:80–7. <https://doi.org/10.1016/j.powtec.2021.04.003>.
 - [24] Otunola BO, Ololade OO. A review on the application of clay minerals as heavy metal adsorbents for remediation purposes. *Environ Technol Innov* 2020;18:100692. <https://doi.org/10.1016/j.eti.2020.100692>.
 - [25] Wang A, Wang W. Vermiculite nanomaterials: Structure, properties, and potential applications. *Nanomater. from Clay Miner. A New Approach to Green Funct. Mater.*, Elsevier Inc.; 2019, p. 415–84. <https://doi.org/10.1016/B978-0-12-814533-3.00009-0>.
 - [26] dos Anjos VE, Rohwedder JR, Cadore S, Abate G, Grassi MT. Montmorillonite and vermiculite as solid phases for the preconcentration of trace elements in natural waters: Adsorption and desorption studies of As, Ba, Cu, Cd, Co, Cr, Mn, Ni, Pb, Sr, V, and Zn. *Appl Clay Sci* 2014;99:289–96. <https://doi.org/10.1016/j.clay.2014.07.013>.
 - [27] Długosz O, Banach M. Sorption of Ag^+ and Cu^{2+} by Vermiculite in a Fixed-Bed Column: Design, Process Optimization and Dynamics Investigations. *Appl Sci* 2018;8:2221. <https://doi.org/10.3390/app8112221>.
 - [28] Stawiński W, Freitas O, Chmielarz L, Węgrzyn A, Komędera K, Błachowski A, et al. The influence of acid treatments over vermiculite based material as adsorbent for cationic textile dyestuffs. *Chemosphere* 2016;153:115–29. <https://doi.org/10.1016/j.chemosphere.2016.03.004>.
 - [29] Bleam WF. *Soil and Environmental Chemistry*. 2nd editio. Elsevier; 2017. <https://doi.org/10.1016/C2015-0-01022-X>.
 - [30] Brião G de V, Silva TL da, Silva MGC da, Vieira MGA. Response surface methodology approach for optimization of dysprosium adsorption onto expanded vermiculite. In: Azevedo DCS de, Bastos-Neto M, editors. 13th Brazillian Meet. Adsorpt., Imprensa Universitaria; 2021, p. 492–7. <https://doi.org/10.51996/9786588492529>.
 - [31] Langmuir I. The Adsorption of Gases on Plane Surfaces of Glass Mic and Platinum. *J Am*

- Chemical Soc 1918;40:1361–403.
- [32] Brunauer S, Emmett PH, Teller E. Adsorption of Gases in Multimolecular Layers. *J Am Chem Soc* 1938;60:309–19. <https://doi.org/10.1021/ja01269a023>.
 - [33] Ebadi A, Soltan Mohammadzadeh JS, Khudiev A. What is the correct form of BET isotherm for modeling liquid phase adsorption? *Adsorption* 2009;15:65–73. <https://doi.org/10.1007/s10450-009-9151-3>.
 - [34] Piccin JS, Cadaval TRS, de Pinto LAA, Dotto GL. Adsorption Isotherms in Liquid Phase: Experimental, Modeling, and Interpretations. In: Bonilla-Petriciolet A, Mendoza-Castillo DI, Reynel-Ávila HE, editors. *Adsorpt. Process. Water Treat. Purif.*, vol. 45, Cham: Springer International Publishing; 2017, p. 19–51. https://doi.org/10.1007/978-3-319-58136-1_2.
 - [35] Al-Ghouti MA, Da'ana DA. Guidelines for the use and interpretation of adsorption isotherm models: A review. *J Hazard Mater* 2020;393:122383. <https://doi.org/10.1016/j.jhazmat.2020.122383>.
 - [36] Van't Hoff JH. *Etudes de dynamique chimique*. Amsterdam: Frederik Muller; 1884.
 - [37] Ghosal PS, Gupta AK. Determination of thermodynamic parameters from Langmuir isotherm constant-revisited. *J Mol Liq* 2017;225:137–46. <https://doi.org/10.1016/j.molliq.2016.11.058>.
 - [38] Lima EC, Hosseini-Bandegharai A, Moreno-Piraján JC, Anastopoulos I. A critical review of the estimation of the thermodynamic parameters on adsorption equilibria. Wrong use of equilibrium constant in the Van't Hoof equation for calculation of thermodynamic parameters of adsorption. *J Mol Liq* 2019;273:425–34. <https://doi.org/10.1016/j.molliq.2018.10.048>.
 - [39] Liu Y. Is the Free Energy Change of Adsorption Correctly Calculated? *J Chem Eng Data* 2009;54:1981–5. <https://doi.org/10.1021/je800661q>.
 - [40] Seaborn DJ, Jameson GJ. Some ion exchange properties of exfoliated vermiculite. *Hydrometallurgy* 1976;2:141–55. [https://doi.org/10.1016/0304-386X\(76\)90024-4](https://doi.org/10.1016/0304-386X(76)90024-4).
 - [41] McNulty BA, Jowitt SM. Barriers to and uncertainties in understanding and quantifying global critical mineral and element supply. *IScience* 2021;24:102809. <https://doi.org/10.1016/j.isci.2021.102809>.
 - [42] Hayes SM, McCullough EA. Critical minerals: A review of elemental trends in comprehensive criticality studies. *Resour Policy* 2018;59:192–9. <https://doi.org/10.1016/j.resourpol.2018.06.015>.
 - [43] Jyothi RK, Thenepalli T, Ahn JW, Parhi PK, Chung KW, Lee J-Y. Review of rare earth

- elements recovery from secondary resources for clean energy technologies: Grand opportunities to create wealth from waste. *J Clean Prod* 2020;267:122048. <https://doi.org/10.1016/j.jclepro.2020.122048>.
- [44] Galamini G, Ferretti G, Medoro V, Tescaro N, Faccini B, Coltorti M. Isotherms, Kinetics, and Thermodynamics of NH_4^+ Adsorption in Raw Liquid Manure by Using Natural Chabazite Zeolite-Rich Tuff. *Water* 2020;12:2944. <https://doi.org/10.3390/w12102944>.
- [45] Giles CH, Macewan TH, Nakhwa SN, Smith D. Studies in Adsorption. Part XI.* A System of Classification of Solution Adsorption Isotherms, and its Use in Diagnosis of Adsorption Mechanisms and in Measurement of Specific Surface Areas of Solids. *J Chem Soc* 1960:3973–93.
- [46] Węgrzyn A, Chmielarz L, Zjezdzała P, Kowalczyk A, Jabłońska M, Baldrich Tolosa X, et al. Adsorbents for iron removal obtained from vermiculite. *Acta Geodyn Geomater* 2013;10:353–61. <https://doi.org/10.13168/AGG.2013.0034>.
- [47] David A. Dzombak FMMM. Surface Complexation Modeling: Hydrous Ferric Oxide Title. Wiley; 1990.
- [48] Li L, Stanforth R. Distinguishing adsorption and surface precipitation of phosphate on goethite ($\alpha\text{-FeOOH}$). *J Colloid Interface Sci* 2000;230:12–21. <https://doi.org/10.1006/jcis.2000.7072>.
- [49] Van Groeningen N, Glück B, Christl I, Kretzschmar R. Surface precipitation of Mn^{2+} on clay minerals enhances Cd^{2+} sorption under anoxic conditions. *Environ Sci Process Impacts* 2020;22:1654–65. <https://doi.org/10.1039/d0em00155d>.
- [50] Doke KM, Khan EM. Adsorption thermodynamics to clean up wastewater; critical review. *Rev Environ Sci Biotechnol* 2013;12:25–44. <https://doi.org/10.1007/s11157-012-9273-z>.
- [51] Inoue A. Thermodynamic study of Na-K-Ca exchange reactions in vermiculite. *Clays Clay Miner* 1984;32:311–9. <https://doi.org/10.1346/CCMN.1984.0320409>.
- [52] Inglezakis VJ, Zorpas AA. Heat of adsorption, adsorption energy and activation energy in adsorption and ion exchange systems. *Desalin Water Treat* 2012;39:149–57. <https://doi.org/10.1080/19443994.2012.669169>.
- [53] Awual R, Yaita T, Kobayashi T, Shiwaku H, Suzuki S. Journal of Environmental Chemical Engineering Improving cesium removal to clean-up the contaminated water using modified conjugate material. *J Environ Chem Eng* 2020;8:103684. <https://doi.org/10.1016/j.jece.2020.103684>.

- [54] Awual R, Hasan M. A ligand based innovative composite material for selective lead (II) capturing from wastewater. *J Mol Liq* 2019;294:111679. <https://doi.org/10.1016/j.molliq.2019.111679>.
- [55] Awual R, Hasan M, Islam A, Asiri AM, Rahman MM. Optimization of an innovative composited material for effective monitoring and removal of cobalt (II) from wastewater. *J Mol Liq* 2020;298:112035. <https://doi.org/10.1016/j.molliq.2019.112035>.
- [56] Awual R. Ring size dependent crown ether based mesoporous adsorbent for high cesium adsorption from wastewater. *Chem Eng J* 2016;303:539–46. <https://doi.org/10.1016/j.cej.2016.06.040>.
- [57] Costa TB da, Silva MGC da, Vieira MGA. Recovery of rare-earth metals from aqueous solutions by bio/adsorption using non-conventional materials: a review with recent studies and promising approaches in column applications. *J Rare Earths* 2020;38:339–55. <https://doi.org/10.1016/j.jre.2019.06.001>.
- [58] Tanner OA. Vermiculite. *US Geol. Surv. Miner. Yearb.*, Reston, VA: 2017. <https://doi.org/https://doi.org/10.3133/mybvl>.
- [59] Javadian H, Ruiz M, Taghvai M, Sastre AM. Novel magnetic nanocomposite of calcium alginate carrying poly(pyrimidine-thiophene-amide) as a novel green synthesized polyamide for adsorption study of neodymium, terbium, and dysprosium rare-earth ions. *Colloids Surfaces A Physicochem Eng Asp* 2020;603:125252. <https://doi.org/10.1016/j.colsurfa.2020.125252>.
- [60] Kaneko T, Nagata F, Kugimiya S, Kato K. Optimization of carboxyl-functionalized mesoporous silica for the selective adsorption of dysprosium. *J Environ Chem Eng* 2018;6:5090–8. <https://doi.org/10.1016/j.jece.2018.09.018>.
- [61] Awual MR, Hasan MM, Shahat A, Naushad M, Shiwaku H, Yaita T. Investigation of ligand immobilized nanocomposite adsorbent for efficient cerium(III) detection and recovery. *Chem Eng J* 2015;265:210–8. <https://doi.org/10.1016/j.cej.2014.12.052>.
- [62] Xu J, Koivula R, Zhang W, Wiikinkoski E, Hietala S, Harjula R. Separation of cobalt, neodymium and dysprosium using amorphous zirconium phosphate. *Hydrometallurgy* 2018;175:170–8. <https://doi.org/10.1016/j.hydromet.2017.11.010>.
- [63] Hoshina H, Chen J, Amada H, Seko N. Chain entanglement of 2-ethylhexyl hydrogen-2-ethylhexylphosphonate into methacrylate-grafted nonwoven fabrics for applications in

- separation and recovery of Dy (III) and Nd (III) from aqueous solution. *Polymers (Basel)* 2020;12:1–12. <https://doi.org/10.3390/polym12112656>.
- [64] Liu E, Xu X, Zheng X, Zhang F, Liu E, Li C. An ion imprinted macroporous chitosan membrane for efficiently selective adsorption of dysprosium. *Sep Purif Technol* 2017;189:288–95. <https://doi.org/10.1016/j.seppur.2017.06.079>.
- [65] Ogata T, Narita H, Tanaka M. Adsorption behavior of rare earth elements on silica gel modified with diglycol amic acid. *Hydrometallurgy* 2015;152:178–82. <https://doi.org/10.1016/j.hydromet.2015.01.005>.
- [66] Zheng X, Zhang Y, Zhang F, Li Z, Yan Y. Dual-template docking oriented ionic imprinted bilayer mesoporous films with efficient recovery of neodymium and dysprosium. *J Hazard Mater* 2018;353:496–504. <https://doi.org/10.1016/j.jhazmat.2018.04.022>.
- [67] Papadopoulos AP, Bar-TaL A, Silver A, Saha UK, Raviv M. Inorganic and Synthetic Organic Components of Soilless Culture and Potting Mixes. *Soil. Cult.*, Elsevier; 2008, p. 505–43. <https://doi.org/10.1016/B978-044452975-6.50014-9>.
- [68] Bragg WL. *The Crystalline State: Volume I*. New York: The Macmillan Company; 1934.
- [69] Ma L, Su X, Xi Y, Wei J, Liang X, Zhu J, et al. The structural change of vermiculite during dehydration processes: A real-time in-situ XRD method. *Appl Clay Sci* 2019;183:105332. <https://doi.org/10.1016/j.clay.2019.105332>.
- [70] Campos A, Moreno S, Molina R. Characterization of vermiculite by XRD and spectroscopic techniques. *Earth Sci Res J* 2009;13:108–18.
- [71] Udoudo O, Folorunso O, Dodds C, Kingman S, Ure A. Understanding the performance of a pilot vermiculite exfoliation system through process mineralogy. *Miner Eng* 2015;82:84–91. <https://doi.org/10.1016/j.mineng.2015.03.023>.
- [72] Tuchowska M, Wołowicz M, Solińska A, Kościelniak A, Bajda T. Organo-Modified Vermiculite: Preparation, Characterization, and Sorption of Arsenic Compounds. *Minerals* 2019;9:483. <https://doi.org/10.3390/min9080483>.
- [73] Kuila U, Prasad M. Specific surface area and pore-size distribution in clays and shales. *Geophys Prospect* 2013;61:341–62. <https://doi.org/10.1111/1365-2478.12028>.
- [74] Thommes M, Kaneko K, Neimark A V., Olivier JP, Rodriguez-Reinoso F, Rouquerol J, et al. Physisorption of gases, with special reference to the evaluation of surface area and pore size distribution (IUPAC Technical Report). *Pure Appl Chem* 2015;87:1051–69.

<https://doi.org/10.1515/pac-2014-1117>.

CHAPTER 9. DYSPROSIUM RECOVERY ON EXPANDED VERMICULITE: CONTINUOUS FIXED-BED ADSORPTION AND DESORPTION

Renewable and selective vermiculite fixed bed for the rare-earth dysprosium recovery⁸

Giani de Vargas Brião, Meuris Gurgel Carlos da Silva, Melissa Gurgel Adeodato Vieira

*University of Campinas, School of Chemical Engineering, Albert Einstein Avenue, 500, 13083-852
Campinas, Brazil*

ABSTRACT

Dysprosium recovery is essential for the sustainable development of clean energies. The present paper investigates the continuous adsorption and recovery of Dy from aqueous solutions using a fixed bed of expanded vermiculite. The study was divided into operational conditions optimizing, modeling, regeneration and reuse cycles, characterization of the regenerated adsorbent, and column selectivity analysis. Under the best conditions, high breakthrough (q_b) and equilibrium (q_e) capacities of 0.31 and 0.42 mmol/g were achieved. The Yan and DualSD models adjusted the data well and can be applied for future scale-up simulations. The fixed bed could operate efficiently, maintaining an average q_b of 0.31 mmol/g and q_e of 0.45 mmol/g over the five cycles. The spent adsorbent presented textural properties different from the original, indicating that the desorption steps did not completely regenerate the material. The selectivity towards dysprosium was confirmed since the removal of Dy (82%) was at least twice the adsorption efficiency of Pb (41.1%), Ni (35.7%), Cd, and Cu (~16.5%). Thus, the recovery of dysprosium using a fixed bed of expanded vermiculite is reproductive along with several uses. Also, the material has a natural selectivity with potential for further advancement of engineered adsorbents based on vermiculite.

Keywords: dysprosium, selectivity, adsorption, vermiculite, fixed bed.

⁸ Manuscript published in *Industrial & Engineering Chemistry Research* (2022).

DOI: 10.1021/acs.iecr.2c01265. Reprinted with the journal's permission (Appendix B.8).

9.1 INTRODUCTION

Human activities, as we know, are only possible due to technological development. Rare earth elements (REEs) are intrinsically related to high-tech applications and renewable energy ¹, i.e., REEs are fundamental for a sustainable future. Dysprosium, one of the most critical REEs, plays an essential role in the production of permanent magnets used in wind turbines, electric vehicles, and consumer electronic devices². Junne et al. ³ simulated distinct green energy scenarios up to 2050, where the maximum annual demand for primary dysprosium demand could exceed 7 to 35 times extraction volumes. Besides the relevance for clean energy development, a circular economy of REEs, including eco-design and urban mining, would be environmentally valuable to mitigate the impacts of primary production ⁴. Thus, recovery of dysprosium from secondary sources is necessary to ensure a maximum contribution of renewable energies to the global energy matrix in the future.

Hydrometallurgical routes used to process secondary wastes bearing REEs have lower production costs, lower waste generation, and lower liberation of harmful gases than other energy-intensive extraction processes like pyrometallurgical methods ⁵. Among the various hydrometallurgical approaches such as solvent extraction, solid-liquid extraction, adsorption, supported liquid membrane, ion exchange, and supercritical extraction methods, adsorption has gained attention due to its simplicity and high efficiency, and performance in diluted systems ⁶. Several studies have been carried out on the sorption of rare earth metals in batch mode, using different adsorbent materials such as clay minerals ⁷, graphene oxide-based materials ⁸, zeolites ⁹, and mesoporous silica ¹⁰. However, research on continuous adsorption on fixed bed is still much scarce ^{11–13}. Also, according to Costa et al.⁶, little attention has been given to regeneration in continuous fixed bed adsorption studies, which are essential for the simulation and prediction of the dynamic performance for further scale-up processes.

Clay minerals are low-cost and ecofriendly materials that present exclusive properties such as high capillarity, degree of swelling, and exceptional thermal and chemical stability, which favor the use in a wide range of applications, including environmental remediation ^{14,15}. Likewise, due to their excellent adsorption potential, clay-based adsorbents have a high regeneration capacity that also increases the sustainability of the process due to the possibility of reusing the adsorbent ¹⁶. Vermiculite, a natural clay mineral with a layered structure with two tetrahedral silica sheets fused to an edge shared octahedral sheet of magnesium, iron, or aluminum hydroxide ¹⁷, has been successfully

applied to the consecutive adsorption and desorption of dysprosium in batch mode¹⁸, which indicates the material's potential for the fixed bed continuous operation.

Thus, this paper aims to study the adsorption and desorption of dysprosium in a continuous operation in a fixed bed of vermiculite. The fluid dynamic and inlet concentration effect was investigated on column efficiency. Mathematical models were fitted to the data to obtain kinetic parameters and define the transfer mass mechanism. Successive cycles of adsorption and desorption were performed to investigate the bed's stability, and the regenerated material was characterized by thermal, structural, and physicochemical properties. Moreover, an adsorption and desorption experiment evaluated the selectivity for dysprosium from a multicomponent system.

9.2 MATERIALS AND METHODS

9.2.1 Adsorbate and adsorbent

A stock solution, 5.0 g of Dy(III)/100 mL of water, was made by dissolving dysprosium pentahydratenitrate (Sigma Aldrich, 99.9% trace metals basis) in deionized water at pH 5.0, prepared by the dripping of diluted HNO₃, and then diluted to the determined concentrations for the experiments. The metals concentration was measured by atomic absorption spectroscopy (Shimadzu, AA7000).

The adsorbent used in this study was the expanded vermiculite (Brasil Minérios, S.A). As received, the material was sieved, and the retained fraction between the sieves 16 and 24 mesh was used in the experiments ($d = 0.855$ mm).

9.2.2 Adsorption and desorption on continuous fixed bed

9.2.2.1 Column system

A glass column of 0.7 cm in inner diameter and 10 cm in height was filled with 0.40 g of adsorbent, forming a bed depth of 7 cm. A peristaltic pump (Masterflex L/S, Cole Parmer) ensured constant flow in the column in ascendant flux. At the exit of the column, an automatic collector FC203 (Gilson, Brazil) was attached to obtain aliquots at predetermined times. Before the adsorption experiments, the bed was washed with deionized water at a 3 mL/min flow rate for 30 min to remove air bubbles and avoid preferential paths in the column.

9.2.2.2 Fixed bed efficiency parameters

The parameters selected to evaluate the column efficiency are adsorption capacity (mmol/g), removal percentage R (%), and height of the mass transfer zone (H_{MTZ}) (Equations 9.1 to 9.5). The adsorption capacity and removal percentage were calculated up to the breakthrough point (q_b and R_b) when $C/C_0 = 0.05$, and the exhaustion point (q_e and R_e) when $C/C_0 = 0.95$.

$$q_b = \frac{C_0 Q}{1000m} \int_0^{t_b} \left(1 - \frac{C}{C_0}\right) dt \quad (9.1)$$

$$q_e = \frac{C_0 Q}{1000m} \int_0^{t_e} \left(1 - \frac{C}{C_0}\right) dt \quad (9.2)$$

$$R_b = \frac{q_b m}{C_0 Q t_b} 100 \quad (9.3)$$

$$R_e = \frac{q_e m}{C_0 Q t_e} 100 \quad (9.4)$$

$$H_{MTZ} = \left(1 - \frac{q_b}{q_e}\right)L \quad (9.5)$$

Where C_0 and C (mmol/L) are the inlet and outlet concentration of dysprosium; Q (ml/min) is the flow rate of the dysprosium solution; m (g) is the amount of adsorbent; t_b and t_e (min) are the breakthrough and exhaustion time, and L (cm) is the bed depth.

9.2.2.3 Fluid dynamic and inlet concentration effect

Experiments with three different flows (0.25, 0.5, and 1.0 mL/min) and concentrations (0.25, 0.5, and 1.0 mmol/L) were performed to comprehend the effect of these parameters on the breakthrough curves and the bed efficiencies and, thus, determine the best condition to fulfill the cyclic adsorption and desorption experiment.

Mathematical models were also fitted to the data to complement the analysis of the kinetic and transfer mass parameters. The empirical models of Thomas, Modified dose-response (MDR) model,

and Yoon-Nelson were adjusted to the data by nonlinear fitting using Origin 6.0 software (Table S.1, Appendix A.7)

Mass transfer-based models (Table S.2, Appendix A.7) were also fitted to the breakthrough curves through numerical solutions using Maple 17, such as the instantaneous local equilibrium (ILE) and the dual-site diffusion (DualSD). ILE and DualSD consider the solid/liquid equilibrium and the conservation of liquid and solid properties during adsorption. The original material balance for both models is represented by Equation 9.6.

$$\frac{\partial C}{\partial t} = D_a \frac{\partial^2 C}{\partial z^2} - u_i \frac{\partial C}{\partial z} - \frac{\rho_B}{\varepsilon} \frac{\partial q}{\partial t} \quad (9.6)$$

Where D_a (cm²/min) is the axial dispersion coefficient; u_i (cm/min) is the interstitial velocity; ρ_B (g/L) is the fixed bed density, and ε is the void fraction.

According to the premises of each model, the adsorption rate ($\partial q/\partial t$) can be changed using the Langmuir model ¹⁹ (Table S.2, Appendix A.7). ILE model presumes an instantaneous mass transfer between the phases and the equilibrium in each bed section. The DualSD model assumes that two specific active sites are involved in the adsorption processes, which means two distinct mass transfer resistances. More information about the ILE and DualSD models' numerical resolution is provided by Georgin et al. ²⁰ and de Andrade et al. ²¹.

The determination coefficient (R^2) and corrected Akaike information criterion (AIC_c) were the criteria of fit assessment ²².

9.2.2.4 Cycles of reuse

The renewability test applied the magnesium hexahydrate nitrate (0.2 mol/L)¹⁸ to recover Dy by ion-exchange mechanism. Five adsorption-desorption runs were accomplished to evaluate the dysprosium recovery and the fixed bed regeneration. A washing step with continuous feeding of deionized water for 30 minutes was done between the adsorption and elution runs. The elution capacity (q_D /mmol/g)) and efficiency ($Des/\%$) were defined by Equations 9.7 and 9.8.

$$q_D = \frac{Q}{m} \int_0^t C_D dt \quad (9.7)$$

$$Des = \frac{q_D}{q_e} 100 \quad (9.8)$$

C_D (mmol/L) is the adsorbate concentration in the eluent solution, and t (min) is time. Also, the maximum concentration factor (C_F) that indicates the times that the adsorbate was concentrated through the desorption process ²³ was calculated according to Equation 9.9. C_{max} (mmol/L) is the maximum concentration achieved in the elution process.

$$C_F = \frac{C_{max}}{C_0} \quad (9.9)$$

9.2.2.5 Dy selectivity from a multimetal solution

The performance of the expanded vermiculite fixed bed to treat a multicomponent solution containing dysprosium was analyzed to mimic a possible effluent containing dysprosium. The equimolar (0.1 mmol/L of each metal) multicomponent inlet solution was prepared by dissolving nickel, lead, cadmium, copper, and dysprosium hydrate nitrates (Sigma Aldrich 99.9% purity). The column operated in adsorption for 3600 min, was washed for 30 min, and then was regenerated.

9.2.3 Adsorbent characterization

Expanded vermiculite, a hydrated silicate magnesium, aluminum, and iron, is the adsorbent material employed in the column. It was characterized in previous studies ^{24,25} which showed some physical-chemical properties such as an interlayer space of 14.1 Å, a layered structure with a surface area of 9.88 m²/g, and elemental composition of Mg (15.7 %), Al (7.63 %), Si (21.8 %), Fe (7.49 %), O (45.9 %), and trace elements (1.48 %). In this study, the material was analyzed after five cycles of reuse. The adsorbent was collected from the column, washed with deionized water, and characterized to verify the influence of these successive cycles on the physicochemical properties of the material. Textural properties such as surface area, bulk, and real densities, were obtained by the surface area analyzer ANOVA-e (Quantachrome), mercury porosimetry (Auto Pore IV, Micromeritics), and Helium picnometry (Accupyc II 1340, Micromeritics), respectively. Fourier-transform infrared

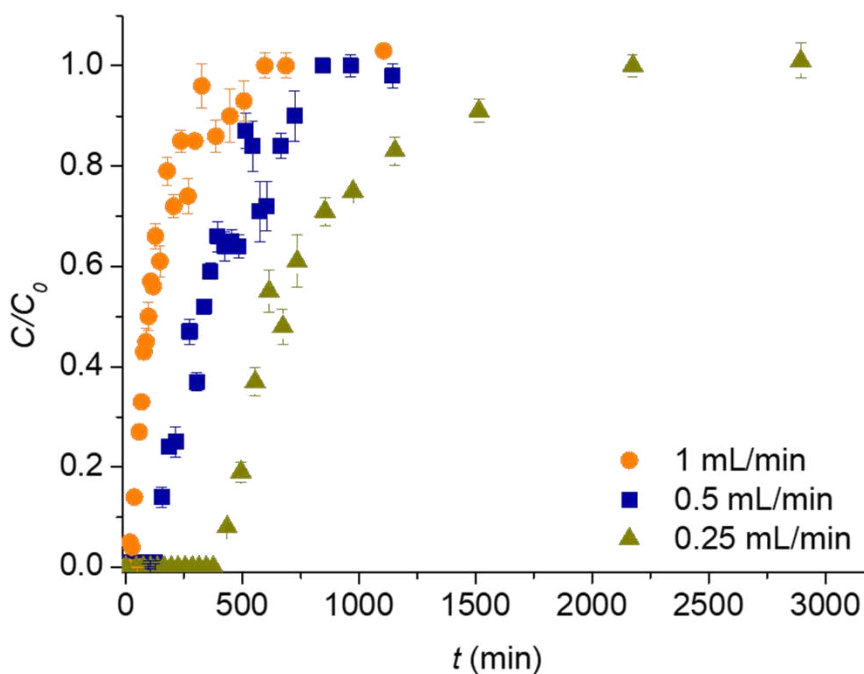
spectroscopy (FT-IR) verified chemical ligands and functional groups ranging from 4000 to 400 cm^{-1} with 4 cm^{-1} resolution in the spectrometer Nicolet 6700 (Thermo Scientific). Also, the zeta charge potential in function of the pH was measured using the SurPASS 2 (Anton Paar).

9.3 RESULTS AND DISCUSSION

9.3.1 Fluid dynamics and inlet concentration effect

The inlet solution flow rate through the column is intrinsically related to the adsorption performance. The longer the fluid and adsorbent contact time, the more significant interaction between solid and liquid, which favors the retention of the adsorbate. Figure 9.1 shows the breakthrough curves for the different flow rates studied. Note that as the flow rate increases, the breakthrough time is shorter, and, consequently, the bed exhaustion occurs earlier. Short breakthrough times may indicate low industrial applicability of the process because it implies more frequent column revitalizations and equipment downtime, which means higher operating costs ⁶. Thus, the flow rate that achieved the longest breakthrough time was 0.25 mL/min, and the efficiency parameters for each flow rate are presented in Table 9.1.

Figure 9.1. Fluid dynamic effect on breakthrough curves of the dysprosium fixed bed adsorption



Quantitatively, some of the best column efficiency indicators (Table 9.1), such as higher adsorption capacities (0.23 and 0.45 mmol/g), lower mass transfer zone height (3.33 cm), and higher removal percentage at the breakthrough (100%), were reached with the lowest flow rate. Thus, the optimal flow rate (0.25 ml/min) was settled for the rest of the experiments.

Table 9.1. Effect of flow rate on the efficiency of the dysprosium fixed bed adsorption

Q (mL/min)	C (mmol/L)	q_b (mmol/g)	q_e (mmol/g)	H_{MTZ} (cm)	R_b (%)	R_e (%)
1	1.0	0.04	0.36	6.14	98.3	24.2
0.5	1.0	0.16	0.45	4.60	99.7	43.0
0.25	1.0	0.23	0.45	3.33	100.0	32.9

Another critical factor associated with column efficiency is the concentration of the inlet solution. Adsorption is known to be efficient at low concentrations ⁶. Since the adsorbent has a maximum adsorption capacity, high adsorbate concentrations saturate the adsorbent quickly. Figure 9.2 shows the effect of the variation of the inlet concentration on the breakthrough curves, where the lowest C_0 (0.25 mmol/L) presented the most considerable breakthrough time. Nevertheless, Table 9.2 indicated that, at 0.25 mmol/L, the column showed efficiency parameters less favorable than those obtained at the concentration of 0.5 mmol/L, except for total column removal (R_e). Thus, due to the higher adsorption capacities (0.31 and 0.42 mmol/g) and the much lower height of the mass transfer zone (1.80 cm), the concentration of 0.5 mmol/L was determined as the optimal concentration to run the continuous adsorption of dysprosium on expanded vermiculite.

Figure 9.2. Effect of the inlet concentration on breakthrough curves of the dysprosium fixed bed adsorption

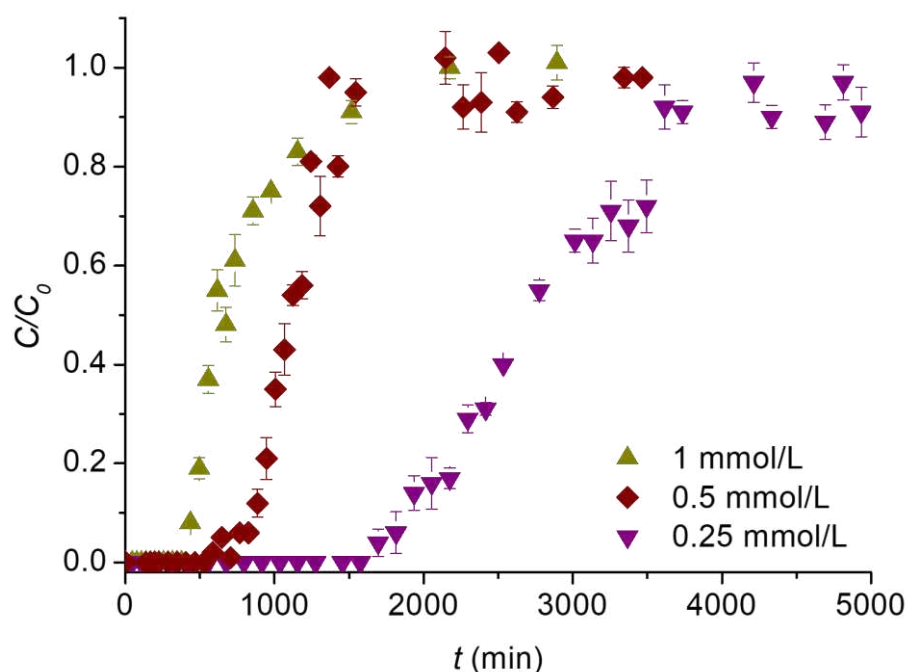


Table 9.2. Effect of C_0 on the efficiency of the dysprosium fixed bed adsorption

Q (mL/min)	C_0 (mmol/L)	q_b (mmol/g)	q_e (mmol/g)	H_{MTZ} (cm)	R_b (%)	R_e (%)
0.25	1.0	0.23	0.45	3.33	100.0	32.9
0.25	0.5	0.31	0.42	1.80	100.0	51.6
0.25	0.25	0.25	0.42	2.90	100.0	63.1

An adequate mathematical description of a dynamic fixed bed column system on small scales can reduce costs in the design fit into an industrial ladder if the models' parameters can sufficiently mimic the large-scale phenomenon. Thus, Table 9.3 shows the adjustment of the mathematical models of Thomas, Yan, and Yoon-Nelson to the experimental data.

Table 9.3. Empirical models fitting results.

Model	C_0 (mmol/L)	1.0	1.0	1.0	0.5	0.25
	Q (mL/min)	1.0	0.5	0.25	0.25	0.25
	q_e (mmol/g)	0.36	0.45	0.45	0.42	0.42
Thomas	k_{Th} (L/mmol.min)	0.02	0.01	0.01	0.012	0.01
	q_{Th} (mmol/g)	0.29	0.43	0.53	0.38	0.44
	R^2	0.9250	0.9574	0.9551	0.9872	0.9845
	AIC_c	-126.7	-165.0	-139.0	-202.6	-221.1

	a_Y (L/min.mmol)	1.95	2.57	3.52	8.19	5.72
Yan	q_Y (mmol/g)	0.26	0.41	0.53	0.35	0.43
	R^2	0.9688	0.9808	0.9760	0.9883	0.9879
	AIC_c	-151.3	-191.4	-157.1	-235.5	-204.5
	k_{YN} (min ⁻¹)	0.02	0.01	0.007	0.008	0.002
Yoon-Nelson	τ (min)	113.2	364.0	695.2	1,114.8	2787.0
	R^2	0.9250	0.9574	0.9551	0.9872	0.9845
	AIC_c	-126.7	-165.0	-139.0	-202.6	-221.1

The Thomas model is widely used to describe fixed bed adsorption. Analyzing the parameters of the Thomas model, through Table 9.3, the rate constant (k_{Th}) had a significant increase only with the increase in flow rate from 0.25 mL/min to 1 mL/min and remained practically constant with the variation of the concentration, at the fixed flow rate of 0.25 mL/min. The increase in flow rate causes decay of q_{Th} , and the concentration of 1 mmol/L returned the highest adsorption capacity (0.53 mmol/g), although it does not correspond to the experimental value (0.45 mmol/g). For the Yoon-Nelson model, the kinetic parameter (k_{YN}) increased as the flow rate and concentration improved. While the τ (min), time in which C/C_0 is 0.5, is enhanced with the decrease in flow and concentration, and it corresponded well to the experimental values. Thomas and Yoon-Nelson's models are mathematically analogous, so the goodness of fit was the same (exact values of the AIC_c and R^2). Despite the mathematical similarity, the two models have different assumptions, thus presenting different information about the system. This difference is confirmed when evaluating the kinetic constants of both models. As described, k_{Th} does not show such a strong correlation with the increase in flow, unlike k_{YN} exhibited a growth that accompanies this flow increase. Thomas and Yan's models decreased their estimated adsorption capacities (q_{Th} and q_Y), increasing inflow. Still investigating Yan's model, the model's constant (a_Y) showed a decreasing behavior when there was an increase in the flow rate in the column. Furthermore, when the flow rate was kept constant, the initial concentration of 0.5 mmol/L returned the highest constant (8.19). The a_Y decreased with the flow rate increase, and a defined tendency was not perceived when the concentration was varied.

The three models obtained the highest values for the respective constant parameter at the concentration of 0.5 mmol/L and flow rate of 0.25 mL/min, which corroborates with the higher efficiency parameters discussed in Table 9.2 at this condition. Also, it is noted that Yan's model exhibited the highest regression coefficient values and the lowest values for the Akaike criterion,

being the most suitable empirical model for predicting the behavior of the fixed bed column in the adsorption of dysprosium in expanded vermiculite.

Table 9.4 shows the adjustment of ILE and DualSD models to the data. The ILE model represents an ideal model in which just the axial dispersion is the dominant effect on the adsorption kinetic, i.e., without mass transfer resistance. This model did not obtain high correlation coefficients; however, the best fit achieved an R^2 of 0.9679 for the condition $Q = 0.25$ mL/min and $C_0 = 0.5$ mmol/L corroborates the best experimental condition. DualSD fitted better the data than ILE for all conditions. The DualSD model assumes that the system has two mass resistances, which leads to two mass transfer coefficients. The k_{s1} had the same order for all essays (10^{-3} 1/min). In turn, k_{s2} was 4.70×10^{-3} 1/min for the essays at 1 mmol/L, and it diminished until the 2.11×10^{-8} 1/min for the lowest concentration. The highest kinetic constant (6.47×10^{-3} 1/min) was achieved under the best conditions. The alpha values did not directly correspond to the fluid dynamics and inlet concentration changing, indicating that both adsorption sites were relevant to the process.

Table 9.4. Mass transfer models fitting results.

Model	C_0 (mmol/L)	1.0	1.0	1.0	0.5	0.25
	Q (mL/min)	1.0	0.5	0.25	0.25	0.25
	q_e (mmol/g)	0.36	0.45	0.45	0.42	0.42
DualSD	k_{s1} (min ⁻¹)	3.43×10^{-2}	5.53×10^{-3}	4.70×10^{-3}	6.47×10^{-3}	2.43×10^{-3}
	k_{s2} (min ⁻¹)	4.70×10^{-3}	4.70×10^{-3}	4.70×10^{-3}	4.58×10^{-4}	2.11×10^{-8}
	D_a (cm ² /min)	0.127	0.067	0.037	0.037	0.037
	α	0.277	1.000	0.999	0.908	1.000
	R^2	0.9719	0.9545	0.9621	0.9885	0.7008
	AIC_c	-148.9	-157.8	-138.7	-201.4	-107.6
	D_a (cm ² /min)	1.39×10^8	1.81×10^8	20.1	2.74	9.59×10^7
ILE	R^2	0.5895	0.8790	0.9376	0.9679	0.7240
	AIC_c	-79.07	-130.5	-129.5	-171.4	-115.6

9.3.2 Batch and fixed-bed equilibrium

The performance of an adsorbent depends on which adsorption mode of operation process is implemented ²⁶. Thus, the comparison between the adsorption equilibrium of dysprosium on expanded vermiculite in batch mode and fixed bed is discussed in this section.

The adsorption of dysprosium on expanded vermiculite in a batch mode at 25 °C occurred by the saturation of a first layer ($q_e \sim 0.45$ mmol/g) with subsequent surface precipitation that reached uptake capacities around of 0.9 mmol/g¹⁸. The experimental adsorption capacity of the first layer (0.45 mmol/g) agrees with the range of the saturation capacities (0.36 to 0.45 mmol/g) of the fixed bed, indicating that the formation of the multilayer by surface precipitation does not occur in continuous operation. The absence of surface precipitation may be related to the constant flow that makes the new layers weakly adhered to the first saturated layer²⁶.

The differences between the maximum adsorption capacities of the adsorbent in batch mode and fixed bed are due to the distinction between the type of equilibrium reached, static and dynamic, respectively. Ideally, under continuous flow, the H_{MTZ} moves through the bed, up or down, depending on the direction of the inlet flow, until it is completely saturated. However, mass transfer limitations and axial dispersion limit the degree of adsorbent utilization^{6,27}. These dynamic equilibrium properties in a fixed bed can cause the adsorption capacity to be lower than batch mode²⁷. However, in real production, the fixed bed operation generally allows the treatment of more significant amounts of effluent than batch mode, being the most applied adsorption mode of operation in the industry²⁸.

9.3.3 Cycles of reuse

The reusability and regeneration of the adsorbent is an operational criterion that defines the process feasibility. This study evaluated five cycles of adsorption and elution (Figure 9.3).

Figure 9.3. Cycles of dysprosium adsorption (a) and desorption (b)

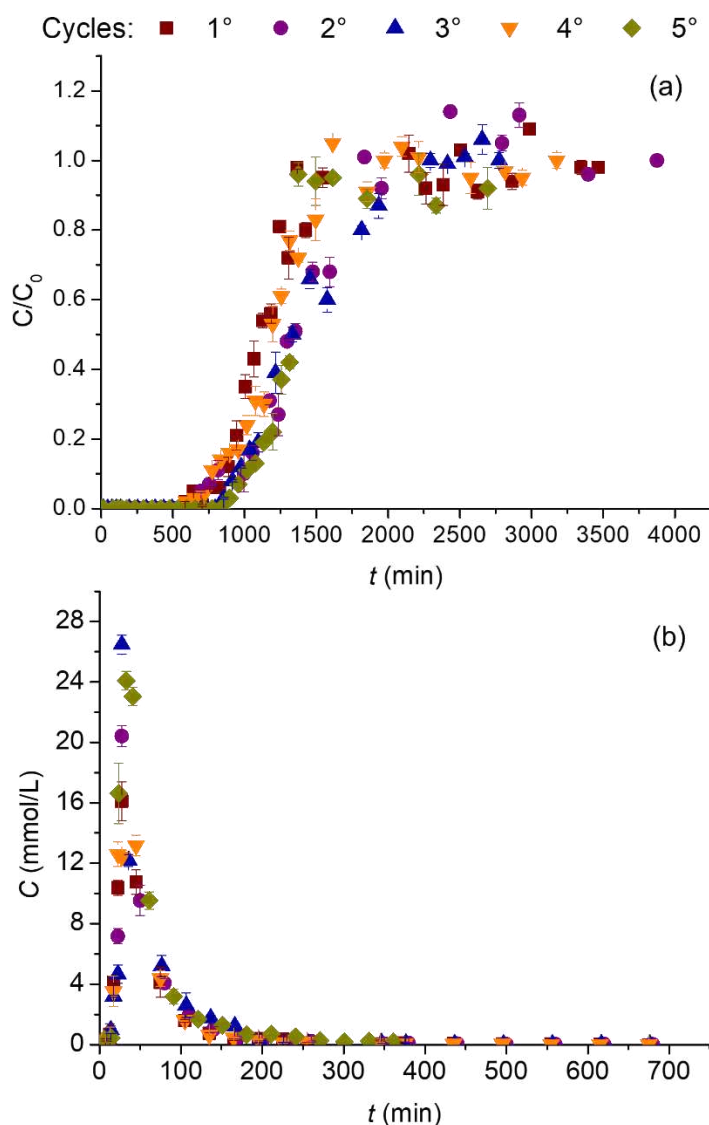


Figure 9.3 (a) reveals that the breakthrough time averaged 809 min ($13.5 \text{ h} \pm 1.1$) along with the cycles, which indicates that the bed efficiency was maintained. Figure 9.3 (b) reveals that the maximum elution occurred at 30 min in all the cycles, and concentrations around 26.5 mmol/L (maximum) were achieved, which means that the column could concentrate dysprosium effectively.

Table 9.5 expresses the quantitative analysis of the sorption cycles. The second cycle achieved the best adsorption capacity (0.53 mmol/g) at the point of exhaustion. However, the fifth cycle obtained the best set of values for the efficiency parameters. The height of the mass transfer zone, an essential parameter of column efficiency, reached the lowest value of 2.0 cm, and the total removal of the column was 91.2 %. The desorption efficiency of the five steps had an average of 94.7%. In the third desorption cycle, the maximum concentration of 26.5 mmol/L was obtained; thus, the metal

was concentrated 53.0 times. Therefore, these adsorption and desorption findings revealed that the dysprosium recovery process in an expanded vermiculite fixed bed is favorable for a possible scale-up due to the high reusability of the bed.

Table 9.5. Efficiency of the cyclic fixed bed sorption process.

Table 3.10: Efficiency of the cyclic fixed bed sorption process.							
Parameters		Cycle					Average \pm Deviation
		1°	2°	3°	4°	5°	
Adsorption	t_b (min)	825	695	855	775	895	809 ± 69
	t_e (min)	2145	1835	2295	1975	1375	1925 ± 316
	R_b (%)	100	97.8	99.9	98.9	99.9	99.3 ± 0.85
	R_e (%)	51.6	62.0	51.6	60.2	91.2	63.3 ± 14.6
	H_{MTZ} (cm)	1.8	2.8	2.0	2.5	2.0	2.21 ± 0.38
	q_b (mmol/g)	0.31	0.31	0.37	0.25	0.28	0.31 ± 0.04
	q_e (mmol/g)	0.42	0.53	0.52	0.39	0.40	0.45 ± 0.06
Desorption	q_D (mmol/g)	0.40	0.46	0.50	0.38	0.38	0.40 ± 0.05
	D (%)	97.4	88.3	96.3	97.7	94.0	94.7 ± 3.48
	C_{max} (mmol/L)	16.1	20.4	26.5	16.1	24.0	20.6 ± 4.15
	CF	32.2	40.8	53.0	32.2	48.0	41.2 ± 8.30

9.3.3.1 Adsorbent characterization after adsorption/desorption cycles

The textural properties of the original adsorbent (Verm) and the material after the reuse cycles (Verm-Reg) are shown in Table 9.6. The successive adsorption and desorption runs significantly modified some textural properties, such as the BET superficial area (S_{BET}), bulk density (ρ_{bulk}), and pore volume. The original adsorbent has an expanded form due to a thermal treatment up to 900°C, in which the steam abruptly expands in the interlayer spaces. This treatment provides a higher surface area and porosity than the compact material. The used vermiculite, which the interlayer rehydrated, lost part of the expansion that reduced the surface area to 5.297 m²/g. This recompacting diminished the volume of pores to 7.5 cm³/g, which increased the bulk density to 0.580 g/cm³ and the real density to 2.306 g/cm³, consequently reducing the void fraction (porosity ε_p).

Table 9.6. Comparison between the textural properties of the original (Verm) and the spent (Verm-Reg) adsorbent.

Samples	S_{BET} (m ² /g)	ρ (g/cm ³)	ρ_{bulk} (g/cm ³)	ε_p	Volume of pores (cm ³ /g)				Reference
					V_{micro}	V_{meso}	V_{macro}	V_{total}	
Verm	9.877	2.167	0.264	0.88	2.47	8.26	0.96	10.7	24,25
Verm-Reg	5.297	2.306	0.580	0.75	1.25	5.22	1.03	7.5	This work

Figure 9.4 shows the pore size distribution (a) and cumulative intruded volume (b) obtained from the mercury porosimetry analysis. Figure 9.4 (a) shows that Verm-Reg has no slits opening lower than 20 μm , and between 20 and 40 μm , there is a plateau indicating that the Hg filled homogeneously different slits sizes in this range. At 80 μm , there is a pronounced peak related to filling void spaces between particles (artificial slits) ^{29,30}. Figure 9.4 (b) demonstrates the mercury intrusion and extrusion behavior into the vermiculite. The mercury cumulative intruded volume was 1.03 mL/g, and the extruded one was 1.02 mL/g, which means a negligible hysteresis between filling and emptying as part of the mercury remains trapped in the material after the extrusion ³⁰. Hg porosimetry indicated the total macropores volume of the Verm-Reg of 1.03 mL/g (Table 9.6).

Figure 9.4. Slits size distribution (a) and cumulative intrusion of mercury (b) of Verm-Reg

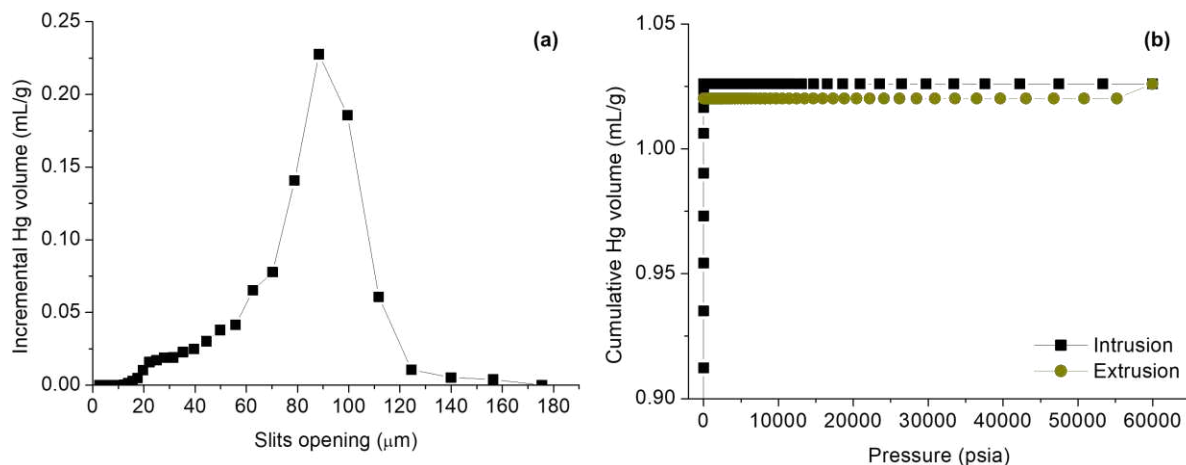
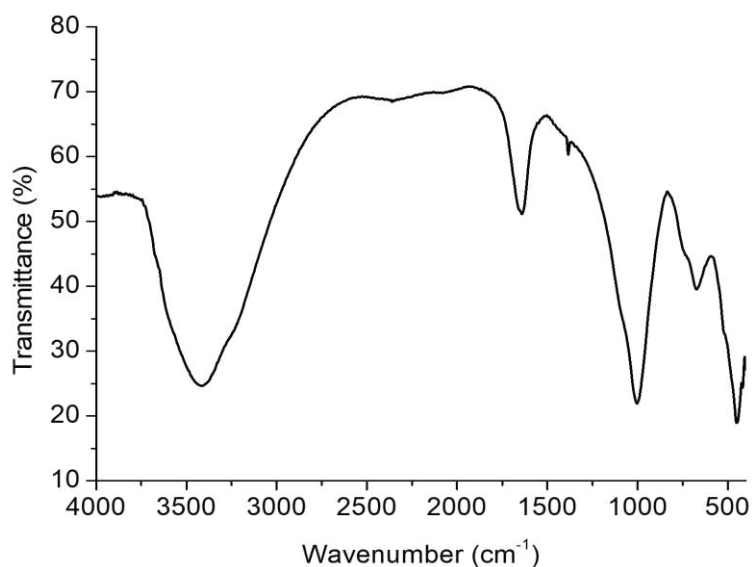


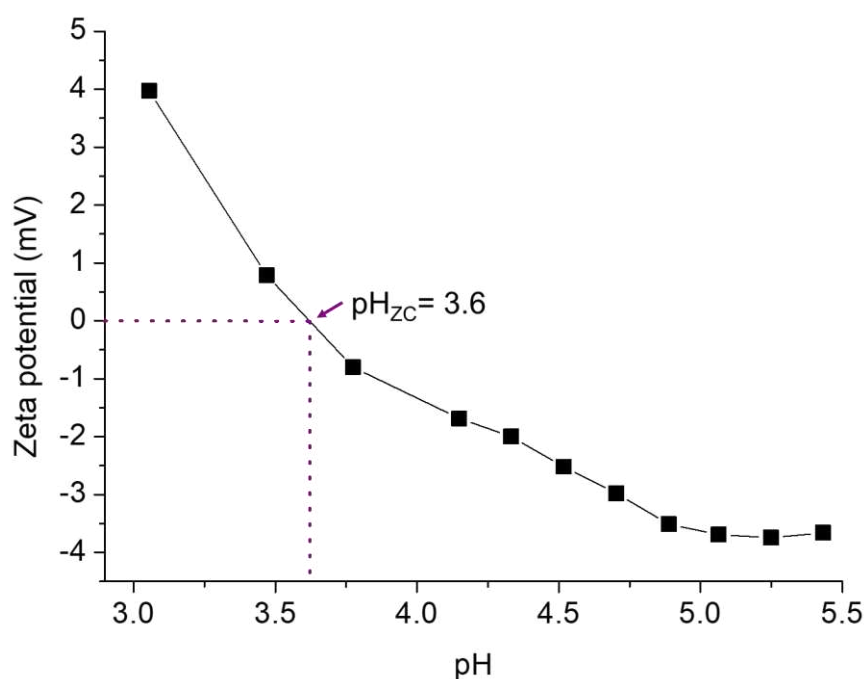
Figure 9.5 presents the FTIR spectra of the spent material that shows peaks referring to interlamellar water, 3400 cm^{-1} and 1630 cm^{-1} , OH stretching and bending vibrations, respectively, and bands located in the $1300\text{--}500\text{ cm}^{-1}$ range that reveals structural characteristics of clay minerals^{31,32}. The silicate characteristic bands are found at 999.5 cm^{-1} , representing Si-O's stretching vibrations, at 745 cm^{-1} indicating the Si-O-Si (Al) stretching, and at lower frequencies 522 and 459 cm^{-1} , meaning Si-O bending³³. At 675 cm^{-1} , the characteristic stretching vibration of the interlayer metal bond (M-O)³⁴ indicates that magnesium, the exchangeable cation of this expanded vermiculite²⁴, replaced dysprosium in the interlayer spaces maintaining the original vibrational characteristic of the M-O bonds.

Figure 9.5. Fourier transform infrared spectroscopy of the Verm-Reg



The surface charge plays a determinant role in sorption processes because it governs the electrostatic interactions in the overall sorption mechanism. Figure 9.6 demonstrates the zeta potential of the regenerated vermiculite as a function of the solution pH. For pH below 5.0, the surface continuously neutralizes the negative charge until zero at pH 3.6. For pH lower than the zero-charge point (pH_{ZC}), the positive charge increases significantly with the acidification of the media. The pH of zero charge of the vermiculite is reported as 2.5, and the negative charges for pH around 5.0 were -20 mV^{35,36}, i.e., the virgin material presents a much more negative surface than the Verm-Reg. The original negative charge of the vermiculite is due to the isomorphic substitution of Si^{4+} by Al^{3+} in the tetrahedral sheet, and magnesium is the interlayer hydrated cation that counterbalances the net charge^{37,38}. The desorption processes could not completely elute the dysprosium from the surface, and the residue may be responsible for neutralizing part of the original negative charge, leading to higher zeta potentials than the virgin adsorbent.

Figure 9.6. Verm-Reg zeta potential in function of the pH



Thus, the desorption using magnesium nitrate solution can regenerate the interlayer magnesium by exchanging the loaded Dy^{18} . However, the successive adsorption and desorption cycles changed the adsorbent's textural properties and the surface charge, indicating that the regeneration steps were

insufficient to avoid partial adsorbent deterioration, despite maintaining the high adsorption and desorption efficiencies.

9.3.4 Selectivity

Selectivity is a keyword in the rare earth recovery field since the rare earth metals on secondary sources are usually mixed with numerous other metals and contaminants ³⁹. This study evaluated the adsorption and desorption of dysprosium from a mix of heavy and base metals solution in a continuous mode to simulate an actual application. Figure 9.7 shows the breakthrough (a) and the desorption (b) curves of the five metals. The inlet concentration of each of them was 0.1 mmol/L, totalizing 0.5 mmol/L of metals in solution.

Figure 9.7 (a) shows the competition between the metals for the sorption sites, revealed by the overshooting ⁴⁰. Also, it is explicit that the column had a higher affinity for dysprosium since the outlet relative concentrations (C/C_0) was the lowest. The adsorption mechanism of the vermiculite is controlled by the exchange with the magnesium cations in the interlayer space. Thus, in Figure 9.7 (a), all ions were removed from the inlet solution until 325 min, and no competition occurred because all metals exchanged with the Mg^{2+} ^{41,42}. When the time increased, the breakthrough happened for cadmium (325 min), nickel (465 min), copper and dysprosium (585 min), and lead (825 min). At 825 min, there was a release peak of copper and lead and a lower dysprosium amount in the outlet solution, which indicates the competition between those cations for the vacancy sites. In terms of exhaustion ($C/C_0 = 0.95$), the column was saturated first by copper at 1750 min, followed by cadmium at 2250 min, nickel at 2500 min, and lead at 2800 min; after that, there was the progressive overshooting of these metals that were substituted by dysprosium on the sorption sites. From 2700 to the end of the experiment (~ 3600 min), the column was able to remove 100% of the dysprosium ($C/C_0 \sim 0$).

Figure 9.7 (b) is the concentration of each metal on the eluate. The elution peak occurs at 27 min for Dy, Ni, Pb, and 37 min for Cd and Cu. The concentrations achieved 1.1, 3.8, 3.0, 2.3, 5.6 mmol/L for Pb, Ni, Cd, Cu, and Dy, respectively, indicating that the process can concentrate Dy more than 50 times ($C_0 = 0.1$ mmol/L). Table 9.7 summarizes the efficiency parameters for each metal in the adsorption and desorption processes.

Figure 9.7. Multimetal adsorption (a) and desorption (b) on expanded vermiculite fixed bed

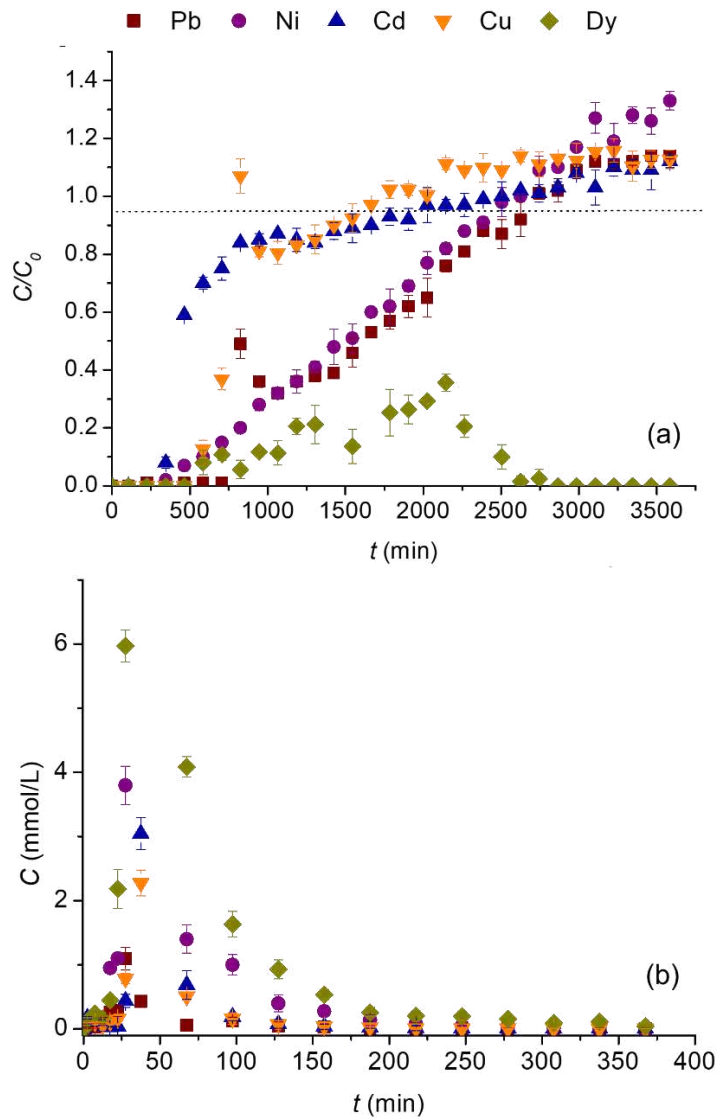


Table 9.7. Efficiency indicators for the multimetal adsorption and desorption on expanded vermiculite fixed bed

Parameters		Metal				
		Dy	Pb	Ni	Cd	Cu
Adsorption	q_e (mmol/g)	0.195	0.092	0.086	0.074	0.059
	R_e (%)	82.1	41.1	35.7	16.5	16.4
	q_eDy/q_eM	-	2.1	2.3	2.6	3.3
Desorption	q_D (mmol/g)	0.192	0.019	0.086	0.061	0.049
	Des (%)	98.3	20.1	100.0	82.3	82.8
	q_DDy/q_DM	-	10.3	2.2	3.1	3.9

The vermiculite adsorbed the metals in the follow downward order: Dy (0.195 mmol/g, 82.1%) > Pb (0.092 mmol/g, 41.1%) > Ni (0.086 mmol/g, 35.7%) > Cd (0.074, 16.5%) > Cu (0.059 mmol/g, 16.4%). In a previous study in batch mode ⁴³, the same affinity order was justified by: the stronger electrostatic attraction between dysprosium trivalent charge and the negative vermiculite surface; the hydration energy ascendant order of the divalent cations Pb^{2+} , Cd^{2+} , Cu^{2+} ⁴⁴, in which lower hydration energies means easier loss of coordinated water and consecutive adsorption ⁴⁵; and exceptionally for Ni, the equivalent hydrated ionic ratio to the Mg^{2+} , 0.72 Å, the most important interlayer exchangeable cation ^{45,46}. The adsorption capacity of Dy on the column was, at maximum, 3.3 times higher than the other metals (M), which confirms the clear preferability for dysprosium.

The eluent could desorb the metals in the follow order: Dy (0.192 mmol/g), Ni (0.086 mmol/g), Cd (0.061 mmol/g), Cu (0.049 mmol/g), and Pb (0.019 mmol/g). The eluent agent was the magnesium container solution that promoted the regeneration of the interlayers. It was expected that the most adsorbed metals were the most desorbed. Withal, lead does not follow this hypothesis. That occurs because the metals were adsorbed on the surface by different mechanisms. The magnesium could replace more efficiently the cations attached to the surface by weak bonds or electrostatic forces. So, Dy that was adsorbed preferable by electrostatic interactions ⁴³ and nickel, retained by the easier magnesium replacement, were practically totally desorbed. Moreover, lead, which possibly was fixed to the vermiculite by inner-sphere complexes (stronger interaction) due to the facilitated loss of coordinated water discussed above, was held by the solid material after the elution process. Thus, the ratio between the desorption capacity of Dy (last line of Table 9.7) was higher as the adsorbent/metal interaction was stronger, indicating that the eluate solution could concentrate dysprosium selectivity depending directly on the adsorption mechanism of the other metals in solution.

Therefore, the vermiculite adsorbs trivalent and divalent cations by different mechanisms determined by charge, hydration energy, and ionic radii. These interactions (inner sphere or out sphere) contribute to the desorption efficiency of each metal and consequently the Dy enrichment on the final solution. Regardless of this selective adsorption mechanism over the bivalent metals, the selectivity of the vermiculite still must be enhanced to reach higher dysprosium or REE separation efficiency since rare earth metals have similar ionic properties. Functionalization, formation of composites, and other physicochemical treatments can be alternatives to augment the original selectivity of the vermiculite towards the REE recovery from multicomponent solutions.

9.4 CONCLUSION

This study applied the expanded vermiculite to recover dysprosium from aqueous solutions in a dynamic fixed bed adsorption process. The flow rate (Q) and the inlet concentration (C_0) had an essential effect on the bed efficiency, and the lowest mass transfer resistance was found and confirmed by the modeling, at $Q = 0.25$ mL/min and $C_0 = 0.5$ mmol/L. The empirical model of Yan and the mass transfer model of DualSD were the most recommended to represent the breakthrough curves of the Dy adsorption. The reusability experiment indicated that the material maintained an average adsorption capacity of 0.31 ± 0.04 mmol/g (breakthrough) and 0.45 ± 0.06 mmol/g (exhaustion), and a mean desorption capacity of 0.40 ± 0.05 mmol/g, the low deviation indicated that the material could repeat the initial efficiency over the cycles. The characterization analyses of the spent material showed that the exchange of the loaded dysprosium by magnesium could regenerate the interlayer cations, and the material presented the same characteristic structural groups. Nevertheless, the textural properties and zeta potential changed significantly.

The selectivity towards dysprosium from a multicomponent solution containing heavy and base metals was confirmed due to each metal's specific mechanism of adsorption, related to their charge, ionic radii, and hydration energies. Thus, vermiculite is an advantageous material for dysprosium recovery by a fixed bed operation regarding the efficiency, reusability, and natural selectivity; nonetheless, the last still needs to be upgraded to achieve optimal dysprosium or rare earth separation efficiency in further studies.

FUNDING

This work was supported by São Paulo Research Foundation/FAPESP (Grant # 2017/18236-1 and Grant # 2019/11353-8), Brazilian National Council for Scientific and Technological Development/CNPq (Grant # 308046/2019-6 and Grant # 147606/2018-7), and Coordination for the Improvement of Higher Education Personnel/CAPES (Financial code 001).

ACKNOWLEDGMENTS

The authors thank Brasil Minérios S.A. for providing the adsorbent material.

REFERENCES

- (1) Opare, E. O.; Struhs, E.; Mirkouei, A. A Comparative State-of-Technology Review and Future Directions for Rare Earth Element Separation. *Renew. Sustain. Energy Rev.* 2021, 143 (March), 110917. <https://doi.org/10.1016/j.rser.2021.110917>.
- (2) Akcil, A.; Ibrahim, Y. A.; Meshram, P.; Panda, S.; Abhilash. Hydrometallurgical Recycling Strategies for Recovery of Rare Earth Elements from Consumer Electronic Scraps: A Review. *J. Chem. Technol. Biotechnol.* 2021, 96 (7), 1785–1797. <https://doi.org/10.1002/jctb.6739>.
- (3) Junne, T.; Wulff, N.; Breyer, C.; Naegler, T. Critical Materials in Global Low-Carbon Energy Scenarios: The Case for Neodymium, Dysprosium, Lithium, and Cobalt. *Energy* 2020, 211, 118532. <https://doi.org/10.1016/j.energy.2020.118532>.
- (4) Dang, D. H.; Thompson, K. A.; Ma, L.; Nguyen, H. Q.; Luu, S. T.; Duong, M. T. N.; Kernaghan, A. Toward the Circular Economy of Rare Earth Elements: A Review of Abundance, Extraction, Applications, and Environmental Impacts. *Arch. Environ. Contam. Toxicol.* 2021, 81 (4), 521–530. <https://doi.org/10.1007/s00244-021-00867-7>.
- (5) Jyothi, R. K.; Thenepalli, T.; Ahn, J. W.; Parhi, P. K.; Chung, K. W.; Lee, J. Y. Review of Rare Earth Elements Recovery from Secondary Resources for Clean Energy Technologies: Grand Opportunities to Create Wealth from Waste. *J. Clean. Prod.* 2020, 267, 122048. <https://doi.org/10.1016/j.jclepro.2020.122048>.
- (6) Costa, T. B. da; Silva, M. G. C. da; Vieira, M. G. A. Recovery of Rare-Earth Metals from Aqueous Solutions by Bio/Adsorption Using Non-Conventional Materials: A Review with Recent Studies and Promising Approaches in Column Applications. *J. Rare Earths* 2020, 38 (4), 339–355. <https://doi.org/10.1016/j.jre.2019.06.001>.
- (7) Fang, Z.; Suhua, H.; Xu, L.; Jian, F.; Qi, L.; Zhiwei, W.; Chuanchang, L.; Yuanlai, X. Adsorption Kinetics and Thermodynamics of Rare Earth on Montmorillonite Modified by Sulfuric Acid. *Colloids Surf. A Physicochem. Eng. Asp.* 2021, 627 (April), 127063. <https://doi.org/10.1016/j.colsurfa.2021.127063>.
- (8) Liao, C.; Liu, Y. P.; Ren, H.; Jiang, X. Y.; Yu, J. G.; Chen, X. Q. Rational Assembly of GO-Based Heterocyclic Sulfur- and Nitrogen-Containing Aerogels and Their Adsorption Properties toward Rare Earth Elementals. *J. Hazard. Mater.* 2021, 419 (March), 126484. <https://doi.org/10.1016/j.jhazmat.2021.126484>.

- (9) Ryu, S.; Fonseka, C.; Naidu, G.; Loganathan, P.; Moon, H.; Kandasamy, J.; Vigneswaran, S. Recovery of Rare Earth Elements (Lu, Y) by Adsorption Using Functionalized SBA-15 and MIL-101 (Cr). *Chemosphere* 2021, 281 (March), 130869. <https://doi.org/10.1016/j.chemosphere.2021.130869>.
- (10) Takei, T.; Takehara, M.; Takabayashi, T.; Yanagida, S.; Kumada, N. Synthesis of Mesoporous Silica Containing Group 2-Metal Cations and Their Performance Behavior in Rare Earth Cation Adsorption. *Colloids Surf. A Physicochem. Eng. Asp.* 2021, 610, 125664. <https://doi.org/10.1016/j.colsurfa.2020.125664>.
- (11) Callura, J. C.; Shi, Q.; Dzombak, D. A.; Karamalidis, A. K. Selective Recovery of Rare Earth Elements with Ligand-Functionalized Polymers in Fixed-Bed Adsorption Columns. *Sep. Purif. Technol.* 2021, 265 (February), 118472. <https://doi.org/10.1016/j.seppur.2021.118472>.
- (12) da Costa, T. B.; da Silva, M. G. C.; Vieira, M. G. A. Biosorption of Lanthanum Using Sericin/Alginate/Polyvinyl Alcohol Beads as a Natural Cation Exchanger in a Continuous Fixed-Bed Column System. *Colloids Surf. A Physicochem. Eng. Asp.* 2021, 627 (May), 127233. <https://doi.org/10.1016/j.colsurfa.2021.127233>.
- (13) da Costa, T. B.; da Silva, M. G. C.; Vieira, M. G. A. Effective Recovery of Ytterbium through Biosorption Using Crosslinked Sericin-Alginate Beads: A Complete Continuous Packed-Bed Column Study. *J. Hazard. Mater.* 2022, 421 (March 2021), 126742. <https://doi.org/10.1016/j.jhazmat.2021.126742>.
- (14) Huang, K.; Rowe, P.; Chi, C.; Sreepal, V.; Bohn, T.; Zhou, K. G.; Su, Y.; Prestat, E.; Pillai, P. B.; Cherian, C. T.; Michaelides, A.; Nair, R. R. Cation-Controlled Wetting Properties of Vermiculite Membranes and Its Promise for Fouling Resistant Oil–Water Separation. *Nat. Commun.* 2020, 11 (1), 1–10. <https://doi.org/10.1038/s41467-020-14854-4>.
- (15) Saha, K.; Deka, J.; Gogoi, R. K.; Datta, K. K. R.; Raidongia, K. Applications of Lamellar Membranes Reconstructed from Clay Mineral-Based Nanosheets: A Review. *ACS Appl. Nano Mater.* 2022. <https://doi.org/10.1021/acsanm.1c03207>.
- (16) Momina, M.; Shahadat, M.; Isamil, S. Regeneration Performance of Clay-Based Adsorbents for the Removal of Industrial Dyes: A Review. *RSC Adv.* 2018, 8 (43), 24571–24587. <https://doi.org/10.1039/C8RA04290J>.
- (17) Brigatti, M. F.; Galán, E.; Theng, B. K. G. *Structure and Mineralogy of Clay Minerals*; 2013; Vol. 5. <https://doi.org/10.1016/B978-0-08-098258-8.00002-X>.

- (18) Brião, G. de V.; da Silva, M. G.; Vieira, M. G. A. Expanded Vermiculite as an Alternative Adsorbent for the Dysprosium Recovery. *J. Taiwan Inst. Chem. Eng.* 2021, 127, 228–235. <https://doi.org/10.1016/j.jtice.2021.08.022>.
- (19) Langmuir, I. The Adsorption of Gases on Plane Surfaces of Glass Mic and Platinum. *J. Am. Chem. Soc.* 1918, 40, 1361–1403.
- (20) Georgin, J.; Franco, D.; Drumm, F. C.; Grassi, P.; Netto, M. S.; Allasia, D.; Dotto, G. L. Powdered Biosorbent from the Mandacaru Cactus (*Cereus Jamacaru*) for Discontinuous and Continuous Removal of Basic Fuchsin from Aqueous Solutions. *Powder Technol.* 2020, 364, 584–592. <https://doi.org/10.1016/j.powtec.2020.01.064>.
- (21) de Andrade, J. R.; Oliveira, M. F.; Canevesi, R. L. S.; Landers, R.; da Silva, M. G. C.; Vieira, M. G. A. Comparative Adsorption of Diclofenac Sodium and Losartan Potassium in Organophilic Clay-Packed Fixed-Bed: X-Ray Photoelectron Spectroscopy Characterization, Experimental Tests and Theoretical Study on DFT-Based Chemical Descriptors. *J. Mol. Liq.* 2020, 312, 113427. <https://doi.org/10.1016/j.molliq.2020.113427>.
- (22) Hurvich, C. M.; Tsai, C. L. Regression and Time Series Model Selection in Small Samples. *Biometrika* 1989, 76 (2), 297–307. <https://doi.org/10.1093/biomet/76.2.297>.
- (23) Lodeiro, P.; Herrero, R.; Sastre de Vicente, M. E. Batch Desorption Studies and Multiple Sorption–Regeneration Cycles in a Fixed-Bed Column for Cd(II) Elimination by Protonated *Sargassum Muticum*. *J. Hazard. Mater.* 2006, 137 (3), 1649–1655. <https://doi.org/10.1016/j.jhazmat.2006.05.003>.
- (24) Brião, G. de V.; da Silva, M. G. C.; Vieira, M. G. A. Efficient and Selective Adsorption of Neodymium on Expanded Vermiculite. *Ind. Eng. Chem. Res.* 2021, 60 (13), 4962–4974. <https://doi.org/10.1021/acs.iecr.0c05979>.
- (25) Brião, G. de V.; Silva, M. G. C. da; Vieira, M. G. A. Neodymium Recovery from Aqueous Solution through Adsorption/Desorption onto Expanded Vermiculite. *Appl. Clay Sci.* 2020, 198, 105825. <https://doi.org/10.1016/j.clay.2020.105825>.
- (26) Dichiarà, A. B.; Weinstein, S. J.; Rogers, R. E. On the Choice of Batch or Fixed Bed Adsorption Processes for Wastewater Treatment. *Ind. Eng. Chem. Res.* 2015, 54 (34), 8579–8586. <https://doi.org/10.1021/acs.iecr.5b02350>.

- (27) Chatterjee, S.; Mondal, S.; De, S. Design and Scaling up of Fixed Bed Adsorption Columns for Lead Removal by Treated Laterite. *J. Clean. Prod.* 2018, 177, 760–774. <https://doi.org/10.1016/j.jclepro.2017.12.249>.
- (28) Costa, T. B. da; Silva, M. G. C. da; Vieira, M. G. A. Recovery of Rare-Earth Metals from Aqueous Solutions by Bio/Adsorption Using Non-Conventional Materials: A Review with Recent Studies and Promising Approaches in Column Applications. *J. Rare Earths.* 2020. <https://doi.org/10.1016/j.jre.2019.06.001>.
- (29) Cuong, N. D.; Hue, V. T.; Kim, Y. S. Thermally Expanded Vermiculite as a Risk-Free and General-Purpose Sorbent for Hazardous Chemical Spillages. *Clay Miner.* 2019, 54 (3), 235–243. <https://doi.org/10.1180/clm.2019.34>.
- (30) Giesche, H. Mercury Porosimetry: A General (Practical) Overview. Part. Part. Syst. Charact. 2006, 23 (1), 9–19. <https://doi.org/10.1002/ppsc.200601009>.
- (31) Derrick, M. R.; Stulik, D.; Landry, J. M. Infrared Spectroscopy in Conservation Science: Scientific Tools for Conservation; The Getty Conservation Institute: Los Angeles, 1999.
- (32) Silva, F. M. N.; Barros, T. R. B.; Barbosa, T. S. B.; Lima, E. G.; Barbosa, T. L. A.; Rodrigues, M. G. F. Expansibility of Vermiculite (Santa Luzia, Brazil) Irradiated with Microwave. *Ceramica* 2021, 67 (382), 230–235. <https://doi.org/10.1590/0366-69132021673823110>.
- (33) Hong, H.; Churchman, G. J.; Yin, K.; Li, R.; Li, Z. Randomly Interstratified Illite-Vermiculite from Weathering of Illite in Red Earth Sediments in Xuancheng, Southeastern China. *Geoderma* 2014, 214–215, 42–49. <https://doi.org/10.1016/j.geoderma.2013.10.004>.
- (34) Marel, H. W. van der; Beutelspacher, H. *Tlas of Infrared Spectroscopy of Clay Minerals and Their Admixtures*; Elsevier: Amsterdam, 1976.
- (35) Padilla-Ortega, E.; Leyva-Ramos, R.; Mendoza-Barron, J. Role of Electrostatic Interactions in the Adsorption of Cadmium(II) from Aqueous Solution onto Vermiculite. *Appl. Clay Sci.* 2014, 88–89, 10–17. <https://doi.org/10.1016/j.clay.2013.12.012>.
- (36) Brião, G. de V.; da Silva, M. G. C.; Vieira, M. G. A. Reusable and Efficient Clay Material for the Fixed-Bed Neodymium Recovery. *Sustain. Chem. Pharm.* 2022, 25, 100623. <https://doi.org/10.1016/j.scp.2022.100623>.
- (37) Campos, A.; Moreno, S.; Molina, R. Characterization of Vermiculite by XRD and Spectroscopic Techniques. *Earth Sci. Res. J.* 2009, 13 (2), 108–118.

- (38) Theng, B. K. G. The Clay Minerals. In *Developments in Clay Science*; Theng, B. K. G., Ed.; Elsevier, 2012; Vol. 4, pp 3–45. <https://doi.org/10.1016/B978-0-444-53354-8.00001-3>.
- (39) Wang, M.; Tan, Q.; Chiang, J. F.; Li, J. Recovery of Rare and Precious Metals from Urban Mines—A Review. *Front Environ Sci Eng.* 2017, 11 (5), 1–17. <https://doi.org/10.1007/s11783-017-0963-1>.
- (40) Zhao, X.; Li, Z.; Tang, W.; Gu, X. Competitive Kinetics of Ni(II)/Co(II) and Cr(VI)/P(V) Adsorption and Desorption on Goethite: A Unified Thermodynamically Based Model. *J. Hazard. Mater.* 2022, 423, 127028. <https://doi.org/10.1016/j.jhazmat.2021.127028>.
- (41) Xiong, W. li; Zhang, J.; Yu, J. xia; Chi, R. an. Competitive Adsorption Behavior and Mechanism for Pb²⁺ Selective Removal from Aqueous Solution on Phosphoric Acid Modified Sugarcane Bagasse Fixed-Bed Column. *Process Saf. Environ. Prot.* 2019, 124, 75–83. <https://doi.org/10.1016/j.psep.2019.02.001>.
- (42) Barros, M. A. S. D.; Zola, A. S.; Arroyo, P. A.; Tavares, C. R. G.; Sousa-Aguiar, E. F. Chromium Uptake from Tricomponent Solution in Zeolite Fixed Bed. *Adsorption* 2006, 12 (4), 239–248. <https://doi.org/10.1007/s10450-006-0500-1>.
- (43) Brião, G. V.; da Silva, M. G. C.; Vieira, M. G. A. Dysprosium Adsorption on Expanded Vermiculite: Kinetics, Selectivity and Desorption. *Colloids Surf. A: Physicochem. Eng. Asp.* 2021, 630, 127616. <https://doi.org/10.1016/j.colsurfa.2021.127616>.
- (44) Marcus, Y. Thermodynamics of Solvation of Ions. Part 5. - Gibbs Free Energy of Hydration at 298.15 K. *J. Chem. Soc. Faraday Trans.* 1991, 87 (18), 2995–2999. <https://doi.org/10.1039/FT9918702995>.
- (45) He, H.; Guo, J.; Xie, X.; Peng, J. Experimental Study of the Selective Adsorption of Heavy Metals onto Clay Minerals. *Chinese J. Chem.* 2000, 19 (2), 105–109. <https://doi.org/10.1007/BF03166865>.
- (46) Persson, I. Hydrated Metal Ions in Aqueous Solution: How Regular Are Their Structures? *Pure Appl. Chem.* 2010, 82 (10), 1901–1917. <https://doi.org/10.1351/PAC-CON-09-10-22>.

CHAPTER 10. RECOVERY OF REM FROM Nd-Fe-B MAGNET LEACHATE

Recovery of rare earth metals from permanent magnet leachate using expanded vermiculite as adsorbent⁹

Giani de Vargas Brião, Meuris Gurgel Carlos da Silva ^a, Claudia Batista Lopes ^b, Tito Trindade ^b,
Carlos Manuel Silva ^b, Melissa Gurgel Adeodato Vieira ^a

^a *University of Campinas – School of Chemical Engineering, Zip code 13083-852, Campinas,
Brazil*

^b *University of Aveiro – Chemical department, Zip code 3810-193, Aveiro, Portugal*

ABSTRACT

The search for new sources, primary or secondary, of critical rare earth metals, such as Nd and Dy, has ensued globally due to the strategic value of these resources for the self-sufficiency and sustainability of the energy sector. Adsorption for the concentration and recovery of REM from alternative sources may be promising as an efficient option to return these metals to the production chain. This work explores the vermiculite potential in the recovery of rare earths from permanent magnet leachates. This study analyzed the equilibrium of the simultaneous adsorption of Nd and Dy, the desorption efficiency of different eluents, and the adsorption and desorption performance from a solution containing Fe, Ni, Zn, Al, Nd, Dy, Pr, Mn, Co that mimics the composition of a real Nd-Fe-B magnet leachate. The equilibrium adsorption capacities were 484.9 and 209.6 $\mu\text{mol/g}$ for Nd and Dy, respectively. The adsorption capacity of vermiculite to remove REM from a magnet leachate solution was higher, but the process was not selective. However, selective elution of Nd occurs using EDTA as eluent. Thus, further improvements in vermiculite, such as functionalization, must be made to achieve high selectivity in real applications.

⁹ Manuscript in elaboration

Keywords: neodymium, dysprosium, adsorption, recovery, permanent magnet leachate.

10.1 INTRODUCTION

Rare earth metals (REM), such as neodymium (Nd) and dysprosium (Dy), are listed as critical resources due to the risk supply and relevance to the technological and energy sector (wind turbines and electric vehicles) (Jowitt et al., 2018). Imminent scenarios of clean energy up to 2050 show the inherent need for high Nd and Dy recycling rates to supply the future demand that can be 35 times higher than the mining capacity (Junne et al., 2020). Thus, recovering rare earth metals is essential for developing the clean energy field. Several technologies for separation and purification have been considered for REM recovery from secondary sources, such as end-of-life NdFeB magnets used in hard disks composed of 32% of REM (München and Veit, 2017). Classical hydrometallurgical routes (leaching, solvent extraction, and precipitation) have been extensively applied for the REM recovery from Nd-Fe-B magnets due to the known high efficiency of separation (Kumari et al., 2018). Nevertheless, adsorption incorporation in typical hydro-processing routes in diluted systems may be advantageous due to the increased potential for reconcentrate and recovery of REM (Jyothi et al., 2020).

Adsorbents of different chemical natures have been proposed for the individual Nd and Dy adsorption from aqueous solution (ideal scenario), such as polymer-based materials (da Costa et al., 2021), metal-organic frameworks (Abdel-Magied et al., 2019), functionalized silica (Ravi et al., 2018), carbon-based materials (Zheng et al., 2022), magnetic particles (Tu et al., 2019), and clays (Brião et al., 2020; Brião et al., 2021a). However, just a few works have been developed to evaluate the adsorbent potential to recover REM from more realistic systems, such as binary (Hoshina et al., 2020; Xu, 2018; Zheng et al., 2018), and simulated or actual samples as NdFeB magnet leachate (Kucuker et al., 2017). Thus, evaluating the adsorbent potential under lifelike conditions is still a gap in the research area of REM adsorption and recovery that must be overcome to achieve the maturity needed to scale up.

Among the adsorbent cited above, clays as expanded vermiculite had great potential for simultaneous multi-component adsorption because this low cost and broadly available material presented promisor results in the single adsorption of Nd and Dy, such as high adsorption capacity, excellent stability during subsequent reuses, and selectivity towards REM over bivalent metals (Brião et al., 2020; Brião et al., 2021a). Those characteristics motivate the present study that aims to evaluate the performance of the expanded vermiculite to recover REM from binary Nd and Dy aqueous

solutions and simulated solution of a NdFeB magnet leachate, which equilibrium isotherms, desorption capacity using different eluents, and performance of adsorption and desorption in the multi-component systems were investigated.

10.2 MATERIALS AND METHODS

10.2.1 Adsorbent Material

Expanded vermiculite clay (Brazil Minérios S.A) is the adsorbent used in this study. The material was sieved, and the particles with an average size of 0.855 mm were selected. The adsorbent was extensively characterized in previous work (Brião et al., 2020; Brião et al., 2021a), and some of the main properties are the surface area of 10 m²/g, majority mesoporosity, a typical composition of hydrated magnesium–aluminum–iron phyllosilicate, cation exchange capacity of 1.41 mmol/g.

10.2.2 Adsorption experiments

10.2.2.1 Binary system

Equimolar Nd and Dy solutions (10 µmol/L, pH= 3.5) were submitted to the adsorption studies. The solutions were prepared by diluting a stock solution of each metal (5 g of REM hydrated nitrate in 100 mL of aqueous solution). The adsorption equilibrium and desorption tests were evaluated at room temperature in an orbital incubator (model ZWYR-240, Labwit) under moderate agitation (200 rpm). The metal concentration was measured by Inductively Coupled Plasma Mass Spectrometry (ICP-MS Agilent 7700). The adsorption capacity and efficiency were calculated by Equations 1 and 2.

$$q = \frac{C_0 - C_f}{m} V \quad (10.1)$$

$$\%R = \frac{C_0 - C_f}{C_0} 100 \quad (10.2)$$

Where C_0 is the initial concentration, C_f is the final concentration at the equilibrium, V is the solution volume (L), and m is the adsorbent mass (g). The molar based-concentration and adsorption capacity were chosen to best compare the efficiencies for each metal.

In the equilibrium study, different mass of vermiculite was put in contact with the REM solution, and the initial and equilibrium concentration (after 24 hours) were collected, acidified, and measured by ICP-MS. The models of adsorption isotherms applied in this study were Langmuir (Langmuir, 1918) (Equation 10.3), Freundlich (Freundlich, 1906) (Equation 10.4), Sips ((Sips, 1948) (Equation 10.5), and Dubinin-Radushkevich (Dubinin and Radushkevich, 1947) (Equations 10.6-10.8).

$$q_e = \frac{q_m K_L C_e}{1 + (K_L C_e)} \quad (10.3)$$

$$q_e = K_F C_e^{n_F} \quad (10.4)$$

$$q_e = \frac{q_{mS} K_S C_e^{m_S}}{1 + (K_S C_e)^{m_S}} \quad (10.5)$$

$$q_e = q_m e^{-\beta \varepsilon^2} \quad (10.6)$$

Where K_L is the Langmuir constant (L/mmol), q_m is the maxima adsorption capacity (mmol/g), K_F (L/g) is the Freundlich constant, and n_F is considered the heterogeneity constant ($0 < n_F < 1$), q_{mS} is the Sips maximum adsorption capacity (mmol/g), K_S is the Sips constant (L/mmol), and m_S is the dimensionless heterogeneity factor, β is the constant associated with the free energy of adsorption (mol^2/J^2) and ε is the Polanyi potential (J/mol).

Equation 10.7 describes the Polanyi potential, and Equation 8 calculates the free energy of adsorption.

$$\varepsilon = RT \ln \left(1 + \frac{1}{C_e/1000} \right) \quad (10.7)$$

$$E = \frac{1}{\sqrt{2\beta}} \quad (10.8)$$

Where R is the ideal gas constant (8.314 J/mol.K), T is the temperature (K), E is the free energy of adsorption (J/mol).

The desorption was investigated by mixing 10 mg of loaded vermiculite with 100 mL of the eluent solutions (0.01 mol/L) for 24 h, and ICP-MS analyzed the final concentration. Six eluent solutions were tested:

- two salts containing exchangeable cations (ammonium chloride (NH_4Cl) and magnesium dichloride hexahydrate ($\text{MgCl}_2 \cdot 6\text{H}_2\text{O}$));
- two complexing agents, ethylenediaminetetraacetic acid (EDTA) and diethylenetriaminepentaacetic acid (DTPA);
- two strong acids to leachate the adsorbed metals, nitric acid (HNO_3) and hydrochloric acid (HCl).

The desorption capacity (q_{el}), and desorption percentage ($\%D$), were calculated by equations 10.9 and 10.10, respectively.

$$q_{el} = \frac{C_f}{m} V \quad (10.9)$$

$$\%D = \frac{q_{el}}{q} 100 \quad (10.10)$$

10.2.2.2 Simulated permanent magnet leachate

The performance of adsorption capacity of the vermiculite to concentrate rare earth metals were tested from a mix of different metals in solution (Fe, Al, Ni, Zn, Co, Mn, Dy, Nd, and Pr).

The leachate solution was prepared based on the components, concentrations, and pH cited in Brewer et al. (2019) study, in which sulfuric acid was used to leach valuable metals from permanent magnet scraps.

In the adsorption essays, vermiculite (0.1 g/L) was added to the simulated leachate solution under 24 h of agitation. The solid was washed with deionized water, dried at 40 °C, and then put in contact with the best eluent solutions defined by the binary study for the multi-component desorption investigation. The metal concentration was measured by inductively coupled plasma optical emission spectrometry (ICP-OES, Perkin–Elmer Optima 4300 DV spectrometer, USA).

The adsorption capacity for each metal (Equation 10.1) and the selectivity coefficient ($S_{REM/M}$) (Equation 10.11) were the parameters evaluated. The experiments were conducted in triplicate.

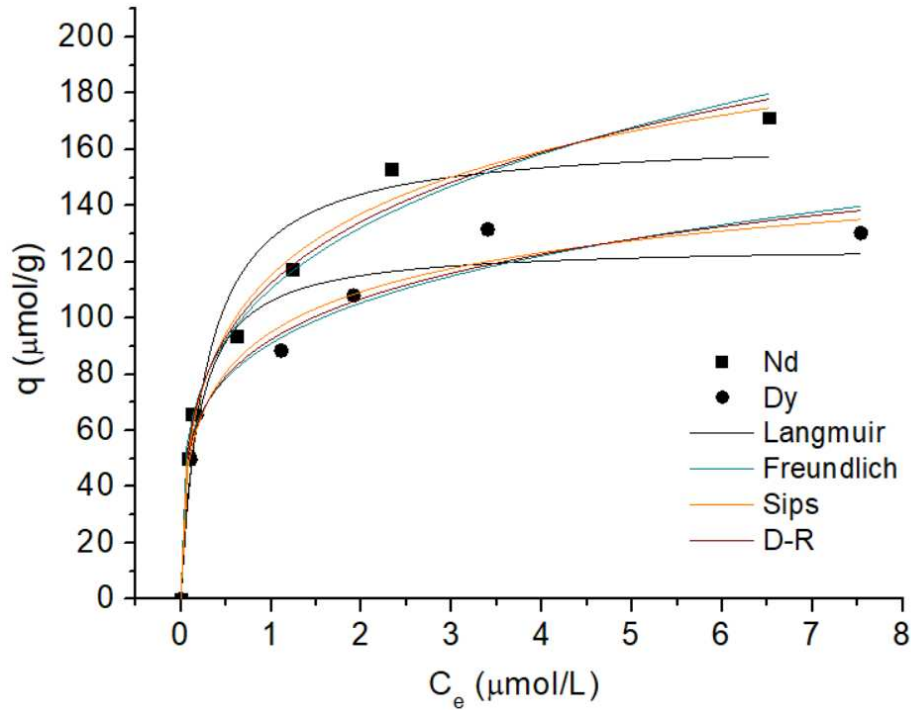
$$S_{Dy/M} = \frac{K_{d(REM)}}{K_{d(M)}} \quad \text{with} \quad K_d = \frac{q_e}{C_e} \quad (10.11)$$

10.3 RESULTS AND DISCUSSION

10.3.1 Binary System

Figure 10.1 shows the isotherms of Nd and Dy adsorption on expanded vermiculite, in which the adsorbent adsorbed more Nd than Dy at this range of low concentrations (10^{-6} mol/L). Table 10.1 presents the isotherm model fitting quality by each model's adjusted correlation coefficient (R^2_{adj}) and their characteristic parameters.

Figure 10.1 – Isotherm of adsorption of Nd and Dy (binary system) on expanded vermiculite



According to the fitting quality criteria (R^2_{adj}), the model that best fitted the data was the Sips model. The model assumes that the surface is homogeneous but that the adsorption is a cooperative process due to adsorbate-adsorbate interactions. This model approximates the Freundlich model at low C_e , and at high C_e , it predicts the Langmuir model (monolayer adsorption) (Ayawei et al., 2017).

The maximum adsorption capacity indicated by the Sips model for Nd and Dy is 484.9 $\mu\text{mol/g}$ and 209.6 $\mu\text{mol/g}$, respectively. The Sips constant for Dy is around double the Nd, which means that the adsorbent saturation with dysprosium occurs at lower C_e than for Nd. The m_s of 0.44 and 0.43 indicated that the adsorption is equally favorable for both metals.

Table 10.1 – Isotherm fitting results

Model	Parameters	Nd	Dy
Langmuir	q_{max} ($\mu\text{mol/g}$)	164.2	125.8
	K_L (L/ μmol)	3.6	5.4
	R^2_{adj}	0.9292	0.9411
Freundlich	K_F (L/g)	110.4	91.0
	n_F	0.26	0.21
	R^2_{adj}	0.9787	0.9681
Sips	q_{mS} ($\mu\text{mol/g}$)	484.9	209.6
	K_S (L/ μmol)	0.39	0.88
	m_s	0.44	0.43
	R^2_{adj}	0.9837	0.9711
D-R	q_{D-R} ($\mu\text{mol/g}$)	689.2	409.6
	E (kJ/mol)	12.6	13.9
	R^2_{adj}	0.9684	0.9334

Table 10.2 – Comparison between different adsorbent matrices performances in the simultaneous adsorption of Nd and Dy.

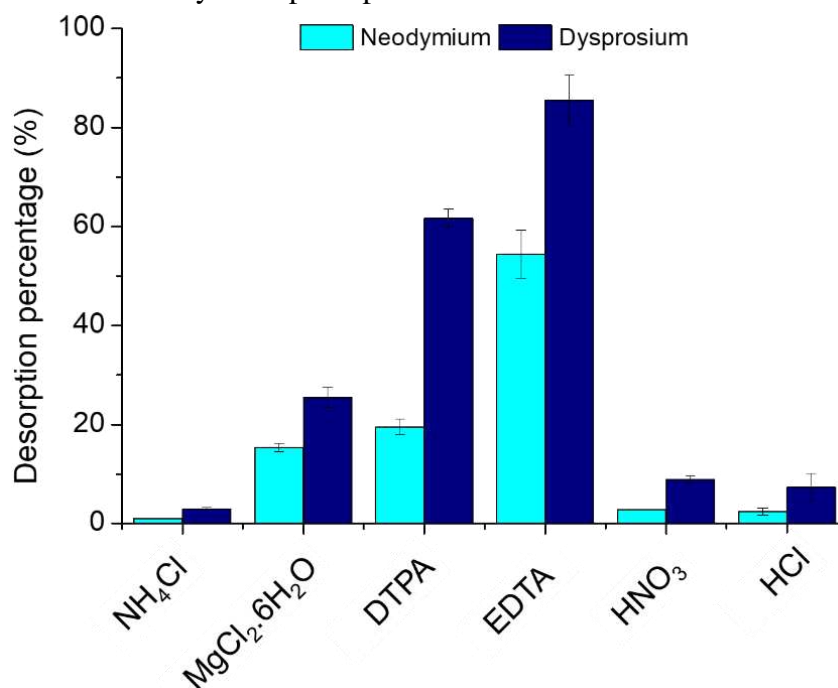
Adsorbent	Binary Solution	Equilibrium	Ref.
Organophosphorus-loaded octadecyl methacrylate film	Nd (693.3 $\mu\text{mol/L}$) Dy (615.4 $\mu\text{mol/L}$) pH 2.0	Nd (* q_m = 6.9 $\mu\text{mol/g}$) Dy (* q_m = 160 $\mu\text{mol/g}$)	(Hoshina et al., 2020)
Ionic imprinted mesoporous bilayer films	Nd (346.7 $\mu\text{mol/L}$) Dy (307.7 $\mu\text{mol/L}$) pH 4.0	Langmuir Nd (q_{max} = 91.5 $\mu\text{mol/g}$) Dy (q_{max} = 114.5 $\mu\text{mol/g}$)	(Zheng et al., 2018)
Expanded Vermiculite	Nd (10 $\mu\text{mol/L}$) Dy (10 $\mu\text{mol/L}$) pH 3.5	Sips Nd (q_{mS} = 484.9 $\mu\text{mol/g}$) Dy (q_{mS} = 209.6 $\mu\text{mol/g}$)	This work

*Experimental

Table 10.2 presents the maximum capacities of different adsorbents in the binary adsorption of Nd and Dy. Compared to other simultaneous adsorption of Nd and Dy, vermiculite achieved higher adsorption capacities than functionalized or ion imprinted polymeric films that are adsorbents more expensive and complex than vermiculite clay. However, the organophosphorus-loaded octadecyl methacrylate film reached a high level of selectivity between Nd and Dy, which can also be advantageous if the objective is the separation at a high degree of purity of each metal.

Figure 10.2 shows that the complexing agents (DTPA and EDTA) desorbed the REM more efficiently than inorganic salts and acids. In this ideal condition experiment, Nd and Dy were adsorbed from an equimolar binary solution (10 $\mu\text{mol/L}$ each) on expanded vermiculite (0.1 g/L). The adsorption capacity for Nd and Dy were 75.2 and 71.1 $\mu\text{mol/g}$, respectively. And the highest desorption efficiencies (84%) were reached using EDTA. In fact, dysprosium was preferably eluted than Nd, indicating that Dy was bonded to the adsorbent by weaker forces.

Figure 10.2 – Nd and Dy desorption performance of different eluents at 0.01 mol/L.



10.3.2 Simulated permanent magnet leachate

A simulated permanent magnet (Nd-Fe-B) leachate solution was prepared according to the final leaching results reported by Brewer et al. (2019) using an H_2SO_4 solution (1 mol/L). Both solutions had a pH of 3.6. The initial concentration of the simulated and real leachate solution is

presented in Table 10.3. The low absolute error between the concentrations indicated that the solution used to perform the adsorption study effectively simulated the leachate. Fe and Mn content varied more than the other metals; yet, it did not compromise the mimic attempting since the leachate concentration can vary significantly in actual applications.

Table 10.3 – Comparison between actual and simulated leachate solution									
Leachate solution	Al	Co	Dy	Fe	Mn	Nd	Ni	Pr	Zn
Simulated (<i>S</i>) (mmol/L)	0.034	0.12	0.048	7.27	0.015	0.74	0.026	0.26	0.43
Real (<i>R</i>) (mmol/L)	0.023	0.10	0.038	5.90	0.003	0.74	0.020	0.21	0.40
$ R - S $ (mmol/L)	0.011	0.02	0.010	1.37	0.011	0.00	0.007	0.05	0.03

Figure 10.3(a) indicates the adsorption capacity of the expanded vermiculite for each metal, in which the decreasing order of uptake efficiency is: Fe > Nd > Zn > Pr > Co > Dy > Ni > Al > Mn. This order agrees with decreasing the initial concentration of each metal in the simulated solution, except for the most diluted components (Ni, Al, Mn). The highest selectivity coefficients in terms of Nd uptake, and the most concentrated REM in the leachate, were obtained when evaluating the performance for Zn (1.6) and Al (1.7). Nonetheless, those values around 1 indicated a low selectivity of the material at the simulated condition, differently from what was pointed out by adsorption studies conducted at more ideal conditions (Brião et al., 2021a; Brião et al., 2021b).

Figure 10.3 – Expanded vermiculite adsorption efficiency (a) and complexing agents (DTPA and EDTA) desorption performances (b) from simulated permanent magnet leachate solution

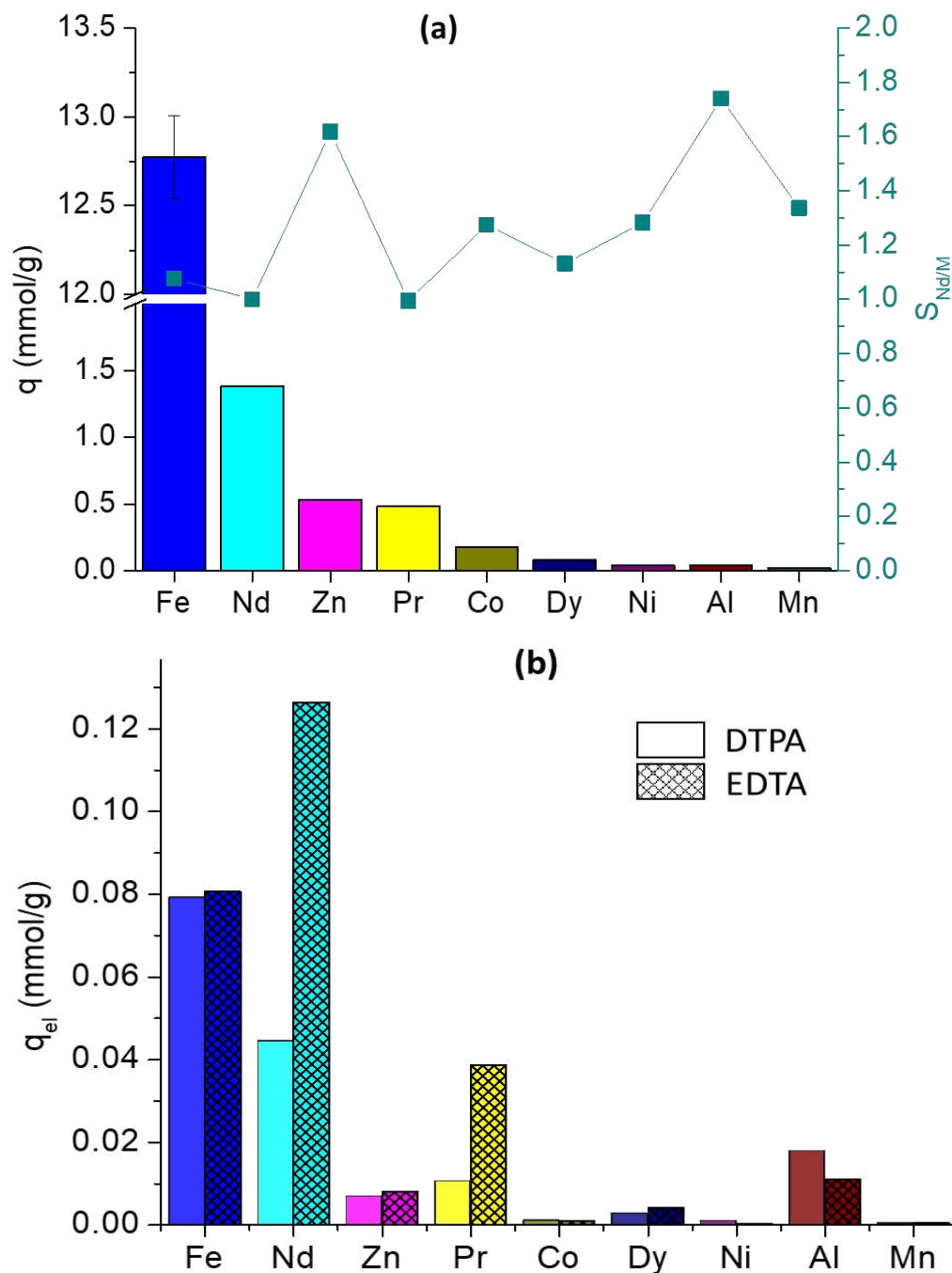


Figure 10.3(b) shows DTPA and EDTA's desorption capacity for each leachate compound. As presented in the binary desorption investigation (Figure 10.2), the EDTA was more efficient than DTPA. And, despite the loaded adsorbent be richer in iron than neodymium, Nd was eluate more efficiently than Fe using EDTA. This means that despite the low selectivity of the vermiculite clay,

the elution can be selective using EDTA as eluent, mainly if optimized desorption conditions of eluent concentration, S/L ratio, and contact time, which should be defined in further studies.

10.4 CONCLUSION

This work investigated the performance of expanded vermiculite in REM recovery from multi-component systems. In a binary adsorption study of Nd and Dy, the equilibrium adsorption capacities for neodymium were higher than for dysprosium in the concentration range studied. The Sips model that best fitted the data predicted maximum adsorption capacities of 484.9 and 209.6 $\mu\text{mol/g}$ for Nd and Dy, respectively. In the desorption essays, dysprosium was desorbed more efficiently than neodymium, indicating that weaker forces bound Dy to the adsorption sites. The desorption efficiency of different eluents for both metals decreased in the following order: EDTA > DTPA > $\text{MgCl}_2 \cdot 6\text{H}_2\text{O}$ > HNO_3 > HCl > NH_4Cl , which means that chelation is more efficient than ion exchange and leaching elution mechanisms. The adsorption efficiency of vermiculite, when applied to a simulated magnet leachate solution, showed that the material reached high adsorption capacities. Nevertheless, the processes were not selective. Desorption using EDTA shows superior performance to desorb Nd than the other metals, suggesting a potential to selectively recover the Nd from the loaded adsorbent. The present study shows that the expanded vermiculite material, despite the high adsorption capacity, is not selective in the REM sorption from the magnet leachate complex solution. However, the elution can be selective if powerful chelating agents are applied. Thus, further functionalization of vermiculite and proper optimization of desorption conditions are recommended to improve the selectivity and desorption efficiency in an attempt to achieve high scale and real applications.

ACKNOWLEDGMENTS

This work was financed by the Fundação de Amparo à Pesquisa do Estado de São Paulo (FAPESP) (Grants # 2017/18236-1), Coordenação de Aperfeiçoamento de Pessoal de Nível Superior (CAPES) (Grant # 88887.571776/2020-00), Conselho Nacional de Desenvolvimento Científico e Tecnológico (CNPq) (Grants # 406193/2018-5 and 308046/2019-6).

REFERENCES

- Abdel-Magied, A.F., Abdelhamid, H.N., Ashour, R.M., Zou, X., Forsberg, K., 2019. Hierarchical porous zeolitic imidazolate frameworks nanoparticles for efficient adsorption of rare-earth elements. *Microporous and Mesoporous Materials* 278, 175–184. <https://doi.org/10.1016/j.micromeso.2018.11.022>
- Ayawei, N., Ebelegi, A.N., Wankasi, D., 2017. Modelling and Interpretation of Adsorption Isotherms. *J Chem* 2017, 1–11. <https://doi.org/10.1155/2017/3039817>
- Brewer, A., Dohnalkova, A., Shutthanandan, V., Kovarik, L., Chang, E., Sawvel, A.M., Mason, H.E., Reed, D., Ye, C., Hynes, W.F., Lammers, L.N., Park, D.M., Jiao, Y., 2019. Microbe Encapsulation for Selective Rare-Earth Recovery from Electronic Waste Leachates. *Environ Sci Technol* 53, 13888–13897. <https://doi.org/10.1021/acs.est.9b04608>
- Brião, G. de V., da Silva, M.G.C., Vieira, M.G.A., 2021a. Efficient and Selective Adsorption of Neodymium on Expanded Vermiculite. *Ind Eng Chem Res* 60, 4962–4974. <https://doi.org/10.1021/acs.iecr.0c05979>
- Brião, G. de V., Silva, M.G.C. da, Vieira, M.G.A., 2020. Neodymium recovery from aqueous solution through adsorption/desorption onto expanded vermiculite. *Appl Clay Sci* 198, 105825. <https://doi.org/10.1016/j.clay.2020.105825>
- Brião, G.V., da Silva, M.G.C., Vieira, M.G.A., 2021b. Dysprosium adsorption on expanded vermiculite: Kinetics, selectivity and desorption. *Colloids Surf A Physicochem Eng Asp* 630, 127616. <https://doi.org/10.1016/j.colsurfa.2021.127616>
- da Costa, T.B., da Silva, M.G.C., Vieira, M.G.A., 2021. Recovery of dysprosium by biosorption onto a biocomposite from sericin and alginate. *Journal of Water Process Engineering* 44. <https://doi.org/10.1016/j.jwpe.2021.102388>
- Dubinin, M.M., Radushkevich, L.V., 1947. The equation of the characteristic curve of activated charcoal. *Proceedings of the Academy of Sciences of USSR* 55, 331.
- Freundlich, H.M.F., 1906. Over the Adsorption in Solution. *urnal of Physical Chemistry* 57, 385–470.
- Hoshina, H., Chen, J., Amada, H., Seko, N., 2020. Chain entanglement of 2-ethylhexyl hydrogen-2-ethylhexylphosphonate into methacrylate-grafted nonwoven fabrics for applications in separation and recovery of Dy (III) and Nd (III) from aqueous solution. *Polymers (Basel)* 12, 1–12. <https://doi.org/10.3390/polym12112656>

- Jowitt, S.M., Werner, T.T., Weng, Z., Mudd, G.M., 2018. Recycling of the rare earth elements. *Curr Opin Green Sustain Chem* 13, 1–7. <https://doi.org/10.1016/j.cogsc.2018.02.008>
- Junne, T., Wulff, N., Breyer, C., Naegler, T., 2020. Critical materials in global low-carbon energy scenarios: The case for neodymium, dysprosium, lithium, and cobalt. *Energy* 211, 118532. <https://doi.org/10.1016/j.energy.2020.118532>
- Jyothi, R.K., Thenepalli, T., Ahn, J.W., Parhi, P.K., Chung, K.W., Lee, J.Y., 2020. Review of rare earth elements recovery from secondary resources for clean energy technologies: Grand opportunities to create wealth from waste. *J Clean Prod.* <https://doi.org/10.1016/j.jclepro.2020.122048>
- Kucuker, M.A., Wieczorek, N., Kuchta, K., Coptý, N.K., 2017. Biosorption of neodymium on *Chlorella vulgaris* in aqueous solution obtained from hard disk drive magnets. *PLoS One* 12, e0175255. <https://doi.org/10.1371/journal.pone.0175255>
- Kumari, A., Jha, M.K., Pathak, D.D., 2018. Review on the Processes for the Recovery of Rare Earth Metals (REMs) from Secondary Resources. pp. 53–65. https://doi.org/10.1007/978-3-319-72350-1_5
- Langmuir, I., 1918. The Adsorption of Gases on Plane Surfaces of Glass Mic and Platinum. *Journal of American Chemiscal Society* 40, 1361–1403.
- München, D.D., Veit, H.M., 2017. Neodymium as the main feature of permanent magnets from hard disk drives (HDDs). *Waste Management.* <https://doi.org/10.1016/j.wasman.2017.01.032>
- Ravi, S., Lee, Y.R., Yu, K., Ahn, J.W., Ahn, W.S., 2018. Benzene triamido-tetraphosphonic acid immobilized on mesoporous silica for adsorption of Nd³⁺ ions in aqueous solution. *Microporous and Mesoporous Materials* 258, 62–71. <https://doi.org/10.1016/j.micromeso.2017.09.006>
- Sips, R., 1948. On the structure of a catalyst surface. *J Chem Phys* 16, 490–495. <https://doi.org/10.1063/1.1746922>
- Tu, Y.-J., You, C.-F., Lo, S.-C., Chan, T.-S., Chung, C.-H., 2019. Recycling of neodymium enhanced by functionalized magnetic ferrite. *Environ Technol* 40, 1592–1604. <https://doi.org/10.1080/09593330.2018.1426643>
- Xu, J., 2018. Recovery of rare-earth elements from NdFeB magnets by zirconium phosphate ion exchangers (ACADEMIC DISSERTATION). Faculty of Science of the University of Helsinki.

- Zheng, X., Sun, W., Li, A., Wang, B., Jiang, R., Song, Z., Zhang, Y., Li, Z., 2022. Graphene oxide and polyethyleneimine cooperative construct ionic imprinted cellulose nanocrystal aerogel for selective adsorption of Dy(III). *Cellulose* 29, 469–481. <https://doi.org/10.1007/s10570-021-04299-3>
- Zheng, X., Zhang, Y., Zhang, F., Li, Z., Yan, Y., 2018. Dual-template docking oriented ionic imprinted bilayer mesoporous films with efficient recovery of neodymium and dysprosium. *J Hazard Mater* 353, 496–504. <https://doi.org/10.1016/j.jhazmat.2018.04.022>

CHAPTER 11. GENERAL DISCUSSION

Diverse governmental agencies and researchers have cited rare earth metals as critical resources due to their application in strategic fields such as energy and high technology and the scarcity of mines with exploitable potential worldwide. These factors direct global efforts to develop a circular economy of the REMs, reusing, recycling, and recovering them from secondary sources to attend the future demand. Diverse classical and innovative methods have been studied to return REM metals from residues, wastewaters, and effluents to the productive chain.

Chapter 2 presented the adsorption potential for the recovery of Nd and Dy from NdFeB magnet scrap (secondary source). Alternative adsorbents such as ion-imprinted polymers, metal-organic frameworks, functionalized silica, and carbon-based materials have been explored for the Nd and Dy recovery from aqueous solutions. Among them, highly porous nano adsorbents and ion-imprinted polymers presented great adsorption capacities and selectivity results. However, the studies have some lacks regarding the economic viability of the adsorbent materials, accurate modeling, development of the desorption towards the REM recovery and reusability, studies of continuous fixed-bed mode, and complete studies of the adsorption in actual or simulated samples. Thus, in the present thesis, the expanded vermiculite, a low-cost and available clay mineral, was proposed as an adsorbent material for the adsorption of Nd and Dy from aqueous solution in batch and continuous fixed-bed modes. The studies focused on the potential of vermiculite for REM recovery. Because of that, desorption was discussed extensively.

This study evaluated the effect of operational parameters such as pH, adsorbent dosage, and particle size over the Nd and Dy adsorption efficiency to guarantee high adsorption performance. Design of experiments and machine learning approaches were used to determine the best conditions and model the effects. The results of these studies are presented in Chapter 3 (Nd) and Chapter 6 (Dy). According to the analyses, the pH and adsorbent dosage greatly influenced the vermiculite performance, independently of the particle size applied. Removal percentages of around 99 % were achieved for an Nd or Dy initial concentration of 3 mmol/L, a volume of 50 mL, using a vermiculite particle of 0.855 mm, at $3.3 \leq \text{pH} \leq 3.5$, and $0.64 \text{ g} \leq \text{adsorbent amount} \leq 0.7 \text{ g}$. Comparing the optimization studies, the best operation conditions were similar for both metals, which is expected since they have similar properties.

The Nd and Dy adsorption kinetics, selectivity, and desorption in batch mode investigation were shown in chapters 3 and 7, where the kinetics of adsorption and magnesium exchange, the

selectivity towards Nd and Dy from a mixture with base and heavy metals, and optimization of the desorption were discussed in detail.

The kinetic experiments indicated that the equilibrium of adsorption of Nd and Dy on expanded vermiculite for an initial concentration of 5 mmol/L occurred at 360 and 180 min, respectively, removing a maximum of 0.34 mmol of Nd and 0.32 mmol of Dy per gram of vermiculite. Both kinetic profiles could be well described by the PSO model, in which the distinct kinetic behavior corroborated the significant difference between the PSO rate constants 0.096 and 0.214 g/mmol.min (Table 10.1). Regarding the mass transfer mechanism, Nd and Dy sorption on expanded vermiculite is influenced by both external film and intraparticle diffusion resistances. The last presents different effective diffusivities of 0.18 and 1.05×10^{-9} m²/min for Nd and Dy, respectively. The difference may be related to the ionic radii of those metals, Nd³⁺ is a larger cation with 1.175 Å of ionic radio, and Dy³⁺ has 1.075 Å (Dangelo et al., 2011) and because of the more substantial affinity towards Dy mentioned above. In the kinetic studies, the exchange with Mg²⁺ that constitutes the octahedral sheets and the interlayer space (Liu et al., 2007) shows a notable influence on the overall adsorption mechanism.

Table 11. 1. Models fitting to the Nd and Dy kinetic experimental data.

Model	Parameters	Nd	Dy
PSO	k_2 (g/mmol.min)	0.096	0.214
	q_e (mmol/g)	0.34	0.32
	R^2	0.997	0.992
Boyd	D_{ef} (m ² /min)	0.18×10^{-9}	1.05×10^{-9}
	R^2	0.996	0.963
EMT	k_{EMT} (m/min)	1.30×10^{-7}	2.86×10^{-7}
	R^2	0.981	0.922

Rare earth metals usually are found with base, noble and toxic metals in actual wastewaters. Thus, in our study, we evaluated the selectivity of vermiculite towards Nd and Dy from a mixture of lead, nickel, zinc, copper, and cadmium. Vermiculite adsorbed preferable Dy, and Nd, over bivalent cations due to the higher positive charge of the REM metals. In the neodymium study, the vermiculite

selectivity occurred in follow the order: Nd (90.8 %) < Ni (66.1 %) < Zn (54.2 %) < Cu (37.8 %) < Pb (23.4 %), agreeing to the ionic radii, in which smaller ions were adsorbed preferably. In the multimetal adsorption using dysprosium mixed with other metals, the selectivity order was Dy (97.6 %) > Pb (80.1 %) > Ni (70.1 %) > Cd (52.0 %) > Cu (51.7%), which the hydration energy had a higher contribution than the cation sizes. Cations with lower hydration energies were rather adsorbed due to the facility losing coordinated water to binding on the adsorbent surface. Those distinct natural selection mechanisms can be helpful when Nd and Dy are mixed with numerous other metals in an actual application. However, further studies were performed to evaluate that in a real scenario, i.e., from permanent magnet leachate solutions (Chapter 10).

Efficient and nondestructive desorption is essential to recover the loaded REM from the adsorbent surface, maintaining the original material properties. The Nd recovery was evaluated using different eluents in chapter 3, in which the calcium chloride (0.5 mol/L) was the most recommended eluent regarding efficiency and safety. Once the exchange with Ca^{2+} recovered Nd, in the study of the Dy desorption (chapter 7), a source of Mg^{2+} (magnesium nitrate) was used as an eluent to regenerate the exchangeable magnesium of the vermiculite. Furthermore, the desorption conditions such as eluent concentration, time, and adsorbent dosage were optimized by a rotational design of experiment and response surface methodologies (chapters 4 and 7), in which elution efficiencies of 80.7% and 89.1% were reached for Nd and Dy, respectively. For Nd, the best conditions were S/L equal to 7.31 g/L, calcium chloride concentration of 0.3 mol/L, and contact time of 3h, and for Dy, they are S/L of 14 g/L, magnesium nitrate concentration equal to 0.2 mol/L and contact time of 3h. The higher efficiency, solid-liquid ratio, and lower eluent concentration needed to recover Dy using magnesium nitrate confirmed that this eluent is more suitable for the desorption and regeneration of the vermiculite than calcium chloride.

The adsorption equilibrium is a critical component of adsorption studies since they inform about the maximum uptake capacity of the adsorbents and if the relationship between adsorption capacity and equilibrium solution concentration is favorable or not. The adsorption equilibrium of Nd and Dy were presented in chapters 4 and 8, in which both isotherms are considered of high affinity. Nevertheless, the dysprosium isotherm indicates the multilayer formation at higher concentrations, while the Nd isotherm follows the Langmuir relation (monolayer saturation) in the studied concentration range. The Langmuir parameters are compared (Table 11.2) to evaluate both performances at 25 °C. The Nd and Dy maximum adsorption capacities were 0.39 and 0.48 mmol/

respectively, which the slightly higher affinity towards the dysprosium corroborates the abovementioned findings. The Langmuir constants 35.6 and 9.35 L/mmol for Nd and Dy equilibrium indicated that the vermiculite saturated with Nd easier than Dy, which also supports the high Dy adsorption capacities achieved at high concentration ~ 0.9 mmol/g due to the surface precipitation (Chapter 8). The thermodynamic study, done using the equilibrium constants at different temperatures, revealed that both are spontaneous and feasible, the neodymium adsorption is exothermic, and the dysprosium adsorption is endothermic. This effect of the temperature on the adsorption capacity can be profitable to improve the selectivity between Nd and Dy in a competitive adsorption study.

Table 11.2. Langmuir fitting to the experimental isotherms of Nd and Dy.

Langmuir parameters	Nd	Dy*
q_m (mmol/g)	0.39	0.48
K_L (L/mmol)	35.6	9.35
R^2	0.974	0.873

*For initial concentrations < 3 mmol/L

Adsorption in batch mode has been widely investigated for the adsorption and desorption of Nd and Dy; regardless, few works have researched the phenomenon in continuous mode, as expressed in Chapter 2. The present thesis evaluated the vermiculite performance on the Nd or Dy recovery in a fixed-bed operation (chapters 5 and 9), contributing to filling that lack by investigating a known low-cost and efficient adsorbent as the vermiculite in a continuous operation. The best fixed-bed performance was achieved with a flow rate of 0.25 mL/min and inlet concentration of 0.5 mmol/L, which also the modified dose-response (Yan et al., 2001) and Dual-SD (de Andrade et al., 2020) models could describe well the breakthrough curves for both metals, being useful for scale-up purposes. Moreover, the bed efficiency was tested through successive adsorption and desorption cycles, and the first and last cycle results are summarized in Table 11.3.

Besides the great results in the reusability experiments in fixed-bed operation, the selectivity towards Dy was also investigated in continuous mode (Chapter 9). The vermiculite adsorbed the metals in the follow downward order: Dy (0.195 mmol/g, 82.1%) $>$ Pb (0.092 mmol/g, 41.1%) $>$ Ni (0.086 mmol/g, 35.7%) $>$ Cd (0.074, 16.5%) $>$ Cu (0.059 mmol/g, 16.4%), which agrees to the order obtained in batch mode (Chapter 7). The adsorption capacity of Dy on the column was, at maximum,

3.3 times higher than the other metals (M), confirming the clear preferability for dysprosium. Regarding the multimetal-loaded column desorption, the eluent could desorb the metals in the follow order: Dy (0.192 mmol/g, 98.3 %), Ni (0.086 mmol/g, 100 %), Cd (0.061 mmol/g, 82.3 %), Cu (0.049 mmol/g, 82.8 %), and Pb (0.019 mmol/g, 20.1%). The most adsorbed metals were expected to be the most desorbed. In addition, Pb did not follow this hypothesis due to the different mechanisms that play a role in the adsorption of each metal. The magnesium could replace, more efficiently, the cations attached to the surface by weak bonds or electrostatic forces. Thus, lead probably was fixed to the vermiculite by inner-sphere complexes (stronger interaction) due to the facilitated loss of coordinated water discussed above and remained in the solid after the elution process. Thus, the eluate solution can concentrate the selectivity of dysprosium depending directly on the adsorption mechanism of the other metals in the solution.

Table 11.3. Comparison between the vermiculite fixed-bed Nd and Dy adsorption efficiencies in the first and fifth cycle.

Parameters		First cycle		Fifth cycle	
		Nd	Dy	Nd	Dy
Adsorption	t_b (min)	847.5	825	790	895
	t_e (min)	2407.5	2145	1930	1375
	R_b (%)	98.9	100	98.9	99.9
	R_e (%)	52.7	51.6	66.3	91.2
	H_{ZTM} (cm)	2.4	1.8	2.7	2.0
	q_b (mmol/g)	0.26	0.31	0.23	0.28
	q_e (mmol/g)	0.40	0.42	0.38	0.40
	q_D (mmol/g)	0.24	0.40	0.19	0.38
Desorption	D (%)	62.1	97.4	48.9	94
	C_F	23.4	32.2	19.2	48

Note that bed rupture occurred for neodymium or dysprosium at around 850 minutes, with less variation over the cycles for the Nd case. Exhaustion occurred at times greater than 2000 minutes in the first cycle, and there was a decrease in this time in the last run. Adsorption efficiencies until failure were approximately 100%, while exhaustion efficiencies were around 50% in the first cycle, increasing to 66.3 for Nd and 91.2 for Dy. The height of the mass transfer zone was from 2.4 to 2.7 cm in the Nd study and from 1.8 to 2.0 cm in the case of Dy, indicating that the bed showed improved

resistance to mass transfer throughout the cycles. The adsorption capacities at the breakthrough and exhaustion were reduced by 0.03 and 0.02 mmol/g for both metals throughout the cycles. Thus, the bed maintained its adsorption potential during the reuse steps with slight variations.

Vermiculite showed a certain selectivity towards REM from mixtures with bivalent metals (Chapters 3 and 7) under idealistic experimental conditions. However, in Chapter 10, the adsorption performance study advanced to more realistic approaches, i.e., the adsorption capacity of vermiculite and selectivity towards Nd and Dy were evaluated from a complex solution containing the main components of Nd-Fe-B magnet leachate, which is a real secondary source rich in REM. The research showed that the clay achieved high adsorption capacities, but the adsorption was not selective. Nevertheless, the desorption by complexation with EDTA (0.01 mol/L) showed the potential to selectively recover REM, but further investigation should be performed to optimize the desorption conditions.

The adsorbent investigated in the study, expanded vermiculite, is a clay mineral that was submitted to a rigorous thermal treatment at around 900 °C (Udoudo et al., 2015), whose characterization before and after the Nd or Dy adsorption and regeneration was raised along with the chapters, according to their pertinence within the scope of the chapter. Table 10.4 summarizes some of the textural and structural properties of the adsorbent, and Table 10.5 presents the elemental composition of the samples.

Table 11.4. Summary of the main properties of the adsorbent in different stages of the adsorption and desorption of Nd and Dy

Property	Original Adsorbent	After Adsorption		After 5 cycles of use	
		Nd	Dy	Nd	Dy
Surface area (m ² /g)	10	5	4	9	5
Density (kg/m ³)	2,167.5	2,582.6	2,612.4	2,544.0	2,306.2
Interlayer space (Å)	14.1	14.8	14.9	15.0	14.3
pH _{zc}	2.5	-	-	3.6	3.6

The surface area, obtained from the nitrogen adsorption isotherm by the BET calculation (Brunauer et al., 1938), was reduced by around 44.3 and 55.1% from the original 10 m²/g after the adsorption of Nd and Dy, respectively, meaning an average reduction of 49.6 % ± 5.3%. This loss of half of the surface area is mainly attributed to the rehydration of the vermiculite's interlayer spaces, which reduces the material's expansion. The regeneration step recovery in part the original surface area and the surface area of the spent material after the successive neodymium adsorption and

desorption processes is much higher than Dy-spent vermiculite. The density of the samples had a similar behavior along to the study step. Independently of the magnitude, the adsorption and desorption processes improved the adsorbent density compared to the original. The REM adsorption enlarged the density from 2,167.5 kg/m³ to around 2,597.5 ± 14.9 kg/m³ due to the compaction mentioned above and to the Nd and Dy loading that turns the material slightly more massive than the original. Once more, the regeneration using the same natural exchangeable cation of the vermiculite showed a more effective result since the Dy-spent vermiculite density was the closest to the original.

The characteristic interlayer space of the vermiculite, found in the X-ray diffractograms, was improved after the adsorption of Nd and Dy because these metals have higher ionic radii and coordination numbers than the exchanged interlayer magnesium. After the reuse cycles, the space is enlarged from the original. As the dysprosium desorption was by magnesium cations in the eluent solution, the interlayer space of the regenerated adsorbent was just slightly higher (~ 1%) than the original. In the neodymium case, the non-desorbed neodymium and the presence of calcium cations in the interlayer could also have contributed to the enlargement of the interlayer space after the regeneration steps.

The pH of zero charge (pH_{zc}) of the vermiculite was 2.5. Meanwhile, the reused material had a pH_{zc} of 3.6 for both metals, which means that the sorptive processes reduced the pH range where the vermiculite has negative charges. The negative charge of the vermiculite is attributed to the isomorphic substitution of silica and aluminum in the tetrahedral sheet, which is counterbalanced by the interlayer cations. The reuse of the adsorbent disarranged the well-organized crystalline structure of the material, as pointed out by X-ray diffraction results, which means a reduction in the effect of the isomorphic substitution.

Table 11.5. Composition determined by SEM-EDS analysis.

Element (%)	Original	After adsorption		After 5 cycles of use	
		Nd	Dy	Nd	Dy
Mg	15.7	16.0	15.5	14.2	17.2
Al	7.63	8.35	6.98	7.40	7.71
Si	21.8	22.7	21.2	21.8	22.3
Fe	7.49	2.83	4.30	6.31	5.44
O	45.9	46.0	44.0	45.3	46.4
Dy	-	-	6.97	-	-
Nd	-	3.62	-	0.51	-
Ca	-	-	-	3.35	-

Others*	1.54	0.54	0.95	1.17	0.87
---------	------	------	------	------	------

*Sum of the elements with content <1%

Table 11.5 confirms the vermiculite's original hydrated magnesium–aluminum–iron phyllosilicate composition. The silica, aluminum, and oxygen content are practically constants (~22%, 7.61%, 45.5%) during all study steps. After the Nd and Dy adsorption, the magnesium content in the vermiculite remains the same since the difference is in the analysis error. However, after the reuse, the relative magnesium amount decreased because the magnesium exchanged with neodymium in the sorption process was not replaced by desorption. Indeed, the calcium took place in the vermiculite composition. Also, a residual Nd is still loaded in the adsorbent after the adsorption, corroborating the partial desorption. In the Mg-regenerated vermiculite (Dy study), the magnesium content improved concerning the original sorbent may be due to the excess of the magnesium employed in the sorption. The Nd and Dy content in the loaded vermiculite was 3.62 and 6.97%, respectively, indicating the affinity order previously discussed. Thus, in general, the sorbent maintained the original composition, even after five cycles of reuse, reflecting the adsorbent stability and how the elution process preserved the vermiculite elemental structure.

Thus, the present thesis evaluated the potential of expanded vermiculite in the recovery of Nd and Dy by adsorption and desorption in batch and fixed-bed mode. The clay material is a promisor alternative adsorbent due to the excellent results regarding reusability and stability. The desorption (recovery) was efficient by exchanging alkaline earth metals or chelant agents instead of the common use of strong acids. Those findings contributed to the development of the REM circular economy, presenting a deep investigation of a low-cost, highly available, and efficient material for recovering such critical metals as neodymium and dysprosium.

CHAPTER 12. GENERAL CONCLUSIONS AND PERSPECTIVES

The present doctoral thesis showed that adsorption using expanded vermiculite is a promising technology for neodymium and dysprosium recovery from aqueous solutions. In general, the main findings are related to the detailed description of the Nd and Dy adsorption mechanisms, the high efficiency in recovering these REM, and the adsorbent regeneration. Moreover, the main challenges and limitations of the approach were also pointed out, such as the lack of selectivity in relations to REM mixed with permanent magnet leachate. Therefore, this thesis may contribute to future research on recovering REM from secondary sources by adsorption. Given the results found, the main conclusions of this work for the REM adsorption and desorption processes are:

- Response surface methodology and machine learning approaches could determine the optimum pH and adsorbent dosages.
- The best pH and solid/liquid ratios for removing Nd and Dy were around 3.3 and 3.5, and 14 g/L and 12.8 g/L, respectively.
- The PSO model described both kinetics behaviors ruled by external and intraparticle diffusion mechanisms.
- Exchange with the interlayer magnesium is essential in the overall adsorption mechanism.
- The maximum experimental adsorption capacities for Nd and Dy were 0.48 mmol/g at 283 K and 0.9 mmol/g at 298 K.
- The equilibrium isotherms of Nd and Dy could be modeled by Langmuir, homogenous monolayer saturation, and by BET, saturation of a first layer followed by surface precipitation.
- The thermodynamics of Nd and Dy adsorption onto vermiculite revealed different natures: Nd adsorption is exothermic and Dy adsorption is endothermic.
- The best eluents were solutions containing alkali earth metals (Ca and Mg).
- The highest Nd and Dy desorption efficiencies were achieved using a solid/liquid ratio of 14 g/L and 7.31 g/L, with calcium chloride (0.3 mol/L) and magnesium nitrate (0.2 mol/L) eluent solutions, with a contact time of 3 h, correspondingly.
- The cyclic reuses, in batch and fixed-bed modes, showed the reproducibility of the original adsorption efficiency along with the cycles.

- The desorption efficiency in batch mode at the fifth cycle (last) was up to 94.0% for both metals, and in fixed-bed mode achieved the maximum values of 96.0% (3rd cycle) and 97.7% (4th cycle) for Nd and Dy.
- The vermiculite is quite selective for Nd and Dy adsorption from mixtures of with bivalent metals, which the selectivity order was Dy > Pb > Ni > Cd > Cu, and Nd > Ni > Zn > Cu > Pb.
- In the dynamic study, both metals achieved the best efficiency parameters at a flow rate of 0.25 mL/min and an inlet concentration of 0.5 mmol/L.
- At the best conditions, the breakthrough and exhaustion capacities were 0.26 and 0.40 mmol/g for Nd and 0.31 and 0.42 mmol/g for Dy.
- The MDR and Dual Site Diffusion models fitted well the breakthrough curves.
- The continuous desorption of the vermiculite bed could concentrate Nd and Dy 25.2 and 41.2 times, respectively.
- The maximum adsorption capacities at equilibrium were 0.48 and 0.21 mmol/g for Nd and Dy, respectively, from an equimolar mixture.
- Vermiculite was not selective towards REM from a Nd-Fe-B leachate, whose descending adsorption capacity order was Fe > Nd > Zn > Pr > Co > Dy > Ni > Al > Mn.
- EDTA as an eluent may desorb REM in preference to other loaded metals, indicating a potential for selective desorption.
- The expanded vermiculite had a layered structure shape with a surface area of 10 m²/g, real density of 2167.5 kg/m³, porosity of 88%, and interlayer space of 14.1 Å.
- After the adsorption of Nd and Dy, the vermiculite reduced the surface area to 5 and 4 m²/g, and porosity to 79 and 72 %, and improved the real density to 2,582.6 and 2,612.4 kg/m³, and the interlayer space to 14.8 and 14.9 Å, respectively.
- The regenerated vermiculite, after the reuses in Nd and Dy sorption, respectively, showed a reduced surface area (9 and 5 m²/g), and porosity (53 and 75%), and an improved density (2,544 and 2,306 kg/m³) and interlayer space (15.0 and 14.3 Å), respect to the original adsorbent.
- The adsorbent also presented homogeneous composition, mesoporous, and thermal stability before and after the Nd and Dy adsorption and subsequent reuses.

- The FTIR and EDS analyses confirmed the aluminum-iron-magnesium silicate composition of the vermiculite. Also, they evidenced that the ion exchange mechanism plays a fundamental role in the removal and recovery of Nd and Dy by expanded vermiculite.

Based on the limitations of the present study and the trends in the REM recovery segment, suggestions for future studies are listed below:

- Vermiculite shows lack of selectivity for REM in real applications, so, if the objective is a selective recovery of the REM, further studies of physical-chemical modifications such as ligand functionalization should be performed.
- Due to the highly stable structure, vermiculite can be a support matrix for forming polymer composites originating efficient and resistant adsorbents for REM recovery.
- Also, based on the above, the polymers used in composites should be preferable from biological sources, such as bio polysaccharides and proteins, contributing to the sustainability of the process. And the ion-imprinted process is also recommended to improve the selectivity between REM.
- The simultaneous Nd and Dy recovery efficiency from complex matrices to mimic real application was just done in batch mode in this thesis, so the investigation in continuous fixed bed mode is also suggested.
- EDTA showed promising results for the selective REM desorption in real operations. Nonetheless, future research should investigate the optimization of desorption conditions, such as S/L ratio, eluent concentration, and contact time to obtain greater efficiencies.
- Novel approaches to elution should also be evaluated, such as eluent recycling, the desorption in steps using eluents with different selectivity between REM, and loaded adsorbent use as a catalyst for the degradation of other contaminants in advanced oxidative processes.
- Economic viability and scale-up studies would also be necessary to improve the proposed technology's maturity.

CHAPTER 13. SCIENTIFIC PRODUCTION OF THE PERIOD (2018/2-2022/2)

Publications on indexed international journals

1. Critical rare earth metal adsorption onto expanded vermiculite: accurate modeling through response surface methodology and machine learning techniques

Authors: **Giani de V. Brião**, Dison S. P. Franco, Flávio V. da Silva, Meuris G. C. da Silva, Melissa G. A. Vieira

Sustainable Chemistry and Pharmacy, v. 31, p. 100938, 2023.

DOI: 10.1016/j.scp.2022.100938

2. Adsorption potential for the concentration and recovery of rare earth metals from NdFeB magnet scrap in the hydrometallurgical route: a review in a circular economy approach.

Authors: **Giani de V. Brião**, Meuris G. C. da Silva, Melissa G. A. Vieira

Journal of Cleaner Production, v. 380, Part 2, 135112, 2022.

DOI: 10.1016/j.jclepro.2022.135112

3. Graphene oxide-safranin modified@polyacrylonitrile membranes for water purification: Reuse and mechanism based on theoretical calculations and XPS analysis.

Authors: Tauany de F. Neves, Natália G. Camparotto, **Giani de V. Brião**, Valmor Mastelaro, Renato F. Dantas, Melissa G. A. Vieira.

Journal of Water Process Engineering, v. 50, p. 103248, 2022.

DOI: 10.1016/j.jwpe.2022.103248

4. Synthesis of Mesoporous P-Doped Carbon and its Application in Propranolol Drug Removal: Characterization, kinetics and isothermal Studies

Authors: Gustavo R. Paixão, Natália G. Camparotto, **Giani de V. Brião**, Juan C. C. Quintero, Rafael L. Oliveira, Patrícia Prediger and Melissa G. A. Vieira

Chemical Engineering Research and Design, v. 187, p. 225 – 239, 2022.

DOI: 10.1016/j.cherd.2022.09.009

5. Inversion of implicit adsorption isotherms by use of the Lambert W function

Authors: **Giani de V. Brião**, Khim H. Chu.

Journal of Chemical Technology & Biotechnology, 2022.

DOI:10.1002/jctb.7189

6. Renewable and selective vermiculite fixed bed for the rare-earth dysprosium recovery

Authors: **Giani de V. Brião**, Fernando A. Agostinho, Meuris G. C. da Silva, Melissa G. A. Vieira

Industrial & Engineering Chemistry Research, v. 61, n. 25, p. 9044–9053, 2022

DOI: 10.1021/acs.iecr.2c01265

7. Ternary adsorption of Auramine-O, Rhodamine 6G, and Brilliant Green onto Arapaima gigas scales hydroxyapatite: Adsorption mechanism investigation using CCD and DFT studies

Authors: Emanuele D.V. Duarte, **Giani de V. Brião**, Nielson F.P. Ribeiro, Meuris G.C. da Silva, Melissa G.A. Vieira, Samira M.L. de Carvalho

Sustainable Materials and Technologies, v. 31, p. e00391, 2022

DOI: 10.1016/j.susmat.2022.e00391

8. Reusable and efficient clay material for the fixed-bed neodymium recovery

Authors: **Giani de V. Brião**, Meuris G. C. da Silva, Melissa G. A. Vieira

Sustainable Chemistry and Pharmacy, v. 25, p. 100623, 2022

DOI: 10.1016/j.scp.2022.100623

9. Correlation of type II adsorption isotherms of water contaminants using modified BET equations

Authors: **Giani de V. Brião**, Meuris G. C. da Silva, Melissa G. A. Vieira, Khim H. Chu.

Colloid and Interface Science Communications, v. 46, p. 100557, 2022

DOI: 10.1016/j.colcom.2021.100557

10. Dysprosium adsorption on expanded vermiculite: Kinetics, selectivity, and desorption

Authors: **Giani de V. Brião**, Meuris G. C. da Silva, Melissa G. A. Vieira

Colloids and Surfaces A: Physicochemical and Engineering Aspects, v. 630, p. 127616, 2021

DOI: 10.1016/j.colsurfa.2021.127616

11. Expanded vermiculite as an alternative adsorbent for the dysprosium recovery

Authors: **Giani de V. Brião**, Meuris G. C. da Silva, Melissa G. A. Vieira

Journal of the Taiwan Institute of Chemical Engineers, v.127, p. 228-235, 2021.

DOI: 10.1016/j.jtice.2021.08.022

12. Efficient and Selective Adsorption of Neodymium on Expanded Vermiculite

Authors: **Giani de V. Brião**, Meuris G. C. da Silva, Melissa G. A. Vieira

Industrial & Engineering Chemistry Research, v. 60, p. 4962–4974, 2021.

DOI: 10.1021/acs.iecr.0c05979

13. Removal of toxic metals from water using chitosan-based magnetic adsorbents. A review

Authors: **Giani de V. Brião**, Júlia R. de Andrade, Meuris G. C. da Silva, Melissa G. A. Vieira

Environmental Chemistry Letters, v. 18, p. 1145–1168, 2020.

DOI: 10.1007/s10311-020-01003-y

14. Neodymium recovery from aqueous solution through adsorption/desorption onto expanded vermiculite

Authors: **Giani de V. Brião**, Meuris G. C. da Silva, Melissa G. A. Vieira

Applied Clay Science, v. 198, p. 105825, 2020.

DOI: 10.1016/j.clay.2020.105825

Submitted articles in indexed international journals

1. Comparative effect of mesoporous carbon doping on the adsorption of pharmaceutical drugs in water: Theoretical calculations and mechanism study by XPS

Authors: Natália G. Camparotto, Gustavo R. Paixão, **Giani de V. Brião**, Rafael L. Oliveira, Patrícia Prediger, Melissa G. A. Vieira

Environmental Toxicology and Pharmacology

Book chapters

1. Biosorption of toxic metals from multicomponent systems and wastewaters

Authors: Heloísa P. S. Costa, **Giani V. Brião**, Talles B. da Costa, Cléophee Gourmand, Caroline Bertagnolli, Meuris G. C. da Silva, Melissa G. A. Vieira

In: Jeferson Steffanello Piccin, Aline Dettmer, Natarajan Chandrasekaran. (Org.). *Toxic metals: generation, disposal, treatment, and valuation*. CRC Press/Taylor & Francis Group.

2. Adsorption and Desorption Aspects of Carbon-Based Nanomaterials: Recent Applications for Water Treatments and Toxic Effects

Authors: Patrícia Prediger, Tauany. F. Neves, Natália. G. Camparotto, Paula. M. M. Da Silva, Melissa G. A. Vieira, **Giani de V. Brião**

In: Uma Shanker, Manviri Rani. (Org.). *Liquid and Crystal Nanomaterials for Water Pollutants Remediation*. 1ed. Boca Raton, US: CRC Press - Taylor & Francis, v. 1, p. 59-87, 2022.

DOI: 10.1201/9781003091486

3. Removal of Emerging Pollutants Using Magnetic Adsorbents

Authors: Julia R. de Andrade, **Giani de V. Brião**, Meuris G. C. da Silva, and Melissa G. A. Vieira

In: Lucas Meili, Guilherme Luiz Dotto. (Org.). *Advanced Magnetic Adsorbents for Water Treatment*. Environmental Chemistry for a Sustainable World. 1ed.: Springer International Publishing, v. 61, p. 187 – 222, 2021.

DOI: 10.1007/978-3-030-64092-7_7

Complete articles published in congress proceedings

1. Response surface methodology approach for optimization of dysprosium adsorption onto expanded vermiculite

Authors: **Giani de V. Brião**, Meuris G. C. da Silva, Melissa G. A. Vieira

In: 13 th Brazilian Meeting on Adsorption, 2020, Fortaleza/CE. Anais 13º EBA, Fortaleza/CE: UFC, 2020.

DOI: 10.51996/9786588492529

2. Avaliação do processo cinético de adsorção do metal terra rara Ítrio (Y3+) em adsorvente argiloso vermiculita expandida

Authors: Thiago L. da Silva, **Giani de V. Brião**, Meuris G. C. da Silva, Melissa G. A. Vieira

In: XXXIX Congresso Brasileiro de Sistemas Particulados, 2019, Belém/PA. Anais do XXXIX ENEMP, Belém/PA: UFPA, 2019.

3. Otimização de condições de operação da adsorção de neodímio em vermiculita expandida pelo método de superfície de resposta

Authors: **Giani de V. Brião**, Thiago L. da Silva, Meuris G. C. da Silva, Melissa G. A. Vieira

In: XXXIX Congresso Brasileiro de Sistemas Particulados, 2019, Belém/PA. Anais do XXXIX ENEMP, Belém/PA: UFPA, 2019.

4. Ensaios de afinidade de íons terras raras em concentrado de vermiculita e vermiculita expandida

Authors **Giani de V. Brião**, Meuris G. C. da Silva, Melissa G. A. Vieira

In: Simpósio Comemorativo 40 Anos da Área de Sistemas Particulados, 2019, São Carlos/SP. Anais do SimAPI, São Carlos, UFSCar, 2019.

Abstract published in congress proceedings

1. Adsorção de disprósio em leito de vermiculita expandida

Authors: Fernando A. Agostinho, **Giani de V. Brião**, Melissa G. A. Vieira.

In: XXIX Congresso de Iniciação Científica Unicamp, 2021, Campinas/SP. Anais do XXIX Congresso de Iniciação Científica Unicamp, Campinas/SP: UNICAMP, 2021.

2. Desenvolvimento de materiais bio/adsorventes para recuperação de íons terras-raras e preparação de partículas de blenda polimérica de sericina e alginato para aplicação farmacêutica

Authors: Nariany A. da Silva, Leandro L. dos Santos Junior, Wedja T. Vieira, **Giani de V. Brião**, Talles B. da Costa, Thiago L. da Silva, Meuris G. C. da Silva, Melissa G. A. Vieira

In: XXIX Congresso de Iniciação Científica Unicamp, 2021, Campinas/SP. Anais do XXIX Congresso de Iniciação Científica Unicamp, Campinas/SP: UNICAMP, 2021.

GENERAL REFERENCES

- ARRUDA, G M. Vermiculite utilization on the treatment of water contaminated with organic compounds. 2005. [S. l.]: 2 nd Mercosur Congress on Chemical Engineering 4 Mercosur Congress on Process Systems Engineering, 2005. p. 1–10.
- BALARAM, V. Rare earth elements: A review of applications, occurrence, exploration, analysis, recycling, and environmental impact. **Geoscience Frontiers**, vol. 10, no. 4, p. 1285–1303, 2019. DOI 10.1016/j.gsf.2018.12.005. Available at: <https://doi.org/10.1016/j.gsf.2018.12.005>.
- BRUNAUER, Stephen; EMMETT, P. H.; TELLER, Edward. Adsorption of Gases in Multimolecular Layers. **Journal of the American Chemical Society**, vol. 60, no. 2, p. 309–319, Feb. 1938. DOI 10.1021/ja01269a023. Available at: <https://pubs.acs.org/doi/abs/10.1021/ja01269a023>.
- CHARALAMPIDES, Georgios; VATALIS, Konstantinos I.; APOSTOLOS, Baklavaridis; PLOUTARCH-NIKOLAS, Benetis. Rare Earth Elements: Industrial Applications and Economic Dependency of Europe. **Procedia Economics and Finance**, vol. 24, no. 15, p. 126–135, 2015. DOI 10.1016/S2212-5671(15)00630-9. Available at: <http://linkinghub.elsevier.com/retrieve/pii/S2212567115006309>.
- CHEN, Liya; WU, Pingxiao; CHEN, Meiqing; LAI, Xiaolin; AHMED, Zubair; ZHU, Nengwu; DANG, Zhi; BI, Yingzhi; LIU, Tongyun. Preparation and characterization of the eco-friendly chitosan/vermiculite biocomposite with excellent removal capacity for cadmium and lead. **Applied Clay Science**, vol. 159, no. December 2017, p. 74–82, 2018. DOI 10.1016/j.clay.2017.12.050. Available at: <https://doi.org/10.1016/j.clay.2017.12.050>.
- DA COSTA, Talles Barcelos; DA SILVA, Meuris Gurgel Carlos; VIEIRA, Melissa Gurgel Adeodato. Effective recovery of ytterbium through biosorption using crosslinked sericin-alginate beads: A complete continuous packed-bed column study. **Journal of Hazardous Materials**, vol. 421, no. March 2021, p. 126742, 2022. DOI 10.1016/j.jhazmat.2021.126742. Available at: <https://doi.org/10.1016/j.jhazmat.2021.126742>.
- DANGELO, Paola; ZITOLO, Andrea; MIGLIORATI, Valentina; CHILLEMI, Giovanni; DUVAIL, Magali; VITORGE, Pierre; ABADIE, Sacha; SPEZIA, Riccardo. Revised ionic radii of lanthanoid(III) ions in aqueous solution. **Inorganic Chemistry**, vol. 50, no. 10, p. 4572–4579, 16 May 2011. <https://doi.org/10.1021/ic200260r>.

- DE ANDRADE, Júlia Resende; OLIVEIRA, Maria Fernanda; CANEVESI, Rafael Luan Sehn; LANDERS, Richard; DA SILVA, Meuris Gurgel Carlos; VIEIRA, Melissa Gurgel Adeodato. Comparative adsorption of diclofenac sodium and losartan potassium in organophilic clay-packed fixed-bed: X-ray photoelectron spectroscopy characterization, experimental tests and theoretical study on DFT-based chemical descriptors. **Journal of Molecular Liquids**, vol. 312, p. 113427, 2020. DOI 10.1016/j.molliq.2020.113427. Available at: <https://doi.org/10.1016/j.molliq.2020.113427>.
- DŁUGOSZ, Olga; BANACH, Marcin. Sorption of Ag⁺ and Cu²⁺ by Vermiculite in a Fixed-Bed Column: Design, Process Optimization and Dynamics Investigations. **Applied Sciences**, vol. 8, no. 11, p. 2221, 11 Nov. 2018. DOI 10.3390/app8112221. Available at: <http://www.mdpi.com/2076-3417/8/11/2221>.
- FREITAS, Emanuelle Dantas de; ALMEIDA, Hewellyn Joacy de; VIEIRA, Melissa Gurgel Adeodato. Binary adsorption of zinc and copper on expanded vermiculite using a fixed bed column. **Applied Clay Science**, vol. 146, no. July, p. 503–509, 2017. DOI 10.1016/j.clay.2017.07.004. Available at: <http://dx.doi.org/10.1016/j.clay.2017.07.004>.
- JOWITT, Simon M.; WERNER, Timothy T.; WENG, Zhehan; MUDD, Gavin M. Recycling of the rare earth elements. **Current Opinion in Green and Sustainable Chemistry**, vol. 13, p. 1–7, 2018. DOI 10.1016/j.cogsc.2018.02.008. Available at: <https://doi.org/10.1016/j.cogsc.2018.02.008>.
- JUNNE, Tobias; WULFF, Niklas; BREYER, Christian; NAEGLER, Tobias. Critical materials in global low-carbon energy scenarios: The case for neodymium, dysprosium, lithium, and cobalt. **Energy**, vol. 211, p. 118532, 2020. DOI 10.1016/j.energy.2020.118532. Available at: <https://doi.org/10.1016/j.energy.2020.118532>.
- KANEKO, Takamasa; NAGATA, Fukue; KUGIMIYA, Shinichi; KATO, Katsuya. Optimization of carboxyl-functionalized mesoporous silica for the selective adsorption of dysprosium. **Journal of Environmental Chemical Engineering**, vol. 6, no. 5, p. 5090–5098, 1 Oct. 2018. <https://doi.org/10.1016/j.jece.2018.09.018>.
- LIU, Enli; XU, Xuechao; ZHENG, Xudong; ZHANG, Fusheng; LIU, Enxiu; LI, Chunxiang. An ion imprinted macroporous chitosan membrane for efficiently selective adsorption of dysprosium. **Separation and Purification Technology**, vol. 189, p. 288–295, 2017. <https://doi.org/10.1016/j.seppur.2017.06.079>.

- LIU, Yong; XIAO, Dan; LI, Hui. Kinetics and Thermodynamics of Lead (II) Adsorption on Vermiculite. **Separation Science and Technology**, vol. 42, no. 1, p. 185–202, Jan. 2007. DOI 10.1080/01496390600998045. Available at: <http://www.tandfonline.com/doi/abs/10.1080/01496390600998045>.
- MORAES, Dorsan S.; RODRIGUES, Elizabeth M.S.; LAMARÃO, Cláudio N.; MARQUES, Gisele T.; RENTE, Augusto F.S. New sodium activated vermiculite process. Testing on Cu²⁺ removal from tailing dam waters. **Journal of Hazardous Materials**, vol. 366, no. November 2018, p. 34–38, 2019. DOI 10.1016/j.jhazmat.2018.11.086. Available at: <https://doi.org/10.1016/j.jhazmat.2018.11.086>.
- PAULA, Ricardo de Freitas; CARVALHÃES, Cássio. Vermiculita. **Sumário Mineral 2016**. Brasília: Departamento Nacional de Produção Mineral, 2018. vol. 36, p. 110–111.
- SAHA, Dipendu; AKKOYUNLU, Sel Didem; THORPE, Ryan; HENSLEY, Dale K.; CHEN, Jihua. Adsorptive recovery of neodymium and dysprosium in phosphorous functionalized nanoporous carbon. **Journal of Environmental Chemical Engineering**, vol. 5, no. 5, p. 4684–4692, 2017. DOI 10.1016/j.jece.2017.09.009. Available at: <http://dx.doi.org/10.1016/j.jece.2017.09.009>.
- UDOUDO, Ofonime; FOLORUNSO, Olaosebikan; DODDS, Christopher; KINGMAN, Samuel; URE, Alex. Understanding the performance of a pilot vermiculite exfoliation system through process mineralogy. **Minerals Engineering**, vol. 82, p. 84–91, 2015. DOI 10.1016/j.mineng.2015.03.023. Available at: <http://dx.doi.org/10.1016/j.mineng.2015.03.023>.
- YAN, G.; VIRARAGHAVAN, T.; CHEN, M. A new model for heavy metal removal in a biosorption column. **Adsorption Science and Technology**, vol. 19, no. 1, p. 25–43, 2001. <https://doi.org/10.1260/0263617011493953>.
- YANG, Yongxiang; WALTON, Allan; SHERIDAN, Richard; GÜTH, Konrad; GAUSS, Roland; GUTFLEISCH, Oliver; BUCHERT, Matthias; STEENARI, Britt-Marie; VAN GERVEN, Tom; JONES, Peter Tom; BINNEMANS, Koen. REE Recovery from End-of-Life NdFeB Permanent Magnet Scrap: A Critical Review. **Journal of Sustainable Metallurgy**, vol. 3, no. 1, p. 122–149, 20 Mar. 2017. DOI 10.1007/s40831-016-0090-4. Available at: <http://link.springer.com/10.1007/s40831-016-0090-4>.

- ZHANG, Lingen; XU, Zhenming. A review of current progress of recycling technologies for metals from waste electrical and electronic equipment. **Journal of Cleaner Production**, vol. 127, p. 19–36, 2016. <https://doi.org/10.1016/j.jclepro.2016.04.004>.
- ZHENG, Xudong; ZHANG, Yi; ZHANG, Fusheng; LI, Zhongyu; YAN, Yongsheng. Dual-template docking oriented ionic imprinted bilayer mesoporous films with efficient recovery of neodymium and dysprosium. **Journal of Hazardous Materials**, vol. 353, p. 496–504, 5 Jul. 2018. <https://doi.org/10.1016/j.jhazmat.2018.04.022>.

APPENDIX A. SUPPLEMENTARY MATERIALS

APPENDIX A.1

Supplementary Material of the Chapter 3

This Supporting Information is available free of charge at <https://doi.org/10.1021/acs.iecr.0c05979>.

Table S1. Experimental domain of RCCD for the neodymium adsorption on EV.

Factor	Code	Levels				
		$-\alpha$	-1	0	+1	$+\alpha$
particle size (mm)	A	0.48	0.65	0.85	1.09	1.30
adsorbent amount (g)	B	0.163	0.300	0.500	0.700	0.836
pH	C	1.3	2.0	3.0	4.0	4.7

Table S2. Comparison of neodymium elution process from different adsorbent matrices.

Adsorbent	<i>S/L</i> (g/L)	Regeneration/Elution process	% <i>D</i> (%)	LD ₅₀ (mg/kg)	GHS class	Reference
Chitosan-Manganese-Ferrite Magnetic Beads	-	Methanol (98% v/v)	90	1,000	Category 4	¹
Core-shell alginate beads	1	HCl 0.2 M	100	277	Category 3	²
Graphene Oxide nanosheets	-	HNO ₃ 0.1 M	99*	> 90	Category 3	³
Gum Arabic grafted polyacrylamide based silica nanocomposite	-	HCl 0.1 M	80	277	Category 3	⁴
Ion imprinted xanthan gum- layered double hydroxide nanocomposite	0.025	HNO ₃ 0.1 M	-	> 90	Category 3	⁵
Ethylenediaminetria- cetic Acid- Functionalized Activated Carbon	-	HCl 0.1 M Washing using acetone and water	99	277	Category 3	⁶
Acrylic Resin (110) resin	0.6	HCl 3.0 M	99.4	277	Category 3	⁷
Expanded Vermiculite	14	CaCl ₂ 0.5 M	43.2	1,000	Category 4	This work

*From a mixture of rare earth metals

Table S3. Selectivity of neodymium from a multicomponent solution

Metal	<i>Kd</i>	<i>q</i> (mmol/g)	<i>S_{Nd/M}</i>
Ni	0.14	0.058	5.07
Zn	0.08	0.052	8.35
Cu	0.04	0.035	16.26
Pb	0.02	0.017	32.26
Nd	0.71	0.065	-

References

- (1) Durán, S. V.; Lapo, B.; Meneses, M.; Sastre, A. M. Recovery of Neodymium (III) from Aqueous Phase by Chitosan-Manganese-Ferrite Magnetic Beads. *Nanomaterials* **2020**, *10* (6), 1204. <https://doi.org/10.3390/nano10061204>.
- (2) Wang, F.; Zhao, J.; Li, W.; Zhou, H.; Yang, X.; Sui, N.; Liu, H. Preparation of Several Alginate Matrix Gel Beads and Their Adsorption Properties Towards Rare Earths (III). *Waste and Biomass Valorization* **2013**, *4* (3), 665–674. <https://doi.org/10.1007/s12649-012-9179-6>.
- (3) Ashour, R. M.; Abdelhamid, H. N.; Abdel-Magied, A. F.; Abdel-Khalek, A. A.; Ali, M. M.; Uheida, A.; Muhammed, M.; Zou, X.; Dutta, J. Rare Earth Ions Adsorption onto Graphene Oxide Nanosheets. *Solvent Extr. Ion Exch.* **2017**, *35* (2), 91–103. <https://doi.org/10.1080/07366299.2017.1287509>.
- (4) Iftekhar, S.; Srivastava, V.; Casas, A.; Sillanpää, M. Synthesis of Novel GA-g-PAM/SiO₂ Nanocomposite for the Recovery of Rare Earth Elements (REE) Ions from Aqueous Solution. *J. Clean. Prod.* **2018**, *170*, 251–259. <https://doi.org/10.1016/j.jclepro.2017.09.166>.
- (5) Iftekhar, S.; Srivastava, V.; Hammouda, S. Ben; Sillanpää, M. Fabrication of Novel Metal Ion Imprinted Xanthan Gum-Layered Double Hydroxide Nanocomposite for Adsorption of Rare Earth Elements. *Carbohydr. Polym.* **2018**, *194*, 274–284. <https://doi.org/10.1016/j.carbpol.2018.04.054>.
- (6) Babu, C. M.; Binnemans, K.; Roosen, J. Ethylenediaminetriacetic Acid-Functionalized Activated Carbon for the Adsorption of Rare Earths from Aqueous Solutions. *Ind. Eng. Chem. Res.* **2018**, *57* (5), 1487–1497. <https://doi.org/10.1021/acs.iecr.7b04274>.
- (7) Xiong, C.; He, R.; Pi, L.; Li, J.; Yao, C.; Jiang, J.; Zheng, X. Adsorption of Neodymium(III) on Acrylic Resin (110 Resin) from Aqueous Solutions. *Sep. Sci. Technol.* **2015**, *50* (4), 564–572. <https://doi.org/10.1080/01496395.2014.955204>.

APPENDIX A.2.

Supplementary Material of the Chapter 4

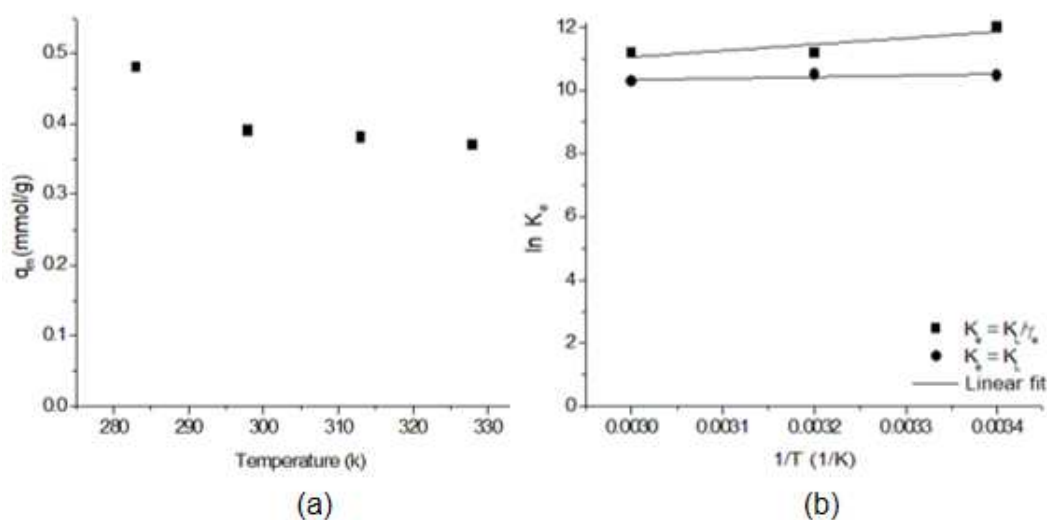
The supplementary material can be consulted at <https://doi.org/10.1016/j.clay.2020.105825>.

Table S.1 – Kinetic model parameters for neodymium adsorption on expanded vermiculite.

Model	Parameter	R^2	ARE (%)	R_a^2	AIC_c	SSE
PFO	q_e (mmol/g)	0.035 ± 0.0003	0.9951	2.16	0.9944	-229.6
	k_1 (1/min)	0.341 ± 0.011				
PSO	q_e (mmol/g)	0.040 ± 0.00073	0.9902	3.17	0.9887	-217.6
	k_2 (g.mmol/min)	11.00 ± 1.023				

Table S.2 – Cost analysis at lab scale.

Inputs	Cost to recover 1 g of Nd (\$/g)
Vermiculite	0.10
Nitric acid	0.0038
Calcium chloride	6.79

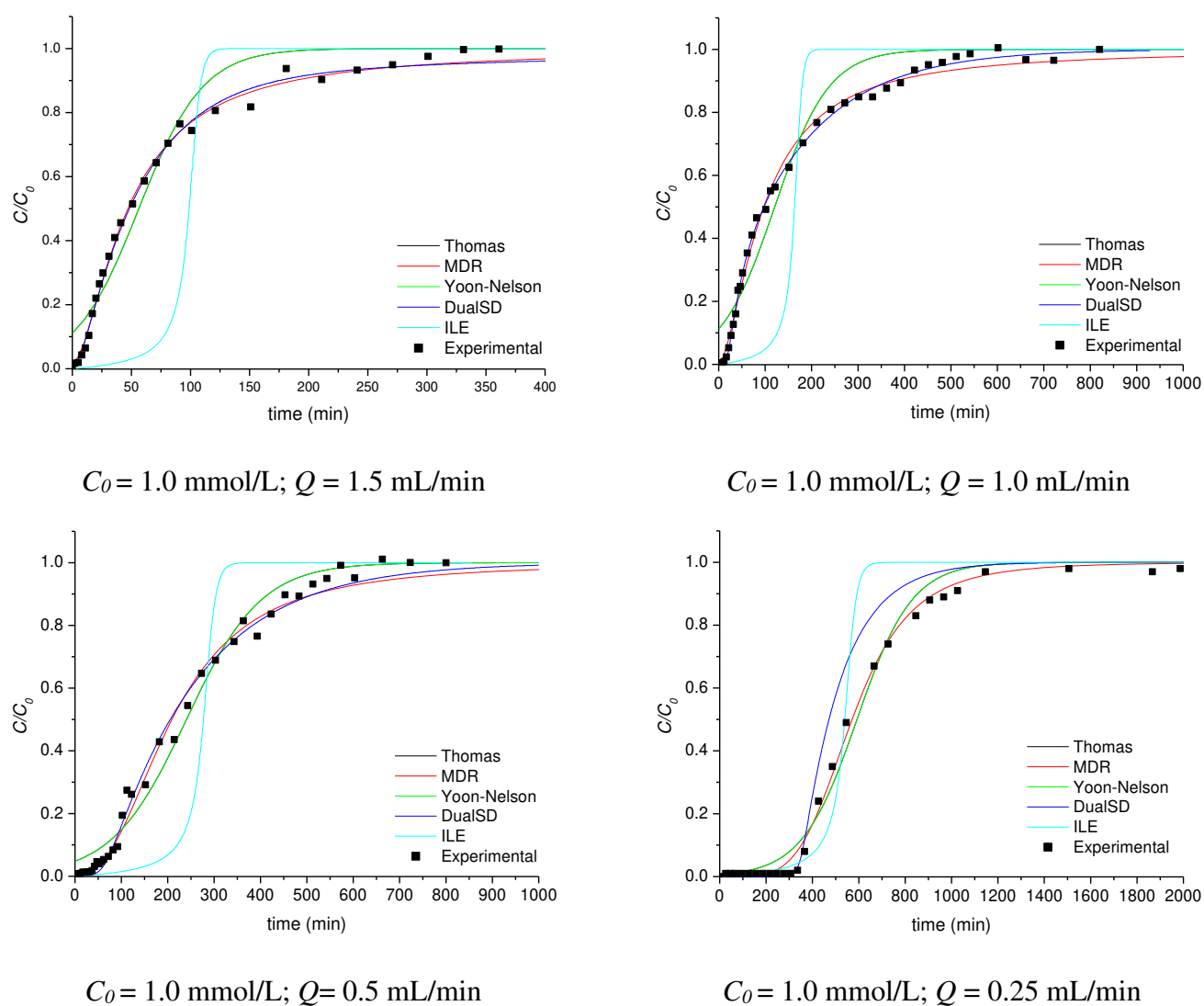
Figure S.1 – Effect of temperature on the q_m of Langmuir (a) and effect of the Nd^{3+} activity on the equilibrium constant (b)

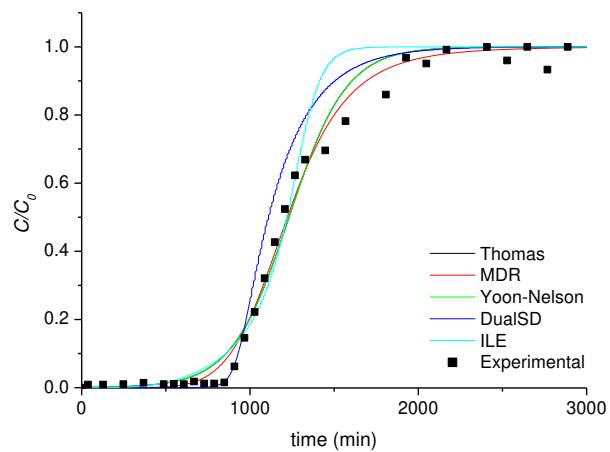
APPENDIX A.3

Supplementary Material of the Chapter 5

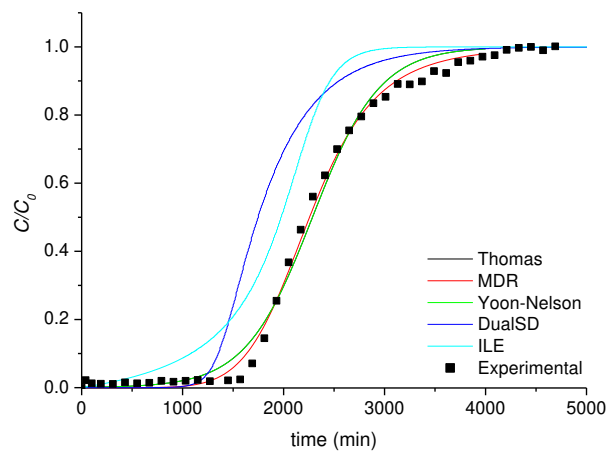
Supplementary data to this article can be found online at <https://doi.org/10.1016/j.scp.2022.100623>.

Figure S.1. Thomas, MDR, Yoon-Nelson, DualSD, and ILE breakthrough curves over the experimental data





$C_0 = 0.5$ mmol/L; $Q = 0.25$ mL/min



$C_0 = 0.25$ mmol/L; $Q = 0.25$ mL/min

APPENDIX A.4

Supplementary Material of the Chapter 6

Supplementary Methodology

Table S1 Parameters of the Dy-loaded adsorbent characterization procedure

Analyzes	Instrument	Experimental Conditions
Physical adsorption and desorption of nitrogen.	ANOVA-e (Quantachrome)	Pressure range from 10 to 800 mmHg, degas treatment for 3 hours at 200°C
Mercury porosimetry	Auto Pore IV (Micromeritics)	Pressure from 0.10 to 60000.00 psia
Helium picnometry	Accupyc II 1340 (Micromeritics)	10 cycles, cycle fill pressure of 16.000 psig, equilibration rate of 0.0500 psig/min.
Thermogravimetric and differential thermal analyses	DTG-60 (Shimadzu)	N ₂ flow of 50 ml/min, a heating rate of 20 °C/min

From the nitrogen adsorption isotherm in the relative pressure range of 0.05 to 0.3, the BET surface area S_{BET} (m²/g) was obtained from a linear regression (Equation S1-S2).

$$\frac{1}{v[(P_0/P) - 1]} = \frac{c - 1}{v_m c} \left(\frac{P}{P_0} \right) + \frac{1}{v_m c} \quad (S1)$$

$$S_{BET} = \frac{v_m N N}{V a} \quad (S2)$$

Where v is the amount of adsorbed N₂; P_0 and P are the saturation and equilibrium pressure of the adsorbate, respectively; c is the BET constant, v_m is the volume of absorbed gas from the monolayer, N is the Avogadro number, s is the cross-sectional area of the adsorbed gas molecule, V is the molar volume of the adsorbate, a is the mass of adsorbent.

Mercury porosimetry provided information on macropores distribution, volume of macropores (V_{macro}) and bulk density (ρ_{bulk}). Helium picnometry analysis provided the real sample density (ρ). The particle porosity (ε_p) was calculated based on these two properties, according to Equation (S3).

$$\varepsilon_p = 1 - \frac{\rho_{bulk}}{\rho} \quad (S3)$$

Supplementary Figures

Fig S1 ANN architectures prediction error

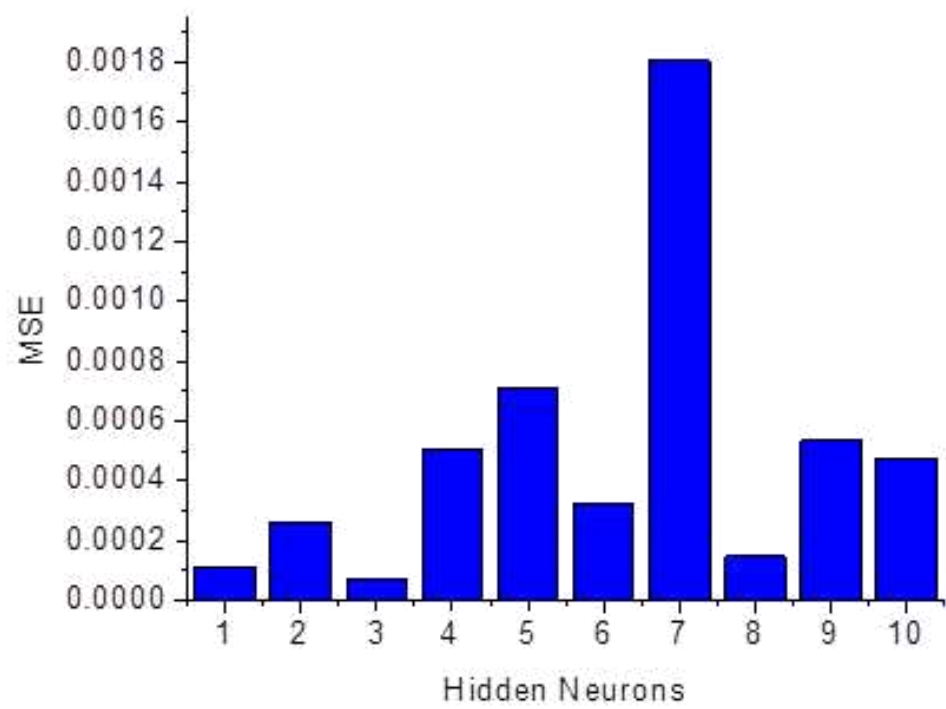


Fig S2 ANN with three hidden neurons performance

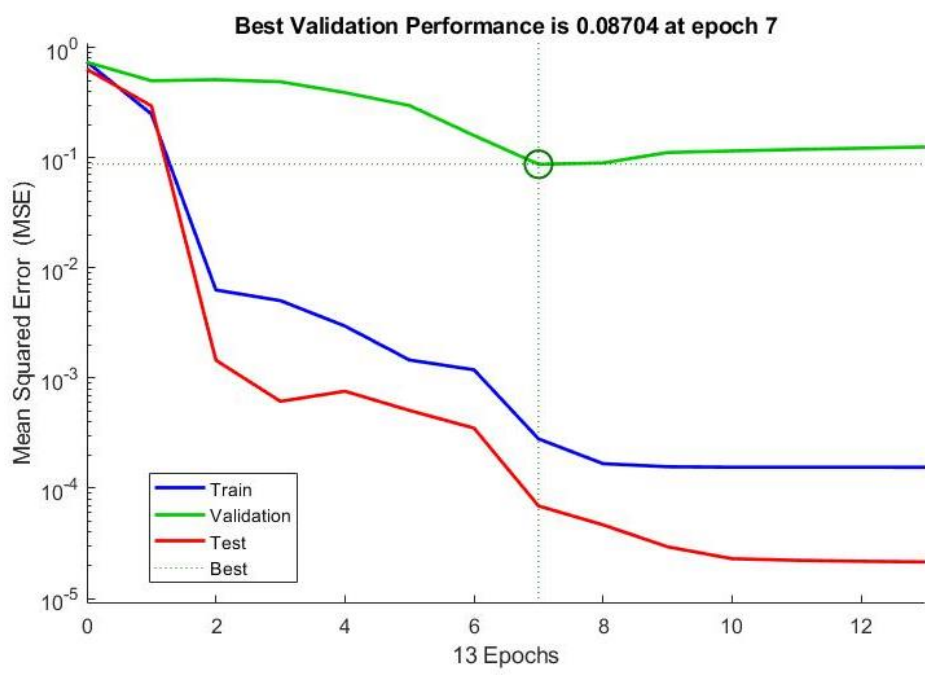


Fig S3 ANFIS architectures prediction error

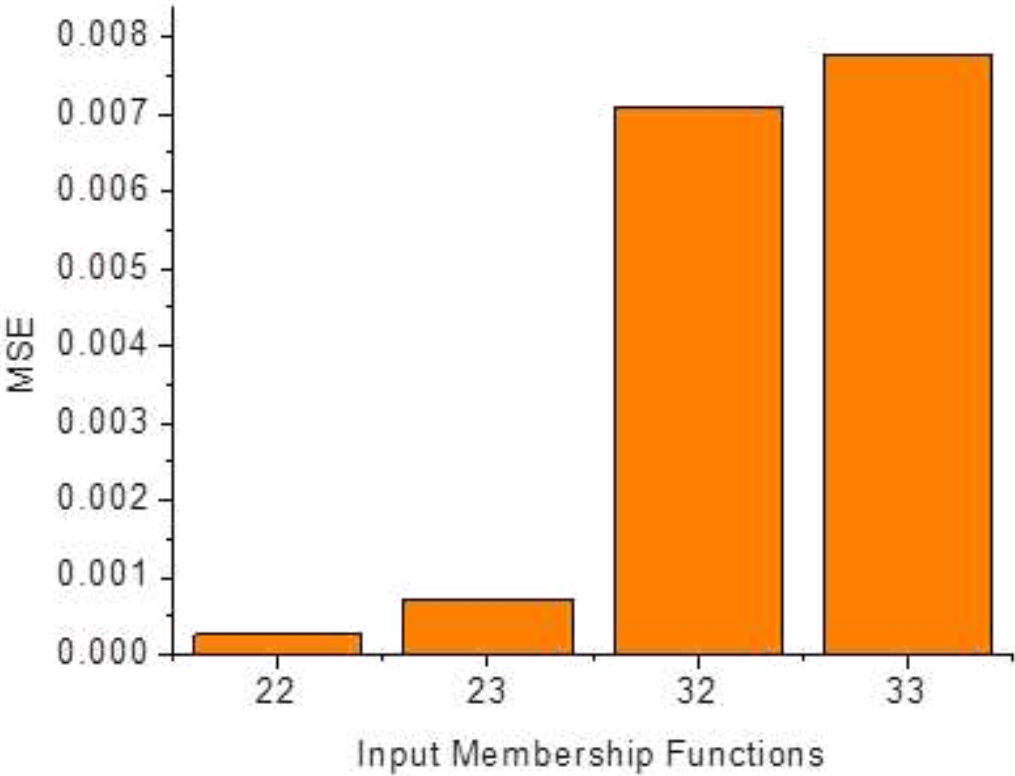
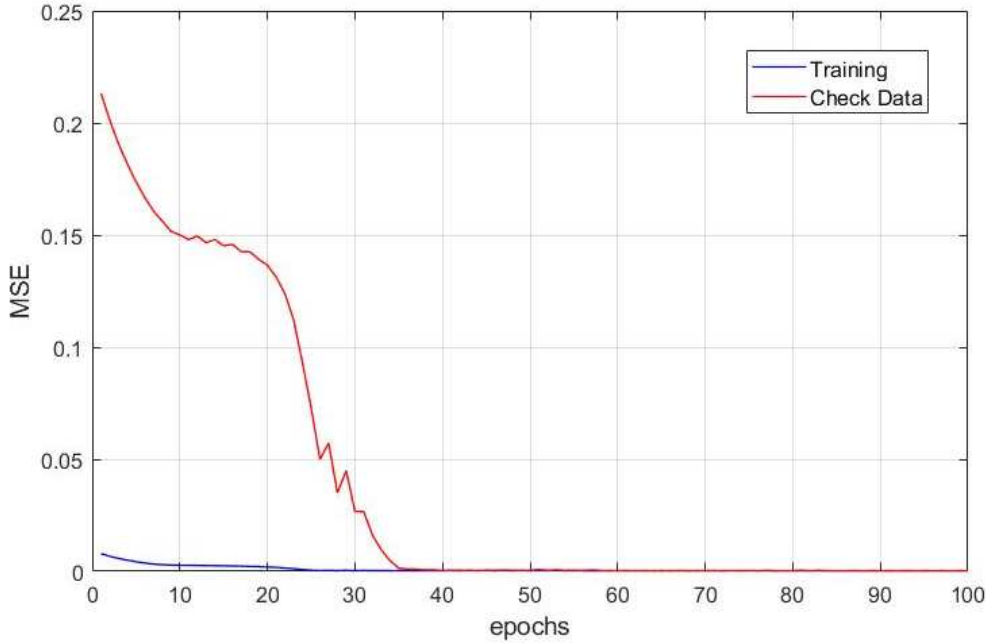


Fig S4 Performance of ANFIS with two membership functions per each input



Supplementary Tables

Table S2 Estimated effects of the complete squared model ($\alpha=0.05$): $R^2 = 0.94555$, $R^2_{adj} = 0.87554$

	Effect	Std.Err.	t	p	-95%	+95%	Coeff.	Std.Err.	-95%	+95%
Mean/Interc.	96.04	5.07	18.95	0.00	84.05	108.03	96.04	5.07	84.05	108.03
A (L)	4.59	4.51	1.02	0.34	-6.07	15.25	2.30	2.25	-3.04	7.63
A (Q)	0.76	4.32	0.17	0.87	-9.47	10.98	0.38	2.16	-4.74	5.49
B (L)	33.39	4.74	7.04	0.00	22.17	44.60	16.69	2.37	11.09	22.30
B (Q)	-19.85	5.29	-3.75	0.01	-32.36	-7.34	-9.93	2.65	-16.18	-3.67
C (L)	29.66	4.74	6.25	0.00	18.44	40.88	14.83	2.37	9.22	20.44
C (Q)	-21.46	5.30	-4.05	0.00	-34.00	-8.93	-10.73	2.65	-17.00	-4.46
A by B	-2.94	6.18	-0.48	0.65	-17.56	11.68	-1.47	3.09	-8.78	5.84
A by C	-4.78	6.18	-0.77	0.46	-19.40	9.84	-2.39	3.09	-9.70	4.92
B by C	-6.82	6.19	-1.10	0.31	-21.46	7.82	-3.41	3.10	-10.73	3.91

Table S3 Variance Analysis (ANOVA) for the complete squared model ($\alpha=0.05$, $F_{tab}=3.68$)

Source of variation	SS	fd	MS	F_{calc}	F_{calc}/F_{tab}
Regression	9318.7	9	1035.4	13.5	3.7
Error	536.6	7	76.7		
Total	9855.4	16			

Table S4 Estimated effects of the reduced model ($\alpha=0.05$): $R^2 = 0.92117$, $R^2_{adj} = 0.89489$

	Effect	Std.Err.	t	p	-95%	+95%	Coeff.	Std.Err.	-95%	+95%
Mean/Interc.	96.58	3.48	27.74	0.00000	89.00	104.17	96.58	3.48	89.00	104.17
B (L)	33.48	4.35	7.69	0.00001	24.00	42.97	16.74	2.18	12.00	21.49
B (Q)	-20.19	4.58	-4.41	0.00085	-30.16	-10.22	-10.09	2.29	-15.08	-5.11
C (L)	29.81	4.36	6.84	0.00002	20.32	39.30	14.91	2.18	10.16	19.65
C (Q)	-21.80	4.59	-4.75	0.00047	-31.80	-11.81	-10.90	2.29	-15.90	-5.90

Table S5 Statistical indices of the machine learning dataset

Parameters	Adsorbent mass (g)	pH	Removal Percentage
Minimum	0.050	1.320	10.448
Maximum	0.900	6.000	99.398
Average	0.502	3.979	85.726
Standard Deviation	0.183	1.206	25.254

APPENDIX A.5

Supplementary Material of the Chapter 7

Fig. A.1. Species from dysprosium nitrate dissolution in aqueous solution for three Dy concentrations (a) 1.0 mmol/L, (b) 3.0 mmol/L; (c) 5.0 mmol/L.

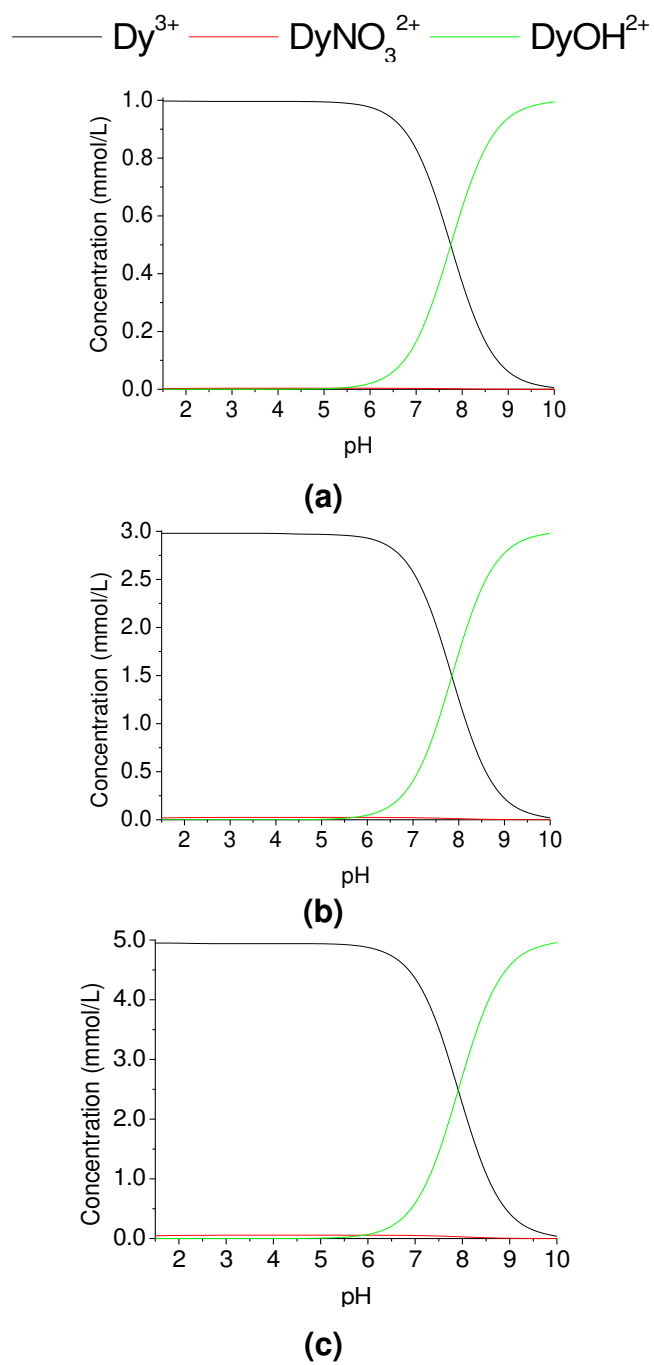


Table A.1. Comparison of the kinetic performance of different adsorbent matrices.

Adsorbent	$*C_{Dy}$ $/C_{ads}$	C_0 (mmol/L)	C_{ads} (g/L)	Stirring (rpm)	t_e (min)	k_2 (g/mmol.min)	q_e (mmol/g)
Hierarchical porous zeolitic imidazolate frameworks nanoparticles	0.05	0.07	0.25	300	420	4.22	0.29
Ion-imprinted macroporous chitosan membrane	0.05	0.3	1	-	240	0.43	0.15
Oxidized carbon materials, graphene oxide, ion imprinted cellulose composite	0.05	0.3	1	100	240	0.13	0.22
	0.01	1.0			40	1.45	0.085
Expanded Vermiculite	0.04	3.0	12.8	200	150	0.19	0.20
	0.06	5.0			180	0.21	0.32

* Ratio of adsorbate/adsorbent concentration, in which C_{Dy} (g/L) = $C_0 \times 10^{-3}$ (mol/L).

162.5(g/mol)

APPENDIX A.6

Supplementary Material of the Chapter 8

Supplementary Methodology*Vermiculite performance in the rare earth adsorption*

In this experiment, the adsorption capacity of the raw and expanded vermiculite was evaluated in the sorption of La, Ce, Nd, Yb, and Dy. The salts used to prepare the rare earth stock solutions were: dysprosium III and ytterbium III nitrates pentahydrate (Aldrich, 99.9%), cerium III nitrate hexahydrate (Neon, 99%), neodymium III, and yttrium III nitrates hexahydrate (Aldrich, 99.9%) and lanthanum III nitrate hexahydrate (Dynamics, 95%).

The adsorption conditions in the batch mode were: the adsorbent dosage of 0.5 g, solution volume of 50 mL, stirring speed of 200 rpm, initial concentration of each metal 3 mmol/L, contact time of 24 h, and pH 4.5 that was maintained adding drops of diluted nitric acid. After the sorption, the adsorbate was separated by filtration using a syringe filter (Chromafil Xtra PES-20/25).

The rare earth metal concentration was determined by spectrophotometry UV- visible (UVmini-1240, Shimadzu) by adding the xylenol orange (0.0045 mol/L) as a complexing agent. The wavelength of maximum absorbance of the xylenol orange was 575 nm. The complex was formed in a volumetric flask (10 mL) by the addition of 2 mL of the metal solution, 3 mL of xylenol orange and filled the volume with a buffer solution of acetic acid/sodium acetate (pH 5.6)[1].

References

- [1] Granados-Correa F, Vilchis-Granados J, Jiménez-Reyes M, Quiroz-Granados LA. Adsorption behaviour of La(III) and Eu(III) ions from aqueous solutions by hydroxyapatite: Kinetic, isotherm, and thermodynamic studies. J Chem 2013;2013. <https://doi.org/10.1155/2013/751696>.

APPENDIX A.7

Supplementary Material of the Chapter 9

Table S.1 Empirical models of breakthrough curves

Models	Equation	Reference
Thomas	$\frac{C}{C_0} = \frac{1}{1 + \exp\left[\frac{k_{Th}}{Q}(q_{Th}m - C_0Qt)\right]} \quad (5)$	1
MDR	$\frac{C}{C_0} = 1 - \frac{1}{1 + \left(\frac{C_0Qt}{q_Y m}\right)^{a_Y}} \quad (6)$	2
Yoon-Nelson	$\frac{C}{C_0} = \frac{1}{1 + \exp(k_{YN}\tau - k_{YN}t)} \quad (7)$	3

Where k_{Th} (L/mmol.min), a_Y , and k_{YN} (1/min) are constants, q_{Th} and q_Y (mmol/g) are bed adsorption capacities at exhaustion. The index $_{Th}$, $_Y$, and $_{YN}$, refers to the models of Thomas, Yan, and Yoon-Nelson, respectively. Moreover, τ (min) is the half-column saturation time according to the Yoon-Nelson model.

Table S.2. Mass transfer models of breakthrough curves

Models	Equation	Reference
ILE	$\frac{\partial C}{\partial t} = D_a \frac{\partial^2 C}{\partial z^2} - u_0 \frac{\partial C}{\partial z} - \frac{\rho_B}{\varepsilon} \left[\frac{\partial}{\partial t} \left(\frac{q_{max} K_L C}{1 + K_L C} \right) \right] \quad (9)$	4
Dual SD	$\frac{\partial C}{\partial t} = D_a \frac{\partial^2 C}{\partial z^2} - u_0 \frac{\partial C}{\partial z} - \frac{\rho_B}{\varepsilon} \left[k_{S1} \left(\alpha \left(\frac{q_{max} K_L C}{1 + K_L C} \right) - q_1 \right) + k_{S2} \left((1 - \alpha) \left(\frac{q_{max} K_L C}{1 + K_L C} \right) - q_2 \right) \right] \quad (10)$	5

Where: q_{max} (mmol/g) and K_L (L/mmol) are the Langmuir's parameters⁶; q_i (mmol/g) and k_{Si} (min^{-1}) are the adsorption capacity, and the mass transfer coefficient of type $i = 1$ or 2 active sites, and α is the impact of the of type-1 sites on the total removed.

References


- (1) Thomas, H. C. Heterogeneous Ion Exchange in a Flowing System. J Am Chem Soc 1944, 66 (10), 1664–1666. <https://doi.org/10.1021/ja01238a017>.






- (2) Yan, G.; Viraraghavan, T.; Chen, M. A New Model for Heavy Metal Removal in a Biosorption Column. *Adsorption Science and Technology* 2001, 19 (1), 25–43. <https://doi.org/10.1260/0263617011493953>.
- (3) Yoon, Y. H.; Nelson, J. H. Application of Gas Adsorption Kinetics I. A Theoretical Model for Respirator Cartridge Service Life. *American Industrial Hygiene Association Journal* 1984, 45 (8), 509–516. <https://doi.org/10.1080/15298668491400197>.
- (4) Georgin, J.; Franco, D.; Drumm, F. C.; Grassi, P.; Netto, M. S.; Allasia, D.; Dotto, G. L. Powdered Biosorbent from the Mandacaru Cactus (*Cereus Jamacaru*) for Discontinuous and Continuous Removal of Basic Fuchsin from Aqueous Solutions. *Powder Technology* 2020, 364, 584–592. <https://doi.org/10.1016/j.powtec.2020.01.064>.
- (5) de Andrade, J. R.; Oliveira, M. F.; Canevesi, R. L. S.; Landers, R.; da Silva, M. G. C.; Vieira, M. G. A. Comparative Adsorption of Diclofenac Sodium and Losartan Potassium in Organophilic Clay-Packed Fixed-Bed: X-Ray Photoelectron Spectroscopy Characterization, Experimental Tests and Theoretical Study on DFT-Based Chemical Descriptors. *Journal of Molecular Liquids* 2020, 312, 113427. <https://doi.org/10.1016/j.molliq.2020.113427>.
- (6) Brião, G. de V.; da Silva, M. G.; Vieira, M. G. A. Expanded Vermiculite as an Alternative Adsorbent for the Dysprosium Recovery. *J Taiwan Inst Chem Eng* 2021, 127, 228–235. <https://doi.org/10.1016/j.jtice.2021.08.022>.

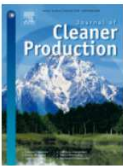
APPENDIX B. LICENCES OF THE PUBLISHED ARTICLES

APPENDIX B.1

Authorizations from Elsevier for the inclusion of the article published in Journal of Cleaner Production in Chapter 2 of this doctoral thesis



 Home
  Help ▾
  Live Chat
  Sign in
  Create Account



Adsorption potential for the concentration and recovery of rare earth metals from NdFeB magnet scrap in the hydrometallurgical route: A review in a circular economy approach

Author: Giani de Vargas Brião, Meuris Gurgel da Silva, Melissa Gurgel Adeodato Vieira

Publication: Journal of Cleaner Production

Publisher: Elsevier

Date: 20 December 2022

© 2022 Elsevier Ltd. All rights reserved.

Journal Author Rights

Please note that, as the author of this Elsevier article, you retain the right to include it in a thesis or dissertation, provided it is not published commercially. Permission is not required, but please ensure that you reference the journal as the original source. For more information on this and on your other retained rights, please visit: <https://www.elsevier.com/about/our-business/policies/copyright#Author-rights>

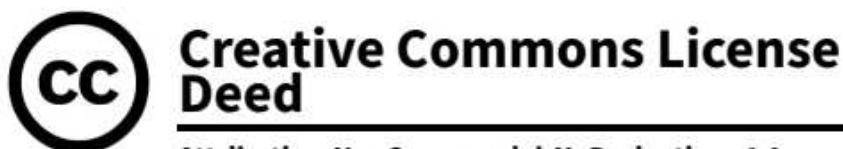
BACK
CLOSE WINDOW

© 2022 Copyright - All Rights Reserved | [Copyright Clearance Center, Inc.](#) | [Privacy statement](#) | [Data Security and Privacy](#)

| [For California Residents](#) | [Terms and Conditions](#) Comments? We would like to hear from you. E-mail us at customer care@copyright.com

APPENDIX B.2

Authorizations from Creative Commons Licence (CC BY-NC-ND 4.0) of the Open Access publication in the Industrial and Engineering Chemistry Research in Chapter 3 of this doctoral thesis.



**Attribution-NonCommercial-NoDerivatives 4.0
International (CC BY-NC-ND 4.0)**

This is a human-readable summary of (and not a substitute for) the [license](#).

You are free to:

Share — copy and redistribute the material in any medium or format

The licensor cannot revoke these freedoms as long as you follow the license terms.

Under the following terms:

Attribution — You must give appropriate credit, provide a link to the license, and indicate if changes were made. You may do so in any reasonable manner, but not in any way that suggests the licensor endorses you or your use.

NonCommercial — You may not use the material for commercial purposes.

NoDerivatives — If you remix, transform, or build upon the material, you may not distribute the modified material.

No additional restrictions — You may not apply legal terms or technological measures that legally restrict others from doing anything the license permits.


Notices:






You do not have to comply with the license for elements of the material in the public domain or where your use is permitted by an applicable exception or limitation.


No warranties are given. The license may not give you all of the permissions necessary for your intended use. For example, other rights such as publicity, privacy, or moral rights may limit how you use the material.

APPENDIX B.3

Authorizations from Elsevier for the inclusion of the article published in Applied Clay Science in Chapter 4 of this doctoral thesis



 Home
  Help
  Email Support
  Sign in
  Create Account



Neodymium recovery from aqueous solution through adsorption/desorption onto expanded vermiculite

Author: Giani de Vargas Brião, Meuris Gurgel Carlos da Silva, Melissa Gurgel Adeodato Vieira
Publication: Applied Clay Science
Publisher: Elsevier
Date: 15 November 2020

© 2020 Elsevier B.V. All rights reserved.

Journal Author Rights


Please note that, as the author of this Elsevier article, you retain the right to include it in a thesis or dissertation, provided it is not published commercially. Permission is not required, but please ensure that you reference the journal as the original source. For more information on this and on your other retained rights, please visit: <https://www.elsevier.com/about/our-business/policies/copyright#Author-rights>






BACK CLOSE WINDOW


© 2022 Copyright - All Rights Reserved | Copyright Clearance Center, Inc. | Privacy statement | Data Security and Privacy
 | For California Residents | Terms and ConditionsComments? We would like to hear from you. E-mail us at customer-care@copyright.com

APPENDIX B.4

Authorizations from Elsevier for the inclusion of the article published in Sustainable Chemistry and Pharmacy in Chapter 5 of this doctoral thesis.



 Home
  Help
  Email Support
  Sign in
  Create Account



Reusable and efficient clay material for the fixed-bed neodymium recovery

Author: Giani de Vargas Brião, Meuris Gurgel Carlos da Silva, Melissa Gurgel Adeodato Vieira
Publication: Sustainable Chemistry and Pharmacy
Publisher: Elsevier
Date: April 2022

© 2022 Elsevier B.V. All rights reserved.

Journal Author Rights

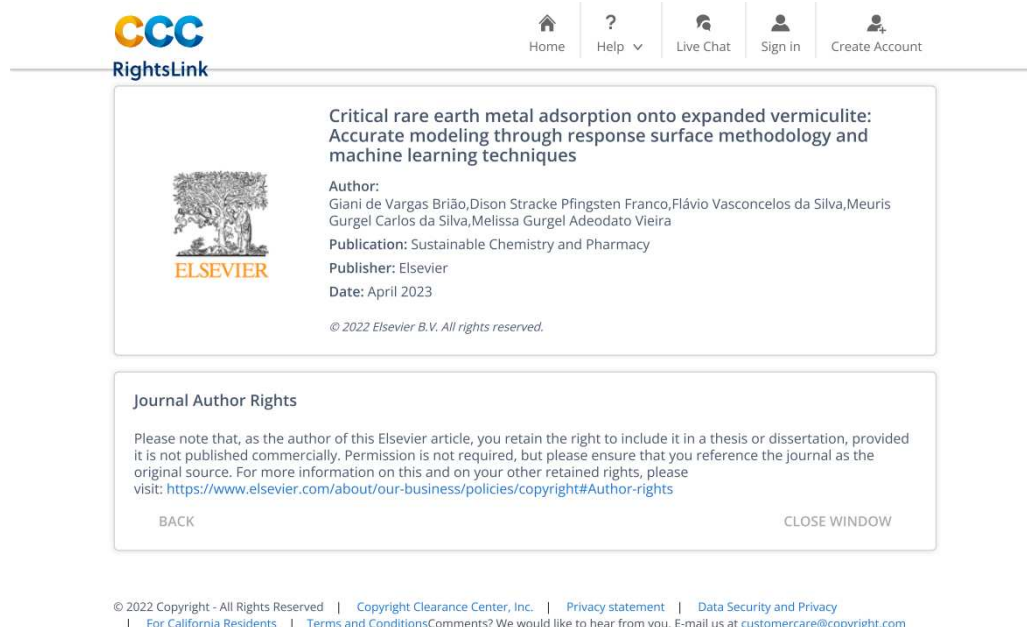
Please note that, as the author of this Elsevier article, you retain the right to include it in a thesis or dissertation, provided it is not published commercially. Permission is not required, but please ensure that you reference the journal as the original source. For more information on this and on your other retained rights, please visit: <https://www.elsevier.com/about/our-business/policies/copyright#Author-rights>

BACK CLOSE WINDOW

© 2022 Copyright - All Rights Reserved | Copyright Clearance Center, Inc. | Privacy statement | Data Security and Privacy
 | For California Residents | Terms and ConditionsComments? We would like to hear from you. E-mail us at customer-care@copyright.com

APPENDIX B.5

Authorizations from Elsevier for the inclusion of the article published in Sustainable Chemistry and Pharmacy in Chapter 6 of this doctoral thesis.



The screenshot shows the CCC RightsLink interface. At the top, there is a navigation bar with icons for Home, Help, Live Chat, Sign in, and Create Account. The main content area displays the article title "Critical rare earth metal adsorption onto expanded vermiculite: Accurate modeling through response surface methodology and machine learning techniques" with the Elsevier logo. Below the title, the author information is listed: "Author: Giani de Vargas Brião, Dison Stracke Pflingsten Franco, Flávio Vasconcelos da Silva, Meuris Gurgel Carlos da Silva, Melissa Gurgel Adeodato Vieira". The publication details are "Publication: Sustainable Chemistry and Pharmacy" and "Publisher: Elsevier". The date is "Date: April 2023". A copyright notice at the bottom states "© 2022 Elsevier B.V. All rights reserved.".

Journal Author Rights

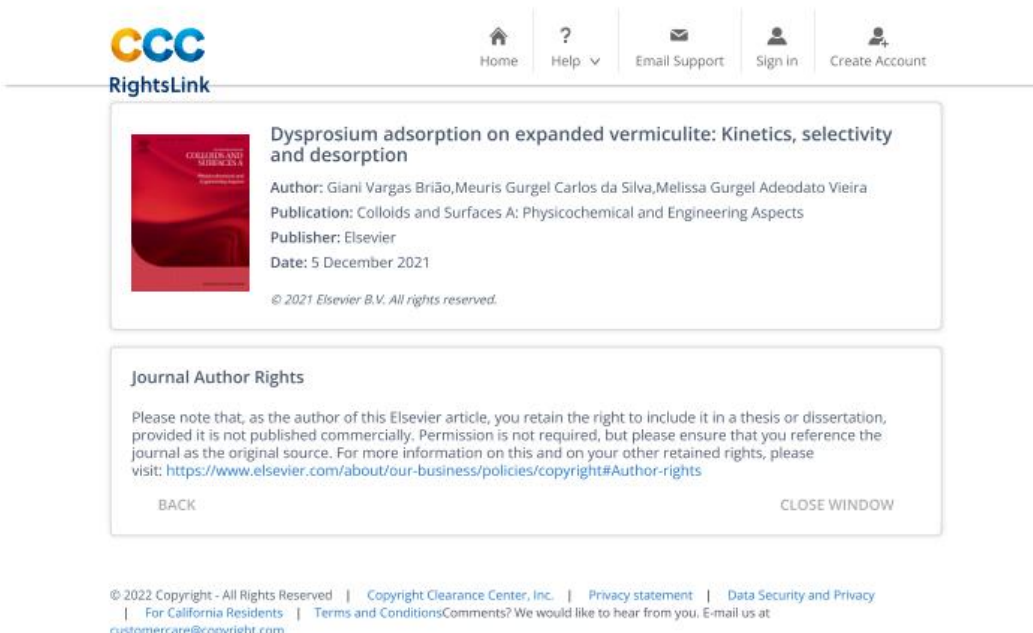
Please note that, as the author of this Elsevier article, you retain the right to include it in a thesis or dissertation, provided it is not published commercially. Permission is not required, but please ensure that you reference the journal as the original source. For more information on this and on your other retained rights, please visit: <https://www.elsevier.com/about/our-business/policies/copyright#Author-rights>

BACK CLOSE WINDOW

© 2022 Copyright - All Rights Reserved | Copyright Clearance Center, Inc. | Privacy statement | Data Security and Privacy
| For California Residents | Terms and Conditions Comments? We would like to hear from you. E-mail us at customer-care@copyright.com

APPENDIX B.6

Authorizations from Elsevier for the inclusion of the article published in Colloids and Surfaces A: Physicochemical and Engineering Aspects in Chapter 7 of this doctoral thesis.



The screenshot shows the CCC RightsLink interface. At the top, there is a navigation bar with icons for Home, Help, Email Support, Sign in, and Create Account. The main content area displays the article title "Dysprosium adsorption on expanded vermiculite: Kinetics, selectivity and desorption" with the Elsevier logo. Below the title, the author information is listed: "Author: Giani Vargas Brião, Meuris Gurgel Carlos da Silva, Melissa Gurgel Adeodato Vieira". The publication details are "Publication: Colloids and Surfaces A: Physicochemical and Engineering Aspects" and "Publisher: Elsevier". The date is "Date: 5 December 2021". A copyright notice at the bottom states "© 2021 Elsevier B.V. All rights reserved.".

Journal Author Rights


Please note that, as the author of this Elsevier article, you retain the right to include it in a thesis or dissertation, provided it is not published commercially. Permission is not required, but please ensure that you reference the journal as the original source. For more information on this and on your other retained rights, please visit: <https://www.elsevier.com/about/our-business/policies/copyright#Author-rights>

BACK CLOSE WINDOW

© 2022 Copyright - All Rights Reserved | Copyright Clearance Center, Inc. | Privacy statement | Data Security and Privacy
| For California Residents | Terms and Conditions Comments? We would like to hear from you. E-mail us at customer-care@copyright.com

APPENDIX B.7

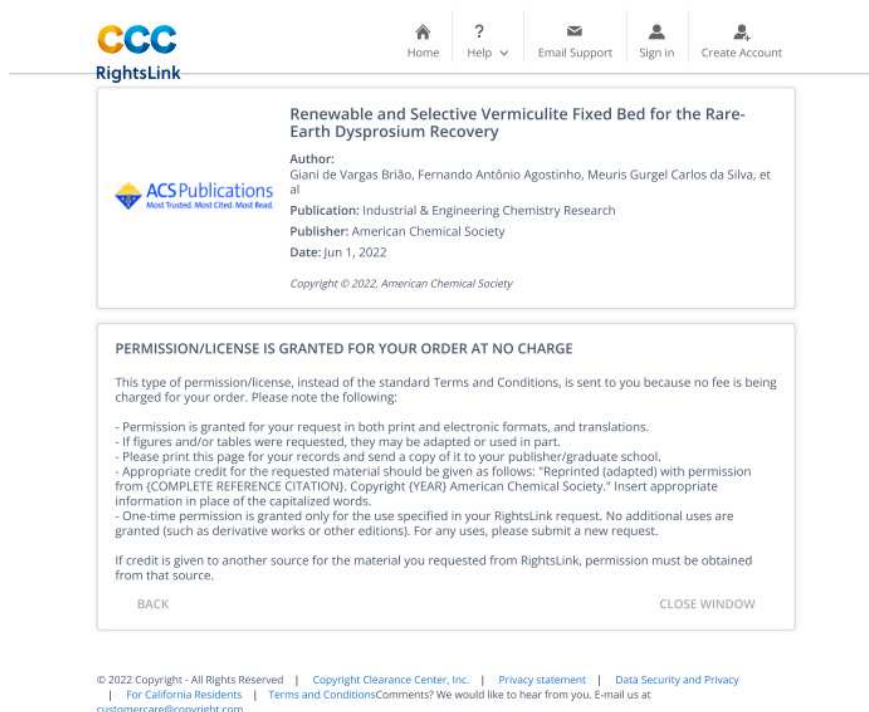
Authorizations from Elsevier for the inclusion of the article published in Journal of the Taiwan Institute of Chemical Engineers in Chapter 8 of this doctoral thesis.



The screenshot shows the CCC RightsLink website. The top navigation bar includes links for Home, Help, Email Support, Sign in, and Create Account. The main content area displays the title "Expanded vermiculite as an alternative adsorbent for the dysprosium recovery" by Giani de Vargas Brião, Meuris Gurgel da Silva, and Melissa Gurgel Adeodato Vieira. The publication is identified as "Journal of the Taiwan Institute of Chemical Engineers" from Elsevier, dated October 2021. Below this, a "Journal Author Rights" section explains that authors retain the right to include the article in a thesis or dissertation, provided it is not published commercially. It includes a link to Elsevier's copyright policy and buttons for "BACK" and "CLOSE WINDOW". At the bottom, there is a footer with copyright information and contact details for the Copyright Clearance Center.

APPENDIX B.8

Authorizations from American Chemical Society for the inclusion of the article published in Industrial and Engineering Chemistry Research in Chapter 9 of this doctoral thesis.



The screenshot shows the CCC RightsLink website. The top navigation bar is identical to the previous one. The main content area displays the title "Renewable and Selective Vermiculite Fixed Bed for the Rare-Earth Dysprosium Recovery" by Giani de Vargas Brião, Fernando Antônio Agostinho, Meuris Gurgel Carlos da Silva, et al. The publication is "Industrial & Engineering Chemistry Research" from the American Chemical Society, dated June 1, 2022. Below this, a "PERMISSION/LICENSE IS GRANTED FOR YOUR ORDER AT NO CHARGE" section provides detailed terms of the permission, including that it covers print and electronic formats, allows for adaptation, and requires appropriate credit. It also states that no additional fees are charged. At the bottom, there are "BACK" and "CLOSE WINDOW" buttons. The footer contains the same copyright and contact information as the previous screenshot.